INEEL/EXT-02-01210

# *Environmental Systems Research FY 2000 Annual Report*

*David L. Miller, Program Manager*
*Peter M. Castle, Deputy Program Manager*
*Robert W. Smith, Deputy Program Manager*

*January 2001*

*Idaho National Engineering and Environmental Laboratory*
*Bechtel BWXT Idaho, LLC*

INEEL/EXT-02-01210

# Environmental Systems Research
# FY 2000 Annual Report

David L. Miller, Program Manager
Peter M. Castle, Deputy Program Manager
Robert W. Smith, Deputy Program Manager

January 2001

Idaho National Engineering and Environmental Laboratory

Idaho Falls, Idaho 83415

Prepared for the
U.S. Department of Energy
Office Of Environmental Management
Under DOE Idaho Operations Office
Contract DE-AC07-99ID13727

# ABSTRACT

The Environmental Systems Research (ESR) Program, a part of the Environmental Systems Research and Analysis (ESRA) Program, was implemented to enhance and augment the technical capabilities of the INEEL. Strengthening the technical capabilities of the INEEL will provide the technical base to serve effectively as the Environmental Management Laboratory for the Office of Environmental Management (EM).

This is a progress report for the third year of the ESR Program (FY 2000). A report of activities is presented for the five ESR research investment areas: (1) Transport Aspects of Selective Mass Transport Agents, (2) Chemistry of Environmental Surfaces, (3) Materials Dynamics, (4) Characterization Science, and (5) Computational Simulation of Mechanical and Chemical Systems. In addition to the five technical areas, the report describes activities in the Science and Technology Foundations element of the program, e.g., interfaces between ESR and the EM Science Program (EMSP) and the EM Focus Areas.

The five research areas are subdivided into 18 research projects. FY 2000 research in these 18 projects has resulted in more than 50 technical papers that are in print, in press, in review, or in preparation. Additionally, more than 100 presentations were made at professional society meetings nationally and internationally. Work supported by this program was in part responsible for one of our researchers, Dr. Mason Harrup, receiving the Department of Energy's "Bright Light" and "Energy at 23" awards.

Significant accomplishments were achieved. Non-Destructive Assay hardware and software was deployed at the INEEL, enhancing the quality and efficiency of TRU waste characterization for shipment. The advanced tensiometer has been employed at numerous sites around the complex to determine hydrologic gradients in variably saturated vadose zones. An ion trap, secondary ion mass spectrometer (IT-SIMS) was designed and fabricated to deploy at the INEEL site to measure the chemical speciation of radionuclides and toxic metals on the surfaces of environmentally significant minerals.

The FY 2001 program will have a significantly different structure and research content. This report presents the final summary of projects coming to an end in FY 2000 and is a bridge to the FY 2001 program.

# CONTENTS

# ENVIRONMENTAL SYSTEMS RESEARCH
# FY 2000 ANNUAL REPORT

## INTRODUCTION

Welcome to the Fiscal Year 2000 annual report of the Environmental Systems Research (ESR) program. The ESR program, initiated in mid-FY 1998, focuses on science and engineering research that addresses EM's technical needs. The ESR program takes a forward-looking view of EM's mission and performs the groundwork to establish the technical foundations that will support both current and anticipated technical issues in disposition, remediation, and waste management. The ESR program is structured to perform two types of research activities. The first is core research, which is basic in tone and focuses on understanding environmental processes, developing new tools, and collecting data. The second type of research is problem-driven and thus is more applied in nature. The composition of research within the ESR program is structured to achieve balance and interaction between the two areas.

The ESR program is organized around five main research areas (see Figure 1, top tier, all but the left box). These five areas are strengthening the INEEL's ability to address EM's technical issues. Each of the five areas is reducing technical uncertainty.

The ESR research portfolio has a three-year planning cycle to accommodate anticipated reanalysis and restructuring (as necessary) of the portfolio content. FY 2000 was the third year of the cycle. Increased emphasis on subsurface science at the INEEL has accelerated the need to restructure the ESR portfolio for FY 2001. Instead of five main research areas, the program will have two main areas with supporting tasks: Subsurface Science and Waste Management Science.

FY 2000 was another productive year. Research projects initiated in mid-FY 1998 continued to make solid technical progress. New staff focused their research expertise to environmental problems, adding to the skill mix of EM's multiprogram national environmental laboratory. Capabilities in computational modeling and tools for studying contaminant surface interactions expanded. In FY 2000, the program added tools to support exploration of fission processes that may lead to new methods for nondestructive assay and subsurface characterization. The Science and Technology Integration activity, in conjunction with the ESR Candidates (ESRC) program, arranged for an external panel review of proposed research projects for the FY 200I ESR portfolio. The peer reviews were positive and offered constructive suggestions, which have been incorporated into program planning for FY 2001.

ESR program research has resulted in more than 50 technical papers in print, in press, in review, or in preparation for FY 2000. Additionally, more than 100 presentations were made at professional society meetings. ESR program participants have also been proactive in working with the Waste Management and Spent Nuclear Fuels programs at the INEEL to understand particular programmatic science needs.

The relationship with the Subsurface Contaminant Focus Area begun in FY 1999 to identify high-priority EMSP projects that might be carried forward through the ESR program in FY 2000 and later years has been maintained. As a result, the ESRC provided continuation funding for one of the EMSP projects, with the purpose of demonstrating a subsurface remediation technique at the INEEL.

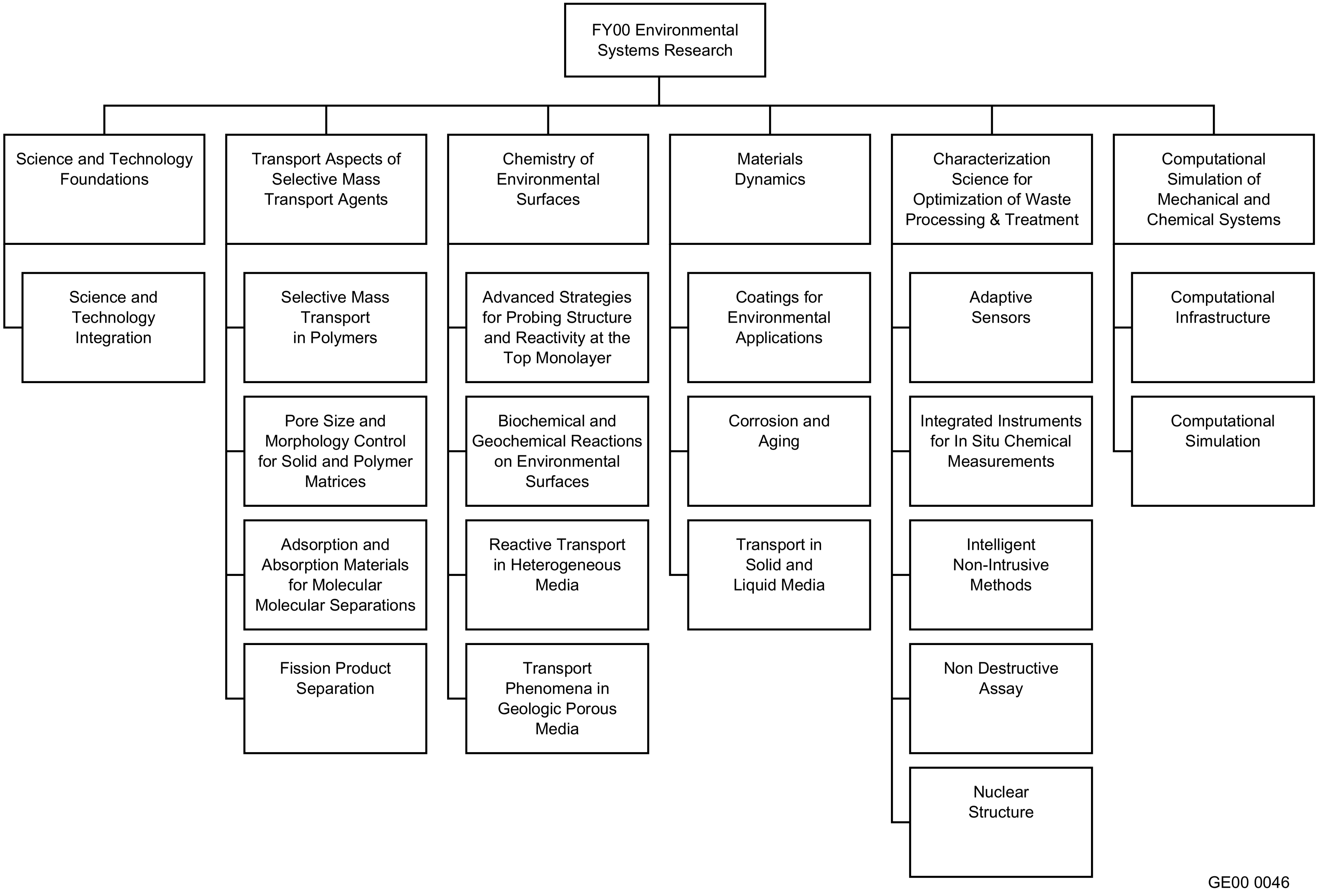

Figure 1. Environmental Systems Research Program.

# Chemistry of Environmental Surfaces

### Gary S. Groenewold, Research Area Leader

Processes that control fate and transport of radionuclides in the subsurface environment are dictated by structure and reactivity considerations on mineral surfaces and by the movement of water. Radionuclide speciation on mineral surfaces is a highly complex topic. It is influenced by a wide range of complexing chemicals that originate from endogenous geochemistry, microbial biochemistry, and industrial waste disposal. Any one of these influences has significant chemical complexity and will affect radionuclide sequestration on mineral surfaces or mobilization through solubility. Compounding this complexity is the movement of water through the subsurface, which is variably saturated in the vadose zone. Water movement through the vadose zone will be irregular as a result of subsurface inhomogeneity and variable saturation. On the basis of these considerations, several salient factors were identified for further investigation:

- Chemical speciation and reactivity on mineral surfaces
- The influence of microbial populations on chemical speciation
- Soil moisture and its movement in the subsurface
- Correlation of chemical speciation and microbial activity to radionuclide adsorption or solubilization.

## Description of Research Activities

In addressing these factors, the Chemistry of Environmental Surfaces research area included five research projects, which are described in detail in the following chapters and overviewed below.

A major problem encountered in characterizing chemical speciation and reactivity on mineralogical surfaces is insufficient sensitivity and specificity using current instrumental strategies. Consequently, we emphasized development of analytical instrumentation and approaches for high-performance characterization of radionuclide surface speciation. The research focused on surface mass spectrometric techniques (laser desorption [LD] and secondary ion mass spectrometry [SIMS]) because they conceptually have the required specificity and sensitivity. A unique LD-Fourier transform mass spectrometer (LD-FTMS) was designed and fabricated that is capable of generating spatially resolved, high-mass, high-resolution, high-accuracy mass spectral information. In addition, a prototype ion trap SIMS was designed and fabricated. This instrument complements the LD-FTMS in that it is a small device capable of operation in radiological environments and uses a bombarding projectile that extracts information only from the top monolayer of the mineral sample. The instrument is also capable of detecting complex and fragile surface species.

These analytical tool development activities were highly successful. The LD-FTMS was demonstrated for high spatial resolution and high mass resolution and is now ready for characterization of heterogeneous contaminated mineralogical systems. The IT-SIMS was demonstrated capable of molecular characterization of mineral surfaces through sputter desorption and analysis of complex surface-derived molecular ions. In addition, the IT-SIMS was used to assess intrinsic reactivity of the surface-derived ions. The possibility arises that mineral oxide moieties could be used as models for reactive sites on mineral surfaces, and reaction pathways and kinetics could be easily determined. The IT-SIMS was applied to characterizing contaminated samples fabricated using clay from the INEEL's Radioactive Waste Management Complex. By performing parallel characterizations using SIMS, the efficacy of sequential extraction for establishing radionuclide speciation was assessed. Effective cesium and uranium speciation was demonstrated based on the SIMS spectra.

The influence of microbial populations on radionuclide adsorption cannot be overemphasized, and we initiated work to identify and to characterize extracellular compounds produced by the iron reducing bacterium *Shewanella putrefaciens*. We found that the microbe selectively seeks iron oxide surfaces under anaerobic conditions, and produces both surface-adhering, and nonadhering strains. The research resulted in the application of a technique using fluorescent probes with excitation via attenuated total reflectance to probe mineral-bacteria interfacial zones, thus providing an invaluable complement to the mass spectrometry approaches pursued in companion projects. Surface complexation in a citrate-uranyl-goethite system was identified (citrate serving as an exudate simulant). This research enabled statistical evaluation of the mass action expression for multidentate surface complexation, which represents an initial step toward a predictive capability regarding the influence of microbial factors in the subsurface.

While the study of isolated species provides highly desirable mechanistic detail, transport or sequestration in the subsurface is in fact influenced by heterogeneous microbe populations that act in an aggregate fashion. This motivated two tasks that investigated the influence of spatial and temporal variations in ecological niches on bacterial community structure-function. In these multicomponent systems, a distribution of microbial metabolisms resulted, that in turn influenced the persistence and mobility of contaminants in both the ground water and the vadose zone. Since the distribution of microbes and contaminant chemicals is influenced by flow and transport of water, a companion study focused on the controlling factors that determine the distribution of soil water in the deep vadose zone as measured by soil water potential.

Clearly, the transport of mineral particulate resulting from water movement in the subsurface represents a factor with potential for moving radionuclides. This possibility has motivated examination of infiltration between alluvial sediment overlying a fractured basalt rock. We developed these examinations in cooperation with the University of Idaho and conducted them at three field sites. The first site was developed on DOE-controlled land at the Jefferson Canal site near Mud Lake. The second site was the IRC 5-well site, which is on DOE-controlled land. This site originally was used to evaluate the INEEL Advanced Tensiometers in fractured basalt. The third site, developed during FY 2000 under land controlled by the University of Idaho, is the University Place Dune Site in Idaho Falls. This site is similar to the IRC 5-well site, except the porous media overlying the basalt is eolian rather than alluvial. We developed a formal strategic alliance with the University of Idaho to devise a framework for collaborative field-oriented vadose zone research. In addition, Dr. Jim Yeh of the University of Arizona and Dr. Gary Pope of the University of Texas made extended INEEL visits.

We have enhanced computational capabilities to simulate complex, nonlinear systems for vadose zone transport. The application of a B-spline collocation method to the solution of differential equations, including sets of coupled, nonlinear partial differential has been shown feasible. We generated a B-spline code that solves the coupled fluid dynamics equations for two-dimensional flow in a channel, including multiple solution algorithms. The unoptimized code has found reasonable solutions in times about half as long as those for the optimized commercial finite element code Fidap.

Finally, we applied INEEL expertise to DOE operational problems. A new version of the advanced tensiometer using cone penetrometer push technology was demonstrated at the Test Buried Waste Facility at Hanford. The standard version of the vadose zone monitoring system was installed at the Savanna River Site. Although Environmental Systems Research Program activities directly support environmental management research needs of the DOE, reaching these goals will have implications beyond the INEEL and DOE. For example, the modeling framework and expertise developed in this project will be transferable to private industries concerned with vadose zone contamination. In addition, many economic activities such as solution mining and farming can benefit from the ability to better simulate biogeochemical processes occurring in the vadose zone.

This research area is enabling the INEEL to make significant progress in understanding radionuclide fate and transport in the subsurface. The ability to understand geochemical and biochemical speciation on mineral surfaces overcomes a substantial hurdle, but new characterization approaches offer the possibility of facile speciation determinations, even for complex, microbially derived complexing species. On an intermediate scale, approaches for characterizing microbial populations adsorbed to mineral surfaces have emerged, and this has enabled correlation with population function relative to metal immobilization. At the field scale, the ability to routinely assess water potential enables gradients to be established, which, ideally, should allow chemical and microbial inhomogeneity to be correlated with water and radionuclide movement.

# Advanced Strategies for Probing Structure and Reactivity at the Top Monolayer

**Gary S. Groenewold, Jill R. Scott, Brittany D. Hodges,**
**Paul R. Tremblay, Anita K. Gianotto**

## SUMMARY

The Advanced Strategies project was initiated to develop instrumentation and methodology for characterizing speciation on real-world surfaces. Motivation for the project is the fact that processes controlling fate and transport of radionuclides are dictated by structure and reactivity of radionuclides on mineral surfaces. The problem is that characterizing structure and reactivity is difficult using current instrumental strategies. This project emphasizes development of instrumentation and analytical approaches for high-performance characterization of radionuclide surface speciation. The project focused on surface mass spectrometric techniques [laser desorption (LD) and secondary ion mass spectrometry (SIMS)] because they conceptually have the required specificity and sensitivity. A unique LD-Fourier transform mass spectrometer (LD-FTMS) was designed and fabricated that is capable of generating spatially resolved, high-mass, high-resolution, high-accuracy mass spectral information. It is also capable of state-of-the-art ion-molecule reactivity investigations. In addition to the LD-FTMS, an ion trap (IT)-SIMS was employed to investigate generation of ions from mineral surfaces and to characterize their intrinsic reactivity. This research produced desorption and reaction information essential to (a) understanding ion behavior in trapped ion mass spectrometry instruments, (b) relating gas-phase phenomena to surface phenomena, and (c) designing effective characterization strategies. This research has resulted in new, more effective approaches for characterizing contaminated oxide surfaces.

## PROJECT DESCRIPTION

### Background and Motivation

Interfacial interactions dictate sequestration or transport of radionuclides and heavy metals in the environment.[1-5] Sequestration can occur by strong ion exchange, intercalation, surface precipitation, or chelation by an immobile organic. Transport, on the other hand, can occur by solubilization, either as a free cation or as a soluble complex. Transport can also be facilitated by adsorption to colloidal matter. Both transport and sequestration are critical outcomes that heavily depend on interfacial interactions, and understanding the macroscopic processes depends on understanding the interface.[6] The problem is that elucidation of interfacial interactions is difficult, because

- Contaminant concentrations on the surface are low
- Surfaces are morphologically and chemically heterogeneous, with multiple neutral and counter ion moieties possible
- Characterization of the microbial surface chemistry is nearly impossible at the molecular level because the organic complexants are too complicated to be deduced with any facility
- Chemical speciation is heterogeneous; oxidation state, oxide form, and hydration are highly variable
- Relative reactivity of multiple contaminants and multiple adsorption moieties are unknown.

Analytical technology has not yet caught up with the challenges posed by these contaminated environmental surfaces. Certainly, infrared and Raman spectroscopies have evolved to a remarkable level of sophistication and offer excellent vibrational information that is directly related to contaminant speciation on the top monolayer of the environmental surfaces.[7-10] They are routinely applied, but they lack sensitivity to characterize contaminants present at low concentrations on surfaces. On the one hand, fluorescence is capable of excellent sensitivity but lacks specificity.[11] X-ray absorption spectroscopy techniques such as EXAFS and XANES, on the other hand, have been applied with remarkable success and are capable of explicitly identifying bonding between adsorptive moieties and contaminants,[12-15] but they sample beyond the top monolayer, and results can be confused by highly heterogeneous samples.

Recognizing these shortcomings in surface characterization, we have endeavored to investigate advanced strategies for probing structure and reactivity at the top monolayer. We have chosen to overcome limitations associated with heterogeneity, complexity, and sensitivity by researching surface mass spectrometry approaches, specifically laser desorption-Fourier transform mass spectrometry (LD-FTMS) and ion trap secondary ion mass spectrometry (IT-SIMS). The motivation behind the choice of these techniques is several-fold:

1. Analytical methods are needed that are more sensitive than the current generation of instrumental approaches, and mass spectrometry is unparalleled for surface sensitivity.
2. A strong need exists to be able to distinguish chemical species (as opposed to elemental detection), and high-performance mass spectrometry approaches have the capability to identify species in chemically complex environments. Specific attributes of mass spectrometry applicable to this problem are
   a. Mass measurement at high resolution and high accuracy for assignment of elemental composition. The adsorbate realm is one monolayer thick, which is beyond the detection limits of most analytical techniques.
   b. “Soft” surface desorption techniques capable of generating gas phase species intact from the surface, without chemically altering the surface.
   c. The capability for ion-molecule reactions that enable characterization of desorbed species in terms of condensation, charge exchange, and fragmentation. This is particularly appealing because of the contaminant surface chemistry, which is highly variable in terms of coadsorbates (most significantly water), and multiple contaminants.

Advances in the field of mass spectrometry over the past 20 years have resulted in instrumental approaches that are capable of high sensitivity and speciation determinations of both inorganic and organic chemicals in complex matrices. What has not been established is whether a mass spectrometric approach can be applied to characterizing inorganic systems localized on the top-most layer of a heterogeneous, contaminated environmental sample. Certainly, developments in the use of polyatomic projectile bombardment and in laser desorption suggest that this is possible. We pursued both of these surface interrogation methods over the course of this research.

INEEL and Texas A&M researchers have demonstrated polyatomic projectiles to be capable of desorbing species intact from the surface into the gas-phase environment of a mass spectrometer. Using $ReO_4^-$ as a projectile, the INEEL group showed that nitrate/nitrite salts can be differentiated[16-17] and that mercury amine complexes can be identified using SIMS. The Texas A&M group was able to differentiate nitrate/nitrite and tetrafluoroborate salts using $Cs(CsI)_n^+$ clusters.[18-19] These and other results suggested that the primary advantage of the polyatomic projectile for surface bombardment was that surface penetration was minimal, and that the majority of the energy is deposited on the top-most monolayers of solid samples. The result was that the secondary ion mass spectra were dominated by surface species, not by the underlying matrix, which suggested that surface speciation could be derived using a polyatomic projectile for surface interrogation.

Similarly, laser desorption is a second surface interrogation approach that had demonstrated capability for producing accurate surface speciation information.[20] Zenobi's group performed surface speciation investigations on environmental particles,[21-22] which are closely related to the sample matrix expected when characterizing environmental and waste samples from the INEEL and other DOE sites. Laser desorption offers potential for a wider range of control in surface interrogation. Variable irradiation wavelength has the potential for ionization selectivity. Variable laser power can be used to vary the character of the analysis from elemental (high-power) to molecular (low-power). Using a high level of optical focusing, the instrument is inherently capable of spatially resolved data acquisition,[23-24] which could overcome spatial variability ubiquitous to environmental samples.

In addition to investigating two surface interrogation approaches, the research evaluated two types of trapped ion mass spectrometers for developing advanced surface speciation strategies: the quadrupole ion trap (also known as *ion trap*) and the Fourier transform mass spectrometer. The advantages of the ion trap are that it is capable of selectively storing ions in preset mass ranges, accumulating ions during long periods of sample irradiation, and performing fragmentation and condensation reactions subsequent to ion storage and accumulation.[25] These latter capabilities offer the possibility for ion identification on the basis of chemical reactivity, and thus offer the possibility for not only species identification but also assessment of the intrinsic reactivity of the ions. The ability to produce multiple levels of information will be critical for identifying the chemistry of complex, contaminated, environmental media.

One other attribute of the ion trap compels comment. The instrument operates using a thermal He bath gas at pressures up to 0.1 millitorr. A consequence of this operating characteristic is that ions that are sputtered into the gas phase with excess internal energy will be *cooled* through collisions with the thermal He.[26] Energy will be transferred from the internal modes of secondary molecular ions energized by the sputtering event to the He atoms in the bath gas. The result of this is that the production of molecular secondary ions is significantly augmented compared to instruments that operate at lower pressures.

The second type of mass spectrometer employed in the research was a Fourier transform instrument (FTMS) capable of high mass resolution, accurate mass measurement sufficient to enable assignment of elemental composition. This is critical for identifying isobaric ions such as *m/z* 137, observed in the spectra of clays. In this example, $Al_2O_5H_3^-$, $AlSiO_5H_2^-$, and $Si_2O_5H^-$ are all possible elemental compositions, and a resolving power ($m/\Delta m$) of 11,000 is required to separate these ions on the basis of mass. The FTMS is easily capable of performing this type of analysis, with achievable resolution beyond $1 \times 10^6$. In addition, the mass range of the FTMS is in excess of *m/z* 10,000, which offers hope for solving problems that will be encountered in characterizing environmental and waste samples, namely, identifying metals complexed with high molecular weight ligands. These ligands could have anthropomorphic, microbial, or vegetative origins, and to date have defied identification in almost all cases.

The FTMS also offers the possibility of ion identification through ion reactivity studies. Ion fragmentation (MS/MS or $MS^2$) enables complex ions to be *taken apart*, which can be a great aid in identifying composition and structure. Ion condensation reactions can also be performed in the FTMS, which augment ion identification and also shed light on species reactivity. This type of study benefits from the low absolute pressure used by the FTMS, and by the fact that ions can be stored for very long times in the instrument, which enables the study of slow reactions.

The present program has pursued development of these two types of surface mass spectrometry instrumentation because the LD-FTMS and the IT-SIMS are complementary in their implementation and, to some extent, their application. The LD-FTMS is a highly complex system, capable of ultra-high vacuum, a superconducting magnet, and high-precision laser optics; as such, it is suited only to an instrument laboratory setting. In contrast, the IT-SIMS is small, more robust, and suited to operate in nonstandard settings such as a radiological laboratory. Hence, the program consists of two parallel thrusts (see Figure 1).

- Task. 1. Design, fabricate, test, and evaluate a state-of-the-art LD-FTMS instrument for surface characterization.
- Task 2. Evaluate an IT-SIMS for surface characterization.

We expect that instrumentation will be developed capable of providing surface characterization support for environmental management and long-term stewardship of INEEL resources. This instrumentation will be capable of new levels of surface speciation, sensitivity, and reactivity measurements heretofore not available in environmental characterization endeavors. In the following tasks, we describe the design, fabrication, and testing of the LD-FTMS (Task 1), and use of the IT-SIMS for metal ion species generation, characterization, and reactivity studies (Task 2). The results of these studies clearly show that these instruments have a vast potential for sample characterization, species identification, and reactivity for complex, contaminated environmental samples.

## Task 1. LD-FTMS Research and Development

The inherent advantages of a LD-FTMS analysis approach motivated procurement of components for fabricating an instrument beginning in mid-1998. This included a 7-tesla superconducting magnet, a vacuum housing, lasers and associated optics, and instrument control and data acquisition software/hardware. The components were assembled into an integrated system during the latter half of FY 1998 and throughout FY 1999. At the end of this period, the instrument was demonstrated to be capable of generating, trapping, mass measuring, and detecting ions from metallic surfaces, thereby providing the laboratory with a research-grade mass spectrometer capable of high-performance surface interrogation capability. However, results from the IT-SIMS research task (see below) revealed the desirability of generating spatially resolved mass spectra and enhanced ion-molecule reaction chemistry.

A significant portion of the scope for FY 2000 (subtask 1a) focused on adding capability to generate spatially resolved mass spectra. This represented a major technological challenge, but once solved, resulted in an instrument capable of generating spectra from a variety of locations, without the need to move the target. This is highly desirable because most real-world sample surfaces are highly heterogeneous, with changeable chemistry across small (μm-size) areas.

The remainder of the scope for the program was devoted to enhancing capabilities for manipulating ions in the trap, for the purpose of improving mass measurement and also for performing ion molecule reactions. The principal emphasis in this research (subtask 1b) was to develop nondestructive ion detection. This accomplishment is highly significant because it enables repeated mass measurement (remeasurement) of the same ion packet. Remeasurement resulted in increased signal-to-noise, which was manifested in improved mass measurement accuracy. Significantly, remeasurement also enables study of reaction kinetics of the same batch of ions, *i.e.*, those produced from a single LD event. This feature is significant because it avoids problems derived from shot-to-shot imprecision, and consequently makes gaseous ion-molecule *derivatization* a more reproducible and desirable characterization technique.

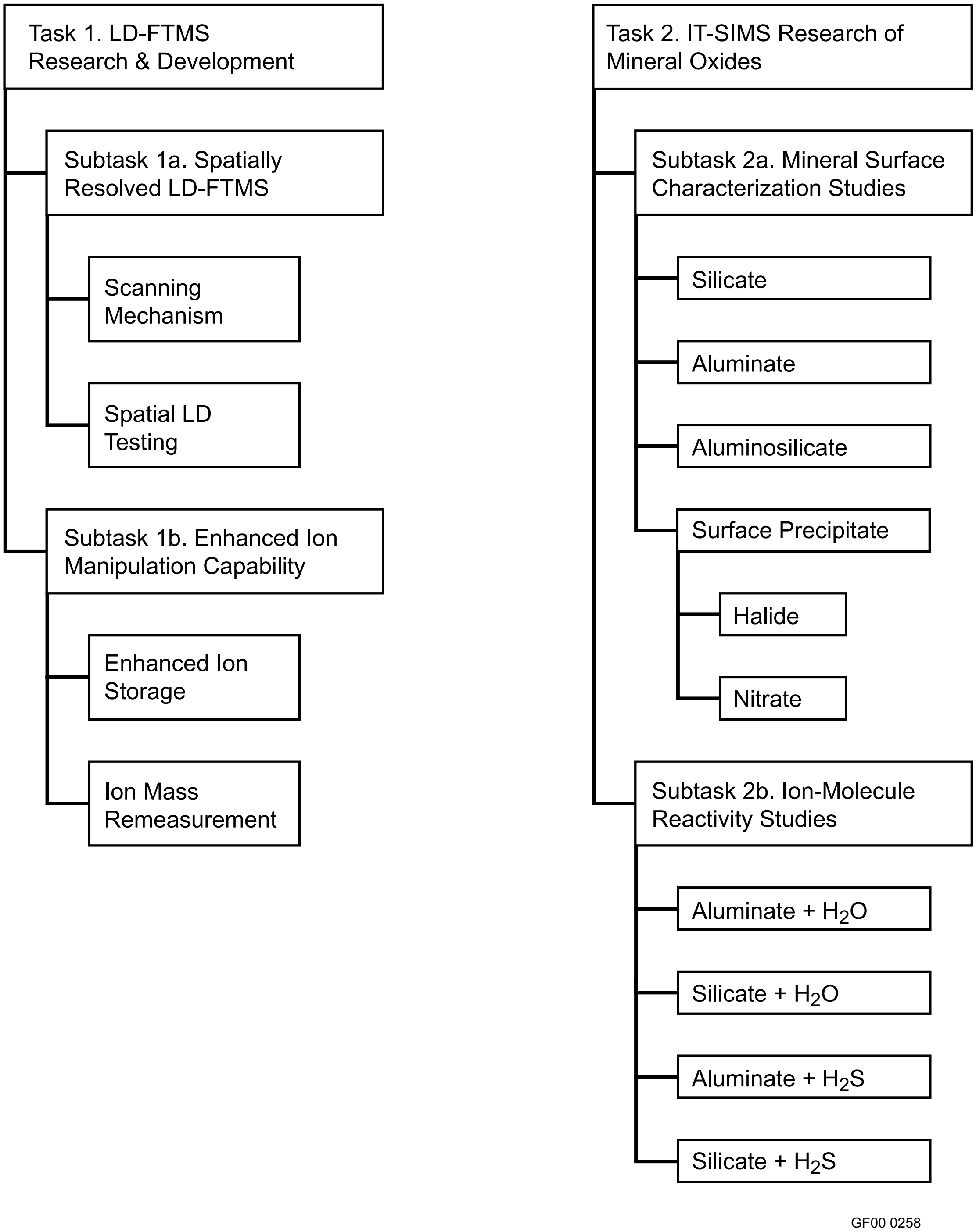

**Figure 1.** Program organization describing the two major thrust areas of the advanced strategies for probing structure and reactivity at the top monolayer.

Because of the high level of inhomogeneity inherent in natural samples, improved precision is difficult to overemphasize.

### *Subtask 1a. Development of Spatially Resolved LD-FTMS*

The primary driving force for developing a scanning mechanism for the laser desorption FTMS is the need to analyze spatially heterogeneous environmental and biological samples. For example, interrogation of selective adsorption of microorganisms on heterogeneous substrates requires the ability to generate molecular data from spatially proximate, chemically distinct areas. This problem in particular is difficult, because microorganism populations are usually heterogeneous, and microbes tend to congregate in colonies, leaving part of the sample probe devoid of organisms. These features can be observed microscopically, but nothing is known about the surficial chemistry underlying this behavior. This is because, on a practical basis, surface analytical instrumentation capable of microscopic scanning has been unable to generate the required level of molecular detail.

Traditionally, mass spectrometry has relied on manipulating the sample target to provide scanning capabilities for laser desorption.[27-30] This is extremely problematic for an internal LD-FTMS owing to (a) the high magnetic field (7 tesla), (b) the geometric constraints of the superconducting magnet bore, and (c) the high vacuum chamber. To overcome these limitations, we have implemented a unique external laser scanning mechanism for the LD-FTMS (Invention Disclosure B028). This mechanism provides adjustable resolution enhancement so that the spatial resolution at the target is not limited to that of the stepper motors at the light source (5 μm/step). The spatial resolution is now limited by the practical optical diffraction limit of the final focusing lens (~0.5 μm).[31] Figure 2 illustrates the operating modes of the scanning device. An index provides for automatic alignment of the device for both uni- and bi-axial (raster) scans. The scanning mechanism employs a *virtual source* that is wavelength independent up to the final focusing lens. The virtual source is located 15 ft from the sample; therefore, it is completely outside of the vacuum system and beyond the 50-Gauss line of the fringing magnetic field. Smaller spot sizes (<1μm) approaching the mechanism step resolution are possible by exchanging the current final focusing optics with one of several more competent multielement lens systems.

The results from the initial tests of the scanning mechanism are highly encouraging. The lens-to-target/lens-to-source distance ratio divides the natural step size of the source to <0.5 μm/step in both horizontal and vertical axes at the target. This scanning capability provides the opportunity to retain the spatial context of analytes in heterogeneous samples. The indexed focus and high-resolution step provide excellent reproducibility, as demonstrated by the scanning electron microscope (SEM) images in Figure 3.

The images in Figure 3 shows two shots (each ~14-μm diameter) separated by 20 μm in an

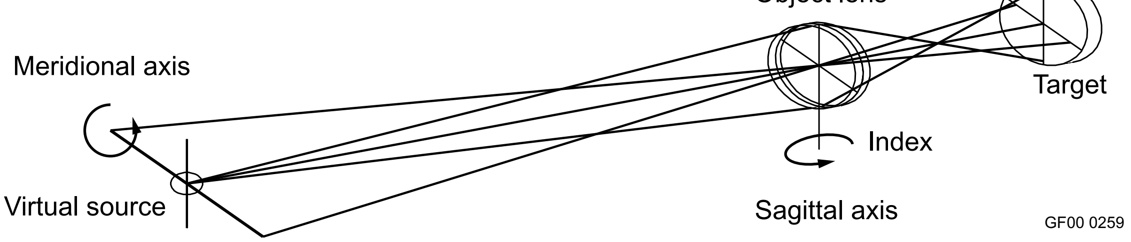

**Figure 2.** Schematic of laser scanning mechanism illustrating modes of operation for horizontal (sagittal axis) and vertical (meridional axis) scanning.

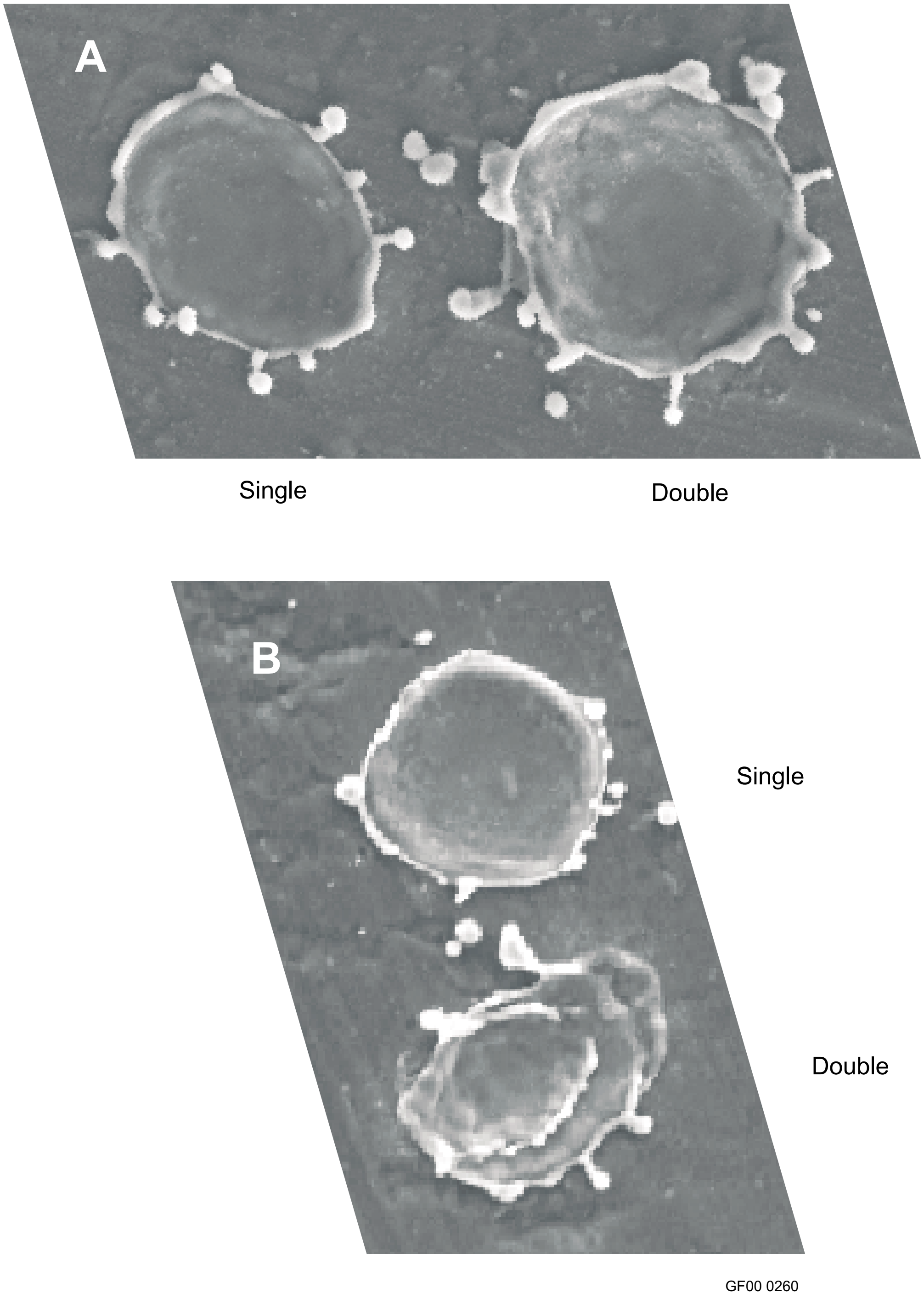

**Figure 3.** SEM images of laser desorption spots on an aluminum sample demonstrating the reproducibility of the scanning laser. (A) Horizontal scan: single shot (left) made during initial scan and double shot (right) made during reverse scan. (B) Vertical scan: single shot (top) made during initial scan and double shot (bottom) made during reverse scan. The internal diameter of single shots is 14 μm.

aluminum target for both horizontal (Fig. 3a) and vertical (Fig. 3b) scanning. The spot on the right has been impacted a second time following a traverse away from the first shot of approximately 300 μm. The reproducibility of the scan position is clearly evident. The distribution of energy across the shot is very nearly Gaussian due to the normal incidence of all elements in the optical scanning mechanism. The slight distortion is due to the distribution of energy exiting from the laser operating at a minimum threshold power level.

In order to evaluate the ability of the unique scanning mechanism as the basis for an imaging internal laser desorption FTMS, a material having a known, chemically variable pattern was needed for benchmark testing. A printed circuit (PC) board was chosen as a heterogeneous test sample. Figure 4 shows a portion of 193 shots taken in six scan lines on the PC board sample. Each spot on the PC board is approximately 200 μm in diameter, spaced at 200-μm intervals. Even though the focus was at the surface of the stainless steel sample holder, sufficient energy impacted the surface of the sample to desorb ions for the FTMS analysis. This experiment successfully demonstrated the ability of the scanning mechanism to generate spatially resolved mass spectra, *without moving the target*. Total time for this manual scan was in excess of two hours. Analysis of each spot required under 2 s, but the traverse to the next shot position was delayed by the manual nature of the user interface to the scanner stepping motors. While the stepper motors are capable of significantly faster response, the manual interface has only a fixed step rate of 5 μm/s. Significant improvement in acquisition time can be achieved by implementing automated scanning.

We chose the first five lines of 34 shots to develop a pseudo image of the sample (Figure 5), which we produced by correlating the physical position of desorption with the mass spectrum obtained from the FTMS at that location. The relatively large spot size (200 μm) used to create this image resulted in 170 files that had to be correlated to the x,y positions by hand. Had a lateral resolution of 10 μm been used, 3400 files would have been collected for the 7-mm$^2$ area. Analysis of the total sample probe area (315 mm$^2$) at a resolution of 10 μm in both ordinates would result in ~3 x $10^7$ files required. The obvious data handling challenges notwithstanding, the mass spectra obtained were easily correlated with the chemical composition of the surface area interrogated, thereby demonstrating the remarkable power of the new instrument for generating spatially resolved mass spectra.

### *Subtask 1b. Development of Enhanced Ion Manipulation Capability*

We recognized that the challenges associated with characterizing complex metal ion species required

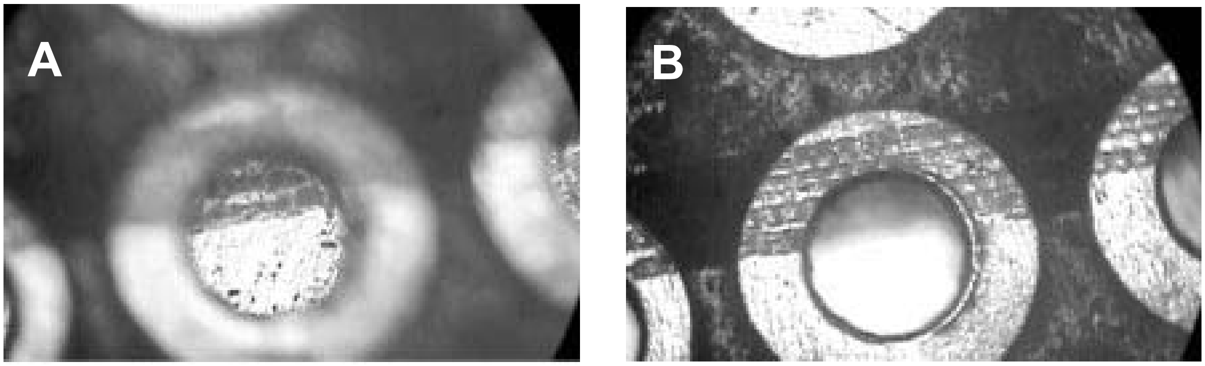

**Figure 4.** Photomicrographs (400x magnification) of PC board. (A) Laser spots focused on probe tip behind the PC board. (B) Defocused laser spots on PC board surface and copper bands.

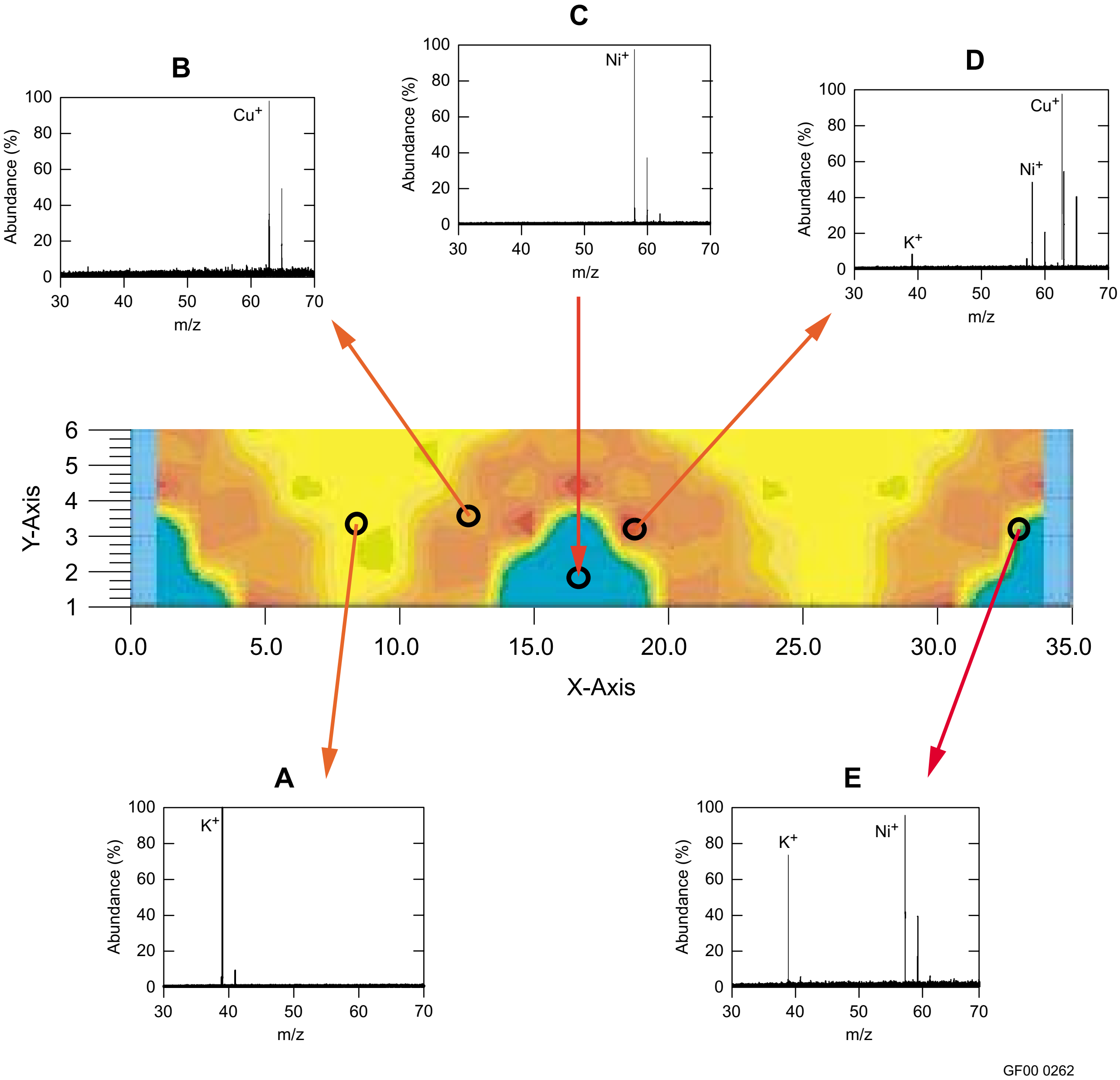

**Figure 5.** Pseudo image produced from the PC board (~7 x 1-mm) section in Figure 4. Colors were arbitrarily assigned based on the appearance of the mass spectra, which was spatially variable. *Pixel* size is 200 µm in a 34 x 5 matrix of spectra correlated with spot position. (A) Spectrum of $K^+$ due to potassium salts on the phenolic portion of PC board. (B) Spectrum of $Cu^+$. (C) Spectrum of $Ni^+$ from laser shots passing through the hole on the PC board and hitting the stainless steel probe tip. (D) Spectrum of $K^+$, $Ni^+$, and $Cu^+$ obtained from the edge of the PC board. (E) Spectrum of $K^+$ and $Ni^+$ from the edge of the PC board.

advanced ion manipulation capabilities. Specifically, the ability to measure and react ions over a range of pressure regimes would be needed, as would the ability to easily change trap geometry. These research needs motivated design and fabrication of a modular cell, and development of instrumental approaches that would enable ion trapping and mass measurement over an extended pressure regime. The effort culminated in a powerful demonstration of ion mass remeasurement that significantly augmented the analytical capability of the instrument.

We initially focused on designing and fabricating a modular cell design that would allow quick and easy interchange of FTMS cells optimized for various experiments. A particularly attractive attribute of the cell design is the simultaneous use of multiple cells having different configurations (see Figure 6). Multiple cells enable ion formation to be separated from reaction and mass measurement, which would be highly advantageous for advanced ion molecule reaction schemes for characterizing complex metal adduct species. Another feature of the modular design is enhanced sensitivity resulting from the carefully matched capacitance of the excitation and detection plates.[32] The increased sensitivity was a key advance, enabling detection of ions at high pressures.

While *trapping* ions at high pressures ($\sim 10^{-6}$ torr) in an FTMS is rather routine, *detection* is still carried out at low pressure ($10^{-8}$ to $10^{-9}$ torr).[33] This is problematic because, for kinetic studies, the pressure of the reagent gas would normally be between $10^{-6}$ and $10^{-5}$ torr. In common practice, the problem is overcome by performing reactions in a high-pressure cell, then transferring the product ions to a low-pressure cell for detection. The problem with this approach is that it negates the possibility monitoring the same packet of ions throughout the course of the reaction, and instead requires the reaction to be stopped for destructive measurement of reactant and product ions at preset time intervals. In principle, the same ions in an ion/molecule reaction could be monitored throughout the experiment using the ion remeasurement capability of the FTMS, if detection at elevated pressure could be achieved. By modifying the vacuum chamber and reagent gas handling apparatus, we demonstrated the ability to maintain high pressures ($10^{-6}$ and $10^{-5}$ torr) around the cell for up to 15 minutes, and detect ions at these high pressures.

To take advantage of the nondestructive detection offered by FTMS to monitor the reaction of the same ions over several time periods for kinetic studies, we investigated various modes for remeasurement

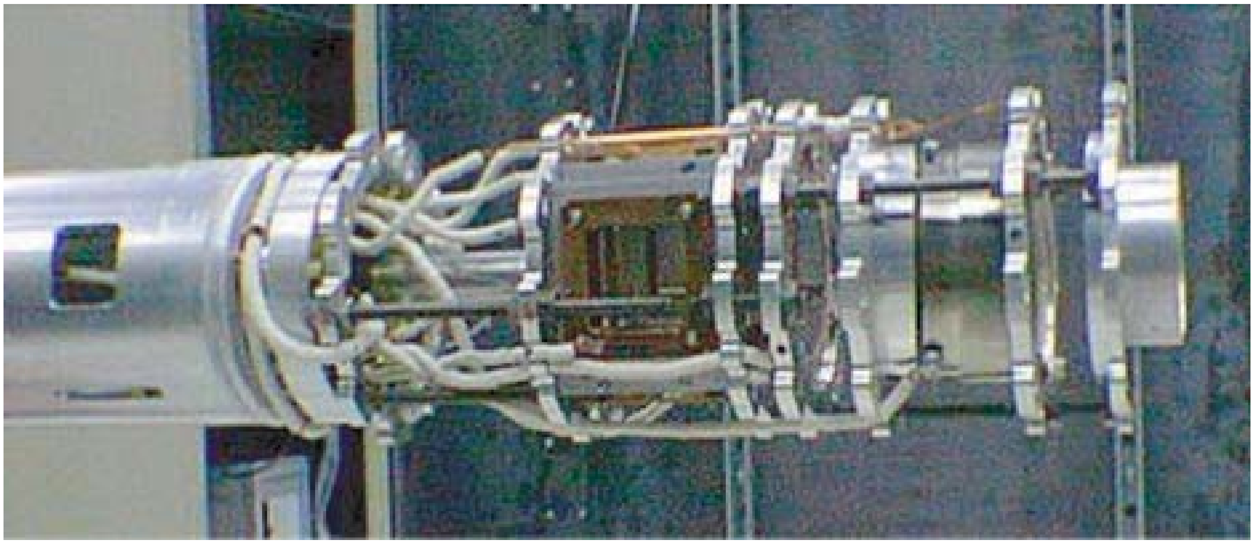

**Figure 6.** Photograph of FTMS cells. Modular design allows multiple cells to be installed simultaneously and for cells to be quickly exchanged.

of ions. Remeasurement is normally accomplished using quadrupolar axialization techniques or by using a collisional cooling bath gas, such as helium. Both of these techniques may affect the internal energy of the ions, which in turn may affect reaction rates. This can be assessed by comparing reaction rates with benchmark experiments performed using the IT-SIMS. Remeasurement without employing some special technique is seldom successful, especially for the closed cubic FTMS cell;[34] however, we obtained excellent remeasurement results using the modular trap design.

While there was a loss in resolution due to the low cyclotron orbits, ions were routinely remeasured without quadrupolar axialization or the presence of a collisional cooling gas. These experiments encompass 10 remeasurement cycles over a 5-minute span. The remeasurement efficiency ranged from 85 to 100% (see Figure 7). Traditionally, remeasurement efficiency has been evaluated as a function of the number of remeasurement cycles because it was being applied over short time intervals for signal averaging. For example, Schmidt et al.[32] report being able to remeasure ions 5 times over 4 ms. Because we are primarily concerned with using this technique for kinetic studies, we have also studied remeasurement efficiency as a function of ion storage time. There is complex interdependence between the number of remeasurement cycles, pressure, trapping voltage, and the ion storage time. However, in these experiments the remeasurement efficiency seemed to depend more on the length of time the ions could be stored in the cell than with the number of remeasurement cycles. These considerations notwithstanding, the results clearly demonstrate superior remeasurement capability and uniquely position the instrument for attacking complex radionuclide speciation issues using high-performance FTMS techniques.

## Task 2. IT-SIMS Research of Mineral Oxides

The INEEL is pursuing ion trap secondary ion mass spectrometer (IT-SIMS) as an advanced characterization tool for radionuclide speciation on real-world mineral samples. Consequently, we performed detailed studies to understand instrument performance when mineral samples were analyzed. Specific questions to be addressed by this research were:

1. Can meaningful molecular information be generated from mineral oxide surfaces?
2. What is the origin of the secondary ion signal and can it be related back to surface speciation?
3. Can the gaseous ion-molecule reactions be used to characterize the resulting secondary ions?
4. Can intrinsic ion reactivity be characterized and exploited for understanding surface speciation and reactivity?

We conducted a research program that addressed these questions and provided a strong set of analytical tools for assessing surface speciation and reactivity. The research keyed on two salient insights, namely, (1) greatly augmented abundances of complex, molecular secondary anions can be generated by bombarding oxide surfaces with a polyatomic projectile in the relatively high-pressure realm of the IT-SIMS, and (2) reactivity of the surface-derived ions can be directly assessed in the gas-phase environment of the IT-SIMS.

These insights are important because they unveil a broad expanse of geochemical investigation

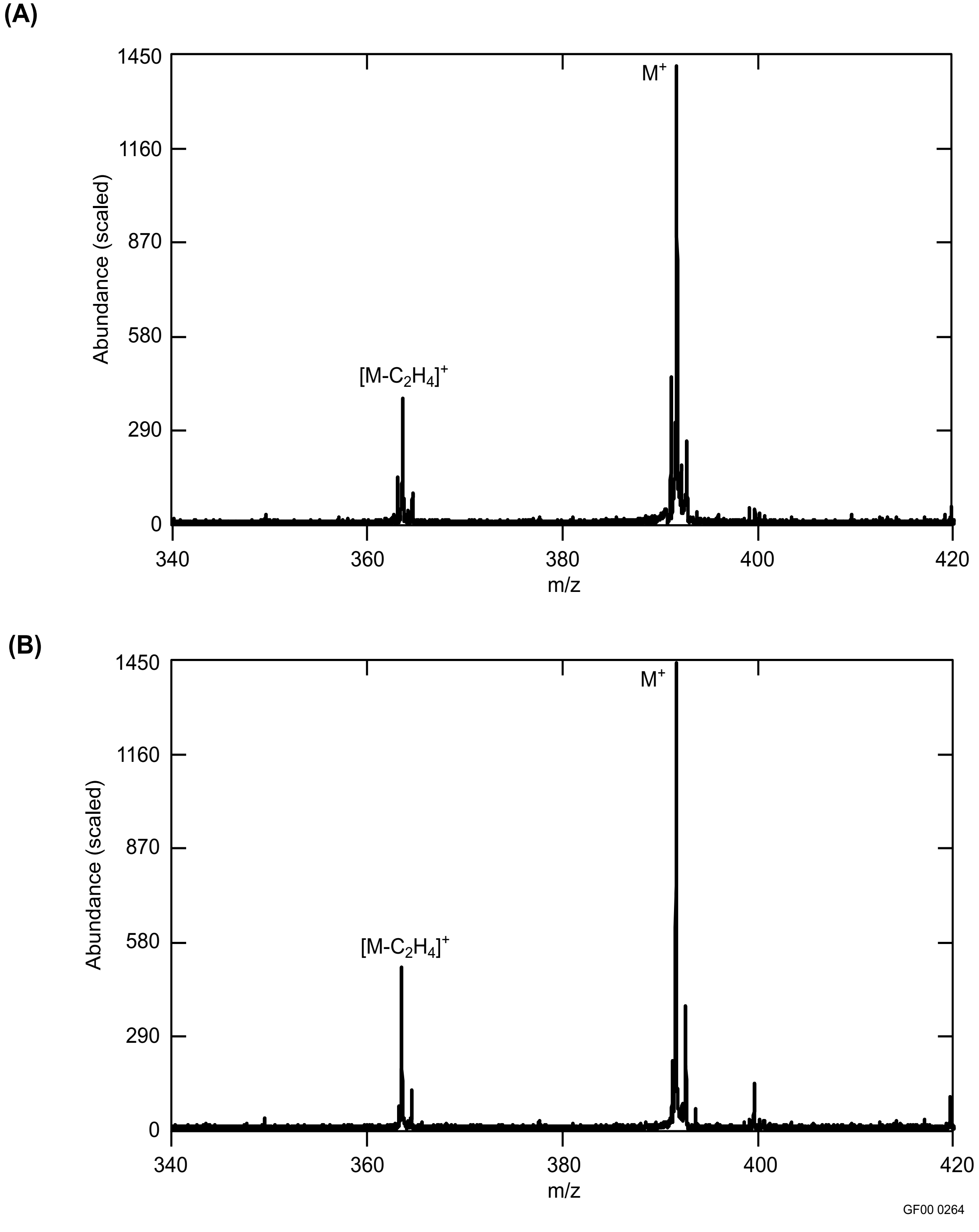

**Figure 7.** FTMS spectra of the same ions remeasured (A) 1 min and (B) 4 min after initial formation. Note that the abundance of the ions in (A) and (B) are essentially identical.

heretofore inaccessible. Surface speciation can be easily and directly interrogated. Adsorbed or adsorptive moieties can be sputtered into the gas phase, and their intrinsic reactivity can be assessed directly with detailed kinetic assessments, which can be backed up by state-of-the-art computation modeling capable of providing structure and thermodynamics.

The dual objectives of this task were (1) to develop IT-SIMS methodologies readily applicable to metal speciation/mineral oxide characterization and (2) to demonstrate these tools through investigation of ion generation and reactivity studies, which define the two subtasks described below. The objectives were addressed in the context of the range of environmental matrices and waste forms likely to be encountered in operations at the INEEL and across the DOE complex. The intent was not to thoroughly canvass these forms, but to perform exploratory research for generating tools applicable to surface speciation of radionuclides on environmental and waste minerals.

### *Subtask 2a. Mineral Surface Characterization Studies*

Conventional classification of adsorbed metals distinguishes five fractions: (1) ion exchangeable, (2) carbonate bound, (3) organic complexed, (4) sesquioxide bound, and (5) residual, which is everything remaining subsequent to a sequential extraction approach.[35] Metals that are bound to aluminosilicate sites constitute most of the exchangeable fraction. Consequently, molecular characterization of aluminosilicate surfaces (i.e., clays, sediments) was emphasized. Prior work on the identification of organic adsorbates on clays and sediments show that they can be readily detected, primarily in the positive ion mode. However, few if any of the ions derived from the aluminosilicate matrix were observable in the cation spectra. In contrast, a reproducible ion series was readily apparent in the anion spectrum (see Figure 8). This ion series was derived from the aluminosilicate matrix and could be more readily observed in the spectra of zeolites.[36] A similar series derived solely from silicate had recently been observed using LD-FTMS.[37-38] The newly observed ion series had the general formula $Al_mSi_nO_{2(m+n)}H_{(m-1)}^-(H_2O)_x$, where (m+n) ranges from 1 to 10, and x from 0 to 3. This result showed clearly that complex, molecular information could be derived from metal/metalloid oxide surfaces, which heretofore had produced principally atomic information under ion bombardment.

A second surprising result was that the abundance of the hydrated ions (x = 1,2,3) increased with increasing ion lifetime in the IT-SIMS. We attribute this to the reaction of $Al_mSi_nO_{2(m+n)}H_{(m-1)}^-$ with $H_2O$ in the gas phase, and we address it in more detail below.

The conclusion of these studies is that aluminosilicate binding moieties can be readily identified in the negative ion spectrum. When combined with metal ion identification from the positive ion spectrum, qualitative surface speciation information could be deduced.

A second type of ion exchangeable species is soluble surface precipitates, such as nitrates and halides. These types of materials are more typically found in waste sites (source terms) than in the subsurface environment. We satisfactorily initiated preliminary research on identifying nitrate and halide species. We observed halides to readily form $M_mX_n^{+/-}$ secondary ions, which are straightforwardly interpreted for alkali and alkaline earth metals but are more complex for transition metals, in that clusters are observed in which the metal exists in multiple oxidation states.[39] Nevertheless, Fe, Mg, and Ca could be observed on mineral surfaces treated with dilute HCl: this resulted in the formation of $MCl_3^-$ in all three cases. This phenomenon has substantial analytical utility.

Nitrate matrices are significant because they are important as a potential waste form. Nitric acid

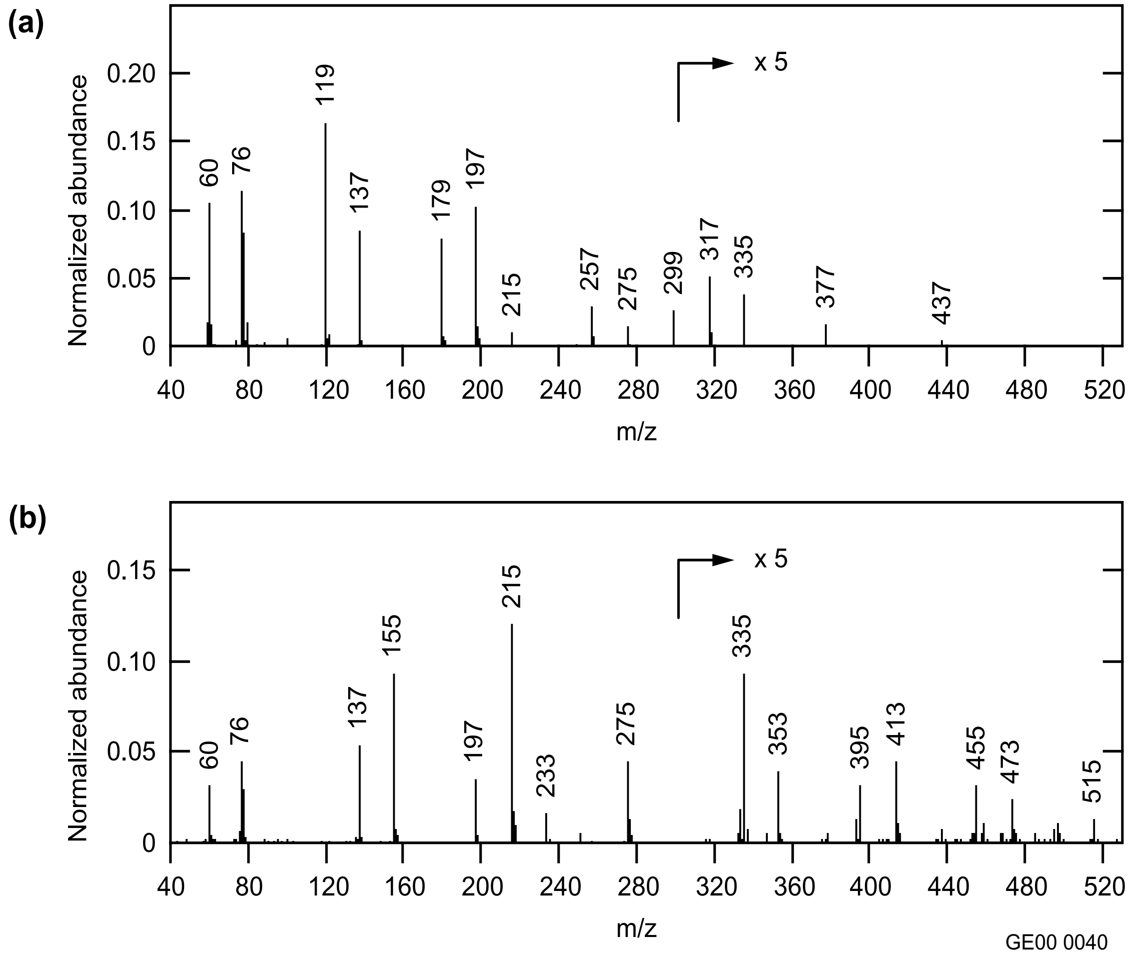

**Figure 8.** IT-SIMS anion spectrum of a cesium zeolite, acquired after variable ion lifetimes in the instrument. (A) Ion lifetime 26 milliseconds. Note the distribution of ion intensities over a range of $H_2O$ adduct states. (B) Ion lifetime 56 milliseconds. Here, the distribution is skewed toward the di- and tri-hydrated species.

was widely used in dissolution processes and is expected in waste burials. Identification of alkaline nitrates had previously been researched in our laboratory.[16] However, transition metals in a nitrate matrix have not been explored, so we examined $Cr(NO_3)_3$ and $Fe(NO_3)_3$ using the IT-SIMS. In the anion spectra of the Cr compound, we observed $NO_3^-$ and $NO_2^-$, as expected, but the most abundant metal-bearing ion was $CrO_3^-$. We also observed lower abundance $CrO_2^-$ and $CrO_4^-$. The observation of the abundant $CrO_3^-$ was surprising because this ion represents Cr in the (V) oxidation state, which means that Cr was oxidized in the bombardment process. Analysis of $Fe(NO_3)_3$ revealed similar behavior; $NO_3^-$ and $NO_2^-$ were observed, but the dominant Fe-bearing ion was $FeO_3^-$ at *m/z* 104. As in the case of $CrO_3^-$, the metal is in the (V) oxidation state.

The $NO_3^-$ counter ion is likely reduced in the bombardment process, forming $NO_2$ and oxidizing Fe to $FeO_3^-$ (Reaction 1). These studies show the relationship between the oxidation state in the condensed phase and that in the gas phase. While SIMS is normally a reducing process, oxidized metal species are observed if the original matrix contains an oxidizing reagent such as $NO_3^-$. Understanding these behavioral characteristics is critical for identifying environmental and waste species. The SIMS ionization process of nitrates also is a means for generating metal oxyanions $MO_x^-$, which are useful for ion-molecule reactivity studies.

$$Fe(NO_3)_3 + e^- \xrightarrow{\text{SIMS}} \underset{m/z\ 104}{FeO_3^-} + 3\ NO_2 \qquad \text{Reaction 1}$$

Curiously, poor spectra were generated from Cr and Fe oxides $Cr_2O_3$, FeO, $Fe_2O_3$, and $Fe_3O_4$. In the cation mode, $Cr^+$ and $Fe^+$ were observed, but this tells nothing about the surface speciation. Abundances of the Fe oxyanions were negligible. Treatment of the surface with HCl, however, resulted in the formation of very abundant $FeCl_3^-$ and thus suggests a simple surface derivatization mechanism for identifying Fe on minerals. We have not yet correlated oxidation state with observed ion species. Derivatization with nitrate or nitrite may also offer a means for characterizing Fe-bearing surfaces, and this may be extendable to more complicated oxide systems such as U or Pu. The ability to characterize Fe oxide surfaces will also directly impact assessment of sesquioxide surface species such as FeOOH, and corresponding Mn species that are thought to be responsible for strong metal bonding.

A significant fraction that has not been extensively explored is carbonate-bound metals. This is an important fraction because carbonate is a significant mineral fraction, and carbonate is known to bind strongly to $UO_2^{+2}$ and other metal species. Analyses of carbonate salts such as $CaCO_3$ yield generally noninformative $Ca^+$ and $CaOH^+$ ions, and little in the way of direct information stemming from carbonate-bearing ions. This is likely because the $CO_3^{-2}$ is not stable under bombardment in vacuum, undergoing decomposition to $CO_2$ and metal oxides.

A significant exception to this behavior is the SIMS analysis of basic, alkali-bearing surfaces, which tend to fix $CO_2$ from the atmosphere. For example, NaOH and $NaNO_2$ both produce significant $Na_3NO_3^+$ when analyzed using SIMS. This suggests that alkaline bases might be useful for *fixing* carbonate on the surface. Generally, however, characterization of carbonate on mineral surfaces is immature using SIMS and constitutes a significant opportunity for improvement.

Metals bound to organic ligands on the surface are thought to constitute a large fraction of many environmental systems. We did not conduct chemical studies designed to specifically address this fraction, but we did lay groundwork for their future study by developing advanced instrumentation, *i.e.*, the LD-FTMS (see above).

### *Subtask 2b. Ion-Molecule Reactivity Studies*

During the course of the aluminosilicate oxide studies, we noted significant reactivity of the sputter desorbed ions, namely, the reaction of $Al_mSi_nO_{2(m+n)}H_{(m-1)}^-$ with $H_2O$. We investigated these reactions in detail for the following reasons:

1. Their understanding is key to control and interpretation of the processes occurring in the IT-SIMS.

2. They offer the possibility of gas-phase derivatization reactions that may be used to develop characterization strategies for metal species in complex matrices. The condensation reactions may be especially valuable in this regard, because many inorganic metal species are very stable and hence not amenable to fragmentation (*i.e.*, MS/MS).

3. They offer insight into the intrinsic reactivity of ionic metal moieties sputtered from the

surface. The ion-molecule reactions thus represent a unique opportunity to directly observe reaction pathways and reaction kinetics.

*Aluminate + $H_2O$.* As noted above, initially the reactivity of aluminosilicate oxyanions with $H_2O$ was observed (Reaction 2):

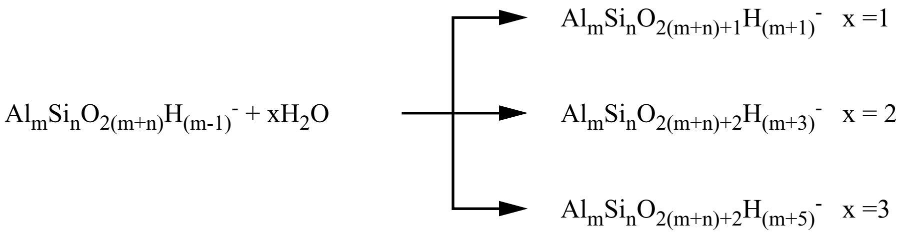

Reaction 2

The reaction products were covalently bound, formed by the hydrolysis of $H_2O$. When $(m+n) \geq 2$, the reactions were fast and highly efficient (50 – 100% compared with the theoretical collision rate). However, when the monomeric species were studied, reactions were observed, but they were very slow.[40] For example, the condensation of $AlO_2^-$ with $H_2O$ (Reaction 3) was only 2% efficient at forming the $AlO_3H_2^-$ product anion (efficiency was assessed by comparing the reaction rate with the theoretical collision rate). We attribute the low efficiency to the lack of a permanent dipole moment on the $AlO_2^-$ ion.

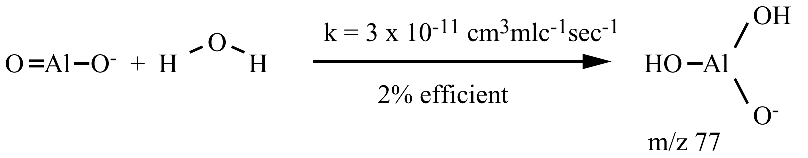

Reaction 3

The product $AlO_3H_2^-$ underwent a sequential reaction with water (Reaction 4), which was substantially more efficient. This result correlated with the presence of a dipole moment in the $AlO_3H_2^-$, while the relative thermodynamics of both water addition reactions were apparently unrelated. *Ab initio* modeling shows that both reactions were approximately 63-kcal mol$^{-1}$ exothermic, and required minimal activation energy.

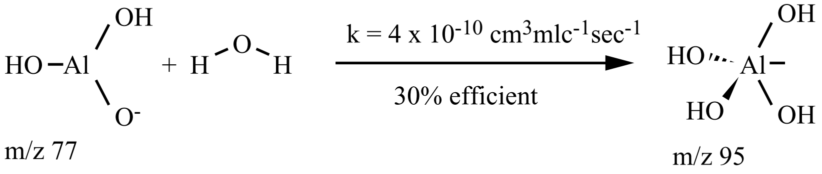

Reaction 4

For comparison, we studied the reactivity of the aluminate dimer $Al_2O_4H^-$. This ion has a substantially larger dipole moment compared with the monomeric aluminate ions, and was found to be 100% efficient in its reaction with water, producing $Al_2O_5H_3^-$ (Reaction 5).

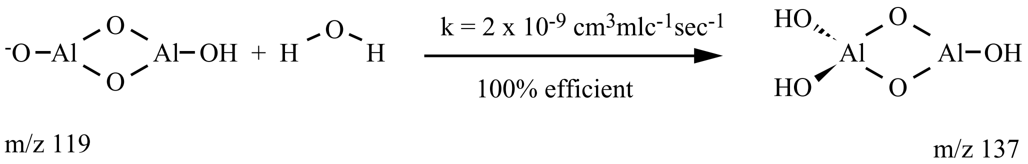

Reaction 5

The product ion $Al_2O_5H_3^-$ will also undergo an efficient hydration reaction to produce $Al_2O_6H_5^-$.

*Silicate + $H_2O$.* Three monomeric silicate oxyanions are generated in the SIMS analysis of silica, $SiO_2^-$, $SiO_3^-$, and $SiO_3H^-$. Like aluminate, silicate sites represent potential reactive moieties on mineral surfaces. When these ions were formed in the IT-SIMS and allowed to react with $H_2O$, their rates of reaction were generally much slower than the rates observed with aluminate oxyanions. $SiO_2$ would react with $H_2O$, but only very slowly. The rate constant for the hydroxyl radical abstraction was $5 \times 10^{-13}$ $cm^3$ $mlc^{-1}$ $sec^{-1}$, or only 0.03% of the collision constant (Reaction 6). The resulting product ion $SiO_3H^-$ reacts 10 times faster than $SiO_2^-$, but it is still slow by gas-phase ion molecule standards (Reaction 7). The reaction pathway results in $H_2O$ addition to $SiO_3H^-$, instead of the OH radical abstraction observed in the reaction of $SiO_2^- + H_2O$. Oligomeric silicate ions tend to be very low abundance, but the $Si_2O_5H^-$ could be isolated and reacted with $H_2O$. The ion adds $H_2O$, at nearly 50% efficiency. As in the case of the aluminates, more complicated structures clearly facilitate reaction with $H_2O$, and at the present time correlation with ion dipole moment remains the best explanation.

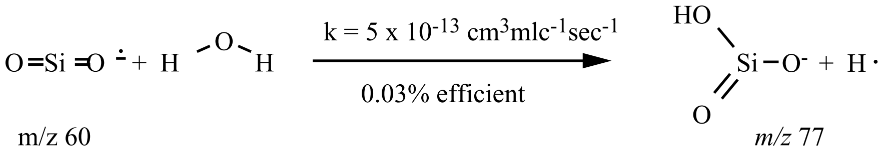

Reaction 6

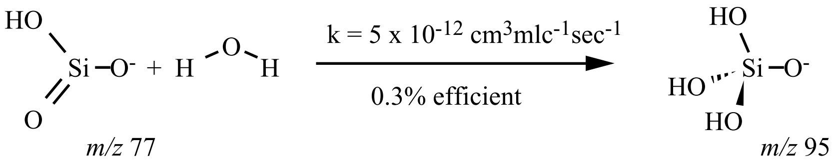

Reaction 7

*Reactions with $H_2S$.* Uncertainty in the elemental composition of aluminosilicate oligomers led to research into the reactivity of $H_2S$ with aluminate and silicate. The ongoing problem is that the assignment of precise elemental compositions for the oligomeric ions $Al_mSi_nO_{2(m+n)}H_{(m-1)}^-$ derived from clays and zeolites is an open question. For example, for $Al_mSi_nO_{2(m+n)}H_{(m-1)}^- 2H_2O$, where (m+n) = 3, the elemental compositions listed in Table 1 are possibilities.

**Table 1.** Isobaric compositions for the $Al_mSi_nO_{2(m+n)+2}H_{(m+3)}^-$ ion observed at *m/z* 155.

| $Al_m$ | $Si_n$ | $O_{2(m+n)+2}$ | $H_{(m+3)}$ |
|---|---|---|---|
| 3 | 0 | 8 | 6 |
| 2 | 1 | 8 | 5 |
| 1 | 2 | 8 | 4 |
| 0 | 3 | 8 | 3 |

Since the number of H atoms is variable, unequivocal identification might be achievable by performing H/D exchange in the gas phase. This experiment assumes that the H's are exchangeable and that the rates will be fast enough to permit quantitative shifting of the ions to higher mass. In this manner, the number of H and, consequently, the elemental composition could be assigned.

Using $D_2O$ as an exchange agent, we observed shifting of the adduct ions to higher mass, but the results were not consistent with a single composition, nor with quantitative H/D exchange. For example, after exchanging *m/z* 155 $(Al_mSi_nO_{2(m+n)}H_{(m-1)} +2H_2O)^-$, the most abundant ion was observed at *m/z* 158, indicating three exchangeable H atoms, and an $Al_0Si_3$ composition (see Table 1). However, we also observed an abundant *m/z* 159, consistent with four exchangeable H and an $Al_1Si_2$ composition. By itself, this is not an ambiguous experiment, except for the fact that ions were observed at *m/z* 156 and 157, which can only occur as a result of incomplete H/D exchange. We concluded that certainly the $Al_1Si_2$ was present, and that the $Al_0Si_3$ was also likely, but a more definitive conclusion was not possible based on these data. The H/D exchange rates were too slow, and for this reason, we employed $D_2S$ as a gaseous reagent.

$D_2S$ is substantially more acidic than $D_2O$, and H/D exchange rates were expected to be more rapid. However, when $D_2S$ was reacted with the Al and Si oxyanions, the product ions observed were principally derived from processes other than H/D exchange. To simplify the interpretation, $H_2S$ was substituted for $D_2S$, and the small oxyanions were studied first. In contrast to its behavior with $H_2O$, the radical anion $SiO_2^-$ reacted rapidly with $H_2S$ by abstracting a sulfuryl radical (SH) to form $SiO_2SH^-$ at *m/z* 93 (reaction 8). The *m/z* 93 goes on to react with a second $H_2S$ to form *m/z* 109 (reaction 9, described below).

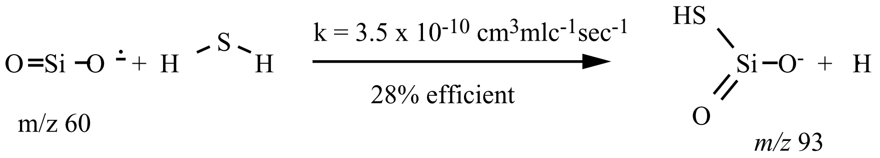

Reaction 8

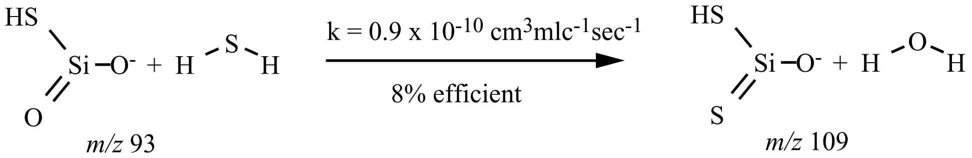

Reaction 9

The reaction of $SiO_2^-$ + $H_2S$ offers a good vehicle for describing how the ion molecule reactivity studies are conducted. Initially, $SiO_2^-$ is sputtered from the silica surface, and is isolated using the filtered noise field capability of the IT-SIMS, which results in a spectrum dominated by $SiO_2^-$ (*m/z* 60, Figure 9a). The reaction time may be varied, during which primary (*m/z* 93) and sequential (*m/z*109) reaction products appear (Figures 9b, c). The disappearance of the initial reactant ion $SiO_2^-$ is described by a single exponential decay, indicating pseudo first-order kinetics (see Figure 10). Dividing the slope by the $[H_2S]$ results in a direct measurement of the rate constant, which for $SiO_2^-$ + $H_2S$ was measured at $3.5 \times 10^{-10}$ $cm^3$ $mlc^{-1}$ $sec^{-1}$, or 28% efficient compared to the collision constant. The rate constant for the consecutive reaction (see below) $SiO_2SH^-$ + $H_2S$ could then be calculated using consecutive reaction modeling, in which two consecutive pseudo first-order reactions are assumed, and the rate constant for the second reaction ($k_2$) is modeled using the measured value for the first reaction ($k_1$). The results of the model are plotted, and the rate constant for the second reaction is estimated by visually fitting the model to the data (see Figure 11).

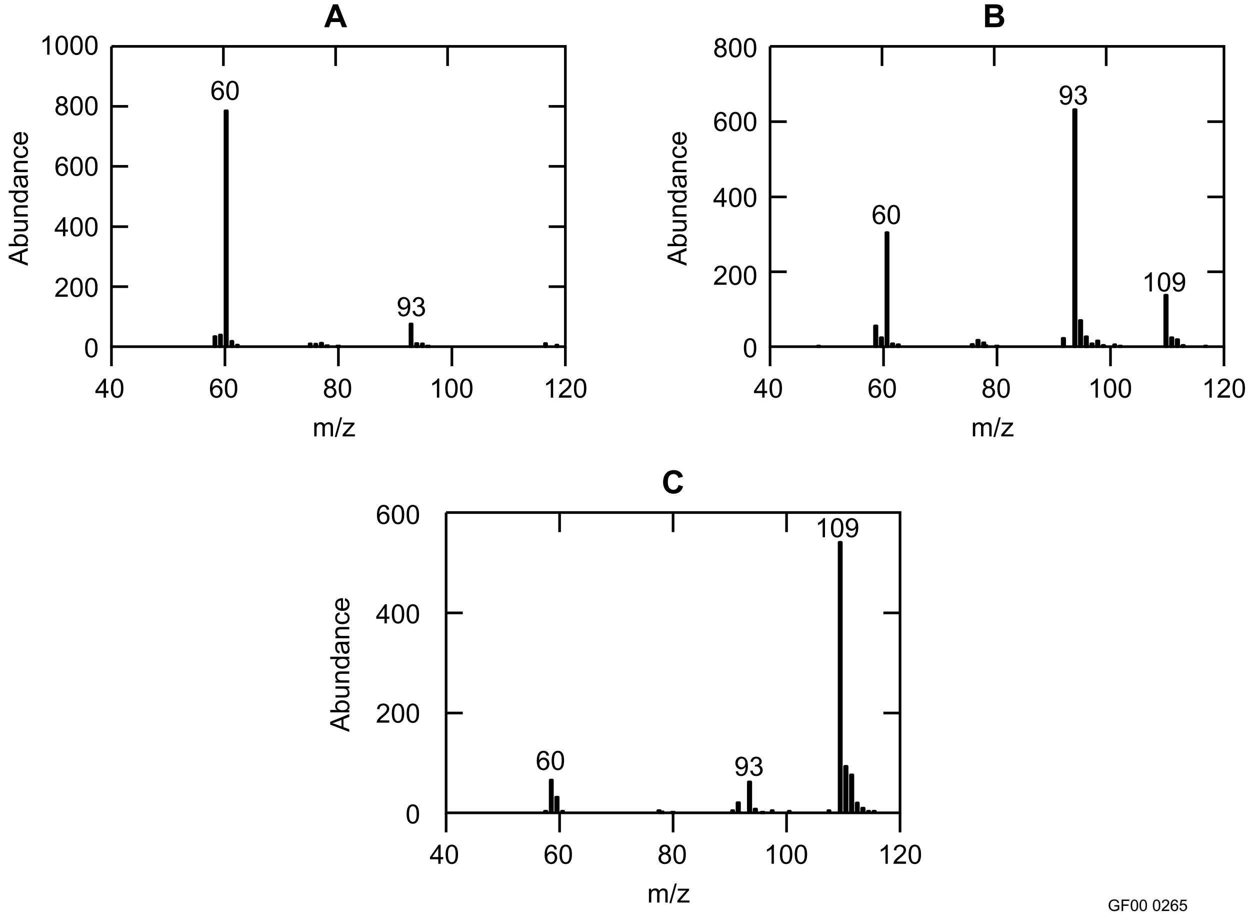

**Figure 9.** Mass spectra of $SiO_2^-$ (*m/z* 60) reacting with $H_2S$ acquired at different ion lifetimes. $SiO_2^-$ was formed and isolated in the IT-SIMS using the filtered noise field. (A) Spectrum acquired 2.4 milliseconds after ion formation. Only a small fraction of *m/z* 60 has reacted with $H_2S$ to form *m/z* 93. (B) After 97 milliseconds, most of the *m/z* 60 has reacted to form *m/z* 93, and a fraction of *m/z* 93 has gone on to react to form *m/z* 109. (C) After 800 milliseconds, no *m/z* 60 exists, and almost all of the *m/z* 93 has reacted to form *m/z* 109.

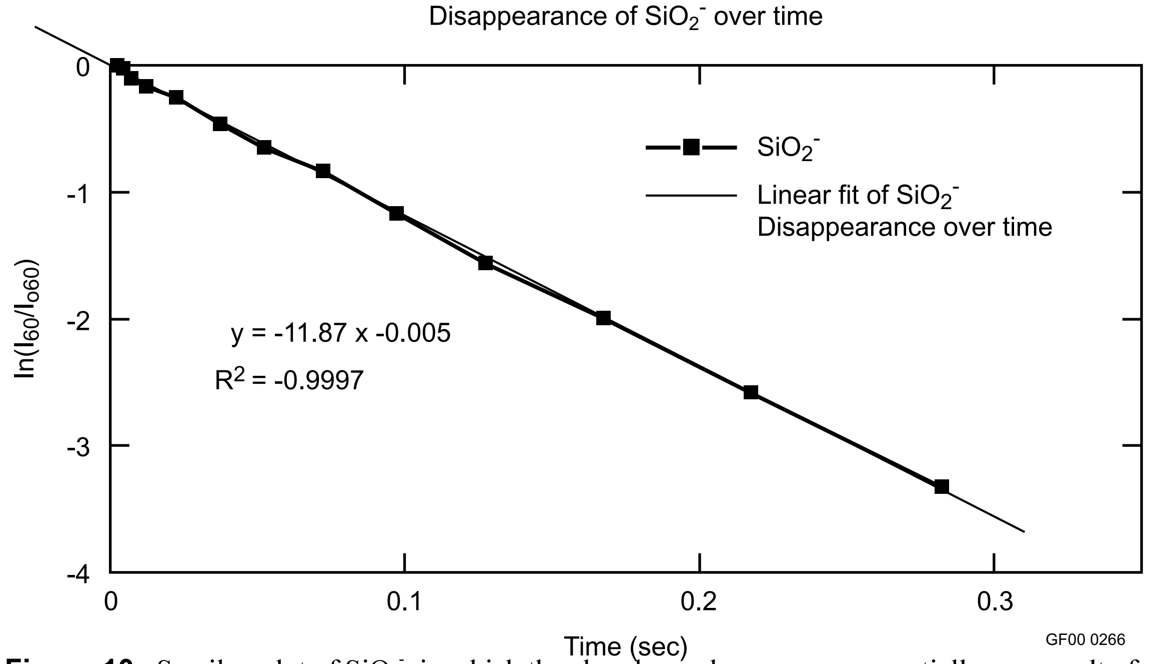

**Figure 10.** Semilog plot of $SiO_2^-$, in which the abundance decreases exponentially as a result of reaction with $H_2S$ with increasing time. The slope of the line corresponds to the phenomenological rate constant, equal to the molecular rate constant multiplied by $[H_2S]$

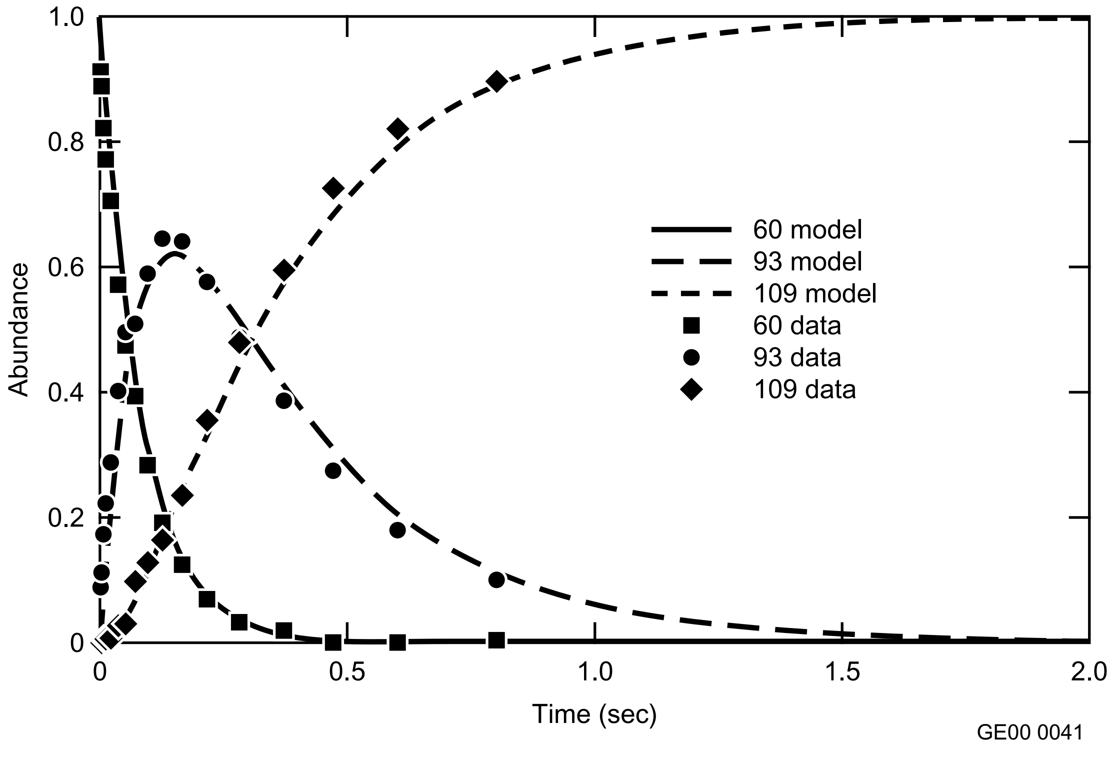

**Figure 11.** Consecutive reaction modeling for $SiO_2^- + H_2S \rightarrow SiO_2SH^-$ followed by $SiO_2SH^- + H_2S \rightarrow SiOS_2H^-$.

After abstracting the sulfuryl radical, the resulting $SiO_2SH^-$ reacts with a second $H_2S$ to form *m/z* 109, which has the composition $SiOS_2H^-$ (Reaction 9). This unique reaction occurs by an S-for-O exchange, and ion formation is accompanied by $H_2O$ elimination. The reaction is surprisingly efficient (30%) given its complexity. The reaction is significant because it reveals the propensity with which heteroatoms may be exchanged on a reactive mineral moiety.

$SiO_3^-$ is a second radical species observed in the SIMS spectrum, and its reaction with $H_2S$ is similar to that of $SiO_2^-$ in that it initially abstracts a radical, followed by S-for-O exchange. However, the molecule does not want additional covalent coordination, and efficiently abstracts an H radical (instead of a sulfuryl), forming $SiO_3H^-$ (Reaction 10). Once formed, the even electron $SiO_3H^-$ reacts consecutively with two additional $H_2S$ to sequentially form $SiO_2SH^-$ (Reaction 11) and $SiOS_2H^-$ (Reaction 9), expelling water in each step.

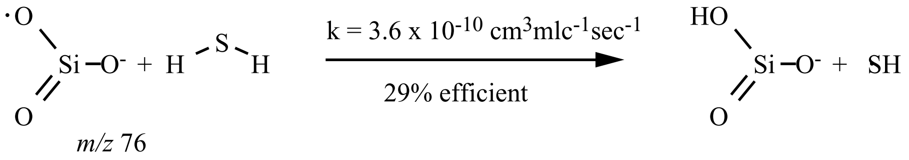

Reaction 10

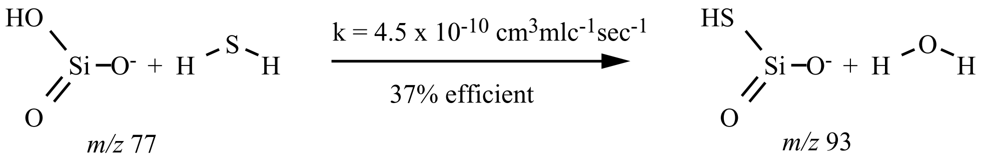

Reaction 11

Since $SiO_3H^-$ is produced directly from the bombardment of silica, the reaction of this ion with $H_2S$ could be studied directly. The behavior of the ion was identical to that of the ion formed from the reaction of $SiO_3^-$. It participated in two consecutive S-for-O exchanges, with rate constants that were in good agreement with the earlier measurements.

*Aluminate + $H_2S$.* The reactivity of $AlO_2^-$ constituted an interesting comparison with $SiO_2^-$, because $AlO_2^-$ is an even electron ion. This may explain the difference in reactivity observed. $AlO_2^-$ does not abstract radicals, but instead undergoes two sequential S-for-O exchanges, forming $AlOS^-$ and $AlS_2^-$ and expelling $H_2O$ at each step (Reactions 12 and 13). The reactions are highly efficient in view of the fact that the mechanism is necessarily complicated. In contrast to the reactivity of $AlO_2^-$ with $H_2O$, there is no tendency to become more highly coordinated.

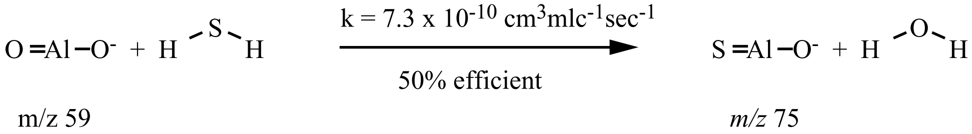

Reaction 12

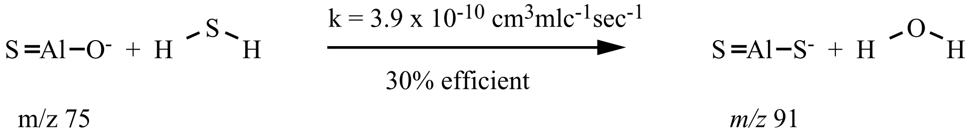

Reaction 13

*Higher Oligomers.* $H_2S$ reactivity studies were initiated with oligomeric aluminate, silicate, and aluminosilicate ions. These preliminary studies clearly show the occurrence of S-for-O switching, but rigorous identification of reaction pathways and kinetics was hindered by fast reactions with residual water. Pursuit of these experiments should be undertaken, because S-for-O switching does not appear to be exhaustive, and the exchange reaction may contain information regarding the chemical environment of the exchangeable O atoms in the oxyanions.

*Transition Metal Reactivity Studies.* Preliminary studies of the reactivity of $FeO_3^-$ and $CrO_3^-$ with $H_2O$ and $H_2S$ were initiated and indicate that reactivity with $H_2O$ is negligible for both ions. Reaction with $H_2S$ did not occur with $CrO_3^-$. We observed ions indicating S-for-O switching in the reaction of $H_2S$ with $FeO_3^-$, but these were low abundance compared with the product ions resulting from reaction with $HNO_3$ that was residual in the ion trap. The $HNO_3$ likely arose from the ferric nitrate nonahydrate salt used as a target for generating $FeO_3^-$. While the results were obfuscatory with regard to iron oxide reactivity with $H_2S$, they show the breadth of the technique for studying reactivity across an incredibly broad range of ions and neutral molecules.

*Summary of Reactivity Investigations.* Combining the results of aluminate and silicate reactivity studies enables several generalizations, which suggest that secondary ion reactivity can be predicted.

1. Al and Si oxyanions react with multiple $H_2O$ molecules in a covalent fashion, which is consistent with the fact that under-coordinated Al/Si on surfaces is reactive.

2. The reactivity of *monomeric* oxyanions is dramatically lower than the reactivity of oligomeric oxyanions, which may be attributable to the existence of significant, permanent dipoles in the oligomeric oxyanions. The least reactive ions are $AlO_2^-$, $SiO_2^-$, and $SiO_3^-$, which have no dipole moment. Similarly, initial reactions with $FeO_3^-$ and $CrO_3^-$ show little or no reactivity with water.

3. $H_2S$ is clearly more reactive with the monomeric oxyanions than is $H_2O$; however, the oligomeric oxyanions are at least as, if not more, reactive with $H_2O$ than they are with $H_2S$.

4. There is a clear difference in reaction path between radical, and even-electron oxyanions. The radical oxyanions initially react by radical abstraction, forming an even-electron oxyanion. The even-electron oxyanions react either by condensation (in the case of $H_2O$) or by S-for-O substitution (in the case of $H_2S$).

5. In the gas-phase environment of the ion trap, Al and Si will tetrahedrally coordinate when reacting with $H_2O$, but will achieve (at most) trigonal coordination when reacting with $H_2S$.

## ACCOMPLISHMENTS

This project focused on developing advanced approaches for probing structure and reactivity at the top monolayer of real-world samples. The project had two thrusts: development of a unique, scanning LD-FTMS, and development of applications using state-of-the-art IT-SIMS instrumentation previously developed at the INEEL.

These projects targeted the challenging problems of identifying metal, specifically radionuclide, speciation on real-world surfaces. Surface was emphasized because the processes that dictate contaminant fate and transport occur in this realm. Characterization has historically been difficult because of complex contaminant and mineral chemistry, low surface concentrations, and insensitive or nonspecific analytical approaches.

Research on the LD-FTMS task resulted in design and fabrication of an instrument capable of desorbing ions from the mineral surface, using a range of wavelengths and power densities. This allows control over the relative amount of atomic versus molecular information generated. The most outstanding achievement, however, is the invention of a laser scanning system that does not require the target to be moved while within the high field of the FTMS magnet. This enables generation of spatially resolved mass spectra from complex, heterogeneous samples typical of those encountered in subsurface environmental or waste characterization activities.

Following laser desorption, the ions are trapped in a high-performance FTMS, capable of high-resolution, accurate mass measurement for elemental composition assignment, at high mass ($\geq 10{,}000$). The instrument is also capable of performing a broad suite of ion-molecule reactions (including fragmentation and condensation), and sophisticated nondestructive ion remeasurement.

We expect this instrument to make significant contributions to understanding radionuclide speciation, including attachment to microbially derived ligands, microbe identification, and metal transformations occurring on surfaces.

The IT-SIMS research of mineral oxides contributed significant understanding of ion generation and ion reactivity behavior critical for instrument control and data acquisition. The research resulted in spectral information needed to identify ion exchangeable and surface precipitated metals, intrinsic hydration reactions, and a novel heteroatom exchange mechanism. These behavioral attributes and chemistries are critical for recognizing the spectral signature of nitrates, aluminates, silicates, aluminosilicates, ferrates, and halides. The results show that the IT-SIMS can be applied to a broad suite of environmental and waste sample types.

Remaining challenges include demonstrating the LD-FTMS for characterizing heterogeneous mineral and microbially modified surfaces with elemental composition assignment. Similarly, the IT-SIMS must be demonstrated for microbially modified surfaces, and for carbonate-bound metals. Further correlation must be established between surface species and gas-phase species sputtered from the sample surface.

Certainly, the level of complexity in these tasks is high, but the approaches offer potential for significant value over the life of DOE and INEEL remediation and stewardship activities. This value will be realized through vastly improved surface characterization, leading to augmented understanding of the structure and reactivity at the top monolayer.

# REFERENCES

1. Evans, L. J., "Chemistry of Metal Retention by Soils," *Environ. Sci. Technol.*, 1989**,** *23*, 1046-1056.

2. Bargar, J. R.; Brown, G. E.; Parks, G. A., "Surface complexation of Pb(II) at oxide-water interfaces .1. XAFS and bond-valence determination of mononuclear and polynuclear Pb(II) sorption products on aluminum oxides," *Geochimica Et Cosmochimica Acta*, 1997**,** *61*, 2617-2637.

3. Bargar, J. R.; Brown, G. E.; Parks, G. A., "Surface complexation of Pb(II) at oxide-water interfaces .2. XAFS and bond-valence determination of mononuclear Pb(II) sorption products and surface functional groups on iron oxides," *Geochimica Et Cosmochimica Acta*, 1997**,** *61*, 2639-2652.

4. Turner, G. D.; Zachara, J. M.; McKinley, J. P.; Smith, S. C., "Surface-charge properties and $UO_2^{2+}$ adsorption of a subsurface smectite," *Geochimica Et Cosmochimica Acta*, 1996**,** *60*, 3399-3414.

5. Zachara, J. M.; McKinley, J. P., "Influence of Hydrolysis On the Sorption of Metal-Cations By Smectites - Importance of Edge Coordination Reactions," *Aquatic Sciences*, 1993**,** *55*, 250-261.

6. Knox, R. C. S., D. A. *Transport and Remediation of Subsurface Contaminants*; American Chemical Society: Washington, D. C., 1992.

7. Akolekar, D. B.; Bhargava, S.; van Bronswijk, W., "Fourier transform Raman spectroscopy of novel aluminophosphate molecular sieves," *Applied Spectroscopy*, 1999**,** *53*, 931-937.

8. Frost, R. L.; Kloprogge, J. T.; Russell, S. C.; Szetu, J., "Dehydroxylation and the Vibrational Spectroscopy of Aluminum (Oxo)hydroxides Using Infrared Emission Spectroscopy. Part III: Diaspore," *Applied Spectroscopy*, 1999**,** *53*, 829-835.

9. Frost, R. L.; Kloprogge, J. T.; Russell, S. C.; Szetu, J. L., "Vibrational spectroscopy and dehydroxylation of aluminum (oxo)hydroxides: Gibbsite," *Applied Spectroscopy*, 1999**,** *53*, 423-434.

10. Knight, C. N. L.; Williamson, M. A.; Bodnar, R. J. In *Microbeam Analysis*; Russell, P. E., Ed.; San Francisco Press, Inc.: San Francisco, *1989*, pp 571-573.

11. Morris, D. E.; Allen, P. G.; Berg, J. M.; ChisholmBrause, C. J.; Conradson, S. D.; Donohoe, R. J.; Hess, N. J.; Musgrave, J. A.; Tait, C. D., "Speciation of uranium in Fernald soils by molecular spectroscopic methods: Characterization of untreated soils," *Environmental Science & Technology*, 1996**,** *30*, 2322-2331.

12. Bach, H., "Advanced Surface Analysis of Silicate Glasses, Ocides and Other Insulating Materials: A Review," *J. of Non-Crystalline Solids*, 1997**,** *209*, 1-18.

13. Dent, A. J.; Ramsay, J. D. F.; Swanton, S. W., "An EXAFS Study of Uranyl Ion in Solution and Sorved onto Silica and Montmorillonite Clay Colloids," *Journal of Colloid and Interface Science*, 1992**,** *150*, 45-60.

14. Manceau, A.; Boisset, M.; Sarret, G.; Hazemann, J.; Mench, M.; Cambier, P.; Prost, R., "Direct Determination of Lead Speciation in Contaminated Soils by EXAFS Spectroscopy," *Env. Sci. Tech.*, 1996**,** *30*, 1540-1552.

15. Moulin, C.; Charron, N.; Plancque, G.; Virelizier, H., "Speciation of uranium by electrospray ionization mass spectrometry: comparison with time-resolved laser-induced fluorescence," *Applied Spectroscopy*, 2000**,** *54*, 843-8.

16. Groenewold, G. S. D., J. E.; Olson, J. E.; Appelhans, A. D.; Ingram, J. C.; Dahl, D. A., "Secondary Ion Mass Spectrometry of Sodium Nitrate: Comparison of ReO4- and Cs+ Primary Ions," *Int. J. Mass Spectrom. Ion Proc.*, 1997, *163*, 185-95.

17. Groenewold, G. S. A., A. D.; Ingram, J. C., "Characterization of bis(alkylamine)mercury Cations from mercury Nitrate Surfaces by Using an Ion Trap Secondary Ion Mass Spectrometry," *J. Amer. Soc. Mass Spectrom.*, 1998**,** *9*, 35-41.

18. Van Stipdonk, M. J.; Justes, D. R.; Force, C. M.; Schweikert, E. A., "Speciation of sodium nitrate and sodium nitrite using kiloelectronvolt energy atomic and polyatomic and megaelectronvolt energy atomic projectiles with secondary ion mass spectrometry," *Analytical Chemistry*, 2000**,** *72*, 2468-74.

19. Van Stipdonk, M. J.; English, R. D.; Schweikert, E. A., "SIMS of organic anions adsorbed onto an aminoethanethiol self-assembled monolayer: an approach for enhanced secondary ion emission," *Analytical Chemistry*, 2000**,** *72*, 2618-26.

20. Neubauer, K. R.; Johnston, M. V.; Wexler, A. S., "Chromium Speciationin Aerosols by Rapid Single-Particle Mass Spectrometry," *Int. J. Mass Spectrom and Ion Proc.*, 1995**,** *151*, 77-87.

21. Zenobi, R., "Advances in Surface Analysis and mass Spectrometry Using Laser Desorption Methods," *Chimia*, 1994**,** *48*, 64-71.

22. Zenobi, R., "In Situ Analysis of Surfaces and Mixtures by Laser Desorption Mass Spectrometry," *Int. J. of Mass Spectrom. Ion Proc.*, 1995**,** *145*, 51-77.

23. Voumard, P.; Zhan, Q.; Zenobi, R., "A New Instrument for Spatially Resolved Laser Desorption/ Laser Multiphoton Ionization Mass Spectrometry," *Rev. Sci. Instrum.*, 1993**,** *64*, 2215-2220.

24. Savina, M. R.; Lykke, K. R., "Chemical Imaging of Surfaces with Laser Desorption Mass Spectrometry," *Trends in Analytical Chemistry*, 1997**,** *16*, 242-251.

25. Todd, J. F. J. In *Practical Aspects of Ion Trap Mass Spectrometry*; March, R. E., Todd, J. F. J., Eds.; CRC Press: New York, 1995; Vol. 1, p 4.

26. Brodbelt, J. S., "Effects of Collisional Cooling on Ion Detection," *CRC Press*, 1995, 209-220.

27. Van Vaeck, L.; Van Roy, W.; H., S.; Adams, F.; Caravatti, P., *Rapid Commun. Mass Spectrom.*, 1993**,** *7*, 323.

28. Brenna, J. T.; Creasy, W. R.; McBain, W.; Soria, C., *Rev. Sci. Instrum.*, 1988**,** *59*, 873.

29. Pelletier, M.; Krier, G.; Muller, J. F.; Weil, D.; Johnston, M., *Rapid Commun. Mass Spectrom.*, 1988**,** *2*, 146.

30. Behm, J. M.; Hemminger, J. C.; Lykke, K. R., *Anal. Chem.*, 1996**,** *68*, 713.

31. Van Vaeck, L.; Struyf, H.; Van Roy, W.; Adams, F., *Mass Spectrom. Rev.*, 1994**,** *13*, 189.

32. Schmidt, E. G.; Fiorentino, M. A.; Arkin, C. R.; Laude, D. A., *Anal. Chem.*, 2000**,** *72*, 3568.

33. Schweikhard, L.; Guan, S.; Marshall, A. G., *Int. J. Mass Spectrom. Ion Processes*, 1992**,** *120*, 71.

34. Campbell, V. L.; Guan, Z.; Vartanian, V. H.; Laude, D. A., *Anal. Chem.*, 1995**,** *67*, 420.

35. Litaor, M. I. I., S. A., *J. Environ. Qual.*, 1996**,** *25*, 1144-1152.

36. Groenewold, G. S. K., G. F.; Scott, J. R.; Gianotto, A. K.; Appelhans, A. D.; Delmore, J. E., "Secondary ion mass spectrometry of zeolite materials observed using an ion trap," *Analytical Chemistry*, 2001**,** *73*, in press.

37. Lafargue, P. E.; Gaumet, J. J.; Muller, J. F.; Labrosse, A., "Laser Ablation of Silica: Study of Induced Clusters by Fourier Transform Ion Cyclotron Resonance Mass Spectrometry," *Journal of Mass Spectrometry*, 1996**,** *31*, 623-632.

38. Lafargue, P. E.; Gaumet, J. J.; Muller, J. F., "Analysis of Thermally Treated Silica Gel Using Fourier Transform Ion Cyclotron Resonance Mass Spectrometry," *Chemical Physics Letters*, 1998**,** *288*, 494-498.

39. Groenewold, G. S. A., A. D.; Gresham, G. L.; Ingram, J. C.; Shaw, A. D., "Characterization of Copper Chloride Cluster Ions Formed in SIMS," *Int. J. Mass Spectrom. Ion Proc.*, 1998**,** *178*, 19-29.

40. Scott, J. R. G., G. S.; Gianotto, A. K.; Benson, M. T.; Wright, J. B., "Experimental and Computational Study of Hydration of Reactions of Aluminum Oxide Anion Clusters," *J. Phys. Chem. A*, 2000**,** *104*, 7079-90.

# Chemical and Biological Reactions at Environmental Surfaces

**William F. Bauer, George D. Redden, Joni M. Barnes**

## SUMMARY

Interpreting contaminant transport, natural attenuation, or active remediation in subsurface environments relies heavily upon the ability to correlate chemical speciation to mobility and bioavailability. Mobility and bioavailability can change in response to variations in chemical or in physical parameters. Surface chemistry plays a central role in this process, because contaminants are in constant contact with mineral surfaces in the subsurface environment. The work described here has been continued from FY 1999 and is designed to address factors that may affect chemical speciation and interactions at mineral surfaces. Our accomplishments have included (a) work to identify and characterize extracellular compounds produced by the iron reducing bacterium *Shewanella putrefaciens*, (b) a study of how microbes interact with mineral surfaces and how surface mineralogical heterogeneities may affect these interactions and the distribution of microbes on mineral surfaces, (c) evaluation of a technique with the potential to probe the interface between surface adhered microbes and the surface, (d) a study on the interaction of "model extracellular compounds" on surface complexation of uranyl ions, and (e) a statistical evaluation of the mass action expression for multidentate surface complexation. Some specific accomplishments and conclusions are (a) determination that the iron-reducing bacteria *Shewanella putrefaciens* selectively seeks out iron oxide surfaces under anaerobic conditions, (b) isolation of surface adhering and nonadhering strains of *Shewanella putrefaciens*, (c) demonstration of a technique using fluorescent probes with excitation via attenuated total reflectance to probe mineral-bacteria interfacial zones, (d) completion of a study concerning the surface complexation in a citrate-uranyl-goethite system, and (e) simulations performed to evaluate the appropriateness of the mass action expression commonly used to describe surface complexation.

## PROJECT DESCRIPTION

### Introduction

Evaluating and interpreting empirical and modeled data concerning contaminant transport, natural attenuation, or active remediation in subsurface environments relies upon the ability to correlate chemical speciation to contaminant mobility and bioavailability. Both can change in response to variations in chemical (pH, ionic strength, co-contaminants, $CO_2$, chelators, etc.) or physical (temperature, flow) parameters. Surface chemistry also plays a large role in this process, since contaminants are in constant contact with mineral surfaces in the subsurface environment. A more thorough knowledge of chemical speciation and surface chemical interactions is necessary to correlate chemical speciation to mobility and bioavailability.

Many microbial species produce iron-sequestering compounds known as siderophores. These primarily consist of hydroxamates and catechols that are expected to play a significant role in environmental surface chemistry, since their function is to make iron from highly insoluble iron oxides available for metabolic processes. These compounds will also affect contaminant transport by either mobilizing or immobilizing the contaminant via complexation chemistry.

Iron reducing bacteria also produce enzymes (e.g., cytochromes) that can reduce Fe(III) sequestered by a siderophore in solution or facilitate electron transport directly at a mineral surface containing Fe(III). The reducing enzymes tend to be found in cell membranes, but preliminary work in our laboratory indicates that they might also be found extracellularly at low concentrations.

The surface chemistry associated with these extracellular chemicals and the bacteria that produce them is largely unknown. Surface complexation models have been developed to describe the macroscopic partitioning of inorganic species (such as heavy metal ions) on mineral or organic substrates. These models are very successful at simulating experimental data but are poorly constrained, as there are a large number of unverified or unverifiable parameters. One particular problem involves the mass action expression for surface reactions that involve more than one reactive surface site. Surface complexation models were originally formulated under the assumption that surface reactions can be represented as analogous to the thermodynamic description of the chemical stoichiometry in homogeneous solutions. However, reactive surface sites are fixed in space, and their geometric distribution depends on the solid matrix. It is inappropriate to use the same stoichiometric coefficients to express surface reactions involving multiple surface sites.

The work described here has been continued from FY 1999 and has included (a) work to identify and characterize extracellular compounds produced by the iron reducing bacterium *Shewanella putrefaciens*, (b) a study of how microbes interact with mineral surfaces and how surface mineralogical heterogeneities may affect these interactions and the distribution of microbes on mineral surfaces, (c) evaluation of a technique with the potential to probe the interface between surface adhered microbes and the surface, (d) a study on the interaction of "model extracellular compounds" on surface complexation of uranyl ions, and (e) a statistical evaluation of the mass action expression for multidentatesurface complexation.

## Microbial Interactions with Mineral Surfaces

### Extracellular Compounds

Microbial activity can affect the mobility of contaminants in the subsurface by direct or secondary interactions. Secondary interactions may be the result of extracellular compounds produced by microbes. Extracellular compounds can affect the chemical speciation of contaminants in the subsurface through either redox chemistry, complexation, or competition for binding sites. During FY 1999, work in our laboratory indicated the presence of multiple extracellular compounds produced by the dissimulatory iron-reducing bacterium *Shewanella putrefaciens*. These compounds included siderophores and, possibly, as many as two extracellular reductases in the form of cytochromes. The two different cytochromes may have been produced in response to different growth conditions. While siderophores are commonly reported, extracellular reductases have not been routinely reported in the literature. During FY 2000, experiments were conducted to verify the presence and identity of extracellular siderophores and reductases. Although other researchers have examined the effect of respiratory substrate on the cytochrome content of *Shewanella putrefaciens*, only soluble or limited kinds of electron acceptors have been typically used and usually a single cytochrome identified.[1-3] The cytochrome identified has been reported with a wide range of different molecular weights. In addition, the effect of available electron acceptors on the production of extracellular reductases has not been reported.

Work was conducted to verify the presence of extracellular reductases and siderophores that were observed previously and to assess the effects of growth conditions on their production. For each extracellar compound detected, the goal was to determine if its production was in response to a particular condition such as contact with an iron oxide surface. In the experiment, *Shewanella putrefaciens* was cultured in M-1 medium containing lactate as a carbon and energy source and either oxygen, nitrate, ferric EDTA (ethylene-diamine-tetraacetic acid), ferric oxide, or manganese oxide as electron acceptors. Cells were grown aerobically, anaerobically, or shifted from aerobic to anaerobic conditions. An increase in cell numbers and significant use of the terminal electron acceptor was used as criteria for growth. Over the course of the experiment, growth medium was collected from each of the cultures filtered and lyophilized. The microbes were found to grow better and more consistently on the natural hematite (Wards Scientific) than with *synthetic* iron oxide (Fisher Scientific). Figure 1 is a photoacoustic-infrared spectrum of the synthetic iron oxide and the natural hematite. Natural hematite contains silicates and several forms of iron oxide, and this complexity is reflected by the spectrum. The lyophilized samples from these experiments are to be analyzed by electrospray ionization mass spectrometry (ESI-MS) and by high-pressure liquid chromatography (HPLC), and possibly HPLC coupled with ESI-MS if the preliminary data is promising. The ESI-MS instrument finally became available for use in August of this year and we have begun preliminary examination of these samples. The ESI-MS and HPLC analyses will be completed in September of this year.

During program review at the end of FY 1999, the suggestion was made to use a "more environmentally relevant" iron-reducing bacterium in these sets of experiments. Therefore, a culture of *Geobacter metallireducens* was purchased from the American Type Culture Collections (ATCC 53774) with the intent of including this microbe in the above described experiments for comparison. Although growth of this organism did occur, at least two other facultative organisms grew as well. Our efforts to isolate the *Geobacter m*etallireducens using plating techniques was unsuccessful. A second culture was ordered from *Deutche Sammlung von Mikroorganismen und Zellkulturen* (DSMZ) in Braunschweig,

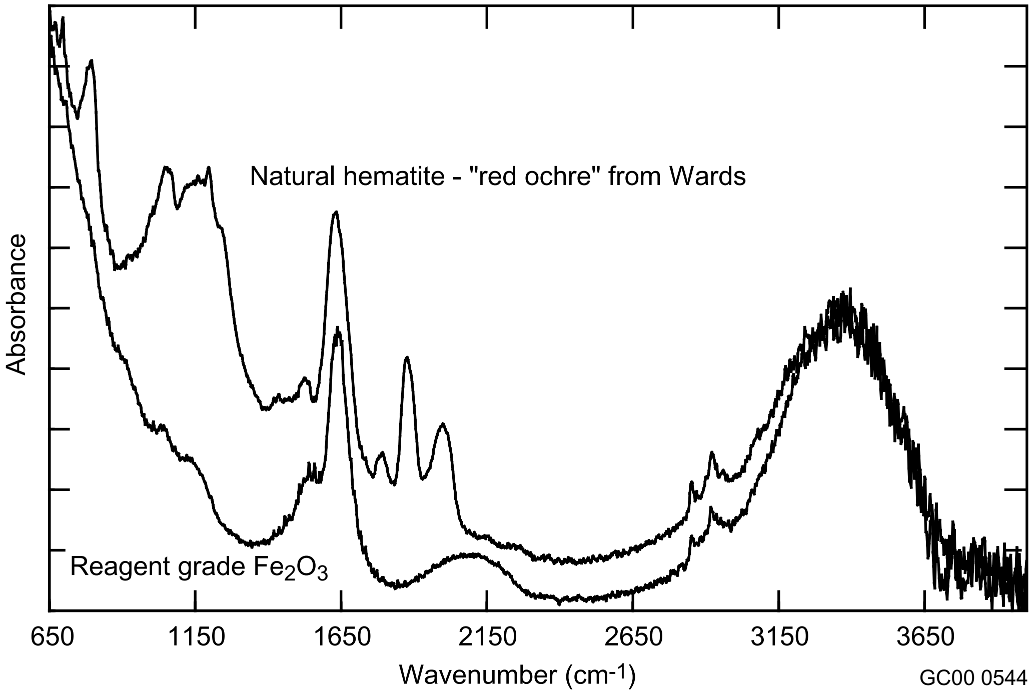

**Figure 1.** PAS infrared spectra of hematite and reagent grade $Fe_2O_3$.

Germany. DSMZ is preparing a live culture and verifying the purity. This culture has not yet been received at the INEEL.

The ultimate research goal is to examine the interaction of bacterial siderophores and iron reducing enzymes with mineral surfaces. A study was conducted to demonstrate the effect of extracellular compounds on the growth of dissimulatory iron-reducing bacteria. A culture of *Shewanella putrefaciens* was grown anaerobically to late log phase in M-1 medium containing natural hematite ground to <38 μm. The growth medium was then harvested by filtration and lyophilized to concentrate extracellular compounds. Anaerobic growth and iron reduction of *Shewanella putrefaciens* in M-1 was then compared to that in M-1 amended with the lyophilate. Cells grown in the presence of ferrous iron and abiotic controls were included in the study. Samples, which were collected over a 23-day period, were analyzed for cell numbers, total iron, ferrous iron, and lactate. The results of this experiment are shown in Figure 2. Growth rates for the lyophilate amended medium were initially as much as five times that of the simple medium. This growth rate difference decreased to only about a factor of two by day 10 of the experiment. The enhanced growth rate results from the presence of extracellular compounds, most likely siderophores already present in the amended medium. The microbes in the amended medium derived immediate benefit from the chelating properties of these compounds, which delivered complexed Fe(III) for use in their respiration. This experiment demonstrated the potential effect that microbially produced compounds may have on the bioavailability of nutrients.

### Surface Colonization by Iron-Reducing Bacteria

Experiments in FY 1999 using atomic force microscopy demonstrated that *Shewanella putrefaciens* tends to populate the surface in tightly packed colony-like groupings firmly associated with a hematite surface. These colony-like groupings make sense from the standpoint of the bacteria, because the tight grouping is much more likely to yield a return on the energy investment of producing extracellular compounds. The close association of the microbes with the hematite surface is interesting, since it is not clear whether direct association with the mineral surface is a requirement.[4-8] To determine whether the observed colonies originate from adhered bacteria or whether the microbes in suspension preferentially attach in clusters, a series of experiments were designed to allow the observation of the development of these groupings. The experiments were also designed to determine if the bacteria selectively colonize Fe(III) mineral surfaces.

For these experiments, a continuous flow anaerobic bioreactor and laminar flow cell containing four different mineral surfaces—silica, labradorite, augite, and hematite—were used. The surface of each mineral was indexed to allow tracking of colony development over time. At select time periods, the flow cell was removed from the continuous flow bioreacter, the flow cell flushed to remove non-adhering cells, the remaining cells stained with the fluorescent nucleic acid stain, 4P-diamidine-2-phenyl indole (DAPI), and images collected at the indexed points on each of the minerals. DAPI was selected because it was reported to have the least effect on the viability of the microbes of any of the common dyes. Initially, the continuous flow bioreacter was charged with $10^8$ cells/mL and one or more solid hematite pellets or powdered natural hematite <38 μm in diameter.

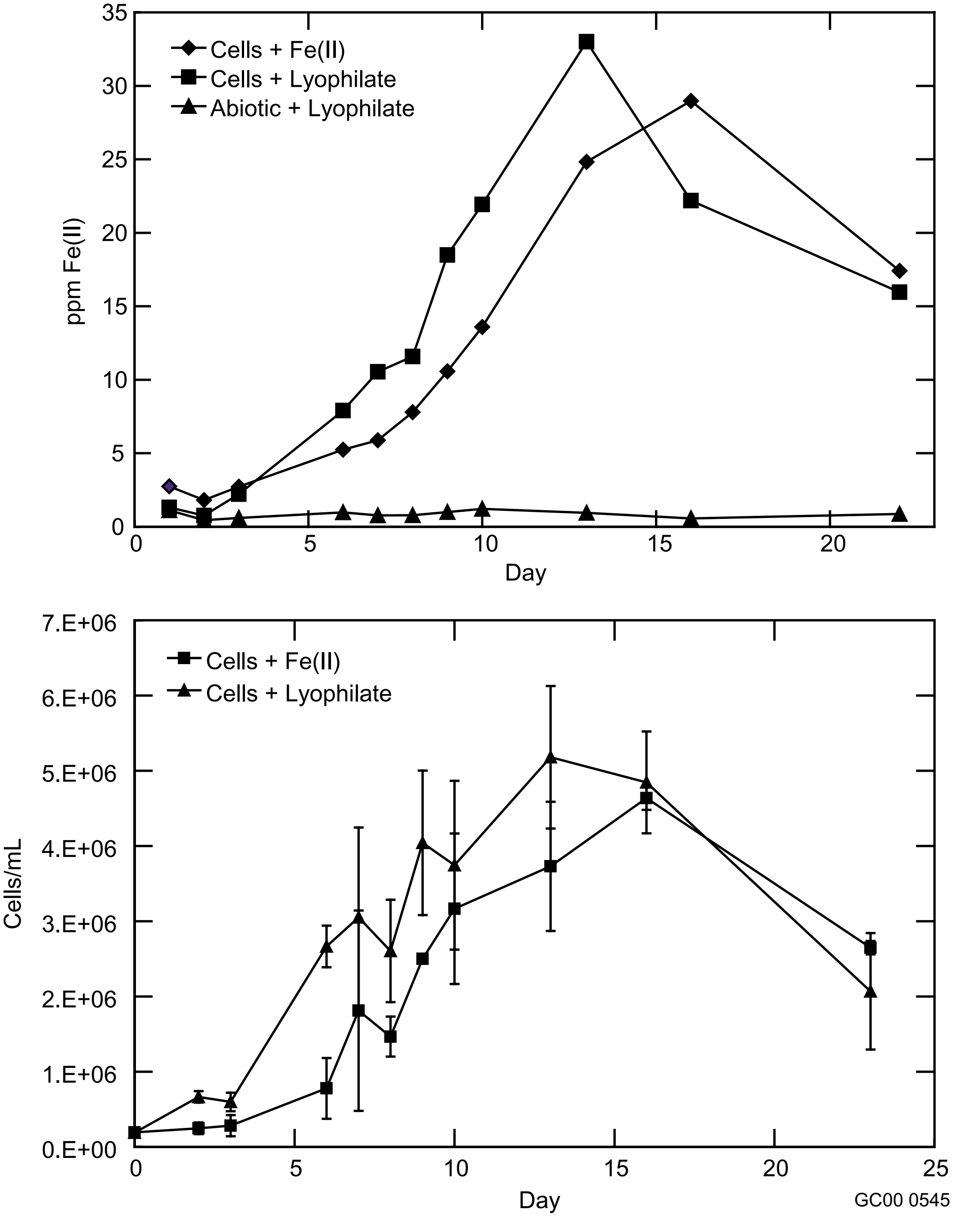

**Figure 2.** Influence of extracellular compounds in a lyphillate from a previous culture on the growth rate of Shewanella putrefaciens in demonstrated by the $Fe^{2+}$ concentration (top) and the total cell numbers (bottom). Initial overall growth rates with the lyophilate were as much at two to five times greater for the first 10 days.

The results from the initial experiments were ambiguous, for a number of reasons. The initial high cell density of $10^8$ cells/mL was selected to ensure that enough cells would be available for colonization in a reasonable time. But this was found to be too many cells, and washing out of any nonadhering cells was extremely difficult. The difficulty in removing the nonadhering cells was exacerbated by the surface potential of the coverslip, which had nearly as many loosely associated cells as the mineral surfaces. The coverslip was silanized for subsequent experiments. Because only the supernatant from the bioreacter was passed through the flow cell containing minerals, *nonadhering* bacteria were likely being selected, because we had now recreated a continuous flow version of the Caccavo experiment in which strains of surface adhesive and surface nonadhesive *Shewanella alga* were isolated.[4] Even with these problems, some strongly surface-associated cell groupings were observed; however, they faded with time and became unobservable. It is likely that these cells died after repeated doses of the DAPI.

Currently, colonization studies are being repeated using a new stock culture of *Shewanella putrefaciens*. Originally, the culture was obtained from the American Type Culture Collection (ATCC). When we received it in the laboratory, it was grown in nutrient broth and split. One portion was used for experimental work and frozen, the other kept for future use. The rational for using the stored cells as the inoculum for the experiment was to remove the possibility that the routine anaerobic culture conditions being used to grow and maintain the bacteria were selecting cells that were adhesion deficient.

Starting with a low cell density ($10^5$ cells/mL) in the bioreactor reservoir and allowing the minerals in the flow cell to be the only source of ferric iron in the system appears to provide favorable operating conditions for selective adhesion of iron-reducing bacteria. The inoculum for the bioreactor was from a culture of *Shewanella putrefaciens* grown aerobically to log phase and then used to inoculate the bioreactor reservoir, which contained 50 mL of anaerobic M-1. The diluted culture ($2.4 \times 10^5$ cells/mL) was then pumped through the flow cell at a rate of 4 mL/hr. The cell is tilted so that the medium first passes over the silica and then up at about a 75-degree angle over the labradorite, augite, and hematite, respectively, before returning to the bioreactor reservoir. After 3 days of operation, the cells were exposed to a fluorescent nucleic acid stain (DAPI) and then viewed microscopically. Cell numbers on the surface of each mineral were counted in 10 randomly selected fields. Staining and viewing of the cells was repeated on day 6 and day 11. Table 1 shows the initial results of these cell counts. The cells are definitely selecting for the hematite and against the other minerals. On day six, the overall count dropped significantly, and several obviously flagellated bacteria were noted. The drop in cell numbers and presence of the *swimming* bacteria are most likely associated with changes in the population dynamics associated with the abrupt change from aerobic to anaerobic conditions and the limited source of terminal electron acceptors. Some of the microbes appear to be firmly adhered, others only loosely bound. The loosely bound cells may be electrostatically adhered. Based upon surface charge, silica should have a negative surface, while the hematite a positive surface.[9] Augite and laboradorite are expected to have surface charges close to neutral at neutral pH.[9] Based upon the observations in Table 1 and the concept of electostatic adhesion, it therefore appears that this particular labradorite has a slightly more positive surface than the augite.

The inability to visualize cells over time due to fading and toxicity of DAPI remains a problem. In an effort to circumvent this problem, we are considering an experiment in which multiple flow cells will be operated concomitantly and one flow cell is removed at each of the predetermined intervals for cell imaging and counting.

**Table 1.** Cell counts in average number of cells per field on the minerals in continuous flow cell.

| | Average Number of Cells in 10 Fields (SD) | | |
|---|---|---|---|
| Mineral | Day 3 | Day 6 | Day 11 |
| Hematite | 60 (13.94) | 28 (6.64) | 78 (29.04) |
| Augite | 3 (2.21) | 7 (1.47) | 10 (8.89) |
| Labradorite | 6 (3.91) | 10 (3.72) | 21 (7.40) |
| Silica | 7 (9.83) | 6 (4.23) | 7 (3.01) |

## Strain Selection

During the initial experiments with the flow cell, it became apparent that we may have been selecting for a nonsurface-adhering strain of the bacterium *Shewanella putrefaciens*. Previously, it had been demonstrated that such a selection could occur for *Shewanella alga*.[4] To verify that this is possible with *Shewanella putrefaciens* under strict anaerobic conditions, we initiated an experiment to isolate a nonsurface-adhering strain of this microbe.

To isolate the surface adhering and nonadhering strains of *Shewanella putrefaciens*, cells are grown under anaerobic conditions in mineral salts medium (M-1) containing lactate and natural hematite. Selection of nonadhering cells involves removing the liquid from the culture, centrifuging it at a low speed to remove any iron oxide particles, and then using the supernatant to inoculate fresh growth medium containing new natural hematite. To select for cells that specifically adhere to the iron oxide, the mineral particles are allowed to settle out of solution and an aliquot of the solids is then transferred into fresh medium containing hew hematite. Subculturing is done every 7 to 10 days, and cell numbers and iron reduction are monitored.

Cell numbers are determined using the following technique. Prior to mixing, a liquid sample is removed from each culture. The culture is then mixed and a sample of the hematite slurry is removed. To determine the number of non-adhering cells present in each culture the liquid sample is centrifuged at a low speed (100 × g, 2 minutes) and an aliquot (100 μL) of the supernatant mixed with acridine orange. After staining, the cells are collected onto a polycarbonate (PC) membrane and then counted using epifluorescent microscopy. The total number of cells in each culture is determined after the cells are dislodged from the surface of the mineral particles. The protocol involves adding an aliquot (100 μL) of the hematite slurry sample to an aqueous mixture of acridine orange (100 μg/mL), glutaraldehyde (1%), and Tween 80 (0.01%). The diluted slurry is then sonicated in a Branson Ultrasonic Cleaner for 30 minutes followed by low speed centrifugation (100 × g, 2 minutes). The supernatant is collected onto a PC membrane and the cells counted. The number of adhered cells is calculated by taking the difference between the total cell number and the number of nonadhering cells.

Table 2 shows the results of this work to date. After 4–5 cycles, it appears that only ~70 % of the cells originating from the cultures initiated with the supernatant are attached to the iron oxide. This is roughly comparable to the results of Caccavo after this many cycles.[4] In cultures inoculated with microbes attached to iron oxides, >90% of all bacteria are attached to the mineral phase. This result confirms the earlier suspicions that selection for nonsurface-adhering microbes can occur unwittingly in laboratory experiments.

**Table 2.** Selection of surface-adhering and nonsurface-adhering strains of *Shewanella putrefaciens* under anaerobic conditions.

| **Nonsurface-Adhering Strain** | | | | |
|---|---|---|---|---|
| | **cells/mL** | | | |
| **Cycle** | **total** | **Unattached** | **attached** | **% attached** |
| 4 | 2.00E+06 | 6.52E+05 | 1.35E+06 | 67 |
| 5 | 4.00E+06 | 1.00E+06 | 3.00E+06 | 75 |
| **Surface-Adhering Strain** | | | | |
| | **cells/mL** | | | |
| **Cycle** | **total** | **Unattached** | **attached** | **% attached** |
| 4 | 4.03E+07 | 3.16E+06 | 3.71E+07 | 92 |
| 5 | 4.20E+07 | 3.70E+06 | 3.83E+07 | 91 |

Caccavo[4] attributed the surface adhesion properties of the surface adhering and nonsurface-adhering strains of *Shewanella alga* to the relative hydrophobicity of the microbial surfaces of his isolates. The surface of the iron oxide adhering bacteria was determined to have a more protein-like surface, while the nonadhering strain was more polysaccharide-like. More recent work indicates that there may be specific proteins on the bacterial surface that bind specifically to the iron oxide surface.[10] A brief experiment was initiated to determine whether infrared spectroscopy could detect the microbes on a powdered hematite surface and subsequently determine whether the microbes had more protein-like or polysaccharide-like surfaces. Photoacoustic infrared spectroscopy was selected because it is relatively sensitive for detecting surface and interfacial chemical properties[11-13] and because changes in the amide I, II, and III bands relative to the bands generally associated with carbohydrates in the 1200-1000 $\text{cm}^{-1}$ region should give a clear indication of the protein versus polysaccharide nature of the cell.

*Shewanella putrefaciens* was grown in M-1 containing lactate and natural hematite that had been crushed and sized to <38 μm. Cells were grown under both aerobic and anaerobic conditions, and cultures were set up in triplicate. On a daily basis, three aliquots (0.5 mL) of the slurried hematite were taken from each culture and allowed the solids to settle out over a 2-hr period. The liquid was then pipetted off and analyzed for total iron. To remove residual growth medium, the solids were resuspended in water, centrifuged, and the liquid decanted. The solids were washed a second time using the same technique and then lyophilized. Infrared spectra were collected using a BioRad FTS 65 FTIR equipped with a MTEC Model 300 Photacoustic Cell (MTEC Photoacoustic, Inc., Ames IA). Each spectrum was the result of 256 coadded scans at a sampling rate of 2.5 kHz. The resulting single-beam spectra were ratioed to a single-beam spectrum of carbon black to obtain an absorbance spectrum.

Visual examination of the spectra of unexposed hematite, the hematite exposed to the M-1 medium, and hematite exposed to the inoculated M-1 medium for various lengths of time under aerobic and anaerobic conditions, failed to identify any unique features. The data set consisting of 129 spectra were then submitted to a factor analysis (i.e., principal components analysis, PCA). The factor analysis generally indicated that >99% of the variance was contained in the first factor. The only major, clearly distinguished group identified from the score plots was the hematite that had not been exposed to any medium. The exposure of the hematite to the medium obviously changed the surfaces of the hematite as more FeOOH species were present. No obvious effects of the microbes could be observed in the spectra. However, one of the statistically significant factors (factor 5) closely matched the spectrum of *Shewanella putrefaciens* (see Figure 3). This factor accounted for much less than 0.1% of the total variance in the data set. Microscopic examination of the hematite particles generally indicates that they are nearly completely covered with the microbes. It is not known why they were not clearly identified by this technique. One possibility is that the surface of the microbes became completely coated with an iron oxide precipitate, as suggested by the work of Ferris.[14-16] However, sampling depths by this technique should be several microns. A faster sampling rate may decrease the significance of the bulk material in the spectrum and enhance the spectral signature of the surface microbes.

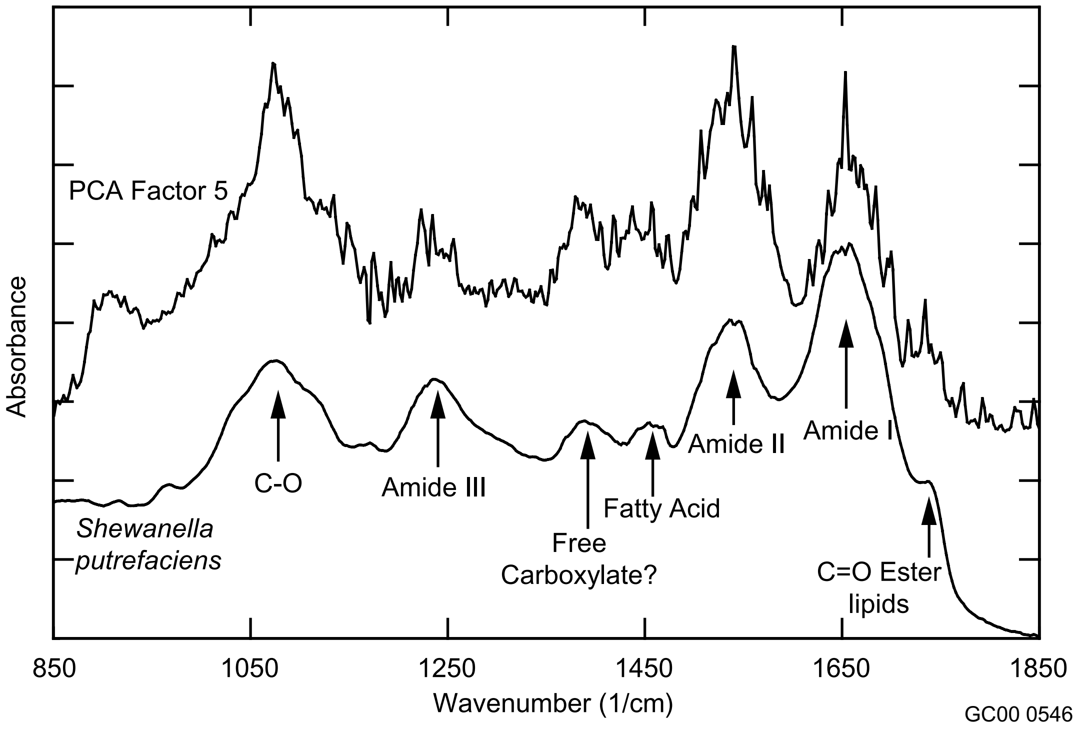

**Figure 3.** Photoacoustic infrared spectrum of Shewanella putrefaciens and PCA factor 5 from analysis of natural hematite exposed to Shewanella putrefaciens.

### Probing Interfacial Regions with Attenuated Total Reflectance

One of the lingering questions concerning microbial interactions with mineral surfaces is what are the chemical conditions in the interfacial zone between the microbe or biofilm and the mineral. It is extremely difficult to directly probe this interfacial zone using common spectroscopic techniques, since they are designed to either measure bulk sample properties or are affected by the bulk sample properties. During the program review at the end of FY 1999, the suggestion was offered that attenuated total reflectance (ATR) techniques may be useful in probing the interfacial zones with certain chemical probes, provided that a sufficiently thin, optically transparent film could be deposited on the ATR element. Since we were ultimately interested in determining such chemical properties as pH and potential, for which there are fluorescent probes available, we attempted to detect fluorescence excited with an evanescent wave. Figure 4 is a schematic of the proposed experiment showing an optical fiber from which the cladding has been removed. The exposed fiber is coated with a thin layer of iron oxide that is then exposed to microbes, which will adhere to the iron oxide film. The system is then exposed to the fluorescent chemical

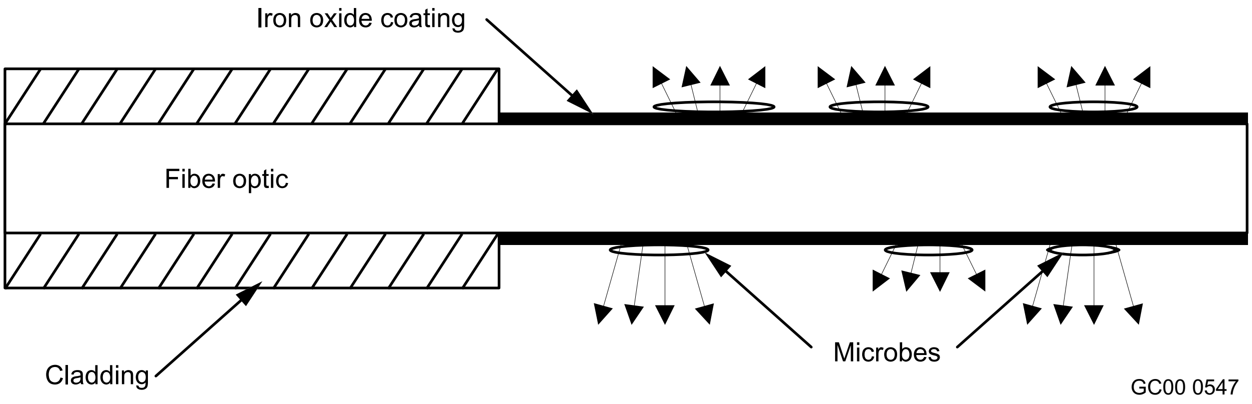

**Figure 4.** Schematic of an experiment to illuminate the interfacial zone between an iron oxide surface and an adhered microbe by attenuated total reflectance using an iron-oxide-coated optical fiber as the ATR element.

probe, which is excited by light passing through the fiber. With a silica fiber and an iron oxide film, we determined that the evanescent wave should penetrate to a depth sufficient to probe the interface between the microbe and the surface and through the cell wall.

Attenuated total reflectance-based materials were prepared for the surface selective excitation of fluorescent probes at FeOOH interfaces. In order to make these materials, it was necessary to prepare FeOOH thin films on silica optical fibers. Polymer-clad optical fibers were obtained from a commercial vendor and removed the polymer cladding from the end portion of the fiber. The exposed silica core was then cleaned using a series of separate chemicals. It was first washed with acetone, then followed by treatments to 30% $H_2O_2$, then NaOH, and finally water. FeOOH films were then prepared on the silica fiber using three different solution deposition methods reported in the literiture.[5,6,17] In the first method, the fiber was placed in a solution of $FeCl_3$ (0.1 M) with NaCl (0.05 M), and the pH was adjusted to the range of 6-7 using NaOH. The fiber was left in the solution for up to 2 days, after which the fiber was removed, rinsed with water, and dried. In the second method, the fiber was suspended in a 0.1-M solution of $FeSO_4$ and 1 drop of 30% $H_2O_2$ was added. After about 24 hours, the fiber was removed, rinsed with water, and allowed to dry. In the third method, $FeCl_3$ solution was mixed with $NH_4OH$, and the FeOOH precipitate was washed with water. The wet FeOOH was then dissolved in 1.0 M $NH_4F{\bullet}HF$, mixed with an equal portion of 0.5 M $H_3BO_3$, and allowed to sit at 30°C for 20 hours. The fiber was then rinsed and allowed to dry.

The films prepared using all three methods were thin and irregular. The fiber preparation conditions, such as the solvent, length of time the fiber was soaked, the temperature, and the concentration of the NaOH solution, were varied with little or no effect. Thicker films were also prepared by repeating the coating process; however, in no case were uniform films obtained.

Even though uniform coatings were not obtained, some fibers were exposed to fluorescing solutions and microbes subsequently stained with a fluorescent dye to confirm the feasibility of the technique. Fluorescence microscopic imaging of microbes stained with acridine orange (AO) on the FeOOH films were obtained using evanescent wave excitation. The fluorescence emission intensity was weak, requiring the use of long integration times and image averaging. The fluorescence emission intensity is low due to the small number of molecules excited at the interface and poor optical coupling of the excitation light to the interface. The top image in Figure 5 shows a representative epifluorescent image of the microbes on the surface of the iron-oxide-coated fiber. The bottom image in Figure 5 shows a portion of the same surface from the bottom up, because it was excited by the evanescent wave created by a 488-nm $Ar^+$ laser beam passing through the fiber. Cells and portions of cells can be discerned in the evanescent-wave-excited image demonstrating that the technique may be useful. In an attempt to acquire more useful data, film preparation conditions were varied in hope of getting more uniform films and thus obtain better coupling of the excitation light to the FeOOH/aqueous interface. As implied above, these efforts were largely unsuccessful. Other film preparation techniques, such as chemical vapor deposition or FeOOH doped sol-gel coatings, may be more suitable for preparing uniform coatings with good optical coupling characteristics. Increasing the sensitivity of the image acquisition system would also be highly desirable and would allow imaging at much lower fluorescence emission intensities.

We will expand the software program developed for this project in the future to allow greater flexibility in the physical and chemical characteristics of adsorbing species and the hypothetical surface.

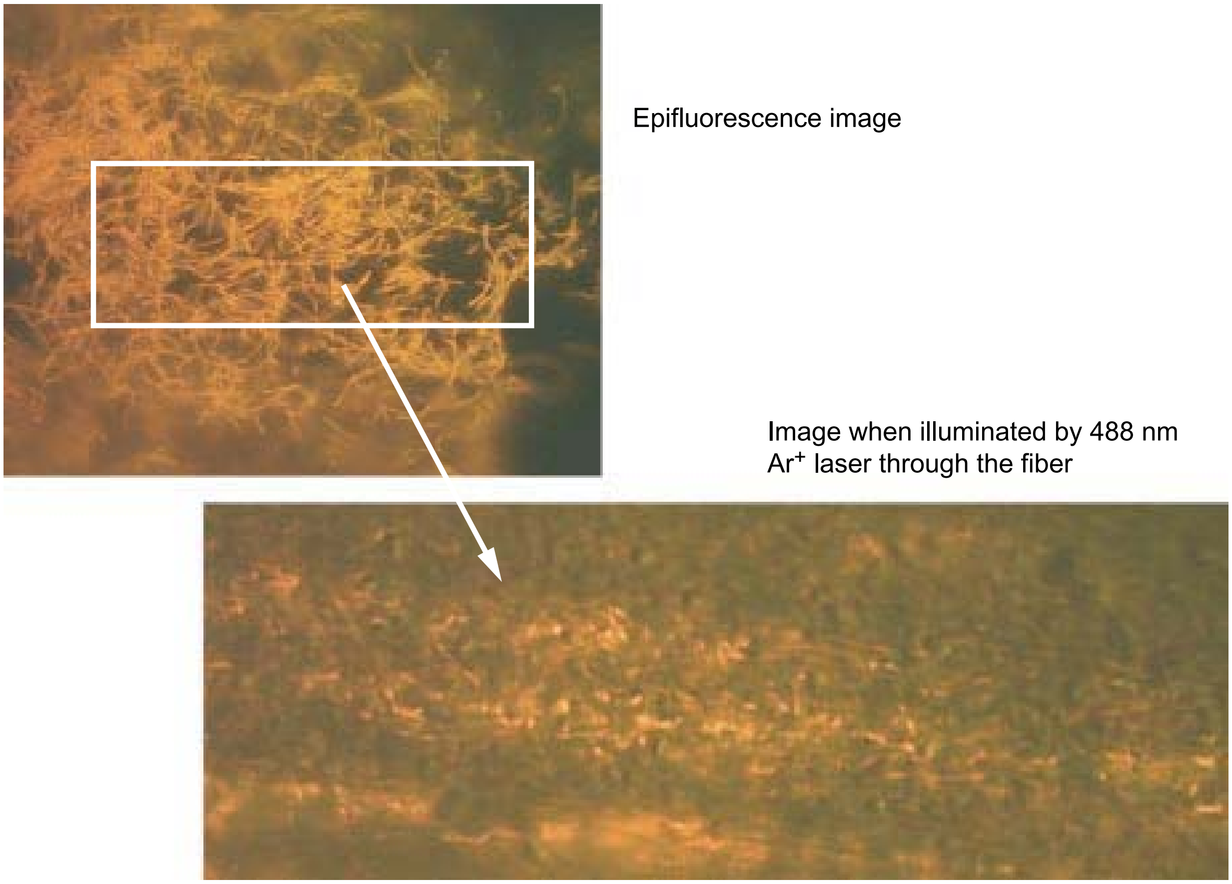

**Figure 5.** Epifluorescence microscope image (top) of acridine orange stained *Shewanella putrefaciens* on iron-oxide-coated optical fiber, the highlighted area illuminated only by the 488-nm line of an $Ar^+$ laser being transmitted by the fiber.

# Complexation at Mineral Surfaces

## Ligand-Metal Interactions at Mineral Surfaces

Natural and anthropogenic metal chelators influence heavy metal and actinide mobility in hydrated porous media. Two experimental projects have been conducted in an effort to determine how polyfunctional organic ligands increase metal adsorption on mineral surfaces. The model system in this particular study included citric acid, uranium(VI) as the uranyl ion ($UO_2^{2+}$), and goethite ($\alpha$-FeOOH) with an emphasis on molecular-level details about the bonding configuration(s). This information will be used to interpret general phenomenological observations at a macroscopic scale and to test models currently used to describe heavy metal partitioning on mineral surfaces.

Extended x-ray absorption fine structure (EXAFS) spectroscopy was used to probe the atomic environment of uranium(VI) in systems where uranium, as the uranyl ion ($UO_2^{2+}$), was adsorbed to goethite in the presence of citrate. Analysis of the spectra includes qualitative comparison against model systems where the uranyl coordination environment or chemical speciation is known. The analysis involves fitting EXAFS spectra using the theoretical model and plausible neighboring atom types and coordination geometries. Figure 6 summarizes the reduced EXAFS spectra, which shows evidence for a bridging goethite-citrate-$UO_2^{2+}$ surface species. The dependence on citrate concentration (and surface coverage) is particularly interesting because a simple stoichiometric relationship between adsorbed citrate and adsorbed uranyl is not evident. This, most likely, reflects the multidentate speciation of citrate at the mineral surface and a species distribution that is a function of surface coverage.

Interpretation of the EXAFS spectra leads to the following conclusions. Citric acid forms a bridge between goethite and uranyl. Coordination with uranyl involves covalent bonding, as opposed to weak electrostatic interactions between a positive uranyl cation and deprotonated carboxyl group(s) from citrate. The bonding appears to be bidentate and involves a single carboxylate group in a bidentate configuration, two carboxyl moieties in monodentate configurations, or one carboxyl and the hydroxyl group. As pH increases from 3 to 8.5, the surface speciation of uranyl changes from the ternary complex involving citric acid to an inner-sphere complex that does not involve citrate. This occurs even though citrate is strongly adsorbed to the goethite surface. The effect of citrate on U(VI) surface complexation is apparent at high surface concentrations of citrate—well above a stoichiometric relationship between citrate and U(VI). As noted above, this may reflect the changing speciation of citrate from a species that is fully coordinated to the surface at low surface concentrations to species with free carboxyl groups exposed to the solution phase at high surface concentrations.

These results have practical implications with respect to the mobility of uranyl in saturated porous media, and will help in the development or evaluation of basic models that predict solid/solution partitioning of ionic solutes at mineral interfaces. Macroscopic adsorption studies were completed in previous years. Model simulations of the macroscopic results will continue given the constraints provided by the spectroscopic analysis.

The EXAFS study was subsequently extended to include the metal chelator EDTA and will be further extended to include systems with analogs to siderophores (polyhydroxamates). The experimental part of the EDTA study (EXAFS spectra acquisition) was successful and is awaiting data reduction.

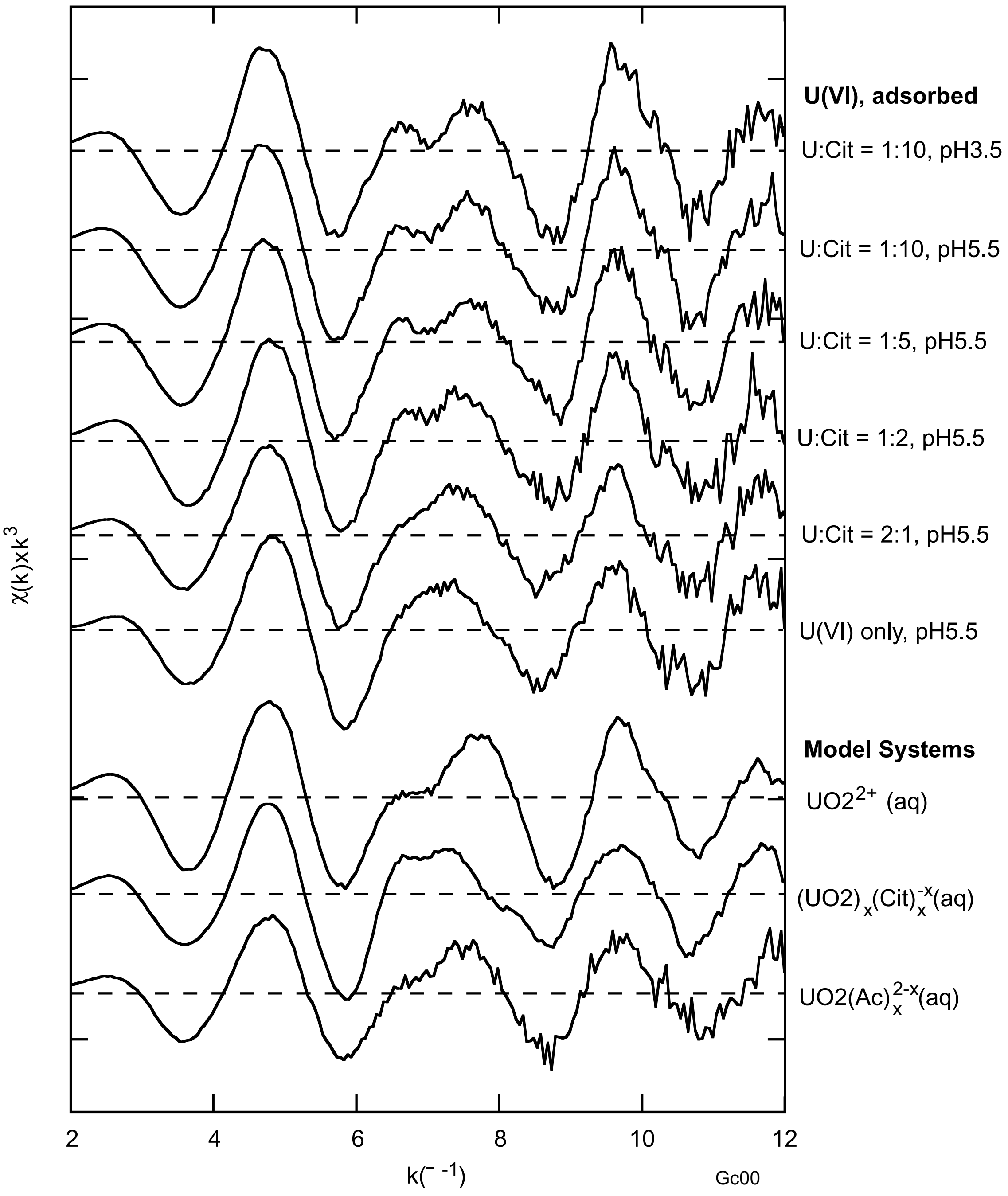

**Figure 6.** Summary of reduced EXAFS spectra, showing evidence for a bridging goethite-citrate-UO22+ surface species. The dependence on citrate concentration (and surface coverage) is also evident.

Attenuated total reflectance Fourier transform infrared (ATR-FTIR) spectroscopy was used to study the bonding of citric acid to goethite and determine whether uranyl influences the bonding. In this study, FTIR is not sensitive tbo uranyl. Instead, it provides information regarding the chemical environment of organic functional groups, including whether they are affected by complexation with uranyl. Data analysis has not been completed, though preliminary results are consistent with those of the EXAFS study.

## An Evaluation and Critique of Modeling Multidentate Complexes on Mineral Surfaces

An issue that relates to the eventual modeling of uranyl adsorption in the presence of citrate and the study of multidentate complexation on mineral surfaces in general concerns the mass action expression for the adsorption reaction. Adsorption described by the *Surface Complexation* modeling approach draws on analogies to chemical equilibrium in homogeneous solution. However, an unresolved problem with the approach occurs when multiple surface sites are involved in a reaction with a single adsorbing solute. This concerns an exponential term that normally reflects the reaction stoichiometry but is known to be inappropriate for fixed surface sites. A simplified description of the problem is described by the following:

A surface reaction involving a single ligand (L) and multiple surface sites (S) is written as

$$nS + L \leftrightarrow S_nL$$

where n = 2, 3, 4….

A conventional mass action expression would be

$$K_{S_nL} = \frac{[S_nL]}{[S^n][L]}.$$

However, since reactive sites on surfaces are fixed in space and cannot participate in multidentate complexation with equal probability, the convention has been to set n = 1. This convention is reasonable, but it is also based largely on intuition. If n has some other value or is a function of surface coverage, it will not be possible to simulate multidentatecomplexation or, more importantly, develop other aspects of surface complexation models, such as the role of electrostatic surface potentials, on the free energy of adsorption.

A Monte Carlo simulation of multidentate surface complexation was conducted in an effort to evaluate the mass action expression for this class of reaction. Figure 7 is an example of the progress of the Monte Carlo simulation as surface sites are filled with tri-dentate L-shaped ligands. An average steady-state condition is achieved within a short time (x-axis). This steady-state condition represents an effective partitioning condition for a given equilibrium constant. Figure 8 is an example of a surface populated by tri-dentate ligands on a regular square lattice at a particular point in time.

The results from this exercise have demonstrated that for very low surface coverage the currently accepted practice of setting n = 1 is a reasonable approximation; however, deviations become apparent as surface coverage increases. It is apparent that n is a complex function of surface coverage even for idealized simulations. At this time, an analytical expression is not known; however, the implications for modeling multidentate surface complexes are clear.

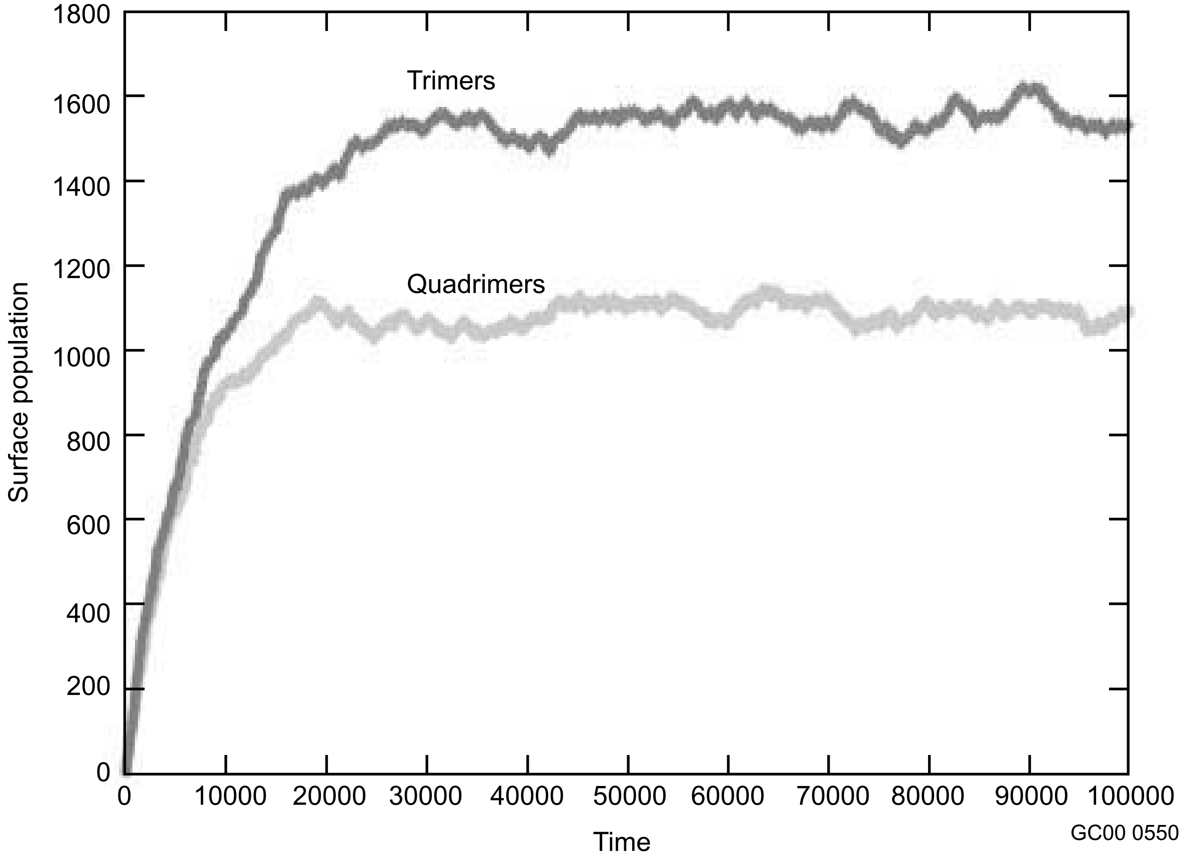

**Figure 7.** Example of the progress of the Monte Carlo simulation as surface sites are filled with tridentate L-shaped or quadrimeric ligands. An average steady-state condition is achieved and represents an effective partitioning condition for a given equilibrium constant.

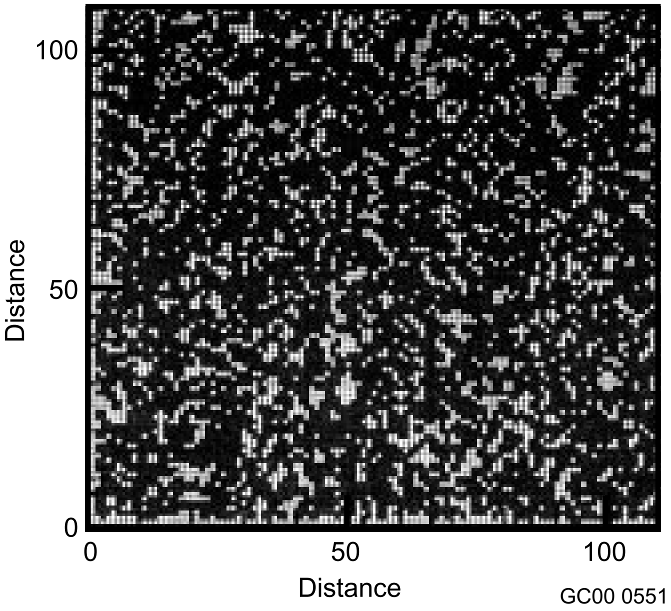

**Figure 8.** Example of a surface populated by tri-dentate ligands on a regular square lattice.

The software program developed for this project will be expanded in the future to allow greater flexibility in the physical and chemical characteristics of adsorbing species andthe hypothetical surface.

## ACCOMPLISHMENTS

- Performed studies to determine the effects of terminal electron acceptors and growth conditions on the production of extracellular complexing and reducing agents by *Shewanella putrefaciens*. Samples from this study are still pending analysis by HPLC and ESI-MS, and will be completed in September of this year.

- Performed studies to determine the selectivity and nature of the adhesion of *Shewanella putrefaciens* to mineral surfaces. To date, the results indicate that the bacteria may adhere to the surface by both loosely and tightly binding mechanisms, and this adhesion to the surface is selective for hematite.

- Initiated experiments to isolate surface adhering and nonadhering strains of *Shewanella putrefaciens* under strictly anaerobic conditions. This work is proceeding and will result in the isolation of bacterial strains not previously reported.

- Demonstrated the potential for using fluorescent probe molecules and attenuated total reflectance excitation to interrogate the interfacial zone between bacteria and the mineral surface to which they adhere. The major problem with this technique arises from the need to get a uniform coating of the mineral onto the surface of the ATR element.

- Completed a study on the metal-ligand interactions at mineral surfaces using the model system of citrate, uranyl, and goethite. The results of this study have been submitted to the *Journal of Colloid and Interface Science*. The study was subsequently expanded with EDTA as the metal chelating ligand. Experiments employing EXAFS on the EDTA-uranyl-goethite study have been performed and the data are currently being evaluated.

- Initiated an effort to evaluate the mass-action expression for multidentate ligand complexation on mineral surfaces. This involved developing a software application for the the purpose, which generated some interesting results that we presented at the National Meeting of the American Chemical Society in August.

- Moved the JEOL Superprobe instrument from the site to our laboratory. Although not listed in any of the previous discussions, significant resources were used to make the move, reinstall, and ensure proper operation in our area. Completion of this activity is scheduled to occur in the last half of September of this year.

# REFERENCES

1. C. R. Myers and J. M. Myers, “Cloning and Sequence of *Cyma*, a Gene Encoding a Tetraheme Cytochrome *C* Required for Reduction of Iron(III), Fumarate and Nitrate by *Shewanella Putrefaciens* Mr-1,” *Journal of Bacteriology*, Vol. 179, No. 4, 1997**,** pp. 1143-1152.

2. A. S. Beliaev and A. S. Daad, “*Shewanella Putrefaciens Mtrb* Encodes an Outer Membrane Protein Required for Fe(III) and Mn(IV) Reduction,” *Journal of Bacteriology*, Vol. 180, No. 23, 1998**,** pp. 6292-6297.

3. F. Picardal, R. G. Arnold, and B. B. Huey, “Effects of Electron-Donor and Acceptor Conditions on Reductive Dehalogenation of Tetrachloromethane by Shewanella- Putrefaciens-200,” *Applied and Environmental Microbiology*, Vol. 61, No. 1, 1995**,** pp. 8-12.

4. J. Caccavo et al. “Role of Hydrophobicity in Adhesion of the Dissimilatory Fe(III)-Reducing Bacterium Shewanella Alga to Amorphous Fe(III) Oxide,” *Applied and Environmental Microbiology*, Vol. 63, No. 10, 1997**,** pp. 3837-3843.

5. M. C. Grantham, and P. M. Dove, “Investigation of Bacterial-Mineral Interactions Using Fluid Tapping Mode Atomic Force Microscopy,” *Geochimica et Cosmochimica Acta*, Vol. 60, No. 13, 1996**,** pp. 2473-2480.

6. M. C. Grantham, P. M. Dove, and T. J. DiChristina, “Microbially Catalyzed Dissolution of Iron and Aluminum Oxyhydroxide Mineral Surface Coatings,” *Geochimica et Cosmochimica Acta*, Vol. 61, No. 21, 1997**,** pp. 4467-4477.

7. D. R. Lovley, “Microbial Fe(III) Reduction in Subsurface Environments,” *FEMS Microbiology Reviews*, Vol. 20, 1997**,** pp. 305-313.

8. H. L. Ehrlich, *Geomicrobiology, 2nd Ed., Rev. And Expanded*; Marcel Dekker, Inc.: New York, 1990, pp 282-346.

9. D. A. Sverjensky, “Zero-Point-of-Charge Prediction from Crystal-Chemistry and Solvation Theory,” *Geochimica et Cosmochimica Acta*, Vol. 58, No. 14, 1994**,** pp. 3123-3129.

10. F. Caccavo, “Protein-Mediated Adhesion of the Dissimilatory Fe(III)-Reducing Bacterium Shewanella Alga Bry to Hydrous Ferric Oxide,” *Applied and Environmental Microbiology*, Vol. 65, No. 11, 1999**,** pp. 5017-5022.

11. J. F. McClelland, et al. “Photoacoustic Spectroscopy”, In *Modern Techniques of Applied Molecular Spectroscopy,* F. M. J. Mirabella, Ed.; John Wiley and Sons, Inc.: New York, 1998, pp 221-265.

12. M. W. Urban, “Surface and Interface Vibrational Spectroscopy - Relevance to Adhesion,” *Journal of Adhesion Science and Technology*, Vol. 7, No. 1, 1993**,** pp. 1-47.

13. B. J. Niu, and M. W. Urban, “Recent Advances in Stratification and Film Formation of Latex Films; Attenuated Total Reflection and Step-Scan Photoacoustic FTIR Spectroscopic Studies,” *Journal of Applied Polymer Science*, Vol. 70, No. 7, 1998**,** pp. 1321-1348.

14. D. Fortin, and F. G. Ferris, “Precipitation of Iron, Silica, and Sulfate on Bacterial Cell Surfaces,” *Geomicrobiology Journal*, Vol. 15, No. 4, 1998**,** pp. 309-324.

15. D. Fortin, F. G. Ferris, and S. D. Scott, “Formation of Fe-Silicates and Fe-Oxides on Bacterial Surfaces in Samples Collected near Hydrothermal Vents on the Southern Explorer Ridge in the Northeast Pacific Ocean,” *American Mineralogist*, Vol. 83, No. 11-12, 1998**,** pp. 1399-1408.

16. L. A. Warren, and F. G. Ferris, “Continuum between Sorption and Precipitation of Fe(III) on Microbial Surfaces,” *Environmental Science & Technology*, Vol. 32, No. 15, 1998**,** pp. 2331-2337.

17. S. Deki, et al., “Preparation and Characterization of Iron Oxyhydroxide and Iron Oxide Thin Films by Liquid-Phase Deposition,” *Journal of Materials Chemistry*, Vol. 7, No. 9, 1997**,** pp. 1769-1772.

# Reactive Transport in Variably Saturated Heterogeneous Media

**Robert W. Smith, Laurence C. Hull, Richard W. Johnson, Earl D. Mattson, Annette L. Schafer, James B. Sisson, David Neil Thompson**

## SUMMARY

For the past three-years, we have been developing a better understanding of the movement and transformation of reactive constituents in heterogeneous, variably saturated subsurface media (e.g., the vadose zone) and using this understanding to improve predictions of the fate and mobility of reactive constituents. Accomplishments in this project have enhanced INEEL capabilities in laboratory equipment and experience, field measurement capabilities and field monitoring sites, and computational expertise and capabilties.

In the laboratory, we constructed three automated titrator systems, installed them at the INEEL Research Center, and used them to perform surface charge titrations on reference minerals and on INEEL soils. For hydrologic studies, in cooperation with the University of Idaho, we established a vadose zone soil physical characterization laboratory at University Place and we purchased and installed a J-6 Unsaturated Flow Apparatus at the INEEL Research Center.

In the field, we developed three field sites, also in cooperation with the University of Idaho. Two sites were developed on DOE-controlled land, one at the Jefferson Canal site near Mud Lake and one at the IRC 5-well site at the INEEL Research Center. A third site developed during FY 2000, on land controlled by the University of Idaho, is the University Place Dune Site in Idaho Falls. INEEL expertise has been applied to DOE operational problems at other national laboratories as well. At the Test Buried Waste Facility at Hanford, we demonstrated a new version of the advanced tensiometer using cone penetrometer push technology. We installed the standard version of the vadose zone monitoring system at the Savanna River Site.

In computational capabilities, we have enhanced computations to simulate complex, nonlinear systems for vadose zone transport. The application of a B-spline collocation method to the solution of differential equations, including sets of coupled, nonlinear partial differential has been shown to be feasible. A B-spline code has been generated that solves the coupled fluid dynamics equations for two-dimensional flow in a channel, including multiple solution algorithms; the unoptimized code has found reasonable solutions in times about half as long as for the optimized commercial finite element code Fidap.

## PROJECT DESCRIPTION

Throughout arid portions of the world, exemplified by the Western United States, both water quantity and water quality are areas of major concern to the general population, agricultural communities, mining and energy resource interests, and local and national governments. Water supplies are becoming critically impacted as population and water demands increase. In many locations, water supplies have been contaminated either by accident or by past waste-disposal practices. Within the United States, for example, activities of the U.S. Department of Energy have resulted in the contamination of large tracts of land with complex mixtures of radionuclides and other contaminants. Much of this contamination results from the migration of wastes disposed of at the land surface into the region between the surface and underlying aquifer. Other activities that occur in, and may result in contamination of, the vadose zone include the following:

- Disposal of municipal and hazardous waste in landfills
- Suburban septic systems
- Mining and milling of ores
- Production and refining of petroleum products
- Application of agricultural chemicals (e.g., fertilizers, pesticides, and herbicides) to crops.

Although the vadose zone is often relied on as the primary protective barrier to prevent groundwater contamination, it is often the conduit for the transport of contamination from the surface to subsurface water supplies. Yet, our current understanding of the movement and transformation of contaminants is inadequate to accurately predict their behavior in the vadose zone. Our inability to adequately describe the subsurface has been identified in numerous articles, books and workshops (Looney and Falta 2000, NRC 2000a and b, EMSP 2000). Simplistic chemical characterizations and supporting modeling of the behavior of actinides and other radionuclides in the vadose zone suggest that these contaminants are immobile. However, at some locations (e.g., the INEEL Radioactive Waste Management Complex [RWMC] and the Hanford Tank Farms), actinides and other radionuclides have migrated hundreds of feet through the vadose zone and are influenced by poorly understood physical, chemical, and biological processes. Centuries of human activity have led to water use and disposal practices that are not environmentally sustainable. Coordinated research and technology development are now needed to improve and sustain stewardship of the vadose zone.

Within the science and engineering community, numerous investigations exist relevant to understanding and modeling the behavior of contaminants in the vadose zone. The ability to predict contaminant fate and transport in the vadose zone, however, requires the ability to model the important physical, biological, and geochemical processes and properties of vadose zone soils and sediments in order to accurately assess transport, retention, and transformation of contaminants and other solutes (nutrients, electron acceptor/donors, etc.).This modeling must include

- A high degree of temporal resolution, so effects on contaminant transport and transformation of events such as snow melt can be evaluated
- A high degree of spatial resolution, so effects on contaminant transport and transformation of physical, chemical, and biological heterogeneities can be evaluated
- Appropriate coupling of the important biological, geochemical, and transport processes, so synergistic and antagonistic effects can be evaluated.

Theoretical derivations, experimental investigations, and field observation will be needed to fill key data or understanding gaps required to successfully develop improved vadose zone predictive capabilities. The unifying theme of the Reactive Transport in Variably Saturated Heterogeneous Media Project research is to develop an enhanced understanding of the cycling of carbon in the spatially and temporally heterogeneous vadose zone and the effect that this cycling has on the mobility of radionuclides and other DOE contaminants. In the vadose zone, carbon can occur in organic and inorganic forms, and in multiple phases (solid, dissolved, gaseous). Because of the existence of a discrete and mobile gas phase in the vadose zone, transport of inorganic carbon in both aqueous and gas phases can occur. The rapid local equilibration between dissolved, solid, and gaseous inorganic carbon can lead to the development of spatially variable pH in the vadose zone and associated variability in contaminant behavior. The presence of organic carbon as either disposed waste or as natural materials can promote microbial mineralization, creating an additional subsurface source for inorganic carbon. Microbial activity, in turn, will be a function of available electron acceptors, such as oxygen in the vadose zone gas phase, and free water (water that microorganism can access). The focus of our research is on the nonlinear interrelationship between movement of the gas and aqueous phases and their effect on microbial activity and, ultimately, contaminant mobility. The research is embodied in the five technical tasks described below.

# Upscaled Effective Reactive Transport Properties in Variably Saturated Heterogeneous Porous Media

## Overview

Field-scale transport through geologically heterogeneous media occurs at scales smaller than the discretization level practical in numerical simulators. This demands use of upscaled parameters to capture the effects of smaller-scale heterogeneity at each discretization level. While evaluation of field-scale transport has widely recognized the importance of the smaller-scale hydraulic heterogeneity in controlling fluid migration, the influence of geochemical heterogeneity at similar scales has not been acknowledged. In this study, we conducted a numerical analysis of geochemical and hydraulic heterogeneity to clarify the concept of effective anisotropy in reactive properties for variably saturated porous media. To support the analysis, we conducted Monte Carlo simulations for two-dimensional, steady-state flow and transient solute transport in hydrologically and geochemically heterogeneous media. In these simulations, we assumed that saturated hydraulic conductivity and the Mualem/van Genuchten parameters were correlated to grain size and reactive surface area, and that they were spatial stochastic variables. We conducted simulations over a range of moisture content and fixed correlation scale and variance, and computed and analyzed moments of the mean plume to obtain upscaled transport parameters.

Results of the simulations support the concept of an anisotropic effective reactive surface area, as indicated by directionally dependent retardation. For unsaturated porous media, we found that geochemical heterogeneity is a function of moisture content in addition to being a function of the hydrologic variability.

## Hypotheses and Significance

The first hypothesis is based on the observation that a reactive surface area should be a hysteretic function manifested during transient wetting and drying cycles. The in situ availability of reactive surfaces is a hysteretic property in vadose zone materials. Based on previously developed relationships between mass-based and surface-area-based surface reactions, and on the dependence of the surface area on grain (and thus pore) geometry, one would expect that unsaturated systems would exhibit hysteretic and moisture dependent adsorption. This should be manifested as a combination of physical exclusion and chemical adsorption as functions of the pore sizes being filled. What has yet to be shown is the relationship and influence of wetting and drying history on the reactive surface area and its relationship to reactive contaminant transport. As a first step in this analysis, this project has looked at the difference in net adsorption as a function of mean moisture content in a two-dimensional porous media.

During the first wetting of a dry soil, small pores fill first, and during subsequent drainage, the large pores empty first, leaving water trapped by capillary forces in the small pore spaces. This water contains contaminants that are in equilibrium with the high-surface area, fine-grained sediments. Subsequent precipitation will carry contaminant-laden water through the next larger, more permeable, and less reactive pore throats, allowing contaminant migration to reach further into the porous media. Repeated cycling of precipitation events in this manner will result in an apparent reduction in effective adsorption over large times and distances. Many geologic systems are essentially binary systems. For example, consider the basalt-sediment sequence at the INEEL, or the silt varves that exist in the coarser sand-gravel matrix at Hanford. In these systems, adsorption parameters obtained from laboratory batch experiments based on well-mixed sediments will overpredict the adsorptive characteristics of the porous media. Numerical or analytical predictions of transport based on these overly optimistic adsorption parameters will underpredict peak concentrations and will over-estimate residence time (and therefore, radioactive contaminant decay) in the vadose zone.

The second hypothesis is based on the observation that the in situ availability of reactive surfaces is a property dependent upon flow magnitude and direction in vadose zone materials. As a function of flow direction and available moisture content, the effective volume-averaged adsorption should be represented by a flux-weighted tensor. It is this effective adsorption coefficient that should be used for field-scale transport predictions.

It is commonly acknowledged that limitations in characterization and transport predictions are introduced by the heterogeneous nature of vadose zone materials through their influence on hydraulic conductivity and on the resultant nonlinear relationships between hydraulic transport properties and state variables. It is not commonly recognized that in field-scale modeling, these hydraulic relationships are anisotropic. Additionally, it has not been commonly recognized that geochemical properties are spatially variable, or that geochemical property variation can have a significant effect on the transport of contaminants that react with the surfaces of vadose zone materials. This lack is evidenced in the single-value parameterization of geochemical properties (e.g., retardation factors) existing in some of the more commonly used vadose zone transport simulators (Porflow, FEHM, and Tetrad [variable but scalar]). Moreover, many field-scale vadose zone characterization studies rely on the use of effective geochemical parameters determined from more abundant aquifer data and transport estimates. Calibrated adsorption parameters based on aquifer data tend to sample in the direction of high-permeability, low-reactivity sediments, as opposed to sampling across these geologic features. As a result, it is highly likely that these “effective” geochemical parameters do not provide realistic estimates of geochemical interactions in the vadose zone.

## Research Results

The first temporal moment of the effluent was used to describe the tracer breakthrough behavior for the following simulations, as defined by Equation 1:

$$T = \frac{\int_0^\infty Ctdt}{\int_0^\infty Cdt} \qquad (1)$$

with the net effect of adsorption on transport for a reactive constituent defined as the ratio of the first temporal moments of reactive and conservative tracers:

$$R = \frac{T_R}{T_C} \ . \tag{2}$$

We conducted Monte Carlo simulations of steady-state flow and transient transport to illustrate the effect of directionally varying hydraulic conductivity anisotropy on transport. In each realization, a saturated hydraulic conductivity field was generated with correlated unsaturated characteristics. A mean pressure head of -20 cm was obtained by specifying upper and lower boundary conditions, and tracers were applied at the upper boundary. The parameter fields were anisotropic, yielding an effective anisotropy in hydraulic conductivity without changing the harmonic mean. We first applied tracers with flow perpendicular to the bedding planes, calculated a mean retardation, and then rotated and used the fields to obtain results for flow and transport parallel to the bedding planes. Figures 1 and 2 below illustrate an example from one realization for flow perpendicular to bedding (representative of vertical

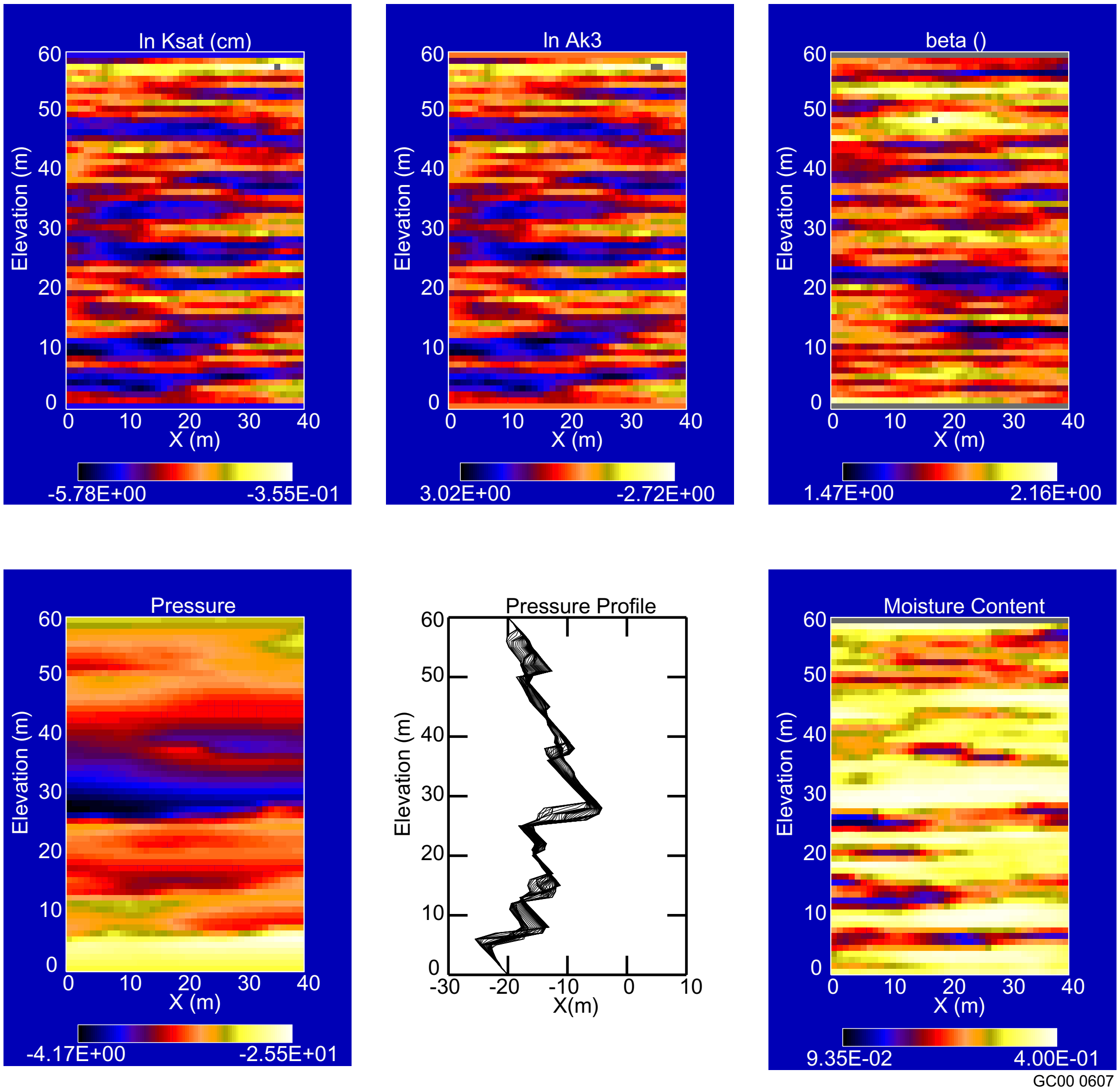

**Figure 1.** Saturated hydraulic conductivity, van Genuchten parameters, pressure head, pressure profile, and moisture content oriented for flow perpendicular to bedding. Correlation lengths are $\lambda_h = 20$ cm, and $\lambda_v = 1$ cm in a 40 × 60-cm domain.

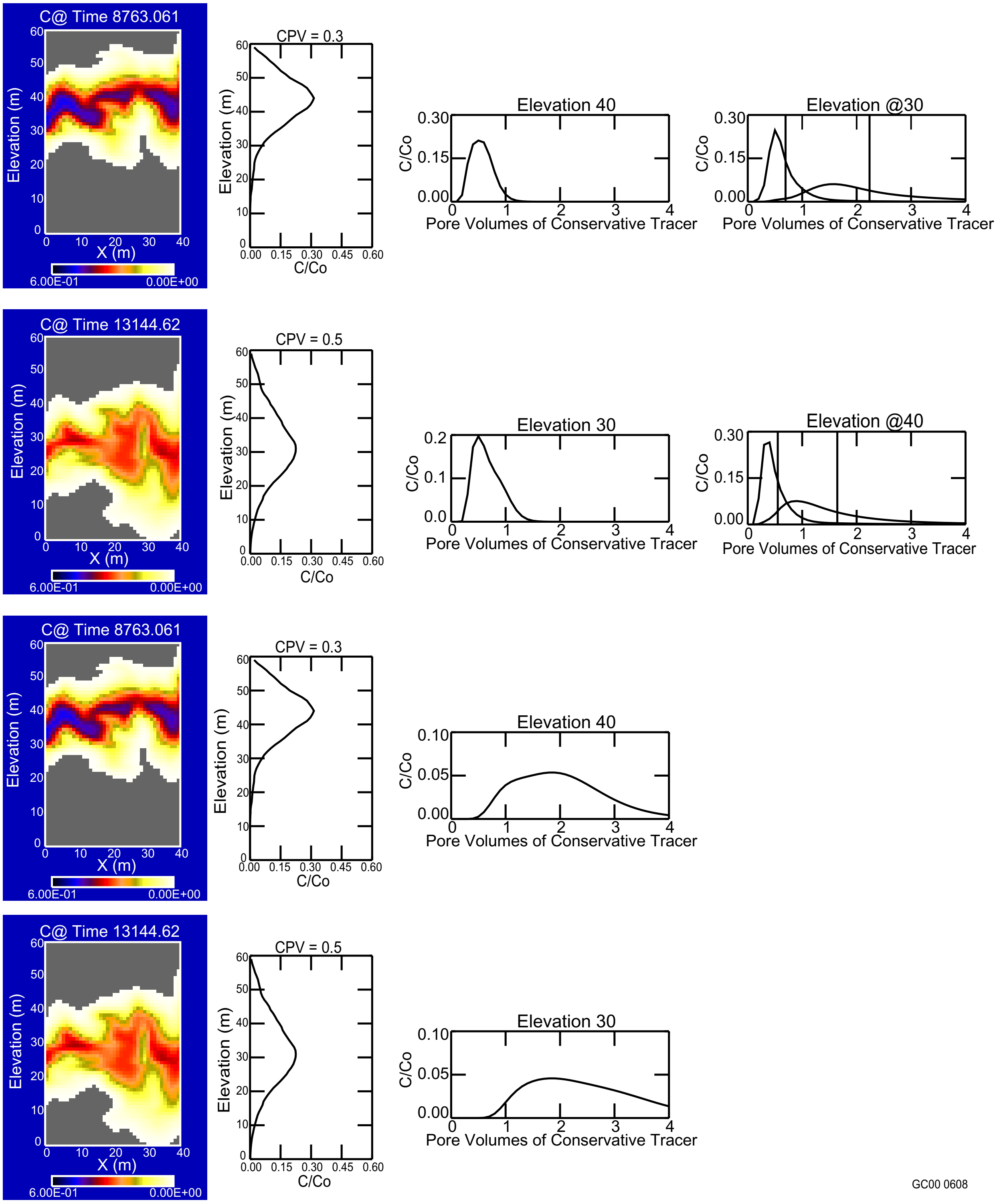

**Figure 2.** Upper left: tracer distribution and horizontally averaged concentration profile for a conservative tracer. Upper center: tracer arrival (effluent concentration) at two elevations for the conservative tracer. Lower left: tracer distribution and horizontally averaged concentration profile for a reactive tracer. Lower center: tracer arrival (effluent concentration) at two elevations for the reactive tracer. Upper right: overlain breakthrough curves for the reactive and conservative tracers. Net retardation effect: R=3.33. Effective Retardation: R = 3.3.

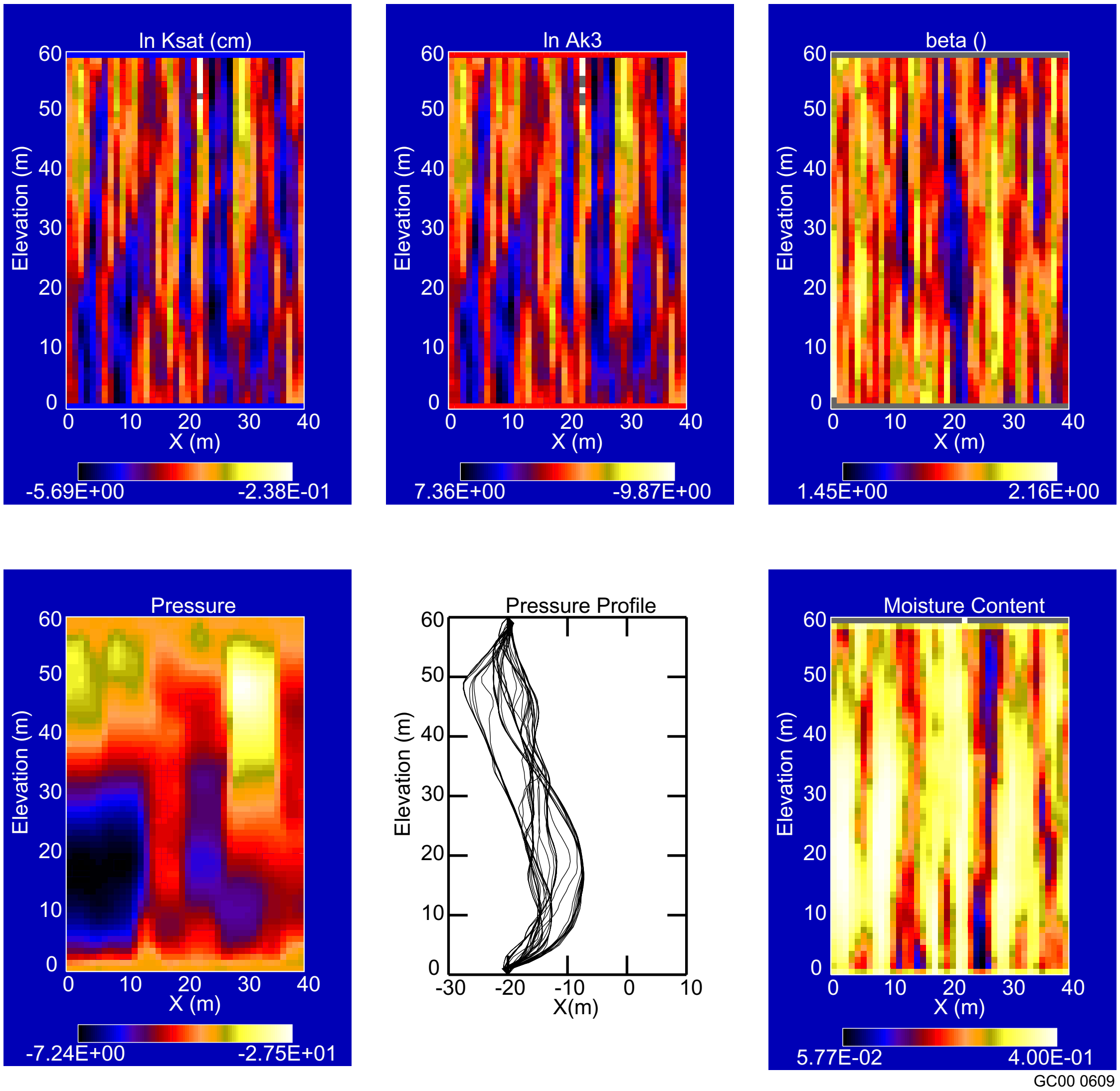

**Figure 3.** Saturated hydraulic conductivity, van Genuchten parameters, pressure head, pressure profile, and moisture content oriented for flow parallel to bedding. Correlation lengths are $\lambda_h = 1$ cm, and $\lambda_v = 20$ cm in a 40 × 60-cm domain.

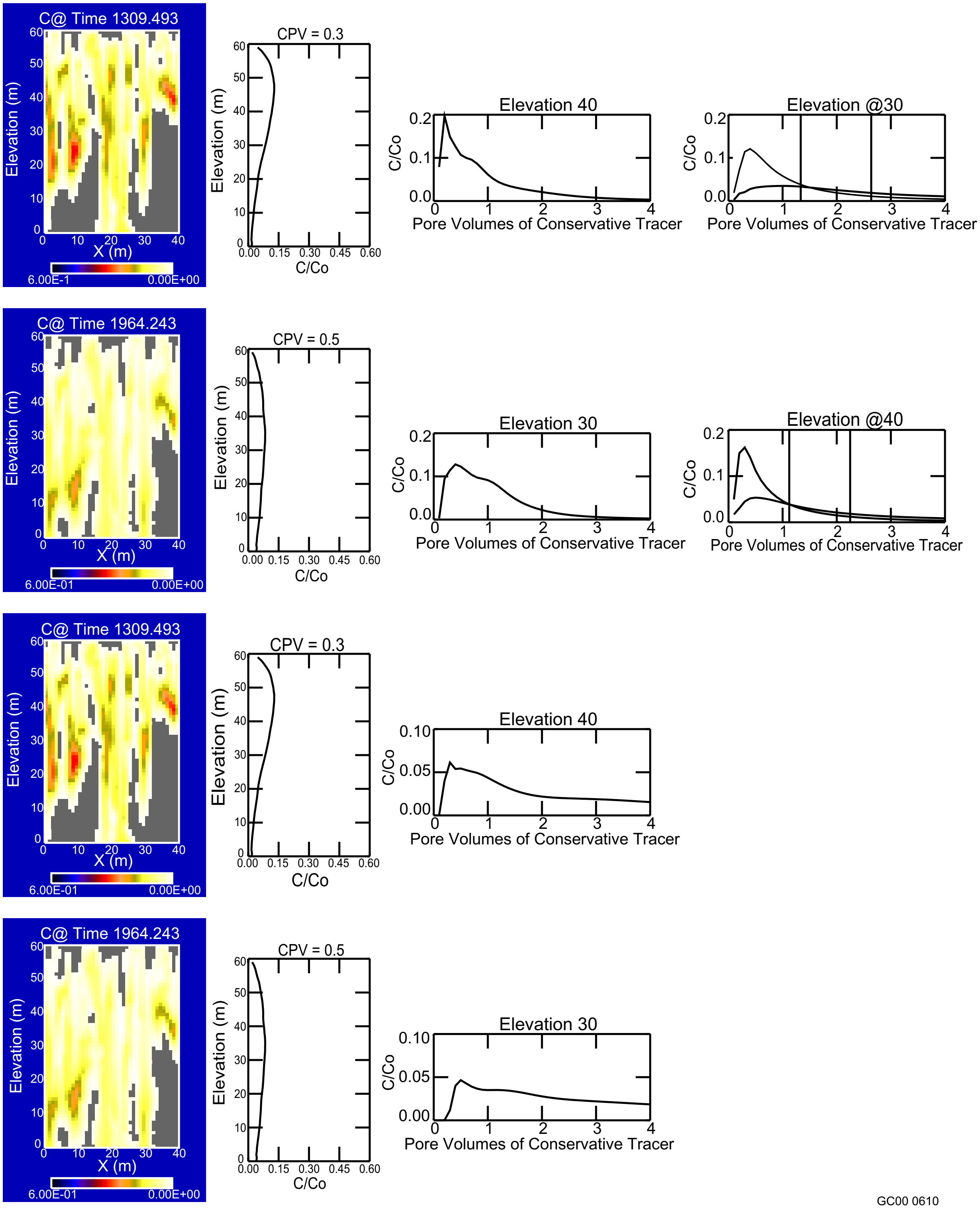

**Figure 4.** Upper left: tracer distribution and horizontally averaged concentration profile for a conservative tracer. Upper center: tracer arrival (effluent concentration) at two elevations for the conservative tracer. Lower left: tracer distribution and horizontally averaged concentration profile for a reactive tracer. Lower center: tracer arrizval (effluent concentration) at two elevations for the reactive tracer. Upper right: overlain breakthrough curves for the reactive and conservative tracers. Net retardation effect: R=1.8. Effective Retardation: R = 1.8.

infiltration) and Figures 3 and 4 for flow parallel to bedding (representative of horizontal fluid migration). The effective retardation given is based on the results of 100 similar realizations and differs by a factor of 2 under this mean pressure head.

We are conducting simulations for varying mean moisture content for publication. Follow-on research will focus on developing the theory for quantifying flux-dependent reactive surface area. As a process correlated with spatially random hydraulic parameters, we will evaluate the conditions for scale-dependence. Further research will also focus on determining the geologic conditions (correlation parameters) under which these processes significantly affect vadose zone transport predictions and characterization.

### Conclusions

Computer simulation of flow and transport in the vadose zone requires discretization of properties at a scale that is courser than the transport properties. Therefore, effective transport parameters must be developed that describe the system over a range of scales, larger than the scale of the processes. Experimental simulation of vadose zone environments provides an effective tool for studying the scaling of properties. Temporal and spatial moments (mean, variance, skewness) can be used to derive effective parameters. However, experimental simulation indicates that the classic advective-dispersive approach is inadequate.

Transport is strongly controlled by reactive surface area. The reactive surface area to which a contaminant is exposed depends on the direction of flow through a heterogeneous material, and therefore must be treated as a tensor, not a scalar parameter. For variably saturated media, reactive surface area is expected to be hysteretic as materials dry and are rewetted. Experimental simulation offers insight into the design of laboratory and field experiments to identify factors that need to be included in experimental design.

## Propagation of Geochemical Environments

### Overview

We conducted proton titration experiments on synthetic goethite and soil in an effort to develop adsorption parameters that will help predict migration of radioactive liquid waste. This is the initial step in a reactive transport project to understand contaminant migration in a system characterized by strong chemical gradients. For this stage, we applied two levels of pretreatment to the soil to remove carbonate minerals and soluble salts to focus on the remaining mineral fraction. Without some sort of treatment or conditioning, native soil has a large buffer capacity that interferes with proton titration experiments.

### Introduction

One of the most significant problems in applying geochemistry to fate and transport modeling is the lack of an approach to adsorption that can account for changes in the subsurface geochemical environment, such as changes in pH, ionic strength, and competing cations. An essential requirement to advance the study of geochemistry is to integrate mechanistic ion exchange and surface complexation into reactive transport models to allow practical application for performance and risk assessment.

At the INEEL, liquid radioactive waste from reprocessing spent nuclear fuel is 1 *M* nitric acid with milligram/liter levels of uranium. Past spills of the liquid waste to the soil were rapidly neutralized by calcite in the soil matrix, with concurrent large pH changes, generation of carbon dioxide gas, strong chemical gradients, and adsorption of uranium onto soil minerals. Adsorption parameters that can accommodate associated changes in the subsurface geochemical environment are needed to understand the migration potential of the waste.

A reactive transport project is under way to study the mechanisms controlling contaminant transport in the vadose zone. The working hypothesis of the project is that uranium transport in the vadose zone is primarily controlled by surface complexation reactions on mineral oxide surfaces and requires knowledge of uranium partitioning on individual soil components under the influence of the carbonate system. Many laboratory experiments have been conducted on the adsorption of uranium on single, synthetic minerals (Hsi and Langmuir 1985, Redden and Leckie 1998, Payne et al. 1998). However, little work has been done to expand these studies to adsorption on mixtures of minerals or on natural soil materials. We conducted proton titration experiments on single minerals and on soil to quantify surface charge and to evaluate buffer capacity.

## Experiments

Goethite ($\alpha$-FeOOH) was prepared under $CO_2$-free conditions following a method similar to that of Atkinson, Posner, and Quirk (1967). Sodium nitrate salts in the goethite suspension were removed by decanting and dialysis exchange with deionized water to yield a final solvent conductivity of less than 20 $\mu$ S. The product was stored at 3°C to prevent microbial growth. Analysis of the solid by x-ray diffraction (XRD) yielded a spectrum consistent with 100% goethite.

Soil from the spreading areas at the INEEL, which is typical of soil from waste disposal areas, was obtained and sieved through a 2-mm sieve and characterized. Bulk mineralogy was determined by XRD analysis. Organic matter was removed with hydrogen peroxide. An absence of $CO_2$-generation suggests that little organic matter was present initially. Next, the soil was treated with dithionite—citrate—bicarbonate to quantify reducible crystalline and amorphous oxides (Klute 1986) A nominal surface area for the soil sample was measured using the Brunauer, Emmett, and Teller (BET) method (Brunauer et al. 1938).

For this stage of the project, the soil was treated to remove calcite. Soil was placed in dialysis tubing and immersed in a sodium acetate/acetic acid buffer solution (pH 5.0) to dissolve carbonates and other soluble salts (Klute 1986). Once $CO_2$ production was complete, the soil was dialyzed against deionized water until the conductivity was less than 20 $\mu$ S. The soil was oven-dried at 30°C and sieved through a 2-mm sieve. A riffle splitter was used to obtain uniform subsamples of treated soil used for characterization and adsorption experiments. An XRD analysis of the treated and untreated soil samples showed that the calcite was removed.

After the initial titration experiments on soil treated with the acetate buffer solution at pH 5.0, we concluded that a more aggressive conditioning of the soil was necessary to remove soluble salts and exchangeable cations because pH stability was difficult to establish during titration experiments. The method used for conditioning the soil was taken from Baeyens and Bradbury (1997). Approximately 0.5 g of soil was added to 50-mL centrifuge tubes. Thirty mL of 0.01 *M* NaCl solution, adjusted to pH 3.5 with HCl, were also added to each tube. The tubes were mixed for 30 minutes on a rotating wheel then taken off and centrifuged. The supernatant was decanted and the pH was measured. This process was repeated until the pH of the supernatant was approximately 3.5. Then the soil in each tube was washed with 0.01 *M* NaCl (without adjusting the pH) following the same process until the pH was approximately equal to the initial pH of the neutral NaCl solution. The conditioned soil samples were stored in a refrigerator at 3°C with 30 mL of 0.01 *M* NaCl.

We used custom automated titrators (Redden 1992) to conduct titrations of soil and mineral samples (Figure 5). Solutions of hydrochloric acid and $CO_2$-free sodium hydroxide were prepared. The NaOH solution was calibrated with potassium hydrogen-phthalate (KHP). The HCl solution was calibrated against the calibrated NaOH. A titration was performed using the background solution (0.01 *M* NaCl) to check for internal consistency of the acid and base reagents.

Proton stoichiometry titrations of the solids for estimating surface charge were performed under nitrogen. Goethite titrations were performed using 1-g/L suspensions in 0.01 *M* NaCl. Soil titrations were performed on an approximately 1.7-g/L solution of soil in 0.01 *M* NaCl. Both solutions had a surface area concentration of about 57 $m^2/L$. The pH of the slurry was lowered to 5.5 and allowed to equilibrate overnight while purging with nitrogen to ensure that the $CO_2$ was removed. The pH was then lowered to 3.0 and allowed to stabilize. Once stable, the slurry was titrated with NaOH to pH 11.0 and then back to pH 3.0 with HCl while constantly purging with nitrogen.

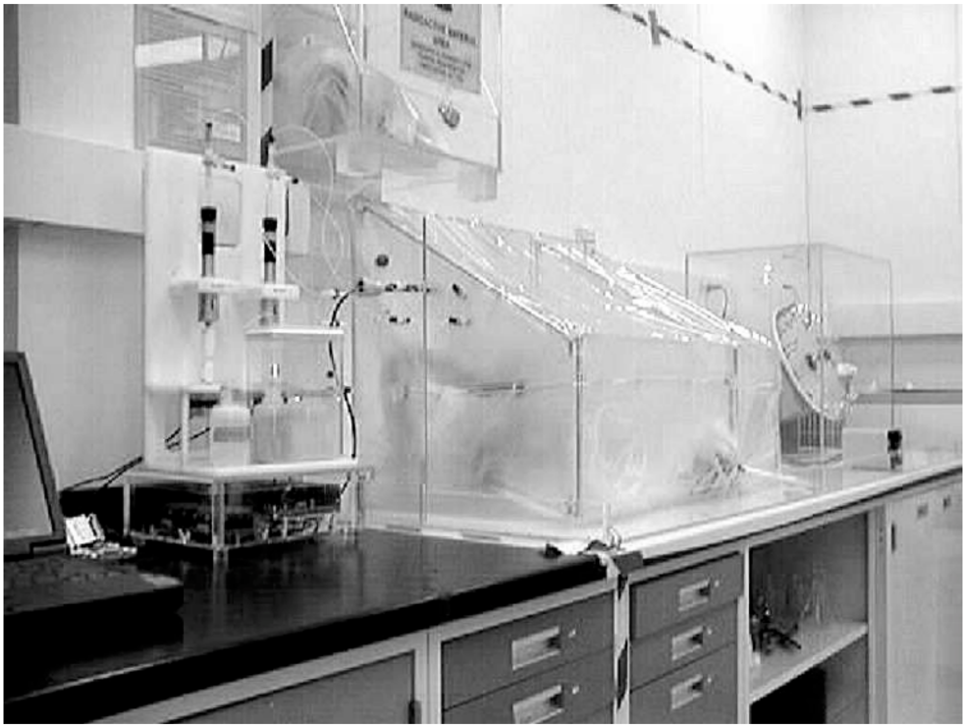

**Figure 5.** Automated titrator dispenses acid and base reagents to measure surface charge on minerals. Experiments are conducted in a glove box to control the gas-phase composition.

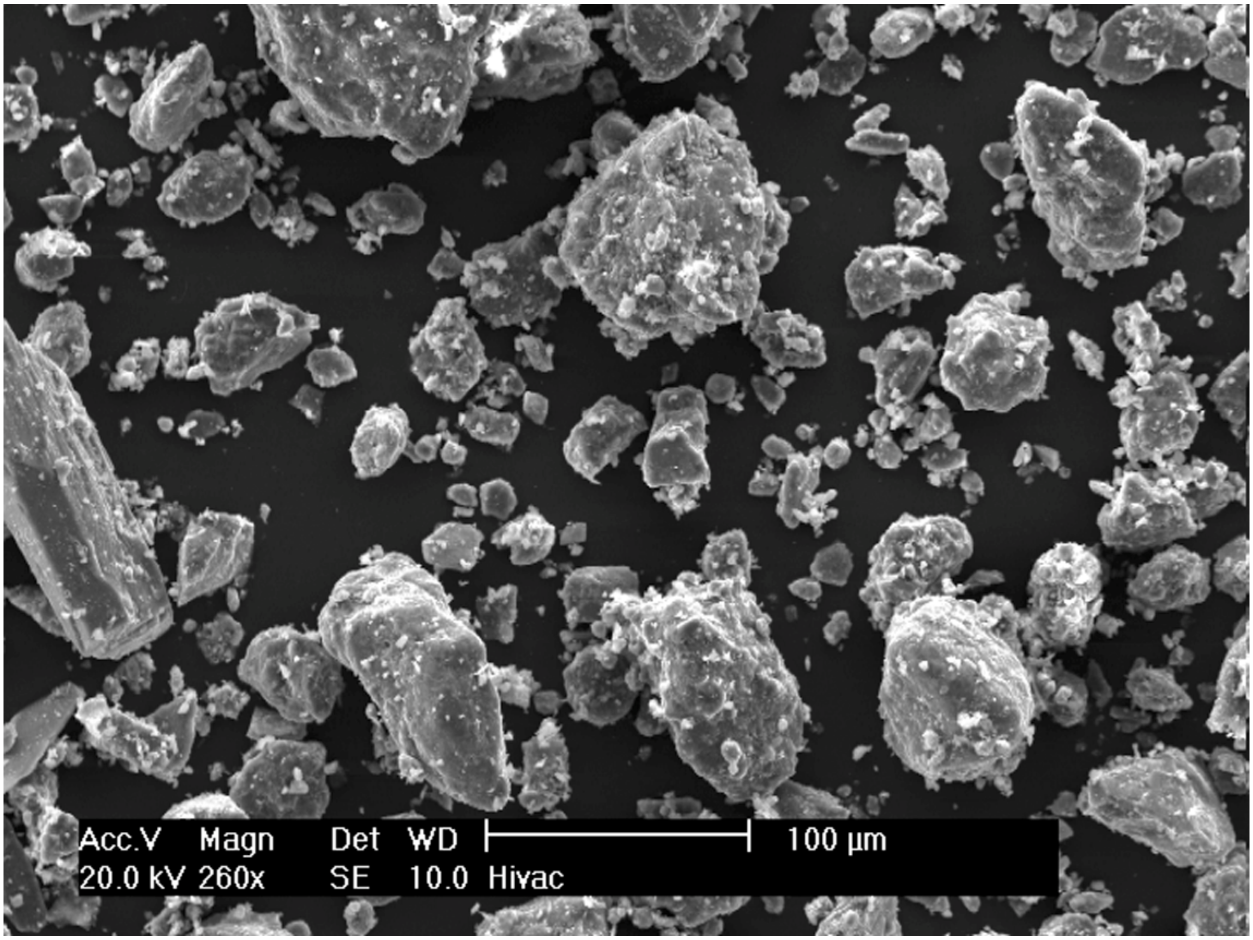

**Figure 6.** Electron microscope picture of soil grains, showing many small, reactive oxide particles on the soil grains.

## Research Results

We used scanning electron microscopy (SEM) to look for crystalline and amorphous iron oxide on the soil. Iron produces higher electron backscattering than most other elements in soil. Iron-containing phases can be seen as lighter areas in Figure 6. Fully crystallized grains of iron minerals, such as magnetite, are not apparent in the soil. Iron-containing phases occur as small particles adhering to the surfaces of mineral grains.

The surface area of the untreated soil was determined to be 30.3 $m^2/g$ ± 0.19% and that of the treated soil 34.2 $m^2/g$ ± 0.08%. We calculated the density of oxide adsorption sites for the soil using the following equation (Kent et al. 1988):

Surrogate sites = (site density * surface area * molecular weight * mole ratio of surrogate oxide to soil oxide * extractable metal) / $10^6$ . (3)

At this point in the process, we are using the information primarily as a guide to identify the oxide phases that will be most important in affecting adsorption. Table 1 lists the calculated site densities for the soils. According to the calculations, iron oxide and manganese oxide provide the greatest number of adsorption sites per gram of soil.

**Table 1.** Estimated oxide site densities for soil.

| Soil Oxide | Extractable Metal (µmol/g) | Surrogate Oxide | Site Density[a] (µmol/m²) | Surface Area[a] (m²/g) | Molecular Weight (g/mol) | Surrogate Sites (µmol/g) |
|---|---|---|---|---|---|---|
| Iron | 23.8 | $\alpha$-FeOOH | 27.2 | 48 | 89 | 2.79 |
| Manganese | 0.91 | $\delta$-$MnO_2$ | 370 | 74 | 87 | 2.16 |
| Aluminum | 4.10 | $\gamma$–$Al_2O_3$ | 13 | 117 | 102 | 0.32 |
| Silicon | 12.7 | am-SiO2 | 8.3 | 170 | 58 | 1.04 |

a. Data for the surrogate oxides were taken from Kent et al. (1988, Table 3-1).

Acid and base titrations were performed to quantify the pH-dependent surface charge of goethite and soil and to compare the behavior of the soil with a well-studied and well-characterized model mineral. Goethite titrations show rapid response and stability during pH changes. Our experiments show that the amount of acid needed to reach a target pH value is greater for treated soil than for goethite (see Figure 7). Even after the target pH value was reached for the treated soil, additional acid was needed to stabilize the pH. We then further conditioned the treated soils with 0.01 *M* NaCl adjusted to pH 3.5 before experimentation on the titrator. The conditioning process is intended to remove adsorbed cations and other soluble salts as well as saturate all exchange sites with sodium. The conditioned soil showed lower buffer capacity than the treated, unconditioned soil, taking less acid to stabilize at a target pH value (Figure 7).

We performed soil dissolution experiments to investigate the stability of treated (unconditioned) soil. Cation concentrations were measured as a function of time for experiments performed at various pH values. All experiments showed an initial rapid release of cations from the soil at all pH values tested (Figure 8). Unconditioned soil will dissolve under conditions used in sorption experiments. Dissolution rates were calculated using the amount (moles/kg of soil) of calcium released from the soil and the surface area of the soil (34.2 $m^2/g$). If sorption experiments last for 24 hours (1,440 min), the soil will dissolve at a rate of 2.14E-6 moles of calcium/$m^2$ at pH 3. If sorption experiments last 1 hr, then the soil will dissolve at a rate of 9.06E-8 moles of calcium/$m^2$ at pH 3.

Surface charges were calculated from the titration curves for goethite. Figure 9 illustrates the relation between surface charge and pH produced from a titration of 1-g/L goethite in 300-mL 0.01 *M* NaCl. We fit titration curves from the laboratory using a triple-layer surface complexation model. A good fit was obtained from the modeling (Figure 9), indicating that equipment and methods used in the laboratory are working as expected.

## Conclusions

The reactive transport project is developing and evaluating an approach to mechanistic adsorption for natural soils. Surface charge titration experiments with native soils indicate that soluble salts and adsorbed cations interfere with titrations. The soluble salts and adsorbed cations can be removed by aggressive conditioning of the soil at pH 3.5. Conditioning of the soil can improve the experimental performance of the surfaces for titrations, but the effects of soil conditioning on adsorption and the ability to predict adsorption onto nonconditioned surfaces based on the measured adsorption isotherms are yet to be determined.

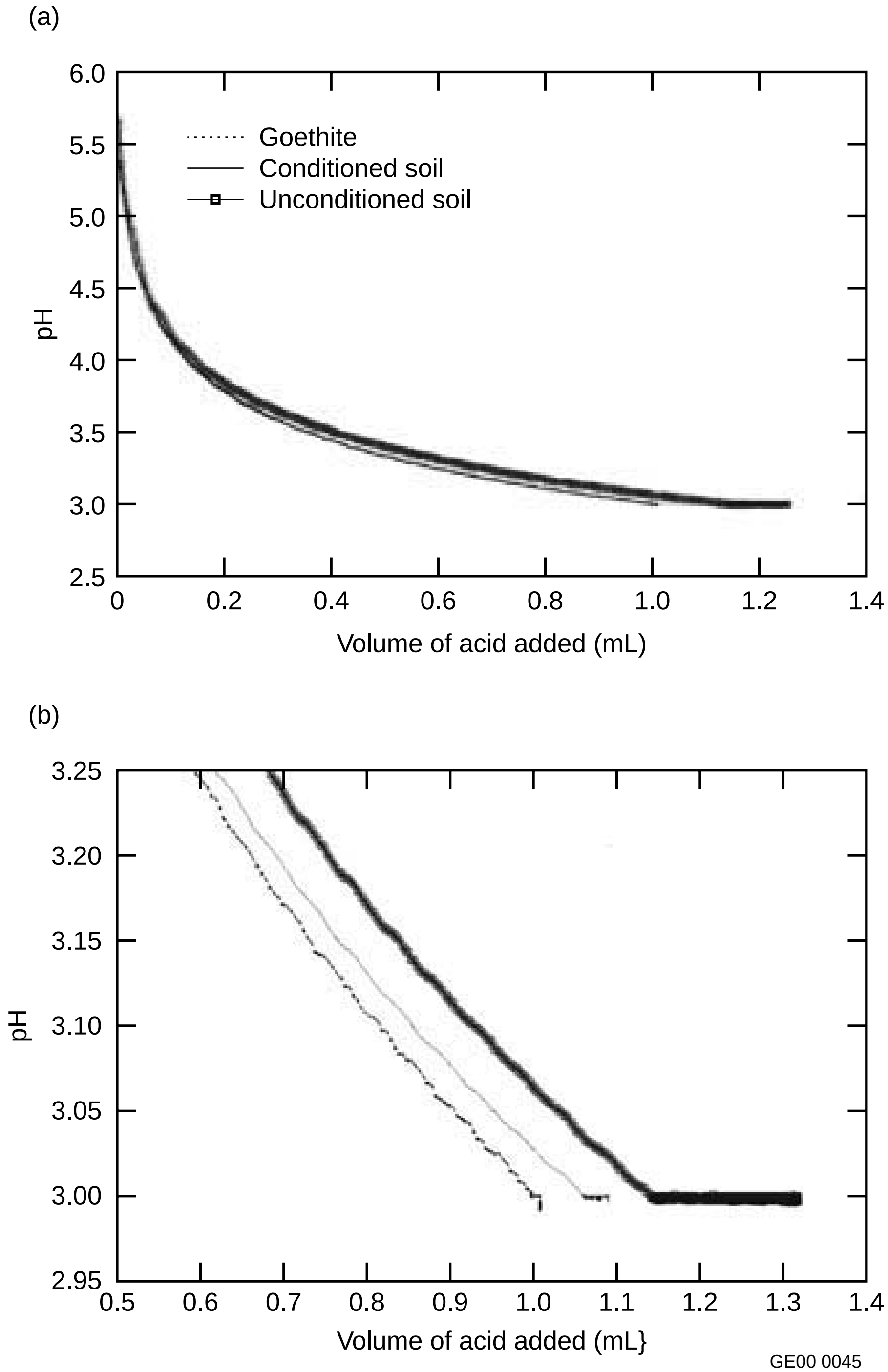

GE00 0045

**Figure 7.** Titration of minerals and soil shows that, in contrast to goethite, unconditioned soil continues to react with the acid and does not stabilize at the new pH value.

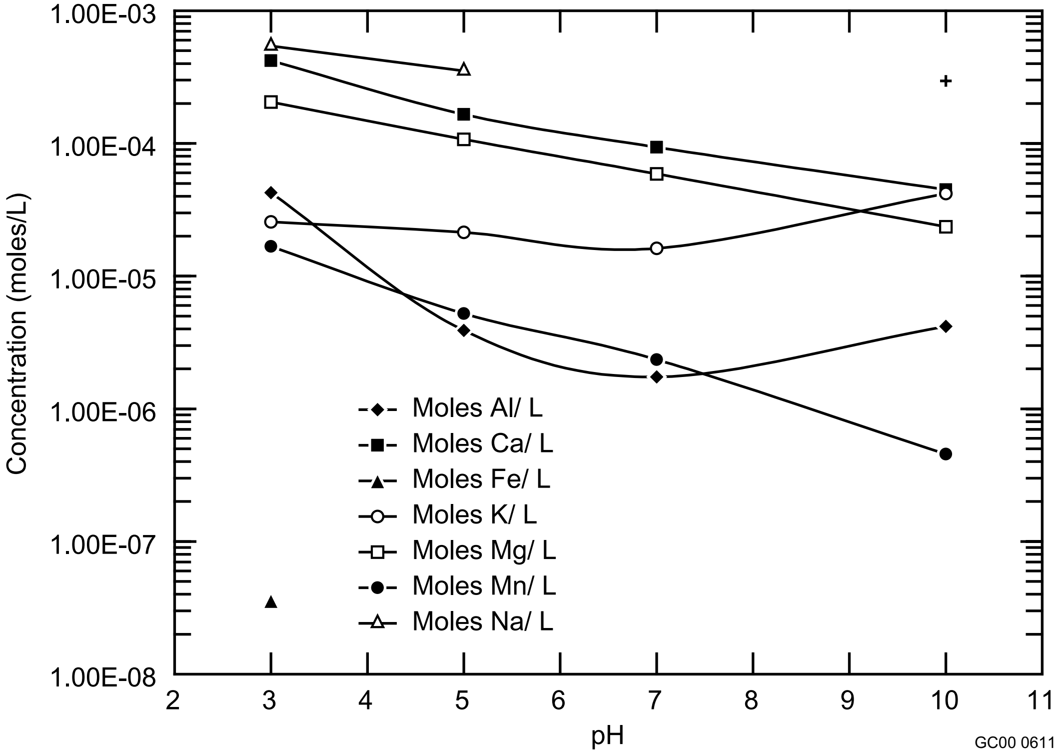

**Figure 8.** Dissolution of soil minerals at all pH values tested will consume hydrogen ions during titration experiments.

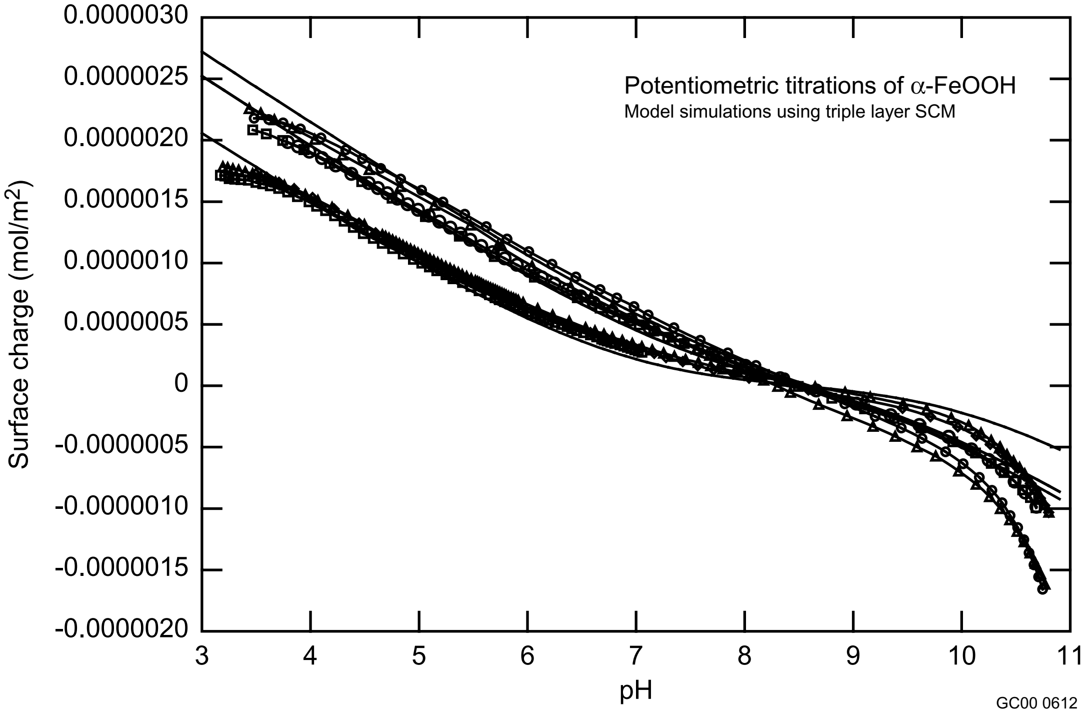

**Figure 9.** Proton stoichiometry titration for goethite at an ionic strength of 0.01 molar.

# Enhanced Computational Methods

## Overview

The transport of various chemical species, including various pollutants, in the subsurface environment is very significantly a function of the dynamics of the fluids present. Typically, these transport processes are modeled by differential equations that describe the transport of solutes, the distribution of pressure head, etc. The complexity of these equations, as well as the heterogeneity of the soils present, requires that the solutions to these transport equations be approximated through application of computer-based numerical techniques. The engineering field used to describe the application of numerical techniques to solve fluid flow equations is called computational fluid dynamics (CFD). Transport in subsurface media is one major branch of computational fluid dynamics. The focus of our project is to develop a numerical technique for approximating differential equations that shows potential for increasing the speed of an accurate solution over traditional methods.

The numerical techniques in use today in commercial CFD codes are still mostly first-generation techniques developed in the 50s, 60s, and 70s. Most of the benefits in reduced analysis times have come from faster, more capable computers, such as parallel processing rather than improved numerical techniques. The B-spline point collocation method shows significant potential as a superior numerical technique, firstly because it avoids grid generation. Secondly, the data required to represent a solution are far fewer than for traditional methods, which should result in much shorter analysis times. Thirdly, the level of accuracy can be as high as desired. It is important in the field of subsurface transport that analysis times be decreased significantly to allow for calibrating field properties and for optimizing remediation strategies, both of which require many simulations of fluid and pollutant transport

We describe the nature of the B-spline collocation method and the approach followed to further its development. Even though development is still in the initial stages, we have made measurable progress.

## Background

The B-spline numerical method can be considered a member of the finite element family of methods, though it is different in important aspects from standard finite element methods (FEM). The approach is to employ advanced geometric functions (e.g., B-splines) as the basis for the usual trial functions used in FEM to represent the solution. Also, for the test function, which appears in the weak statement and represents the weighting function, the method uses the Dirac delta function, which essentially returns the original differential equation upon integration. Because there is essentially no integration required over finite elements/volumes, the solution is found by evaluating the residual to the differential equation at various points, called collocation points. The solution process involves seeking the functions that minimize the magnitude of the residuals computed at the collocation points. Hence, the method is a point collocation method.

The B-spline method may also be viewed as a spline collocation method. As a method for approximating solutions to differential equations, spline collocation has also been around for some time. Collocation is considered to be more efficient than methods that require integration of the differential equations (Celia and Pinder 1990; Fairweather and Meade 1989). Fairweather and Meade extensively surveyed spline collocation methods. They classify spline collocation methods into four categories: nodal, orthogonal, extrapolated/modified, and collocation/Galerkin. Spline collocation methods are said to perform better than collocation/Galerkin methods, which perform better that Galerkin methods.

The type of collocation scheme relates to the locations of the collocation points. Orthogonal collocation is widely used and is shown to yield optimal order of accuracy (de Boor and Swartz 1973). Here, the collocation points are located on the intervals between junctions at the Gaussian integration points. Others have determined that an upwind collocation method is appropriate when convection-dominated convection-diffusion equations, often true for fluid dynamics equations, are being solved (Sun 1999; Shapiro and Pinder 1981). Ganesh and Sloan (1999) introduce a cost-effective alternative to orthogonal collocation with stability and convergence similar to orthogonal collocation. They have discovered that by using splines that have $C^m$ continuity for an mth order ordinary differential equation, they need far fewer data values to define the spline, even as few as half the number needed for $C^{m-1}$ splines.

B-splines and nonuniform rational B-splines (NURBS) are very popular in commercial computer-aided design (CAD) software. They are used to represent curves and surfaces for solid modeling. The field of research that encompasses geometric design is called computer-aided geometric design (CAGD) (Farin 1997; Hoschek and Lasser 1993). The value of B-splines has also received some attention in the numerical analysis community. Shariff and Moser (1998) and Kravchenko, Moin, and Moser (1996) have used B-splines as basis functions in a Galerkin method to resolve near wall eddies in large eddy simulation and direct numerical simulation (LES/DNS) of turbulence. They embed special meshes near the wall where the B-splines are used. They also discuss the attractive features of using B-splines, including the arbitrary order of accuracy and high resolution attainable, drastic reduction of numbers of grid points, and automatic $C^{n-1}$ continuity for n-degree B-splines.

The fact that collocation is employed means that a grid need not be generated. The time required to generate grids for complex problems can represent a significant portion of the solution process. Furthermore, B-spline curves and surfaces can represent solutions to differential equations using far fewer data than traditional CFD methods (finite difference, finite volume, linear finite elements). Solution matrices are much smaller and should require less time to solve than do the traditional approaches.

The finite element method was in the process of development (Baker 1998) at about the same time as were parametrically based Bezier curves. Although finite element developers looked at using splines as basis functions, they may not have been aware of the development or the functionality of these kinds of functions. Employing the parametrically based technique to describe a spline function is far easier and has some advantages over using a standard Cartesian-based approach. Some of the features of the B-spline are that

- B-splines are easily defined and manipulated because they are defined parametrically. That is, instead of being defined as a spline of curves in Cartesian space with Cartesian variables, they are defined in parametric space using parametric variables.
- B-splines have definitive end points.
- B-splines provide automatic $C^{n-1}$ continuity at junction points for a degree 'n' spline.
- B-splines can be represented by the well-known Bernstein polynomials, which are easy to calculate and numerically stable. Each segment of an 'n'-degree B-spline is defined by 'n+1' Bernstein polynomials (not an infinite series).

The B-spline curve is defined by the locations of the junctions (or knots) between individual curve segments, and the values of associated control points (de Boor points) (Farin 1997). Because a B-spline curve is a series of analytically defined curve segments splined together, derivatives can be analytically evaluated along the spline. The differentiability of the spline is limited only at the junctions (knots) by the degree of the individual curves. For a cubic B-spline, 2nd order (parametric) derivatives are defined at the knots. Figure 10 shows two curves that represent an approximate solution profile for the streamwise velocity component for flow in a channel at 1.25 channel widths downstream of the inlet. Shown is the finite element solution using bilinear elements and a B-spline fitted to the finite element solution. The B-spline data required to approximate the finite element solutions are far fewer than the number of finite element data. The finite element solution comprises the locations and values at 35 interior nodes (70 pieces of data). The B-spline consists of a knot vector with five interior data values and seven de Boor points, or 12 data values.

A B-spline surface can be defined using a tensor product of B-spline curves. B-spline surfaces are commonly used in the computer-aided design (CAD) world where objects having arbitrary geometry are rendered. The B-spline surface is defined at every point within the domain of the surface. Derivatives can be evaluated analytically at any point on the surface. A B-spline surface, which approximates the solution of a 2D differential equation to some tolerance, can be found using one of many known search algorithms. The approach, described in detail below, employs a two-dimensional problem for which the solution is a series of surfaces. These are approximated using tensor-product B-spline surfaces.

## Approach

The objectives of the Enhanced Computational Methods Task for Fiscal Year 2000, which constitute the subtasks, are as follows:

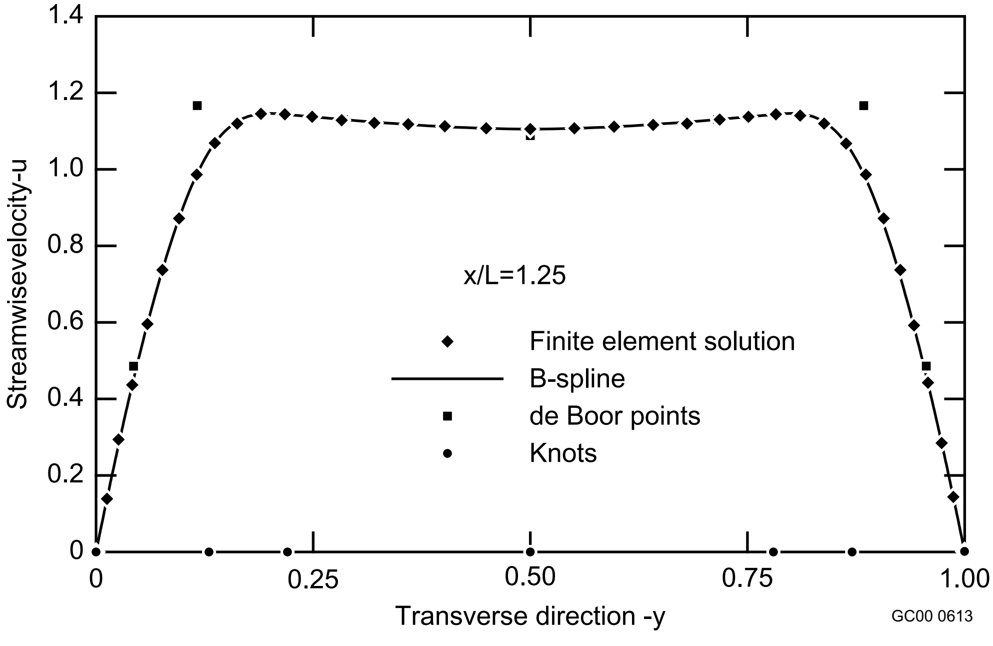

**Figure 10.** The finite element solution for the test problem for the streamwise velocity in a channel flow at 1.25 channel widths from the true inlet compared to a B-spline fitted to the finite element solution. Also shown are the knots (spline junctions) and control (de Boor) points that together define the B-spline. This B-spline is used as the inlet for the computational domain for the B-spline code.

1. Finish development of the solver and code in order to obtain the correct solution for the test problem.

2. Incorporate the appropriate equations for solute transport in the vadose zone.

3. Develop a knot insertion algorithm to increase numerical resolution.

4. Publish a report of accomplishments.

We chose a test problem to solve for subtask 1. The problem is a geometrically simple two-dimensional, incompressible, laminar flow in a channel. The flow has a plug flow (flat) inlet profile. Boundary layers develop along each wall until they merge and attain fully developed flow. The flow was simulated using a commercial finite element CFD code (Fidap 1999), for comparison. Initially, the flow has components in both the streamwise and transverse directions. As the flow becomes fully developed, the transverse component decays to zero. At this point, the flow equations reduce to one equation, which can be solved analytically, the solution being a simple parabolic profile. The equations that describe the flow in the initial region of the channel are given as

$$\begin{aligned}
&\rho u\frac{\partial u}{\partial x}+\rho v\frac{\partial u}{\partial y}=-\frac{\partial p}{\partial x}+\mu\left[\frac{\partial^2 u}{\partial x^2}+\frac{\partial^2 u}{\partial y^2}\right] \quad \text{(conservation of axial momentum) .}\\
&\rho u\frac{\partial v}{\partial x}+\rho v\frac{\partial v}{\partial y}=-\frac{\partial p}{\partial y}+\mu\left[\frac{\partial^2 v}{\partial x^2}+\frac{\partial^2 v}{\partial y^2}\right] \quad \text{(conservation of transverse momentum) .}\\
&\frac{\partial u}{\partial x}+\frac{\partial v}{\partial y}=0 \quad \text{(conservation of mass) .}
\end{aligned} \tag{4}$$

The inlet for the test problem for the B-spline method is set at 1.25 channel widths downstream of the true inlet, because the Fidap solution is spatially oscillatory up to almost this point. The outlet for the test problem is set at 13 step heights downstream from the true inlet. The axial and transverse velocities at these cross-sections from the Fidap solution are fitted with B-splines. These are used in the B-spline code for the inlet and outlet conditions. The velocity components are set at zero along both walls. The Reynolds number for the test problem (Re = $\rho$LV/$\mu$) is set to 500. Here, $\rho$ is the density, L is the channel width, V is the mean axial velocity, and $\mu$ is the dynamic viscosity. The pressure is not set except at the outlet, where it is set to zero.

Last year we created a B-spline code to solve for the test problem. This early version of the code was designed to interface with a commercial optimization code to demonstrate feasibility of the B-spline method. Feasibility was demonstrated and reported in Johnson and Landon (1999). The commercial code proved to be very slow, however, and we initiated coding of a solution algorithm internal to the B-spline code. In order to provide for the internal solution algorithm(s), and the successful completion of subtask 1, several issues needed to be addressed. A detailed discussion of the issues follows.

**Choice-of-solution method**. The solution can be found either by setting the problem up as a minimization (optimization) problem and applying a minimum-finding algorithm or as a standard problem where a zero (vector) is sought, using a zero-finding algorithm. We have tried both zero finding and minimization algorithms. For the minimization problem, we tried both a conjugate gradient and a quasi-Newton (variable metric) algorithm. The latter employs the well-known BFGS update algorithm. For the zero-finding algorithm, we used a globally convergent method for nonlinear systems of equations.

Furthermore, methods using individual matrices for each dependent variable were compared to methods that used one large matrix that included all variables. These algorithms were adapted from Press et al (1992). Eventually, it will be expedient to employ the most efficient solution method in order to realize the potential speed of B-spline collocation. Though, at this time, we simply desire to have a solution method that produces a solution. It does appear, however, that the zero-finding algorithm converges fastest to a solution.

**Points used as collocation points**. Theoretically, the equations should be solved for the infinite number of points in the flow domain. Practically, the equations are evaluated at a finite number of points, called collocation points, in order to determine how well the equations are solved. For the minimization solver, the number of points can be any number if enough to generate a good solution but not so many that computing times are excessive. The reason for this is that a function is identified for minimization that can be the sum of the absolute values of the residuals for any desired number of points. The residual is the difference between the approximated solution and the differential equation at a point. For the zero-finding solution, the number of collocation points needed is exactly the number of B-spline control points needed to define the solution. The issue is what points should be used for these collocation points. A number of groups of points can be used. The knots are points where the spline segments join; there are fewer of them than there are control points. There are also the Gaussian integration points identified by de Boor as the points that yield optimal order of accuracy. However, for one-point Gaussian integration, there are not enough points. For two-point integration, there are too many. There are the actual locations of the control points. These are called the Greville abscissae and are the locations of the control points themselves. There are also hybrid sets of points that use combinations of the above in order to obtain enough points. We have obtained reasonable results using hybrid sets consisting of Gaussian points and Greville abscissae.

**Residuals used**. The equations to be solved are coupled, with most dependent variables appearing in each equation. Hence, the equations must be solved simultaneously. The solution procedure starts with an initial guess and attempts to drive the errors (residuals) to zero. The solution algorithm uses a specific search procedure to find improved values for the solution. The solution for each dependent variable (u, v, p) is constructed from B-spline surfaces. One of the ways in which the method has potential to save time is by recognizing the fact that the solution for each dependent variable can be constructed from its own unique B-spline surface. For the test problem used, it appears that the surface for the transverse velocity, v, should require the most B-spline patches to describe it. (A patch is formed from spline segments in two dimensions.) The other two require fewer patches. For the zero-finding algorithm, the residual function for each unknown variable can be formed in various ways. It appears that carefully summing the residuals for mass and the particular momentum equation for each velocity component, and all three residuals for the pressure surface, is the best scheme.

**Line search**. For both the minimum and the zero-finding algorithms used, the solution procedure requires a line-search algorithm. That is, the solution algorithms determine a search direction in which to look for a solution. If the equations were linear, only one search would be needed. However, for nonlinear equations, the search direction computed is only approximate. When the search direction is found, the line-search algorithm proceeds in the search direction until a minimum is found. At this point, a new search direction is computed and the process repeats. Press et al (1992) provide a line-search algorithm that goes until a minimum is bracketed, and then it fits a cubic curve to approximate the minimum. This algorithm worked for a few iterations and then failed. We modified this line search algorithm to use a quadratic fit to make it work. Also, we created a separate, more efficient line search algorithm.

**Numerical gradients**. The solution algorithms all required calculation of numerical gradients in order to determine the search directions. Numerical gradients are formed by calculating the function at different points and performing a finite difference approximation. A centered difference formula is used with a perturbation of 0.01% of the dependent variable in each direction. This appears to produce an accurate finite difference approximation to the gradient.

**Scaling**. The numerical reference of Press et al (1992) indicates that dependent variables that are not of the order of 1.0 should be rescaled so that they are, making the solution algorithm more efficient. For the test problem employed, the values of the control points for the u velocity component are of the order of 1.0, while the v component parameters are a few orders of magnitude lower. Nevertheless, we found that attempting to scale the v component variable led to poorer results.

**Numbers of knots**. Although the number of knots in the transverse direction is set by the number needed to represent accurately the inlet profiles, the number of knots in the streamwise direction is variable. We employed enough knots such that the solution could be adequately approximated. This was determined by comparing with the Fidap solution as well as a solution found using B-splines. We based the latter on a sufficiently fine knot network and on the application of a minimum finding algorithm where the minimization (objective) function was the sum of the residuals on a very fine grid of collocation points.

## Research Results

These several issues all had to be successfully addressed in order to obtain a reasonable solution to the test problem. Results are presented for two different sets of collocation points: a hybrid set involving various Gaussian integration points and other points, and a set based on the locations of the control points, referred to as the Greville points. Figure 11 is a schematic of the computational domain for the streamwise velocity, u, with the locations of the hybrid collocation points, the Greville collocation points, and the knots. The knots define the corners of the Bezier patches that constitute the B-spline surface. Figure 12 illustrates the B-spline surface computed for the streamwise velocity component. Also shown are the several control or de Boor points, which, along with the knots, define the B-spline surface.

Figures 13a-b and 14a-b show results for profiles for the streamwise and transverse velocity components at two cross sections, $x/L = 4.0$ and 6.5, respectively. The results for the hybrid and Greville collocation points, employing the zero-finding algorithm, are compared to the solution for the commercial CFD code, Fidap, and the B-spline solution using the minimum finding algorithm (BFGS data) on the very fine grid ($48 \times 51$ points). That is, the zero-finding algorithm evaluates the residuals for just the collocation points, ($4 \times 7$) for the u velocity and ($4 \times 10$) for the v velocity, while the minimum finder computes the residuals at 2448 points. The latter, of course, computes a more accurate solution, because far more information is used. However, the latter also is quite slow. The results shown in these figures are reasonable, though not as accurate as the fine grid solution. The time required for the hybrid and Greville collocation points using the zero-finder is approximately half the time used by Fidap, though the algorithms have not been fully optimized.

Figure 15 compares the streamwise profile for the pressure along the channel centerline for the same four solutions as above. Figure 16 compares the same solutions for the streamwise profile of the streamwise velocity. As can be seen, the solutions for the hybrid and Greville collocation points using the zero-finding algorithm are reasonable, though not as accurate as the fine-grid solution. The fine-grid solution is deemed to be the most accurate solution because of the fineness of the grid and because it is very close to the Fidap solution.

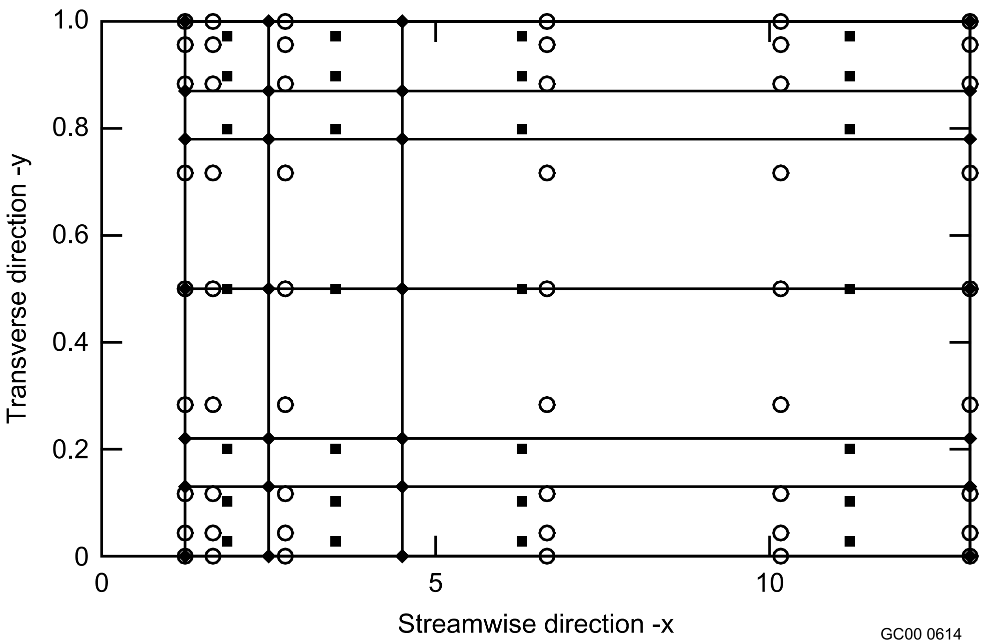

**Figure 11.** A schematic of the computational domain for the streamwise (u) velocity component, showing the hybrid set of collocation points ( ), the Greville collocation points (O) and the knots (♦). The knots form the corners of the Bezier patches that constitute the B-spline surface.

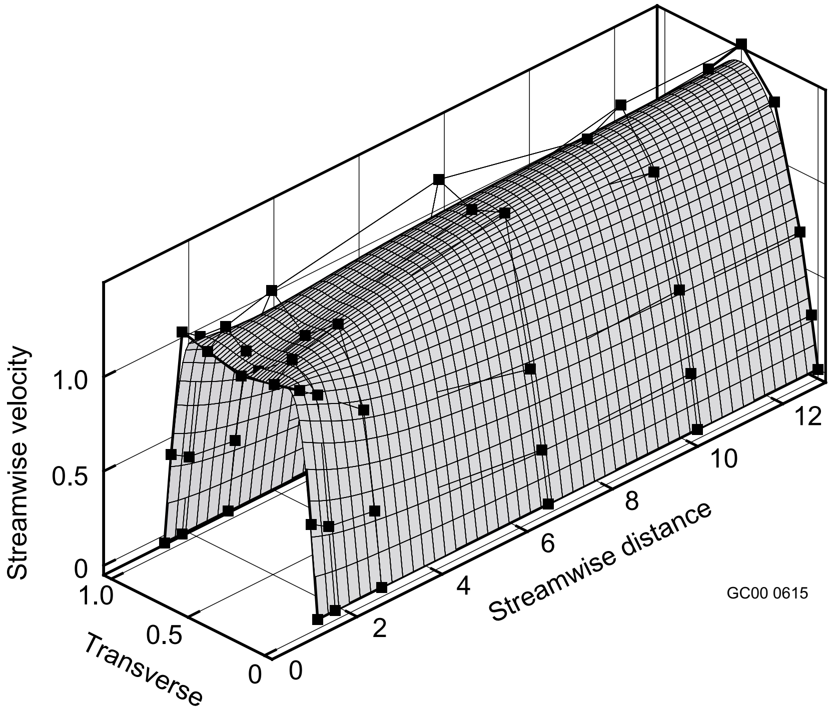

**Figure 12.** The B-spline surface, which represents the solution for the streamwise velocity component for the test problem. The de Boor points are shown as square symbols.

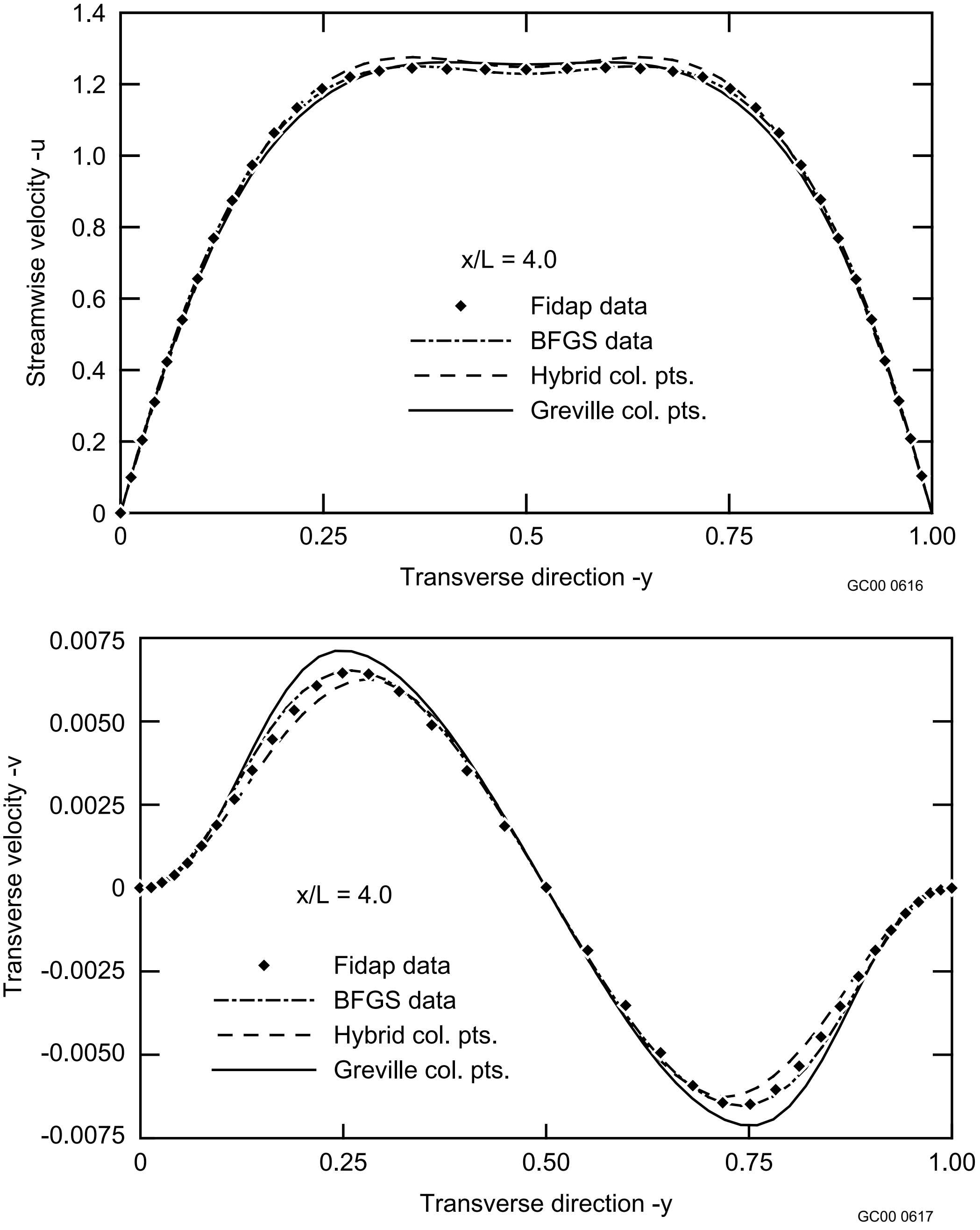

**Figure 13.** Cross-stream profiles for the (a) streamwise and (b) transverse velocities at x/L = 4.0, for the Fidap data, the fine-grid B-spline results (BFGS data), the hybrid collocation points, and the Greville points.

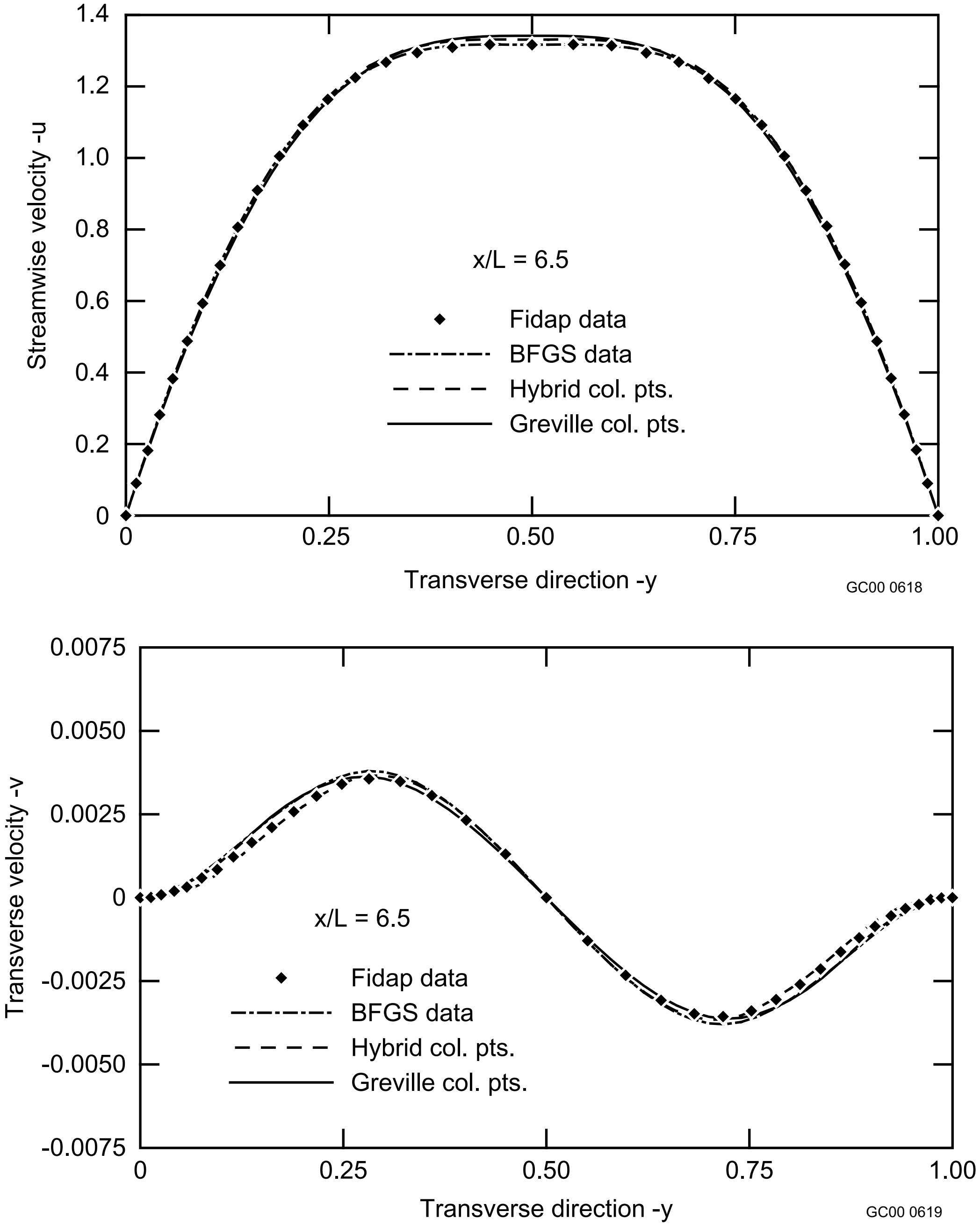

**Figure 14.** Cross-stream profiles for the (a) streamwise and (b) transverse velocities at x/L = 6.5, for the Fidap data, the fine-grid B-spline results (BFGS data), the hybrid collocation points, and the Greville points.

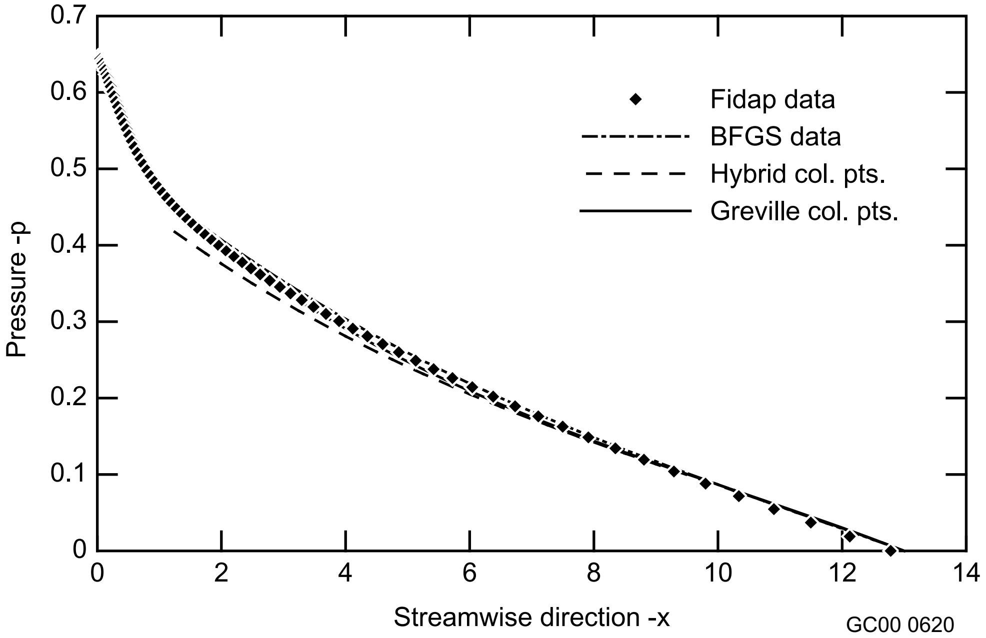

**Figure 15.** Streamwise profile for the pressure along the channel centerline for the Fidap data, the fine-grid B-spline results (BFGS data), the hybrid points, and the Greville points.

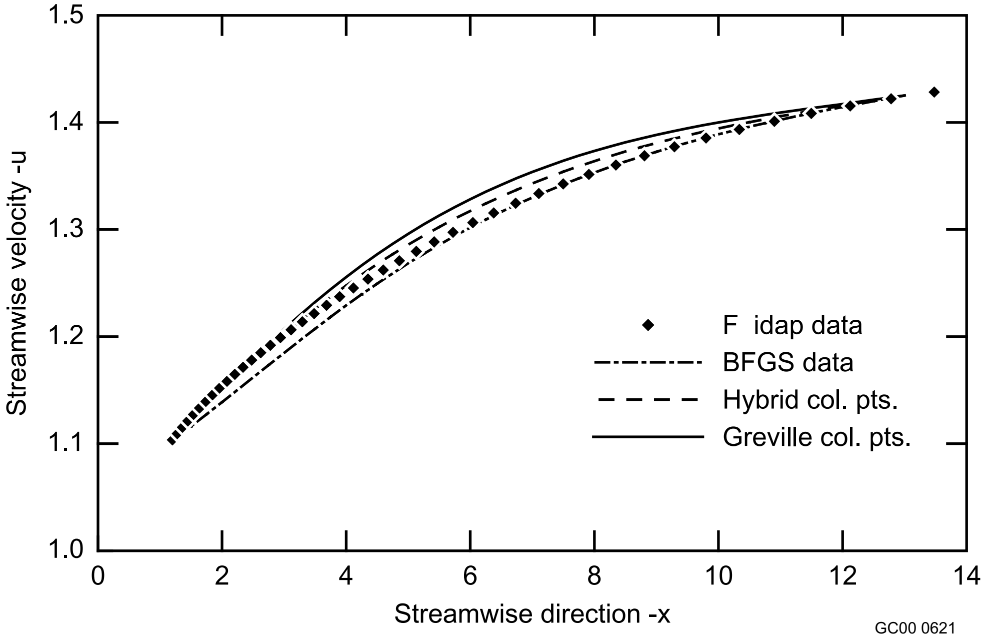

**Figure 16.** Streamwise profile for the streamwise velocity along the channel centerline for the Fidap data, the fine-grid B-spline results (BFGS data), the hybrid points, and the Greville points.

We have obtained preliminary results for the second subtask listed above, the application of the method to a solute transport problem. The problem involves the solution of a simplified version of the solute transport equation. This equation is given as

$$D_L \frac{\partial^2 C}{\partial x^2} + D_T \frac{\partial^2 C}{\partial y^2} - u_x \frac{\partial C}{\partial x} = S \tag{5}$$

where $C$ is the solute concentration, x is the direction of a (uniform) subsurface fluid velocity $u_x$, y is the direction transverse to x, and $D_L$ and $D_T$ are the longitudinal and transverse hydrodynamics dispersion coefficients, respectively. $S$ is a constant sink of the solute that occurs uniformly in the subsurface. The equation above has been simplified to be able to accommodate the current status of the B-spline collocation method.

## Vadose Zone Moisture Movement

### Overview

The advective transport of water and gases is the primary method controlling the distribution of contaminants, nutrients, and moisture in the vadose zone. These fluid pathways are determined by the distribution of the permeability distribution within the subsurface and the boundary conditions. Numerous controlled-boundary field-scale studies (e.g., Las Cruces Trench site, New Mexico Tech Golf Course site, Sisson and Lu's PNNL Borehole site) have indicated that the heterogeneity (i.e., distribution) of fluid transport properties is the controlling factor in the direction of fluid movement in the subsurface. An adequate description of the transport properties' variability requires a large number of data points that are rarely obtained due to the enormous difficulty (cost, time, and subsurface access) of obtaining the data. Laboratory estimates of the transport properties seldom correlate well with field results. Thus, in situ methods are desired for estimating transport properties. Inadequate characterization of the heterogeneity has led to ineffective remedial designs, which lead to risk estimates with a high degree of uncertainty, higher costs, and longer remediation times. DOE has indicated their recognition of this problem with statements such as "Fundamental improvements in the abilities to characterize contaminant geologic settings and chemistry, to assess data, and to predict the movement and fate of contaminants are needed" (EMSP 2000). The INEEL Exfiltrometer has the potential to produce estimates of transport properties at sufficient spatial density and at acceptable cost.

### Research Results

Numerous instruments have been designed in the past few years (e.g., the tension infiltrometer, the mini air permeameter, Geulph permeameter) to provide field measurements in part for spatial variability analysis. Recent analysis of these instruments (by Holt et al., 1999) suggest that the error incorporated in taking these measurements and in the inversion-model used may overshadow the spatial variability in the parameter being measured. We suggest evaluating an instrument that measures the hydraulic properties in a single direction and computes water flux directly.

The Exfiltrometer has been tested to evaluate its ability to measure unsaturated hydraulic conductivity while concurrently measuring the drainage moisture characteristic relationship. The Exfiltrometer measures the transport parameter (e.g., hydraulic conductivity) directly, quickly, and inexpensively. Testing at the INEEL (Mattson and Sisson, 1999) illustrates that this permeameter could supply repeatable results in a silty sand material. Results obtained during FY 2000 include development of a rapid calibration method for dielectric soil water content sensors. Figure 17 shows the calibration curve resulting from one type of water content sensor, the CS505 (Campbell Scientific, Inc., Logan, UT).

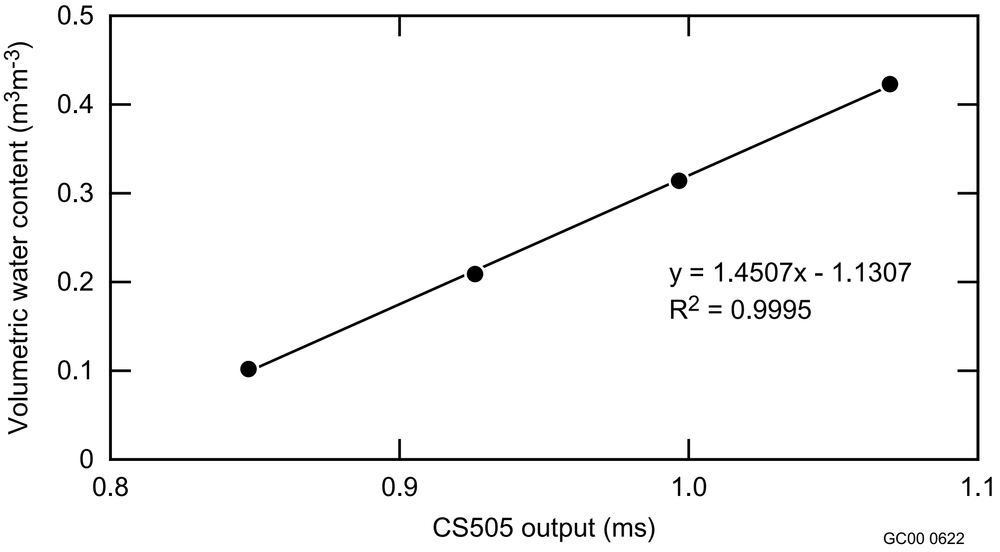

**Figure 17.** Campbell Scientific CS505 water content sensor calibration as a function of moisture content.

Ongoing work includes evaluating new classes of water content sensors, which are an integral part of the Exfiltrometer. The expected result of the ongoing work will be a water content sensor that is nearly independent of soil type and electrical conductivity effects.

Overland flow and surface ponding have often been observed at the INEEL Subsurface Disposal Area during spring snowmelt and occasionally during heavy rainfall. These surface flow events result in focused infiltration in small, local areas at many times greater than the average infiltration rate. Monitoring data indicate that these episodic infiltration events result in the formation of a perched water table on the sediment/basalt interface. This perched water body subsequently infiltrates into the underlying fractured basalt, likely carrying contamination from the waste pit to the aquifer.

It is speculated that the mechanisms for enhanced surface infiltration result from a number of factors, including water equivalent in snow pack, rate of snowmelt, antecedent conditions prior to snow pack, and topography. Little study has been done to verify the mechanisms, quantify the enhanced surface infiltration at the INEEL, and understand the effects of this phenomenon on contaminant transport. An additional mechanism that has been ignored is the effect of the subsurface geologic structure as an additional enhanced recharge mechanism (i.e., funnel flow) within the vadose zone. We do not know how much lateral flow occurs at this interface or what mechanism creates the perching of infiltrated water at the sediment/basalt interface. Recharge in the form of rain and snowmelt often provides the downward driving force for contaminant migration. These rapid infiltration events force large volumes of water through the soil and often result in perching of water at the upper sediment/basalt interface. Lateral movement of the perched water may intercept contaminants in the waste pits and transport these contaminants deep into the vadose zone.

We hypothesize that the textural component of the sediment immediately overlying the basalt, as well as the topography of the basalt surface, will focus recharge to a relatively small number of the fractures. These fractures may be in-filled with sedimentary material or the interface surface may be covered with a noncontinuous low permeable lens. The field-scale impacts of these enhanced infiltration events are not well quantified, and have not been examined in fractured systems. We will evaluate this hypothesis in cooperation with the University of Idaho at the INEEL 5-well site and through laboratory experiments examining equipment response.

We will evaluate the enhanced subsurface infiltration hypothesis at the 5-well research site by creating either a natural recharge event or an artificial recharge event at the soil surface. An electromagnetic survey conducted at the 5-well site (Figure 18) indicates an iso-electrical conductivity depression that extends from the northern boundary of the site to the existing monitoring boreholes. We speculate that this contour profile is caused by either the topography of the underlying basalt/sediment interface or by clay lenses lying on the basalt surface. Soil samples will be collected at the end of FY 2000 to evaluate these hypothesis.

Monitoring the vadose zone below buried waste provides an early warning of contaminant transport toward the groundwater. To quantify the transport mechanisms, vadose zone transport characteristics and chemical concentrations need to be obtained. Unfortunately, equipment necessary for obtaining the transport/concentration data temporal and spatial trends is not available. We have designed and

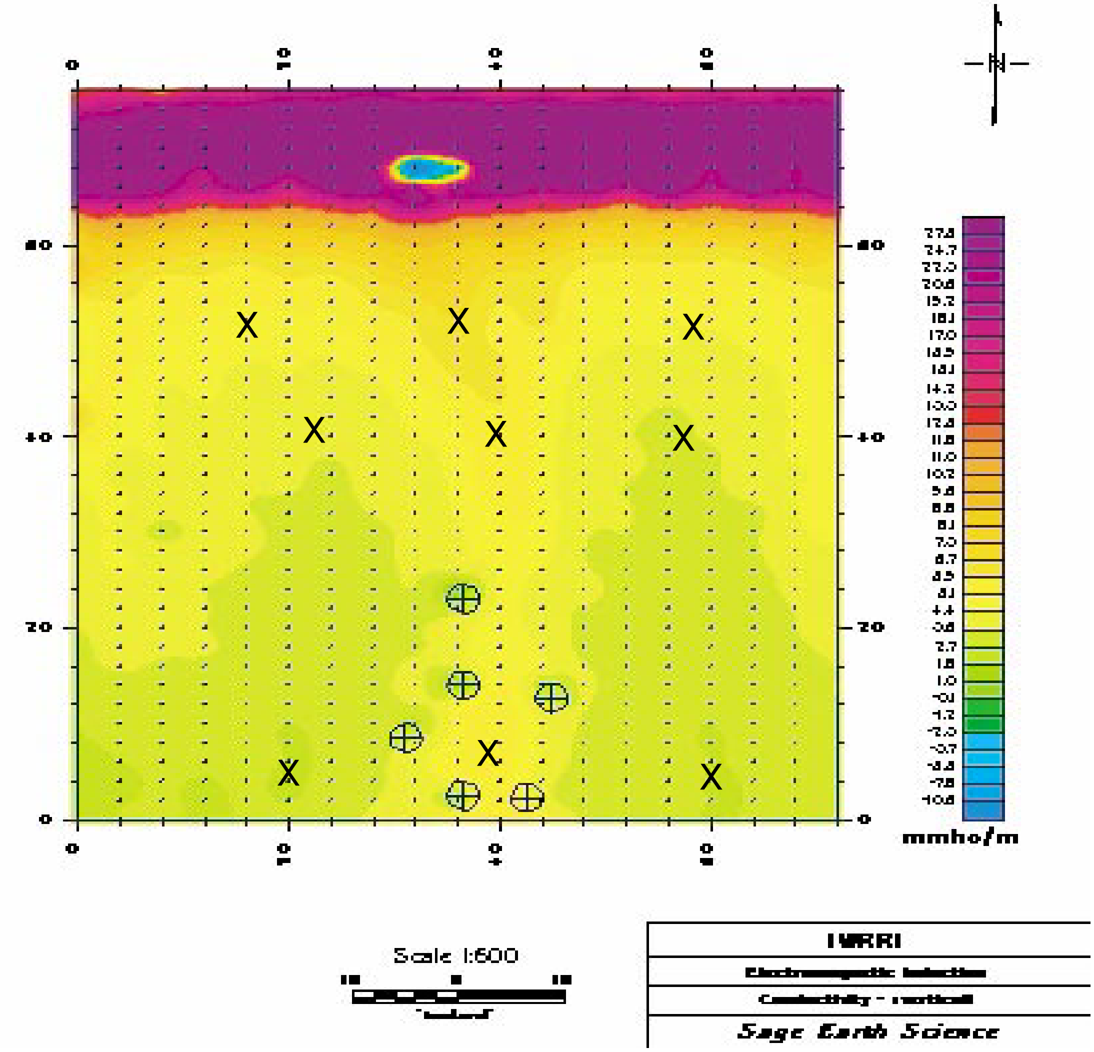

**Figure 18.** Electromagnetic surface survey results of the INEEL 5-well site. Dark blue at the top represents subsurface utility corridor. The letter X represents a proposed soil sampling location. The letter O represents an existing open and instrumented borehole.

implemented a vadose zone monitoring system to monitor and sample three state variables of the vadose zone: water potential, water content, and chemical concentration. These state variables are monitored using an advanced tensiometer, a borehole water content sensor, and a vacuum lysimeter, respectively. The system was installed during FY 1999 and greatly expanded in FY 2000 at the Savannah River Site, E-Area disposal site, where low-level wastes have been disposed of in shallow trenches, and at the Troy watershed research site in FY 2000. These systems have operated for several months, providing nearly continuous water content and water potential data.

An area of scientific neglect has been the collection of a long-term data set of both soil physics properties and long-term trends of chemical analysis. In an attempt to remedy this neglect, we adapted the advanced tensiometer such that we could measure the in situ chemical composition of the vadose zone. Previous researchers (Riga and Charpentier 1998; Moutonnet et al. 1993) have described that the water contained in the tensiometer will come into chemical equilibrium with the surrounding soil water through diffusion through the porous cup. These studies indicate that the time to reach chemical equilibrium is in the range of approximate ten days (a function of soil type and its soil water potential) for unsaturated soil. This long equilibrium time may not be a factor in measuring monitoring vadose zone chemical concentrations in a nondynamic system where the temporal response is seasonal. Such a situation may exist in the vadose zone where biological activity changes temporally in response to temperature and precipitation events. In the case where there is an infiltration event, the soil water potential will become more positive and will cause an advective flux of water, along with its solute, to enter the tensiometer cup, decreasing the equilibrium time. Even if the advective flux were ignored, Moutonnet et al. (1993) suggest that the response time is compatible to the rate of soil water migration.

Previous studies extracted water samples from the tensiometers for subsequent laboratory analysis in much the same way as suction lysimeters. These samples were taken at discrete intervals, possibly missing episodic chemical transport events. The research at INEEL has examined the installation of chemical sensing probes directly into the advanced tensiometer to be used as long-term chemical sensors. Preliminary analyses of laboratory testing of various porous materials indicate that porous nylon material has approximately ten times greater diffusion coefficient than other commercially available porous materials (i.e., ceramic and porous steel). Concurrent testing of commercially available sensors indicate that electrical conductivity measurements are the most suitable to use as long-term indicators of changes of in situ chemical conditions. Electrolyte leakage from ion-specific electrodes and temporal drift of solid-state pH probes readings eliminated use of these sensors.

We are also evaluating carbon dioxide soil-gas sensing probes under this funding. $CO_2$ produced by plant roots and subsurface microorganisms subsequently effects soil water pH and chemical composition. Long-term continuous measurements of subsurface $CO_2$ concentrations that describe the coupling of biological/chemical processes to soil physics measurement are not available. We evaluated and found commercially available infrared light $CO_2$ sensing transmitters suitable for subsurface installation, with minor modifications. These probes are currently being installed at the Jefferson Canal Vadose Zone Research site to evaluate the long-term temporal trends of gas movement within the vadose zone. Results of this effort are not yet available to report.

The expected result will be improved understanding of transport of water, gases, and chemicals in complex heterogeneous subsurface matrices. This knowledge will lead to better monitoring and characterization strategies. The strategies will allow improved parameter estimation for predictive contaminant migration models and development of integrated remediation strategies.

# Relationships between Moisture Content, Tension, and Biogeochemical Activity in the Vadose Zone

One of the most significant difficulties facing in situ bioremediation today is the biodegradability of the contaminant. The remediation takes place in the vadose zone, where water content can vary significantly within a small volume. While volume-averaged water content measurements can sometimes adequately predict flow patterns and mobility of contaminants, they have been less successful at predicting the remediation potential because of inconsistent results regarding microbial activity. The activity of microorganisms in the subsurface is controlled in part by the availability of water and water-borne nutrients (Skopp et al. 1990; Kieft et al. 1993). The availability of water and its mobility in soil is, in turn, controlled to varying degrees by the activity of soil microorganisms and their production of $CO_2$. For example, hydraulic conductivity (a measure of water mobility in soil) is strongly influenced by the concentration of $Ca^{2+}$ (through precipitation and dissolution of calcium carbonate), and the $CO_2$ level influences the $Ca^{2+}$ concentration. The influences of $Ca^{2+}$ and $CO_2$ levels on the water retention curve are also unknown, and many microorganisms produce biofilms that may modify flow path. Finally, the production and migration of $CO_2$ significantly influences the migration of radionuclides in the vadose zone. We expect the relationship between water content and microbial activity to be complex. Laboratory- and field-scale unsaturated experiments will be conducted to test hypotheses and to develop an understanding of the relationship between microbial activity and moisture characteristics. This may include various soil types, ranging from sandy to clay soils, but will be generally limited to water potentials in the range 0.1 to 6 bar. Adequate correlation of water content with biodegradability will be important in assessing remediation potential at most DOE sites and other contaminated sites. This task supports ongoing work to develop vadose zone instrumentation, including the Exfiltrometer and the dielectric soil water content sensors.

In porous media, microbial activity decreases at both very high and very low water contents (Figure 19). This has generally been attributed to higher osmotic pressures at low water contents and to oxygen limitations at high water contents. We hypothesize that this behavior also depends on the amount of water that is *available* to the microbes (Figure 20). In effect, at very low water contents, water in unsaturated soil becomes unavailable for microbial use because the bulk of the water is held in pores smaller than or similar in size to the bacteria. Thus, not all of the water in unsaturated soils is available, and the amount available would depend directly on the pore size distribution of the soil (Figure 21). This project is divided into two subtasks, soil characterization and aerobic microbial activity. In the first subtask, we measured several properties of the model soil to understand the distribution of the water in the soil at the various water contents. These included, among others, surface area, interstitial volume, pore volume, and pore size distribution. In the second subtask, we will adjust soil to the desired water content using the Unsaturated Flow Apparatus (UFA). The solution used to adjust the water content will be either $^{13}C$-UL-glucose or a solution of $^{12}C$-glucose spiked with $^{14}C$-UL-glucose. Microbial activity in the soil will then be measured by $^{13}CO_2$ or $^{14}CO_2$ evolution under aerobic conditions. These experiments will be conducted at water potentials ranging from 0.1–6 bar, and will be done in sealed batch systems. Small enough amounts of substrate will be added to ensure that the cells remain in maintenance metabolism.

## Approach

Soil water content will be adjusted by centrifugation (Hassler and Brunner 1945; Hoffman 1963) using an UFA rotor, manufactured by UFA Ventures, Inc., Richland, WA (Conca and Wright 1992, UFA Ventures 1996). This method of desorption is expected to maintain a uniform substrate distribution throughout the sample during drainage, which is necessary to quantitatively observe the effects of

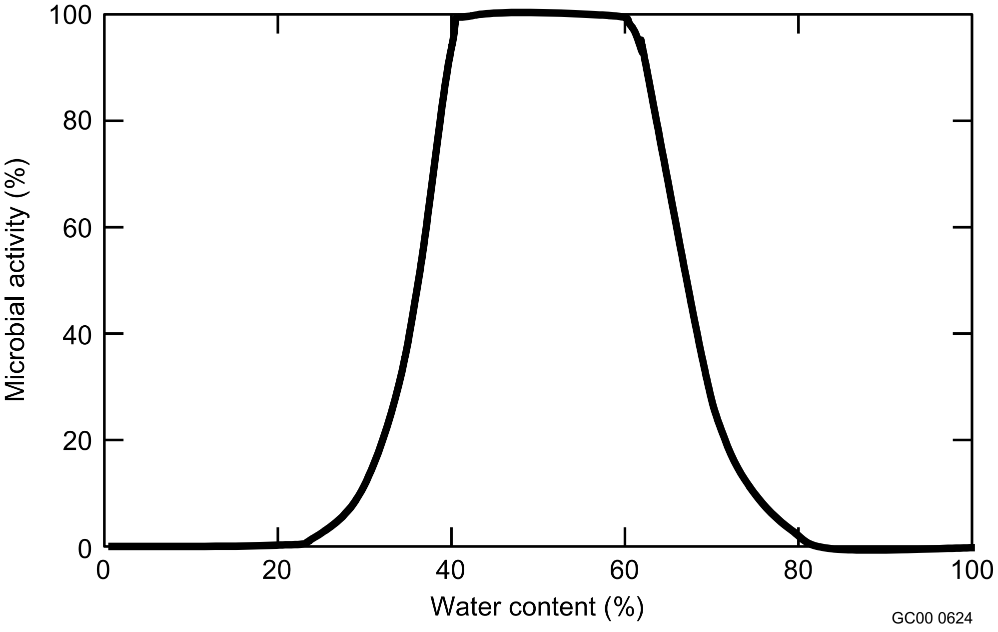

**Figure 19.** Observed variation of microbial activity with water content. This behavior is similar for various microporous supports, including soils and compost.

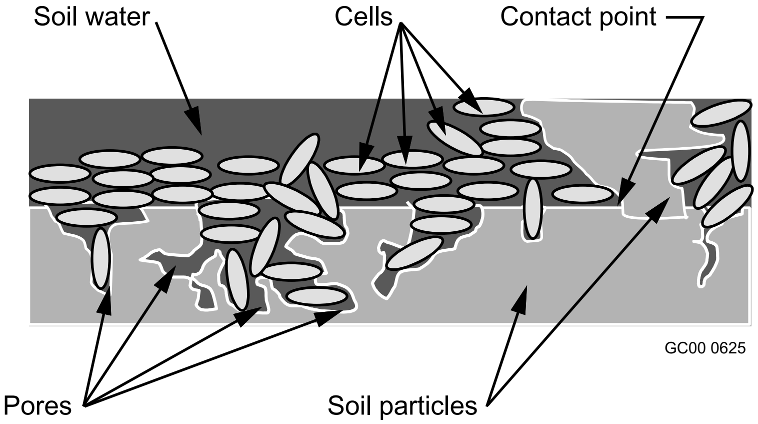

**Figure 20.** Diagram of a control volume of saturated soil. As depicted, not all of the soil water is in pores large enough for cells to enter.

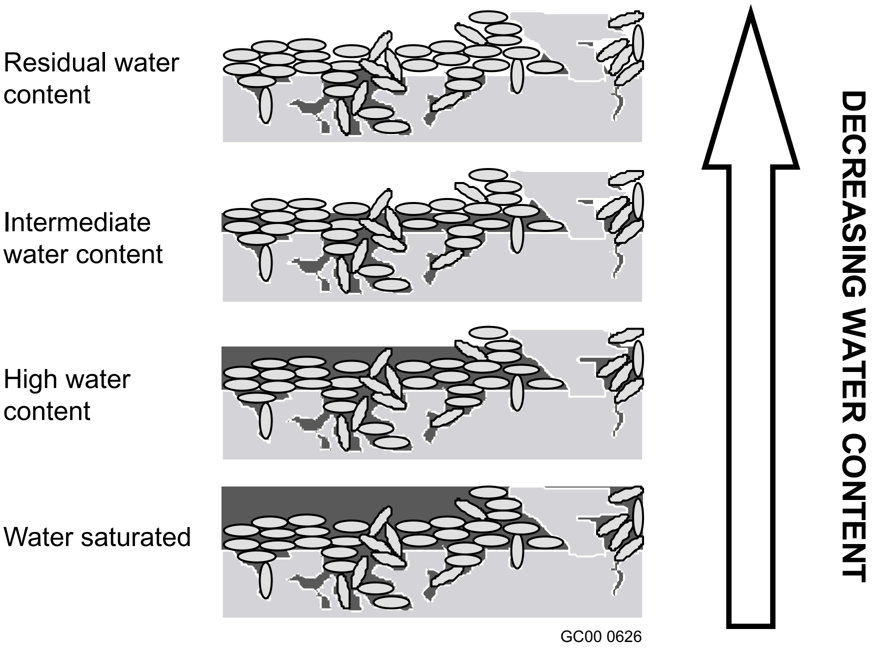

**Figure 21.** As the control volume dries out, the fraction of water unavailable to the cells increases. Even before reaching residual water content, very little of the soil water may be available to the bacterial cells.

decreasing water content on degradation of the added substrate. We purchased a UFA apparatus for use on this and other projects, which subjects the sample to large fluid driving forces up to 10,000 ×*g* in an open-flow centrifugation device, or in separate drainage cells. A rotating seal assembly allows an ultra-low flow pump to deliver fluid to the sample surface during rotation. Because of the large driving forces, steady state is reached within hours, even at hydraulic conductivities as low as $10^{-10}$ cm/s, removing the traditional time barrier to these types of experiments (ASTM D18.21 2000). Knowledge of how soil physical properties limit microbial activity will be useful in estimating the potential microbial activity in a soil over a wide range of water contents. For example, soil physical properties, including pore volume, pore size distribution, percentage sand/clay, etc., could be measured. The relationships developed in this project could be used to predict the range of microbial activities seen at different water contents based on the physical distribution of the water in the soil and its availability to the microbes. The process of in situ biodegradation could thus be better understood, and a method based on soil physical properties and local water contents could be devised to predict biodegradability. This result would directly benefit bioremediation efforts.

### Summary of Results to Date

Soil from the U.S. Department of Agriculture, Sheep Experiment Station near Dubois, Idaho was used as the model soil. The soil was collected from just below the root horizon (~3-foot depth) from the sides of a trench dug by a backhoe. A thin layer of soil was first scraped from the side of the trench, and tarred soil cans were pushed into the side wall of the trench. The cans were closed with lids, sealed with parafilm, and weighed. The sealed cans were then stored in a cold room at 4°C until use. We describe soil characterization below.

The soil was classified as a sandy loam based on percent sands, silts, and clay-size particles (using USDA triangle and standard procedures for particle size analysis), as shown in Table 2. Percent

**Table 2.** Particle size analysis of the Dubois model soil.

| Property | Population Mean |
|---|---|
| Particle density (g/cm$^3$) | 2.06 ± 0.03 |
| Particle Size Analysis: | |
| Particle diameter (mm) | 0.01 |
| $C_u$ value | 10.0 |
| $d_{10}$ value (mm) | 0.01 |
| %> 2 mm by wt | 4.91 |
| % sand by wt | 56.9 |
| % slit | 30.2 |
| % clay | 8.00 |
| Soil classification | SANDY LOAM |

carbonate and organic matter (7.5% and 1.7% by wt, respectively) listed in Table 3 are included in the percentage of silt and clay-size particles. The coefficient of uniformity ($C_u$) indicates that the soil is poorly sorted, and that 10% of the particles are less than 0.01 mm. Table 4 shows the metal content of the soil, both total and soluble (pH 7.0). Not surprisingly, calcium was present in the highest amounts, followed by iron. More calcium was also soluble than the other metals, followed closely by magnesium.

Intraparticle (micropore) pore size and surface area distributions were measured using nitrogen adsorption (Brunauer et al. 1938), with the following modifications to the standard procedure (Klute 1986): (1) organic matter and carbonates were not removed prior to measurement; and (2) the soil was dried under a vacuum at room temperature rather than oven-dried at 105°C. These modifications were made to preserve as much as possible the pore structure seen by the bacterial cells. Figures 22 and 23 show the cumulative micropore volume and surface area distributions . Since some pores in organic

**Table 3.** Mass balance for the Dubois soil.

| Component | % of Total |
|---|---|
| Sand | 56.9 ± 6.9 |
| *Silt | 38.1 ± 8.01 |
| Clay | 7.58 ± 4.11 |
| Total | 102.6 ± 11.3 |
| * % silt and clay include: | |
| Carbonate | 7.51 ± 0.81 |
| Organic matter | 1.69 ± 0.37 |

**Table 4.** Metal content of the Dubois soil, including total and soluble (pH 7.0) metals.

| Metal | Total (mg/kg) | Soluble (mg/kg) |
|---|---|---|
| Mg | 16,500 ± 900 | 9.38 ± 2.37 |
| Ca | 58,700 ± 2,900 | 10.6 ± 3.0 |
| Fe | 20,800 ± 1,000 | 0.643 ± 0.297 |
| K | 16,600 ± 800 | 0.954 ± 0.547 |
| Na | 7,800 ± 400 | 2.32 ± 0.36 |

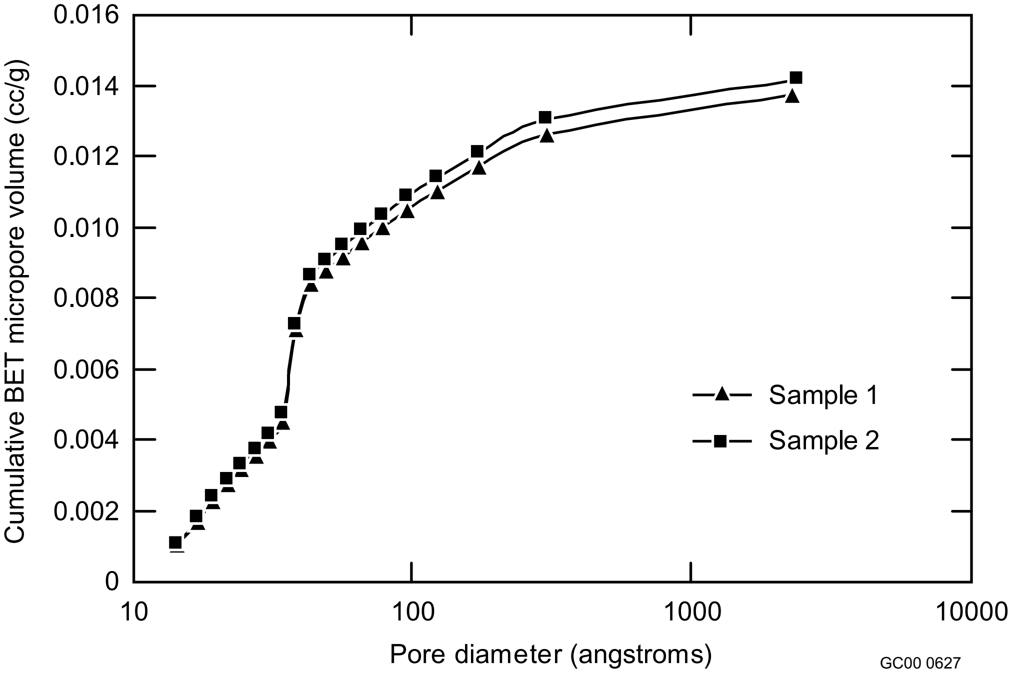

**Figure 22.** Cumulative micropore size distribution of the Dubois soil, measured by nitrogen adsorption. This represents the intraparticle pore volume and is low because of the high sand content. There is relatively little pore volume in pores smaller than about 3000 Angstroms, which is about 30% of the size of a bacterial cell (≈1 μm).

matter can collapse under dry conditions due to formation of hydrogen bonds between adjacent molecules, another independent estimate of the pore size distribution under water-saturated conditions is planned. Accordingly, the pore size distribution will also be measured by a "solute exclusion" technique in which the dilution of solutes of different molecular diameters is measured and used to construct a micropore-size distribution (Stone and Scallan 1968, Stone et al. 1969, Thompson et al. 1992). This measurement is being conducted at the time of this writing.

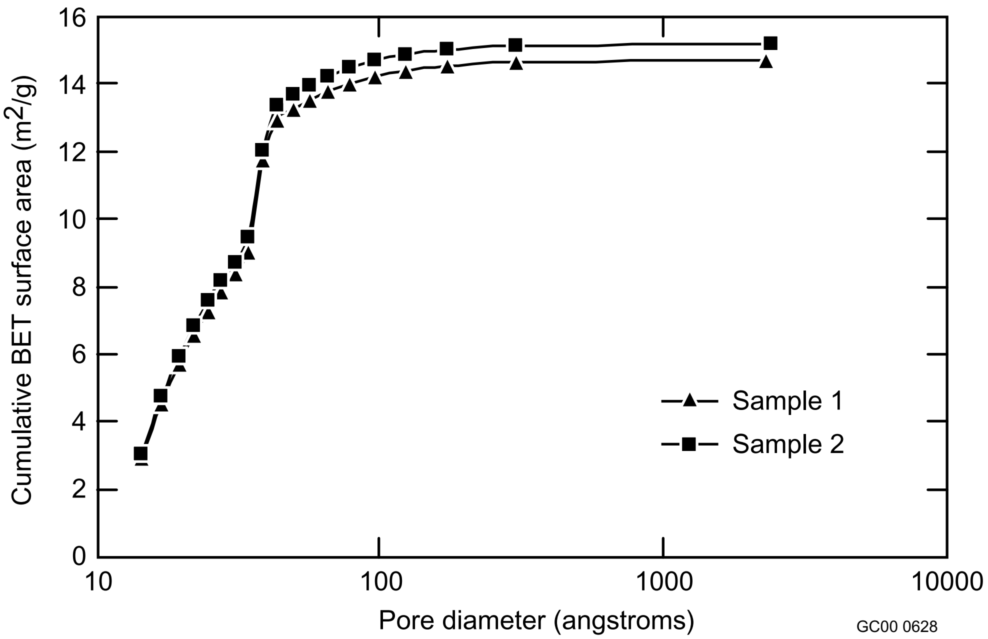

**Figure 23.** Cumulative micropore surface area distribution of the Dubois soil, measured by nitrogen adsorption. A total of about 15 $m^2$ of surface per gram of soil is present in pores smaller than 3000 Angstroms.

Hydraulic properties of the soil were measured using traditional laboratory procedures, which included hanging columns and pressure cells for moisture retention curves, constant head permeameters for saturated hydraulic conductivity, and soil sieves and hydrometers for particle size distributions (Klute 1986). Table 5 present the results. We estimated air entry pressure by fitting the van Genuchten functional form to the moisture retention data by taking the inverse of the fitting parameter $\alpha$. The estimated value for air entry pressure was approximately 145-cm $H_2O$ (2.06 psig). The estimated residual moisture content was 0.16 $cm^3/cm^3$ (assumed to equal the moisture content at ~10 bars pressure). The porosity calculated from dry bulk density and particle density was 92% of the measured porosity,

**Table 5.** Hydraulic properties of the Dubois soil. Properties are for intact cores taken from the trench wall with brass sampling rings, using traditional soil columns and pressure cells.

| Property | Population Mean |
|---|---|
| Porosity (measured) | 0.471 ± 0.023 $cm^3/cm^3$ |
| Porosity (calculated) | 0.432 ± 0.037 $cm^3/cm^3$ |
| $K_{sat}$ | (6.91 ± 3.70) x $10^{-5}$ cm/s |
| Bulk density | 1.46 ± 0.10 $g/cm^3$ |
| van Genuchten "n" | 2.25 ± 0.24 |
| van Genuchten "$\alpha$" | 0.007 ± 0.001 $cm^{-1}$ |
| Estimated air entry pressure | 144.7 ± 24.8 cm |
| Residual moisture content | 0.159 ± 0.018 $cm^3/cm^3$ |

primarily because direct porosity measurements include water absorbed along edges of the sample ring and the cotton cloth that holds the sample intact during the analysis. The measured value needs to be adjusted to account for the moisture contributed by the sample ring. The saturated hydraulic conductivity ($K_{sat}$) was measured at $6.9 \times 10^{-5}$ cm/s, while the van Genuchten fitting parameters $\alpha$ and $n$ were estimated to be 0.007 $cm^{-1}$ and 2.25, respectively.

Figure 24 shows the moisture characteristic curves of intact and repacked cores of Dubois soil. Also included is a curve measured using a UFA centrifuge apparatus (obtained via a subcontract with UFA Ventures, Inc., Richland, WA). While the traditional and UFA-measured curves are similar, the UFA-measured samples compacted from 1.30 $g/cm^3$ to 1.55 $g/cm^3$ during centrifugation (see Figure 24) Additional funding was obtained through the Environmental Systems Research Candidates Program (ESRCP) in May of FY 2000 to explore methods to account for this compaction in the UFA. As part of the new project, which was a direct outgrowth of this task, we have begun collaboration with Clark Lindenmeier at the Pacific Northwest National Laboratory (PNNL) to do soil compaction characterization in the UFA via x-ray microtomography. This technique can be also very useful in tracer flow characterization and modeling, so the collaboration should ultimately benefit other tasks within this program as well. Mr. Lindenmeier is also an expert in the use of the UFA, so is a valuable resource for INEEL.

Preliminary microbial activity measurements are underway, using traditional methods (Kieft et al. 1993), in which the substrate is dripped onto a sample of soil and $CO_2$ evolution is measured. We are testing whether uniformly labeled $^{13}C$-glucose can be used as the substrate, while still maintaining the sensitivity (versus $^{14}C$) needed to characterize soils with low microbial activity.

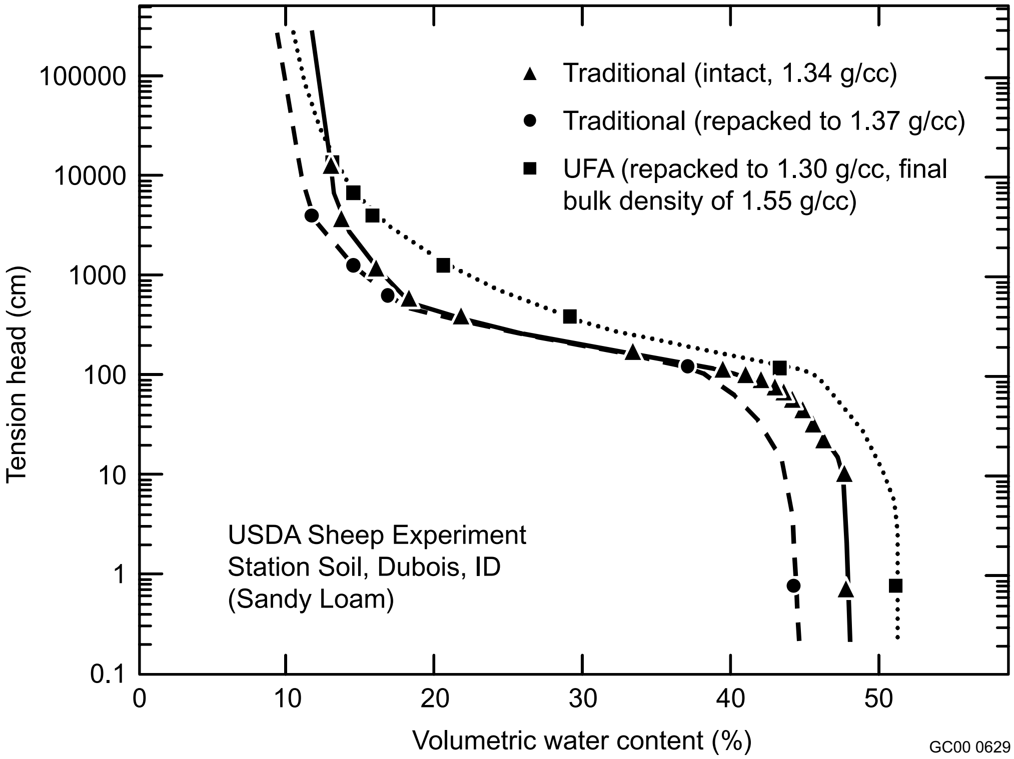

**Figure 24.** Comparison of traditionally measured moisture characteristic curves and a UFA-measured curve for the Dubois soil.

# ACCOMPLISHMENTS

Accomplishments in this project have enhanced INEEL capabilities in the areas of laboratory equipment and experience, field measurement capabilities and field monitoring sites, and computational expertise and capabilties.

## Laboratory Equipment and Experience

- Three automated titrator systems were constructed and installed at the INEEL Research Center. Titrator systems were used to perform surface charge titrations on reference minerals and on INEEL soils. Results of the experiments demonstrate that systems and procedures are fully functional.
- A J-6 Unsaturated Flow Apparatus has been purchased and installed at the INEEL Research Center.
- Two weeks of special training in the use of the UFA was completed by Kristine Baker in Clark Lindenmeier's laboratory at PNNL
- A vadose zone soil physical characterization laboratory was established in cooperation with the University of Idaho (at University Place in Idaho Falls). This laboratory accommodates standard hydrologic characterization of cores.
- A valuable collaboration was initiated with Clark Lindenmeier at PNNL to use x-ray microtomography to characterize vadose zone cores.
- An additional \$350K research project was funded through the Environmental Systems Research Candidate program titled "Unified Hydrogeophysical Parameter Estimation Approach to Subsurface Contaminant Transport – Subsurface Imaging Collaboration" with the Center for Subsurface Sensing and Imaging Systems (CenSSIS).
- An additional \$250K research project was funded through the Environmental Systems Research Candidate program titled "Water Flow Through INEEL Subsurface Samples — Innovative Approaches to Characterize Vadose Zone Hydraulic Properties."

## Field Sites and Capabilities

- Vadose zone monitoring systems were installed at national laboratories throughout the United States. A new version of the advanced tensiometer using cone penetrometer push technology was demonstrated at the Test Buried Waste Facility at Hanford. The standard version of the vadose zone monitoring system was installed at the Savanna River Site and at the University of Idaho's Troy research site.
- Jefferson Canal field site is being developed to evaluate long-term chemical and physical monitoring strategies under natural recharge conditions. Four 50-foot boreholes were instrumented with PVC casing for cross-borehole geophysical evaluations. Spatial variability analysis of infiltration is ongoing.
- A surface geophysical survey indicates possible basalt-sediment interface structure that may promote subsurface funnel flow phenomena at the IRC 5-well site. Soil sampling and additional Advance tensiometers are being installed to examine this hypothesis.

- Two 50-foot geophysical boreholes were installed at the University Place Dune Site. Preliminary analysis of cross-borehole radar data suggests fast preferential flow pathways through the overlying sedimentary material.

### Computational Expertise and Capabilities

- Computer simulation codes have been developed to compute the spatial and temporal moments for the 2-D FE-MMOC variably saturated code.

- We determined that the existing 2-D FE-MMOC code cannot be effectively extended computationally to 3-D, therefore requiring development of a finite difference replacement for parallel implementation.

- The application of a B-spline collocation method to the solution of differential equations, including sets of coupled, nonlinear partial differential has been shown feasible.

- A rudimentary B-spline code has been generated that solves the coupled fluid dynamics equations for two-dimensional flow in a channel, including multiple solution algorithms; the unoptimized code has found reasonable solutions in times about half as long as for the optimized commercial finite element code Fidap.

- A version of the B-spline code has been created to solve an idealized version of the Advection-Dispersion Equation for Subsurface Solute Transport.

- The INEEL joined a consortium of universities and national laboratories headed by the University of Illinois for developing and sharing codes for simulation of reactive contaminant transport.

## REFERENCES

ASTM D18.21, "Test Method For Determining Unsaturated Hydraulic Conductivity In Porous Media By Open-Flow Centrifugation," Subcommittee on Ground Water, *Annual Book of ASTM Standards*, 2000.

Atkinson, R. J., A. J. Posner, and J. P. Quirk, "Adsorption of Potential-Determining Ions at the Ferric-Oxide-Aqueous Electrolyte Interface," *J Phys. Chem.*, 71, 1967, pp. 550–558.

Baeyens, B. and M. H. Bradbury, "A Mechanistic Description of Ni and Zn Sorption on Na-montmorillonite Part I: Titration and Sorption Measurements," *J. of Contam. Hydrology*, 27, 1997, pp. 199-222.

Baker, A. J., "Finite Element Method," Chap. 28, in: Johnson, R. W., ed., The Handbook of Fluid Dynamics, CRC Press, Boca Raton, 1998, p. 28-2.

Brunauer, S., P. H. Emmett, and E. Teller, "Adsorption of Gases in Multimolecular Layers," J*ournal of American Chemical Society*, 60, 1938, pp. 309-319.

Celia, M. A. and G. Pinder, "Generalized Alternating-Direction Collocation Methods for Parabolic Equations. I Spatially Varying Coefficients," Numer. Methods Partial Differential Eq., vol. 6, 1990, pp. 193-214.

Conca, J. L. and J. V. Wright, “Flow and diffusion in unsaturated gravel, soil and whole rock,” *Applied Hydrogeology*, 1, 1992, 5-24.

de Boor, C. and B. Swartz, “ Collocation at Gaussian Points,” SIAM J. Numer. Anal., vol. 10, 1973, pp. 582-606.

EMSP, 2000, Environmental Management Science Program, Science Needs by Focus Area, Environmental Restoration Directed Research, **URL:http://emsp.em.doe.gov/focus_area.htm**

Fairweather, G. and D. Meade, “A Survey of Spline Collocation Methods for the Numerical Solution of Differential Equations,” in: Diaz, J.C., ed., Mathematics for Large Scale Computing, Lecture Notes in Pure and Applied Mathematics 120, Marcel Dekker, New York, 1989, pp. 297-341.

Farin, G., Curves and Surfaces for Computer Aided Geometric Design, 4th ed., Academic Press, San Diego, 1997.

Fidap, version 8.5, Fluent Inc., Centerra Resource Park, 10 Cavendish Court, Lebanon, New Hampshire, 03766, 1999.

Ganesh, M. and I. H. Sloan, “Optimal Order Spline Methods for Nonlinear Differential and Integro-Differential Equations,” Appl. Num. Math., vol. 29, 1999, pp. 445-478.

Hassler, G. L. and E. Brunner, “Measurement of capillary pressures in small core samples,” *Trans. Am. Inst. Min. Metall. Petrol. Eng.*, 160, 1945, 114-123.

Hoffman, R. N. A., *Soc. Petrol. Eng. J.*, 3, 1963, 227-235.

Holt R. M., R. Glass, J. Wilson, 1999, personal communication.

Hoschek, J. and D. Lasser, Fundamentals of Computer Aided Geometric Design, translated by L. L. Schumaker, A. K. Peters, Wellesley, Massachusetts, 1993.

Hsi, C. D. and D. Langmuir, “Adsorption of uranyl onto ferric oxyhydroxides: Application of the surface complexation site-binding model,” *Geochim. et Cosmochim Acta*, 49, 1985, p. 1931-1941.

Hubbell, J. M. and J. B. Sisson, 1998, Advanced tensiometer for shallow or deep soil water potential measurements,” Soil Sci. 163(4): 271-276.

Johnson, R. W. and M. B. Landon, “A B-Spline Collocation Method To Approximate The Solutions To The Equations Of Fluid Dynamics,” Proceedings of the 3rd ASME/JSME Joint Fluids Engineering Conference, July 18-23, San Francisco, Forum F-217, 1999.

Kent, D. B., V. S. Tripathi, N. B. Ball, J. O. Leckie, and M. D. Siegel, *Surface Complexation Modeling of Radionuclide Adsorption in Subsurface Environments*, NUREGCR-4807, Division of High-Level Waste Management, Office of Nuclear Material Safety and Safeguards, U.S. Nuclear Regulatory Commission, 1988.

Kieft, T. L., P. S. Amy, F. J. Brockman, J. K. Fredrickson, B. N. Bjornstad, and L. L. Rosacker, “Microbial abindance and activities in relation to water potential in the vadose zones of arid and semiarid sites,” *Microb. Ecol.*, 26, 1993, 59-78.

Klute, A. *Methods of Soil Analysis, Part 1 Physical and Mineralogical Methods,* Second Edition, Soil Science Society of America, Inc., Madison, WI, 1986.

Kravechenko, A. G., P. Moin, and R. Moser, "Zonal Embedded Grids for Numerical Simulations of Wall-Bounded Turbulent Flows," *J. Comput. Phys*., vol. 127, 1996, pp. 412-423.

Looney, B.B. and R.W. Falta, *Vadose Zone Science and Technology Solutions*, editors, Battelle Press, Columbus OH, 2000.

Mattson, E. D. and J. B. Sisson., "Vadose zone characterization equipment development at the INEEL," presented at the Advanced Vadose Zone Characterization Workshop, Hanford, WA, 1999.

Moutonnet, P., J. F. Pagenel, and J. C. Fardeau, "Simultaneous Field Measurements of Nitrate-Nitrogen and Matric Pressure Head," *Soil Sci. Soc. Am. J*., 57, 1999, pp. 1458-1462.

NRC, *Research Needs in Subsurface Science*, U.S. Department of Energy's Environmental Management Science Program, National Research Council, National Academy Press, Washington, D.C., 2000a.

NRC, *Seeing into the Earth*, Noninvasive Characterization of the Shallow Subsurface for Environmental and Engineering Application, National Research Council, National Academy Press, Washington, D.C., 2000b.

Payne, T. E., G. R. Lumpkin, and T. D. Waite, "Uranium(VI) Adsorption on Model Minerals," in: *Adsorption of Metals by Geomedia*, Academic Press, San Diego, CA, 1998, pp. 75-97.

Press, W. H., S. A. Teukolsky, W. T. Vetterling, and B. P. Flannery, Numerical Recipes in Fortran 77, The Art of Scientific Computing, 2nd ed., Volume 1 of Fortran Numerical Recipes, Cambridge Press, Cambridge, 1992.

Redden, G., J. Li, and J. Leckie, "Adsorption of U(VI) and Citric Acid on Goethite, Gibbsite, and Kaolinite," in: *Adsorption of Metals by Geomedia,* Academic Press, San Diego, CA, 1998, pp. 291-315.

Riga, P. and S. Charpentier, "Ionic-Equilibrium Time inside Ceramic Cups in Unsaturated Porous Media," Soil Sci. Soc. Am. J. 62, 1998, pp. 574-579.

Shapiro, A. G. F. and Pinder, "Analysis of an Upstream Weighted Collocation Approximation to the Transport Equation," J. Comput. Physics, vol. 39, 1981, pp. 46-71.

Shariff, K., and R. D. Moser, "Two-Dimensional Mesh Embedding for B-spline Methods," J. Comput. Phys., vol. 145, 1998, pp. 471-488.

Skopp, J., M. D. Jawson, and J. W. Doran, "Steady-state aerobic microbial activity as a function of soil water content," *Soil Sci. Am. J.*, 54, 1990, 1619-1625.

Stone, J. E. and A. M. Scallan, "A structural model for the cell wall of water-swollen wood pulp fibres based on their accessibility to macromolecules," *Cellulose Chem. Technol.*, 2, 1968, 343-358.

Stone, J. E., A. M. Scallan, E. Donefer, and E. Ahlgren, "Digestibility as a simple function of a molecule of similar size to a cellulase enzyme," *Adv. Chem. Ser.*, 95, 1969, 219-238.

Sun, W., “Spectral Analysis of Hermite Cubic Spline Collocation Systems,” SIAM J. Numer. Anal., vol. 36, no. 6, 1999, pp. 1962-1975.

Thompson, D. N., H.-C. Chen, and H.E. Grethlein, “Comparison of pretreatment methods on the basis of available surface area,” *Bioresource Technol.*, 39, 1992, 155-163.

UFA Ventures, Inc. *Matric Potential Technical Brief.* http://www.UFAVENTURES.COM/ ufa_ventures/ tech_briefs/matric_potential.html, 1996.

# Transport Phenomena in Geologic Porous Media

**G. A. Bala, J. M. Hubbell, B. D. Lee, R. M. Lehman, and J. B. Sisson**

## SUMMARY

This program investigated the relationships between bulk-scale (g–Kg, or ml–L) biological, chemical, and physical heterogeneities in the subsurface by integrating three hypothesis-driven research thrusts. The thrusts were driven by identification of critical deficiencies in the existing knowledge base that limit in situ remedial applications. The underpinnings of this program are based on the tenet that microorganisms are the primary agents of geochemical change and that these changes mediate transport phenomena. The first two tasks investigated the influence of spatial and temporal variations in ecological niches on bacterial community structure-function in multicomponent systems and the resulting distribution of microbial metabolisms that influence the persistence and mobility of contaminants in both the ground water and the vadose zone. The third task focused on the controlling factors that determine the distribution of soil water potential in deep vadose zone that effect flow and transport of moisture. Program output is the production of new knowledge that provides the foundation for remedial applications by DOE-EM. Where appropriate, intellectual property is protected and further development is pursued to accomplish DOE tech-transfer objectives. Endpoint applications of this work include mining, resource recovery (energy), aquifer contamination, waste disposal, and remediation of contaminated geologic media at Department of Energy (DOE) sites and facilities nationwide, and industrial sites throughout the world.

## Microbial Partitioning Between Mobile and Immobile Phases in Geologic Media

Hypothesis: Structure-function relationships of microbial communities in multicomponent systems are influenced by spatial and temporal variations in ecological niches that result in a distribution of microbial metabolisms that influence fate and transport of contaminants.

The segregation of microorganisms in aquifers between the immobile phase (i.e., geologic media) and the mobile phase (i.e., ground water) can have profound effects on the metabolism of individual cells and the collective community of cells. Differences in the mobility of microorganisms and their metabolisms will alter contaminant fate and transport in subsurface environments. The segregation of microbial populations and their functions were studied in laboratory core floods constructed of basalt. Emerging techniques to adequately describe in situ microbial community structure and function were developed and applied.

A long-term goal of subsurface microbiological investigations is to develop a predictive knowledge base concerning the distribution of microorganisms and their activities in subsurface environments so that activities such as remediation can be accomplished efficiently with a minimum of costly site characterization studies at each location. Many of these locations that are amenable to remediation are saturated. A prime consideration in developing a field or lab model for determining overall degradation potential for a compound(s) is whether the organisms are sessile (attached) or planktonic (unattached). Ambiguous findings have been reported regarding the relative partitioning of microbes and their functions between the mobile and immobile phases and the conditions that may predictably alter this distribution (Lehman, unpublished literature review). Many reports in the literature exist that document radical changes in the physiology (i.e., enzyme expression) when single organisms become attached to or detached from substrata during laboratory experimentation. Predictive knowledge drives design of relevant laboratory biodegradation and numerical models, which allows site characterization to focus on either core or ground waters and to determine which should be subsequently monitored. To achieve degradation (or other desirable interaction), it is necessary to place the substrate, transforming population, and stimulus at the same location simultaneously.

Task objectives are to empirically determine the segregation of bacterial populations and functions as mixed ground-water communities interact with geologic media so that in situ biotransformations can be effectively modeled and implemented. The primary questions are as follows: Are the populations attached to porous media different than those suspended in the ground water and are their activities different? Is the biomass significantly higher at one location over the other? How does the segregation of microbes differ at different sites? These primary questions will be addressed under controlled laboratory conditions using several experimental models related to the TAN mixed-waste plume. An example hypothesis for these studies might be: “Segregation of community structure and function will occur according to the mobility (attached vs. unattached) of bacteria in saturated subsurface environments.” Integral to the solution to these questions is the microbiological analytical approach used. The methods to be used are all emerging molecular and surface analytical techniques to investigate and link the structure and function of natural microbial communities while minimizing loss of their spatial relationship with the organisms’ in situ microenvironment. It is this latter criteria that will allow solutions to the following questions: Are there physical and chemical measures that are useful in predicting whether attached or unattached bacteria will predominate? Is the location of populations or activities predictable by more easily-gained measures (i.e., remote sensing)?

Several experimental subtasks were initiated to empirically address the questions raised above.

### Subtask 1

Subtask 1 centered around the use of a laboratory core flood apparatus constructed with basalt and perfused with Snake River Plain Aquifer ground water to simulate the aquifer and provide materials that were subjected to microbiological analyses. Subtask 1 also includes development of appropriate methodologies for analyzing micro-organisms indigenous to ground water and geologic media.

Laboratory core flood experiments were performed to examine the partitioning of indigenous ground-water bacteria between basalt and the ground water. Replicated experiments were performed to determine any differences in partitioning between fracture-flow and porous flow hydrological regimes. The findings from these and other associated laboratory experiments and analyses are as follows:

- Differences exist between attached and unattached communities using culture-dependent and -independent microbiological assays.

- Little difference in the cultural community can be attributed to hydrologic regime while culture-independent assays showed some difference (see No. 6 below).

- Extraction efficiencies (e.g., from the basalt) could not explain the differences observed.

- Extraction procedures for removing basalt were tested and optimized using a replicated ANOVA experimental design.

- Units of reference for biomass were examined and extensive morphometric analyses of basalt fracture surfaces and particle surfaces were performed to develop a tortuosity index that can be used in conjunction with substrata geometry to calculate substrata surface area. Biomass results can then be expressed in various units to approximate equivalency between attached and unattached components; i.e., by weight, by volume, by surface area (internal and external), and by bacterial-accessible surface area.

- Development and optimization of protocols for quantifying relative abundance of bacteria populations using 16S rRNA-directed oligonucleotide probes that are conjugated with different fluors. This procedure is termed whole cell fluorescent in situ hybridization (FISH) and allows distinction of different microbial phylotypes. The attractiveness of the technique is twofold: one, cells are not cultured, and two, cells can potentially be observed on their natural substrata. A variety of protocols have been published in the literature although a single protocol has not emerged as being reliable by a consensus of practitioners. The application of FISH to environmental samples with low cell numbers and low activities per cell has been particularly problematic although the potential return of in situ culture-independent identification of microorganisms provides substantial stimulus to pursue optimization of FISH protocols. Over 50 FISH trials were performed in the development of defensible protocols and the generation of data evaluating relative abundance of different phylogenetic groups in situ from geologic materials and in ground water. The following probes were used in these studies: eubacterial (Eub338), high G+C gram positives (GmPos1901), alpha proteobacteria (Alpha19), beta proteobacteria (Bet42A) and gamma proteobacteria (Gamma42A). These phylogenetic groups include representatives that are commonly found in subsurface environments. Figure 1 shows the distribution of phylotypes

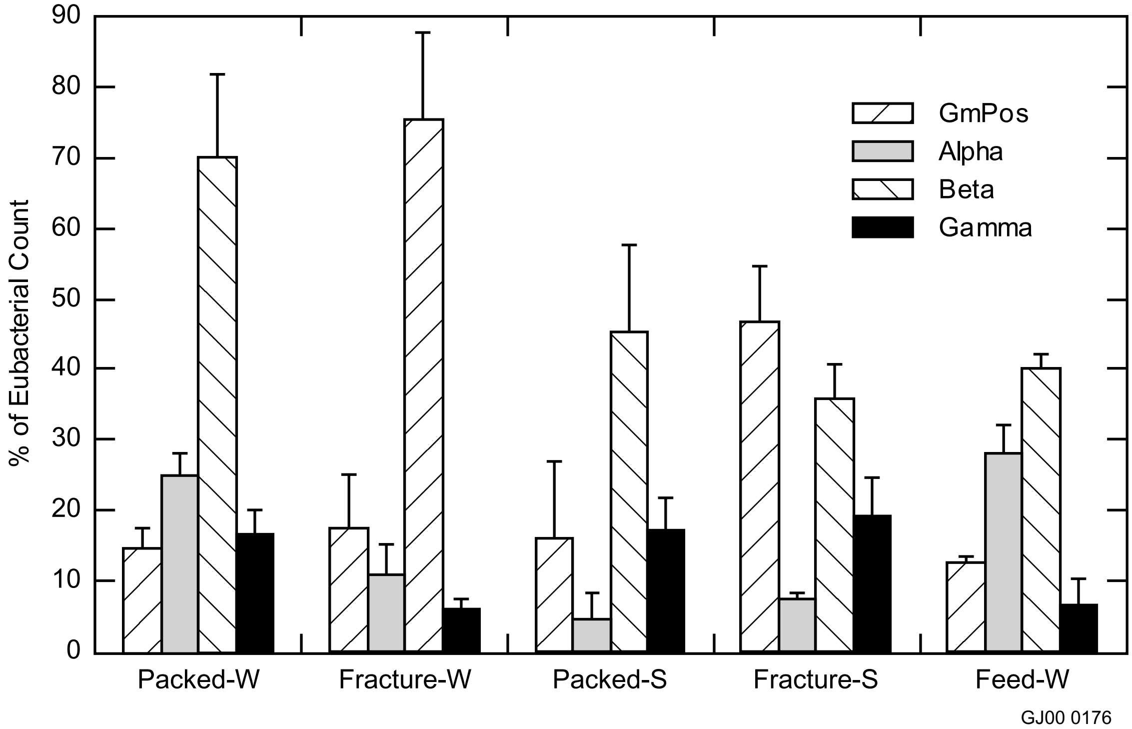

**Figure 1.** Phylogenetic affiliation of attached and unattached bacteria in laboratory core floods 16S rRNA oligonucleotide probes.

between rock and water in the laboratory core floods. In comparison to the basalt, ground waters were enriched with beta-Proteobacteria. With respect to hydrologic regime, fracture-flow basalt surfaces were significantly enriched with respect to gram positive bacteria versus porous-flow basalt. INEEL personnel contributing to progress on this subtask are Mike Lehman supported by Eric Robertson and Joni Barnes.

To assist in reducing the bias (i.e., matrix effects) of comparing microbiota extracted from solids to those already existing in aqueous solution, several efforts were initiated to develop and refine emerging techniques for culture-independent assays and in situ surface analyses of bacteria attached to environmental surfaces. Much experimental work was involved in applying FISH to extracts of (low activity) cells from the basalt as described above. The next step would be FISH analyses of stained cells in situ, i.e., on the basalt. This step necessitates large advancements in boosting the signal-to-noise ratio and other technical challenges. Parallel work involved use of bulk nucleic acid extraction, purification, amplification, and separation technologies on low biomass subsurface samples.

Work was initiated on developing spectral and hyperspectral methods for simultaneously determining multiple microbial phylotypes in a single sample spectrum or spectral image after labeling with FISH probes. Each of the FISH probes are labeled with a different fluorophore with spectral characteristics different than any of the other probes in the assay. Ideally, each probe is completely resolved from the other probes and single excitation or emission wavelengths can be used for each probe. However, excitation and emission spectra for the available probes are very broad and overlap can be a severe problem, particularly when 10–30 nm bandpass filters are used. This spectral overlap problem can be overcome mathematically by collecting, at a minimum, images (i.e., spectral data points) at n excitation or emission wavelengths for n FISH probes and solving for the contributions of each of the probes. Ideally, the images at the n excitation or emission wavelengths will be recorded simultaneously to limit translocation problems. Images at multiple wavelengths can be collected using the confocal laser scanning microscope (CLSM) or a microspectroscopy system equipped with an appropriate CCD camera to collect spatially resolved spectra of cells along the entrance slit. Once reduced to practice, other microbial indices may be measured, e.g., enzyme activity in situ. The use of CLSM with its laser excitation confers several advantages to overcome the deficiencies in detection of environmental microorganisms by use of 16S rRNA-directed oligonucleotide probes, i.e., lower number of ribosomes. The specific advantages of CLSM are that laser excitation results in a stronger emission signal than epifluorescent illumination, digital imaging allows amplification and image analysis to improve the signal-to-noise ratio and the ability to scan vertically allows integration of the signal from multiple cross-sections of a stained cell. Progress on this subtask has included a few pilot studies and substantial procurement of increased hardware and software capabilities. The PARISS microspectrometer system mounted on a Nikon E600 microscope was upgraded by adding a more sensitive Dage DC-330 CCD camera to the spectrometer. The CLSM (Nikon PCM2000) has also been upgraded to allow use of laser excitation wavelengths of 488 nm (Ar+), 514 nm (Ar+), 543 (HeNe), and 633 nm (HeNe) and simultaneous detection on three channels. With the upgraded CLSM system, it is now possible to spatially and spectrally resolve three probes with each image (i.e., one excitation wavelength and three emission wavelengths), even if they are not completely spectrally resolved. The hardware and software for the image analysis system have also been upgraded to provide capability commensurate with upgrades to the image acquisition software. At present, the arrival of a prototype tunable crystal filter (to resolve spectral overlap) is awaited to allow further experimental work to continue. INEEL personnel contributing to progress on this subtask are Bill Bauer, Mike Lehman, Joni Barnes, and Pete Pryfogle.

Research using bulk DNA analyses to examine the response of ground water and sediment/rock microbial communities to contaminants is being performed by Sean O'Connell (ISU Ph.D. candidate supported on ACE fellowship). O'Connell is examining the diversity of subsurface communities as an indicator using three different methods of assessment: traditional culturing, polymerase chain reaction (PCR), denaturing gradient gel electrophoreses (DGGE) banding patterns, and dilution-extinction of community phenotypic patterns. The focus of the work has been on the technical challenge of retrieving sufficient quantities of amplifiable (by PCR) DNA from low biomass subsurface samples. Central to this work is the quantification of DNA extraction efficiency that has only rarely been reported in the literature. Protocols have been developed and optimized for this procedure (in association with researchers at other institutions: Dr. Fred Brockman, PNNL and Dr. Mark Wilson, Humboldt State University) in addition to procurement and configuration of required software and hardware. O'Connell has also trained with collaborator Dr. Jay Garland at NASA's Kennedy Space Center (KSC) and conducted analyses of ground water microbial diversity by terminal restriction fragment length polymorphism (t-RFLP) at KSC. The t-RFLP estimates of community diversity will be contrasted with those from PCR-DGGE analyses performed in the INEEL's Geomicrobiology Laboratory. The goal of this work is to achieve the ability to perform the most relevant molecular analysis of community diversity on low biomass ground water and aquifer media samples so that these communities can be contrasted independent of cultural bias. An understanding of the limitations of each approach is critical to the final interpretation of this data. Laboratory microcosm studies using Snake River Plain Aquifer communities and TCE as the contaminant are currently ongoing. O'Connell authored a related methods paper and Lehman authored a related methods paper which are both cited below. INEEL personnel contributing to progress on this subtask are Sean O'Connell supported by Mike Lehman.

### Subtask 2

Subtask 2 involves noninvasive assessment of in situ microbial activities using low-energy infrared radiation. A collaboration was established with Dr. Hoi Ying Holman (LBNL) to explore a promising method for nondestructive assessment of microbial presence and activities in situ. This work includes study of the surface associations of organisms, target substrate, and mineral type on basalt surfaces by application of synchrotron radiation-based Fourier transform spectromicroscopy (SR-FTIR). The SR-FTIR instrument is located the Advanced Light Source (ALS) at LBNL. The use of infrared spectromicroscopy for examining microorganisms on natural substrata has only recently been reported by Dr. Holman. Advantages of this nondestructive method are the resolution conferred by a 10 micron spot size and the high intensity but low energy infrared radiation source. An ACE subcontract was initiated to Mary Kauffman (interdisciplinary Microbiology and Geology Master's degree candidate at ISU) who is studying the degradation kinetics of aromatic and chlorinated hydrocarbons by attached and unattached organisms. Kauffman's proposal ("Investigation into the Spatial Distribution and Synchrotron FTIR Absorption Microspectra of G4 Attached to Basalt and Exposed to Toluene, Phenol, Trichloroethylene, or 3-Hydroxyphenylacetylene") for beam time at ALS at LBNL was submitted and approved by ALS administrators. An experimental work plan for this project has been generated to direct this investigation that uses organisms similar to those isolated from the TAN mixed-waste plume (i.e., Burkholderia cepacia), basalt as the substrate and TCE as the organic substrate/contaminant. The induction of the enzymes that co-metabolically degrade TCE are being studied with toluene and phenol as an inducer and 3-hydroxyphenyacetylene as an analogue substrate and activity indicator. Major findings from four 2-week stretches of beam time at the ALS at LBNL and the use of light (epifluorescent and diffracted light illumination) microscopy at the INEEL include the following:

- Spectra of the distinct mineral phases in the basalt were defined by comparison to spectra obtained for individual mineral standards.

- Spectra for *B. cepacia* (absorption peaks near 1740, 1650, and 1550 $\text{cm}^{-1}$ that correspond to the phospholipids in the outer membrane of Gram-negative bacteria, protein Amide I, and protein Amide II, respectively) were detected on basalt and differentiated from mineral and other background spectra.

- Spectra for 3HPA and TFMC (toluene mono-oxygenase, TMO, analogue substrates) were defined.

- Collected spectra for TMO induced vs. noninduced bacterial cells from agar plates and the same cells exposed to 3HPA and TFMC.

- Collected spectra for free-living, noninduced bacterial cells, and the same cells exposed to 3HPA and TFMC.

- Collected spectra for mineral standards thin sections with G4 cells attached. All four minerals, in thin section, were exposed to the same bacterial culture. Based upon spectral markers, there was preferential attachment to one mineral (plagioclase).

- Obtained background data for abiotic basalt thin sections in lactate only, lactate and phenol, and lactate and toluene minimal salts media (carbon sources are TMO inducers).

- Collected spatial maps of the distribution of noninduced bacteria attached to a basalt thin section.

- Compared spectra for free-living and attached organisms on basalt. Evidence suggests physiological changes can be detected upon cell attachment. Initial data indicates observable spectral marker variations between bacterial cultures introduced onto calcic plagioclase, augite, ilmenite, and olivine. Also, observable spectral marker variations exist between bacterial cells attached to gold vs. basalt surfaces. Initial data indicate an uneven 3-D spatial distribution of bacterial attachment (pure culture) to a single mineral phase. See Figure 2 for a sample spectrum.

In addition, numerous technical obstacles have been addressed in the course of this research: (1) access and logistical concerns at the ALS; (2) maintenance of proper sample moisture content during SR-FTIR analyses; (3) procurement, installation and debugging of spectral analysis software; (4) development of a suitable lab model for obtaining a high quantity of vigorous cells grown in a submerged biofilm on basalt at the expense of a volatile substrate, (5) maintenance of thin section stability throughout all experimental procedures; (6) consistent relocation of a specific position on thin section; (7) autofluoresence of mineral phases interfering with epifluorescent microscopy of tagged cells; (8) control of vapor (i.e., substrate) during SR-FTIR analysis. A sample cell for the FTIR microscope stage was machined at LBNL. The sample cell can accommodate 3 × 1 inch slides, seal air-tight for volatile organics, and can accommodate the maximum ZnSe crystal window with the minimum thickness. The new sample holder will allow a variety of sample sizes and mounting techniques, optimize the optical resolution with the thinner crystal window, and minimize volatile loss in the toluene and TCE degradation studies. INEEL personnel contributing to progress on this task are Mary Kauffman supported by Pete Pryfogle and Mike Lehman.

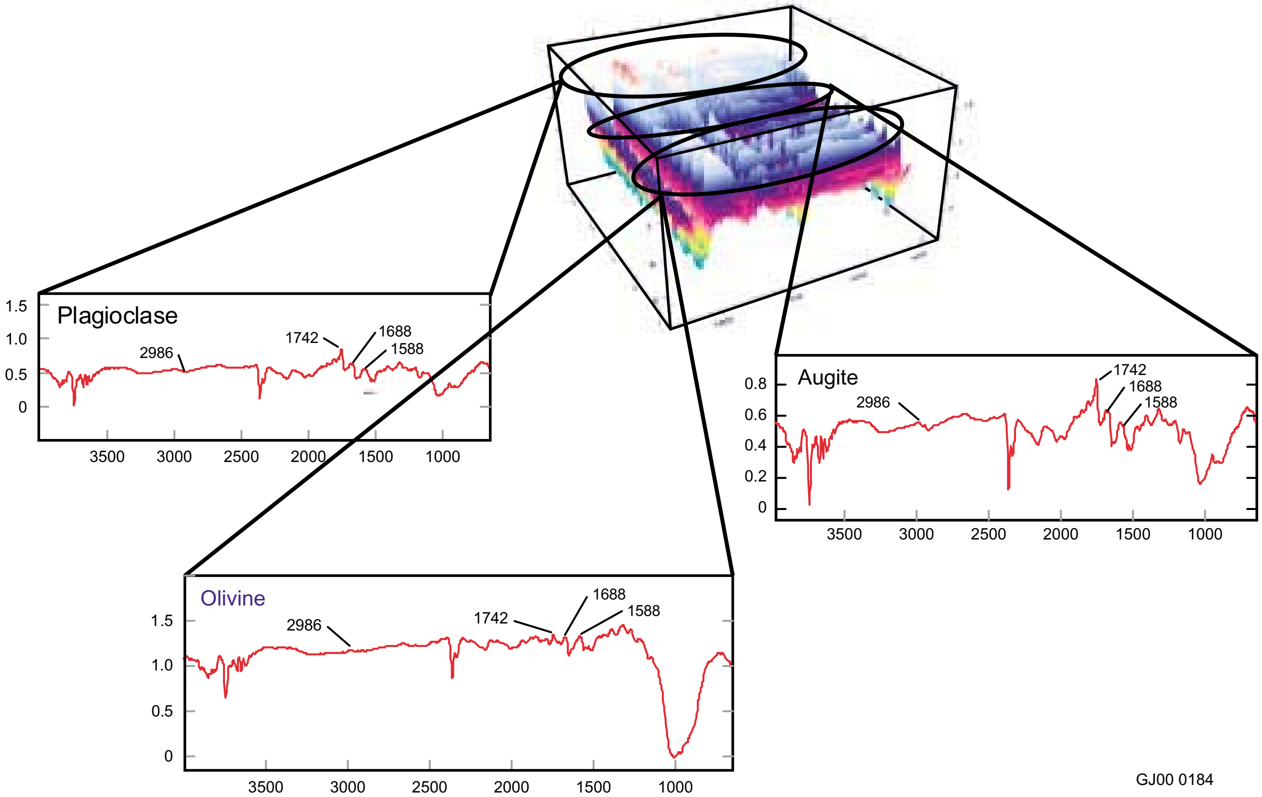

**Figure 2.** Sample spectra from SR-FTIR showing the localization of *Burkholderia cepacia* on different mineral phases on a basalt specimen. Peaks at 1742, 1688, and 1588 are markers for bacterial cells.

## Subtask 3

Subtask 3 involves microbiological analyses of field samples of geologic media and ground water taken across temporal and spatial scales with respect to contaminant introduction and elimination. A collaboration was established with Dr. Mike Barcelona, University of Michigan, Director of the National Center for Integrated Bioremediation Research and Development (NCIBRD) and with Dr. D. C. White, University of Tennessee, to participate in Michigan Integrated Remediation Technology Laboratory (MIRTL) field experiments at Wurtsmith Air Force Base, Oscoda, MI. MIRTL2: A Natural Gradient Reactive Fate and Transport Experiment at NCIBRD, was commenced in November of 1998 by (regulatory agency-approved) intentional injection of labeled contaminants (BTEX and MTBE) into the aquifer. In this case, the quantity, type, and exact time of contaminant introduction is known. Further, the site had been previously characterized for contaminant dispersion parameters. The dissolved plume has been followed by periodic sampling of established transects of multilevel well installations along the flow axis in this relatively shallow, sandy aquifer. Our role in this experiment is to examine the response of the indigenous microbial communities in both the ground water and associated with sediment during introduction of and subsequent elimination of hydrocarbon contaminants. In the last 2 years we have analyzed over 500 ground-water samples and over 300 sediment samples using Community-Level Physiological Profiling (CLPP) that fingerprint the community according to functional potential. Dr. White has analyzed splits of these same samples for phospholipid fatty acid (PLFA) community profiles that fingerprints the community according to structural (i.e., cell wall) components. The immense challenge of analyzing the large multivariate data matrices, correlating the results of CLPP and PLFA, and correlating the biology with the chemistry remains to complete this multiyear experiment. This work has included INEEL participation in field sampling for ground water and cores at the NCIBRD as well as a subcontract let to University of Michigan to defray sampling costs. Preliminary data analysis demonstrates a large difference in the attached and unattached community profiles and a divergence in their response to introduction of the contaminants. INEEL personnel contributing to progress on this subtask are Mike Lehman supported by Sean O'Connell.

## Biologically Mediated Actinide Transport in the Subsurface

Hypothesis: Decreased redox potential and supplementary electron transfer associated with chlorinated solvent bioremediation may effect the mobilization of actinides that have become chemically complexed to mineral oxides.

The primary objective of this task was to better understand the coupling of microbial processes and surface geochemical reactions that affect the migration of actinides, such as uranium, through saturated zones in the subsurface. Technical information generated from this research may meet numerous science and technical needs at the Idaho National Engineering and Environmental Laboratory (INEEL), as well as Pacific Northwest National Laboratory (PNNL), including the need to understand the microbial alteration of heavy metal and radionuclide partitioning at mineral surfaces. Laboratory research was performed to understand the effect of anaerobic enrichments for the purpose of trichloroethylene (TCE) degradation on the mobility of uranium in basaltic aquifers. Interacti on of uranium and hydrous iron oxide moieties on the mineral oxide surfaces was maximized by using iron oxide-coated quartz from Oyster, Virginia. Major accomplishments for this fiscal year included: the determination that adsorption and desorption to iron oxide-coated sand appears to be affected by anaerobic enrichments and is culture dependent. Specifically, enrichments for sulfate reducing bacteria (SRB) and iron reducing bacteria (IRB) from a laboratory culture caused the release of low concentrations of absorbed uranium into the growth medium, followed by a steady decrease in the soluble fraction with a concomitant increase in particles filterable through a 0.2 μm filter. Enrichments of SRB and IRB from ground water taken from Test Area North were able to chemically reduce the iron on the surface of the sand that may reduce the reactive surface area on mineral surfaces significantly affecting adsorption of uranium and subsequent mobility in the ground water. Both SRB and IRB enrichments from the TAN ground water were able to reduce both soluble and bound U(VI) to U(IV).

Weapons production and energy research activities have resulted in widespread contamination of subsurface sediments and ground water with chlorinated organics, metals, and radionuclides. More than 5,700 known DOE plumes have contaminated over 600 billion gallons of water and 50 million cubic meters of soils and sediments. Some of the more prevalent contaminants that have been co-disposed at DOE sites are chlorinated solvents (e.g., perchloroethylene (PCE) and TCE), metals (e.g., lead, chromium and mercury) and radionuclides (e.g., uranium, cesium, and strontium) (Riley et al. 1992). These contaminants, especially the metals and radionuclides, can persist in the environment for extremely long periods. Migration of contaminants within these plumes threatens local and regional water sources, and in some cases has already adversely impacted offsite receptors (DOE August 1996).

Over the past several years, biological treatment of chlorinated organic contaminants has gained popularity in research and development as well as application of the technology to field sites (Ellis et al. 2000; Harkness et al. 1999; Sorenson 1998). When considering biotreatment of the chlorinated organic component of a mixed contaminant plume in saturated porous media, a number of related chemical and biological interactions must be considered. First, and most obvious, is the interaction of the microbial population of interest with the contaminant to be remediated. As stated, a large amount of fundamental and applied knowledge has been gained regarding reductive dechlorination of chlorinated organic contaminants (Adriaens and Vogel 1995; Fetzner 1998). Second, is the interaction of co-disposed inorganic contaminants, such as metals and actinides, with geological media within the contaminant plume. A wide variety of laboratory research has gone into understanding the partition coefficients and surface complexation of compounds such as uranium on the surface of mineral oxides (Waite et al. 1994; Kohler et al. 1996; Reich et al. 1998; Rosentreter et al. 1998; Bargar et al. 1999). Finally, the interactions between the microbial populations (specifically those capable of degrading the chlorinated organic contaminants), the actinide contaminants, and the mineral oxides in the growth environment, must be determined. The focus of this research project has been the interaction of microbial populations capable of degrading TCE contaminants with actinides that are chemically complexed to mineral surfaces. Microorganisms may affect the mobility of the actinide directly by changing the speciation, or indirectly by transforming the mineral matrix to which the metal has complexed. Once the uranyl ion has been released, it is available for complexation to counter ions in solution, allowing for mobilization of the actinide. During the reduction of the iron oxides and liberation of soluble ferrous iron, potential sites for adsorption are also lost. Knowledge gained from the project will be directly applicable to the following Environmental Management Needs:

- Microbial alteration of heavy metal and radionuclide partitioning at mineral surfaces.
- Detection/distribution of contaminants—chemical binding on site-specific mineral surfaces.
- Transport of contaminants—rates of coupled abiotic and biogeochemical reactions involving contaminants in the Hanford subsurface.
- Remediation—interaction of remedial processes with Hanford subsurface.
- Cost-effective, in situ remediation in the vadose zone of one or more of the following radionuclides: uranium, plutonium, cesium, cobalt, and strontium-90.
- Understand, quantify, and develop descriptions of biogeochemical reactions and interactions between contaminants of concern and aquifer sediments to describe biochemical reactive transport.

Bench-scale laboratory research performed during the past year attempted to address a largely ignored issue associated with in situ remediation: that is the potential enhancement of mobility of co-disposed radionuclides resulting from remediation of chlorinated organic contaminants in ground water. The guiding hypothesis for the research was that when microbial growth conditions are established in the subsurface for chlorinated solvent biotransformation, changes in redox chemistry and direct reduction by microbes will affect the fate of uranium that has become chemically complexed to the mineral oxides. Anaerobic microorganisms require certain environmental factors to be favorable to maintain their baseline physiology as well as dechlorination activity. One important factor is the redox potential (Eh) of the growth medium. A change in Eh facilitated by microorganisms has a strong possibility of affecting chemical speciation in the area of changed Eh (Tsang et al. 1994). The hypothesized mechanism of uranium release from the U-mineral oxide complex is similar for enrichments for sulfate reducers and sulfate free enrichments. In this mechanism uranyl ions sorb to mineral oxides such as iron oxide, ferric oxyhydroxides, or manganese oxides. Once accelerated bioremediation is initiated, the required redox for microbial growth and supplementary electron transfer occurring in the system leads to the reduction and loss of the iron oxide and uranyl ions. The uranyl ions will complex with carbonate forming dioxouranium (VI) carbonate complexes. The iron is lost as ferrous iron, which may form carbonate complexes. Under conditions of enrichment without sulfate, the uranium carbonate will stay in solution depending on the microbial activity occurring or will be precipitated as solid uranous oxide. Uranium solubility will be affected under conditions of sulfate reduction due to the formation of metal sulfides, specifically iron sulfide. Two potential effects of the iron sulfide would be abiotic reduction of the U(VI) and reprecipitation onto the mineral matrix, or adsorption to iron sulfide particles followed by precipitation.

The effect of remediating trichloroethylene using enrichments with and without sulfate on actinide mobility was determined. Previous research at the INEEL has shown that sulfate reducing and methanogenic enrichments are able to transfer electrons to organometallic compounds affecting the valence state of transition metal involved (Lee et al. 2000). The initial research task for the current project was to determine the interaction of redox conditions on uranium using simulated materials to mimic the mineral matrices found on the surface of basalt. When culture conditions are established in the subsurface, changes in chemistry will affect the fate of uranium that has sorbed to basalt. After remediation of the plume is complete the aquifer in the area will naturally return to oxidative conditions. The effect of the positive oxidation-reduction potential on the chemically sorbed uranium will be determined.

Batch testing was performed during this phase of research. Figure 3 represents the general configuration used for testing. Boxes to the left of the test vial photograph contain components added to the vials, while the box to the left of the bottle represents analyses performed on the vials. Each series of assays contained two blanks, one with TCE and one without, one killed control, one enrichment for SRB, and one enrichment for IRB. All vials contained nitrogen phosphorus growth medium and iron oxide-coated quartz.

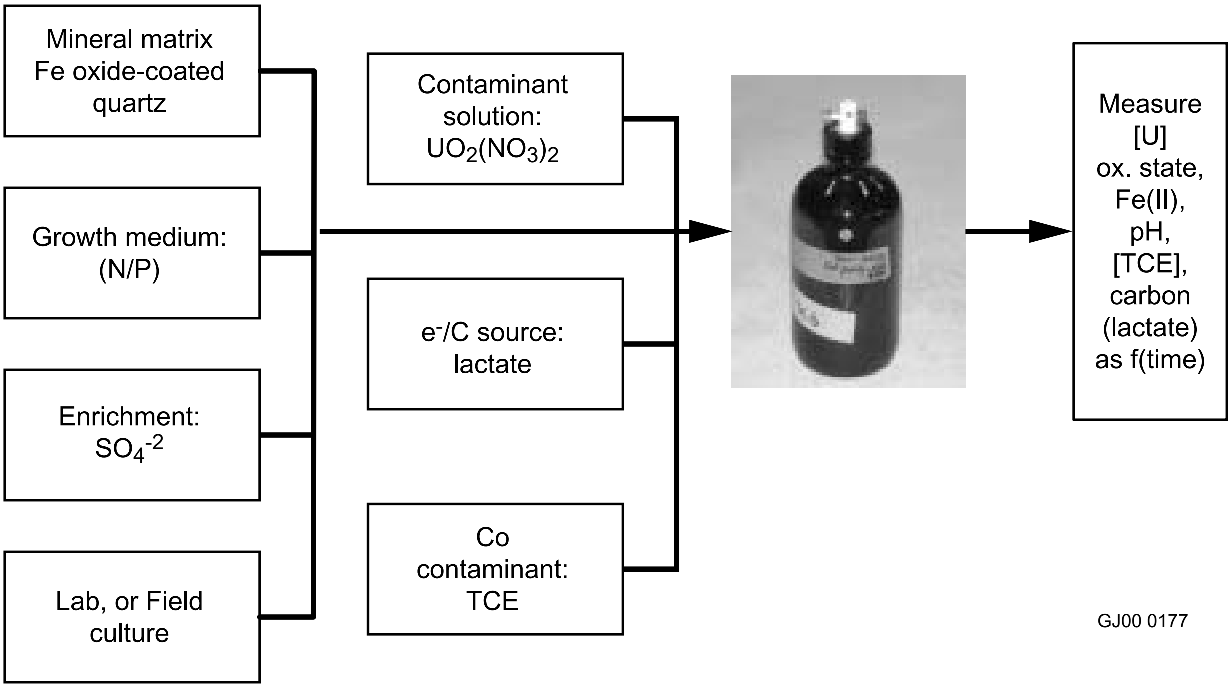

**Figure 3.** Flow diagram of basic experimental configuration used to determine the effect of anaerobic enrichments on uranium adsorption and desorption to iron oxide coated sand.

There were two sources of inoculum for the experiments run during the past year. Initial experiments were run using a microbial culture enriched from TAN ground water that had been used to determine TCE removal kinetics. This culture had been maintained in the laboratory for numerous generations prior to use in the adsorption/desorption experiments. For presentation of results this culture will be called the "Laboratory Culture." The second culture used was enriched from ground water obtained from sampling well TAN-37. A 1-liter sample of ground water was filtered and the filter was added to growth medium for enrichment. This culture was designated as the "field culture" for presentation of results.

Uranium (VI) was measured using kinetic phosphorimetry, total U was measured using inductively coupled plasma with atomic adsorption (ICP-AA), ferrous iron was measured using the ferrozine dye method, pH and Eh were measured using probes, TCE using solid phase microextraction and methane via direct sampling of headspace were measured using gas chromatography, and lactate and associated breakdown products were measured using high pressure liquid chromatography.

Two problems encountered during research performed during FY 1999 were the lack of TCE reductive dechlorination and less than desirable mass balances for uranium in the batch system. Research during FY 2000 focused on solving these problems prior to initiating column studies. An attempt to overcome the lack of TCE reductive dechlorination was performed by obtaining an enrichment culture from the ongoing enhanced in situ bioremediation of TCE project taking place in the source area of TAN. Better uranium recovery was attempted by looking more closely at solution and surface species of uranium.

### Assay Optimization

Adsorption and desorption testing performed during the initial year of research utilized a destructive sampling technique in which multiple vials were sacrificed at each sampling point. This type of sampling led to considerable variability between sampling points and a low mass recovery of total uranium for each individual experiment and adequate U(IV) information was not gathered to allow for appropriate mass balance calculations. Some of the error was thought to be caused by the overall heterogeneity between batches of iron oxide sand used in the individual vials. While samples of sand were well mixed and the same batches were used for all of the vials used in the destructive sampling matrix, a wide range of variability for U(VI) adsorbed to the sand was noted. Per analysis of the U(VI) adsorption medium and the iron oxide-coated sand via nitric oxide digestion following adsorption, there was a 2× difference in U (VI) concentrations on the sand and 2 to 3× in the adsorption medium. Mineralogical characteristics of the sand may explain some of the variability noticed in the initial experiments. Rosentreter et al (1998) determined the mineralogical characteristics of 25 sediment samples collected from the Oyster, Virginia site. Three characteristics that would have affected the U(VI) adsorption were surface area, reducible iron and partition coefficient. Surface area for the 25 samples varied from 0.13 to 3.21 m2 $g^{-1}$; reducible iron varied from 0.97 to 73.28 $\mu$mol · $g^{-1}$; and finally, the partition coefficient for adsorption of U(VI) at pH 5.0 varied from 1.02 to 2.05 ml · $g^{-1}$.

During the past year, the adsorption and desorption testing was performed using nondestructive sampling with larger masses of sand and volumes of media. While there may have been differences in the various legs of each assay, variability for each assay was decreased. ICP-AA analyses of the growth medium as well as the sand for total U was also performed in order to close or nearly close the mass balance for uranium in the samples. Uranium recovery in the current experiments is greater than 90% of the mass added to the vials for testing.

## Adsorption/Desorption Testing—Laboratory Culture

Enrichments of the Laboratory Culture caused the initial desorption of uranium followed by a longer-term loss of uranium from the growth medium in batch experiments in which iron oxide-coated sand had been exposed to uranium prior to inoculation. Figure 4 shows U(VI) concentration over time for SRB and IRB enrichments. In both enrichments, the soluble U(VI) was less than the mass that was filterable through 0.2 µm filters. In the IRB enrichments, the soluble U(VI) decreased steadily over the duration of the experiment. The filterable fraction of U(VI) initially decreased, but then began to increase as the experiment neared completion. This disparity in results between the filterable and soluble fraction may be due to the formation of fine particles or colloids rather than readsorption to the surface of the iron oxide. Formation of fine particles or colloids may lead to the mobility of U(VI) in ground water of microbially impacted aquifers with mixed contamination (Beak and Pitt 1996).

U(VI) in the SRB enrichments showed a similar decrease as the experiment continued, but there was little difference in the rate of U(VI) disappearance between the filtered and unfiltered fractions. The amount of U(VI) desorbed initially was less for the SRB enrichment than for the IRB enrichment. The difference may have been caused by the chemical precipitation of uranium by the presence of sulfides produced by the culture. Precipitation of black iron sulfide on the surface of the iron oxide was the primary indicator of sulfate reduction in the test vials. In contrast, no buildup of the black encrustation of the iron oxide-coated sand was noted in the IRB enrichments.

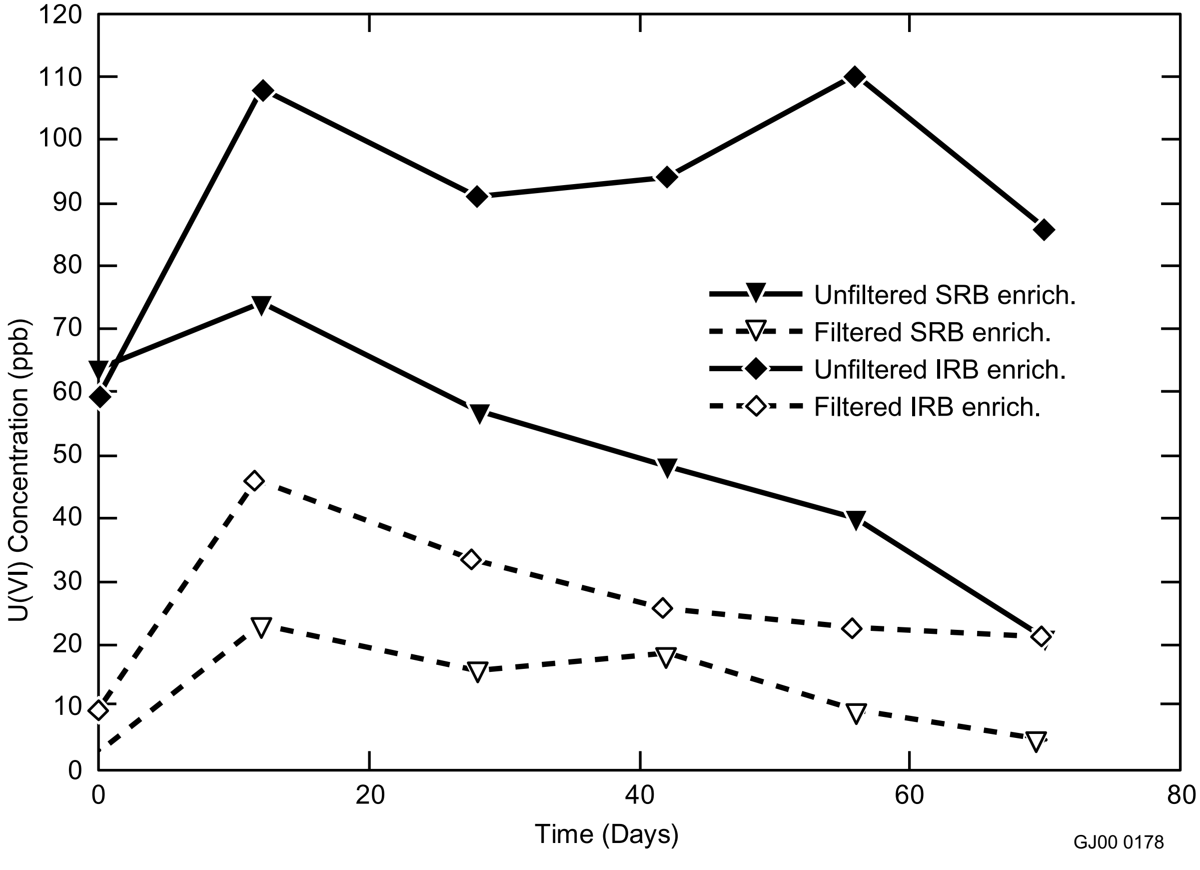

**Figure 4.** U(VI) concentration in SRB and IRB enrichments comparing filtered and unfiltered fractions over time for the “Laboratory culture.” Experiment was performed to determine the effect of SRB and IRB enrichments on uranium desorption from iron oxide coated sand.

Analysis of the growth medium using ICP-AA indicated no significant difference between the total uranium and the U(VI) measured using the kinetic phosphorescence analyzer (KPA). Neither of the enrichments were able to reductively dechlorinate the TCE that was added to the assay vials as a cocontaminant with the U(VI).

### Adsorption/Desorption Testing—Field Culture

Due to the inability of the laboratory culture to reductively dechlorinate TCE, measures were taken to obtain a culture that was demonstrating reductive dechlorination of TCE in the field. A 1-l sample of ground water from TAN (TAN 25) was filtered through a 0.2 μm filter membrane using a sterile filter apparatus. The filter was then submerged in nitrogen/phosphorus growth medium containing lactate, sulfate and iron oxide-coated sand. Following growth the culture was transferred to fresh growth medium and then a culture was set up for use in the adsorption/desorption testing. The culture was fed lactate at the start of the experiment.

Enrichment for SRB and IRB significantly affected the initial adsorption of U(VI) in the assay vials compared to the killed control and the blanks with and without TCE (Figure 5). Within the first 24 hours, the U(VI) concentration had decreased to about 400 ppb and steadily decreased to about zero by the completion of the experiment. The initial decrease in U(VI) noted in the killed control may be due to

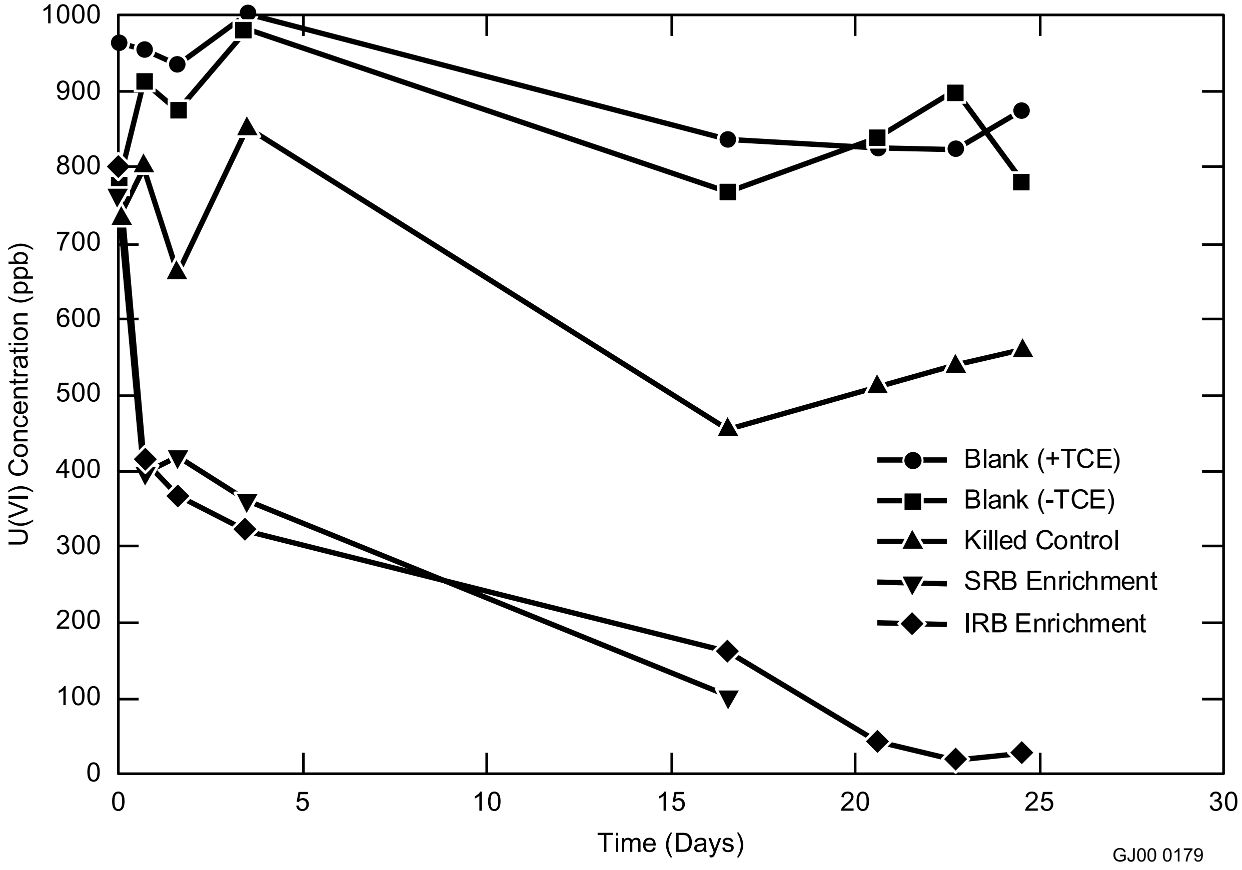

**Figure 5.** U(VI) concentration in SRB and IRB enrichments over time for the "Field Culture." Experiment was performed to determine the effect of SRB and IRB enrichments on uranium adsorption to iron oxide coated sand.

transfer of an exudate from the inoculation culture causing a chemical reaction with the U(VI) in solution. The blanks for the experiment showed a minimal decrease in uranium compared to the enrichments. On day 17 the SRB enrichment vial broke, ending this leg of the experiment.

ICP-AA analysis of nitric acid digests of the iron oxide-coated sand from the IRB enrichments yielded evidence that the microbial culture was able to chemically reduce the U(VI) to lower oxidation states. At the completion of the experiment KPA and ICP-AA analysis of the sand and the growth medium indicated a total uranium mass of 148.4 µg and a U(VI) mass of 99.2 µg. A similar analysis for the SRBs was not performed due to the breaking of the flask.

Solubility changes of the U(VI) due to pH are not likely since the pH remained stable between 6.5 and 7 during the entire experiment. As with previous experiments using the Laboratory Culture, there was no reductive dechlorination of TCE noted in either enrichment. Activity of the IRB diminished the number of iron oxide sites on the surface of the sand as indicated by the presence of ferrous iron in the growth medium. A loss of iron oxide in an aquifer impacted by IRB may decrease the number of uranium adsorption sites, potentially increasing the mobility of uranium.

### Adsorption/Desorption—Field Culture with Lactate Addition

A second adsorption/desorption experiment was set up using the Field culture to determine the effect of lactate depletion and addition on U(VI) concentration in the enrichments. Vials were set up in a manner similar to that indicated in the previous experiment, but additional lactate was added to the enrichment vials after 20 days of incubation.

Figure 6 shows uranium concentration in adsorption/desorption assay vials set up to determine the effect of lactate addition on U(VI) adsorption/desorption. As with the previous experiment, U(VI) in the enrichments decreased to near zero. Interestingly, the U(VI) concentration in the killed control also dropped to zero, indicating contamination or significant chemical precipitation of uranium in solution. By day 10 the initial supply of lactate was depleted in the SRB and IRB enrichments (Figures 7 and 8). Following this time the amount of propionate and acetate produced by fermentation of the lactate in the culture began to decrease. During this time period (between days 10 and 20) the U(VI) concentration began to increase. Upon addition of lactate on day 20, the U(VI) concentration again dropped to near zero. Upon depletion of lactate on day 28 the U(VI) again began to increase.

Metal reducing microorganisms appeared to be dominant in both enrichments, especially the IRB enrichment. Samples analyzed for total uranium after 46 days of incubation indicated high concentrations of reduced forms of uranium compared to U(VI) in the samples (Figure 6). The ferrous iron concentration in both enrichments, as well as the killed control and blank can be seen in Figure 9. Both the SRB and IRB enrichments showed the ability to reduce the iron present on the iron oxide-coated quartz. When lactate was depleted, the ferrous iron concentration in the IRB enrichment stabilized. Upon addition of lactate, the ferrous-iron concentration in solution increased. In contrast, when lactate was depleted in the SRB enrichment, the ferrous iron concentration began decreasing, but did come back when lactate was added. The loss of ferrous iron in the SRB enrichments may have been due to the formation of ferrous sulfide as indicated by the formation of a dark precipitate on the iron-oxide surface of the sand. Ferrous iron concentration in the killed controls and blanks remained near zero for the duration of the experiment.

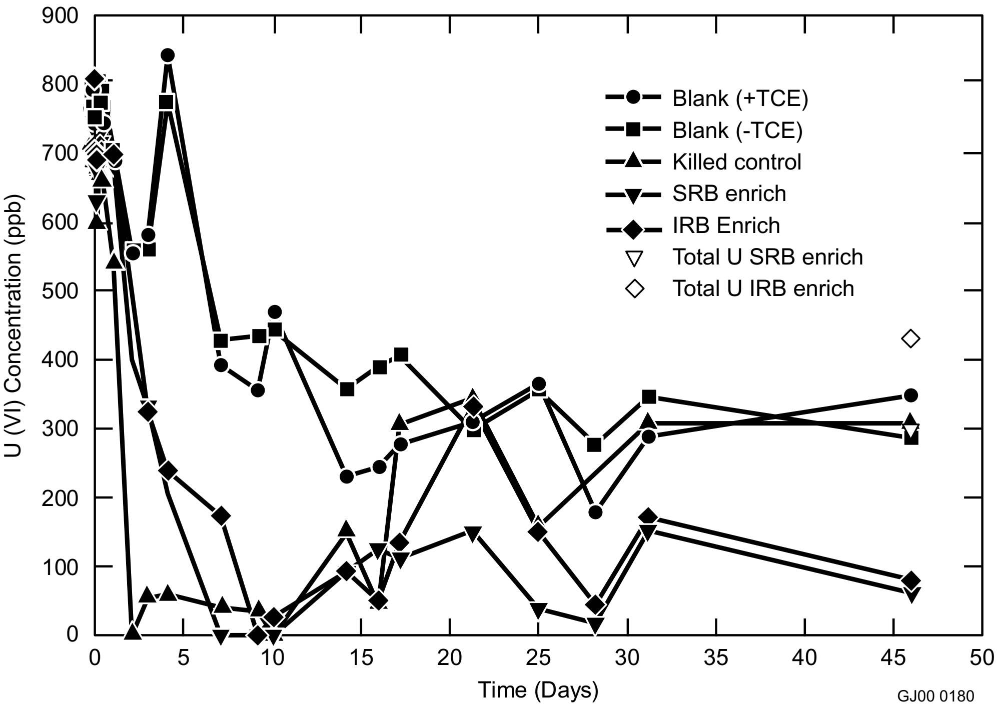

**Figure 6.** U(VI) concentration in SRB and IRB enrichments over time for the "Field Culture" during lactate addition and depletion experiments. Experiment was performed to determine the effect of SRB and IRB enrichemnets on uranioum adsorption to iron oxide coated sand. Symbols containing cross' indicate reduced forms of uranium.

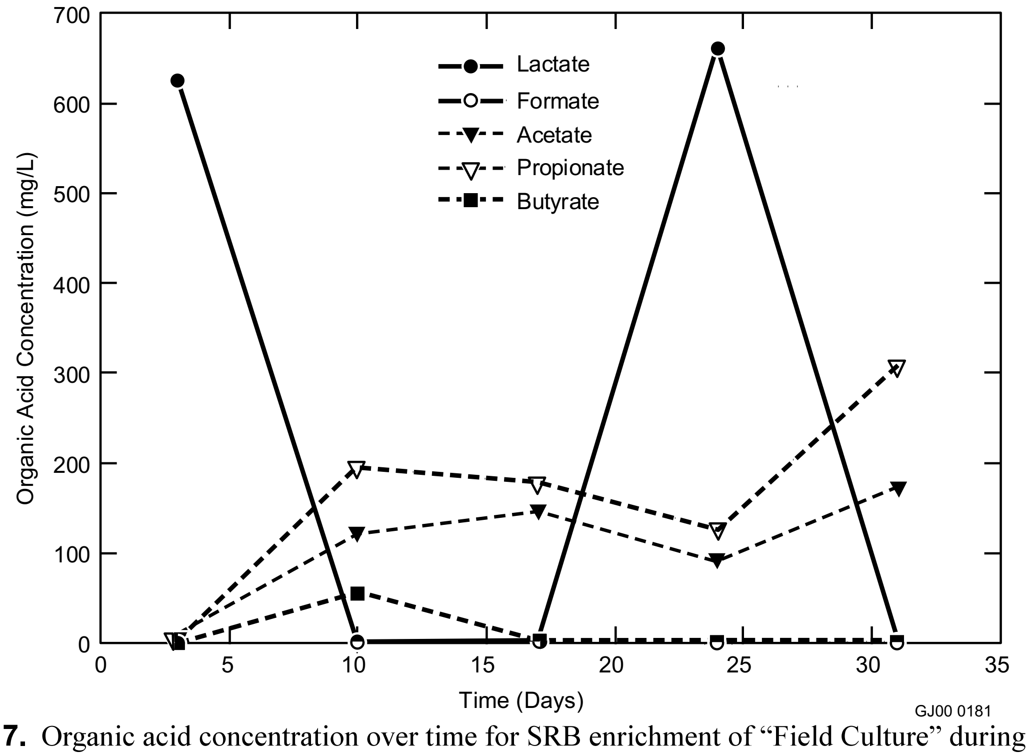

**Figure 7.** Organic acid concentration over time for SRB enrichment of "Field Culture" during lactate addition and depletion experiments.

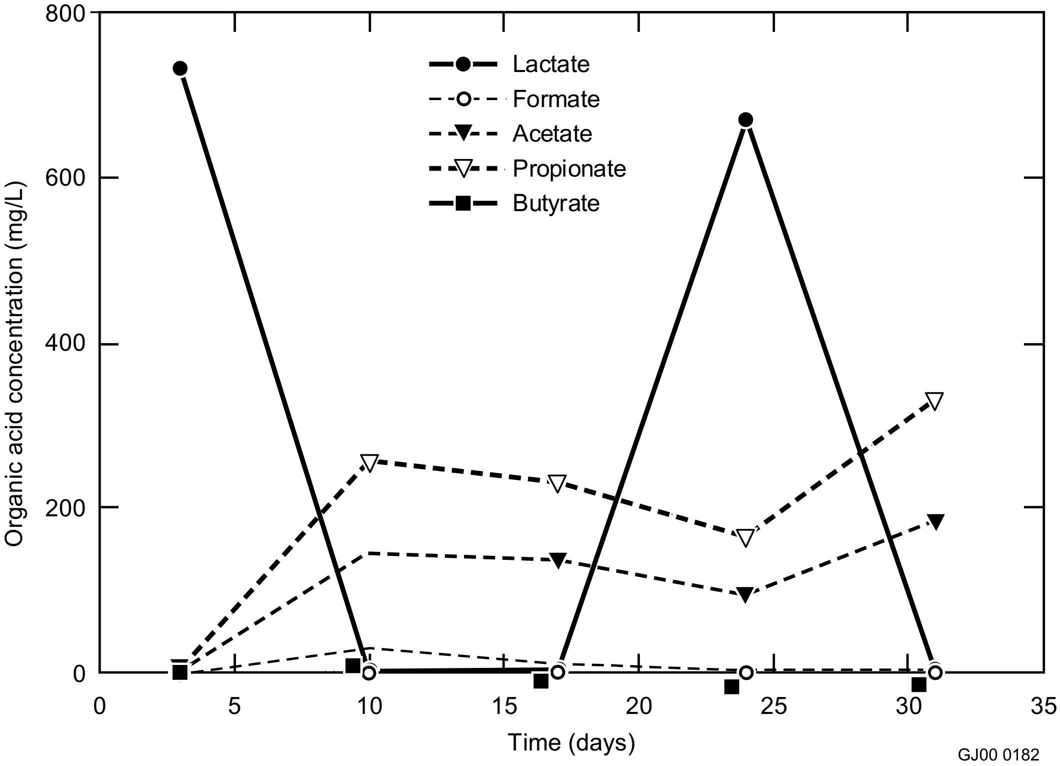

**Figure 8.** Organic acid concentration over time for IRB enrichment of "Field Culture" during lactate addition and depletion experiments.

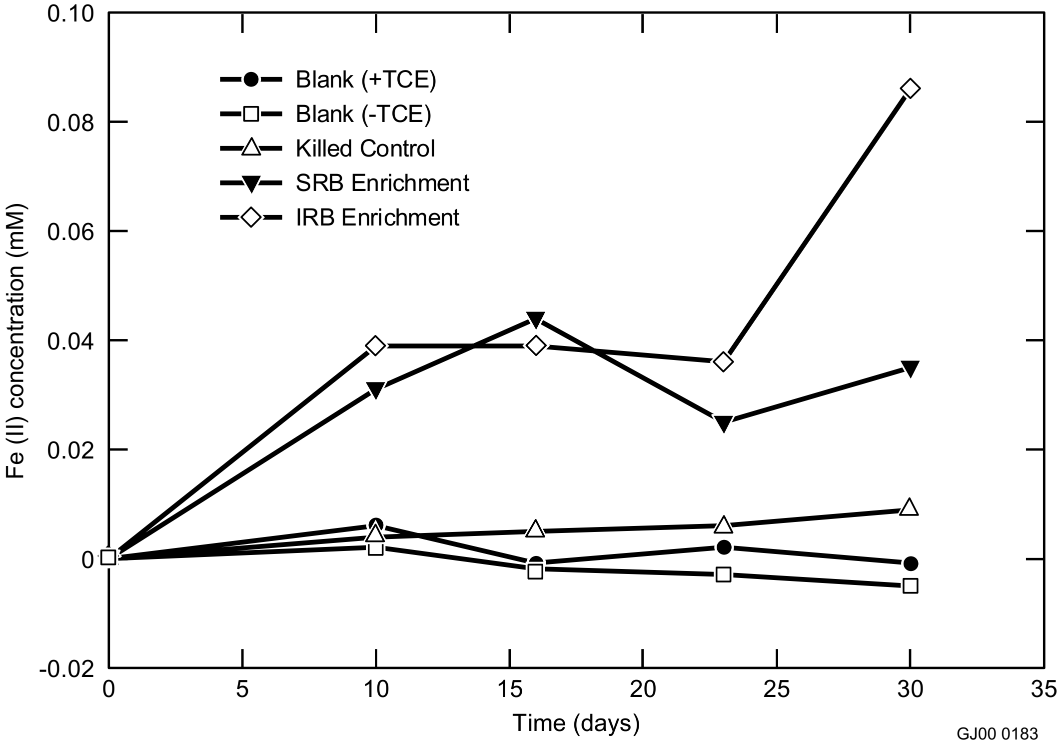

**Figure 9.** Ferrous iron concentration in SRB and IRB enrichments over time for "Field Culture" during lactate addition and depletion experiments.

As with previous experiments, the enrichments were not able to reductively dechlorinate TCE. Enrichment for SRB and IRB may be selecting for metal reducing microbes in the culture, shifting the community away from TCE degraders that were prevalent in the field. The loss in some TCE dechlorination capacity appears to be inherent with the culture from TAN. Microcosms set up specifically to monitor reductive dechlorination of TCE have encountered similar problems, including lags in rates of dechlorination and initiation of dechlorination (Kent Sorenson, personal communication).

Column experiments that are currently being set up will decrease the probability for selection of metal degrading microbial populations. The columns will be set up using crushed basalt from TAN that will decrease the amount of ferric iron present and may allow for reductive dechlorination of the TCE. Basalt in the columns will be exposed to uranium for a short period; the columns drained; followed by inoculation with a culture enriched from TAN-25. The test column will receive an inlet solution containing nitrogen/phosphorus growth medium, lactate, and sulfate. One control column will receive growth medium without lactate and a control that has not been exposed to uranium will be run to monitor the effect of uranium on the culture used for inoculum. These experiments are being set up with online monitoring of pH and Eh at various levels over the length of the columns. Columns will also be monitored over the length for U(VI), total uranium, TCE, and lactate concentration.

## Using Deep Tensiometers to Interrogate and Validate Numeric Models and Existing Field Data in the Subsurface

Hypothesis: Measured soil water potential of arid and humid sites are substantially similar.

The primary means by which contaminants are transported through the vadose zone to underlying aquifers is by subsurface movement of moisture. This task used advanced tensiometers to characterize soil water potential distributions in deep vadose zones over time in different geologic and climatic environments. These field data are required to characterize sites, develop site-specific conceptual models of flow and transport at sites, provide data for predictions of contaminant transport and model calibration, and monitor migration phenomena for long-term stewardship.

Moisture movement in the subsurface is the primary means by which contaminants are transported through the vadose zone and to the aquifer. Field data are required to monitor these migration phenomena and provide data for model calibration. Deep monitoring in the vadose zone has been limited by the availability of accurate instruments to provide data on the primary state variables. The advanced tensiometer provides data not previously attainable that is critical for understanding transport through deep vadose zones. These data are needed to monitor and evaluate contaminant plume movement and verify the landfill and hazardous waste site conditions. Advanced tensiometers are one of the vadose zone instruments used to determine the potential for moisture movement, to determine initial moisture conditions, to obtain characterization data for input to risk assessment modeling, and as part of long-term stewardship monitoring systems to ensure remedial actions are effective. This exploratory investigation has obtained the first-ever continuous measurements of water potential in deep vadose zones, in various geologic environments under distinct climatic conditions, at numerous sites. This information will be used to provide a framework for characterizing water transport in deep vadose zones.

The general objectives of this project are to: install and maintain advanced tensiometers in various geologic media for extended time periods to generate background information on water potential in deep vadose zones, continue development of the advanced tensiometer and other complementary monitoring instruments, and conduct technology transfer activities. Specific objectives on producing a data base of water potential in deep vadose zones includes (a) characterization of the vertical distribution of soil water potential in deep vadose zones using the advanced tensiometer, (b) collection and interpretation of deep water potential data over time periods relevant to transport processes, (c) acquisition of soil water potential profiles in different geologic environments, and (d) acquisition of soil water potential at sites with different climates. Development of the advanced tensiometer includes improving and developing variations of the advanced tensiometer for specific field applications, and inventing vadose/ground-water monitoring and characterization instruments that complement the advanced tensiometer. Technical transfer activities include presentations, papers, interfacing with potential users of the instruments (INEEL operations, ER and outside investigators), support to users, and patent preparation.

### Field Investigations

Wells with multiple advanced tensiometers collected data at the INEEL, Oak Ridge, Savannah River Site (SRS), Hanford, and other sites to characterize the vertical distribution of soil water potential in deep vadose zones. The instruments at the INEEL Idaho Research Center, Radioactive Waste Management Complex, INTEC, Site 14 (about 16 km south of Test Area North), and the Savannah River Site were maintained and monitored on an hourly basis. Data were downloaded from these sites, stored in a database, and plotted to evaluate the data. These wells contain multiple tensiometers with instruments at depths ranging from 3 to over 30 m. Field measurements indicate that water potential has the greatest variation in the few meters below land surface while measurements beneath this depth are relatively stable over the majority of the year. Several of the sites exhibited significant and rapid changes in water potential to depths over 15 m in response to recharge events. The general, vertical profile of water potential with depth appears similar between sites at the INEEL and SRS, despite significant differences in the amount of precipitation and geologic conditions. Water potential measurements at all these sites were within the tensiometric range, from approximately +100 to -250 cm of water. This suggests that most deep vadose zone sites can be monitored with tensiometers. Previous results from these investigations are documented (Hubbell and Sisson 1998; Sisson and Hubbell 2000; and Miller 2000).

Multiple advanced tensiometers have been installed in boreholes to depths of 143 m. The number of instruments placed in a well is limited by the sizes of the instrument and the complexity of installing suitable backfill material. Tensiometers require servicing (refilling with water) as frequently as monthly in shallow/dry sites, once every two months in most sites, and as little as yearly or every few years at sites that are at or near saturation.

Water potentials were obtained from deep vadose zones to examine and evaluate long-term water potential. Water potential measurements were collected for periods up to 4-½ years. The tensiometer data indicated there is an initial period while the instruments and backfill comes into equilibration with the surrounding materials. This can last from a few days to months, dependant on the geologic and hydrologic conditions as well as the characteristics of the backfill. The tensiometers then provide relatively stable measurements indicative of a water potentials near field capacity, with water moving by the force of gravity (unit hydraulic gradient) much of the year. Several sites showed periodic recharge events where the water potential increased in response to a pulse of water moving through the vadose zone which then drains slowly, approaching the initial water potential measurement. The recharge events are frequently rapid, suggesting that continuous monitoring is required to capture these recharge events.

Tensiometers were successfully installed in geologic materials that represent most materials found at most sites. They were installed and operated in sedimentary materials ranging from clay, silt, sand, and course gravel. Wells were also installed in fractured rock such as basalt, sandstone, and semi-consolidated sediments of the Ogallala formation in Kansas. Data from these sites suggest that the dominant water potentials are related to the field capacity of the matrix. Fine-grained sediments have dampened responses to recharge events while course material and rock have sharper responses to recharge events. In fractured rock, the tensiometers are able to obtain measurements from both the matrix and pulses of water moving within preferential pathways.

Tensiometers were installed at sites with arid to humid climates. A comparison of the water potential data from these sites suggests that the amount and distribution of precipitation is important but that difference in geologic setting may be a larger contributing factor than precipitation. It is difficult to distinguish water potential data from the INEEL as compared to data obtained from SRS. The data from the INEEL, an arid to semiarid site shows more recharge events than does SRS. This is attributed to the differences in site geology.

The INEEL has assisted several other DOE, USGS, and university sites to install, operate, and interpret data from advanced tensiometers. These projects are primarily funded by these other organizations. The INEEL-ER program installed over 40 advanced tensiometers and suction lysimeters in wells drilled at the Radioactive Waste Management Complex. These wells monitor water potential (or the formation of perched water) at the 110 and 240 ft interbeds and provide samples from these depths. Specifically, the information to be generated from these instruments are intended to assist in defining the lateral and vertical extent of perched water at the RWMC, provide evidence of the mechanisms controlling the formation of perched water, and provide data for evaluating lateral and vertical water transport in deep vadose zone. Advanced tensiometers and borehole water content sensors developed under this project were installed in 11 wells at the Savannah River Site for monitoring the vadose zone at the Mega trench and E-slit trenches.

Ten advanced tensiometers were installed in three wells at the Sand Hollow recharge site (St. George, Utah) in November and December 1999. The INEEL is cooperating with the USGS, Bureau of Reclamation, and University of Utah on this project for the Bureau of Reclamation. Two wells were instrumented to monitor water movement in the vadose zone to 60 ft beneath an infiltration pond located on the Navaho formation. These instruments along with gas sampling ports, heat dissipation sensors, and suction lysimeters will be used for estimating infiltration rates, water travel times, and level of saturation for this recharge investigation. Four advanced tensiometers were also installed from depths of 15–95 ft at a "background" site to evaluate the distribution of soil water potential in deep vadose zones under natural conditions within the Navaho formation. Data from the infiltration pond site has indicated that background water potentials are at or below the tensiometer range to depths of 15 m. Preliminary data from the infiltration test indicate low flow rates into the formation at this site, suggestive of matrix-dominated flow.

A collaborative project was started with the Kansas Geological Survey at The University of Kansas on defining the quality and quantity of recharge in the Ogallala Formation of the High Plains. Advanced tensiometers were placed in ground-water wells drilled by the USGS on irrigated and nonirrigated farm land to differentiate the effects of irrigation on deep vadose zone recharge processes. Four sets of advanced tensiometers were installed in three boreholes in Finney County, Kansas. Results are not yet available from this ongoing investigation. Over 50 advanced tensiometers are planned to be installed at the new INTEC percolation ponds in FY 2001 to characterize the water distribution and water movement prior to and following operation of these ponds.

### Development of Technologies and Intellectual Properties

The design of the advanced tensiometer has been modified and adapted to improve measurements, extend field applications, and enhance field reliability. The details of the specific improvements will not be enumerated in this report to preserve these intellectual properties. Overall, nine invention disclosures have been submitted with four more in process, in response to activities performed in this investigation. Several design changes have been incorporated into the design to reduce the effect of water level and barometric pressure changes in the water potential measurements. These modifications will provide more precise soil water measurements to detect subtle changes required for long-term (stewardship) monitoring at DOE/commercial sites. These designs have been successfully tested in the laboratory and field with prototype instruments.

Five of the submitted invention disclosures relate to extending the range of use of the advanced tensiometer for sampling and monitoring. One of these is the drive cone tensiometer that was shown at the DOE Science and Technology Complexwide Exhibit in Washington and the Environmental Management Science Program National Workshop in Atlanta. This instrument can be deployed using drive cone technology where no drill cuttings are generated in the installation process. Several of these devices have been installed at test facilities at the INEEL and Hanford. Discussions have been held with a commercial vendor that is interested in licensing this technology.

The field reliability of the advanced tensiometer has been addressed by several modifications to the design. These changes improve the ruggedness of the installation and provide a better sealing mechanism for selected applications. Several other invention disclosures have been submitted and are in preparation at the time of this report for complementary, vadose/ground-water monitoring and characterization instruments that would enhance or supplement existing instruments.

The field deployments of the advanced tensiometers are presented in the field investigations section. In addition, discussions have been held with other INEEL and DOE sites, as well other groups that are planning or considering utilizing the advanced tensiometer for their applications. At the INEEL, instruments are being considered for use at INTEC for monitoring around the tank farm and the existing percolation ponds to characterize the distribution and movement of moisture in the underlying sediments and basalt. The University of Idaho and University of Texas are using these instruments for an infiltration/geophysical test and barriers study, respectively. Instruments are being used/evaluated by the USGS at sites in the Mojave Desert and Yucca Mountain.

A patent for the Isobaric Ground-water Well was granted by the U.S. Patent and Trademark Office. The isobaric ground-water well resulted from research and development that was supported by this project during previous years' efforts. Two patent applications prepared for this investigation were submitted for consideration to the U.S. PTO. An innovative technology summary report is being prepared on the advanced tensiometer.

## ACCOMPLISHMENTS

*Microbial Partitioning Between Mobile and Immobile Phases in Geologic Media.*

See Appendix for list of published abstracts and referred papers.

1. In addition to the papers listed in the appendix, it is expected that experimental work performed under this project funding will produce at least seven additional papers:

    a. Calculation of basalt surface area based on micromorphometry (Lehman)

    b. Comparison of bacterial cell extraction methods (Lehman)

    c. Results of MIRTL2 field experiment (Lehman)

    d. Two papers associated with SR-FTIR task (Kauffman)

    e. Two papers associated with the PCR-DGGE task (O'Connell).

2. Two additional abstracts were submitted and are pending decision:

    a. Abstract submitted to the ALS Users' Conference, Lawrence Berkeley National Laboratory, Berkeley, California, October 16, 2000, Kauffman.

    b. Abstract submitted to the AGU Fall Meeting, San Francisco, CA, Dec. 15–19, 2000. Kauffman

3. Task supports an M.S. and 2 Ph.D. degrees through ISU in collaboration with Dr. Maribeth Watwood.

4. Both O'Connell and Kauffman won awards for best student presentation at regional professional meetings (see Appendix).

5. Lehman co-wrote and submitted a proposal to SERDP in collaboration with Bill Bauer and Jill Scott at the INEEL and D. C. White and C. Lytle at the University of Tennessee, "Relating TNT Contaminant Form, Soil Composition and Microbial Activity to Bioavailability."

6. Kauffman is session co-chair for International Professional Meeting: "Microbial-Mineral Interactions in Deep Subsurface Environments" at the Fall Meeting of the American Geophysical Union to be held in San Francisco, December 15–19, 2000.

*Biologically Mediated Actinide Transport in the Subsurface.*

During FY 2000 testing continued to determine the effect of anaerobic enrichment on uranium adsorption and desorption from iron oxide-coated sand. During the past year the following important determinations were made:

1. Optimization of adsorption/desorption assay for increased recovery of uranium and increased accuracy over the sampling period.

2. Uranium adsorption and desorption from iron oxide-coated sand appears to be affected by anaerobic enrichments and also appears to be culture dependent.

3. Enrichments for sulfate reducing and iron reducing bacteria cause the release of low concentrations of adsorbed uranium into the growth medium.

4. Once uranium was released into solution, the soluble fraction decreased while the fraction filterable through 0.2 μm filters increased, a possible indication that some sort of colloid is forming over the course of the experiment.

5. Enrichments for sulfate reducing and iron reducing bacteria chemically reduce iron on the surface of iron oxide-coated sand, as indicated by ferrous iron in solution. Reduction of reactive surface area may significantly affect adsorption of uranium and subsequent mobility in ground water.

6. Microbial enrichments from ground water from Test Area North (from enhanced in situ bioremediation of TCE in fractured rock source remediation operation) appear to significantly affect uranium concentration in solution; the culture also appears to reduce uranium.

Adsorption/desorption data gathered during FY 1999 has been included to allow for a comprehensive analysis of all data gathered during the project.

Utilization of Deep Tensiometers to Interrogate and Validate Numeric Models and Existing Field Data in the Subsurface

1. Soil water potential measurements were collected at multiple sites from arid and humid sites in geologically diverse materials including sediments (gravel, sands, clay, and silts) and porous rock (basalt and sandstone) to improve the baseline understanding of water distribution and movement in deep vadose zones.

2. Water potentials were analyzed from a deep vadose zone at a semi-arid site in southeast Idaho to examine long-term water potential. Water potential measurements were in the range of approximately +100 to -250 cm of water in both arid and humid sites. Beneath 4 m, the water potentials were steady most of the year with a unit-gradient downward flux. Tensiometers located near the surface exhibited water potential standard deviations greater than 25 cm, likely due to evapotranspiration and drainage. Several of the fractured rock sites recorded episodic infiltration events indicating recharge pulses occurring to depths exceeding 15 m. Water potential during these episodic infiltration events varied both temporally and spatially indicating preferential flow pathways through the fractured media.

3. Drive cone tensiometers were designed and installed for testing purposes at the Hanford Buried Waste Test Facility (BWTF), the Sisson and Lu Site at Hanford, and the Idaho Research Center at the INEEL. These tensiometers were placed adjacent to existing instruments (water content sensors, neutron access tube and conventional tensiometers installed using an instrument caisson) to allow comparison of data. The drive cone tensiometers are planned to be deployed at the Radioactive Waste Management Complex in FY-01.

4. The patent for the Isobaric Ground-water Well (number 5,969,242) was granted by the U.S. Patent and Trademark Office, October 19, 1999. This invention is an outgrowth of work on the advanced tensiometer.

5. Nine invention disclosure records were prepared and submitted to the Technology Transfer Office on vadose zone and ground water monitoring devices.

6. Developed capabilities to monitor water movement in deep vadose zones for long-term stewardship at disposal facilities.

7. Worked with the Environmental Restorations for their deployment of advanced tensiometers and lysimeters at the INEEL Radioactive Waste Management Complex in FY-00. Continued to provide consultation for interpretation of the field data from these sites.

# REFERENCES

Riley, R. G., J. M. Zachara, and F. J. Wobber, “Chemical Contaminants on DOE Lands and Selection of Contaminant Mixtures for Subsurface Science Research,” DOE/ER—0547T, April 1992.

U. S. Department of Energy, Subsurface Contaminants Focus Area, Summary Report, Washington, D. C., August, 1996.

Ellis, D. E., E. J. Lutz, J. M. Odom, R. J. Buchanan, Jr., C. L. Bartlett, M. D. Lee, M. R. Harkness, and K. A. Deweerd. 2000. “Bioaugmentation for Accelerated In Situ Anaerobic Bioremediation.” *Environ. Sci. Technol.* 34: 2254–2260.

Harkness, M. R., A. A. Bracco, M. J. Brennan, Jr., K. A. Deweerd, and J. L. Spivack. 1999. “Use of Bioaugmentation to Stimulate Complete Reductive Dechlorination of Trichloroethene in Dover Soil Columns.” *Environ. Sci. Technol.* 33: 1100–1109

Sorenson, K. S., 1998, “Design of a Field-Scale Enhanced In Situ Bioremediation Evaluation for Trichloroethene in Ground Water at the Idaho National Engineering and Environmental Laboratory,” ASAE, St. Joseph MI, Paper no. PNW98-113.

Adriaens, P. and T. M. Vogel, “Biological Treatment of Organics, In Microbial Transformation and Degradation of Toxic Organic Chemicals,” L. Young and C. Cerniglia, eds. John Wiley & Sons, Inc. New York. 1995 pp. 435–486.

Fetzner, S., “Bacterial Dehalogenation,” *Appl. Microbiol. Biotechnol.* 1998, 50: 633–657.

Waite, T. D., J. A. Davis, T. E. Payne, G. A. Waychunas, and N. Xu. 1994. “Uranium(VI) Adsorption to Ferrihydrite: Application of a Surface Complexation Model.” *Geochem. Cosmochem. Acta* 58: 5465–5478.

Kohler, M., G. P. Curtis, D. B. Kent, and J. A. Davis. 1996. “Experimental Investigation and Modeling of Uranium(VI) Transport under Variable Chemical Conditions.” *Wat. Resources Res.* 32: 3539–3551.

Reich, T., H. Moll, T. Arnold, M. A. Denecke, C. Henning, G. Geipel, G. Bernhard, H. Nitsche, P. G. Allen, J. J. Bucher, N. M. Edelstein, and D. K. Shuh. 1998. “An EXAFS Study of Uranium(VI) Sorption onto Silica Gel and Ferrihydrite.” *J. Electron Spec. Related Phenomena* 96: 237–243.

Rosentreter, J. J., H. S. Quarder, R. W. Smith, and T. McLing. 1998. “Uranium Sorption onto Natural Sands as a Function of Sediment Characteristics and Solution pH. In Adsorption of Metals by Geological Media.” E. A. Jenne (Ed.) Academic Press, pp. 181–192.

Bargar, J. R., R. Reitmeyer, and J. A. Davis. 1999. “Spectroscopic Confirmation of Uranium(VI)-Carbonato Adsorption Complexes on Hematite.” *Environ. Sci. Technol.* 33: 2481–2484.

Tsang. K. W., P. R. Dugan, and R. M. Pfister, “Mobilization of Bi, Cd, Pb, Th, and U Ions from Contaminated Soil and the Influence of Bacteria on the Process,” In Emerging Technologies in Hazardous Waste Management IV (D. Tedder and F. Poland, eds.) American Chemical Society, Washington, D. C., 1994, pp. 78–93.

Lee, B. D., K. D. Schaller, M. E. Watwood, and W. A. Apel. 2000. "Transition Metal Catalyst-Assisted Reductive Dechlorination of Perchloroethylene by Anaerobic Aquifer Enrichments." *Biorem. J.* 4: 97–110.

Beak, I., and W. W. Pitt, Jr., "Colloid-Facilitated Radionuclide Transport in Fractured Porous Rock," *Waste Manag.,* 1996, 16(4): 313–325.

Miller, D. L., 2000, "Environmental Systems Research, FY-99 Annual Report," INEEL/EXT-99-01008, pp. 387.

Sisson, J. B. and J. M. Hubbell, 2000, "Water Potential to Depths of 30 Meters in Fractured Basalt and Sedimentary Interbeds," in Characterization and Measurement of Hydraulic Properties of Unsaturated Porous Media, ed. by M. Th. van Genuchten and F. J. Leij, U.S. Salinity Laboratory, Riverside, Calif., pp. 855–865.

Hubbell, J. M. and J. B. Sisson, 1998, "Advanced Tensiometer for Shallow or Deep Soil Water Potential Measurements," *Soil Science*, April, Vol. 163, No. 4, pp. 271–277.

# Surface Speciation of Radionuclides in Environmental Media

**Gary S. Groenewold, Tony Appelhans, Robert V. Fox,**
**Jani C. Ingram, and Bruce J. Mincher**

## SUMMARY

Radionuclides can exist in a variety of chemical forms, which are referred to as the chemical species of the radionuclide. The chemical species has a profound bearing on environmental fate and transport, and consequently risk assessment. Determining radionuclide chemical speciation present on the reactive top monolayer of naturally occurring mineral surfaces is a challenging task that is beyond the capability of current analytical methods and instrumentation. Our research combines rigorous bulk speciation characterization with unique secondary ion mass spectrometry (SIMS) surface analysis to generate accurate, radionuclide surface speciation information and, more importantly, general methods and instrumentation for facile radionuclide surface speciation determinations. Specifically, we initiated studies of Cs, Sr, Re, U, Pu, and Am in contact with soils from the INEEL's Radioactive Waste Management Complex using adsorption, sequential extraction, and SIMS approaches. Substantial information was gained for the Cs, Sr, and U-contaminated systems that described surface- and bulk-phase speciation. The SIMS investigations were conducted using nonradioactive nuclides or surrogate metals because a SIMS instrument capable of handling radioactive samples does not currently exist. For this reason, a longer-term goal is to design and fabricate a SIMS instrument capable of performing surface speciation studies on radioactive samples. We assembled a prototype instrument and initiated initial function testing . Our principal objective for this instrument is to transport it to a radioactive laboratory to begin assessing performance using radiologically contaminated samples, scheduled for FY 2001.

## PROJECT DESCRIPTION

### Background and Motivation

Radionuclide contamination in the surficial soils of the Radioactive Waste Management Complex (RWMC) Subsurface Disposal Area (SDA) is a significant problem because it is a radioactive hazard to personnel and the environment.[1] The RWMC is a restricted-access area located in the southwest quadrant of the INEEL in a depression circumscribed by basaltic and lava ridges. The ground surface is relatively flat, lying about 5,000 feet above sea level, and about 600 feet above the Snake River Plain Aquifer. The Subsurface Disposal Area is a 97-acre area in a western section of the RWMC. The SDA was dedicated to permanent shallow-land disposal of solid, low-level transuranic waste generated by national defense programs from 1954 to 1970. The chemistry, biology, and geology of the SDA and surrounding area define a complex system in which radionuclide behavior is difficult to predict.

The radionuclide contamination is complex because the buried metals and radionuclides can exist in a variety of chemical forms or *species*[2-4] that strongly influence mobility in the environment, and they present a variety of remediation approaches. In addition to chemical complexity, the geology of the area is complex, with multiple basaltic, eolean, and sedimentary mineral forms present. Over long time periods, radionuclides can be incorporated into the bulk of these minerals; however, a more immediately controlling factor relative to radionuclide sequestration or mobility in a heterogeneous mineralogical environment is interactions with the mineral surfaces. Ideally, radionuclide surface behavior as a function of chemical species and mineral form is desired to predict migration or sequestration outcomes in the environment.

Addressing chemical speciation on environmental surfaces is a difficult proposition. The technique recognized as providing the most informative analytical information is extended x-ray absorption fine structure (EXAFS) spectroscopy,[5-6] which can provide bonding information for adsorbed metals. However, even the tremendous power of this technique encounters limitations when addressing radionuclide-contaminated environmental samples. The concentrations of surface-adsorbed species can be too low for observation using EXAFS,[7] and highly heterogeneous samples can result in uninterpretable information. Furthermore, ready access to a synchrotron accelerator facility is required, and this can be limiting for support of ongoing remediation or stewardship activities. Certainly, other surface techniques have been applied to characterizing contaminated environmental samples, among them x-ray photoelectron, Auger, low-energy electron diffraction, infrared, and Raman spectroscopies. Generally, if the techniques are sensitive enough to detect surface-adsorbed radionuclides, they generate limited molecular information; conversely, if they are specific enough to distinguish molecular forms, sensitivity tends to be limited. Another technique that has enjoyed some application to the characterization of mineral surfaces is secondary ion mass spectrometry (SIMS),[8] which is the primary subject of the present research .

Historically, SIMS has been employed for analyzing the elemental composition of a variety of materials, including minerals. SIMS analyzes sample surfaces by bombarding them with an energetic projectile, which causes ‘secondary’ ions to be ‘sputtered’ from the surface, where their masses can be measured using mass spectrometry techniques. Normally, *atomic* projectiles have been employed, which result in highly energetic surface impacts and production of primarily *atomic* secondary ions. However, recent research by the INEEL SIMS group and others has clearly shown that using *polyatomic* projectiles results in sputtering of *molecular* secondary ions,[9-11] which can be highly indicative of the surface speciation of adsorbed radionuclides. The specific projectile used by the INEEL group is $ReO_4^-$ (a.k.a. perrhenate), which is generated as a gas-phase anion by heating a $Ba(ReO_4)_2/Eu_2O_3$ ceramic to $>800^oC$ in vacuum and accelerated to 5 KeV for surface bombardment.[12] This projectile was used on all INEEL SIMS spectrometers, and was subsequently applied to a wide variety of organic surface adsorbate molecules.[13]

Foundational work in developing SIMS for probing metal species present on mineral surfaces indicate that speciation can be determined. Specific studies relevant to this project include the micron-scale spatial correlation of adsorbed $Cs^+$ with Al-bearing phases on silicate surfaces,[14] the correlation of reduced tri-*n*-butylphosphate with high Fe(II)-bearing basalts,[15] the interrogation of Hg-nitrate surfaces using an organic amine,[16] and the identification of basalt mineral phases.[17] These studies strongly suggest that improved metal speciation can be determined by using SIMS for characterizing radionuclide-contaminated mineral surfaces.

Applying SIMS for speciation determination of adsorbed radionuclides required us to obtain knowledge and develop methods in several areas. We needed test samples in which the metal speciation was well understood, so that we could evaluate speciation determination using SIMS. We expended significant effort to characterize unmodified RWMC soil samples in terms of elemental composition and physical attributes. We then exposed these samples to nonradiological metals relevant to radiological contamination at the RWMC; these metals were Sr, Cs, Re, and U. Sr, Cs, and U all have radioactive nuclei of direct interest as contaminants. We studied Re because it is an effective surrogate for Tc, which is a radioactive element that may be significant at the RWMC.

Once the samples were exposed, we then recharacterized them for metal content, also using a sequential extraction approach.[18] The sequential extraction indicated how the metals were bound to the soil particles. Hence, the exposed soil samples served as benchmarks to evaluate SIMS instrumentation for determining speciation. We performed the initial, nonradiological SIMS analyses using instrumentation at the INEEL and at the Image and Chemical Analysis Laboratory (Montana State

University). But we could analyze no radiological samples because no instrumentation was located in a radiological laboratory.

To enable analysis of radiological samples, we designed and fabricated an ion trap SIMS for eventual transport to a radiological laboratory. The ion trap design was adopted for its high degree of instrumental flexibility; namely, the instrument is capable of collisionally stabilizing complex metal species indicative of surface speciation and can be used to study MS/MS to determine ion composition, and study ion-molecule condensation reactions to assess ion reactivity.

These activities comprised the tasks for the metal speciation program (Figure 1), and are highly integrated (see Table 1). Studies of nonradiological metal speciation provide samples and characterization requirements to the characterization and instrument R&D tasks, which provide information back to the soil research task. Characterization Task 2 provides requirements to the IT-SIMS R&D task, which in turn provides characterization tools back to Task 2. This tandem strategy results in speciation data describing contaminated RWMC soils, but, more importantly, it will generate tools and methods for routine speciation determinations for a wide range of samples.

### Task 1. Radioactive Waste Management Complex Soil Research

Our objectives for the RWMC soil research task were twofold, namely, to thoroughly understand the physical and chemical soil attributes and to understand the adsorption/desorption behavior relative to salient radionuclides. Our initial subtask was to identify a RWMC soil sample typical of the SDA area. Owing to the presence of several different soil lenses, variations in RWMC soil physical and chemical properties are known to exist, depending on the exact location and depth from which samples are obtained. From a historical perspective, it is known that the pits and trenches at the RWMC were typically excavated to 18 ft, or to the top of the basalt, filled with drums and boxes, then backfilled. Thus, the soil beneath the SDA (below the 18-ft level) is, for the most part, undisturbed, whereas the backfilled soil is a mixture of excavated materials. To satisfy the criteria of the initial subtask, we chose soil samples from the in situ vitrification demonstration pit and Spreading Area B, for three reasons: first, soils originating from those locations had been previously established to be typical of those in the RWMC area. Second, the samples contain only naturally occurring radionuclides at background levels. Third, because the areas are not within the RWMC site boundary and the samples were not radiologically contaminated, the samples did not require a treatability study permit and could be collected and used without fear of contaminating the nonradiological analysis laboratories. The third reason for using the Spreading Area B soil was to have a standard soil against which to compare our characterization results with results found by others. The in situ vitrification pit samples afforded additional opportunity to retrieve “undisturbed” RWMC area soils at varying depths.

The in situ vitrification pit is located immediately outside the RWMC at the INEEL. It is a 30-ft-long by 30-ft-wide by 18-ft-deep excavation approximately 220 ft north of the north SDA fence, approximately 60 ft northeast of the northeast corner of the United States Geographical Survey fence, and approximately 175 ft west of the west Pit 9 fence (see Figure 2). The spreading areas are approximately 1 mile south of the SDA. The spreading area soils were previously analyzed and are routinely used for top-soil at various locations around the INEEL. Data are presented below for the in situ vitrification pit soils at the 18-ft level and every 3 ft up the pit face to the surface. For comparison, data are also presented for Spreading Area B soil.

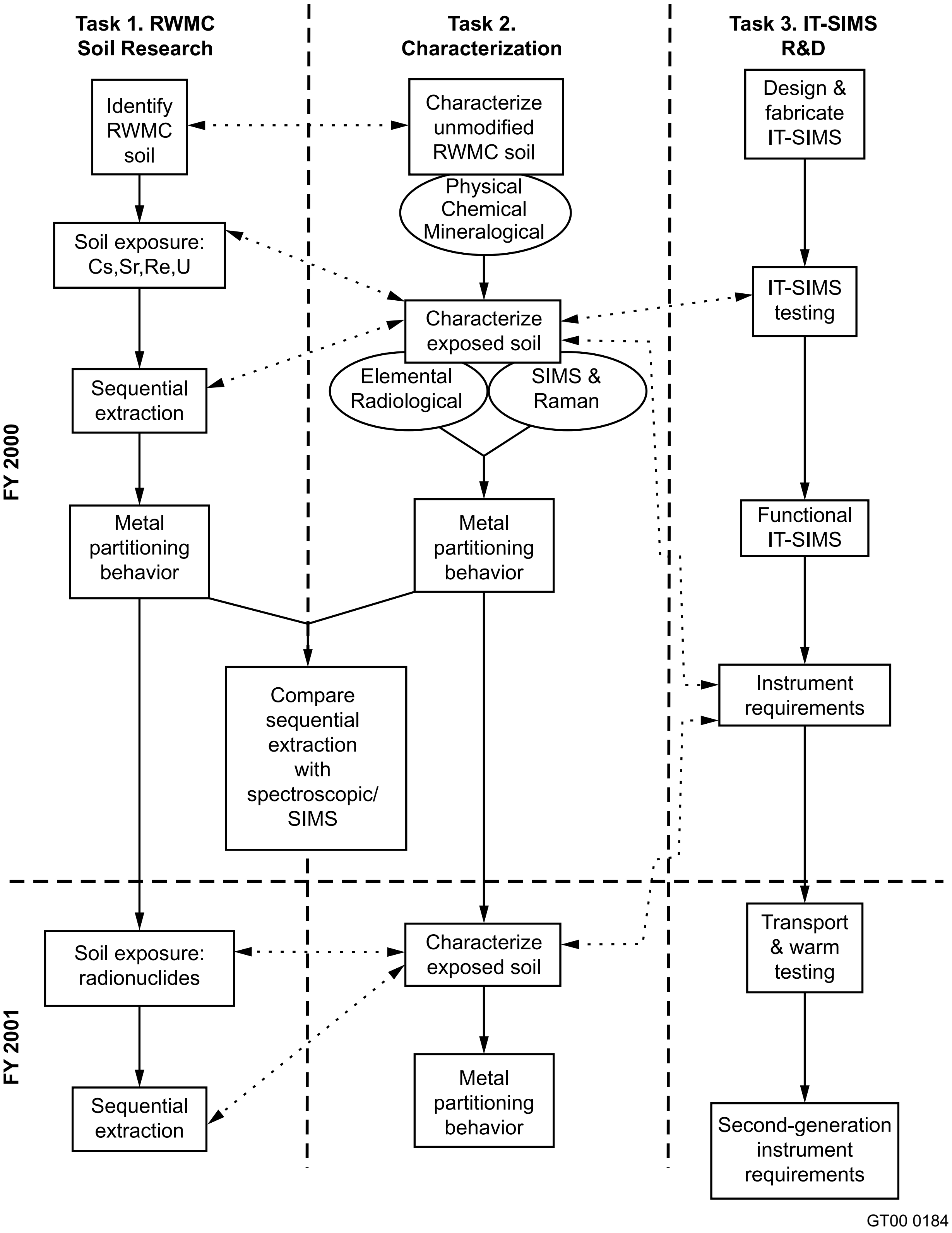

**Figure 1.** Tasks, with interrelationships, and projected activities for FY 2000.

**Table 1.** Summary of tasks and interrelationships in the surface speciation of radionuclides in the environmental media program.

| Task | Title/Description | Relationships to Other Tasks |
|---|---|---|
| 1 | RWMC soil research, including sample identification, physical and elemental characterization, metal exposure, and sequential extraction. | Provides unmodified and exposed samples for Task 2, Characterization. Provides sequential extraction information relating to metal speciation |
| 2 | Characterization: surface speciation determinations emphasizing SIMS. | Provides characterization data back to Task 1, RWMC soil research, for unmodified, exposed and extracted samples.<br>Provides operating performance information to Task 3, IT-SIMS R&D. Provides samples for evaluating instrument analytical capability. Provides requirements for second-generation instrumentation. |
| 3 | Ion Trap SIMS Research and Development, including design and fabrication of an instrument to be transported to a radiological laboratory, and generation of requirements for a second-generation instrument specifically tailored to radiological analyses. | Provides analytical capability to Task 2, Characterization. Influences methodology choices for speciation measurements. |

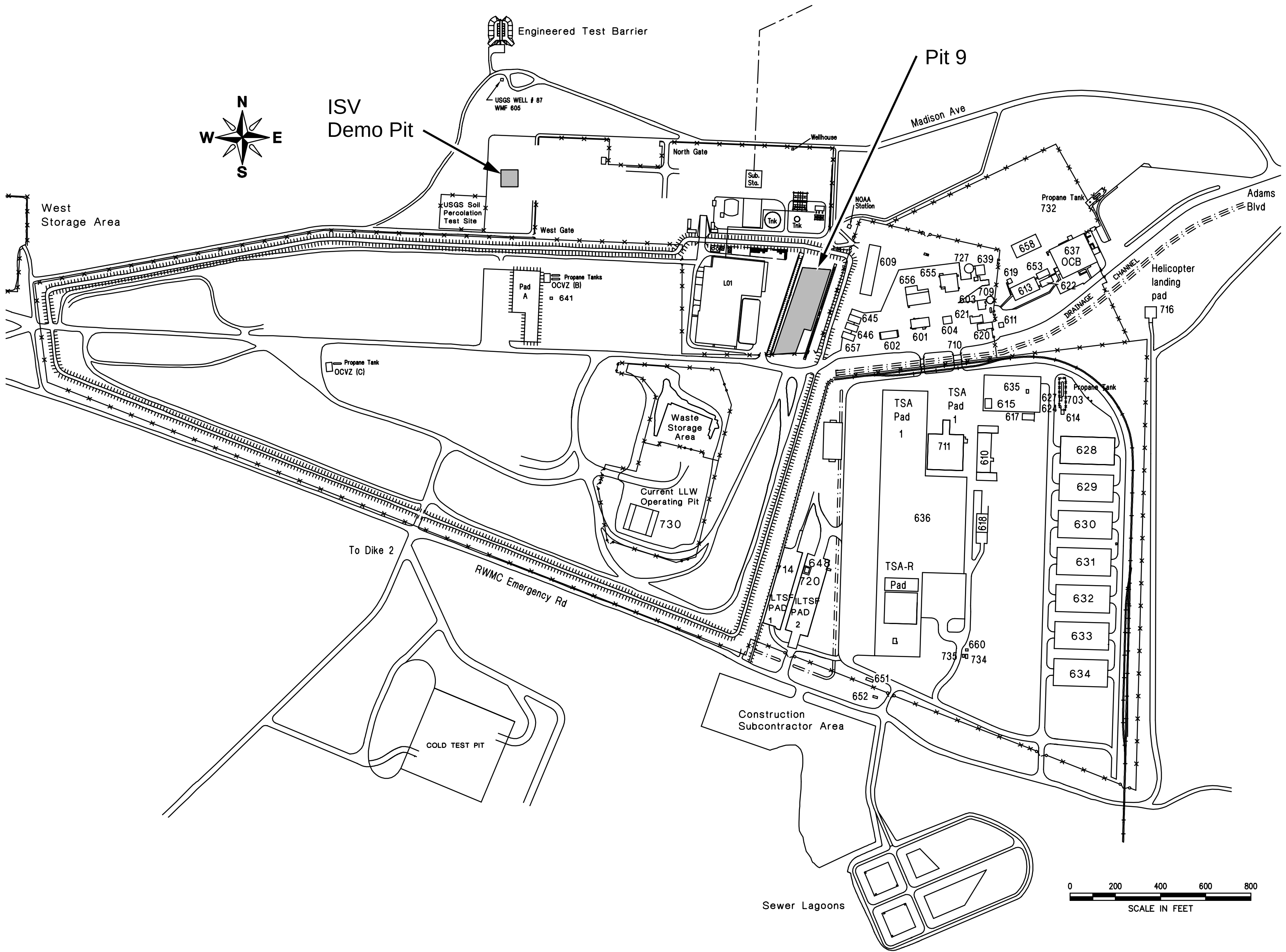

**Figure 2.** Location of the sampling location for the RWMC soils used in the speciation project.

### *Physical and Chemical Characterization of RWMC Soil*

A series of characterizations were undertaken to establish the physical and chemical properties of the soil samples. These are summarized in Table 2.

**Table 2.** Physical and chemical characterizations applied to RWMC soil samples.

| Characterization | Description |
|---|---|
| Particle size spectrum | Soil particle size analysis used the Coulter (laser diffraction) method, the wet sieving method, and the calibrated hydrometer method.[19] |
| Specific surface and average pore size | Surface area was determined using a Quantachrome Autosorb 1-CLT particle size analyzer. The Autosorb unit employs nitrogen physisorption and BET isotherm analysis. The average pore size was also determined using the Autosorb 1-CLT and nitrogen physisorption techniques. Average pore size was calculated by the MP method described by Brunaeur.[20] |
| Bulk density | Bulk soil density was determined using the excavation method.[21] |
| pH | Soil pH in water was determined by electrometric measurement.[22] |
| Redox potential (eH) | Soil redox potential was determined by electrometric measurement. [23] |
| Cation exchange capacity (CEC) | CEC was determined using the ammonium chloride method.[24] Barium chloride exchangeable cations were also determined by displacing cations with barium. |
| Soluble soil cations and anions | Analysis used atomic absorption spectroscopic and ion chromatographic analysis of the liquid extracts resulting from displacement of exchangeable cations and anions and direct dissolution of soil anions and cations into an aqueous phase. |
| Elemental analysis | Elemental analysis was performed by lithium hydroxide and boric acid fusion at 1000°C, then dissolution and analysis via inductively coupled plasma atomic emission spectroscopy (ICP-AES). |
| Organics and carbonates | Soil organic content was determined by a modified rapid dichromate oxidation technique in sulfuric acid.[25] Soil carbonates were determined by acid dissolution and gas evolution analysis.[26] |
| Determination of Fe/Mn mineral content | Total soil iron and manganese were determined by lithium meta-borate fusion of a 1-gram soil sample, followed by ICP-AES, as described under elemental analysis. Free iron and manganese (hydrated oxides or oxyhydroxides, a.k.a. sesquioxides) were determined by the citrate-dithionite and citrate-bicarbonate-dithionite methods.[27] |
| Sequential extractions | Sequential extractions with cation analysis were performed at each step.[18,28] |

When characterized on the basis of particle size, the RWMC in situ vitrification pit soil is predominantly a silty-clay (see Table 3). There is some variation in particle size distribution, surface area, or porosity in the samples collected at the different depths, but the 18-ft sample is most representative. The bulk of the in situ vitrification pit soil particles resided in the 2 to 53-µm range, with the remainder split between finer and coarser particles. Only slight variation exits between the soil density of the in situ vitrification pit samples collected at the different depths (see Table 4).

Chemical analysis of the soil samples identified them as predominantly aluminosilicate, with higher concentrations of Ca/Mg carbonates near the surface. Consistent with this observation was the measurement of a slightly alkaline pH. The soil elemental and soil mineralogical analyses (data not shown) indicate the soil is predominantly clay minerals (illite, smectite, mixed illite-smectite 2:1 clays, and some kaolinite). Parent minerals found in the samples include calcium carbonate, feldspars, quartz, and diopsides. The pH of the soil is basic (7.5 to 8.0 for all samples), and the redox potential (eH) varies from –400 to +200 mV for all samples. The cation exchange capacity is relatively low (<20 meq/100g; see Table 5), which is typical of the illite, smectite, and mixed illite-smectite 2:1 clay minerals. The exchangeable cations (see Table 5) were dominated by $Ca^{+2}$ and $Mg^{+2}$. In addition, both the cation composition and cation exchange capacities were fairly constant from the surface to the 18-ft level. When we contrasted the elemental compositions of the rock-forming minerals, again, we observed relatively minor differences from the surface to the 18-ft level (see Table 6). The material is predominantly aluminosilicate, with significant contributions from Fe, Mg, Ca, and K, and minor amounts of Ti and Na. The Ca is somewhat more concentrated near the surface. Of these elements, total soil Fe is potentially the most significant, ranging from approximately 2 wt% to ~5 wt%. Even though total soil Fe constitutes as much as 5 wt%, from sequential aqueous extraction studies, we determined that only 0.0002 to 0.0004 wt% of the soil Fe resides in the sesquioxide phase.

**Table 3.** In situ vitrification pit, 18-ft depth, soil particle size distribution, surface area, and pore size.

| | |
|---|---|
| <2 microns (clay) | 14 wt% |
| 2 to 53 microns (silt) | 73 wt% |
| >53 microns (sands) | 13 wt% |
| Specific surface | 32.6 $m^2/g$ |
| Average pore size | 26 Å |

**Table 4.** Bulk soil density (g/ml).

| | |
|---|---|
| 18-ft in situ vitrification pit | 1.20 |
| 15-ft in situ vitrification pit | 1.17 |
| 12-ft in situ vitrification pit | 1.00 |
| 9-ft in situ vitrification pit | 1.05 |
| 6-ft in situ vitrification pit | 1.09 |
| 3-ft in situ vitrification pit | 1.16 |
| Spreading Area B soil | 1.08 |

**Table 5.** Exchangeable cations, cation exchange capacities.

| | $Ba^{+2}$ Exchangeable Cations, Cation Exchange Capacity | | | | | $NH_4^+$ Cation Exchange Capacity (CEC) | |
|---|---|---|---|---|---|---|---|
| ppm/g soil | $Mg^{2+}$ | $Na^+$ | $K^+$ | $Ca^{2+}$ | Total meq/100g | meq/100 g soil | |
| 18-ft in situ vitrification pit | 40 | 61 | 12 | 131 | 12.8 | 18-ft in situ vitrification pit | 7.3 |
| 15-ft in situ vitrification pit | 44 | 41 | 14 | 129 | 12.2 | 15-ft in situ vitrification pit | 6.5 |
| 12-ft in situ vitrification pit | 48 | 66 | 11 | 125 | 13.3 | 12-ft in situ vitrification pit | 9.5 |
| 9-ft in situ vitrification pit | 57 | 67 | 8 | 106 | 13.1 | 9-ft in situ vitrification pit | 8.2 |
| 6-ft in situ vitrification pit | 71 | 7 | 2 | 134 | 12.9 | 6-ft in situ vitrification pit | 9.6 |
| 3-ft in situ vitrification pit | 29 | 2 | 1 | 137 | 9.3 | 3-ft in situ vitrification pit | 3.6 |
| Spreading Area B soil | 58 | 8 | 23 | 215 | 16.4 | | |

**Table 6.** Elemental analysis of major rock forming minerals.

| Calculated as wt% most common oxide | Si | Fe | Mg | Mn | Cu | Cr | Ti | Al | Sr | Ca | Na | K |
|---|---|---|---|---|---|---|---|---|---|---|---|---|
| 18-ft in situ vitrification pit | 34.6 | 2.93 | 2.86 | 0.089 | 0.019 | 0.011 | 0.40 | 5.87 | 0.0051 | 0.88 | 0.7 | 2.5 |
| 15-ft in situ vitrification pit | 32.7 | 2.67 | 2.50 | 0.11 | 0.060 | 0.014 | 0.47 | 5.85 | 0.0063 | 0.77 | 0.9 | 2.6 |
| 12-ft in situ vitrification pit | 31.8 | 4.71 | 5.34 | 0.19 | 0.042 | 0.015 | 0.64 | 6.90 | 0.0064 | 1.54 | 0.9 | 2.0 |
| 9-ft in situ vitrification pit | 34.1 | 2.40 | 2.73 | 0.037 | 0.055 | 0.011 | 0.41 | 5.73 | 0.0064 | 0.88 | 0.9 | 2.2 |
| 6-ft in situ vitrification pit | 30.5 | 2.79 | 3.14 | 0.057 | 0.023 | 0.0098 | 0.41 | 5.88 | 0.0076 | 2.02 | 0.8 | 2.1 |
| 3-ft in situ vitrification pit | 28.1 | 1.93 | 3.48 | 0.041 | 0.039 | 0.0074 | 0.33 | 4.54 | 0.0095 | 5.73 | 0.9 | 2.0 |
| Spreading Area B soil | 34.0 | 2.19 | 3.02 | 0.034 | 0.024 | 0.0069 | 0.356 | 5.04 | 0.0075 | 2.98 | 0.80 | 1.8 |

The in situ vitrification pit soil contains soluble and leachable cations (see Table 7). The dominant cations are Ca, Ba, and Cs, with lower quantities of K, Na, Mg, Al, and Si. No systematic trends could be observed when we compared samples from the different depths. No significant anionic species were present except carbonate, which is typical of a calcareous soil and points strongly to precipitation of metal carbonate salts as a plausible surface complexation mechanism (see Tables 8 and 9). The total carbonate concentration ranges from ~0.3 wt% at the 18-ft level to ~8.8 wt% near the surface of the ground. Organic carbon also tends to concentrate near the surface. We measured fractions as high as 0.5% in the 3-ft sample, but this decreased to <0.2% in the samples collected from the greatest depths (see Table 10).

**Table 7.** Soluble soil cations.

| ppm/g soil | Ca | K | Na | Mg | Al | Ti | Mn | Zr | Si | Fe | Cu | Ni | Cs | Ba |
|---|---|---|---|---|---|---|---|---|---|---|---|---|---|---|
| 18-ft in situ vitrification pit | 205 | 12 | 18 | 19 | 0.57 | 0.006 | 0.008 | <0.01 | 3.6 | <0.05 | <0.05 | <0.1 | 63 | 210 |
| 15-ft in situ vitrification pit | 143 | 16 | 11 | 28 | 0.48 | 0.012 | 0.003 | <0.01 | 3.6 | <0.05 | <0.05 | <0.1 | 65 | 199 |
| 12-ft in situ vitrification pit | 124 | 18 | 20 | 32 | 0.38 | 0 | 0.002 | <0.01 | <0.1 | <0.05 | <0.05 | <0.1 | 80 | 188 |
| 9-ft in situ vitrification pit | 200 | 11 | 15 | 29 | 1.5 | 0.036 | 0.004 | <0.01 | 3.8 | <0.05 | <0.05 | <0.1 | 95 | 182 |
| 6-ft in situ vitrification pit | 270 | 10 | 3 | 36 | 0.78 | 0 | 0.001 | <0.01 | 5.1 | <0.05 | <0.05 | <0.1 | 70 | 197 |
| 3-ft in situ vitrification pit | 238 | 5 | 1 | 10 | 760 | 0.001 | 0.006 | <0.01 | 1.1 | <0.05 | <0.05 | <0.1 | 100 | 241 |
| Spreading Area B soil | 285 | 14 | 2 | 28 | 0.99 | 0.016 | 0.011 | <0.01 | 3.5 | <0.05 | <0.05 | <0.1 | 95 | 227 |

**Table 8.** Soil inorganic carbon, nitrogen, phosphorous, and sulfur.

| Calculated as wt% | Carbon as wt% Carbonate | Nitrogen as wt% Nitrate | Phosphorous as wt% Phosphate | Sulfur as wt% Sulfate |
|---|---|---|---|---|
| 18-ft in situ vitrification pit | 0.3 | 0.05 | 0.006 | 0.02 |
| 15-ft in situ vitrification pit | 0.6 | 0.02 | <0.005 | 0.02 |
| 12-ft in situ vitrification pit | 0.6 | <0.005 | 0.05 | <0.005 |
| 9-ft in situ vitrification pit | 0.7 | <0.005 | <0.005 | <0.005 |
| 6-ft in situ vitrification pit | 2.4 | <0.005 | <0.005 | <0.005 |
| 3-ft in situ vitrification pit | 8.8 | <0.005 | <0.005 | <0.005 |
| Spreading Area B soil | 4.4 | <0.005 | <0.005 | <0.005 |

**Table 9.** Soluble soil anions.

| Calculated as wt% of soil | Soluble Carbonates | Soluble Chlorides | Soluble Nitrates | Soluble Sulfates |
|---|---|---|---|---|
| 18-ft in situ vitrification pit | ~0.13 | <0.05 | ~0.05 | <0.05 |
| 15-ft in situ vitrification pit | ~0.18 | <0.05 | ~0.05 | <0.05 |
| 12-ft in situ vitrification pit | ~0.12 | <0.05 | ~0.05 | <0.05 |
| 9-ft in situ vitrification pit | 1.2 | <0.02 | 0.06 | <0.02 |
| 6-ft in situ vitrification pit | 1.9 | <0.02 | 0.05 | <0.02 |
| 3-ft in situ vitrification pit | 2.8 | <0.02 | 0.05 | <0.02 |
| Spreading Area B soil | 5.7 | <0.02 | 0.025 | <0.02 |

**Table 10.** Soil organic carbon.

| | |
|---|---|
| 18-ft in situ vitrification pit | 0.15 wt% |
| 15-ft in situ vitrification pit | 0.16 wt% |
| 12-ft in situ vitrification pit | 0.27 wt% |
| 9-ft in situ vitrification pit | 0.2 wt% |
| 6-ft in situ vitrification pit | 0.21 wt% |
| 3-ft in situ vitrification pit | 0.53 wt% |
| Spreading Area B soil | 0.3 wt% |

### *Metal Sorption Characteristics of RWMC Soil*

We exposed the characterized soil samples to cesium, strontium, rhenium, uranium, plutonium, and americium for adsorption/desorption studies. Three types of studies were performed. Short-term kinetics studies revealed the rate at which equilibrium was established. Adsorption/desorption studies provided macroscopic evidence of the degree to which RWMC soils interact with radionuclides, and the reversibility of the process. Sequential aqueous extractions provided a macroscopic measure of which chemical components of the soil interact with the radionuclides. The data generated in these studies are important for determining metal speciation, transport of those metals in the soil column, and eventual fate. The results are presented below, element-by-element.

### Cesium

We exposed soil from the 18-ft level to solutions having known concentrations of $^{137}$Cs. The $^{137}$Cs $\gamma$ activity was measured before and after exposure, and we determined the quantity adsorbed by difference. Our qualitative evaluations of the kinetics of $^{137}$Cs adsorption show that the process was practically instantaneous, and the concentration of Cs remained constant for hours after initial exposure. We concluded that initial Cs adsorption could be accomplished using 15-minute exposures.

We initially contrasted $Cs^+$ sorption with the cation exchange capacity, which was determined to be 7 meq/100 g (from $NH_4^+$, Table 5); however, we found these soils to sorb 70 meq/100 g. The results suggest that cation exchange cannot solely be responsible for the sorption of Cs on RWMC soils when loaded using CsCl solutions.

We generated Freundlich adsorption *and* desorption isotherms by varying the initial concentration of $^{137}$Cs and measuring the equilibrium concentration. The data were modeled using

$$S = K\, C_{eq}^{\,n}$$

where S is the metal concentration on the soil (mmol/kg), $C_{eq}$ is the solution concentration at equilibrium (mmol/L), K is the distribution coefficient for the given $C_{eq}$, and n is a dimensionless fitting parameter normally close to 0.5 (when n = 1, the equation is linear, and K becomes $K_d$).

The K values determined for Cs adsorption did not agree with the desorption values, which indicates a hysteresis effect. For example (see Figure 3), the equilibrium obtained from Cs adsorption (K=74) is not reobtained in the Cs desorption experiments. When we used 0.01M $Ca^{+2}$ as the desorption

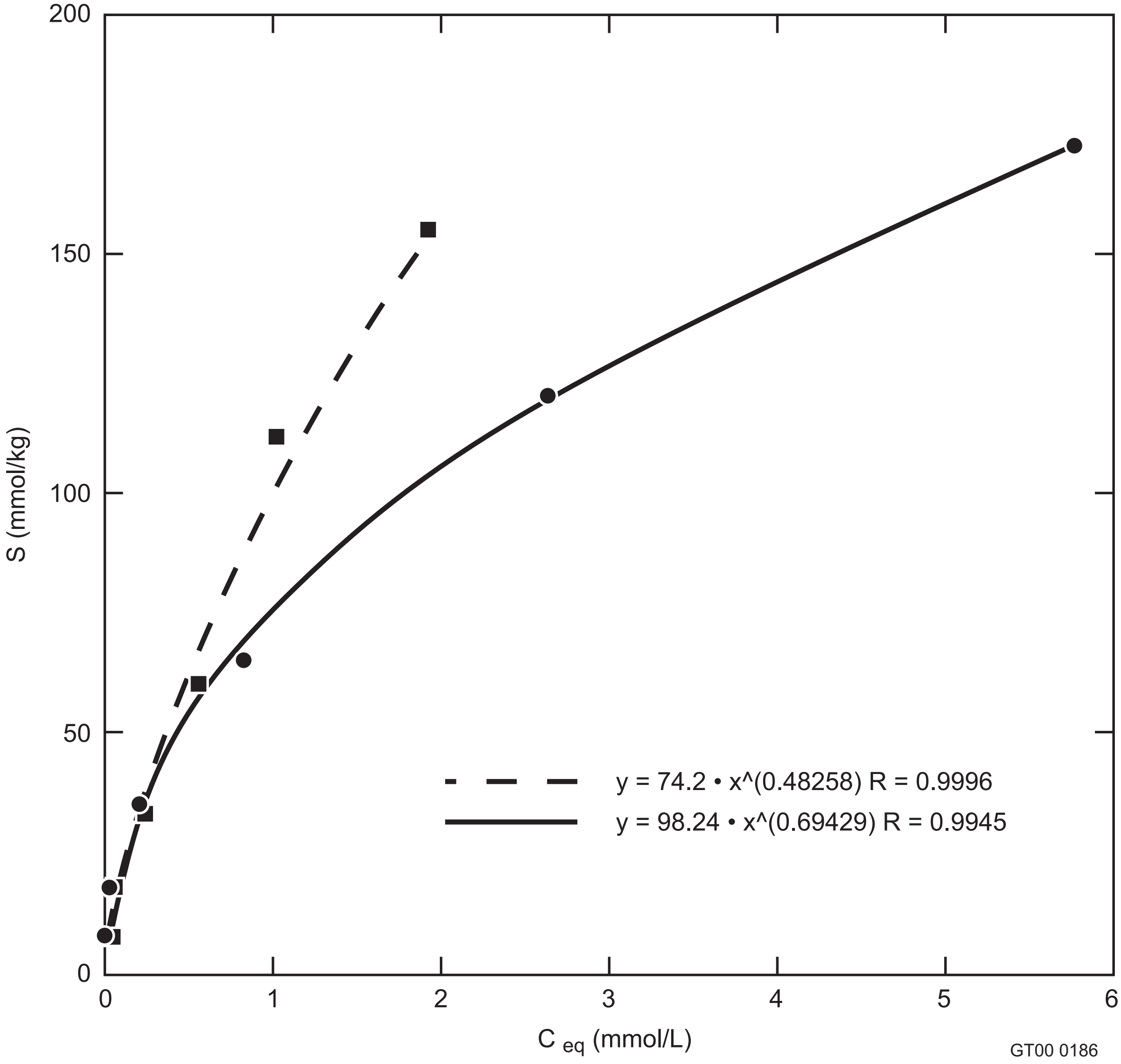

**Figure 3.** Freundlich isotherms for cesium absorption at pH 9. Adsorption isotherm is represented by the circle data points. Desorption isotherm was generated using 0.01M $Ca^{+2}$ and is represented by the squares.

solution, we measured an increased K value of 98, which indicates that, once loaded, cesium is tightly bound, and that cation exchange plays, at most, a minor role in the $Cs^{+}$ adsorption. The general result of $K_{adsorption} < K_{desorption}$ was achieved for experiments that used both deionized water and $Ca^{+2}$ for desorption, across a range of Cs and Ca concentrations.

We used sequential extraction to evaluate partitioning of the Cs into different soil fractions using the method of Litaor and Ibrihim.[18] Table 11 summarizes the method, with the results for $Cs^{+}$, $Sr^{+2}$, and Pu. A surprising result is the case of $Cs^{+}$, the very large residual fraction, or not removable using the most aggressive extraction in the sequence. This “residual” fraction would likely require very strong acid or complete soil dissolution to remove. We believe cesium is adsorbed into the mineral lattice, perhaps between the octahedral-tetrahedral planes of the clay particulate. The result is consistent with the hysteresis observed when comparing the adsorption and desorption isotherms.

### Strontium

We exposed soil from the 18-ft level to solutions having known concentrations of $^{85}$Sr. Bulk adsorption/kinetics studies revealed that only about 20% of the available strontium was absorbed at all contact durations up to a maximum of ~28 hr. Strontium had a much lower affinity for soil than did cesium, which was nearly quantitatively absorbed at pH 9. As in the case of cesium, the distribution of strontium to the soil phase occurs within 5 minutes. All subsequent exposures were of 15-minute duration.

Adsorption of strontium to RWMC soil resulted in an average K = 20, and desorption isotherms did not display noticeable hysteresis (see Figure 4). Complementary sequential aqueous extractions (see Table 11) of strontium-loaded soil revealed that most of the $Sr^{+2}$ was bound to carbonate, and that the bulk of the remainder was ion exchangeable. In contrast to $Cs^+$, very little of the $Sr^{+2}$ was nonextractable.

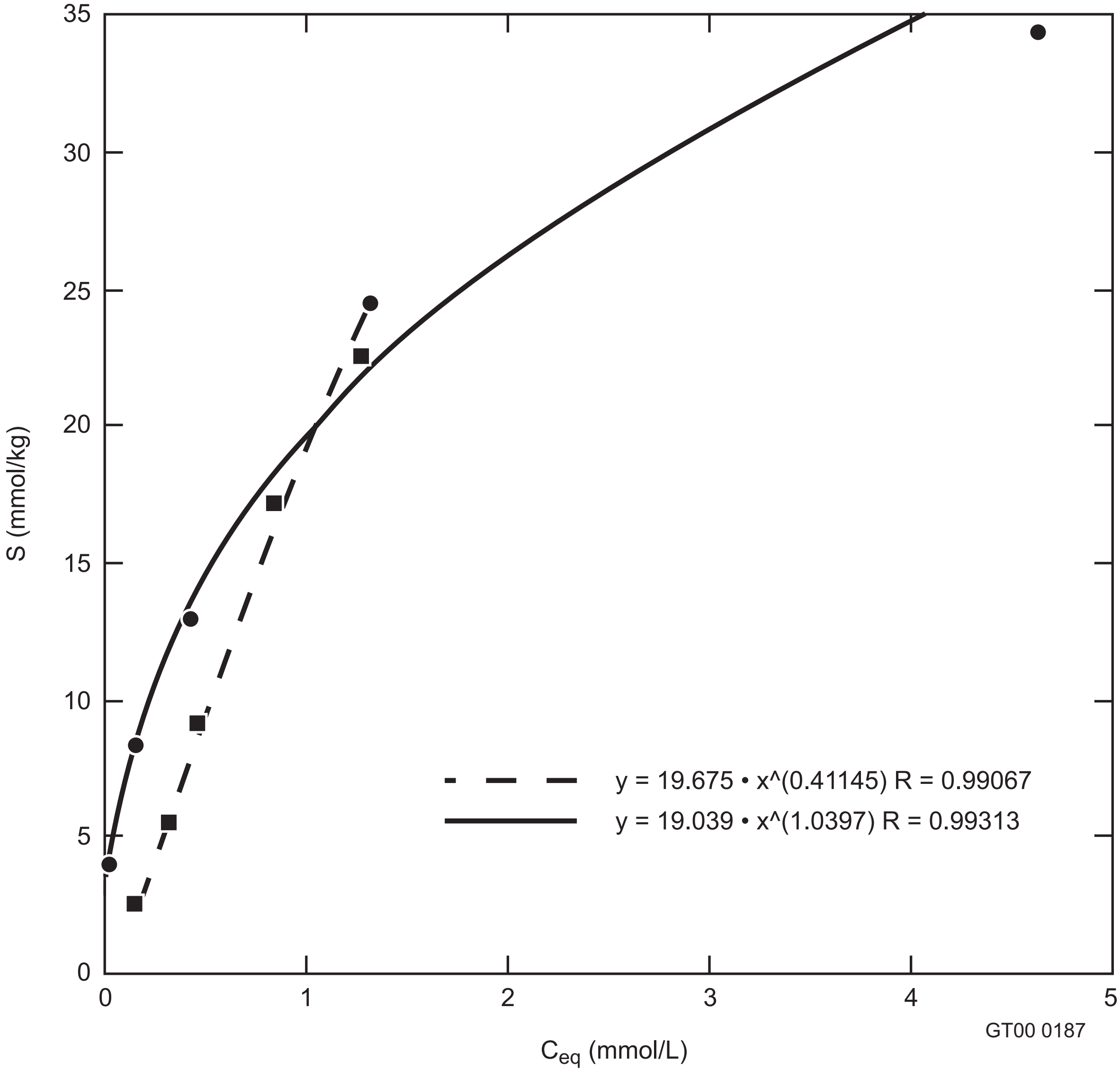

**Figure 4.** Freundlich isotherms for strontium absorption at pH 6. Adsorption isotherm is represented by the circle data points. Desorption isotherm was generated using 0.01M $Ca^{+2}$ and is represented by the squares.

**Table 11.** Sequential extraction results for RWMC soils exposed to Cs, Sr, and Pu.

| Fraction | Extractant | $Cs^+$ wt% | $Sr^{+2}$ wt% | Pu wt% |
|---|---|---|---|---|
| Ion-exchangeable | 0.01 M $Ca^{+2}$ | 2.3 | 25 | <1 |
| Carbonate-bound | Acetic acid/sodium acetate (pH 5) | 8.2 | 67 | 13 |
| Organic-bound | Sodium hypochlorite (adjusted to pH 10 with HCl) | 27 | 3.1 | 25 |
| Fe/Mn sesquioxide bound | Citrate-bicarbonate-dithionite | 11 | 12 | 35 |
| Residual (nonextractable) | none | 51 | 2.2 | 27 |

### Plutonium

We obtained in situ vitrification pit and Spreading Area B soil samples containing plutonium. Kinetics and adsorption/desorption isotherms have not yet been generated, but sequential extraction experiments (see Table 11) show that Pu was distributed between the carbonate, organic, sesquioxide, and residual soil fractions. We found no appreciable Pu to reside in the ion-exchangeable fraction.

### Uranium

We obtained and analyzed RWMC soil samples containing sorbed uranium using SIMS, but we have not yet performed kinetics, adsorption/desorption, or sequential extractions.

### Americium

We obtained RWMC and Spreading Area B soil samples containing americium. Preliminary results from sequential extraction experiments indicate that americium resides primarily in the sesquioxide fraction. We have not yet performed kinetics, adsorption/desorption, rigorous sequential extraction, or surface analysis on these samples.

### Rhenium

We obtained RWMC and Spreading Area B soil samples containing rhenium, but we have not yet characterized them.

## Task 2. Surface Characterization

Our objectives of surface characterization included identifying adsorbed radionuclides on sample surfaces, surface distribution, and metal speciation. The principal tool used in these studies was secondary ion mass spectrometry (SIMS). We employed three SIMS instruments. Two were designed and constructed in-house: an ion trap (modified Varian ITMS) and a triple quadrupole (Extrel). Both systems are equipped with $ReO_4^-$ primary ion guns. The third was a Charles Evans TRIFT-TM Time-of-Flight SIMS, equipped with a $Ga^+$ primary ion gun, which we used in collaboration with the Image and Chemical Analysis Laboratory at Montana State University in cooperation with Dr. Recep Avci.

We investigated the cesium and uranium-contaminated soil samples in some detail; the results of these investigations are described below.

### *Cesium Sorption on RWMC Soil*

We used SIMS to investigate $Cs^+$ sorption for samples that had been exposed to CsCl solutions and then washed with $H_2O$ to remove any soluble $Cs^+$. In the SIMS spectrum (see Figure 5), we observed $Cs^+$ together with molecular Cs cations: $CsSiO^+$ or $CsAlOH^+$, $Cs_2^+$, $Cs_2O^+$, $Cs_2Cl^+$, $Cs_2(NO_3)^+$, and $Cs_3Cl_2^+$ (see Table 12). The abundances of the CsCl cluster ions change with increasing $Cs^+$ concentration (see Figure 6). As the $Cs^+$ exposure increases, so do ions corresponding to CsCl clusters. In contrast, the abundance of the $CsSiO^+/CsAlOH^+$ remains relatively constant. The $CsSiO^+/CsAlOH^+$ ion is interpreted in terms of Cs sorbing at aluminosilicate sites, whereas the $Cs_2Cl^+$ ion indicates Cs sorbing as a surface precipitate. This result is surprising, because we washed the sample subsequent to exposure, which should have removed soluble Cs salts.

Raman spectroscopy supported the presence of a CsCl surface precipitate, which revealed a line at identify it, but shifted to high energy. The blue shift is consistent with stronger bonding and limited solubility.

Based on our experiments conducted with Cs-loaded RWMC soils, we draw the following conclusions :

1. The cation exchange, SIMS, and sequential extraction results indicate that $Cs^+$ sorption onto RWMC soils occurs via multiple mechanisms. The adsorption/desorption $Cs^+$ isotherms indicate that the $Cs^+$ is strongly sorbed to RWMC soils, which is consistent with the sequential extraction results, and indicates that up to half of the $Cs^+$ is contained in the nonextractable ‘residual’ fraction. The residual fraction may represent $Cs^+$ that is intercalated between the aluminosilicate tetrahedral/octahedral planes that constitute the clay.

2. The $CsSiO^+/CsAlOH^+$ ion must derive from aluminosilicate sites. In the context of the sequential extraction experiments, aluminosilicate sites could reside in the cation exchange, sesquioxide, or residual fractions, and, hence, the presence of these ions would be consistent with any or all of these fractions. The ions are not consistent with binding to carbonate or organic sites. The cation exchange or sesquioxide fractions are most likely responsible for the generation of these ions, because these fractions can reside on the surface of the clay particles. However, the two fractions cannot be distinguished on the basis of the SIMS results. We believe it less likely that the $CsSiO^+/CsAlOH^+$ ions are derived from the residual fraction, on the basis that this is not likely to be on the surface of the clay, and, hence, not accessible to SIMS or Raman detection.

3. When $Cs^+$ is loaded onto the RWMC soil from a CsCl solution, surface precipitation of the CsCl occurs at loadings in excess of 1 wt%, or 0.01 monolayer Cs surface coverage. This conclusion is supported by both the SIMS and the Raman spectroscopy experiments, but not explicitly identified by the sequential extractions. One would expect that the surface precipitate would ‘show up’ under the ‘cation exchangeable’ fraction. This result highlights the focus of the project; namely, surface speciation can result from multiple adsorption processes not revealed using sequential extraction. On the other hand, the sequential extractions could identify a ‘residual’ $Cs^+$ that may not be accessible to a SIMS or Raman spectroscopy analysis.

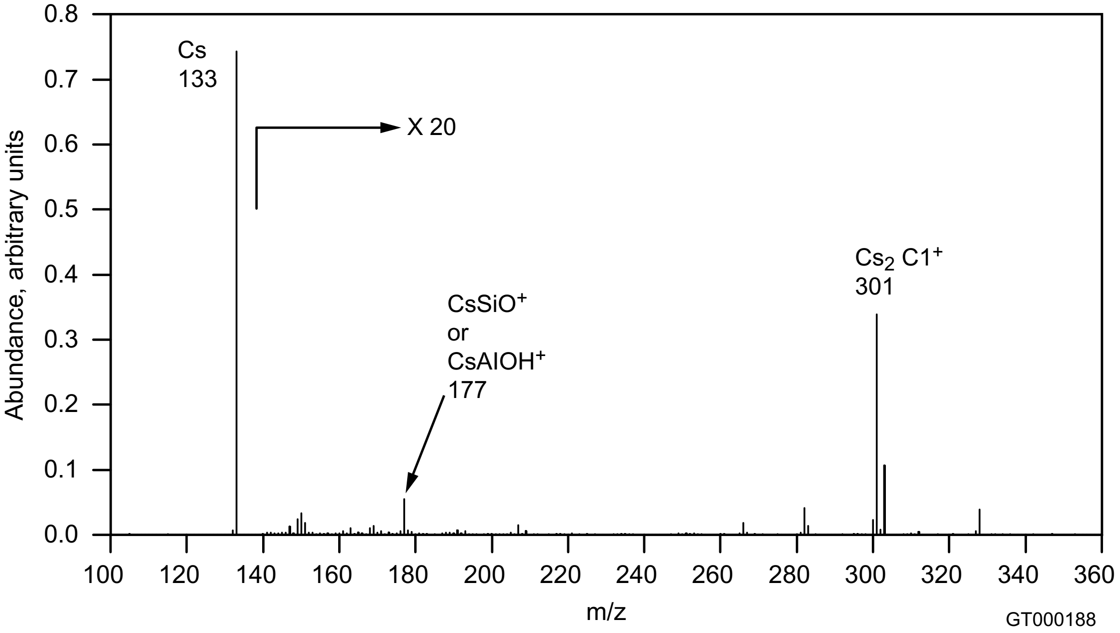

**Figure 5.** Cation spectrum of RWMC soil exposed to CsCl solution, then washed.

**Table 12.** Secondary cations observed in the SIMS spectrum of RWMC clay exposed to a CsCl solution.

| m/z | Composition | m/z | Composition |
|---|---|---|---|
| 133 | $Cs^+$ | 266 | $Cs_2^+$ |
| 149 | $CsO^+$ | 282 | $Cs_2O^+$ |
| 150 | $CsOH^+$ | 301/303 | $Cs_2Cl^+$ ($^{35}Cl$ and $^{37}Cl$ isotopic peaks |
| 151 | $CsOH_2^+$ | 328 | $Cs_2(NO_3)_2^+$ |
| 177 | $CsSiO^+$ or $CsAlOH^+$ | 469 | $Cs_3Cl_2^+$ |

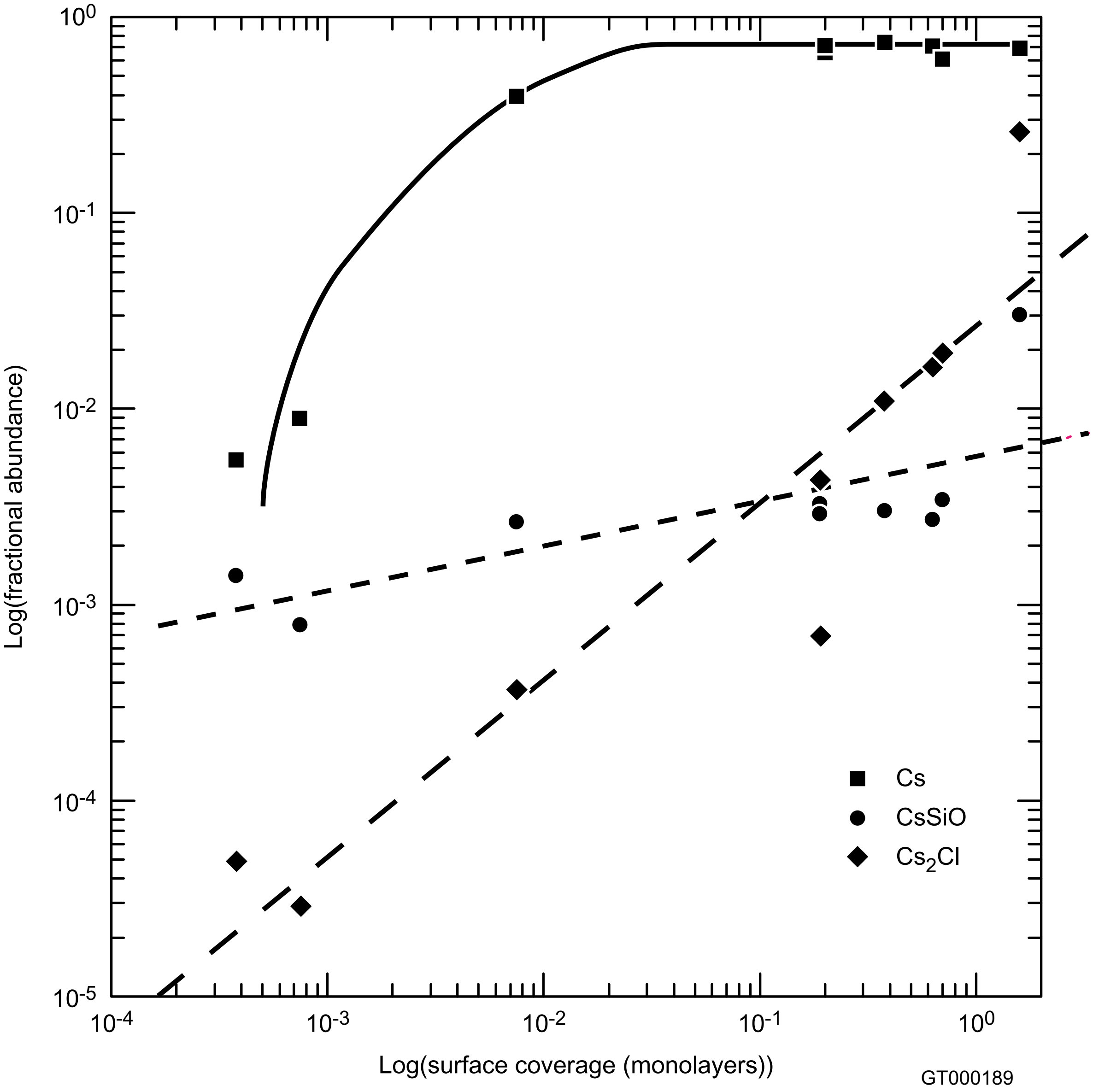

**Figure 6.** Relative abundances of molecular $Cs^+$-bearing ions generated from RWMC soils exposed to CsCl solutions. Note that the $Cs_2Cl^+$ ion increases over more than three orders of magnitude, indicating enhanced surface precipitate as the exposure solution concentration increases. In contrast, the ion – exchange-derived ions $CsSiO^+$ / $CsAlOH^+$ are constant, indicating a limited number of these sites.

These conclusions point to several open questions regarding the nature of $Cs^+$ on the clay particles and the capability of the SIMS/Raman approach for surface speciation. The questions suggest experiments that may answer them:

1. Is the ‘residual’ fraction observable using SIMS, and is the signature constituted of the $CsSiO^+$/$CsAlOH^+$ ions? A depth profiling experiment in which the spectrum is recorded as a function of primary ion dose may provide information on the depth distribution for $Cs^+$. If $Cs^+$ is intercalated between the aluminosilicate planes, then a bimodal or polymodal $Cs^+$ would be expected. In contrast, $Cs^+$ that is solely surface adsorbed would have a depth profile in which $Cs^+$ is localized near the surface.

2. Can sesquioxide-bound $Cs^+$ be distinguished from cation-exchangeable? Benchmark experiments to identify the SIMS signature of $Cs^+$ bound to Al/Si/Fe sesquioxide are needed to identify whether molecular ions could originate from this fraction, and whether they differ from those bound to aluminosilicate (*i.e.*, $CsSiO^+$/$CsAlOH^+$).

### *Uranium Sorption on RWMC Soil*

Our strategy for assessing characterization of uranium speciation on soil particles was similar to that employed for $Cs^+$. We stirred RWMC soil samples with 8 M and 0.6 M nitrate solutions containing $UO_2(NO_3)_2$,, then put them in a vacuum oven a low heat to evaporate the solvent. The final U concentration on the soil was 300 pCi/g, which is equivalent to ~900 ppm U (w/w). Some of the samples were washed for 5 minutes with DI water.

We used SIMS to investigate U sorption. The cation SIMS spectrum (see Figure 7a) is dominated by atomic ions corresponding to $Mg^+$, $Al^+$, $Si^+$, $K^+$, $Ca^+$, and $Fe^+$. In addition, numerous low abundance ions are observed at almost every mass, which are derived from organic adsorbates. Close examination of the uranium region of the spectrum shows that ions having augmented abundances are observed at *m/z* 254 and 270, which correspond to $UO^+$ and $UO_2^+$ (see Figure 7b). This signature certainly reflects the presence of uranyl on the clay surface. We observed these ions in both the 8M and 0.6M $HNO_3$-exposed samples, and they were generally more abundant than the organic background; however, the background was limiting for detecting lower concentrations of surface-adsorbed uranium. Therefore, we employed high-beam density surface sputtering to attempt to selectively remove the organic contamination layer, leading to a more clear observation of the uranium species. We used 22 KeV $Ga^+$ at 2.5 mA to sputter clean the surface for 60 seconds. The mass spectrum that was subsequently acquired was nearly devoid of ions derived from organic contamination but still contained reasonably abundant U-containing ions (see Figure 8).

The relative abundances of the $UO^+$ and $UO_2^+$ cations may indicate the nitrate content of the clay surface. We noted that the abundance ratio $UO_2^+/UO^+$ was up to four times greater in the samples that had been treated with the uranyl/8M $HNO_3$ solution, compared with the 0.6M $HNO_3$ exposure solution. The anion spectra clearly showed abundant nitrate on the surface of the 8M-exposed soil. In addition to $NO_3^-$ and $NO_2^-$ (which were as abundant as the silicate-derived ions), we observed Ca-nitrate complex anions to at least *m/z* 500. These ions clearly reflect the nature of the soil surface and certainly indicate destruction of $CaCO_3$ on the clay surface. In contrast, the 0.6M-exposed soil exhibited negligible nitrate in the anion spectrum. Instead, the spectrum contained only aluminosilicate-derived anions. The result demonstrates facile anion characterization directly from the clay surfaces.

The uranyl cations were resistant to resolubilization during subsequent exposure to water. We repeatedly washed both samples with water, then dried and analyzed them. This showed that the abundances of the uranyl signature $U^+/UO^+/UO_2^+$ were practically unchanged, which suggests that binding to the clay surface is relatively strong, and, more importantly, that the SIMS approach is viable for monitoring adsorption progress as environmental conditions change.

Based on the experiments conducted with the uranyl nitrate-loaded RWMC soils (from 8M and 0.6M $HNO_3$ solutions), we draw the following conclusions:

1. The cation SIMS spectra clearly show evidence for the presence of the uranyl cation on the surface of the clay soils. For high- to mid-ppm level concentrations, the abundances of these cations is low compared to the atomic ions derived from the matrix, but the dynamic range of the SIMS instrument is well capable of performing the detection.

2. The uranyl cations are isobaric with ions derived from organic surface adsorbates, which can obfuscate spectral interpretation, especially at low abundances. The organic adsorbates may be preferentially removed in the SIMS spectrometer by sputter cleaning the sample for a short time, using a mA primary ion beam. This action reduces the abundance of the uranyl signature but can eliminate the organic contribution entirely, which enables unambiguous identification.

3. The anion SIMS spectrum is valuable for identifying counter anions present in the same vicinity as the uranyl, which is highly suggestive of salt speciation on the surface. In particular, chloride and nitrate were demonstrated to be readily detectable in the present study, and we believe that a range of counter anions is identifiable. The detection of Ca nitrate cluster anions is highly indicative of the high Ca/high nitrate content of the surface from which these were detected. We detected no abundant uranium-bearing anions, though a low abundance *m/z* $286^-$ may well be $UO_3^-$.

4. Distribution of adsorbed uranium on the RWMC clay particles appeared to be homogeneous, which indicates that for these types of samples mm-scale imaging is not necessary. This may not be the case, however, when studying more heterogeneous samples, such as basalt particles.

The research presented in this section raises several important questions:

1. That the uranyl cations could be generated using a polyatomic projectile such as $ReO_4^-$ was not established. Nonquantitative comparison of $Ga^+$ with $Cs^+$ indicated that the more massive $Cs^+$ was superior for generating the uranyl-derived ions. Extrapolation to a polyatomic, however, is not warranted based on these few experiments. Instrumental evaluation of the production of uranyl cations using $ReO_4^-$ will be required.

2. Detection of anionic complexing ligands with uranyl on the surface has not been established. In particular, detection of carbonates using SIMS is an open question.

3. The ability of SIMS to track changes in surface chemistry over the course of a sequential extraction has not been established.

4. Research to address these questions and other related issues will require attention in FY-01 in order to proceed toward more analytically mature methods and eventual application.

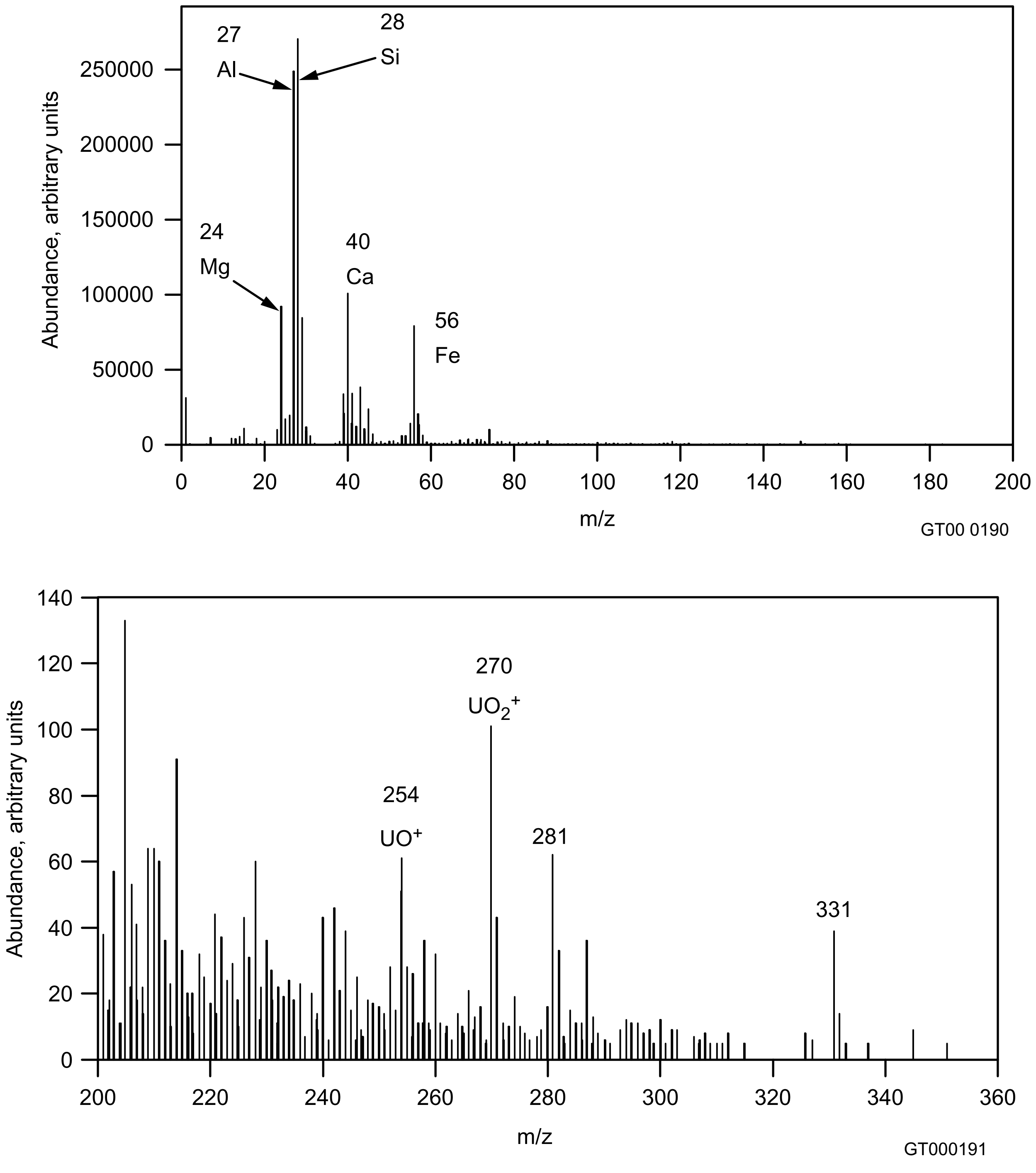

**Figure 7.** (a) Cation SIMS spectrum of RWMC soil exposed to uranyl nitrate in a 0.6 M $HNO_3$ solution. (b) High mass region, with expanded abundance axis.

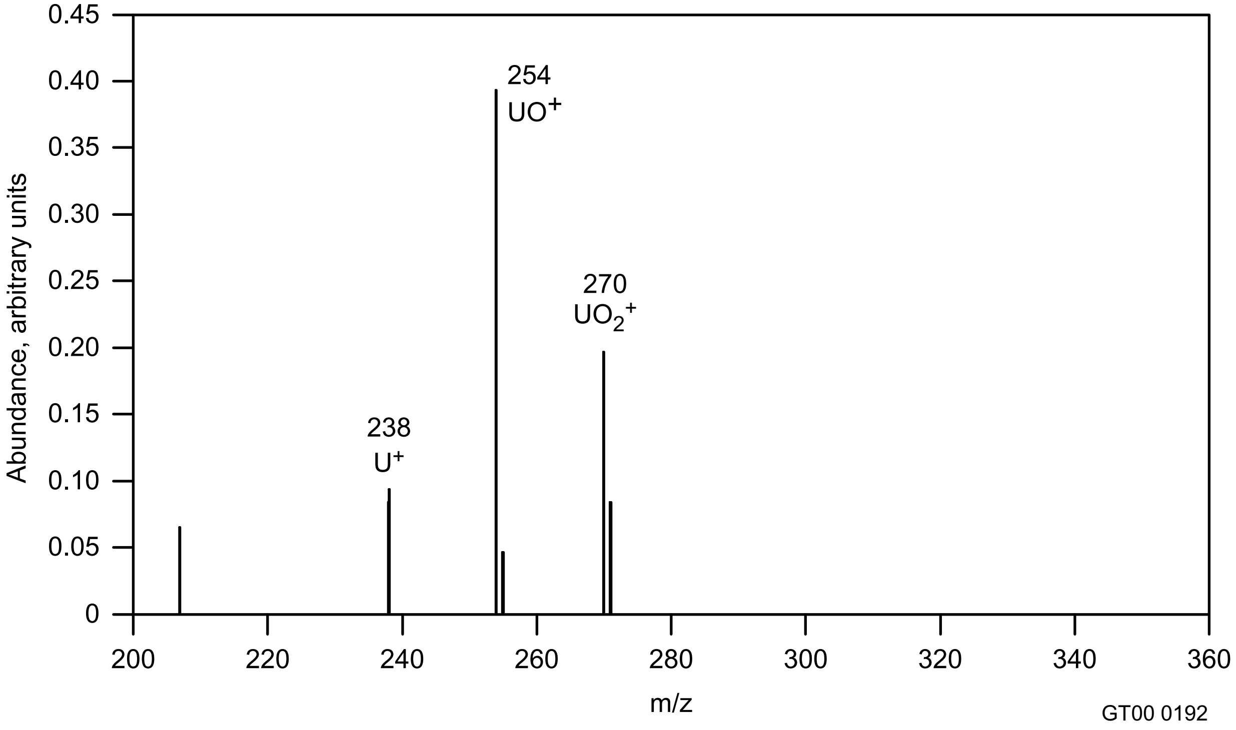

**Figure 8.** Cation SIMS spectrum of RWMC soil exposed to uranyl nitrate in a 0.6 M $HNO_3$ solution, subsequent to sputter cleaning the surface with a 2.5 mA $Ga^+$ beam for 60 seconds. High mass region is displayed.

### Task 3. Ion Trap SIMS Research and Development.

Our objective of Task 3 was to fabricate an ion trap secondary ion mass spectrometer based on current state-of-the-art design. This IT-SIMS instrument is to be used to develop analytical methods for speciation of radionuclides on environmental sample surfaces and to help define the requirements for design of an IT-SIMS that can be used for routine analysis of radioactive environmental samples.

The INEEL developed the IT-SIMS to analyze trace levels of chemicals on surfaces. It has been applied to a wide range of analyses and has demonstrated the potential for providing information needed to determine the speciation of metals such as Cs, Sr, Tc, U, Pu, and other transuranic elements present on environmental surfaces (soil, minerals). The current state-of-the-art design of the IT-SIMS was defined by the capabilities of the instrument constructed for the U.S. Army's Mobile Munitions Assessment System, modified as needed to better meet the needs of a research instrument operated in a fixed laboratory. Four primary modifications were included:

1. The sample insertion system uses a small probe with a reduced-volume roughing port and manual sample insertion. In addition, an oil-free vacuum pumping system was used for the insertion lock. This offered faster sample turn-around and additional flexibility for sample mounting.

2. The energy of the primary ion gun was increased to 7 kilovolts to provide added flexibility in analysis of samples that suffer from sample charging.

3. A system for controlling electron emission from the samples during analysis was added to provide additional flexibility in analysis of samples that suffer from sample charging.

4. A rotatable Faraday cup for measuring the primary beam current incident on the sample was designed and installed directly in the vacuum housing.

The IT-SIMS is based on a Varian Corporation ion trap mass spectrometer. The unit was modified at the INEEL to perform secondary ion mass spectrometry. The vacuum housing of the Varian instrument was replaced with an alternate housing that includes an off-axis detector capable of positive and negative ion detection, a polyatomic primary ion gun, and a rotatable Faraday cup assembly. The rotatable Faraday cup design allows the primary beam current to be measured without removing the sample from the vacuum housing. Figure 9 shows a schematic of the vacuum housing and internals. Figure 10 shows a photograph of the IT-SIMS and electronics mounted on a mobile cart.

The instrument control software was modified for additional flexibility during the analysis. The modification permits longer sampling and reaction times to support the anticipated needs of the metal speciation application.

The system was constructed and tested and is currently being used in methods development activities. Initial studies show comparable or improved sensitivity for detecting adsorbed organic compounds on soil surfaces. In addition, vacuum characteristics are improved, which will facilitate analysis of environmental samples.

## ACCOMPLISHMENTS

The ability to accurately assess radionuclide speciation is critical for predicting fate and transport, and for assessing risk to personnel and the environment. Current analytical ability to do this is limited. Certainly, synchrotron radiation techniques are capable, but this approach struggles with inhomogeneous samples and is not readily applicable to a large sample flux from the field or from a meso-scale experiment. This research addresses the limitation.

During the course of the research, we developed capability to do bulk speciation for radionuclides. This consisted of adsorption and sequential extractions for radioactive samples. Initial experiments applied these techniques to representative RWMC soil samples deliberately spiked with metals having radionuclides of interest at the RWMC, or surrogates for those metals. These were Cs, Sr, Re, U, Pu, and Am.

During initial studies, which focused on Cs, Sr, and Pu partitioning, we observed that the behavior of the three different metals varied significantly. Cs prefers to strongly bind within the mineral lattice, which we speculate to be intercalation between the octahedral and tetrahedral planes of the clay minerals. A smaller amount of Cs was bound with the soil organic fraction. In contrast, Sr tends to bind much more loosely and prefers ion exchange and carbonate sites. The case for Pu is more complicated. It tends to distribute between the carbonate, soil organic sesquioxide, and residual soil fractions, a result that illustrates the complexity of Pu chemistry, as manifest in a range of bulk phase species.

The bulk-phase speciation research provided benchmark samples that we then analyzed using SIMS and, in some cases, Raman spectroscopy. The $Cs^+$-spiked soils produced spectra that contained signals indicative of aluminosilicate and surface precipitate-adsorbed species. Both chloride and nitrate species were detectable. Other counter ions that provide a clear picture of the $Cs^+$ environment were

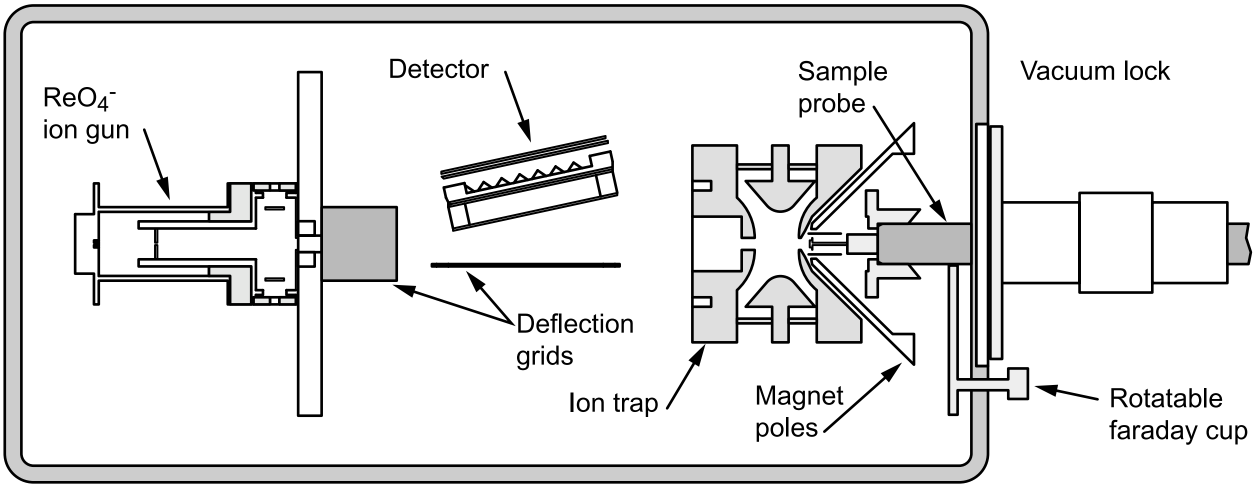

GT00 0193

**Figure 9.** Schematic of the IT-SIMS fabricated for metal speciation studies on environmental surfaces.

**Figure 10.** Photograph of the IT-SIMS fabricated for metal speciation studies on environmental surfaces.

clearly discernable. SIMS spectra acquired for the U-spiked soils contained ions derived from the uranyl cation $UO_2^{+2}$, which shows that this was the form adsorbed on the surface. As in the case of $Cs^+$, counter anions in the SIMS data reveal the chemical environment of the uranyl cation on the soil surface.

The results of the research conducted to date constitute preliminary indication of the utility of SIMS for quickly and easily assessing radionuclide surface speciation. This has motivated design and fabrication of a prototype ion trap SIMS instrument that can be evaluated in a radiological laboratory and that will enable rigorous comparison of SIMS results with results acquired from the sequential extraction methods. The experiments should provide assessment of SIMS performance and evaluation of the sequential extraction approach. We have scheduled the instrument to be moved to the radiological laboratories at the Test Reactor Area in early 2001.

## REFERENCES

1. J. C. S. Long, *Research Needs in Subsurface Science*, National Academy Press, Washington, D.C., 2000, p. 159.

2. P. Benes, “Radiotracer Method in the Study of Environmental Speciation and Migration of Contaminants,” in *Biological Trace Element Research*, Schrauzer, G. N., ed., **1994**, Humana Press, Inc., p. 79.

3. G. M. Desmet, L. R. V. Loon, B. J. Howard, “Chemical Speciation and Bioavailability of Elements in the Environment and Their Relevance to Radioecology,” *The Science of the Total Environment,* 100, p. 105. 1991.

4. H. R. V. Gunten and P. Benes, “Speciation of Radionuclides in the Environment,” *Radiochimica Acta,* 69, p. 1. 1995.

5. A. J. Dent, J. D. F. Ramsay, and S. W. Swanton, “An EXAFS Study of Uranyl Ion in Solution and Sorved onto Silica and Montmorillonite Clay Colloids,” *Journal of Colloid and Interface Science,* 150, 1, p. 45. 1992.

6. A., Manceau et al., “Direct Determination of Lead Speciation in Contaminated Soils by EXAFS Spectroscopy,” *Env. Sci. Tech.,* 30, 5, p. 1540. 1996.

7. C. Moulin et al., “Speciation of Uranium by Electrospray Ionization Mass Spectrometry: Comparison with Time-resolved Laser-induced Fluorescence,” *Applied Spectroscopy,* 54, 6, p. 843. 2000.

8. N. D. MacRae, “Secondary-Ion Mass Spectrometry and Geology,” *The Canadian Mineralogist,* 33, p. 219. 1995.

9. M. J. Van Stipdonk et al., “Speciation of Sodium Nitrate and Sodium Nitrite Using Kiloelectronvolt Energy Atomic and Polyatomic and Megaelectronvolt Energy Atomic Projectiles with Secondary Ion Mass Spectrometry,” *Analytical Chemistry,* 72, June 1, p. 2468. 2000.

10. O. W. Hand, T. K. Majumdar, and R. G. Cooks, “Effects of Primary Ion Polyatomicity and Kinetic Energy on Secondary Ion Yield and Internal Energy in SIMS,” *Int. J. Mass Spectrom. Ion Proc.,* 1997, p. 35.

11. J. E. Groenewold, J. E. Olson, A. D. Appelhans, J. C. Ingram, D. A. Dahl, “Secondary Ion Mass Spectrometry of Sodium Nitrate: Comparison of ReO4- and Cs+ Primary Ions,” *Int. J. Mass Spectrom. Ion Proc.,* 163, p. 185. 1997.

12. Delmore, J. E., Appelhans, A. D., and Peterson, E. S., "A Rare Earth Oxide Matrix for Emitting Perrhenate Anions," *Int. J. Mass Spectrom. Ion Proc., 146/147,* p. 15-20. 1995.

13. G. S. Groenewold, J. C. Ingram, A. D. Appelhans, "Analysis of Environmental Surfaces using Static Secondary Ion Mass Spectrometry," *Current Topics in Analytical Chemistry,* 1, p. 73. 1998.

14. G. S. Groenewold, J. C. Ingram, T. McLing, A. K. Gianotto, R. Avci, "Cs+ Speciation on Soil Particles by TOF-SIMS Imaging," *Analytical Chemistry,* 70, 3, p. 534. 1998.

15. G. S. Groenewold, J. E. Delmore, A. D. Appelhans, "Static SIMS Analysis of Tributyl Phosphate on Mineral Surfaces: Effect of Fe(II)," *J. Amer. Soc. Mass Spectrom.,* 6, p. 165. 1995.

16. G. S. Groenewold, J. C. Ingram, "Characterization of bis(alkylamine)mercury Cations from Mercury Nitrate Surfaces by Using an Ion Trap Secondary Ion Mass Spectrometry," *J. Amer. Soc. Mass Spectrom.,* 9, p. 35. 1998.

17. Ingram, J. C., Groenewold, G. S., Olson, J. E., Gianotto, A. K., and McCurry, M. O., "Identification of mineral phases on basalt surfaces by imaging SIMS", *Analytical Chemistry,* 71, 9, pp. 1712. 1999.

18. M. I. Litaor, Ibrahim, S. A. *J. Environ. Qual.* 25, p. 1144. 1996.

19. G. W. Gee, *Methods of Soil Analysis Part 1: Physical and Mineralogical Methods*, Madison, WI, Soil Science Society of America, Inc., 1986.

20. T. Allen, *Particle Size Measurement*, New York, NY: Chapman and Hall, 1981.

21. G. R. Blake, *Methods of Soil Analysis Part 1: Physical and Mineralogical Methods*, Madison, WI: Soil Science Society of America, Inc., 1986.

22. G. W. Thomas, *Methods of Soil Analysis Part 3: Chemical Methods*, Madison, WI, Soil Science Society of America, Inc., 1996.

23. W. H. Patrick, S. P. Faulkner, *Methods of Soil Analysis Part 3: Chemical Methods*, Madison, WI, Soil Science Society of America, Inc., 1996.

24. M. E. Sumner, *Methods of Soil Analysis Part 3: Chemical Methods*, Madison, WI, Soil Science Society of America, Inc., 1996.

25. D. W. Nelson,. *Methods of Soil Analysis Part 3: Chemical Methods*, Madison, WI, Soil Science Society of America, Inc., 1996.

26. R. H. Loeppert, *Methods of Soil Analysis Part 3: Chemical Methods*, Madison, WI, 1996.

27. R. L. Loeppert, *Methods of Soil Analysis Part 3: Chemical Methods*, Madison, WI, Soil Science Society of America, Inc., 1996.

28. A. P. Tessier, G. C. Campbell, M., Bisson, *Analytical Chemistry,* 51, 7, p. 844. 1979.

# Transport Aspects of Selective Mass Transport Agents

**Eric Peterson, Research Area Leader**

The ability to separate radioactive and hazardous components from bulk matrices is necessary to effectively treat and process the wide variety of wastes for which the U.S. Department of Energy, Office of Environmental Management, is responsible. This research covers the areas of polymer membrane science, controlled transport properties in polymers, controlled pore sizes in solids such as ceramics, and extraction technology. The research resulting from this crosscutting program focuses on two critical issues that relate to separation methods targeted for waste treatment and disposal, pollution prevention, subsurface remediation, and waste characterization and monitoring. These issues are (1) the physical characteristics of the separation media, and (2) the intermolecular and intramolecular interactions involved in transport/retention mechanisms. Better understanding these two issues provides the basis for developing new separation tools for DOE EM's applications. Program implementation consisted of four projects: (1) Selective Mass Transport In Polymers, (2) Pore Size and Morphology Control For Solid and Polymer Matrices, (3) Adsorption and Absorption for Molecular Separations, and (4) Fission Product Extraction Process.

## Description of Research Activities

### Selective Mass Transport in Polymers

The key to developing new materials for challenging environmental separations is understanding the mechanics of the molecular aspects of selective mass transport through a host matrix. This project focused on the intermolecular and intramolecular interactions of selected permeates and macromolecular solid matrices, which are identified strategies for developing and probing selective mass transport matrices based on materials synthesis, testing, evaluation, characterization, and modeling capabilities. These will yield fundamental understanding of membrane transport and how it can be described and predicted.

Beyond determining the nature of the significant molecular interactions that occur in separations materials, we must choose general chemoselective characteristics, and we must understand their effect on the macroscopic properties of the materials. The macroscopic physical properties to be understood and controlled are ruggedness, inherent stability (chemical, thermal, and radiation), and film forming ability. Likewise, designing a material for an exact physical property can have a deleterious effect on the desired chemoselectivity; therefore, the two factors (permeate affinity and macroscopic physical properties) are linked and clearly have an effect on each other.

### Pore Size and Morphology Control for Solid and Polymer Matrices

One of the biggest challenges in making membrane separations technologies viable for EM's applications is increasing the rate of permeation through the membrane while maintaining high selectivity. We must achieve this with a durable material, capable of withstanding harsh environments, without making the material prohibitively expensive. Membrane materials that allow for a high transmission rate generally swell to a great degree and lose their physical integrity, which leads to rapid membrane failure. To combat this problem, all manner of cross-linking strategies have been explored and recorded in the literature. While this type of strategy does increase membrane durability, it has had limited success owing to incomplete understanding of the interactions at the molecular level. Through this research, we gained better fundamental understanding of the mechanisms of transport into and through polymer and composite matrices. The enhanced understanding has facilitated rational molecular design improvements of existing materials used for challenging environmental separations. The research had two focuses: (1) molecular composites for enhanced selective mass transport and durability, and (2) polymer morphology effects on selective mass transport and durability.

### Adsorption and Absorption Materials for Molecular Separations

Selective mass transport has two common critical issues that form the basis for nearly all separation methods: (1) the physical characteristics of the separation media, and (2) the intermolecular and intramolecular interactions involved in the transport/retention mechanisms. Research focused in these two areas should help develop understanding of transport phenomena needed to design useful separation methods targeted for waste treatment and disposal, pollution prevention, waste characterization and monitoring, and such.

Our research focused on physical adsorbents and absorbents. Adsorbents and absorbents are critical in today's environmental control work. Typically, solid adsorbent and absorbent materials are made using either sol-gel or related methodologies. Our approach used molecular composite methodologies, coupled with some of the newer template generation approaches to obtain specific properties in materials of interest to DOE EM. The ultimate result will be new materials with higher than currently known selectivity for gas and liquid separations. To enhance the sorption properties of these materials, we will develop a series of specific materials that have unique surface morphology characteristics and give direction for the next generation of materials. Our work will focus primarily on materials having a propensity for capturing mercury vapor and aqueous phase mercury, both being prevalent DOE and industrial waste constituents. These new-solid phase materials were developed with specific reactive site, surface, and pore modifications to offer either hydrophobicity or hydropholicity, plus molecular/ionic recognition.

### Fission Product Extraction Process

We developed the fission product extraction process based on cobalt dicarbollide and polyethylene glycol in an appropriate diluent for simultaneous removal of cesium and strontium from simulated tank waste at the Idaho Nuclear Technology and Engineering Center. We have optimized the process to minimize the final volume of high activity waste and low activity waste fractions and to demonstrate technical feasibility for tank wastes. The research included process development, using small, laboratory-scale batch contactors to generate distribution data, modeling efforts based on the batch contactor data to establish countercurrent flowsheet parameters, and testing of the counter-current process in a centrifugal contactor mockup.

# Selective Mass Transport in Polymers

**Frederick F. Stewart, Christopher J. Orme, Robert P. Lash,
Thomas A. Luther, Donald H. Weinkauf, Kelly S. Houston**

## SUMMARY

Novel separations processes are required to ensure effective and efficient cleanup of storage tanks and sites within the Department of Energy (DOE) community. In this regard, membranes may be able to play a role. A recent publication reports that the industrial outlook for membrane separation technologies is robust, having 8.2% growth expected yearly.[1] We investigated new strategies toward forming chemoselective membranes.

Our approach was to synthesize materials with chemical compatibility with a target permeate, namely water. We did this by synthesizing polymers with functionality that resembles water to a certain degree. Specifically, we synthesized membranes capable of hydrogen bonding using modified literature procedures in an attempt to increase the solubility of the target permeate within the polymer matrix. We synthesized and characterized eight new materials for composition, molecular weight, thermal properties, gas transport properties, and solubility parameters. Additionally, we explored plasma membrane formation using model polyphosphazenes as a substrate for the polymerization and application of thin (angstrom) chemoselective films.

Membrane performance was investigated through pervaporation experiments, where we separated water-dye and water-alcohol mixtures. Membranes were formed as homogeneous thin dense films cast onto porous ceramic supports. We quantified the membrane flux gravimetrically for all experiments and further analyzed the separation factor for the alcohol-water separations by gas chromatography.

We estimated three-point Hanson solubility parameters through each polymer's behavior in selected solvents. From these determinations, we increased the hydrogen-bonding capabilities and the polarities of the polymers, consistent with tailoring for water permeation. However, the magnitude of the increases did not represent a wholesale shift of polymer solubility to a water-like parameter set. We attribute this to contributions from the polymer backbone to the overall solubility of the polymer.

## PROJECT DESCRIPTION

Mechanistic understanding of the molecular aspects of selective mass transport through a host matrix is the key to developing new materials for challenging environmental separations. This work focuses on the intermolecular and intramolecular interactions of selected permeates and macromolecular solid matrices. A plan is outlined here that identifies strategies and tasks for developing and probing selective mass transport matrices. The plan draws on materials synthesis, testing, evaluation, characterization, and modeling capabilities to build a fundamental understanding of membrane transport and how it can be described and predicted.

Beyond determining the nature of the significant molecular interactions that occur in separations materials, general chemoselective characteristics must be chosen, and the effect of these choices on the macroscopic properties of the materials must be understood. Macroscopic physical properties to be understood and controlled are ruggedness, inherent stability (chemical, thermal, and radiation), and film forming ability. Likewise, design of a material for an exact physical property can have a deleterious effect on the desired chemoselectivity; thus, the two factors of permeate affinity and macroscopic physical properties can be linked and clearly affect each other.

In this work, we sought to further understanding of separations material design by determining and ultimately predicting clear structure-function relationships in polymeric matrices for factors such as backbone morphology, crosslinking, and chemical content. Outlined below are the findings of the four tasks that investigate intermolecular interactions between a membrane permeate and the membrane itself. The first task entailed synthesis of materials to be characterized for their gross physical properties and molecular inclusion phenomena with materials consisting of amorphous polymers. The second task formed materials developed in Task 1 into thin film membranes. The third task provided characterization data necessary to form structure-function relationships. The fourth task concerned prediction and characterization of molecular permeability within polymeric matrices.

## Material Synthesis

### Linear and Cyclomatrix Materials

We investigated linear and cyclomatrix phosphazene polymers but synthesized only linear polyphosphazene models. Cyclomatrix chemistry for membrane formation requires good film forming ability to be effective. We examined a survey of potential crosslinking strategies with respect to previously performed research and determined that this pathway was not optimal for forming effective pervaporation membranes. Note, however, that this method of membrane synthesis does hold promise for efficient gas separation membranes.

Polyphosphazenes are hybrid polymers that consist of an inorganic backbone of phosphorus and nitrogen with two organic pendant groups attached to each phosphorus. The inorganic backbone imparts into the polymer a very high level of thermal and chemical stability. For example, thermal stabilities as high as 400°C have been reported.[2] Organic pendant groups, such as alkoxides, aryloxides, and amines, have been readily attached to the phosphazene backbone through straightforward nucleophilic substitution processes[3] conducted on poly(dichlorophosphazene). Poly(dichlorophosphazene) is itself synthesized from the ring opening polymerization of the commercially available hexachlorocyclotriphosphazene.

We synthesized linear polymers with the goal of increasing both the polarity and the hydrogen-bonding ability within the polymer to enhance the solubility of water within the matrix. We adopted the synthetic scheme based on earlier work,[4] which suggests that a balance of hydrophilic and hydrophobic groups on the polymer provides an effective pathway for polymer tailoring. Modification of the hydrophilic group to enhance hydrogen-bonding capabilities was conducted through a two-step process[5,6] designed to incorporate hydroxyl functionality into the polymer. Due to the nucleophilic activity of hydroxyl moieties, we employed a protection-deprotection scheme where diacetone-d-glucofuranose (DADG) served as the *masked hydroxyl precursor*. DADG has one free hydroxyl, which we employed to attach the pendant group to the polymer followed by deprotection to reveal four hydroxyls per pendant group, see "Scheme 1."

**Scheme 1.** Synthesis scheme employed for DADG containing polymers.

Using the method above, we incorporated DADG into the polymer matrix with a hydrophobic pendant group with the goal of creating good film forming polymers suitable for membrane application. Previous work shows that including a hydrophobic group into the polymer matrix can yield a polymer suitable for membrane use through control of swelling. Polymers with an excessive amount of hydrophilicity have been found to have poor mechanical stability due to an excessively swollen structure. We included two different substituted phenols into the polymer matrix to add not only hydrophobicity but also an increased degree of free volume through increased steric bulk. The phenols used were 4-*sec*-butylphenol and 4-*tert*-butylphenol. We synthesized two polymers to maximize hydrophilic behavior by using the polyether 2-(2-methoxyethoxy)ethanol (MEE). MEE is hydrophilic and served in that capacity during previous efforts. However, we noted that MEE is a poor match for enhancing water permeability due to a lack of a hydrogen-bonding functionality. We envisioned that MEE would serve as the hydrophobic component and give the material excellent film forming characteristics. Additionally, all polymers were synthesized with targeted 15% *o*-allylphenol content to provide for thermally initiated free radical crosslinking processes. Table1 shows the compositions of the polymers synthesized in this work as determined using $^1$H NMR spectroscopy.

All four polymers synthesized were deprotected using a modified literature procedure. We unmasked the hydroxyl functionality by treating the polymers with 90% trifluoroacetic acid in water for 0.5 to 4 hr at room temperature. All deprotected polymers were isolated and collected in 50–80% yield. Modification of the literature procedure was necessary due to polymer degradation caused by the extreme acidity required for hydrolysis of the DADG pendant groups. In general, polymers with lower amounts of DADG were deprotected in higher yield. In fact, we isolated no deprotected polymer from 100% DADG linear phosphazene polymer due to complete acid catalyzed hydrolysis of the backbone.

The performance of polymeric membranes in gas separation applications is largely governed by the permeability-selectivity characteristics and thickness of the dense separating layer. The achievable thickness of high integrity, selective layers using conventional membrane formation techniques seems to have reached a physical limitation on the order of 100 nm. At the same time, the permeability-selectivity trade-off for conventional polymers has also reached some apparent limitations. To push the boundaries of polymeric membrane performance beyond the current state, it is imperative to consider new materials (e.g., nonconventional polymers) and new approaches to membrane formation. This work explored the effect of plasma surface treatment on the gas transport properties of rubbery polymers, specifically poly(dimethylsiloxane) (PDMS) and polyphosphazene. Argon plasma treatment greatly reduces PDMS gas permeability coefficients. The same treatment had no effect, however, on polyphosphazene. The decrease in permeability coefficients of PDMS is accompanied with varying degrees of change in gas pair selectivity, which is consistent with the literature. We analyzed the variability in plasma-treated PDMS

**Table 1.** Pendant distribution of the DADG containing polymers.

| Polymer | DADG (%) | 4-*sec*-butylphenol (%) | 4-*tert*-butylphenol (%) | 2-*o*-allylphenol (%) | MEE (%) |
|---|---|---|---|---|---|
| 084 | 46 | — | 25 | 29 | — |
| 096 | 61 | 3 | — | 36 | — |
| 104 | 31 | — | — | 29 | 40 |
| 116 | 29 | — | — | 18 | 53 |

permeability-selectivity characteristics using activation energy studies and electron microscopy of neat and treated PDMS.

We also examined the effect of plasma treatment on gas transport properties of six polyphosphazene materials. A series of four polyphosphazenes were prepared[8] during FY 1999 with systematic variation of hydrophobic side groups. The results showed little effect of plasma treatment, suggesting that these polyphosphazene materials are good substrate candidates for rubbery polymer/plasma polymerized thin-film composite membranes. Surface treatments, such as halogenation or plasma polymer deposition, can be performed using polyphosphazene without gross changes in the bulk substrate permeability such as that observed with PDMS.

## Materials Processing and Testing

### Membrane Formation

We formed membranes from all of the new polymers by solution casting. Pervaporation membranes were typically cast from tetrahydrofuran (THF) onto Whatman Anopore ceramic disks with 0.2-μm pore size. This method was successful with the MEE containing polymers 104 and 116. Application of this method to the non-MEE containing polymers, 084 and 096, was not successful due to low solution viscosity where the polymer penetrated into the pores of the ceramic. We found replacing the THF with a chlorinated solvent such as methylene chloride yielded homogeneous films on the ceramic supports.

Prior to installing the membranes into an appropriate housing, we thermally cured the membranes to effect crosslinking. Free radical initiators such as benzoyl peroxide were doped into the casting solutions prior to membrane casting. Upon thermal treatment, the membranes crosslink through the allylic moieties, yielding materials far more durable than uncrosslinked membranes. Curing was conducted at 130°C for at least ten minutes. Previous work shows this to be the optimum temperature for thermal curing and that excessive heating times do not result in higher crosslink densities.[7] Note, however, that we formed the membranes from the deprotected polymers without crosslinking due to the low decomposition temperatures of these polymers.

### Pervaporation experiments

The ultimate measure of a polymer membrane synthetic scheme is analysis of the performance of the membranes formed. We used pervaporation to assess membrane performance for water-dye separations and water-alcohol separations. Pervaporation is a membrane process that includes a low-pressure liquid feedstream circulated on the upstream side of the membrane and a vacuum on the permeate side. Permeate transport during pervaporation typically occurs by selective sorption of the permeate into the membrane, diffusion through the membrane, followed by vaporization and trapping.

Of the polymers synthesized, we assessed several for pervaporation performance using water-dye feedstreams. Table 2 presents the results of these experiments. In all experiments, transport of water is low due to the hydrophobicity of the four protected polymers. Polymers 084, 096, and 104 show no temperature dependence to flux, which suggests that water does not interact with these polymers and has a poor solubility within the matrix. Polymer 116 does stand out from this group, having increased fluxes observed for increased temperatures. This behavior is attributed to a limited interaction of MEE with the permeate.

**Table 2.** Pervaporation data for polymers 084, 096, 104, and 116.

| Polymer | Temperature (°C) | Flux (L/m$^2$h) |
|---|---|---|
| 084 | 40 | 0.02 |
| 084 | 52 | 0.03 |
| 096 | 26 | 0.04 |
| 096 | 55 | 0.04 |
| 104 | 29 | 0.05 |
| 104 | 50 | 0.05 |
| 116 | 29 | 0.01 |
| 116 | 47 | 0.19 |
| 116 | 56 | 0.30 |
| 116 | 62 | 0.40 |

For insight into membrane separations behavior, we investigated polymers synthesized as a part of INEEL's FY 1999 effort[8] for alcohol-water separations. These data are briefly discussed in the referenced report. Polymer M2D was employed for these tests, where the composition was 48% MEE, 48% *p*-methoxyphenol, and 4% *o*-allylphenol. During FY 2000, more membranes were formed and studied. Aqueous solutions containing methanol or isopropanol (typically 50 to 80% alcohol) were separated. Figure 1 shows an example of an methanol-water separation conducted at 54°C. The trend observed was relatively high levels of transmembrane flux, with the composition favoring the methanol. The separation factor favoring methanol increased as the concentration of alcohol in the feed decreased. Additionally, fluxes also lowered with the decreasing concentration of alcohol.

Increases of methanol up to 80% in the feedstream resulted in the same type of separations behavior (see Figure 2). However, the fluxes are much higher, reflecting the higher content of methanol both in the permeate and the feed. These data suggest that the polymer membrane has a higher affinity for methanol than for water. This conclusion seems to be supported by the solubility parameter experiments where M2D had a better solubility match with methanol than water.[8]

## Characterization of Polymeric Membranes

### Chemical and Physical Characterization of Polymers and Membranes

We characterized the polymers synthesized in this project using Nuclear Magnetic Resonance (NMR) spectrometry, thermal analysis (DSC and TGA), and dilute solution techniques for molecular weight determination (see Table 3).

We performed NMR analysis to study the extent of reaction and speciation of pendant groups on the backbone. The backbone phosphorus atoms and the hydrogens on the pendant groups were observed by NMR. $^{31}$P NMR data revealed two major signals for the DADG-aromatic pendant group polymers (084

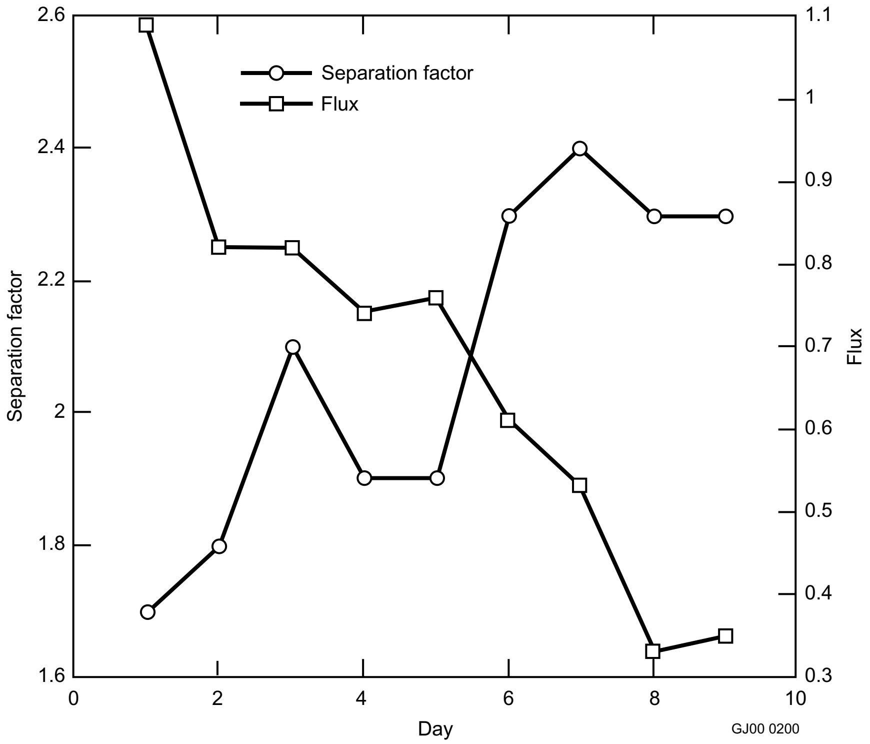

**Figure 1**. Flux and separation factor plot for methanol-water pervaporation experiment using polymer M2D and a 50% methanol feed. The units for flux are L/m$^2$h.

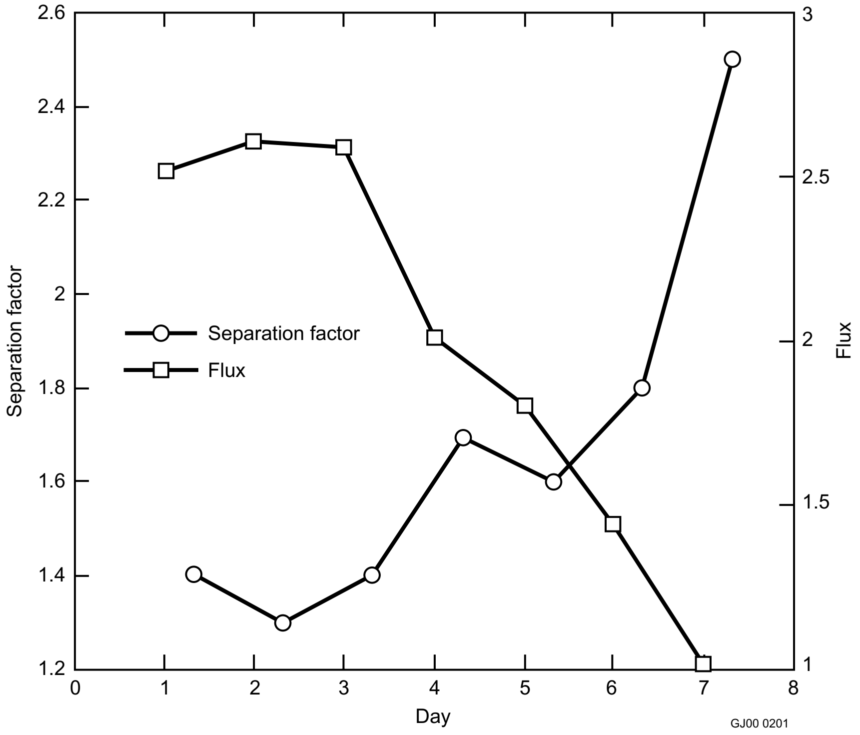

**Figure 2**. Flux and separation factor plot for methanol-water pervaporation experiment using polymer M2D with an 80% methanol feed.

**Table 3**. Characterization data for polymers 084, 096, 104, and 116.

| Polymer | $^{31}$P NMR (ppm) | Tg (°C) | $T_d$ (°C) | Mw (g/mol) | Polydispersity Index |
|---|---|---|---|---|---|
| 084 | -11.9, -17.3 | 56 | 281 | $7.7 \times 10^5$ | 1.4 |
| 096 | -14.2, -17.5 | 48 | 263 | n/a | n/a |
| 104 | -8.3, -12.9 | 12 | 275 | $1.5 \times 10^6$ | 1.9 |
| 116 | -8.3, -12.9 | -15 | 288 | $2.6 \times 10^6$ | 2.3 |

and 096), generally centered around -12 ppm and -17 ppm corresponding to the DADG and the aromatics, respectively. The MEE containing polymers also showed two dominant resonances; these were observed at -6 and -13 ppm, corresponding to MEE and DADG containing phosphorus atoms, respectively. These data are consistent with previous work.[9,10]

Additional polymer characterization was performed using differential scanning calorimetry (DSC), thermomechanical analysis (TMA), and thermogravimetric analysis (TGA). Two features dominate the thermal behavior of these polymers: a glass transition ($T_g$) and a decomposition temperature ($T_d$). In these data, the influence of the MEE pendant group was observed where the $T_g$ was substantially lower than what were observed for the aromatic containing polymers. The $T_d$ values do not appear to reflect this trend, with thermal stabilities evident from 260 to 290°C. We performed additional analysis through gel permeation chromatography, where the materials were shown to be high polymers with low polydispersities.

We cast all polymers into membranes using the above-mentioned solution casting method. Thicknesses were determined using a Mitutoyo micrometer. Membrane thicknesses were easily controlled by using consistent polymer concentration casting solutions. Membranes for pervaporation were generally between 10- and 20-μm thick, while the gas permeability membranes were substantially thicker, between 80 and 100 μm.

The deprotected polymer series 090, 142b, 109, and 122 were primarily characterized using thermal analysis where they were observed to decompose at much lower temperatures than the protected materials. For example, the $T_d$ for polymer 109 was measured at 153°C as compared to 275°C for the precursor polymer, 104. Additionally, $^{31}$P NMR spectroscopy revealed similar spectra as the precursor polymers with the indicative change being a slight shift of the DADG resonance to lower field for polymers 116 and 122. For polymer 090, the changes in the spectrum were more subtle, however reaction was evident.

## Gas Permeability Measurements

Gas permeabilities for polymers 084, 096, 104, and 116 were determined using the time-lag method[11,12,13] (see Table 5). These data are consistent with previous reports.[14] Using these data, ideal separation factors ($\alpha$) can be calculated from a ratio of the pure gas permeabilities, yielding a permselectivity. Ideal separation factors are of particular value as a predictive tool to determine structure-function relationships between gas permeability and phosphazene pendant group substitution.

**Table 4**. Characterization data for polymers 090, 142b, 109, and 122.

| Polymer | Precursor polymer | $T_g$ (°C) | $T_d$ (°C) | $^{31}$P NMR (ppm) |
|---|---|---|---|---|
| 090 | 084 | 58 | 149 | -11.9, -17.3 |
| 142b | 096 | 45 | 138 | -11.4, -17.4 |
| 109 | 104 | 17 | 153 | -5.5, -11.2 |
| 122 | 116 | -11 | 150 | -5.7, -11.6 |

Figure 3 is a plot of $\alpha$ versus permeability of $O_2$ for the $O_2/N_2$ gas pair for polymers 084, 090, 096, 104, 109, 116, and 122. The upper bound on the plot is defined as the boundary of membrane effectiveness, as defined by Robeson.[15] The goal of membrane design is to move toward the upper bound, gaining both increased permeability and separation. Clearly, there does not appear to be a trend where the maximization of any one component on the polymer backbone correlates to increased permeability and selectivity. This is consistent with previous data collected on phosphazene polymers using oxygen and nitrogen as analyte gases.[16]

We performed a similar analysis using the $CO_2/CH_4$ gas pair (see Figure 4). In this analysis, a general trend can be seen for the two MEE containing polymers, where an increased amount of MEE gives higher permeabilities and separation factors. This observation is also consistent with previously reported data.[16] Transport of $CO_2$ through a membrane can be strongly influenced by the solubility behavior of that polymer and the compatibility of $CO_2$ with the polymer. Furthermore, this interaction with the polymer can be strong enough to overwhelm many morphological changes within the polymer that would inhibit higher fluxes. From the data shown in Figure 4, the DADG or the aromatic pendant groups appear to have little interaction with $CO_2$, and the transport of gas depends upon segmental chain motion in the polymer matrix.

The link between MEE content on the polymer backbone and $CO_2$ permeability was established using the FY 1999 MEE containing polymers.[8] All of these polymers were heteropolymers containing MEE, *p*-methoxyphenol, and *o*-allylphenol. Pure gas carbon dioxide and methane permeability experiments reveal a direct linear correlation between permeability of $CO_2$ and MEE content within the polymer matrix (see Figure 5). This is shown in Figure 5 as a trend that moves toward the upper bound as MEE content is increased.

The trend in Figure 5 is significant, because the mechanism of transport of permanent gases identified in these polymers is segmental chain motion. For $CO_2$, interaction with the polar MEE pendant group dominates the transport mechanism. Poly((2-(2-methoxyethoxy)ethoxy)phosphazene), MEEP, is a polymer with 100% MEE on the backbone. We tested MEEP and found it to have the highest permeabilities *and* separation factors for $CO_2/CH_4$. This was a surprising result due to the very dense nature of MEEP. Transport induced by segmental chain motion is enhanced by increasing intermolecular voids within the polymer. These voids tend to reduce the density of the polymer. MEEP is a dense semi-fluid material that could only be tested after crosslinking. In this instance, the solubility of the permeate was the controlling property to effect improvements in membrane transport.

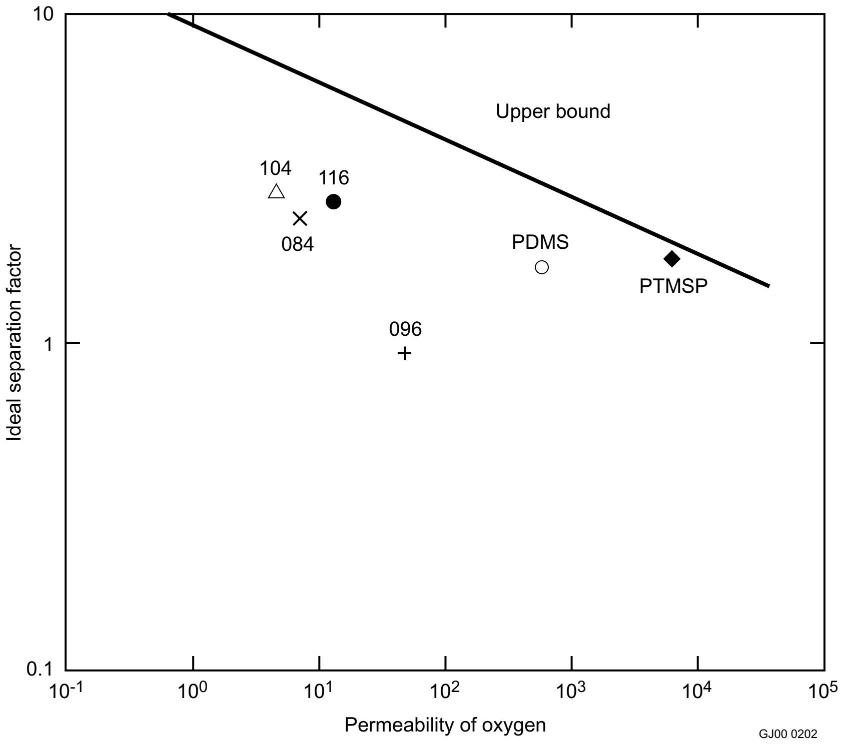

**Figure 3.** Plot of permselectivity versus permeability for the $O_2/N_2$ gas pair. Poly(dimethylsiloxane) (PDMS) and Poly(Trimethylsilylpropyne) (PTMSP) are added as references.

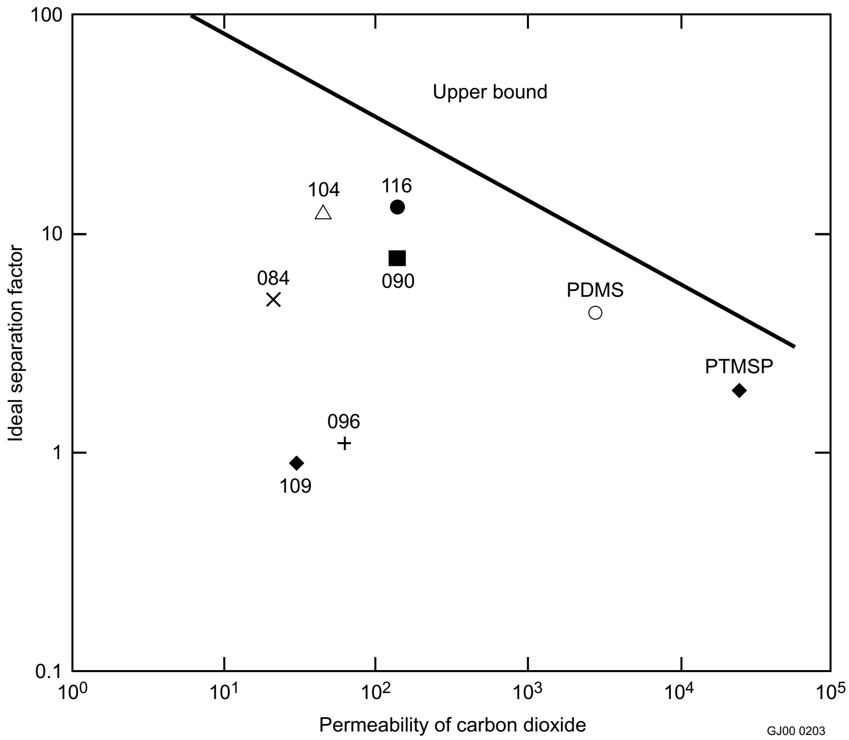

**Figure 4.** Plot of permselectivity versus permeability for the $CO_2/CH_4$ gas pair.

**Table 5.** Gas permeabilities of selected phosphazenes.

| Polymer | $H_2$ | He | $N_2$ | $O_2$ | $CH_4$ | $CO_2$ | $\alpha O_2/N_2$ | $\alpha CO_2/CH_4$ |
|---|---|---|---|---|---|---|---|---|
| 084 | 27.2 | 29.2 | 2.9 | 7.1 | 3.7 | 21.1 | 2.4 | 5.7 |
| 096 | 141.3 | 105.3 | 52.5 | 48.7 | 56.9 | 62.0 | 0.9 | 1.1 |
| 104 | 25.5 | 19.7 | 1.6 | 4.7 | 3.6 | 45.3 | 2.9 | 12.6 |
| 116 | 37.1 | 28.9 | 4.8 | 13.0 | 10.6 | 139.7 | 2.7 | 13.2 |
| 090 | 179.7 | 149.9 | 8.1 | 30.5 | 17.6 | 135.9 | 3.8 | 7.7 |
| 109 | 45.6 | 38.7 | 24.2 | 21.3 | 32.8 | 30.1 | 0.9 | 0.9 |

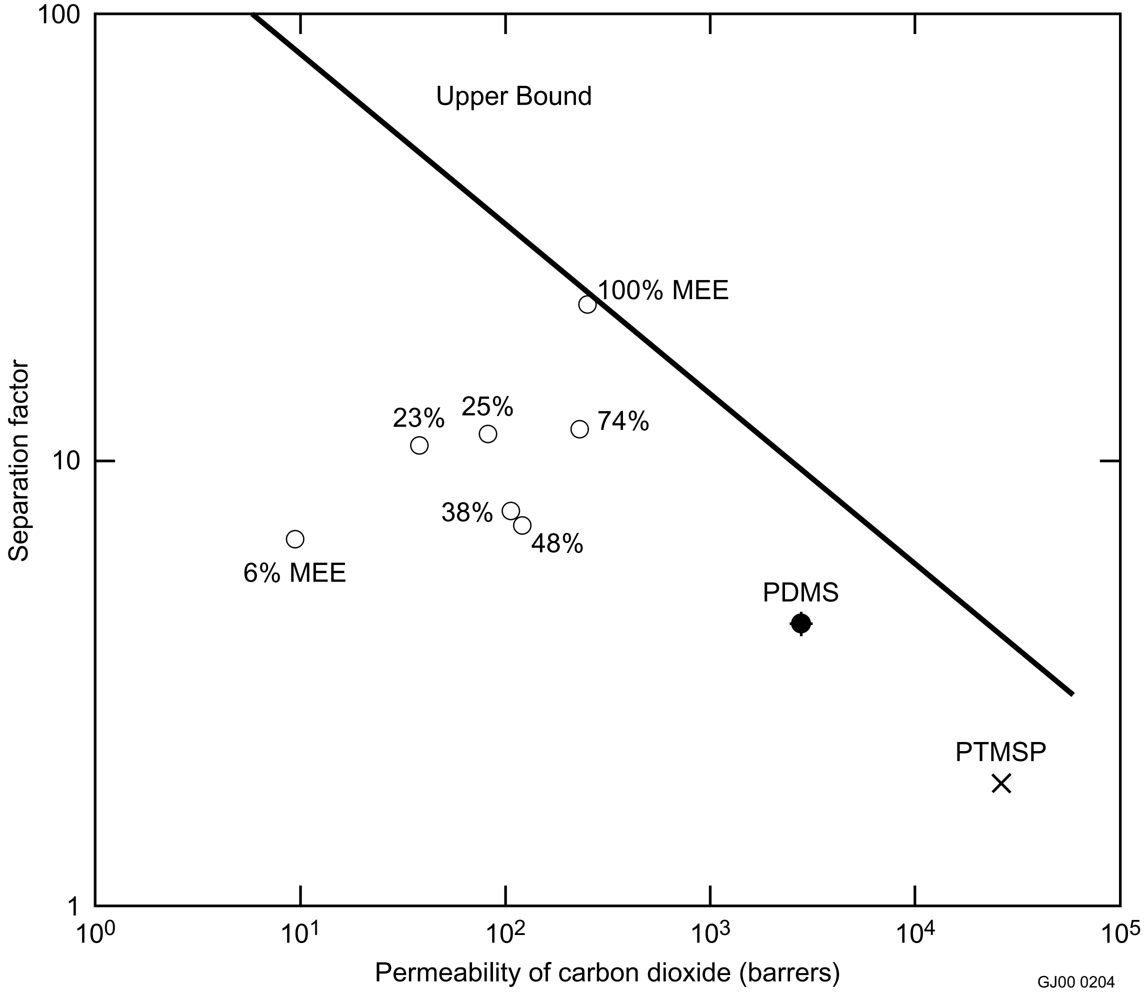

**Figure 5.** Plot of permselectivity versus permeability for the $CO_2/CH_4$ gas pair for the FY 1999 MEE containing polymers.

Segmental chain motion as a dominant influence on transport can be readily observed for the $O_2/N_2$ gas pair on the FY 1999 MEE polymers. The data in Figure 6 show a trend parallel to the upper bound, suggesting that as the content of MEE is increased in the polymer, permeability of $O_2$ also increased. However, this increased permeability was obtained with a loss of separation factor. This behavior can be attributed to morphological changes in the polymer with increasing MEE in the absence of strong intermolecular interactions between the gas permeate and the polymer. In this instance, the morphological changes correspond to lower $T_g$ values for each polymer as the percentage of MEE is increased, leading to increased segmental chain motion within the matrix at room temperature as the $T_g$ is decreased.

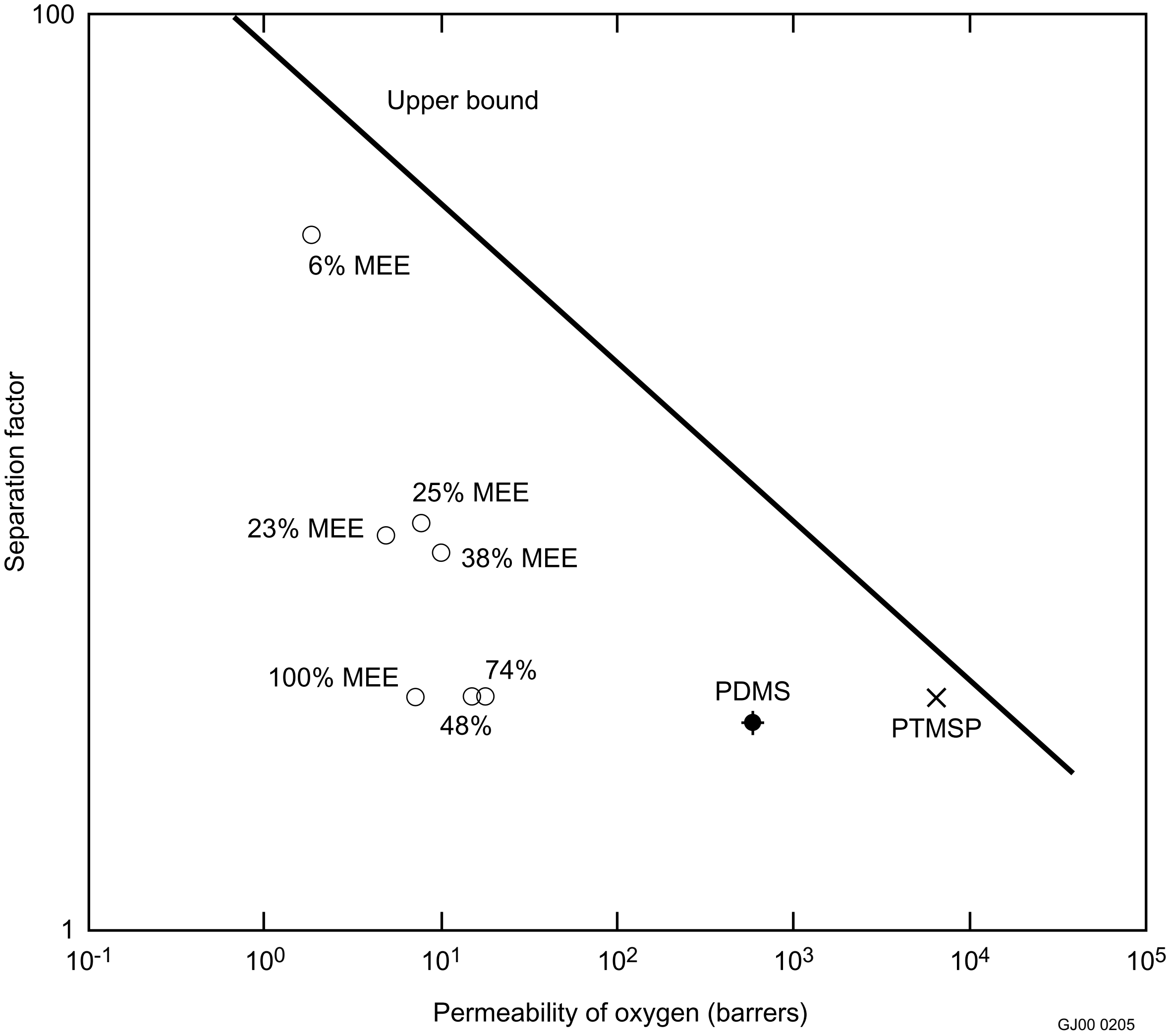

**Figure 6.** Plot of permselectivity versus permeability for the $O_2/N_2$ gas pair for the FY 1999 MEE containing polymers.

# Prediction of Polymer Properties and Membrane Efficacy

## Solubility Parameter Determinations

We determined three-point Hanson solubility parameters for seven polymers. Hanson solubility parameters ($\delta$) separate out aspects of solubility interactions into three types: dispersion ($\delta_d$), polar ($\delta_p$), and hydrogen bonding ($\delta_h$). The goal of this work was to increase the hydrogen bonding aspects of the polymers through creation of hydroxyl sites. Thus, solubility parameter determination experiments served as a method for investigating the effects of these hydroxyl sites on solubility behavior.

We performed these investigations by immersing polymer samples in twelve different solvents with varying solubility parameters. The duration of the immersion was 2 weeks. We visually determined *goodness* of a solvent as one that completely dissolved the polymers described as *good*. Likewise, we labeled solvents that failed to dissolve the polymer samples as *poor*. We estimated the polymer Hanson parameters through a simple average of the Hanson parameters for *good* solvents for each polymer (see Table 6). An additional parameter, $\delta_T$, was calculated as the square root of the sum of the squares of each individual Hanson parameter. We did this to obtain a contrast for the single-point Hildebrand parameters.

Analysis of the data shows that for the 084/090 and 104/109 polymer pairs, $\delta_p$ and $\delta_h$ are enhanced toward an increased affinity of the polymers for water. Additionally, the $\delta_T$ is significantly increased. However, this trend was not observed for the 116/122 polymer pair where the data were essentially unchanged. This behavior, when examined in light of the above-mentioned polymer pairs, does suggest that the effect of the DADG inclusion and deprotection is small. Solubility of the polymer is not only controlled through the DADG pendant group, but it is influenced by the other pendant groups and the backbone itself. In fact, the solubility behavior of phosphazenes appears to be a competition between conflicting influences. This has been seen for 100% DADG (deprotected) and MEEP polymers where complete water solubility was observed, in addition to solubility in solvents such as THF and toluene, leading to a broader solubility profile. For polymers such as 100% aromatic substituted systems, solubility is restricted to a narrow region represented by THF and toluene. Consistent solubility of phosphazenes in THF and toluene has, therefore, been attributed to the influence of the polymer backbone.

**Table 6.** Estimated Hanson solubility parameters.

| Polymer | $\delta$d | $\delta$p | $\delta$h | $\delta$T |
|---|---|---|---|---|
| 084 | 17.7 | 2.9 | 4.7 | 18.5 |
| 090 | 17.2 | 6.0 | 9.6 | 20.6 |
| 096 | 17.9 | 3.7 | 5.8 | 19.2 |
| 104 | 17.4 | 4.0 | 5.9 | 18.8 |
| 109 | 16.2 | 10.5 | 15.0 | 24.4 |
| 116 | 17.2 | 6.0 | 9.6 | 20.6 |
| 122 | 17.5 | 5.0 | 8.4 | 20.0 |

# ACCOMPLISHMENTS

## Material Synthesis

- Synthesized four model polymers and examined the influence of placing hydroxyl precursors on the phosphazene backbone.

- Performed a deprotection process on the four new polymers and formed new hydroxylated polymers with the potential of having a higher degree of interaction with water.

- Investigated the use of polyphosphazene membranes as a stable substrate for plasma polymerization. The plasma treatment does not compromise the transport characteristics of the phosphazenes, which leads to an important development for creating chemoselective thin dense films.

## Materials Processing and Testing

- Formed asymmetric polymer-ceramic composite membranes for liquid pervaporation and gas separations.

- Conducted more than 10 pervaporation experiments to characterize membranes through the separation of water-dye and water-alcohol feedstreams.

## Characterization of Polymeric Membranes

- Characterized seven new polymers using Nuclear Magnetic Resonance spectrometry, Gel Permeation Chromatography, and thermal analysis (DSC, TGA, and TMA).

- Determined the permeability of the new materials to hydrogen, helium, nitrogen, oxygen, carbon dioxide, and methane.

- Observed a direct linear relationship between the amount of MEE within the polymer matrix and the permeability of $CO_2$. This result is exciting due to the need for effective $CO_2$ sequestration technologies.

## Prediction of Polymer Properties and Membrane Efficacy

- Group contribution theory was used in conjunction with Hanson parameters to predict and explain polymer solubility behavior.

- Determined Hanson solubility parameters for the seven new polymers through immersion in 12 different solvents. These parameters allow prediction of transport behavior and observation of changes in polymer solubility.

# REFERENCES

1. R. Roger, "Membrane Materials Market to Grow Steadily," *Chemical and Engineering News*, Vol. 76, No.34, 1998, p.38.

2. R. E. Singler et al., "Synthesis and Characterization of Polyaryloxyphosphazenes," *J. Poly. Sci. Polymer Chem. Ed.,* Vol.12, 1974, p. 433.

3. J. E. Mark, H. R. Allcock, R. West, *Polyphosphazenes, Inorganic Polymers*, Prentice Hall, Englewood Cliffs, NJ, 1992, pp. 61-140.

4. F. F. Stewart, M. K. Harrup, T. A. Luther, C. J. Orme, R. P. Lash, "Formation of Pervaporation Membranes from Polyphosphazenes Having Hydrophilic and Hydrophobic Pendant Groups: Synthesis and Characterization," *J. Appl. Polym. Sci.* In Press.

5. H. R. Allcock, S. R. Pucher, "Polyphosphazenes with Glucosyl and Methylamino, Trifluoroethoxy, Phenoxy, Or (Methoxyethoxy)Ethoxy Side Groups," *Macromolecules*, Vol.24, 1991, p.23.

6. H. R. Allcock, A. G. Scopelianos, "Synthesis of Sugar-Substituted Cyclic and Polymeric Phosphazenes and Their Oxidation, Reduction, and Acetylation Reactions," *Macromolecules*, Vol.16, 1983, p. 715.

7. F. F. Stewart, *Selective Mass Transport in Polymers*, INEEL/EXT-98-01023, April 1999, p.9.

8. F. F. Stewart, T. A. Luther, R. P. Lash, C. J. Orme, "Selective Mass Transport in Polymers," INEEL/EXT-99-01008, January 2000, p.139.

9. F. F. Stewart, M. K. Harrup, R. P. Lash, M. N. Tsang, "Synthesis, Characterization and Thermal Stability of Phosphazene Terpolymers with 2-(2-Methoxyethoxy)ethoxy and Diacetone D-Glucofuranosyl Pendant Groups," *Polymer International*, Vol. 49(1), 2000, p. 57.

10. F. F. Stewart, E. S. Peterson, M. L. Stone, R. E. Singler, "Synthesis and Characterization of Polyphosphazene Copolymers Using Phosphorus-31 NMR Spectroscopy," *Amer. Chem. Soc., Polymer Preprints,* Vol. 38(1), 1997, p. 836.

11. C. Rogers, J. A. Meyer, V. Stannett, M. Szwarc, "Studies In The Gas and Vapor Permeability of Plastic Films and Coated Papers, Parts I And II," *TAPPI*, Vol. 39, 1956, p. 737.

12. R. M. Barrer, "Permeation, Diffusion, and Solution of Gases in Organic Polymers," *Trans. Faraday Soc.,* Vol. 35, 1939, p. 628.

13. G. J. van Amerongen, "The Permeability of Different Rubbers to Gases and Its Relationship to Diffusivity and Solubility," *J. Appl. Phys.,* Vol. 17, 1946, p. 972.

14. E. Drioli, S.-M Zhang, A. Basile, G. Golemme, S. N. Gaeta, H.-C. Zhang, "Gas Permeability of Polyphosphazene Membranes," *Gas Separat. Purif.*, Vol. 5, 1991, p. 252.

15. L. M. Robeson, "Correlation of Separation Factor versus Permeability for Polymeric Membranes," *J. Membrane Sci.,* Vol. 62, 1991, p.165.

16. C. J. Orme et al., "Characterization of Gas Transport in Selected Rubbery Amorphous Polyphosphazene Membranes," *J. Membrane Sci*.,. Submitted.

# Pore Size and Morphology Control for Solid and Polymer Matrices

**Mason K. Harrup, Alan K. Wertsching, Thomas A. Luther, and Robert P. Lash**

## SUMMARY

The separation needs of the Department of Energy's Office of Environmental Management are extremely demanding on separation materials due to the highly aggressive thermal and chemical environments, and also due to the presence of high levels of radiation. Typical organic membrane materials employed for this purpose do not maintain structural integrity in these types of environments. In order to address this pressing need, this project has focused on two aspects of the transport of small molecules through solid polymer and composite materials that exhibit great promise for solving these problems.

The first aspect of this project extended the investigation of novel hybrid organic/inorganic materials named molecular composites. This program first explored composites of this kind at the INEEL during FY 1998 and 1999. Factors that control structure property relationships and other pertinent synthetic aspects of these composites were more fully explored. The most important result to come from this area was our ability to transfer the synthetic techniques and expertise gained through the investigation of phosphazene-based composite model systems to more conventional organic polymer-based systems. Synthetic routes to molecular composites formulated with commercially available polymers were opened and synthetic method/composite property relationships explored. This opens exciting new possibilities for these materials, as there now exists a means for stabilizing a broad range of polymers, not just the prohibitively expensive phosphazenes, for challenging EM separations and sequestration problems.

The second focus of this project involved the investigation of phosphazene skeletal morphology. Polymer morphology is a little studied phenomenon that could significantly impact membrane lifetimes and transport rates. Two series of polymers, one catalyzed one not, were synthesized and evaluated to assess skeletal morphology and our ability to control this morphology. It was found that skeletal morphology could indeed be influenced by the synthetic conditions employed. Further work in this area is needed to fully understand the effects observed and to quantify the magnitude of the advantage gained by this selective stabilization strategy. The separate aspect of our investigations of skeletal morphology involved the synthesis and analysis of special nuclear magnetic resonance active polymers that possessed the isotope $^{15}N$ in the polymer backbone. Multinuclear nuclear magnetic resonance (NMR) experiments were performed at both high and low fields, and revealed a wealth of information about the nature of the backbone and its interactions with organic and ionic species. This information aids in understanding the role that the backbone plays in transport through phosphazene membrane materials, and could enable us to design better materials for challenging EM separations.

## PROJECT DESCRIPTION

### Objectives

One of the biggest challenges in making membrane separations technologies viable for EM applications is increasing the rate of permeation through the membrane while maintaining high selectivity. This must be achieved with a durable material, capable of withstanding harsh environments, without making the material prohibitively expensive. Membrane materials that allow for a high transmission rate generally swell to a great degree and lose their physical integrity leading to rapid failure of the membrane. To combat this problem, all manners of crosslinking strategies have been explored in the open and patent literature. While this type of strategy does increase membrane durability, it has met with limited success due to an incomplete understanding of the interactions at a molecular level. In this work, we seek a better fundamental understanding of the mechanisms of transport into and through polymer and composite matrices. This enhanced understanding will facilitate rational design improvements upon existing materials used for challenging environmental separations. The scope of this project focuses on two research areas:

1. Molecular composites for enhanced selective mass transport and durability
2. Polymer skeletal morphology effects on selective mass transport and durability.

## Technical Approach

The technical approach to this work is to examine the research areas delineated above in detail and draw conclusions about molecular interactions/transport from the combined results of these efforts. Each area of research will be executed separately; initially, with crossovers anticipated to occur as data is collected and the work progresses. Five tasks in these two research areas are described below.

### Molecular Composites

The first of these research areas that offers promise to address the above stated problems is the investigation of molecular composites.[1,2] These composites combine polymers with ceramic components in a novel manner, retaining the beneficial aspects of both. The resulting material is more physically and chemically robust than the polymer alone, yet the material loses none of the desired qualities of the parent polymer. Recent research in the area of molecular composites (funded by the ESRA program) has yielded a wealth of new composite materials that exhibit promise for a variety of EM applications. The efforts in this part are designed to enhance the fundamental understanding of these composites and to develop new synthetic strategies that will provide access to a wider variety of polymer composites.

*Task 1. Aqueous-Based Molecular Composites.* Previous research into molecular composites (ESRA 99) has focused on polymers and ceramic precursors that are water-soluble. Based on this new understanding, this task will expand the synthetic techniques employed to form this type of composites to include nonphosphazene polymers. Well-studied organic polymers that are currently used in commercial separation processes, such as polyvinyl alcohol (PVA), will be used as the polymer component to form novel molecular composites. These new materials will be fully characterized to study the composite materials in fine detail at the molecular level. After this rigorous characterization, these composite materials will be evaluated using water and gas transport tests and the results compared to the parent systems to determine the advantages gained with these materials.

*Task 2. Hydrophobic Molecular Composites.* The solution to many EM relevant problems depends on low polarity membranes to effect the desired separations. All of the development work to date on molecular composites has been in a highly polar (aqueous) environment due to the need for small amounts of water to effect the condensation of the ceramic. This task will explore synthetic strategies designed to form new molecular composites in a very low polarity environment. By using ceramic precursors and catalysts that possess significant solubility in less polar solvents, such as toluene, composites will be formed using hydrophobic phosphazenes. These new materials will be fully characterized and, if suitable, evaluated in practical pervaporation tests with the results compared to the parent polymer system.

*Task 3. Molecular Composites for Gas Separations.* Molecular composites also exhibit great promise as gas separation membranes. Results from previous research (ESRA 1999) suggest that these composite materials possess a higher porosity than that for the parent polymer due to the rigid ceramic superstructure within the composite matrix. This task will investigate this phenomenon in greater detail and assay the gas transport characteristics through these materials. A series of representative phosphazene polymers with widely varying physical properties, from rubbery to glassy, will be formed into molecular composites using identical polymer/ceramic ratios to validate polymer to polymer comparisons. After full characterization (vide supra), these membranes will be subjected to rigorous gas testing protocols using a range of representative gasses and the results compared to the parent systems.

## Polymer Morphology

Batch-to-batch reproducibility is a pressing problem in working with linear polyphosphazenes as separation materials. Since the substitution of organic ligands for chlorine on the polymer skeleton is readily controllable and highly reproducible, it must be some other factor—polymer morphology—which accounts for the differences in the observed separations properties. Previous research has indicated that ligand-based morphological factors do play a significant role in the performance of the membrane, but the hydrophilic/hydrophobic balance possessed by the ligands alone remains insufficient to account for the observed differences in membrane performance. Little attention has been given to the morphology based upon the polymer skeleton in polyphosphazenes. The efforts in this part are designed to address the effect that skeletal morphology has on the separation performance of phosphazene membranes.

*Task 4. Backbone Morphology.* Thermal crosslinking or branching of the polymer increases in frequency as polymerization progresses and the supply of starting trimer is consumed. It is therefore reasonable to assume that at early reaction times (5–15% complete) the polymer strands are the closest to truly linear structures, while having a high enough molecular number to be true polymers. The polymerization reaction will be terminated at this stage and the polymer purified. A complete analysis of this material by viscometry, laser light scattering, and gel-permeation chromatography (GPC) will render benchmark values for a polyphosphazene that possesses a minimum of branch points. This benchmark material will then be thermally crosslinked in a vacuum/Argon oven to various degrees, either lightly to produce a branched material or heavily to produce a hyperbranched material. Viscometry, laser light scattering, and GPC will again be employed to test these materials and the results will be tabulated along with those of the linear benchmark. A second series of polymers is to be synthesized employing a catalyst. This should result in a polymer that has a lower molecular weight than those of the uncatalyzed series. These can then be subsequently crosslinked at the backbone using thermal methods to produce a material that is much more branched than those generated by conventional methods, yet still have a similar molecular weight. With this strategy, materials of identical composition and similar molecular number will be generated that differ only in backbone morphology. The full battery of analytical testing will then be performed to adequately characterize these materials.

*Task 5. NMR Studies of Backbone Interactions*. Previous morphological studies (ESRA 99) generated a series of phosphazene polymers with an NMR active backbone ($^{15}N$). These polymers will be further investigated using NMR spectroscopy both alone and in the presence of probe species, such as solvents and lithium ions. In this manner, information about the nature of the interaction between the backbone component of the polymer and the probe molecules can be gained. This will lead to an evaluation of the relative importance of this component of the polymer and shed light on its function during small molecule transport through these matrices.

# Results and Discussion

## Molecular Composites

**Catalysis of Silicate Networks.** Polyphosphazene-silicate nanocomposites are a relatively new material created from the *in situ* polymerization of a silicate matrix within a dissolved solution of phosphazene polymer. An interpenetrating network (IPN) results from the sol-gel reaction, which combines the physical properties of both materials. This technique which improves the mechanical and elastic properties of many polyphosphazenes has important implications for gasket, membrane, barrier, and electrolyte research.

The pioneering work of Ferrar[3] described a single experimental protocol for synthesizing these materials, particularly the poly[bis(2-(2-methoxyethoxy)ethoxy)phosphazene] (MEEP)/silicate composites. Deviation from the standard acid catalysis of these composites is virtually unknown until the present work. In addition, a recent review of polyphosphazene-silicate materials has suggested that salt content within some acid or base catalyzed systems had no effect on the final composite physical properties.[4] However, throughout sol-gel literature neutral salt catalysis can be found, it is therefore reasonable to assume changes in the silicate matrix could occur from this salt addition.[1,5]

As use of other common sol-gel techniques, such as sol aging before casting, has never been described for these systems, it appears that some catalysts may have been rejected before proper evaluation. The desire to create unique and novel network morphologies became the impetus for establishing these new catalysis protocols. Multiple series of composites were produced using a variety of synthetic conditions in an attempt to create and optimize desirable physical properties. The synthetic variables initially identified as critical and subsequently explored include the nature of the catalyst (acid, base or ionic salt), concentration of catalyst, and aging times used for the synthetic solution mixtures before casting. Composites, once formed, were subjected to mechanical testing and chemical analyses to evaluate their potential usefulness in solid electrolyte and/or membrane separation applications.

**Mechanical Analysis.** Each molecular composite was cast as a thin film and was cut to specific dimensions before analysis with TA Instruments Dynamic Mechanical Analyzer (DMA), equipped with a thin-film clamp accessory. The DMA can place specific load forces on composite films in order to obtain relevant mechanical data. The stress-strain (force ramp) experiment was the most common analytical experiment performed on these composite films. Ramped force experiments involve stretching a film sample under ever-increasing force until failure. The resulting plot can reveal important mechanical characteristics of the composite. It becomes critical to remain within the linear range when removing films from casting moulds to obtain an unstressed, undeformed membrane. Tables 1 and 2 contain data from force ramp experiments.

**ESEM Measurements.** Various thin films were imaged as an unstressed, swelled, or stretched composite with a Philips XL30ESEM. A 10 to 20 kV electron beam was used. Wet mode employed a 500 μm pressure-limiting aperture (PLA). To image the topography either a gaseous secondary electron detector (wet mode) or secondary electron detector (HiVac) was used.

**Gel Permeation Chromatography Measurements.** The MEEP in this study was dissolved in a freshly prepared solution of THF containing 0.1% tetrabutylammonium bromide (TBABr). The resulting solutions were filtered through a 0.45 μm PTFE syringe filter prior to injection into the chromatographic analysis system. This system consisted of a Waters Alliance 2690 separations module, and two Waters Styragel HR-5E solvent efficient columns (4.6 × 300 mm) connected in series to a Wyatt Technologies

Dawn DSP laser light scattering detector and a Rainin Dynamax RI-1 refractive index (RI) detector. The elunt for the separations was THF/0.1 % TBABr at a flow rate of 0.3 mL/min. The light scattering detector uses polarized light (633 nm) to measure scattered light intensities at 16 angles ranging from 12.3 to 165.1 degrees. The detector was calibrated with toluene, which was filtered through a 0.02 µm filter. The RI detector constant was determined via calibration using known concentrations of polystyrene standards whose dn/dc values are well known.

**Degradation Studies.** Use of strong acids or bases as catalysts have some pitfalls, namely degradation of the polyphosphazene component of the composite. To determine the effects of acid base exposure and duration simple degradation studies were performed on MEEP. Short and long term exposure to 1.0 M HCl or KOH, the most severe of the sol-gel reaction conditions undertaken, were performed without tetraethylorthosilicate (TEOS). The neutralized MEEP and control samples were then examined with GPC instrumentation. The results showed a slight reduction in molecular weight without a significant increase in polydispersity. This validates our results in that the parent polymer is essentially unchanged due to composite synthesis, and the differences observed in mechanical and chemical properties are indeed due solely to the presence of the ceramic component, and not due to modifications to the polymer component.

**Acid Catalyzed Composites.** In the course of experiments, the use of lower critical solubility temperature (LCST) purified MEEP, instead of dialysis purified MEEP, prevented our attempts to successfully reproduce the mechanical properties reported for MEEP composites using the Ferrar method.[6] Only after trace amounts of salt (as NaCl) were incorporated as a co-catalyst in the MEEP (obtained without using rigorous lower critical solubility temperature (LCST) purification), did the Ferrar method produce tractable composites in our hands.[7] Figure 1 is an ESEM of HCl/NaCl catalyzed composite, NaCl crystals can be observed from the surface to approximately 10µm into the composite (left). Even after curing, some crystals extrude at the surface as seen in a cross-sectional cut (right).

Even though acid catalysis fails at lower concentrations without salt contamination, use of acid solutions of increased molarity can produce usable composites. These composites typically require ten times the acid the standard literature preparations report in order to form. Unfortunately acid catalyzed membranes have all performed poorly in aqueous systems. Figure 2 is of an aqueous swelled/deswelled membrane, which has fractured from the hydrostatic pressure. However all acid catalyzed composites are glassy and brittle when compared to salt or base catalyzed membranes.

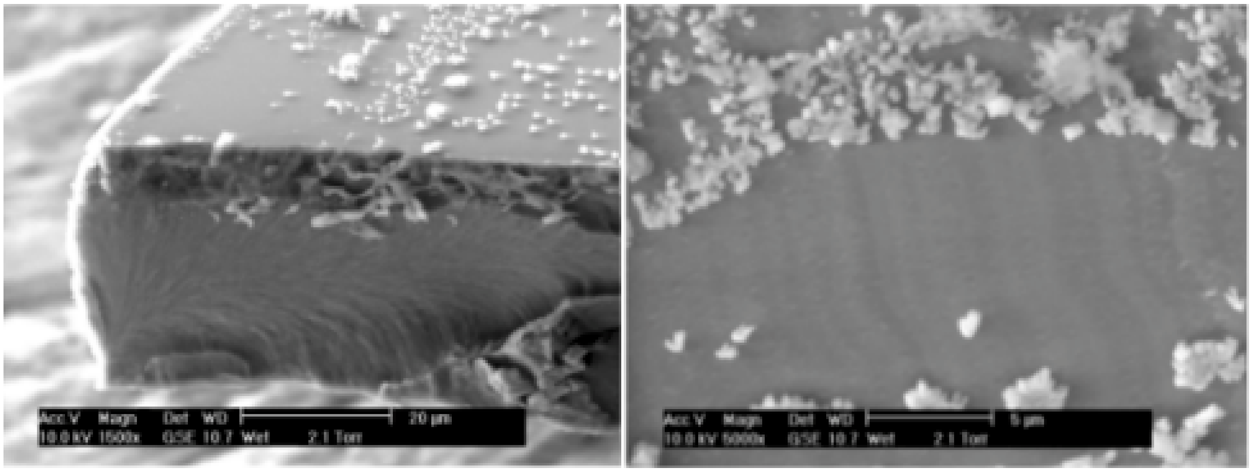

**Figure 1.** ESEM of HCl/NaCl catalyzed composite at 1,500× and 5,000× magnification.

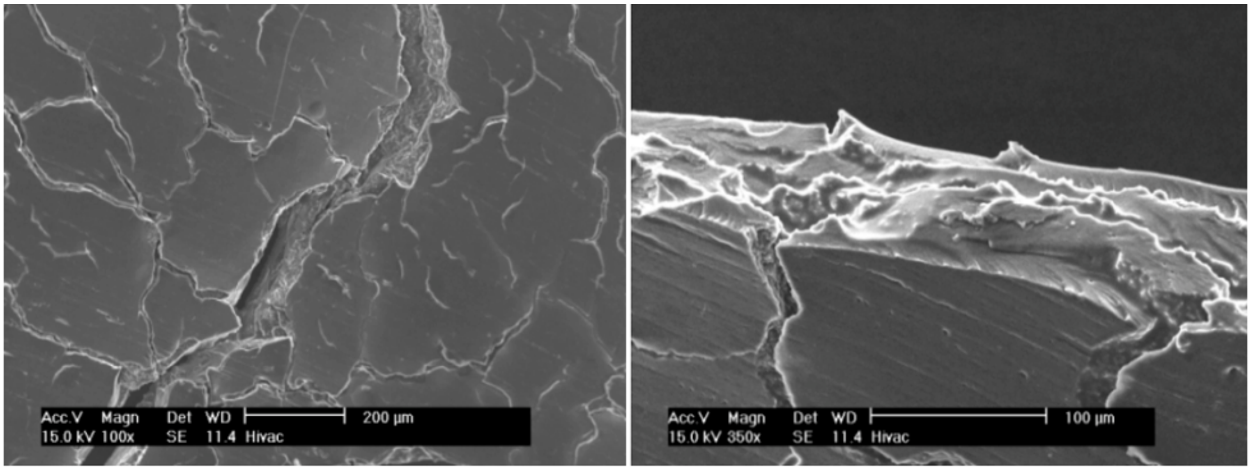

**Figure 2.** HBr catalyzed MEEP/TEOS composite after one cycle of swell/deswell in water.

**Base Catalyzed Composites.** Base catalyzed composites have the best elastic and aqueous swell characteristics of all the nanocomposites. Increasing the silicate composition of the membrane can improve the overall strength of the membrane under hydrostatic stress. Figure 3 is an image of a membrane, with four times the standard silicate composition, swollen with water. The creases of the villae-like structure indicate the underlying structure of the composite, areas of higher silicate composition. Before swelling, the composite has a featureless uniform appearance, after swelling, these creases reveal the cross-linked global view of the silicate superstructure. Radically increasing silicate composition of these composites need not produce ceramic like properties as seen in Table 1.

Under DMA stretch tests, increasing the silicate component results in a stronger composite without sacrificing elasticity, as seen in total displacement. However, as improved as the swell characteristics may be, damage does occur upon repeated swell/deswells. Three immediate swell/deswell iterations result in an approximately ten-fold decrease in composite strength. The repeated application of hydrostatic force has a damaging accumulative effect. As seen, a single swell/deswell, over the course of a week, retains much of its original strength.

**Salt Catalyzed Composites.** After establishing that fluoride anion salts are superior catalysts over other halide salts, a course of fluoride salts with various large to small alkali counter-cations was examined.

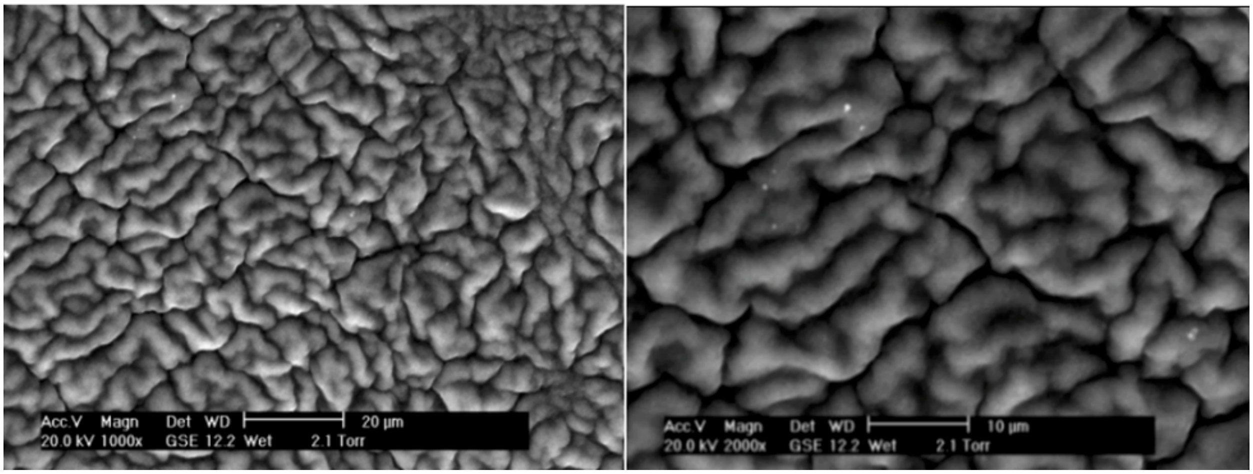

**Figure 3.** ESEM (wet mode) of aqueous swollen 4× TEOS base-catalyzed composite.

**Table 1.** DMA results for base-catalyzed composites.

| TEOS (360 μL) | Failure Force (N) | Displacement (μm) | Thickness (μm) |
|---|---|---|---|
| 1X TEOS | 0.5146 | 10,610 | 85 |
| 2X TEOS | 0.7529 | 4,105 | 98 |
| 3X TEOS | 1.0200 | 6,340 | 107 |
| 4X TEOS | 1.8900 | 8,830 | 125 |
| 4X (1 s/d) | 0.9021 | 5,965 | 90 |
| 4X (3 s/d) | 0.1463 | 4,935 | 92 |

The initial results indicated that large cations like cesium perform better than small ones, such as lithium. Intuitively hard ions such as lithium should perform well as catalysts. However, strong electronegative fluoride ion with a poor association towards large polarizable cesium may suggest that hard naked ions are an important necessary characteristic for sol-gel catalysts. In order to validate this, tetrabutylammonium fluoride (TBAF) was used as the sole catalyst in a standard MEEP/silicate composite reaction. Higher concentration TBAF solutions that were employed were too reactive and silica polymerized out of solution before an IPN could form. Diluted TBAF solutions were more successful. The TBAF composites have better swell-deswell characteristics than all other fluoride salt catalyzed composites to date. This suggests a more intimately woven IPN results from this approach. Choice of salt catalyst is limited by solubility and relative disassociative concentration. Naked anions are a more efficient choice, i.e., lower concentration of ionic species in the sol, which lower the risk of salt precipitation (Figure 1) and the resulting defects.

**Organic Polymer-Based Composites.** The use of organic acid (acetic acid) as solvent and catalyst has resulted in the first known PVA-silicate thin film composite. Initial synthesis involving inorganic acids and alcohol, although common in sol-gel procedures, were deemed inappropriate for PVA composites because of the resulting ether modification to the PVA alcohol groups. Control reaction of PVA with acetic acid without the addition of TEOS (silicate component) indicate exposure to organic acids do not chemically alter the structure of the PVA, as often is the case with inorganic acids. The resulting PVA-silicate composite has radically different solubility in aqueous media when compared to the parent PVA. Both PVA and PVA-silicate composites form hard brittle glassy thin films; however, PVA readily dissolves in water and PVA-silicate films swell only slightly.

**Table 2.** DMA results for fluoride salt-catalyzed composites.

| Catalyst (0.1M) | Failure Force (N) | Displacement (μm) | Thickness (μm) |
|---|---|---|---|
| LiF | 0.1968 | 6,418 | 85 |
| NaF | 0.4504 | 5,556 | 87 |
| KF | 0.7420 | 7,420 | 95 |
| CsF | 0.9321 | 6,896 | 90 |
| TBAF | 0.9046 | 1,417 | 110 |

However in time, PVA-silicate composites created by the sol-gel method become brittle and highly resistant to aqueous swelling. Arresting the silica sol-gel reaction at a specific point in time can permanently change the swelling and flux of these composites in aqueous systems. Repeated solvent washes of precured PVA-silicate composite stops the sol-gel reaction and can markedly change the flexibility and durability of the composite.

The quality of the PVA polymer starting material is critical to the strength of the final composite. PVA with even low percentages of unhydrolyzed acetyl groups (2–5%) form macroscopic pockets of polymer in the composite. These pockets form fracture sites under applied force or under hydrostatic pressure. PVA with high hydroxide content (99+%) form stronger, clearer, smooth composite films. These improved films are hard and clear like glass. Whereas old composites would severely fracture in water, these new composites become soft and flexible in water without breaking. The water swollen composites can be cast into different shapes through the use of moulds and dried back to a hard glass.

The effects of high water content necessary to dissolve the PVA, during the sol-gel silicate matrix formation, are a concern. Controlling water concentration during the sol-gel process is critical to controlling silicate morphology. High water content, during the sol-gel process, favor silanol formation. Which in turn favors formation of brittle, heavily cross-linked silicate structures. Low water content favors formation of a more flexible linear fibrous silicate structures. Experiments involving lower molecular weight PVA are ongoing with the hope of lowering the overall water content during silicate formation and to increase the resulting strength of the silicate matrix.

Synthesis of additional water-soluble polymer/silicate nanocomposites has been achieved. Polyethylene glycol (PEG) block co-polymers (2,000 MW) are oily, viscous materials which upon addition to TEOS and an acid catalyst, form hard clear glassy materials. The optically clear materials suggest a very homogeneous composite. In aqueous swelling tests the material holds its shape, appears to swell very little, but form cracks under hydrostatic pressure. The current formula of 40/60 PEG/TEOS by weight is being adjusted because these composites are brittle and sensitive to bending. In addition, other catalyst formulations are under consideration.

Poly(ethylene oxide) (PEO)-poly(propylene oxide) (PPO) block polymer silicate composites were also synthesized. Although weak and brittle the composites are thick and gel-like. This is unusual for acid catalyzed composites, which tend to form hard, glassy composites.

# Polymer Morphology

## Characterization of Poly(Dichlorophosphazene) Backbone Morphology

A series of ring opening polymerizations were performed on hexachlorocyclotriphosphazene in a solventless process without the addition of any catalysts. The reaction times were varied in an attempt to control the molecular weight of these “under reacted” polymerizations. The polymers were separated from the unreacted trimer species and analyzed by both batch-mode laser light scattering analyses and GPC using the methods described below. The results of these analyses are shown in Table 3. One of the most surprising results of these experiments was the extreme difference in the kinetics of the ring-opening polymerization in this solventless process as opposed to those reported in the literature[8,9] for this same polymerization in an inert solvent system. It was expected that the molecular weights would drop off with decreasing reaction time and total yield, yet, to a large extent, this was not observed. Even at very low conversions, the molecular weights remained near one million. This is strong evidence that the kinetics of the ring-opening step in the polymerization reaction is several orders of magnitude lower than

**Table 3.** GPC results from uncatalyzed polydichlorophosphazene production.

| Reaction Set # | Reaction Time (h) | Yield (%)[a] | Mw[a] | PDI[a] |
|---|---|---|---|---|
| 1 | 28 | 54 | 2.06e6 | 1.64 |
| 2 | 15 | 21 | 1.59e6 | 1.22 |
| 3 | 8.5 | 14 | 7.84e5 | 1.11 |
| 4 | 6.0 | 8 | 7.88e5 | 1.08 |

a. Value reported is an average of two or three individual polymerization reactions run concurrently and averaged.

that for the propagation step. This results in the observed trends that yields decrease linearly with decreasing reaction time, yet molecular weights do not. One point that was consistent with what was expected was the polydispersity of the polymers. The PDI approaches unity at low conversions due to the fact that the unreacted trimmer to living polymer ratio is maintained at a very high value throughout the entire reaction and chain-chain interactions (crosslinking or skeletal scission) are rare.

To further expand on our surprising discoveries, it was decided to study the catalyzed production of dichlorophosphazene. The catalyst first selected was $AlCl_3$, based on its similarity to the literature-employed catalyst, $BCl_3$. As it turns out, $AlCl_3$ was not the best choice for the morphological study. As the $AlCl_3$ remained a solid at the polymerization temperatures employed (250°C), unwanted heterogeneity was introduced during the polymerization process. This was caused as diffusion to the catalytically active surface (of the still solid $AlCl_3$) dominated the process, leading to a wide variation in results from batch to batch, even though total mole percent loading of catalyst was rigorously controlled. The molecular weight for a representative sample was low (720,000), yet the root mean square radius, a reliable semi-quantitative measure of the degree of branching in these polymers, was quite large. This indicates a high random degree of branching exists within the polymer—not at all desirable for a morphological study. To overcome this problem, we synthesized an additional series of catalyzed polymers using molecular sulfur ($S_8$). This catalyst was chosen because it has a literature precedent[10] as an effective catalyst for the ring-opening polymerization of phosphazene trimers, and it is a neat, easily diffusing liquid at the polymerization temperature. Further, initial experiments demonstrated that liquid sulfur was completely miscible with liquid hexachlorocyclotriphosphazene.

A series of poly(dichlorophosphazenes) were then prepared from hexachlorotriphosphazene to evaluate the kinetics and mechanisms of the reaction in the presence of sulfur as a catalyst. The polymers were dissolved in anhydrous toluene that was filtered through a 0.2 μm filter prior to use. All dissolutions were allowed to proceed overnight to insure that all of the polymer had dissolved. Since it appeared that there was a significant amount of insoluble material remaining, a solubility determination was performed. This was done by filtering the polymer solution through a 0.45 μm PTFE syringe filter and evaporating a 5.0 mL aliquot of the sample to constant weight under a stream of dry nitrogen. A refractive index increment, dn/dc, determination was performed on one of the filtered sample solutions in the series and applied to all of the remaining samples for calculation of light scattering results. Individual polymer solubility results were used to correct dn/dc and light scattering results. Dn/dc determinations were performed on a Rainin Dynamax RI-1 RI detector. Molecular weight and RMS radius moments were determined by GPC separation coupled to multiangle laser-light scattering (MALLS) and RI detectors. The GPC system consisted of a Waters Alliance Model 2690 solvent/sample delivery system incorporating two HR5E, 4.6 × 300 mm, solvent efficient Styragel columns operating at a flow rate of

0.3 mL/min. The MALLS detector was a Wyatt Technologies Dawn DSP system that measures scattered light intensities at 17 angles ranging from 16.8 to 155.4 degrees. A typical chromatogram with overlaid detector responses is shown in Figure 4.

The molecular weight and polydispersity data collected from the most illustrative of the sulfur catalyzed polymerizations are shown in Table 4. In the first group of samples (PCL2-0.5 through PCL22.0), which represent increasing amounts of catalyst and constant reaction time, there is a gradual decrease in both the molecular weight and size of the polymer molecules. However, the PDIs remain constant and therefore the amount of catalyst has only a small inverse effect on the polymer molecular weights and sizes and no effect on the PDIs over the range of catalyst used in this group of samples. In the second group of samples (PCL2-2B and 2C), which represent a constant amount of catalyst as used in sample PCL2-2.0 above and an increasing reaction time, there appears to be a small increase in molecular weights. However, the sizes and PDIs remain constant and therefore the reaction time appears to have only a small direct effect on the polymer molecular weights and no effect on the sizes or PDIs. In the third group of samples (PCL2–1B and 1C), which represents a constant amount of catalyst as used in sample PCL2-1.0 above and an increasing reaction time, there is a significant decrease in the molecular weights and sizes but the PDIs again remain constant. In this group it appears that the reaction time has a significant inverse effect on the molecular weights and sizes, but again, no effect on the PDIs.

The molecular weight and size trends shown by groups 2 and 3 contradict one another and need to be resolved. The PDIs throughout the entire series of samples remained unchanged at a value close to unity indicating that the variables over the ranges studied herein have no effect on the degree of branching of the polymers.

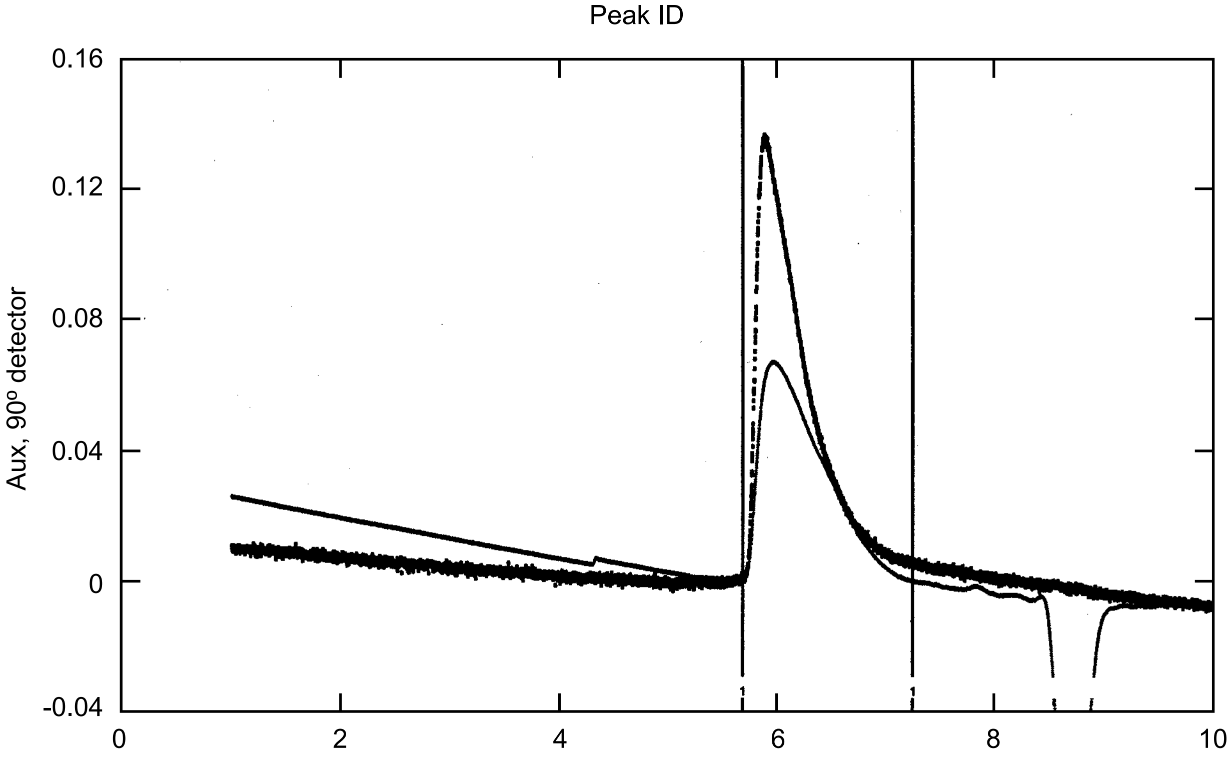

GJ00 0211

**Figure 4.** Chromatogram with overlaid detector responses: upper trace (LS), lower

**Table 4.** Molecular weight and RMS radius moments along with polydispersity indices (PDI) for sulfur catalyzed poly(dichlorophosphazenes).

| Sample | $M_w$, g/mol. | $R_w$, nm | Mn, g/mol. | $R_n$, nm | PDI |
|---|---|---|---|---|---|
| PCL2-0.5 | (3.43+0.07)e5 | 24.7+2.5 | (3.22+0.07)e5 | 25.4+2.6 | 1.06+0.03 |
| PCL2-1.0 | (2.36+0.05)e5 | 19.8+3.2 | (2.25+0.05)e5 | 20.8+3.2 | 1.05+0.03 |
| PCL2-2.0 | (1.86+0.04)e5 | 17.1+4.4 | (1.76+0.05)e5 | 19.1+4.2 | 1.05+0.04 |
| PCL2-2B | (1.74+0.03)e5 | 18.6+3.6 | (1.63+0.04)e5 | 19.9+3.7 | 1.07+0.03 |
| PCL2-2C | (2.32+0.05)e5 | 17.5+3.9 | (2.21+0.05)e5 | 18.3+4.0 | 1.05+0.04 |
| PCL2-1B | (6.35+0.2)e5 | 48.4+5.1 | (6.30+0.2)e5 | 48.3+5.1 | 1.01+0.04 |
| PCL2-1C | (2.49+0.06)e5 | 22.6+3.1 | (2.35+0.06)e5 | 23.5+3.5 | 1.05+0.04 |

Table 5 shows the solubility behaviour of the polymer samples. The solubility percentage is high but not unity, as one would expect. This is primarily due to the presence of some colloidal sulfur (the catalyst) that has become unavoidably entrained within the polymer during reaction workup. The percentage recoveries of the mass injected onto the GPC columns were low and relatively constant (range: 45–59%). We take this as an indication that approximately 50% of the polymer is irreversibly adsorbed to the column packing during chromatographic analyses.

## NMR Studies of Backbone Interactions

Polyphosphazenes are a class of materials that have been recently studied for use as solid polymer electrolytes. The first polyphosphazene shown to have ion conducting properties when complexed with a metal salt was poly[bis(2-(2-methoxyethoxy)ethoxy)phosphazene] (MEEP).[11] The proposed transport mechanism of the metal ions through the MEEP matrix has been modeled on the transport mechanism of metal ions through poly(ethylene oxide) (PEO). This model describes the mechanism as "hand-to-hand" transport by the lone electron pairs of the oxygen atoms on the side chains and that the backbone nitrogen

**Table 5.** Individual polymer solubilities, dn/dc and the percentage of the mass recovered from each injection onto the GPC.

| Sample | Solubility % | dn/dc | % Recovery of Injected Mass |
|---|---|---|---|
| PCL2-0.5 | 89 | — | 58 |
| PCL2-1.0 | 94 | 0.076 | 59 |
| PCL2-2.0 | 88 | — | 55 |
| PCL2-2B | 92 | — | 52 |
| PCL2-2C | 94 | — | 45 |
| PCL2-1B | 76 | — | 53 |
| PCL2-1C | 80 | — | 52 |

atoms are not significantly involved.[12] The natural abundance amount of the spin active $^{15}N$ nuclei that can be observed by NMR spectroscopy is too low to be effectively studied (natural abundance $^{15}N$ is only 0.345%). In order to investigate the nitrogen atoms involvement with metal ion transport in polyphosphazenes by NMR spectroscopy, the polyphosphazenes in this study needed to be synthesized from $^{15}N$ labeled starting materials.

A comprehensive set of NMR experiments with isotopically $^{15}N$ labeled poly[bis(2-(2-methoxyethoxy)ethoxy)phosphazene] ($^{15}N$ MEEP) was performed ($^{1}H$, $^{13}C\{^{1}H\}$, $^{15}N$, $^{31}P$, and variable temperature $T_1$'s) at a magnetic field strength of 7.04 Tesla ($^{1}H$ NMR operating frequency of 300 MHz). Another set of NMR experiments with $^{15}N$ MEEP and a $^{15}N$ labeled heteropolyphosphazene, $^{15}N$ poly[((2-allylphenoxy)$_{0.12}$(4-methoxyphenoxy)$_{1.02}$(2-(2-methoxyethoxy)ethoxy)$_{0.86}$)phosphazene] ($^{15}N$ HPP), was carried out ($^{1}H$, $^{13}C\{^{1}H\}$, $^{15}N$, and $^{31}P$) at the University of Washington at a magnetic field strength of 17.63 Tesla ($^{1}H$ NMR operating frequency of 750 MHz). The NMR samples were typically prepared with 100-200 mg $^{15}N$ MEEP or $^{15}N$ HPP and approximately 0.5 mL solvent in a NMR tube. Tetrahydrofuran-d$_8$ (THF-d$_8$) and chloroform-d ($CDCl_3$) were used as solvents. Experiments were also performed with $^{15}N$ MEEP using deuterium oxide ($D_2O$) and a neat sample (approx. 1.5 g $^{15}N$ MEEP) in a NMR tube with $CDCl_3$ in a coaxial insert was also prepared.

As expected, some solvent effects are exhibited in the solution spectra primarily as a small change in the observed chemical shifts along with some slight resolution differences. The sharpness of the resonances in the $^{1}H$ NMR spectrum, with THF-d$_8$ as the solvent, allows for measurable proton-proton coupling (5.0 Hz, previously unreported). In contrast, the NMR spectra of the neat $^{15}N$ MEEP sample exhibit extremely broad resonances. A single broad resonance (approx. 2 ppm in width) in the $^{1}H$ NMR spectrum allows for very little spectral interpretation. The full-width half-height linewidth ($\Delta\nu_{1/2}$) of the resonance in the $^{31}P$ NMR spectrum is approximately 10 times of that which is observed in the solution spectra ($\approx$200 Hz vs. 18 Hz). The resonances in the $^{13}C\{^{1}H\}$ (proton decoupled) and $^{15}N$ NMR spectra are also broaden compared with what is observed in the solution spectra but not to the extent observed in the $^{1}H$ and $^{31}P$ NMR spectra.

The $^{15}N$ NMR spectrum exhibits a major resonance at $\delta$ 63.1 (THF-d$_8$) with a $\Delta\nu_{1/2}$ of 75 Hz (Figure 5). The broad featureless resonance that is evident in the $^{31}P$ NMR spectra downfield (0 to -5 ppm region) of the major resonance is also seen in the $^{15}N$ NMR spectra ($\delta$ 71.9). The intensity of this resonance in the $^{15}N$ NMR spectra is 2.5% of the intensity of the major resonance. Similar resonances are observed in the $^{31}P$ and $^{15}N$ NMR spectra of $^{15}N$ HPP. These downfield resonances are attributed to polymer degradation during synthesis and/or chain-end effects.[6]

The increased resolution and chemical shift dispersity that is evident in the $^{1}H$ NMR spectrum with THF-d$_8$ are also observed in the $^{13}C\{^{1}H\}$ NMR spectrum. This allows for the unambiguous assignment of the carbon resonances of the $^{15}N$ MEEP polymer. The chemical shift assignments (Figure 6) were determined by various NMR techniques including two-dimensional proton homonuclear (COSY) and proton-carbon heteronuclear (HETCOR) correlation experiments. The assignments are consistent with the results of NMR spin-lattice relaxation ($T_1$) experiments. The relaxation times of carbon atoms in flexible side chains increase with distance from the polymer backbone due to the increased mobility.[13]

Various NMR experiments including variable temperature $T_1$ were performed to probe the lithium ion residency in the polymer matrix. Lithium trifluoromethanesulfonate (LiOTf) was added to the $^{15}N$ MEEP in incremental amounts in a NMR tube. NMR spectra were taken to observe the expected changes in the chemical shifts of the resonances of the various nuclei ($^{13}C\{^{1}H\}$, $^{31}P$, and $^{15}N$). After 104 mol % of LiOTf was added to the polymer dissolved in THF-d$_8$, the change in the observed chemical

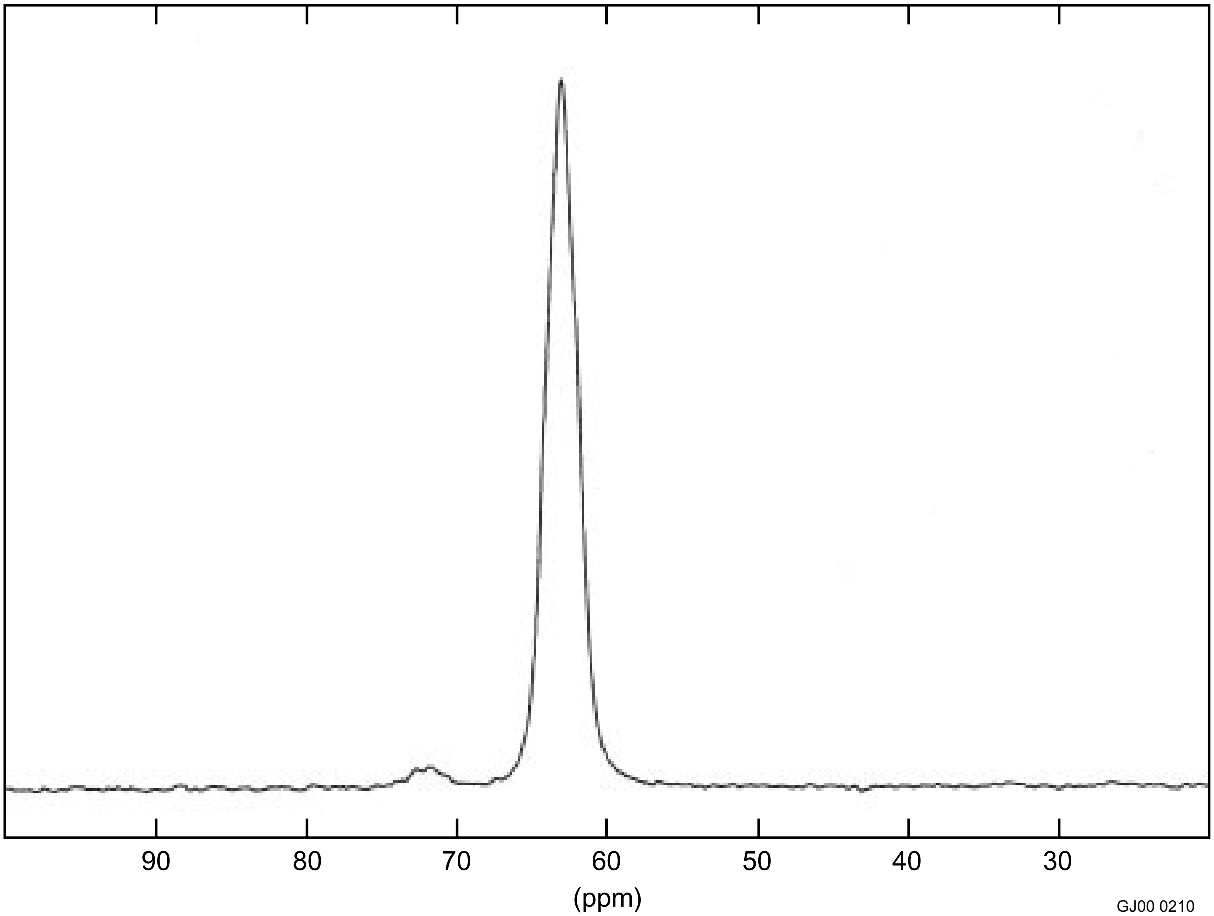

**Figure 5.** $^{15}$NMR spectrum of $^{15}$N MEEP in $CDCl_3$.

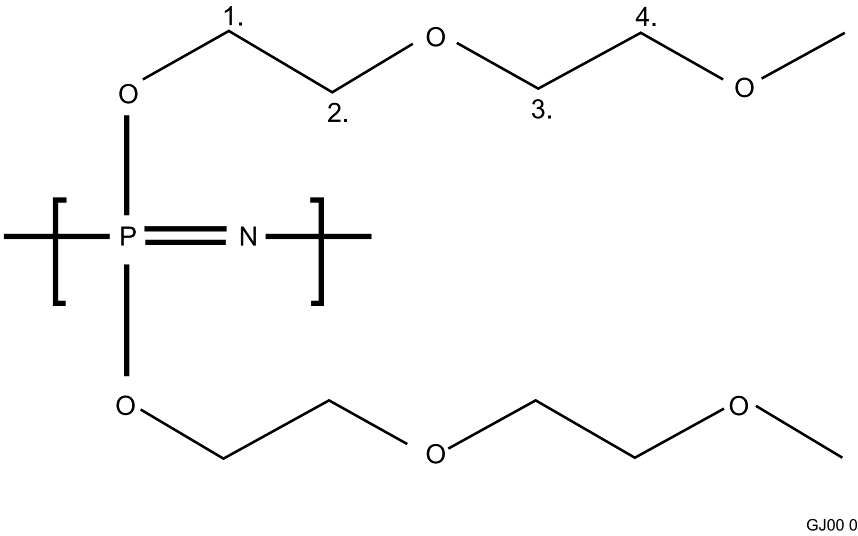

**Figure 6.** Carbon assignments for $^{15}$N MEEP.

shift of the resonance in the $^{31}P$ NMR spectrum was less than 0.5 ppm. The observed changes in the signals in the $^{13}C\{^1H\}$ NMR spectrum were less than 0.15 ppm and no significant change was observed for the resonance in the $^{15}N$ NMR spectrum. This indicates that as expected the THF-$d_8$ has the ability to compete with the polymer to solvate the lithium ions. NMR experiments with $CDCl_3$ were also performed, since LiOTf is not soluble in $CDCl_3$ but is soluble in the polymer matrix. Linear changes in the chemical shift in the resonances of the $^{13}C\{^1H\}$, $^{31}P$, and $^{15}N$ NMR spectra were observed for the incremental addition of LiOTf to the polymer. After a 40 mol% addition of LiOTf, the $^{13}C$ NMR chemical shift changes were 0.16 ppm for C1, -0.14 ppm for C2, 0.63 ppm for C3, -0.62 ppm for C4, and -0.01 ppm for C5. The observed downfield $^{31}P$ and $^{15}N$ NMR chemical shift changes were 1.51 and 0.70 ppm respectively. The $\Delta n_{1/2}$ of the $^{15}N$ and $^{31}P$ NMR resonances for $^{15}N$ MEEP were relatively unchanged after the 40 mol% addition of LiOTf.

Variable temperature $T_1$ values were measured for the internal spin = ½ nuclei ($^{13}C\{^1H\}$, $^{31}P$, and $^{15}N$). When a molecule is tumbling isotropically in solution, the dominant source of relaxation for these nuclei is from dipole-dipole interactions. The relaxation rate ($R_{DD}$) will increase with temperature, pass through a maximum, and decrease with increasing temperature. At low temperatures when the molecule is tumbling slowly in solution, the $R_{DD}$ is inversely proportional to the rotational correlation time of the molecule ($\tau_c$) and the strength of the magnetic field squared. At high temperatures, when the molecule is tumbling quickly, the $R_{DD}$ is proportional to $\tau_c$ and is independent of the magnetic field strength. Since the relaxation rate is the inverse of the $T_1$, the relaxation time will decrease, pass through a minimum, and then increase with increasing temperature. The minimum $T_1$ values ($T_{1min}$) for the nuclei will be influenced by intermolecular and intramolecular dipole-dipole interactions and are proportional to the internuclear distances.[14,15]

The variable temperature $T_1$ experiments were conducted to explore the observed changes in the $T_{1min}$ values and the temperature where the $T_{1min}$ occurs before and after the addition of LiOTf. The addition of LiOTf to the polymer causes a decrease in the flexibility of the polymer. This decrease in flexibility is evident by an increase of the temperature where the $T_{1min}$ occurs. However, the $T_{1min}$ values for the nuclei are influenced by intermolecular and intramolecular dipole-dipole interactions and are proportional to the internuclear distances. These values will be affected by the presence of lithium ions coordinating to the polymer and thereby provide insight as to the location of the lithium ions in the polymer matrix.

The $^{13}C\{^1H\}$ NMR variable temperature $T_1$ data only exhibit distinct minimum values for carbons C1 and C2, which is approximately 0.11 seconds at 235 K for both nuclei. At the lowest temperature recorded (225 K), the $T_{1min}$ for C3 had reached a constant value of 0.15 seconds. The $T_1$ values for C4 and C5, 0.16 and 0.58 seconds respectively, were still slightly decreasing with the decrease in temperature. Relaxation times at lower temperatures were not obtainable due to broadening of the resonances. After the 40 mol% addition of LiOTf, the $T_{1min}$ values showed the expected increase in temperature to approximately 285 K for all the carbon resonances except for the C5 resonance. The $T_1$ values for C5 were still slightly decreasing at the lowest obtainable temperature (1.30 seconds at 265 K). The $T_{1min}$ values showed the expected increases in relaxation times of approximately 0.04 seconds for C1 and C2, and approximately 0.07 seconds for C3 and C4. The variable temperature $^{31}P$ NMR $T_1$ data indicate a $T_{1min}$ value of 1.55 seconds at 260 K. After the addition of the LiOTf, the $T_{1min}$ increases to 1.76 seconds at 305 K (Figure 7). However, the $T_{1min}$ value for the $^{15}N$ NMR resonance decreases with the addition of LiOTf, approximately 7.5 seconds at 255 K to 5.0 seconds at 300 K (Figure 8). This data indicate that the dominant source of relaxation for the nitrogen nuclei is no longer from dipole-dipole interaction. This decrease in $T_{1min}$ is consistent with significant lithium ion involvement with the nitrogen atom of the $^{15}N$ MEEP.

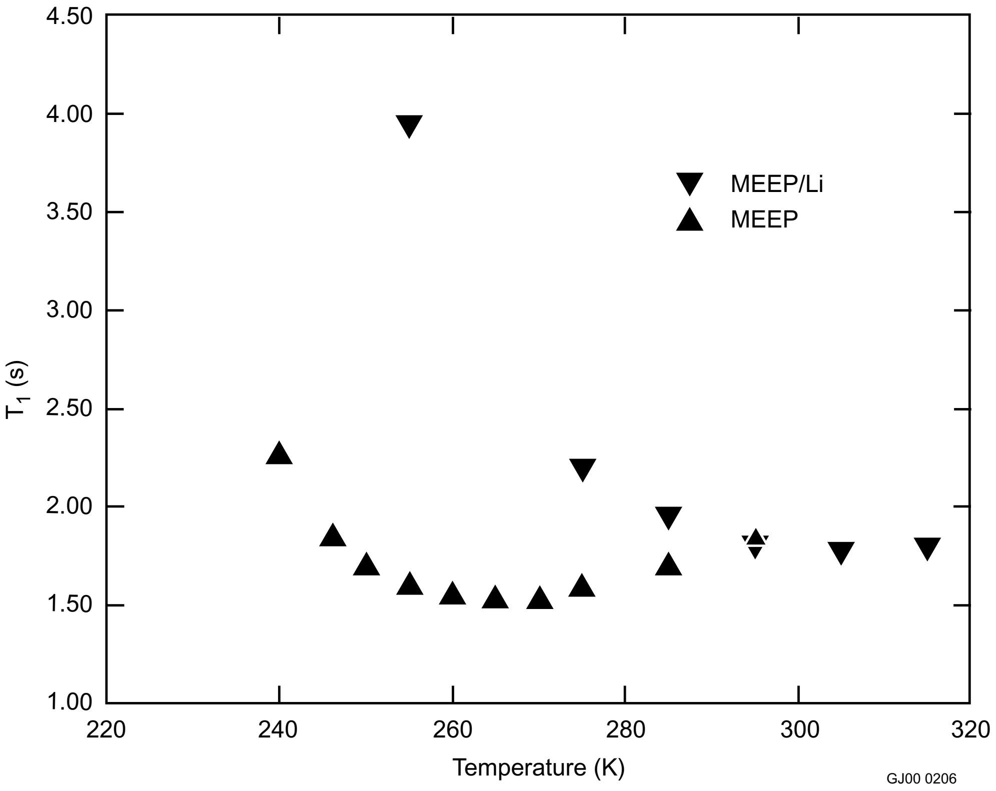

**Figure 7.** $^{31}$P NMR variable temperature $T_1$ graph for $^{15}$N MEEP in $CDCl_3$.

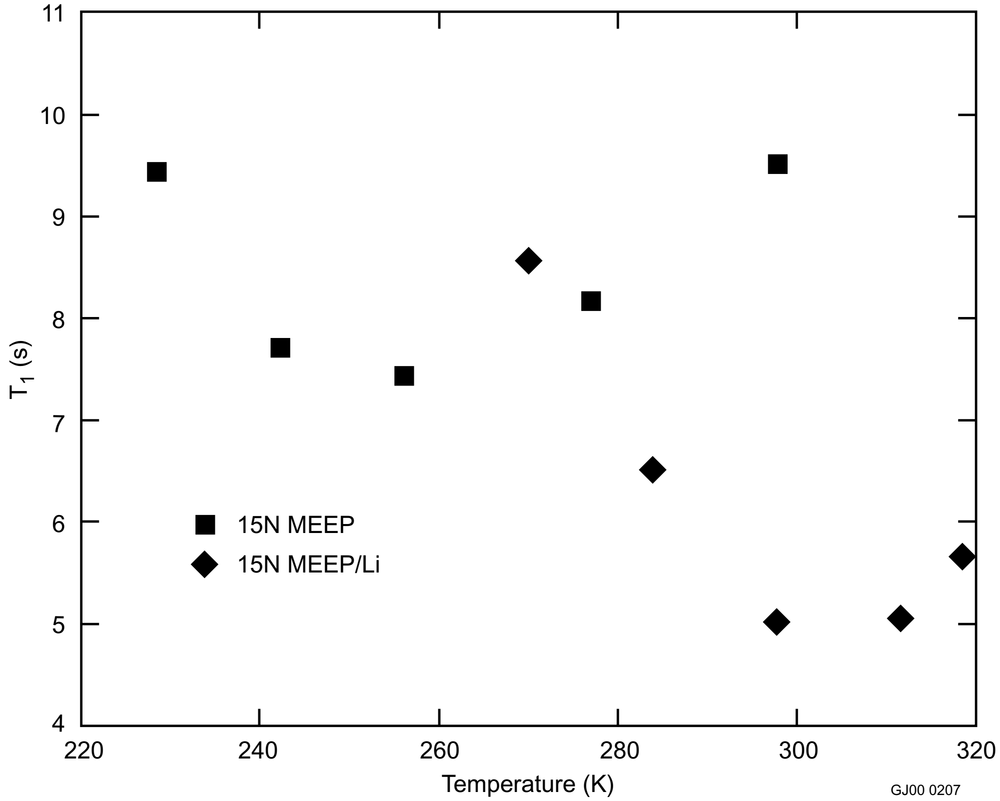

**Figure 8.** $^{15}$N NMR variable temperature $T_1$ graph for $^{15}$N MEEP in $CDCl_3$.

NMR samples of $^{15}N$ MEEP and $^{15}N$ HPP were taken to the Department of Chemistry at the University of Washington to perform experiments on a Bruker DMX 750 NMR spectrometer. The DMX750 has a magnetic field strength of 17.63 Tesla ($^{1}H$ operating frequency of 750 MHz). This work was undertaken to corroborate the $^{1}H$, $^{13}C\{^{1}H\}$, $^{15}N$, and $^{31}P$ NMR chemical shift data that was previously acquired on the Bruker DMX 300WB and to examine some spectral dispersity and coupling data not observable at 7.04 Tesla.

The observable coupling in the $^{1}H$ NMR spectra and the chemical shift changes in the $^{13}C\{^{1}H\}$, $^{31}P$, and $^{15}N$ NMR spectra of $^{15}N$ MEEP after addition of LiOTf in $CDCl_3$ were similar to the previously observed data. However, the $^{31}P$ NMR spectrum of the $^{15}N$ HPP exhibits five separate resonances (only 3 resonances are observed at 7.04 Tesla). Four of the resonances are due to the $^{31}P$ nuclei that have as the attached side chains either 2 methoxyethoxyethoxides (MEE), 1 MEE and 1 methoxyphenoxide (MeOP), 1 MEE and 1 *o*-allylphenoxide (*o-Al*), or 2 MeOP. The fifth resonance is broadened due to a combination of resonances corresponding to $^{31}P$ nuclei that has either 1 MeOP and 1 *o*-Al or 2 *o*-Al. The $^{15}N$ NMR spectrum of $^{15}N$ HPP at 7.04 Tesla is a single very broad resonance ($\Delta\nu_{1/2}$ ~260 Hz). The $^{15}N$ NMR spectrum acquired at 17.63 Tesla exhibits five separate resonances (Figure 9). These resonances are due to the neighboring $^{31}P$ environments (the number of aryloxide side chains versus the number of MEE side chains). When the neighboring $^{31}P$ nuclei have four aryloxides (resonance A), the $^{15}N$ resonance exhibits $^{15}N$-$^{15}N$ and $^{15}N$-$^{31}P$ coupling of 40 Hz. As the number of aryloxide side chains decrease, resonances B to D, the resolution of the resonance decreases. Resonance E, the furthest upfield, has the immediate environment similar to what is experienced in MEEP and therefore the observed chemical shift at 62 ppm is similar. After approximately 40 mol% addition of LiOTf the significant change in the $^{15}N$ NMR spectrum is that the chemical shift of E moves downfield to

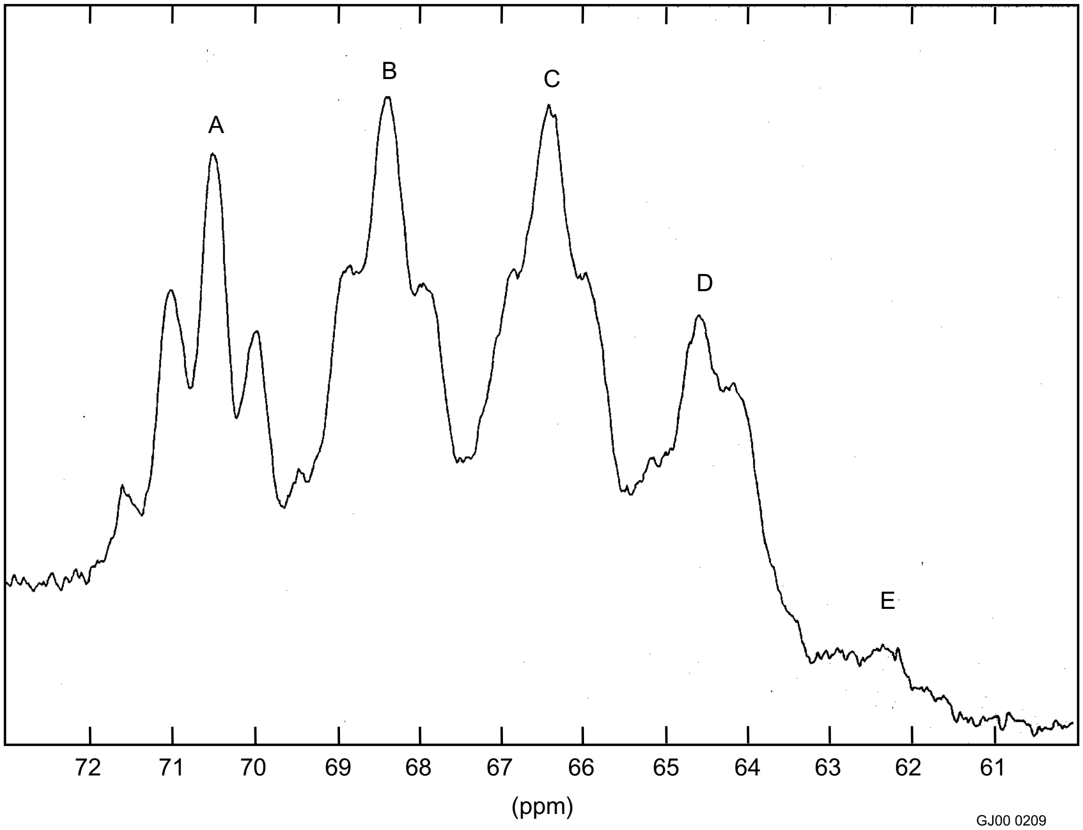

**Figure 9.** $^{15}N$ NMR spectrum of $^{15}N$ HPP in $CDCl_3$.

approximately 63 ppm. This change in chemical shift in the $^{15}N$ NMR spectra is also similar to what is observed for $^{15}N$ MEEP.

# ACCOMPLISHMENTS

## Molecular Composites

1. Further developed and refined synthetic protocols for formation of molecular composites. These included not only synthetic conditions, but also film formation protocols that provide a convenient pathway for adaptation of these materials as membranes for challenging EM relevant applications.

2. Extensive dynamic mechanical analysis of these composites was performed. This has provided information crucial to accurately assessing the potential usefulness and limitations of these materials.

3. Correlated the observed physical properties of phosphazene-containing composites to form the basis for understanding the structure-property relationships in these materials.

4. Extrapolated the structure-property relationships found for phosphazene systems to more conventional all organic polymer systems. Extensive method development was performed to optimize synthetic strategies for organic-based composites.

5. Performed elementary gas transport studies on selected phosphazene-based composites.

## Polymer Morphology

1. Two separate series of poly(dichlorophosphazenes) were successfully synthesized—one uncatalyzed and one catalyzed by elemental sulfur.

2. The above mentioned series of polymers were all characterized by GPC and by laser light scattering molecular weight determination experiments. This information was translated into a better understanding of the kinetics of the ring-opening polymerization in solventless systems and a better understanding of how to control skeletal morphology.

3. Multinuclear NMR studies of specially synthesized NMR active ($^{15}N$) polyphosphazenes were carried out, both at low field (7.04T) and high field (17.63T). These studies were performed with and without ionic dopants and were used to probe the importance of the influence of the polymer skeleton during transport of such species.

# REFERENCES

1. B. M. Novak, “Hybrid Nanocomposite Materials-Between Inorganic Glasses and Organic Polymers,” *Advanced Materials*, 5(6), 1993, 422–433.

2. B. K. Coltrain, W. T. Ferrar, C. J. Landry, T. R. Molaire, and N. Zumbultadis, “Polyphosphazene Molecular Composites 1. In Situ Polymerization of Tetraethoxysilane,” *Chem. Mater.,* 4, 1992, 358.

3. Coltrain, B. K.; Ferrar, W. T.; Landry, C. J. T.; Molaire, T. R.; Schildkraut, D. E.; Smith, V. K., "Polyphosphazene Molecular Composites. II.," *Polymer Preprints (ACS),* 34 (1), 1993, 266.

4. Guglielmi, M.; Brusatin, G.; Facchin, G.; Gleria, M., "Poly(organophosphazene)s and the Sol-gel Technique" *Appl. Organometal. Chem*., 13, 1999, 339.

5. Pope, J. A.; Mackenzie, J. D.; "Sol-Gel Processing of Silica," *Journal of Non-Crystalline Solids*, 87(3), 1986, 185–198.

6. Harrup, M. K.; Stewart, F. F., "Improved Method for the Isolation and Purification of Water-Soluble Polyphosphazenes" *J. Appl. Poly. Sci.*, 2000, 78(5), 1092.

7. Harrup, M.K.; Wertsching, A. K.; Stewart, F.F., "Phosphazene Silicate Nanocomposites. A Survey of Materials Properties and Synthetic Methods Using New Catalysts." *PM:SE Preprints (ACS)*, 2000, 82, 307.

8. Sennett, M. S.; Hagnauer, G. L.; Singler, R. E.; Davies, G.; "Kinetics and Mechanism of the Boron Trichloride Catalyzed Thermal Ring Opening Polymerization of Hexachlorocyclotriphosphazene in 1,2,4-Trichlorobenzene Solution" Macromolecules, 1986, 19, 959.

9. Mujumdar, A. N.; Young, S. G.; Merker, R. L.; Magill, J. H.; "A Solution Study of Polymerization of Polyphosphazenes" *Macromolecules*, 1990, 23, 14.

10. Sun, Y.; Lin, C.; Chen, Y.; Wu, C.; *J. Mem. Sci.*, 1997, 134 , 117.

11. Blonsky, P. M.; Shriver, D. F.; Austin, P.; Allcock, H. R. "Polyphosphazene Solid Electrolytes," *Journal of the American Chemical Society* 1984, 106, 6854-6855.

12. Allcock, H. R.; Napierala, M. E.; Olmeijer, D. L.; Best, S. A.; Merz, K. M. "Ionic conduction in polyphosphazene solids and gels: C-13, P- 31, and N-15 NMR spectroscopy and molecular dynamics simulations" *Macromolecules* 1999, 32, 732-741.

13. Krajewski-Bertrand, M.-A.; Lauprêtre, F.; Monnerie, L., *Dynamics of Solutions and Fluid Mixtures by NMR*; John Wiley & Sons: Chichester, 1995.

14. Desrosiers, P. J.; Cai, L. H.; Lin, Z. R.; Richards, R.; Halpern, J. "Assessment of the T1 Criterion for Distinguishing between Classical and Nonclassical Transition-Metal Hydrides - Hydride Relaxation Rates in Tris(Triarylphosphine)Osmium Tetrahydrides and Related Polyhydrides," *Journal of the American Chemical Society* 1991, 113, 4173-4184.

15. Luo, X. L.; Crabtree, R. H., "Testing the T1 Method - a Comparison of T1(Min) and Structural Data," *Inorganic Chemistry* 1990, 29, 2788-2791.

# Adsorption and Absorption Materials for Molecular Separations

**Glenn A. Moore, Phil Martellaro, Tammy Reichert, and Eric Peterson**

## SUMMARY

Our research during FY 2000 focused primarily on processing and characterizing high surface area mesoporous silicas and precipitated copper sulfides. These materials are being developed to provide a cost effective way to capture heavy metal and radionuclides in solid and liquid waste forms for DOE's Environmental Management (EM) program. During FY 1999, we demonstrated enhanced mercury reactivity for nanocrystalline copper sulfide powders and oxalic acid-treated copper sulfide powders. During FY 2000, we prepared and characterized novel mesoporous silicas and nanocrystalline zirconia plasma spray coatings, investigated key copper sulfide synthesis parameters, and conducted ionic mercury reactivity experiments directed at elucidation of the reaction mechanism for $Hg^{2+}$ with $Cu_2S$.

As part of our efforts we prepared mesoporous silicas using precipitation and sol-gel techniques and surfactant templating agents; prepared and characterized silicas that have replicated lamellar, hexagonal, and cubic pore structures; and prepared copper sulfides using precipitation techniques with cationic surfactant cetyltrimethylammonium bromide (CTAB) serving as a particle size mediating agent.

## Mesoporous Silicas

Mesoporous materials are of interest as catalysts, molecular sorbents, chromatograph separation media, and separation membranes. Mesoporous templating of silica using liquid-crystal-forming surfactants was discovered by scientists at Mobil Oil Corporation in 1992.[1] This discovery has led to a new class of materials and associated descriptive nomenclature. Mobil's original mesoporous material having a regularly ordered hexagonal pore arrangement was designated (Mobil Composition of Matter) MCM-41. Figure 1 shows a schematic diagram of the structural evolution of the MCM-41 hexagonal mesostructure.[2] Temporal variation of the condensing silicate species' charge density is responsible for the lamellar to hexagonal mesostructure transformation. Other distinct mesoporous materials, having distinct morphologies, include hexagonal mesoporous silica (HMS) where textural or aggregation based packing structures evolve and mesoporous silica units (MSU) materials having disordered channels.

Our FY 2000 effort in this area included manipulation of the surfactant templating process in order to form hybrid silica materials containing cyclodextrins (CDs). CDs are cyclic oligosaccharides made up of six, seven, or eight glucose residues per molecule; referred to as $\alpha$-, $\beta$- and $\gamma$- CD respectively (Figure 2).[3] These molecules form a toroidal/hollow truncated cone structure containing a central hydrophobic core and a hydrophilic exterior.

CDs have been used extensively to increase the solubility, dissolution rate, and bioavailability of poorly water-soluble drugs, as well as increase the stability of labile drugs.[4] These properties result from the inclusion of the drugs within the central hydrophobic cavity of the CDs. The inner diameter and depth of the $\beta$-CD central cavity is 7 Å resulting in a volume of 270 Å$^3$. The complexation of a CD host and a guest compound (drugs or dyes) is a dynamic process involving Van der Waals dipole-dipole and hydrophobic interactions. We envision two sorbent capture schemes involving CD-silica hybrid materials: functionalized pores/cavities in the silica matrix, and guest-host sorbents based on incorporated

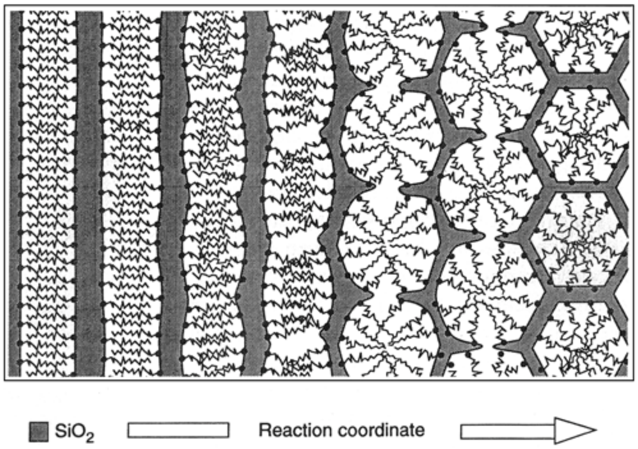

**Figure 1.** Schematic diagram of the lamellar to hexagonal mesophase structure evolution in the surfactant-templated sol-gel process.[2]

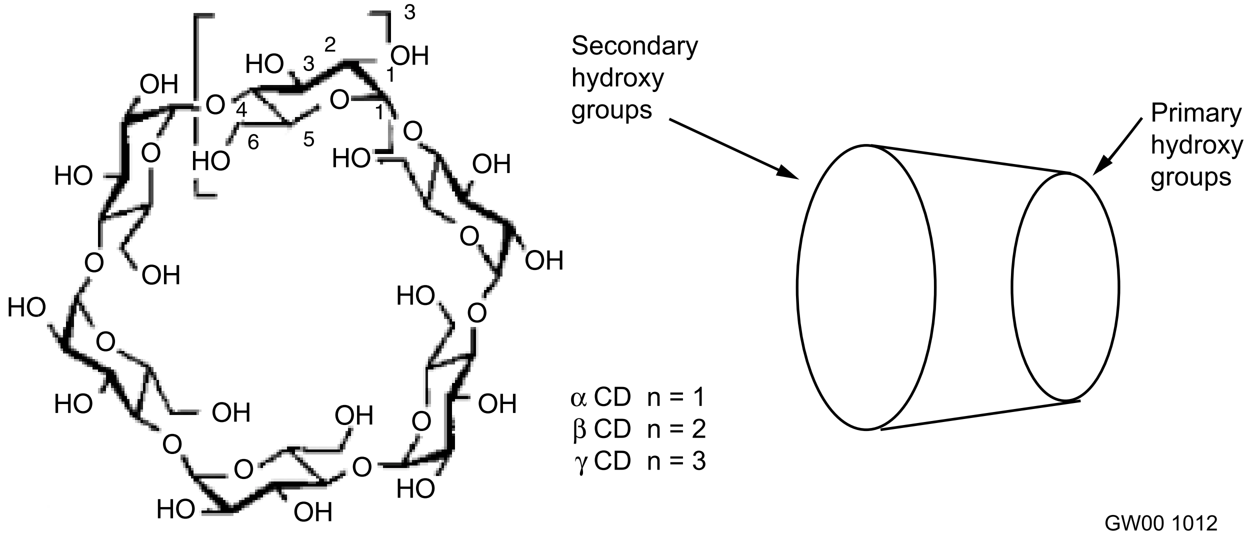

**Figure 2.** Diagram of CD chemical structure and molecular geometry.[3]

CDs.

Processing of mesoporous silicas and their organic-inorganic hybrid counterparts is accomplished using the sol-gel process. The sol-gel process consists of the acid or base catalyzed hydrolysis and condensation of a metal alkoxide, e.g., tetraethyl orthosilicate (TEOS), to form an amorphous metal oxide network "gel"; in this case silica. In our studies templated mesoporosity was imparted via the incorporation of a cationic surfactant, e.g., cetyltrimethyl-ammonium bromide (CTAB). The CDs investigated included the "parent CDs" alpha, beta, gamma, and 2-hydroxypropylated β-CD (HPBCD), a chemically modified CDs purchased from Wacker Biochem. Stable mesoporous powders for use in removing the surfactant and CD constituents were obtained by pyrolysis of gels in air at 550°C. The resulting mesoporous powders were characterized for surface area, pore size distribution, and mesophase composition.

Three distinct processing schemes were experimentally investigated: (1) gel powder precipitation using low surfactant concentration base catalyzed TEOS sols, (2) thin film formation via spin coating of a acid hydrolyzed tetramethyl orthosilicate (TMOS) sols, and (3) gel powder preparation via spray drying of acid hydrolyzed TMOS sols.

## Precipitated Mesoporous Silica Powder

Our investigation of the gel powder precipitation scheme involved the method reported by Cai et al.[6] for producing MCM-41 silica. Of interest are four samples prepared using the $H_20:NH_4OH:CTAB:TEOS$ molar ratios shown in Table 1. In sample BP-4, an equimolar HPBCD:CTAB addition was made. Precipitated powders were water rinsed, air dried at RT-70ºC, and calcined in air at 550ºC for 4 hours to remove the templating agent CTAB.

The calcined precipitate powders were characterized for surface area and pore size distribution using nitrogen adsorption analysis and mesoporous phase analysis using X-ray diffraction (XRD) and transmission electron microscopy (TEM). Figure 3 is a TEM micrograph showing a typical precipitated particle. Mesopores and hexagonal faceting are apparent. The surface area of the precipitate powders ranged from 1,032 to 1,589 $m^2/g$. The Kurk, Jeromiec, Syari (KJS) method was applied to the nitrogen adsorption data in order to calculate pore size distributions for the powder.[7] The nitrogen adsorption isotherms and the calculated $W_{JKS}$ pore distributions are shown in Figure 4. When HPBCD was present in the sol formulation (sample BP-4), an asymmetric pore size distribution was produced. This result infers that a portion of the HPBCD was included in the CTAB liquid crystal phase and served as a swelling agent. Thus, it has been demonstrated that hybrid mesoporous silicas can be prepared using the

**Table 1.** Formulation and characterization data of basic precipitate (BP) samples.

| Sample | Formulation Molar Ratio $H_20:NH_4OH:CTAB:TEOS$ | Characteristic HKL (100) d-spacing (nm) | Effective Pore Diameter $W_{KJS}$ (nm) | BET[a] Surface Area ($m_2/g$) |
|---|---|---|---|---|
| BP-1 | 422:26.0:0.1:1.0 | 3.37 | 3.06 | 1465 |
| BP-2 | 397:30.4:0.1:1.0 | 3.48 | 3.08 | 1032 |
| BP-3 | 437:26.4:0.1:1.0 | 3.16 | 2.83 | 1589 |
| BP-4 | 437:26.4:0.1:1.0b | 3.48 | 3.15 | 1145 |

---

a. Brunauer, Emmett, and Teller.

b. An equimolar HPBCD:CTAB addition was also made.

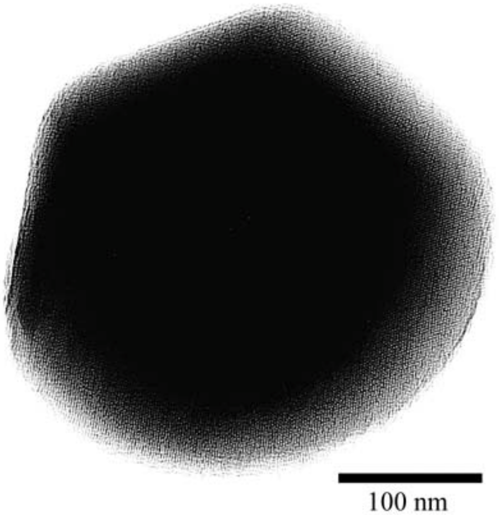

**Figure 3.** TEM micrograph of a precipitated mesoporous silica particle. Hexagonal particle morphology and structured porosity at the particle's perimeter are evident.

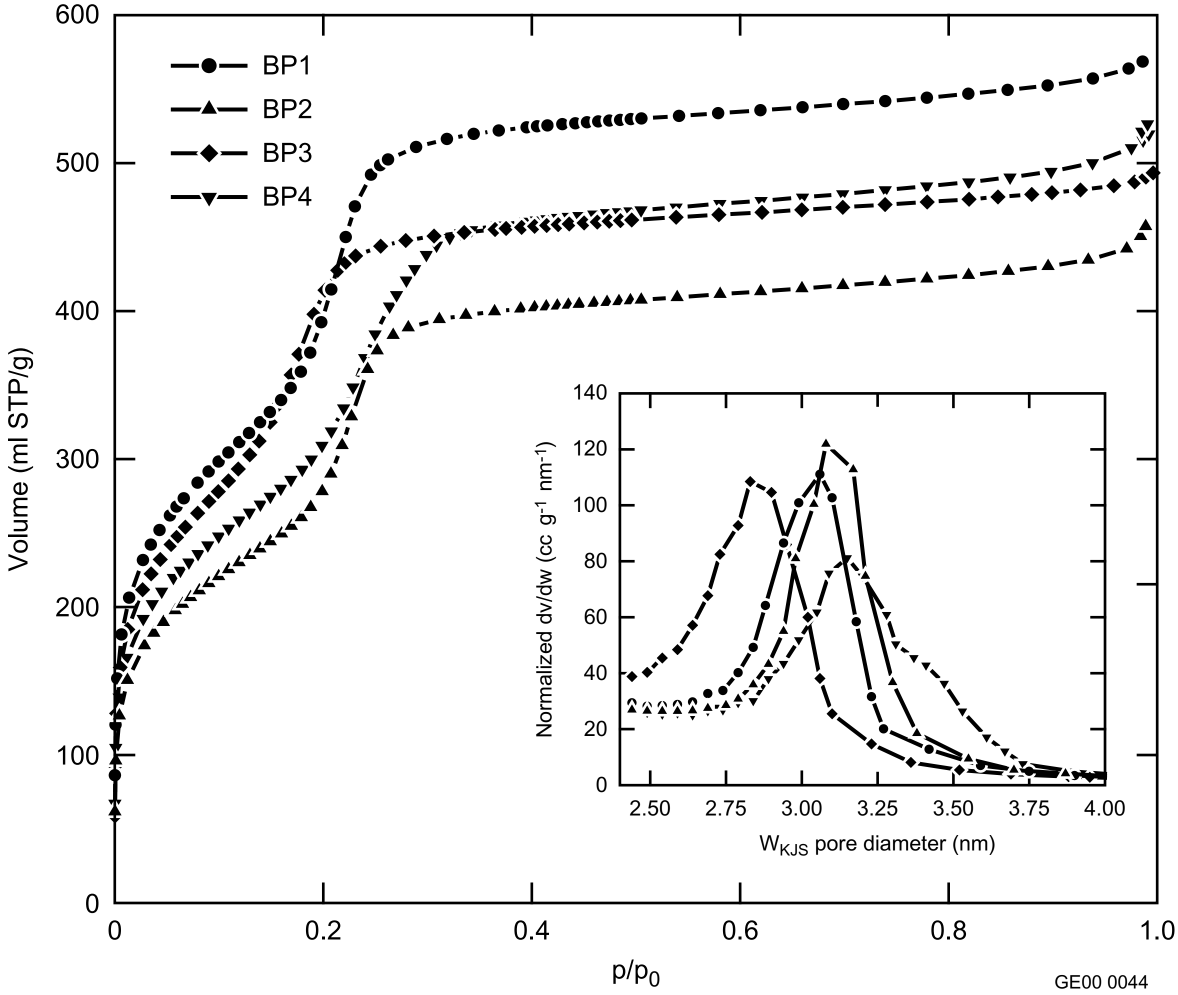

**Figure 4.** BET adsorption isotherms and the corresponding calculated $D_{KJS}$ pore diameter distributions.

acid catalyzed TEOS:CTAB scheme. Future studies will investigate the influence of CD-concentration on templated porosity and the use of nonionic surfactants.

## Mesoporous Films

Mesoporous thin films, 0.5 to 1.0 µm thick, were produced on silicon and borosilicate substrates via spin coating at 3,000 rpm. The acid catalyzed sol formulation scheme use was taken from Ogawa et al.[8] The advantage of this film preparation scheme being the direct formation of lamellar, hexagonal, or cubic ((Pm3n) films by variation of the TMOS (tetramethyl orthosilicate):surfactant (cetyltrimethylammonium chloride CTAC) ratio in the range of 2:1 to 8:1. Table 2 lists the sol formulations investigated and the resulting primary mesophase observed. Film samples were calcined at 550°C for 3 hours to remove the template prior to characterization.

**Table 2.** Mesoporous thin film formulations and resulting primary mesophase formed.

| Sample | Formulation Molar Ratio H20:CTAC:TMOS | Primary Mesophases Observed via TEM |
|---|---|---|
| AF-00, AF-01, AF-6 (ACF-1) (UT-2, -3) | 184:1.0:8.1 | Hexagonal, cubic |
| AF-02 (ACF-2) | 176:1.0:4.1 | Hexagonal |
| AF-5 (UT-1) (ACF-3) | 187:1.0:9.73 | Hexagonal |
| AF-7 (UT-4) (ACF-4) | 184:1.0:8.1 (HPBCD:0.5) | Amorphous |

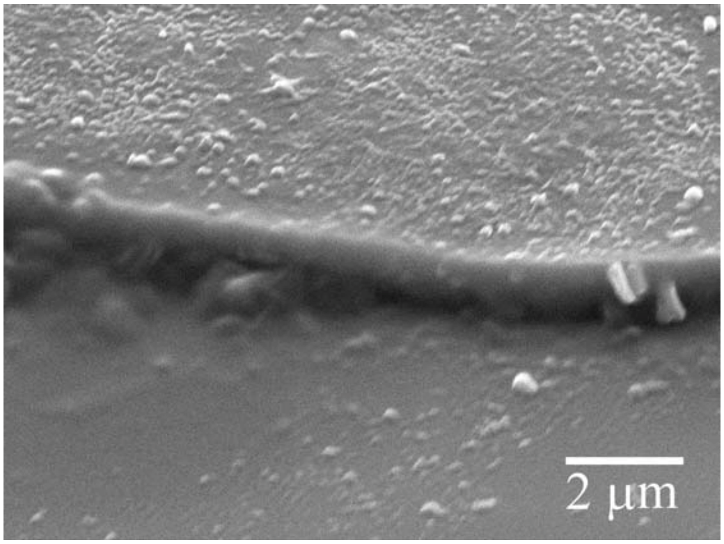

**Figure 5.** SEM micrograph of a mesoporous calcined film, top portion, on a borosilicate substrate.

Scanning electron microscopy (SEM) analysis showed the prepared films to be 0.5 to 1.0 mm thick and crack-free. Figure 5 shows a SEM micrograph of a ~1.0-mm-thick mesoporous film on a borosilicate substrate.

Mesoporous film samples were prepared for transmission electron microscopy (TEM) by scraping a portion of a film with a razor blade and transferring film fragments to a carbon coated TEM grid. In the case of a film prepared using an 8:1 TMOS:CTAC sol, a Pm3n cubic mesostructure was expected, however, TEM analysis revealed a mixture of lamellar, hexagonal, and cubic pore ordering. Figure 6 shows two TEM micrographs from an 8:1 film sample. In Figure 6a, the pores (white spots) are arranged in a cubic array; in Figure 6b, we observe a pore arrangement characteristic of the lamellar-to-hexagonal transition.

The observed mesostructure morphology variation is thought to be a consequence of the stoichiometric gradients created during the drying process. As methanol/water evaporate from a sol, the TMOS:(methanol/water) ratio increases; at the same time, the film consolidates in the direction perpendicular to the substrate surface. Additionally, the film can be viewed as having three graded regions: a solid/sol-gel interface region, a core sol-gel region, and an air/sol-gel interface region. It is surmised that as the spin coating/drying process takes place, stoichiometric and interfacial considerations produce mesostructure morphology variations in the film. At some critical point in the drying process each mesostructure type looses its ability to reconfigure/evolve due to viscosity constraints. Our TEM characterization results capture the "established" temporal mesostructure evolution sequence proposed by Monnier et al[2]; namely, transitional microstructures associated with the lamellar-to-hexagonal-to-cubic liquid crystal phase evolution. As the cubic mesostructure, having interconnected porosity, is most desirable for the envisioned molecular sorbents, we are working to optimize our processing conditions .

In pursuit of our aim to develop a processing scheme for incorporating CDs in the silica wall structure of mesoporous materials, we investigated the addition of hydroxypropyl β-cyclodextrin (HPBCD) at a level of 0.5 HPBCD:CTAC in a 8:1 TMOS:CTAB batch (ACF-4). Good film forming

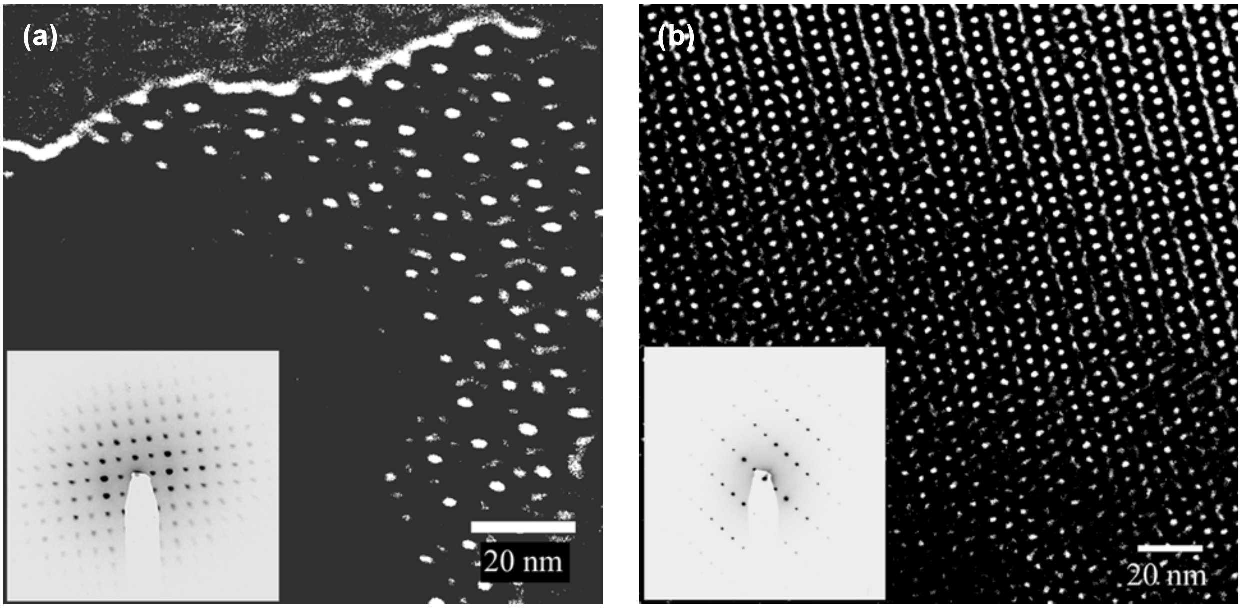

**Figure 6.** TEM micrographs from a mesoporous thin film: (a) cubic mesostructure, (b) lamellar-hexagonal transition region. Inlaid are the selected area diffraction patterns.

qualities were observed, however, the films produced were strictly amorphous. Thus, the HPBCD modifier addition resulted in the elimination of mesoporosity. It is known that CTAB forms a 1:1 inclusion complex with β-CD and that the critical micelle concentration (CMC) of the CTAB/B-CD (~$2 \times 10^{-3}$ mol/L) complex is approximately twice that of just β-CD (0.92 × 10-3 mol/L). In this case, the CTAC surfactant concentration is approximately two orders of magnitude above the CMC in pure water. At this time, our TEM characterization results indicate that the addition of HPBCD in a 1:2 ratio with the templating surfactant results in a suppression of CTAC micelle formation during the sol to gel transition. Thus, in order to form CD-mesoporous hybrid materials using this approach, we need to better understand the interactions of the CD with the templating agent and hydrolyzed silicate species.

## Spray Dried Mesoporous Powders

In the course of developing mesoporous powders for pollutant separation and sequestration applications, the need for industrially scalable process schemes should not be overlooked. As such, we investigated the formation of mesoporous powders via spray-drying. The spray drying process is an established "scalable" process widely used in the ceramics and specialty chemicals industries. As the name implies, spray drying involves spray atomization of a solution or slurry and in-flight drying of the droplets. This process typically produces spherical particles with an average diameter of 10 to 100 μm. Spray dried powders have several advantages over submicron precipitate powders, these include reduced static charging, less nuisance dust, good flowability, and high packing efficiency. These powder-media attributes lend themselves to packed column, fluidized bed, and pressed media preparations.

We investigated the applicability of TMOS:CTAC sol formulations, discussed in the previous section, to the spray drying process. Comparable with spin coating, the spray drying process involves rapid evaporation of a sol's free liquid contents and the rapid coalescence of gel network forming species. Here, heat and/or reduced pressure were used to control the drying rate. A series of experiments were conducted using the sol formulations listed in Table 3, a Sono-Tek 48 kHz ultrasonic spray nozzle, and the 4-cm-ID by 50-cm-long tube assembly shown is Figure 7. Spray dried powder was calcined at 550°C for 3 hours in air to remove the templating agent.

Spray dried powders were characterized for surface area and pore size distribution via nitrogen adsorption, mesophase via XRD, pore morphology via TEM, and particle morphology via SEM. As can be seen in Figure 7, two types of particle morphologies were obtained depending on the experimental

**Table 3.** Spray drying formulation, process conditions, and material properties of spray dried mesoporous powders.

| Sample | Molar Ratio H20:CTAC:TMOS | Temp (°C) | BET Surface Area ($m^2$/g) | Pore Dia. (nm) | Mesophase |
|---|---|---|---|---|---|
| UT-1 | 187:1.0:9.73 | 40-50 | 737 | 3.3[a] | hexagonal |
| UT-2 | 184:1.0:8.1 | 70-80 | 777 | 3.2[a] | hexagonal |
| UT-3 | 184:1.0:8.1 | 90-110 | 866 | 3.1[a] | hexagonal |
| UT-4 | 184:1.0:8.1(HPBCD :0.5) | 80-100 | 444 | — | amorphous |

a. The FWHM of the $W_{JKS}$[7] pore diameter distribution was 0.4 nm.

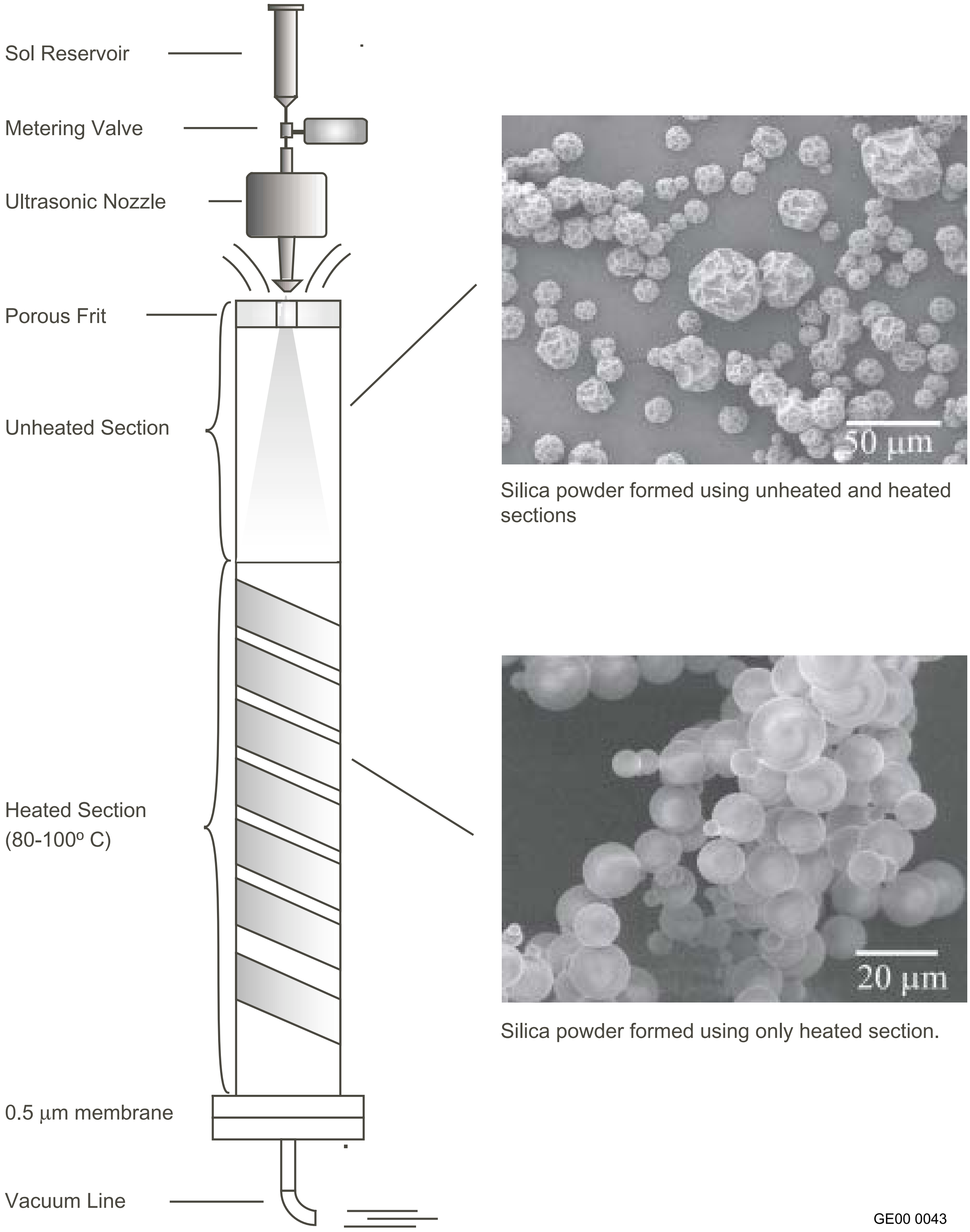

Silica powder formed using unheated and heated sections

Silica powder formed using only heated section.

**Figure 7.** Diagram of ultrasonic spray drying apparatus used in preparing mesoporous powders. The two particle morphology types obtained are shown in the corresponding SEM micrographs.

configuration. Smooth spherical particles in the 5 to 20-um range were obtained when the sol was directly sprayed into the heated portion of the drying tube. When a dual-rate drying configuration was used (i.e., an unheated riser tube placed above the heated tube section), pleated particles 5 to 50 um in diameter were produced.

A summary of the materials characterization data for the spray dried powders is shown in Table 3. In samples UT-1, 2, and 3 hexagonal mesostructures were observed. A typical pore morphology arrangement for these powders is shown in Figure 8. Distinct mesoporous domains of the hexagonal type are apparent, much like those in a dense polycrystalline ceramic material. However in this case the domains consist of ordered pore regions. The UT-1, 2, and 3 powders showed a notable decrease in pore diameter of 3.3 to 3.1 nm and an increase in surface area of 737 to 866 $m^2/g$, with an increasing drying temperature of 40 to 110°C. The breadth of the JKS pore size distribution (0.4 nm FWHM) was consistent throughout the experimental series.

In the case of sample UT-4, a 0.5 molar equivalent addition of HPBCD was made to the sol formulation of UT-1 and 2. As was the case for films prepared using this formulation, no mesoporosity developed. The resulting amorphous, microporous UT-4 powder had approximately half the surface area of the other three samples.

This experimental investigation demonstrated the applicability of the spray drying process with acid catalyzed TMOS:CTAC sols. Further, the pore size of these mesoporous powders can be controlled via the temperature and reduced pressure “drying rate” conditions employed. While cubic mesostructure was not observed in this initial spray drying study, the processing method appears very favorable to processing of mesoporous powder media.

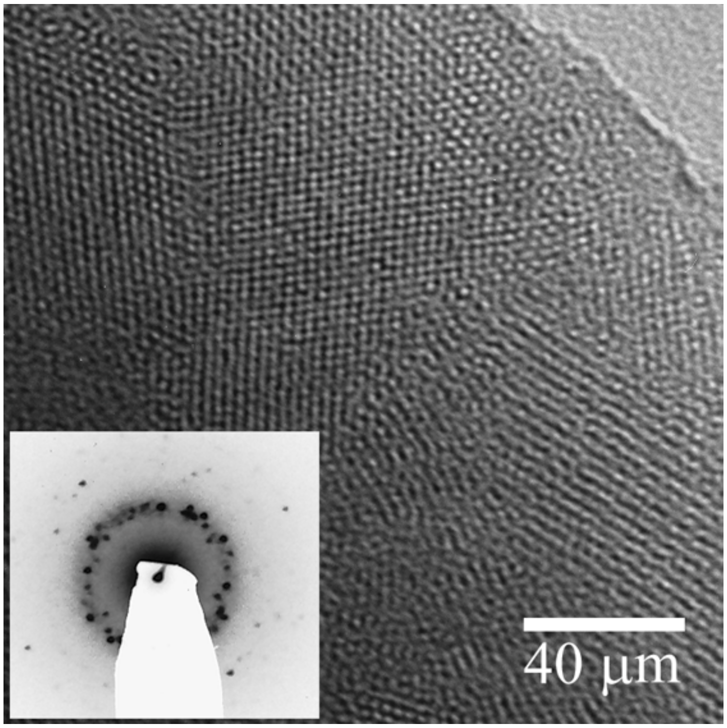

**Figure 8.** TEM micrograph of spray dried particle having mesoporous domain structure. Selected area diffraction pattern, inlay, confirms polymesoporous morphology.

## Plasma Spray Deposition of Zirconia Layers

An experimental effort was initiated for producing porous zirconia nanoparticulate coatings on porous substrates. Previous work at the INEEL demonstrated that zirconium acetate can be converted to zirconia nanoparticle in an argon plasma when oxygen serves as the ceramic precursor carrier gas. Our experimental objective here was to determine if the zirconia nanoparticles could be controllably deposited on a porous substrate to form a coherent, defect free, controlled porosity membrane. A series of deposition experiments were performed using porous stainless steel substrates and a 2 kW plasma torch system configured for injection of a zirconium acetate/oxygen mixture. X-ray diffraction was used to confirm that a nanocrystalline zirconia layer was deposited on the porous stainless-steel substrate. However, the coatings were not physically robust and could be easily removed from the substrate with light scratching. SEM analysis showed the zirconia coating to be ~100 μm thick, with minimal micron-scale pores (see Figure 9). The observed gap between the coating and substrate may have been produced during the deposition process, as a result of thermal expansion mismatch stresses when the sample was cooled, or during the SEM sample polishing operation. After these initial experiments, it was concluded that alternative coating processes, i.e., sol spin coating, would be more amenable to the development of controlled micro and mesoporosity coatings. Thus, the activity was discontinued.

## Copper(II) Sulfide Particle Size Control Study

Our previous work demonstrated the advantage of nanocrystalline copper sulfide for capture of mercury vapor. When the surfactant CTAB was used to mediate the particle size of precipitated Cu(II) sulfide (CuS covellite), a five fold increase in the Hg(0) capture rate resulted.[9,10] In the previous study, CuS was precipitated upon addition of an $H_2O$/ethanol solution of $Cu(NO_3)2.3H_2O$ to an aqueous solution of $Na_2S.9H_2O$ containing the surfactant CTAB. When a 1:1 molar ratio of CTAB:$Na_2S.9H_2O$ was used, and the overall CTAB concentration being 0.13 M, a median particle size (MPS) of 250 nm was obtained. This compares to a median particle size of ~2,500 nm for commercial grade CuS.

To investigate the effect of surfactant concentration on CuS particle size, a series of synthesis experiments were conducted using two different solvent systems, i.e., water and a 50/50 mixture of water

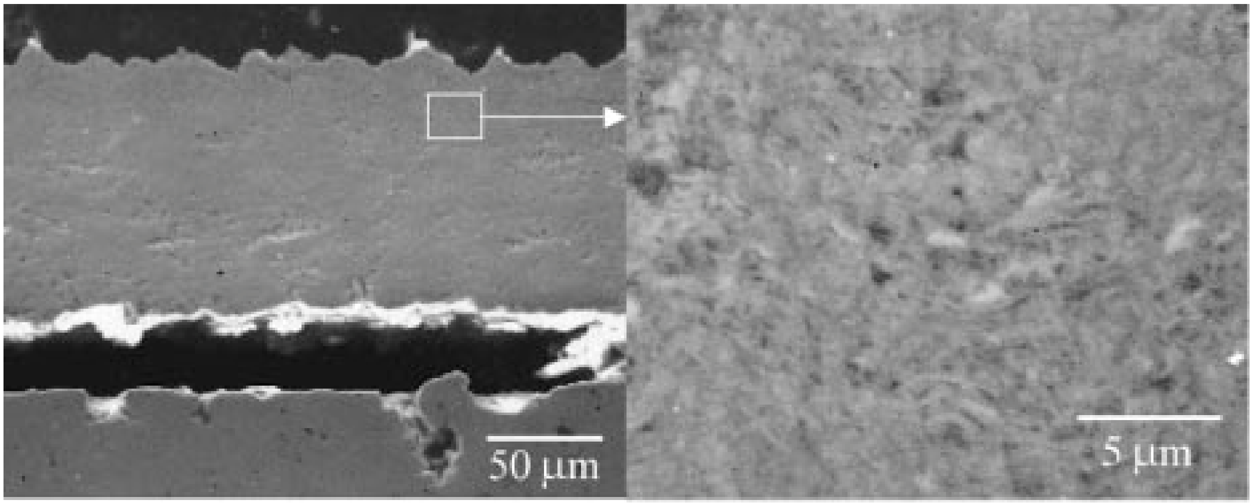

**Figure 9.** SEM micrographs of plasma spray deposited zirconia film on porous steel substrate. (crossection).

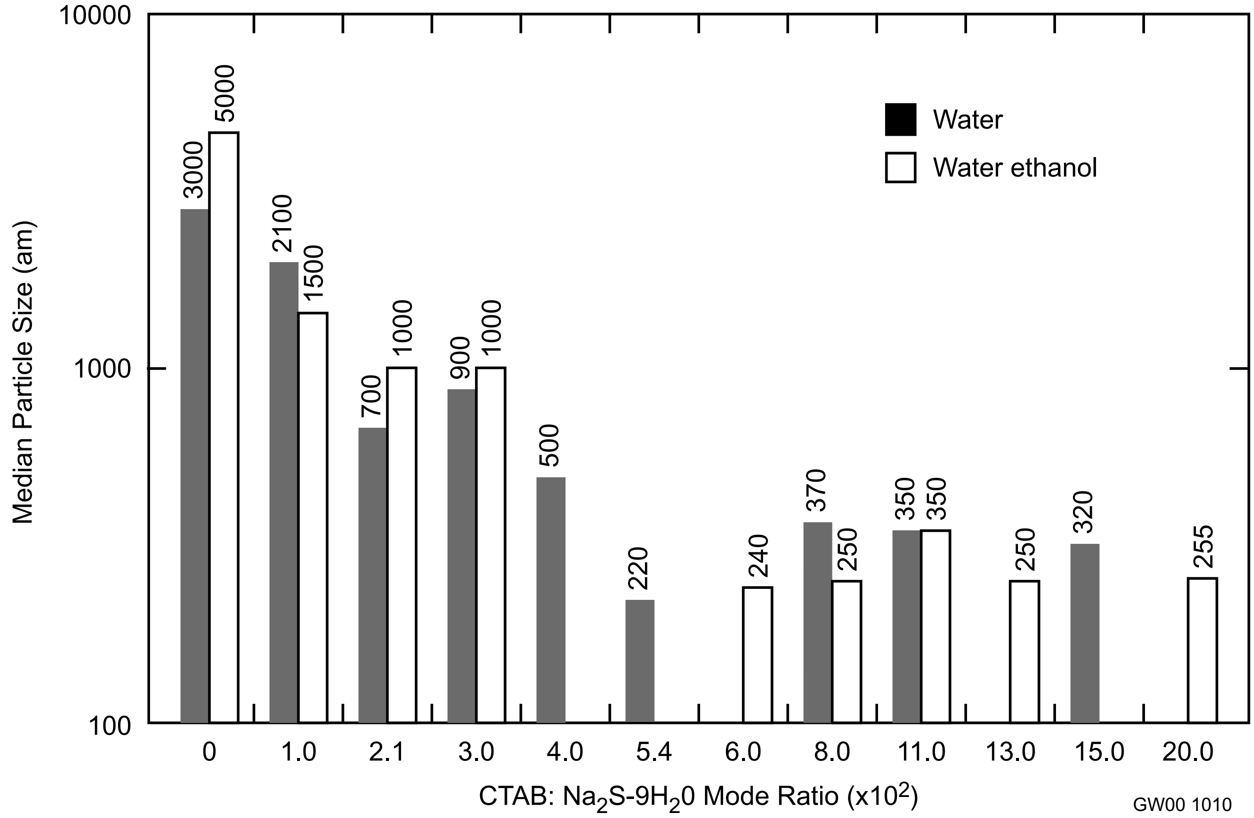

**Figure 10.** Median particle size distribution for CuS synthesized in water and water/ethanol solvent systems.

and ethanol. For the aqueous based experiments, the CTAB:$Na_2S{\cdot}9H_2O$ molar ratio was varied over the range of 0.01 to 0.2. The precipitate was collected via vacuum filtration, water rinsed, and air dried. Particle size analysis was performed using a Beckman-Coulter N4 particle size analyzer. The median particle size results for these analyses are shown in Figure 10.

The MPS of CuS precipitated without CTAB present was ~5,000 nm. The median particle size of the precipitate rapidly decreased from 1,500 to 250 nm as the CTAB:$Na_2S{\cdot}9H_2O$ ratio was increased from 0.01 to 0.05. For this water based series, unimodal particle size distributions were observed. It was determined that a CTAB:$Na_2S{\cdot}9H_2O$ ratio greater than 0.05 did not further reduce particle size. The overall CTAB concentration associated with the 0.01 to 0.05 CTAB:$Na_2S{\cdot}9H_2O$ ratio is $1\text{-}5 \times 10^{-3}$M. The critical micelle concentration (CMC) of CTAB in water is $\sim 1 \times 10^{-3}$M. The formation of surfactant micelles or microemulsions are known to influence precipitation reactions.[11,12] Thus, from this data, we conclude that CTAB micelles serve as nucleation sites for the precipitate particles and that the competing particle nucleation and growth reactions reach a balance as the CTAB concentration approaches approximately five times the CMC; resulting in a MPS of ~250 nm thereafter.

Likewise, a CTAB:$Na_2S{\cdot}9H_2O$ molar ratio in the range of 0.01 to 0.15 was investigated for the 50:50 water:ethanol solvent system. The median particle size analysis results are also shown in Figure 10. The MPS for CuS precipitate prepared without CTAB was determined to be 3,000 nm, two thirds of that measured in the corresponding water-based sample. Otherwise, with respect to the MPS, the same decreasing particle size trend with increasing surfactant concentration was observed, up to a CTAB:$Na_2S\cdot 9H_2O$ ratio of 0.05. The particle size distribution data for the water:ethanol series was distinguished from the water based data in that bimodal distributions were obtained.

For samples having a MPS of ~250 nm, approximately 20 to 30% of the particles were in the 800 to 900 nm size range, and the remaining fraction of particle distributed in the 150 to 200 nm region. At this time, an explanation for the bimodal precipitate formation has yet to be established.

## Oxalic Acid Treatment of Copper(II) Sulfide

In our previous work, it was demonstrated that CuS treated with an oxalic acid solution had a 2× mercury vapor capture rate increase.[4,5] Initially, it was suggested that the effect dealt with enhanced scission of the metal-sulfur bond.[11,12] We performed particle size and surface area analysis on commercial grade CuS samples before and after treatment with an oxalic acid solution. Our results indicate that the acid treatment results in a 4× CuS surface area increase (1.0 to 4.0 $m^2/g$) and a ~4× reduction in mean particle size (~2,500 to 600 nm). It is suggested from these measurements, that the oxalic acid serves as an agent for deagglomeration of the layered CuS particles without appreciable sulfide dissolution. Thus, the observed 2× increase in the mercury vapor sorption rate is attributed to the 4× increased in surface area provided by the oxalic acid treatment.

## Reaction Study of Copper(I) sulfide with Ionic Mercury

A series of experiments were conducted in order to establish the mechanism of ionic mercury ($Hg^{2+}$)capture by $Cu_2S$ in acidic, aqueous solution. A series of $Hg^{2+}$ sorption experiments were conducted at three different temperatures (20, 30, and 40°C) in order to determine the thermodynamic parameters of the sorption process in acidic media (pH=1) containing 300 ppm of $Hg^{2+}$. For each temperature series, 11 samples of $Cu_2S$(10-33 mg) were stirred in the ionic $Hg^{2+}$ solutions for 24 hours. The residual $Hg^{2+}$ concentration in the solutions was analyzed using Inductively Coupled Plasma-Atomic Emission Spectroscopy (ICP-AES) and the equilibrium coefficient for the reaction, $K_D$, was calculated. Solid constituents of the reaction were analyzed using Atomic Absorption (AA) spectrometry and XRD. The results of which established that the $Hg^{2+}$ was removed via precipitation of HgS. The ICP-AES results revealed that, in most cases, the quantity of $Hg^{2+}$ removed directly corresponded with the quantity of dissolved sulfide ion in the final solutions; as calculated from the quantity of dissolved copper in solution. This reaction is shown in Reaction (1).

$$Cu_2S \xrightarrow{\text{Dissolution}} 2Cu^{2+} + S^{2-} + Hg^{2+} \xrightarrow{\text{Precipitation}} HgS + 2Cu^{2+} \qquad \text{Reaction (1)}$$

Formation constants were calculated from the $Hg^{2+}$ equilibrium concentration data obtained via the ICP-AES analysis. The enthalpy of reaction was determined to be +147kJ/mole as derived from the van’t Hoff plot shown in Figure 11. The $Cu_2S$ dissolution values measured in these experiments are within 20% of those reported in the literature.[15] The positive slope of the van’t Hoff plot line is an indication that nearly all the $Hg^{2+}$ is removed by precipitation and not by an endothermic sorption process. The magnitude of the reaction enthalpy is exemplified by the fact that the formation of HgS would give some negative contribution (-50kJ/mole) to the overall reaction enthalpy however, its magnitude is small compared to the large positive enthalpy for dissolution of $Cu_2S$.

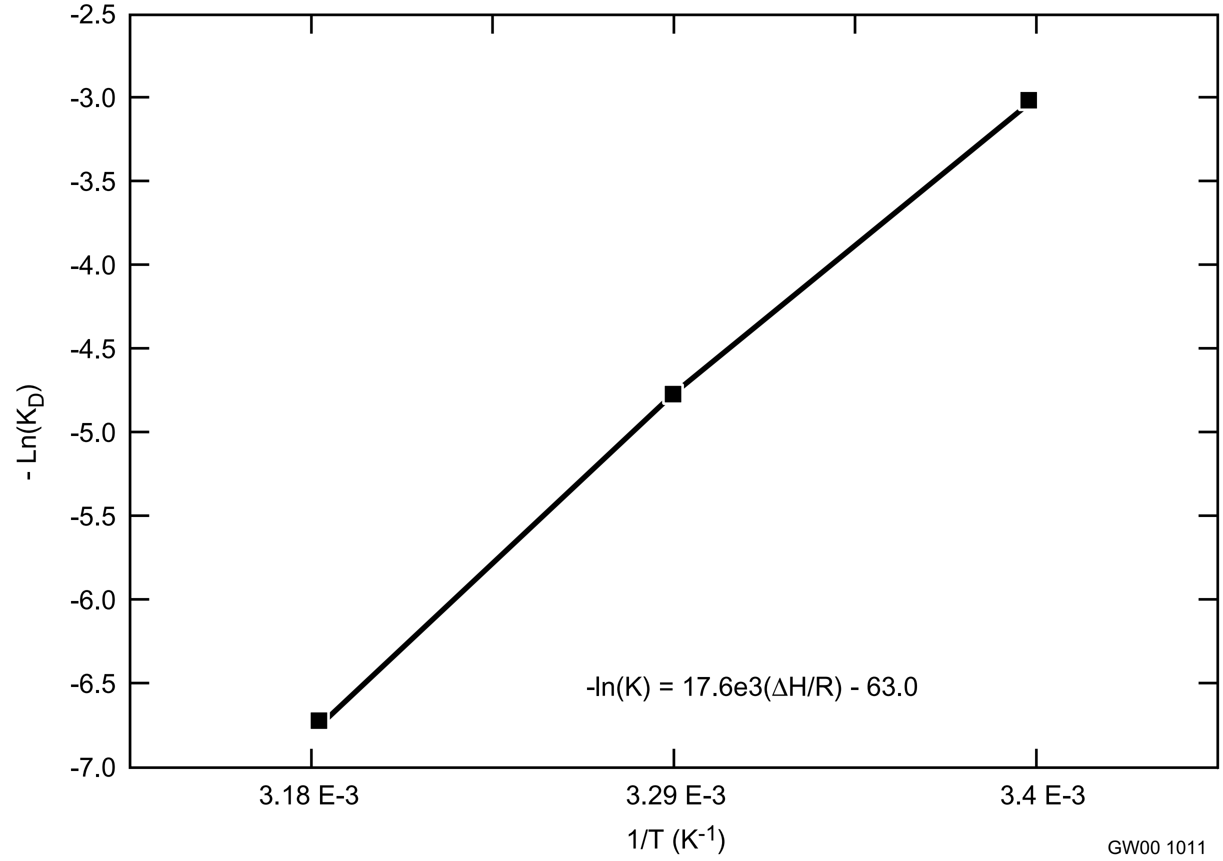

**Figure 11.** Van't Hoff plot for the dissolution of $Cu_2S$ in 0.1M $HNO_3$.

## ACCOMPLISHMENTS

Novel mesoporous silicas were prepared using precipitation and sol-gel techniques in conjunction with surfactant templating agents. Silicas having replicated lamellar, hexagonal, and cubic pore structures were prepared and characterized. Precipitated powder, thin films, and spray dried powder were processed. The incorporation of hydroypropyl Beta-CD was accomplished in the base catalyzed system studied.

This work serves as a foundation for the future development of mesoporous-based sorbent media and separation membranes with and without CDs. The spray drying process employed is of particular relevance.

Nanocrystalline CuS powders were prepared from $Cu(NO_3)_2{\cdot}3H_2O$ and $Na_2S{\cdot}9H_2O$ with surfactant CTAB serving as a particle size mediating agent. Using ethanol as a co-solvent in the precipitation process provided a similar median particle size compared to the aqueous system. In both systems a CTAB:$Na_2S{\cdot}9H_2O$ molar ratio of 0.2 or greater, at least five times the CMC, was found effective for obtaining a precipitate powder having a median particle size of 200 to 400 nm. In the case of the co-solvent system, the particle size distribution was found to be bimodal. The bimodal distributions contained a greater number fraction of particles <200 nm. Thus the increased mercury vapor reactivity previously observed for mediated CuS relative to commercial grade CuS is attributed to an increased surface area and a reduced median particle size as established in this study.

Oxalic acid treated commercial grade CuS also was previously shown to provide a two-fold rate increase in elemental mercury vapor capture. Our present work has shown that the oxalic acid treatment is responsible for a four-fold increase in surface area and a corresponding four-fold decrease in the median particle size of the commercial grade CuS. Thus, providing an explanation for the increased mercury vapor capture rate.

A water-based sorption study was conducted using $Cu_2S$ in order to characterize the $Hg^{2+}$ capture mechanism. Our experiments demonstrated that the metal sulfide does not physically or chemically adsorb $Hg^{2+}$ in acidic aqueous solution. Powder XRD revealed the presence of HgS in the post-reaction solid phase and ICP-AES experiments confirmed the mass balance for a precipitation reaction; namely, a one-to-one reaction of $Hg^{2+}$ with dissolved sulfide ions to form the solid precipitate HgS.

## REFERENCES

1. C. T. Kresge, M. E. Leonowicz, W. J. Roth, J. C. Vartuli, and J. S. Beck, *Nature* 1992, *359*, 710.
2. A. Monnier, F. Schuth, Q. Huo, D. Kumar, D. Margolese, R. S. Maxwell, G. D. Stucky, M. Krishnamurty, P. Petroff, A. Firouzi, M. Janicke, and B. F. Chmelkz, *Nature* 1993, *261*, 1299.
3. C. J. Easton and S. F. Lincoln, S. F. “Modified Cyclodextrins,” *Imperial College Press*, London, 1999.
4. W. Saenger, *Angew. Chem. Int. Ed.*, 1980, *19*, 344-362.
5. G. Wenz, *Angew. Chem. Int. Ed.*, 1994, *33*, 803-822.
6. Q. Cai, W. Y. Lin, F. S. Xiao, W. Q. Pang, X. H. Chen, and B. S. Zou, *Microporous and Mesoporous Material*s, 1999, *32*, 1.
7. M. Kurk, M. Jaroniec, and A. Sayari, *Langmuir*, 1997, 13, 6267.
8. M. Ogawa, N. Masukawa, *Microporous and Mesoporous Materials*, 2000, 38, 35.
9. P. J. Martellaro, G. A. Moore, A. E. Gorenbain, E. H. Abbott and E. S. Peterson, *Sep. Sci. Technol.,* 2000 in press.
10. G. A. Moore, P. J. Martellaro, and E. S. Peterson, “Studies in Surface Science and Catalysis 129,” *Elsevier Science*, 2000, 765.
11. J. H. Fendler, *Chem. Rev*., 1987, 87, 877.
12. S. G. Dixit, A. R. Mahadeshwar, and S. K. Haram, *Colloids and Surfaces A.*, 1998, 133, 69.
13. A. J. Parker, and N. Kharasch, Chem. Rev., 1959, 35, 583.
14. A. E. Gorenbain, A. Rebitser, D. Paul, and Y. F. Linov, “The Method of Producing the Sorbents for Scrubbing the Mercury from Gases,” Russian Patent #2,035,993, 1988
15. D. R. Lide, Editor, *Handbook of Chemistry and Physics*, Chapman and Hall, CRCnetBase, 1999.

# Fission Product Extraction Process

**R. S. Herbst, J. D. Law, T. A. Todd, INEEL, Idaho Falls, Idaho**
**V. N. Romanovskii, V. A. Babain, V. M. Esimantovski, B. N. Zaitsev, I. V. Smirnov**
**Khlopin Radium Institute, St. Petersburg, Russia**

## SUMMARY

This project was a collaborative effort with the Khlopin Radium Institute (KRI) in St. Petersburg, Russia to initially test the fission product solvent extraction technology for simultaneous extraction of Cs and Sr from the current 5 million liter inventory of acidic tank waste stored at the INEEL. The fission product extraction process is an alternative technology to feasibly provide a method of meeting the Batt Settlement Agreement milestones to cease use of the INTEC tank farm by 2012. Predominate fission products that contribute to the radioactivity of the tank wastes are Cs-137 and Sr-90. The fission product extraction process is based on an immiscible organic phase comprised of chlorinated cobalt dicarbollide (CCD, Cs extractant) and polyethylene glycol (PEG, Sr extractant) dissolved in a poly-fluorinated sulfone diluent. Batch contact experiments and preliminary flowsheet testing were used to define potential solvent composition and flowsheet configuration. This information was used to specify an initial flowsheet for countercurrent testing with simulated tank waste in the 3.3-cm centrifugal contactor mockup at INTEC. This flowsheet consisted of 13 extraction stages, 2 scrub stages, and 11 stripping stages. Millimolar quantities of stable (nonradioactive) Cs and Sr were added to the simulated feed to facilitate analytical detection; such quantities are several orders of magnitude higher than anticipated in the actual tank wastes. The initial extractant composition was 0.08 M CCD, 0.6 vol% PEG-400 in phenyl trifluoromethyl sulfone (FS-13) diluent. Approximately 1.5 L of solvent was used (with continuous recycle) to treat 43 L of simulated tank waste during 75 hours of continuous operation. Greater than 99.992% of the Sr and 97.45% of the Cs were extracted from the simulated tank waste and recovered in the strip product based on the raffinate composite sample for the duration of the run. Approximately 99.9% of the Eu, added as a surrogate for the transuranic (TRU) elements remained in the raffinate, attesting to the excellent separation factors of the fission products over the TRU elements in the process. The matrix components Ba (>99.6%), Pb (99.8%), and Ca (10.6%) were also extracted from the simulated tank waste and recovered in the strip product. Less than 1% of the K, Na, Fe, Zr, and Mo were extracted from the tank waste simulant. The only physical problem encountered throughout the course of the experiment was slight flooding (~0.3 vol% carryover of organic solvent in the aqueous phase) in the strip product stream. While <1% flooding is typically acceptable from a processing standpoint, the flooding was attributed to limitations of the centrifugal contactors and could be readily solved with the appropriate flowsheet or equipment modifications. The PEG-400 used in the organic solvent is known to have limited solubility in the aqueous process solutions. Consequently, ~0.6 g/L PEG-400 was added to the strip product to compensate for losses of this component from the solvent. As a result of the PEG-400 addition, the concentration was estimated to increase from the initial 0.6 vol% in the solvent to ~1.3 vol% at the conclusion of the test. Finally, none of the analytically determined waste components were observed to build up in the organic solvent.

## PROJECT DESCRIPTION

### Background

The fission product extraction process is a solvent extraction technology for the simultaneous extraction, concentration, and recovery of Cs and Sr from acidic radioactive wastes. Predominant fission products contributing to the radioactivity of INTEC wastes are Cs-137 and Sr-90. This process is amenable to the current inventory of aqueous tank wastes and acidic solutions of redissolved calcine wastes stored at INTEC.

Cobalt dicarbollide was first synthesized and characterized by Hawthorne and Warren[1,2] at the University of California in 1965. Rais et al. first reported the applicability of cobalt dicarbollide in solvent extraction processes.[3] The CCD anion is a large hydrophobic species that exhibits the properties of a strong acid.

Chlorinated cobalt dicarbollide selectively extracts cesium through an uncommon cation-exchange mechanism with dissociation of the solvated species in the organic phase. Dipicrylamine, tetraphenylborate, polyiodide, and heteropolyacids extract cesium by the same mechanism, but only CCD is simultaneously a strong acid, such as heteropolyacids, and extremely hydrophobic, such as tetraphenylborate. This combination of properties enables CCD to extract cesium from acidic media and provides low solubility of CCD in aqueous solutions. Aliphatic and aromatic nitro-compounds, such as nitrobenzene, are the best diluents for CCD.[3] However, nitrobenzene and nitroaromatic compounds are unacceptable diluents in the U.S. due to technical, environmental, health, and safety considerations.

The unsubstituted cobalt dicarbollide has a high resistance to acid hydrolysis, reductants, and radiation, as well as having excellent thermal stability.[4] Halogenated derivatives of cobalt dicarbollide, especially chlorinated cobalt dicarbollide, exhibit even greater stability.[5,6] Therefore, the hexachloro-derivative of cobalt dicarbollide have historically been used in development efforts associated with radioactive waste treatment.

Many mixtures incorporating CCD are of particular interest for the synergistic extraction of other components. Rais et al. observed a large synergistic effect on the extraction of micro-quantities of $Ca^{2+}$, $Sr^{2+}$, $Ba^{2+}$, and $Pb^{2+}$ in the presence of polyethylene glycols (PEG) and CCD.[4,7] Polyethylene glycol remains as a neutral molecule when associated with ionic strontium, disrupting the hydration sphere of $Sr^{+2}$ and creating a hydrophobic species that is transferred from the aqueous phase into a nitrobenzene phase containing the CCD anion.[4] Experimentally derived data were used to validate theoretical results, which indicated the charged species $PEG{:}Sr^{2+}$ and protonated polyethylene glycol ($PEG{:}H^{+}$) were competing counter-ions of the CCD anion in the organic phase.[4]

The unique extraction properties of CCD/PEG mixtures allows for the separation of Cs and Sr from acidic high activity wastes (HAW). However, the industrial use of this process was not feasible due to the lack of an appropriate diluent for CCD. Acceptable diluents for use in radioactive waste treatment must have high chemical and radiation stability, low aqueous solubility, low viscosity, and a density substantially different than the aqueous process solutions. Furthermore, the extractants (CCD and PEG), and their solvated metal complexes, must be readily soluble in the diluent to prevent formation of an immiscible third phase or solid precipitates. Finally, the diluent should be nontoxic, inexpensive, and readily available or produced.

Identification of an optimal CCD diluent is complicated by the fact that CCD and its salts are highly polar compounds and are essentially insoluble in low-polar solvents like saturated and aromatic hydrocarbons. Consequently, nitrobenzene and its mixtures with carbon tetrachloride and saturated hydrocarbons were initially proposed as diluents.[3] The high solubility of nitrobenzene in water and acidic solutions, renders its use under industrial conditions technically impractical. Commercial scale processing of high level waste (HLW) in Russia was initiated after the development of m-nitro-trifluoromethyl benzene (MNTFB), a diluent technically amenable to large-scale use.[8] Approximately

800 $m^3$ of acidic HLW were commercially processed using the CCD/PEG/MNBTF system at the Mayak Production Association (Russia), and approximately 12 million Ci of Cs and Sr were recovered.[9]

Collaborative efforts between the INEEL and the Khlopin Radium Institute (KRI) were initiated in 1994 to evaluate the applicability of the CCD/PEG process as applied to INEEL tank and dissolved calcine wastes. This early testing used nitroaromatic diluents and hydrazine as a strip reagent, both unacceptable in the U.S. for commercial use. Ongoing efforts have since focussed on development and demonstration of the Universal Extraction (UNEX) process to simultaneously extract all the major radionuclides (Cs-137, Sr-90, and the actinides) from INEEL wastes.[10–13] The UNEX process incorporates CCD, PEG, and diphenylcarbamoylmethyl-phoshine oxide (CMPO) in an appropriate diluent to simultaneously extract the radioisotopes. UNEX development efforts have recently culminated with the identification of phenyl trifluoromethyl sulfone (FS-13) as a suitable diluent for the UNEX process solvent. The FS-13 diluent exhibits excellent radiolytic and chemical stability, is innocuous, and provides ample solubility of CCD, PEG, and CMPO and their respective metal complexes. Finally, the physical properties of density and viscosity are suitable for countercurrent processing applications.

## Scope and Objectives

Currently, there are 5 million liters of radioactive acidic waste stored in the INTEC tank farm. The residual tank wastes were a result of solvent wash and equipment decontamination activities associated with previous reprocessing activities. One of the current, economically appealing methodologies for the disposal of INTEC tank waste involves chemically separating and concentrating the radionuclide fraction into a relatively small volume for disposal as a remote handled waste at the Hanford Reservation or the Nevada Test Site. The residual bulk of the separated waste would be grouted and disposed of as contact-handled Transuranic waste (TRU) at the Waste Isolation Pilot Plant (WIPP). This disposal alternative is contingent on obtaining a Waste Incidental to Reprocessing (WIR) determination for the wastes currently stored in the INTEC tank farm.

The scope of this project was to demonstrate the applicability of the fission product extraction process for Cs and Sr removal from simulated INTEC tank wastes. The Batt Settlement Agreement between the INEEL, State of Idaho, and Department of Energy is a court mandated agreement to cease use of the existing INTEC tank farm by 2012. The path forward with respect to meeting the tank farm milestone is contingent on the Idaho High Level Waste and Facility Disposition Environmental Impact Statement (EIS) and subsequent Record of Decision (ROD). The significance of this effort is the initial development of a robust process, and the associated data, supporting current and future feasibility studies for a treatment facility and the capability of meeting the milestones in the Batt Agreement.

The purpose of the effort was to evaluate a viable process flowsheet based on CCD/PEG in FS-13 for the simultaneous removal of Cs and Sr from simulated INTEC tank waste during extended countercurrent flowsheet testing. To this end, the objectives of this program included:

- Identify a precursory diluent and solvent composition (CCD and PEG) for testing
- Define a potential flowsheet and perform dynamic countercurrent testing
- Evaluate the ability to control PEG losses by addition to PEG to the strip feed solution
- Verify the potential to eliminate the solvent wash section used in previous flowsheets

- Evaluate the solvent loading and compositional changes with multiple solvent turnovers in the countercurrent flowsheet.

## Centrifugal Contactors

Flowsheet testing at the INEEL was performed using 3.3-cm diameter centrifugal contactors installed at INTEC. The contactor mockup consists of 26 available stages, reagent feed and receiving vessels, and feed pumps with associated controllers. The 3.3-cm centrifugal contactor mockup is pictured in Figure 1.

The 3.3-cm contactors were designed and fabricated in Moscow, Russia by the Research and Development Institute of Construction Technology (NIKIMT). Table 1 lists the operating specifications of the contactors. A total of 26 contactors were obtained from NIKIMT for testing purposes. Each stage can be operated independently allowing numerous combinations for changing flowsheet configurations.

Solutions are fed to the contactors using valveless metering pumps with controllers. Surge suppression tubes, 4 inches long and 1 inch in diameter, were placed on the pump outlets to dampen solution flow fluctuations. Flow rates were adjusted by controlling pump speed using a 10-turn potentiometer or by manual adjustment of the piston stroke length and/or a combination of the two. Once solutions enter the contactors, flow through the equipment is by gravity, i.e., the solutions in the contactors are not under pressure. The product solutions from the contactors drain by gravity to the product vessels.

Solvent exiting the strip section was cooled prior to recycle to the extraction section by pumping the solvent through a cooling coil submerged in an ice water bath.

## Tank Waste Composition

Beginning in FY-01, the tank waste stored at INTEC will be concentrated from the current inventory of ~5 to ~4.2 million L using the High-Level Liquid Waste Evaporator. The expected composition of select constituents in the evaporated waste is indicated in Table 2. The simulated waste used in this

**Figure 1.** 3.3-cm. centrifugal contactors used for dynamic flowsheet testing at the INEEL.

**Table 1.** Operating specifications for the 3.3 cm contactors.

| | |
|---|---|
| Size | 3.3-cm rotor diameter |
| Mixing Chamber Volume | 22 mL |
| Separating Chamber Volume | 32 mL |
| Overall Dimensions: | |
| Length | 105 mm (4.13 in) |
| Width | 132 mm (5.2 in) |
| Height | 286 mm (11.26 in) |
| Volumetric Capacity | 25 L/hr (for the system TBP-kerosene/2 M $HNO_3$) |
| Mass | 5 kg per stage (includes electric motor) |
| Motor | 160-180 volt, 50-60 Hz, 0.04 kW (Russian Design) |
| RPM | 2700 rpm (slightly adjustable) |
| Material of construction | 12X18H10T stainless steel (Russian designation) |
| Inlet and outlet ports | 3/8 inch o.d. tubing |
| Configuration | Single stage units, which can be configured as desired. Stages connected using U-tubes. |

project was prepared with the appropriate chemicals to approximate the anticipated composition of the actual waste (less the radionuclides) indicated in Table 2. Approximately 40 L of the simulated waste were prepared for the development efforts at the INEEL, including the countercurrent flowsheet testing. Approximately 39 L of simulated waste was diluted by 20 vol% with water to a final volume of 48.75 L for use as feed in the flowsheet test. The aqueous feed was diluted to reduce the acid and metals concentration, thus enhancing the extraction of Cs and Sr *(vide infra)*. Additionally, at the desired flow rates, approximately 50 L of the feed was required to allow the test to continue for the prescribed length of time. The concentration of stable Cs, Sr, and Eu (actinide surrogate) in the simulated waste was several orders of magnitude higher than that in the actual waste. The increased composition of these elements was necessary to facilitate ICP and AA analyses of the process samples.

## Preliminary Experimental Efforts

Specialists at the Khlopin Radium Institute (KRI) have many years experience with the development and industrial application of the fission product extraction process based on earlier diluents such as nitrobenzene and *m*-nitrotrifluoromethyl benzene (MNTFB, *m*-$CF_3C_6H_4NO_2$). A goal of this project was to evaluate a new class of diluents, polyfluoro-substituted sulfones, as applied to the fission product extraction process. The significant advantages of these compounds include their low toxicity and high radiation and chemical stability relative to the previous diluents; however, these types of compounds are presently not available from commercial sources. The KRI expertise also includes the synthesis and purification of numerous sulfone derivatives. Consequently, KRI collaborated to perform initial experimental work comparing properties of several different diluents and propose potential flowsheets based on batch contact information. Ultimately, KRI also provided the necessary quantity of the selected diluent for experimental work at the INEEL.

**Table 2.** Tank waste and simulant composition.

| Component | Composition | Component | Composition |
|---|---|---|---|
| Acid (*M*) | 1.96[a] | Na (*M*) | 1.59 |
| Al (*M*) | 0.61 | NO3 (*M*) | 5.64 |
| Ba (*M*) | 6.5E-05 | Zr (*M*) | 0.014 |
| Ca (*M*) | 0.060 | Radionuclides | |
| Cs (*M*) | 8.9E-06 | $^{137}$Cs (Ci/m$^3$) | 42 |
| F (*M*) | 0.099 | $^{90}$Sr (Ci/m$^3$) | 38 |
| Fe (*M*) | 0.023 | Alpha (nCi/g) | 576 |
| Pb (*M*) | 1.1E-03 | $^{241}$Am (nCi/g) | 65 |
| Hg (*M*) | 2.9E-03 | $^{238}$Pu (nCi/g) | 454 |
| Mo (*M*) | 9.8E-04 | $^{239}$Pu (nCi/g) | 57 |
| K (*M*) | 0.18 | $^{99}$Tc (Ci/m$^3$) | 0.016 |

a. Acid concentration may be up to 50% higher depending on the tank farm management scenario.

Two different sulfone diluents were evaluated: phenyl trifluoromethyl sulfone (FS-13, $C_6H_5SO_2CF_3$) and phenyl-1,1,2,2-tetrafluoroethyl sulfone (FS-24, $C_6H_5SO_2CF_2CF_2H$). Several properties of these two diluents are indicated in Table 3. The properties of MNTFB, a diluent used in Russia on the industrial scale, are also indicated in Table 3 for comparison. Note that FS-24 exhibits a slightly higher Cs distribution coefficient ($D_{C\sigma}$≡$[Cs]_{Organic}/[Cs]_{Aqueous}$ at equilibrium) and lower solubility in 3 M $HNO_3$, but also has a correspondingly higher viscosity than FS-13.

The distribution coefficients of Cs and Sr were determined by performing batch contacts with simulated INEEL tank waste solution using CCD and PEG-400 to further elucidate the selection of an appropriate sulfone diluent. The results of these experiments are indicated in Table 4. The measured distribution coefficients are high enough for the acceptable recovery of Cs and Sr in the extraction section of a countercurrent flowsheet. The recovery of Sr from the tank waste is considered to be more difficult (relative to Cs), and the higher Sr distribution along with the dramatically lower viscosity associated with

**Table 3.** Experimentally determined physical properties of several diluents.

| Diluent | Density (20°C) | Viscosity (mPa·s) | Solubility in 3 M $HNO_3$ (g/L) | DCs (from 3 M $HNO_3$ with 0.06 M CCD solution) |
|---|---|---|---|---|
| *m*-$CF_3C_6H_4NO_2$ (MNTFB) | 1.44 | 3.0 | 1.23 | 16 |
| $C_6H_5SO_2CF_3$ (FS-13) | 1.41 | 3.6 | 0.6 | 3.8 |
| $C_6H_5SO_2CF_2CF_2H$ (FS-24) | 1.47 | 9 | <0.5 | 4.9 |

**Table 4.** Cs and Sr distributions from simulated INEEL tank waste.

| Extractant Composition | $D_{Sr}$ | $D_{Cs}$ |
|---|---|---|
| 0.08 M CCD, 0.6 vol% PEG-400 in FS-13 | 2.3 | 1.5 |
| 0.08 M CCD, 0.6 vol% PEG-400 in FS-24 | 1.7 | 2.3 |

the FS-13 diluent is desirable. For these reasons, the extractant based on CCD and PEG-400 in the FS-13 diluent was that of choice.

Several potential stripping reagents were also evaluated by measurement of Cs and Sr batch distribution coefficients. The stripping reagents evaluated were ammonium nitrate ($NH_4NO_3$), methylamine ($CH_3NH_2$), guanidine nitrate ($CH_5N_3 \times HNO_3$), and dimethylformamide ($HCON(CH_3)_2$), each in a nitric acid matrix. The experimentally measured stripping distribution coefficients are indicated in Table 5. Ammonium nitrate is the least favored stripping reagent due to the rather high distribution coefficients obtained (strip distributions should be as small as possible), particularly for Sr. Guanidine nitrate and dimethylformamide are both very effective at stripping Sr and Cs from the organic phase; however, these compounds may be difficult to wash out of the organic phase. Methylamine in nitric acid is the most interesting of the strip reagents studied since it allows for a high degree of concentration of Sr and Cs in the strip solution based on the low distribution coefficients for both these elements. Furthermore, methylamine should be easily washed from the organic phase with nitric acid solutions. However, methylamine, as well as dimethyl-formamide, have a serious drawback due to the safety concern that hydrazine nitrate is formed from the compounds in the presence of nitric acid in the aqueous strip solution.

## Dynamic Flowsheet Testing at the Khlopin Radium Institute

Based on the results of the laboratory experiments and modeling calculations, a conceptual flowsheet was developed for countercurrent testing. The developed flowsheet fundamentally differs from predecessors in that the solvent wash section for extractant regeneration could be completely eliminated.

**Table 5.** Cs and Sr stripping distributions from 0.1 M CCD and 1 vol% PEG in FS-13.

| Strip Reagent | Concentration (M) | $HNO_3$ Concentration (M) | $D_{Cs}$ | $D_{Sr}$ |
|---|---|---|---|---|
| $NH_4NO_3$ | 1.0 | 4.0 | 0.24 | 0.18 |
| | 2.0 | 6.0 | 0.037 | 0.034 |
| $CH_3NH_2$ | 3.0 | 4.5 | 0.053 | 0.033 |
| | 3.5 | 3.5 | 0.048 | 0.019 |
| | 1.0 | 1.0 | 0.22 | 0.064 |
| $CH_5N_3{\cdot}HNO_3$ | 1.5 | 2.0 | 0.037 | 0.049 |
| $HCON(CH_3)_2$ | 1.5 | 4.0 | 0.012 | 0.018 |

Such a dramatic change would substantially simplify the flowsheet and eliminate the solvent wash secondary waste stream. The ramifications of this revolutionary change include alteration of the organic extractant composition and an increase in the necessary number of stages in the extraction section to compensate for carryover of entrained or dissolved strip reagent recycled to the extraction section in the organic phase. The proposed flowsheet developed in accord with these considerations was tested at KRI's Gatchina Facility near St. Petersburg, Russia in June 2000. The INEEL investigators intended to be present during the Gatchina tests; however, circumstances did not allow this interaction to occur. The countercurrent flowsheet tested at Gatchina is schematically depicted in Figure 2.

The flowsheet indicated in Figure 2 used 0.13 M CCD as the Cs extractant and 0.3 vol% Slovafol-909 (Czech product, which is an analog of PEG-400) in FS-13 diluent. The increased concentration of CCD and Slovafol (relative to the previous development efforts) was thought necessary to enhance the Cs and Sr extraction in the absence of a solvent wash section for the removal of methylamine from the

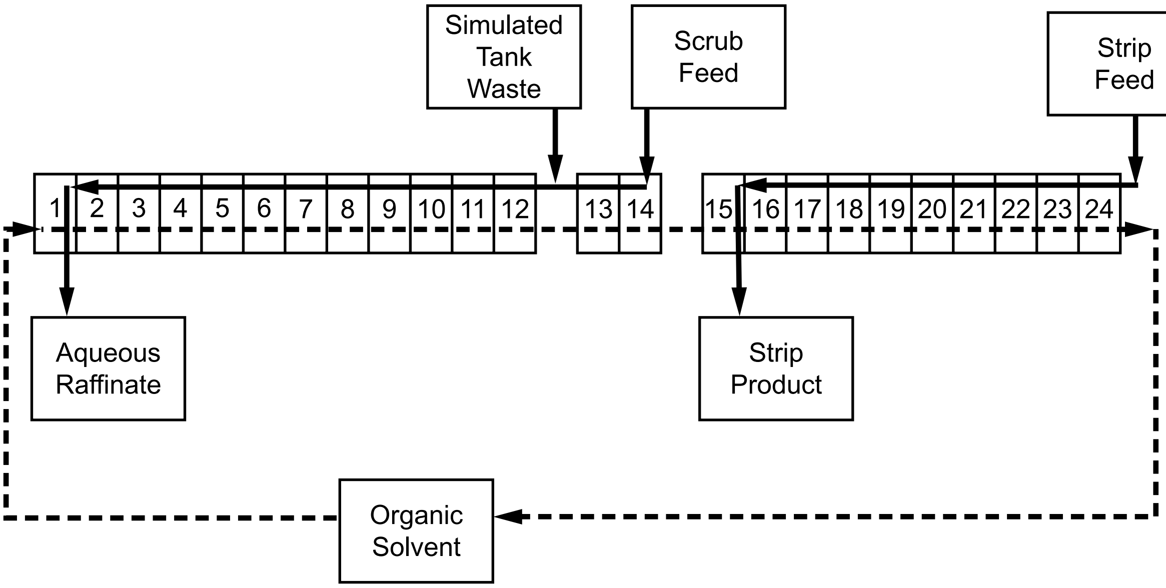

| Stream | Composition | Flowrate (mL/min) |
|---|---|---|
| Simulated INEEL Tank Waste | Refer to Table 2 (undiluted)<br>3 g/L $H_2C_2O_4$ added | 2.1 |
| Organic Solvent | 0.13 M CCD, 3 vol% Slovafol-909 in FS-13 | 3.2 |
| Scrub Feed | 0.1 M $HNO_3$, 3 g/L $H_2C_2O_4$ | 0.80 |
| Strip Feed | 3 M methylamine nitrate, 3 M $HNO_3$ | 0.45 |
| Raffinate | - - - | 2.9 |
| Strip Product | - - - | 0.45 |

GJ00 0185

**Figure 2.** Fission Product Extraction Process flowsheet tested by KRI at atchina, Russia.

organic phase prior to recycle of the solvent to the extraction section. Slovafol-909 was substituted for PEG-400 in the organic extractant due to the lower solubility of Slovafol in the aqueous process streams. Additionally, 3 g/L oxalic acid was added to the simulated feed and scrub solutions in an attempt to reduce the amount of co-extracted Fe and Zr that would be carried over into the strip product phase. The analytical results of this flowsheet test are summarized in Table 6.

The results in Table 6 indicate 99.7% of the Cs and 99.98% of the Sr in the simulated waste feed was extracted and quantitatively recovered in the strip product. Virtually all of the Ba and Pb were also extracted from the feed and recovered in the strip product. The extraction of Ba and Pb was anticipated since these elements typically compete with and follow the Sr in the process. The extraction and recovery of the other reported elements is less clear due to the rather poor material balances obtained, i.e., the material balance for Na is ~132% (% in raffinate + % in strip). Due to the dynamic nature of the test and the use of ICP and AA analytical methods, acceptable material balances are typically in the ±10% range. The data in Table 6 indicate that up to 13.4% of the Ca, 6.6% of the Na, 2.6% of the Ni, and 1.9% of the Cd (relative to their concentration in feed) were extracted and exited in the strip product. Less than 1% of the other metals examined were extracted. CCD potentially extracts Na and K as competing ions with Cs in the process. Considering the bulk concentration of Na relative to Cs in the simulated waste, the selectivity from Cs was quite high. Data were not available regarding the behavior of K in this particular test. The KRI scientists also indicated that the addition of oxalic acid to the tank waste and scrub feed solutions would be unnecessary in future flowsheet tests.

## Dynamic Flowsheet Testing at the INEEL

During July of 2000, the KRI scientists visited the INEEL and participated in flowsheet testing of the related UNEX process *(vide supra)*. The results of these tests (currently being prepared for publication) provided valuable insight for the upcoming INEEL dynamic test of the fission product extraction process. In collaboration with the KRI specialists, several necessary flowsheet parameters were defined and tested, largely due to the preliminary results of the UNEX testing. A joint decision was made to evaluate an extractant composition of 0.08 M CCD and 0.6 vol% PEG-400 in FS-13 for the INEEL dynamic test. Computer modeling efforts for the number of available contactor stages indicated that the distribution coefficients for Cs and Sr should be $D_{Cs}{}^{3}$ 1.5 and $D_{Sr}{}^{3}$ 2.2 in the extraction section for high recovery (>99.9%) of these target species. Additionally, distribution coefficients of $D_{Cs}$ and $D_{Sr}$

**Table 6.** Distribution of feed components in the KRI dynamic test (% of content in feed).

| | Component | | | | | | | |
|---|---|---|---|---|---|---|---|---|
| Stream | Cs | Sr | Ba | Pb | Ca | Na | Al | Cr |
| Raffinate | 0.3 | 0.02 | <0.1 | <0.001 | 111 | 127 | 115 | 115 |
| Strip Product | 104 | 107 | 103 | 127 | 13.4 | 6.6 | 0.03 | 0.4 |

| | Component | | | | | | |
|---|---|---|---|---|---|---|---|
| Stream | Cd | Fe | Mo | Mn | Ni | Pd | Zr |
| Raffinate | 123 | 121 | 111 | 121 | 117 | 114 | 110 |
| Strip Product | 1.9 | 1.0 | 0.2 | 0.8 | 2.6 | 1.1 | 0.03 |

£ 0.2 in the strip section for effective stripping of these elements. Much of the previous data, including that from the UNEX testing, indicated that the above-prescribed solvent composition would likely be capable of achieving the necessary distribution coefficients. The other conditions discussed included use of a 0.3 M $HNO_3$ solution in the scrub section, and a strip solution consisting of 100 g/L (0.56 M) guanidine carbonate (GC, $CH_5N_3 \times HCO_3$) and 20 g/L (0.05 M) diethylenetriaminepentaacetic acid (DTPA, $C_{14}H_{23}N_3O_{10}$). The DTPA was deemed necessary in the strip solution to prevent the formation of insoluble carbonates. Several of these changes, particularly in the choice of suitable strip reagents, were a substantial departure from the KRI flowsheet tested previously, and were founded on the technical basis provided by the more recent UNEX testing at the INEEL.

Several batch contact experiments were performed using Cs-137 and Sr-85 traced feeds to determine the batch distribution coefficients under the proposed conditions of extraction and stripping for the INEEL dynamic flowsheet. These batch contact tests were performed with two different feed solutions. The first feed solution was the simulated waste plus 20 vol% of 0.3 M $HNO_3$ (scrub solution) to emulate the scrub dilution of the feed in the extraction section. The second feed solution was simulated waste +20 vol% of 0.3 M $HNO_3$ (scrub solution) + 20 vol% $H_2O$ (total dilution of 40 vol%); the water dilution in this feed was intended to observe the effect of decreasing (diluting) the acid and metals concentration on Cs and Sr distribution coefficients. The feed solutions were spiked with trace quantities of the radionuclides Cs-137 and Sr-85 to facilitate analysis by gamma spectroscopy. The organic extractant (0.08 M CCD, 0.6 vol% PEG-400 in FS-13) was contacted three consecutive times with fresh aliquots of the respective feed solutions (contacts E1, E2, E3) and the extraction distribution coefficients of Cs and Sr were measured after each contact. The organic from the contacts with the feed solutions (loaded with the extracted species) were subsequently contacted two consecutive times with fresh strip solution (contacts St1 and St2) and the strip distribution measured for each contact. The results of these laboratory tests are indicated in Table 7.

The data in Table 7 indicate that the 20 vol% scrub dilution of the simulated waste does not provide sufficiently high Cs and Sr distribution coefficients for effective removal of the these components in the extraction section. The additional 20 vol% water dilution (for a total feed dilution of 40 vol%) does produce marginally acceptable distribution coefficients for Cs and Sr recovery. In all cases, the distribution coefficients in the strip contacts were very low and therefore acceptable. The St2 stripping distributions are indicated to be much less than one since all detectable quantities of Cs and Sr were removed from the organic phase in the second strip contact.

**Table 7.** Batch distribution coefficients with 0.08 M CCD, 0.6 vol% PEG-400 in FS-13.

| Feed 1: Simulated INEEL tank waste + 20 vol% $HNO_3$ | | | | | |
|---|---|---|---|---|---|
| Contact: | E1 | E2 | E3 | St1 | St2 |
| $D_{Cs}$ | 0.66 | 0.93 | 0.63 | 0.22 | <<1 |
| $D_{Sr}$ | 1.47 | 1.42 | 1.05 | 0.02 | <<1 |
| Feed 2: Simulated INEEL tank waste + 20 vol% $HNO_3$ + 20 vol% $H_2O$ | | | | | |
| Contact: | E1 | E2 | E3 | St1 | St2 |
| $D_{Cs}$ | 1.36 | 1.19 | 1.18 | 0.20 | <<1 |
| $D_{Sr}$ | 2.73 | 2.17 | 1.81 | <<1 | <<1 |

There was a concern that the reported extraction distributions were artificially high for the feed solutions used to generate the data shown in Table 7. Millimolar quantities of stable Cs and Sr had not been added to the simulated waste solution prior to performing the batch contacts [~0.001 M concentration of stable Cs and Sr were to be added to the feed to facilitate analysis by ICP (inductively coupled plasma emission spectroscopy) for Sr and AA (atomic absorption) for Cs]. The small volume of extractant used in the batch contact tests had been washed with $K_2CO_3$ and $HNO_3$ solutions (to remove impurities from the CCD) after the PEG-400 had been added. These washes should have been performed prior to preparing the solvent for the batch contacts to prevent washing PEG out of the extractant. Consequently, there was also some concern that the PEG-400 concentration in the organic extract used in the batch contacts was lower than the required 0.6 vol% due to the wash procedures used to prepare the solvent for the batch contacts. Due to the uncertainties in the batch distribution data arising from these concerns, the batch contact experiments were partially repeated. The required 0.001 M Cs and 0.001 M Sr were added to the simulated tank waste prior to dilution with scrub and/or water for the repeat experiments. A small aliquot of stock (0.16 M) CCD solution was washed with $K_2CO_3$ and $HNO_3$ prior to preparing the final extractant used in the batch contacts. In these experiments, a single extraction contact was performed with the freshly prepared extractant and each waste feed solution. The results of these experiments are presented in Table 8.

The extraction distribution coefficients shown in Table 8 indicate that a 40 vol% dilution of the simulated tank waste feed solution is required to obtain high enough Cs distribution coefficients for effective Cs recovery for the extractant composition identified for the dynamic test. Note that alteration of the extractant composition, likely increasing the CCD concentration and perhaps reducing the PEG-400 concentration, could potentially produce the necessary increase in the Cs extraction distributions. Such a study is a rather entailed effort and the necessary time and resources were unavailable to evaluate such alterations in solvent composition. Optimization of the extractant composition is recommended for future efforts. Consequently, a 40 vol% dilution of the feed was necessary for the dynamic testing at the INEEL. There are two potential methods to achieve a 40 vol% dilution of the waste. One approach is to simply increase (double) the scrub solution feed flow rate, which already accounts for a 20 vol% dilution in the proposed dynamic test, resulting in an overall dilution of 40 vol%. While this approach is operationally quite simple, it would result in a slightly different (higher) acidity than was tested in the above batch contacts. Alternatively, the feed could be diluted by 20 vol% with water and the additional 20% dilution would occur with the scrub solution in the flowsheet, essentially the conditions used to determine the above batch distribution coefficients. In order to prepare the necessary volume of simulated tank waste required to operate the dynamic flowsheet test for 80 hours (~50 L), the latter approach was taken.

The fundamental purpose of this effort was to validate that the fission product extraction process, with numerous modifications relative to previous efforts, is a viable method to selectively partition and recover Cs and Sr from the tank waste under dynamic flowsheet conditions. To this end, experience,

**Table 8.** Repeated distribution coefficients for 0.08 M CCD, 0.6 vol% PEG-400 in FS-13.

| | Feed 1: Simulated INEEL tank waste + 20 vol% $HNO_3$ | Feed 2: Simulated INEEL tank waste + 20 vol% $HNO_3$ + 20 vol% $H_2O$ |
|---|---|---|
| $D_{Cs}$ | 0.85 | 1.4 |
| $D_{Sr}$ | 3.8 | 6.3 |

laboratory data and modeling results culminated in a countercurrent flowsheet proposed for testing at the INEEL as indicated in Figure 3.

The dynamic test was operated continuously for 74.9 hours and processed a total of 43 L of (20 vol% diluted) simulated tank waste using 1.57 L of organic solvent. Based on the 74.9 hour duration, 1.57 L of solvent, and an average organic flow rate of 1.1 L/hr, the solvent was estimated to recycle through the system 52 times.

It is of interest to note that the concentration of the organic phase could potentially vary due to solubility of the PEG-400 and sulfone in the aqueous process solutions. Solubility of the sulfone diluent is estimated to be 200 mg/L in the raffinate stream and 120 mg/L in the guanidine carbonate strip solution. Samples of the initial organic solvent, the solvent after 45 hours of operation, and the end of the test were taken for CCD analysis. The resulting concentrations are indicated in Table 9. The CCD concentration was determined independently by: (1) X-ray fluorescence (XRF) for Co concentration, and (2) ICP analysis of Co and B following destructive digestion. The results indicate an initial concentration of 0.08 M CCD that remained constant during the experiment. Although there is currently not an

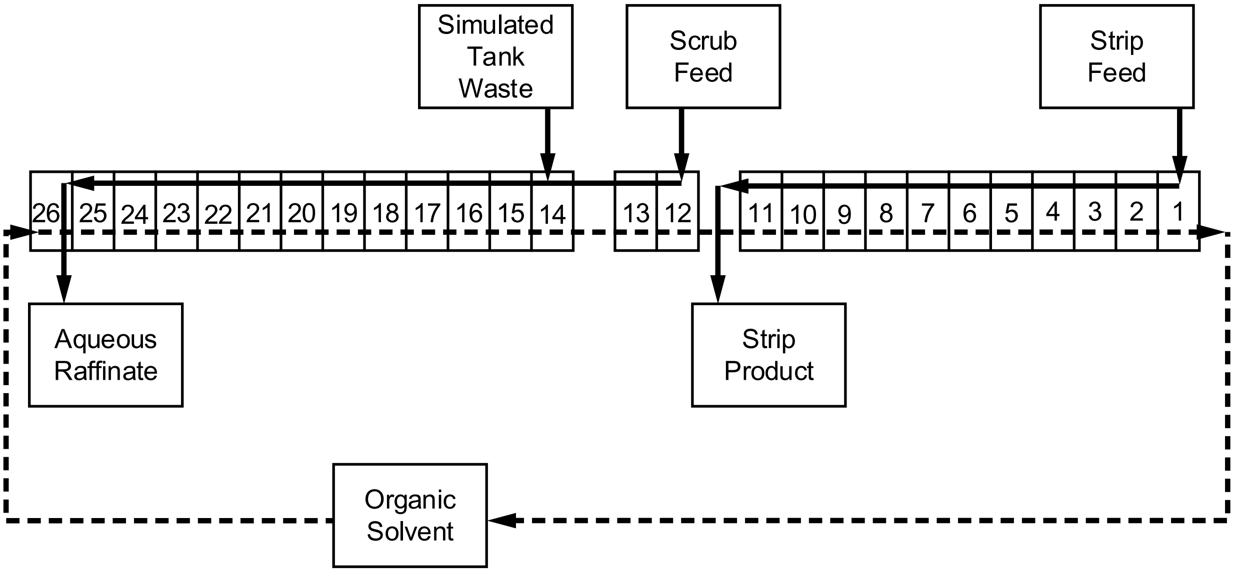

| Stream | Composition | Flowrate (mL/min) |
|---|---|---|
| Simulated INEEL Tank Waste | Diluted 20 vol% with water | 10 |
| Organic Solvent | 0.08 M CCD, 0.6 vol%<br>PEG-400 in FS-13 | 15.5 |
| Scrub Feed | 0.3 M $HNO_3$ | 2.5 |
| Strip Feed | 100 g/L Guanidine Carbonate<br>20 g/L DTPA | 8.7 |
| Raffinate | - - - | 12.5 |
| Strip Product | - - - | 8.7 |

GJ00 0186

**Figure 3.** Fission Product Extraction Process flowsheet tested at the INEEL.

**Table 9.** CCD analyses in the organic solvent from the dynamic test.

| | Organic Phase CCD Concentration (M) | | |
|---|---|---|---|
| Method | Initial | 45 Hours | Conclusion |
| ICP | 0.080 | 0.081 | 0.081 |
| XRF | 0.081 | — | 0.082 |

available analytical method to determine sulfone concentration, the constant CCD concentration implies sulfone losses were minimal since the CCD (virtually insoluble) concentration would increase with a corresponding decrease (loss) of diluent.

One of the objectives of this test was to determine if losses of PEG-400 from the organic solvent (due to solubility of PEG) could be controlled by addition of PEG to the process strip solution. The solubility of PEG-400 is estimated to be 50 mg/L (0.005 vol%) in the raffinate stream and 250 mg/L (0.025 vol%) in the guanidine carbonate strip solution. The solubility losses can be partially controlled by use of a different, less soluble polyethylene glycol, such as Slovafol-909. Analytical methods are currently unavailable at the INEEL to accurately estimate PEG-400 concentration in the organic phase. NMR analysis was explored with inconclusive results. To control PEG losses from the solvent, 600 mg/L (0.06 vol%) PEG-400 was added to the strip feed solution beginning at 17 hours during the test. A material balance was used to estimate the final PEG-400 concentration in the organic phase. Based on the solubility in the raffinate and strip streams, the average strip and raffinate flow rates (*vide infra*), and the addition of 600 mg/L PEG-400 to the strip feed during the test, the final PEG-400 concentration was estimated as 1.28 vol%. Thus, th3% flooded. The flooding is postulated to be associated with the design of the centrifugal contactors. As opposed to completely redesigning and reengineering the contactor stages, the flooding could likely be eliminated by increasing the residence time of the solutions in the separating zone of the current contactors. This could be most simply accomplished by decreasing the flow rates of the organic and aqueous phases. Alternatively, it may be possible to use a single contactor stage (placed as the final or product stage in the strip section) as a centrifugal separator by diverting the organic flow around that stage and allowing only the (flooded) aqueous phase to enter. These methodologies to eliminate the flooding would be explored in continued development efforts.

Analysis of process samples taken early in the run indicted Cs removals (relative to the feed) of 98.4% and 99.3% at 15 and 25 hours, respectively. Sr removal was >99.99% for both of these samples. Since the Cs removal efficiency was lower than anticipated, the flow rate of the organic solvent was increased approximately 50% (from 14.8 to 22.3 mL/min) in an attempt to increase the Cs removal efficiency. To ensure Cs stripping remained acceptable due to the increased organic flow, the strip feed flow rates were increased by ~40% (from 8.5 to 14.1 mL/min). These flow rates were increased at approximately 39 hours into the run, and were maintained for the duration of the test. The target flow rates, actual flow rates, and O/A phase ratios during the dynamic test are indicated in Table 10. Note that the actual flow rates of the organic solvent and strip feed are a time-weighted average for the entire test and reflect the increased flows mentioned earlier, while the target values are those for the initial startup of the test. Despite the increased solvent and strip flow rates during the test, the actual and target flow rates and O/A ratios indicate reasonable agreement. The flow rates in Table 10 were used to calculate the overall removal efficiencies and material balances based on the composite product samples.

The key data used to evaluate overall flowsheet performance are from the composite product streams. Samples of the composite raffinate and strip product were collected at the conclusion of the test and represent the cumulative, average behavior of the key components for the duration of the test. The composition in the various streams, removal efficiencies, material balance data, and other pertinent information is summarized in Table 11.

The data in Table 11 reflect the rather poor removal efficiency of 97.45% for Cs from the simulated waste solution. It was anticipated that >99.9% of the Cs would be extracted from the simulated waste during the dynamic test. The reason for the low Cs recovery is unclear at this point and warrants future study. The most plausible explanation for the low Cs removal efficiency is a low CCD concentration relative to the amount of PEG in the organic solvent. Due to competition between the Cs and K with the PEG complexes of Sr, Ba, Pb, and Ca for the available CCD extractant, the PEG complexes consume much of the extractant and result in suppressed Cs extraction.

While the Cs extraction efficiency was somewhat lower than expected, Table 11 indicates that the extracted Cs was stripped quantitatively by the guanidine carbonate solution. The overall Cs material balance is marginal at 108.2%, with much of the discrepancy likely associated with the analysis of the strip product sample. Analysis of the organic phase indicated Cs was not present, further indicating excellent Cs stripping was achieved.

The removal and stripping efficiency of Sr was excellent with >99.992% of the strontium extracted and recovered in the strip product stream. Detectable quantities of Sr were not found in the organic phase, supporting the excellent stripping efficiency. The overall material balance was very good at 101.3%.

Barium and Pb were also efficiently extracted by the solvent and recovered in the strip product. This is not surprising, since these matrix components tend to behave very similar to Sr in the process flowsheet. Calcium is chemical similar to Sr and could potentially follow Sr through the flowsheet, some of the Ca, 10.1%, was also extracted and recovered in the strip product.

**Table 10.** Target and actual flow rates in the INEEL dynamic tests.

| | | Flow rate (mL/min) | | O/A Ratio | | |
|---|---|---|---|---|---|---|
| Section | Phase | Target | Actual | Target | Actual | Total Flow (mL/min) |
| All | Organic | 15.5 | 18.3 | — | — | — |
| Extraction | Aqueous | 12.5 | 11.6 | 1.24 | 1.58 | 29.9 |
| Scrub | Aqueous | 2.5 | 2.4 | 6.20 | 7.56 | 20.7 |
| Strip | Aqueous | 8.7 | 11.1 | 1.78 | 1.65 | 28.4 |

**Table 11.** Components and parameters in the composite product samples.

| Component | Simulated Tank Waste | Aqueous Raffinate | Strip Product | Organic Solvent[a] | Material Balance[b] |
|---|---|---|---|---|---|
| Cs (mg/L) | 105 | 2.20 | 95.5 | <0.05 | — |
| % per stream | — | 2.55 | 105.7 | <0.09 | 108.2 |
| Sr (mg/L) | 67.9 | <0.004 | 59.2 | <0.06 | — |
| % per stream | — | <0.008 | 101.3 | <0.2 | 101.3 |
| Ba (mg/L) | 6.74 | <0.02 | 5.96 | 0.25 | — |
| % per stream | — | <0.38 | 102.8 | 7.01 | 103.1 |
| Pb (mg/L) | 186 | 0.26 | 164 | <1 | — |
| % per stream | — | 0.23 | 102.1 | <1 | 102.3 |
| K (mg/L) | 6140 | 3650 | 1500 | 107 | — |
| % per stream | — | 72.4 | 28.4 | 3.35 | 100.8 |
| Na (mg/L) | 33,400 | 25,400 | 800 | 174 | — |
| % per stream | — | 92.7 | 2.78 | 1.0 | 95.4 |
| Ca (mg/L) | 1760 | 1220 | 152 | 174 | — |
| % per stream | — | 84.8 | 10.1 | 0.72 | 94.9 |
| Fe (mg/L) | 1050 | 831 | 6.18 | 7.73 | — |
| % per stream | — | 96.3 | 0.68 | 1.41 | 97.0 |
| Zr (mg/L) | 1040 | 819 | 3.24 | 1.48 | — |
| % per stream | — | 95.8 | 0.36 | 0.27 | 96.1 |
| Mo (mg/L) | 50.0 | 41.4 | <0.03 | <0.1 | — |
| % per stream | — | 100.8 | <0.06 | <0.5 | 100.9 |
| Eu (mg/L) | 784 | 609 | 0.09 | <0.2 | — |
| % per stream | — | 94.6 | 0.014 | <0.04 | 94.6 |
| Final Volume[c] (L) | — | 52.9 | 50.2 | — | — |
| Flow rate (mL/min) | 9.5 | 11.6 | 11.1 | 18.3 | — |

a. Organic composition was not used in the material balance due to recycle.
b. Material balance calculated as a percentage of material in/material out.
c. Does not account for samples removed during the experiment or the volume remaining in the contactor stages after shutdown.

Approximately 28% of the K was extracted and recovered in the process flowsheet. A small amount of Na, 2.8%, was also extracted and recovered. Due to their chemical similarities, these two matrix components would tend to follow Cs in the flowsheet. Based on relative concentrations of Na, K, and Cs in the feed, the excellent selectivity of the process solvent for Cs over Na and K is apparent.

Other key data pertinent to the evaluation of overall process performance are the stagewise distribution coefficients obtained for the extracted species. At the conclusion of the test, the contactors and feed pumps are shut down simultaneously, leaving the two phases in each stage at their respective equilibrium concentrations. The stages can then be drained, and the phases separated and sampled to determine stagewise distribution coefficients and evaluate concentration profiles through the system.

Additionally, equal volume samples of the organic and aqueous phases from each stage can be spiked with trace quantities of radionuclides (in this case, Cs-137 and Sr-85). Thus, the distribution coefficients can be determined radiometrically for those stages where the concentrations of stable Cs and Sr are below the analytical detection limits for ICP or AA analyses. The measured stagewise distribution coefficients, including the distributions determined radiometrically from Cs-137 and Sr-85, are listed in Table 12.

The Cs distributions in the strip section (Stages 1 through 11) were very consistent at 0.3 to 0.4 for both stable and radioactive Cs. The distribution data in the strip section are consistent with those obtained in the batch contacts (Table 7) and are sufficiently low for the number of stages and flow rates to insure complete Cs stripping from the organic phase. The distribution coefficients for stable Cs on Stages 1 through 5 are meaningless since the Cs concentration in one or both of the phases were below analytical detection limits; this trend is observed for many of the analyzed species in the different stages. The Cs distributions measured on the scrub stages (12 and 13) were sufficiently high to insure that the Cs was not scrubbed from the organic phase and recycled to the extraction section. The unanticipated low Cs removal efficiency during the test is related to the low Cs distribution coefficients measured in the extraction section. The Cs extraction distribution coefficients were consistently lower than the anticipated value of ~1.4 obtained in the batch contacts (refer to Tables 7 and 8). The Cs distribution on the raffinate stage was ~0.2, and continuously increased toward the feed stage to a value of ~1. The measured extraction stage distributions are consistent with overall Cs removal efficiency of ~97 %.

The Sr distributions in the strip section (stages 1 through 11) for both the stable and radioactive Sr indicate very effective Sr stripping. The distributions based on stable Sr were meaningless for Stages 1 through 9 since the Sr concentration in the organic phase was at or below the analytical detection limits, indicating Sr stripping occurred on the first two strip stages (11 and 10). The strip distributions based on the Sr-85 spiked samples exemplify effective Sr removal; the less than values reflect the fact that Sr-85 was consistently below detection limits in the organic phase. The stripping distribution data are consistent with those obtained in the batch contacts (Table 7) and indicate an excessive number of strip stages to insure that Sr was removed from the organic phase. The Sr distributions measured on the scrub stages (12 and 13) were extremely high and ensure that the Sr was not scrubbed from the organic phase and recycled to the extraction section. The excellent Sr removal efficiency observed in the test is consistent with the large Sr distribution coefficients measured in the extraction section. All of the Sr removal occurred on the first four extraction stages (14 through 17), and the Sr-85 distributions are consistent with the batch data (Table 7).

The distribution data measured for the other elements show consistent trends with their respective extraction and stripping, and parallels the Cs and Sr distributions. It is interesting to note that the scrub distribution coefficients for Pb, K, and Fe indicate these bulk matrix components were not effectively removed from the organic phase in the scrub section. The Zr distribution coefficient of 0.24 on Stage 13 indicates some scrubbing of Zr was occurring. The only other species potentially removed in the scrub section were Na and Ca; distribution data were not requested for these components. The only utility of the scrub section may be removing acid from the solvent (to prevent foaming from carbonate neutralization in the strip solution) and/or the dilution of the waste to enhance Sr and Cs recoveries. This observation suggests it may be possible to modify or eliminate the scrub section, further simplifying the flowsheet and waste volumes. Such an assumption must be validated in future experiments.

The increase in Cs and Sr distributions from the product end of the cascade to the feed point is of particular interest. The primary purpose of a solvent wash section, following the strip section, in the process flowsheet would be to remove entrained or soluble strip solution (guanidine carbonate/DTPA) from the organic prior to solvent recycle to the extraction section. The carryover of residual strip solution

**Table 12.** Stagewise distribution coefficients at shutdown of the INEEL dynamic test.

| | | Component | | | | | | | |
|---|---|---|---|---|---|---|---|---|---|
| Flowsheet Section | Stage No. | Cs | Cs-137 | Sr | Sr-85 | Pb | K | Fe | Zr |
| Strip | 1 | — | 0.38 | — | <0.0003 | — | 7.9 | 27 | >6.1 |
| | 2 | — | 0.36 | — | <0.0002 | — | 18 | 17 | 4.98 |
| | 3 | <0.25 | 0.36 | — | <0.0003 | — | 4.1 | 27 | >5.2 |
| | 4 | <0.11 | 0.37 | — | <0.0003 | — | 2.7 | 27 | 5.0 |
| | 5 | 0.07 | 0.40 | — | <0.0003 | — | 1.7 | 24 | >5.1 |
| | 6 | 0.21 | 0.35 | — | <0.0002 | <4.2 | 1.1 | 29 | >5.1 |
| | 7 | 0.28 | 0.35 | — | <0.0003 | — | 0.76 | 26 | <4.6 |
| | 8 | 0.30 | 0.38 | — | <0.0003 | — | 0.61 | 13 | — |
| | 9 | 0.29 | 0.31 | — | <0.0003 | — | 0.46 | 15 | <2.4 |
| | 10 | 0.30 | 0.36 | 0.33 | <0.0003 | <0.36 | 0.38 | 3.4 | <0.7 |
| | 11 | 0.30 | 0.33 | 0.005 | <0.0003 | <0.008 | 0.33 | 1.6 | 0.20 |
| Scrub | 12 | 36 | 14 | 2200 | 1000 | >870 | 7.2 | 30 | 1.7 |
| | 13 | 21 | 8.6 | 700 | 460 | >880 | 4.4 | 5.6 | 0.24 |
| Extraction | 14 | 1.2 | 0.81 | 6.0 | 6.0 | 54 | 0.18 | 0.02 | 0.003 |
| | 15 | 0.64 | 0.67 | 5.9 | 5.5 | 8.7 | 0.18 | 0.02 | 0.003 |
| | 16 | 0.60 | 0.71 | 7.6 | 5.6 | <4.7 | 0.15 | 0.02 | 0.003 |
| | 17 | 0.59 | 0.67 | 24 | 5.8 | <3.8 | 0.16 | 0.02 | 0.002 |
| | 18 | 0.56 | 0.73 | — | 6.0 | <4.3 | 0.17 | 0.02 | 0.003 |
| | 19 | 0.54 | 0.65 | — | 5.8 | <4.6 | 0.15 | 0.02 | 0.003 |
| | 20 | 0.49 | 0.66 | — | 5.6 | <3.2 | 0.15 | 0.02 | 0.003 |
| | 21 | 0.49 | 0.56 | — | 5.5 | <3.4 | 0.15 | 0.02 | 0.003 |
| | 22 | 0.44 | 0.61 | — | 5.4 | <3.9 | 0.15 | 0.02 | 0.004 |
| | 23 | 0.41 | 0.35 | — | 5.0 | <4.7 | 0.16 | 0.02 | 0.004 |
| | 24 | 0.39 | 0.50 | — | 5.2 | <4.0 | 0.16 | 0.02 | 0.004 |
| | 25 | 0.28 | 0.34 | — | 4.9 | <4.0 | 0.16 | 0.02 | 0.006 |
| | 26 | 0.15 | 0.20 | — | 3.8 | <3.8 | 0.14 | 0.02 | 0.008 |

with the recycled organic could potentially impede the extraction of target species in the extraction section and reduce the overall extraction efficiency of target components. Unfortunately, a solvent wash section also requires input of additional wash solutions ($HNO_3$ in this process), which increases secondary waste volumes generated and adds additional complexity to the process. The fundamental concept used in eliminating solvent washing in the flowsheet tested was to perform solvent wash in the first few extraction stages. Thus, the Cs and Sr distribution coefficients would be suppressed in the early stages (the raffinate end of the cascade where the organic is introduced) due to the recycle of guanidine, then approach an equilibrium value after several of the extraction stages. The data for the first two extraction stages (Stages 25 and 26) indicate suppressed Cs distribution coefficients, which then approach an equilibrium value of 0.4 to 0.6 in the remainder of the extraction section. Thus, two extraction stages appear to provide sufficient washing of residual strip components from the organic phase. The Cs-137 and Sr-85 distribution data also strongly support this conclusion.

Samples of the product solutions (strip and raffinate) and the organic solvent were taken every hour for the first six hours, and at 10-hour intervals thereafter until the conclusion of the test. These time-wise samples were all analyzed for Cs and Sr. The Cs concentration in the raffinate as a function of time is of particular interest, and is as indicated in Figure 4. Note that the rapid increase in Cs concentration to approximately 1 mg/L early in the test indicate steady state operation was achieved by approximately 3 hours into the test. The interesting features of the data are the cyclic behavior observed during the course of the run and the general increase in Cs concentration toward the end of the test. Cesium extraction (the Cs distribution coefficient) is temperature dependent, increasing as the temperature decreases. Thus, at higher temperatures, the extraction efficiency would tend to decrease. The cyclic behavior tends to follow ambient temperature in the lab, which ranged from ~18 to 32°C, during the course of the experiment. Consequently, the Cs concentration in the raffinate samples tends to be higher during the hotter parts of the day. Time zero corresponds to 7 a.m., and the higher Cs concentrations observed at 15, 40, and 65 hours coincide with warmer ambient temperature during afternoon and early evenings. Note that the flow rate of the organic solvent was increased immediately after the 40 hour sample was taken and that the Cs concentration generally increased for the duration of the test. Operationally, temperature dependence poses no serious problem, provided the temperature dependence is understood, since the process solutions or even the individual contactors can be temperature controlled. The information in Figure 4 tends to indicate that the increased organic flow was actually detrimental to Cs

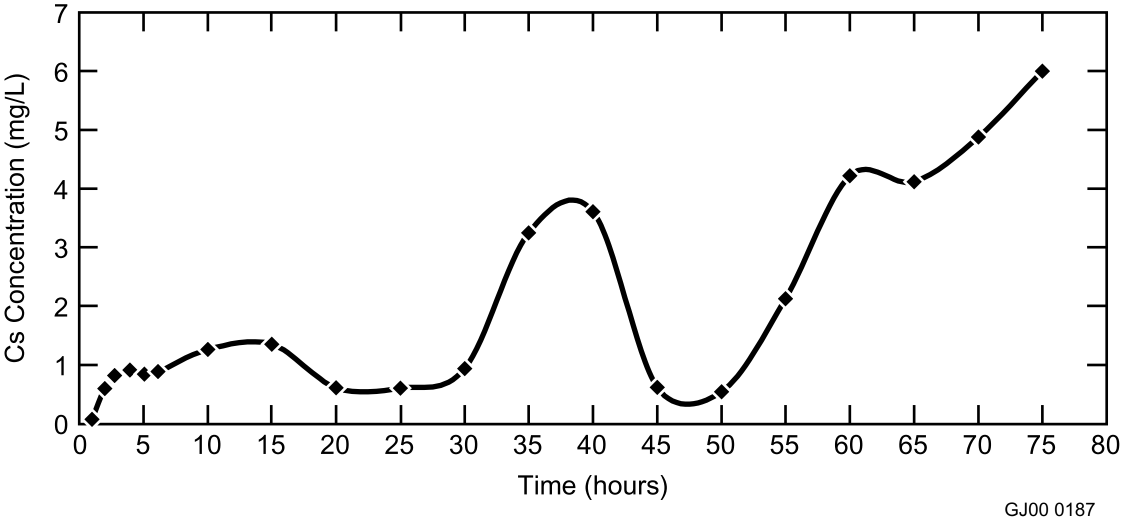

**Figure 4.** Time-wise concentration of Cs in the raffinate.

extraction efficiency. However, the data are inconclusive and it is uncertain whether the increase in Cs concentration would have continued or would have cycled to a lower value due to a reduction in ambient temperature. Further experimental work is required to quantify the temperature dependence of the Cs distribution coefficient and allow accurate predictions of extraction efficiency.

The Cs and Sr concentration in the strip product are indicated as a function of time in Figure 5. The rapid increase in initial Cs and Sr concentrations indicate that the strip section reached steady-state operation after less than 3 hours of operation. The concentration decrease after 40 hours reflects the increase is strip feed and organic solvent flow rates immediately after taking the samples at 40 hours. Following the adjustment in flow rates, the strip section returned to steady state operation, which remained constant for the duration of the test.

The dynamic test and associated data fulfilled the objectives of the FY-00 program and indicate the viability of the process as applied to INEEL tank waste. The use of FS-13 as the diluent in the organic solvent provides acceptable process performance. The composition of PEG-400 in the organic phase can be adequately controlled by adding PEG to the aqueous strip feed solution. The flowsheet was substantially simpler than previous renditions in that the solvent wash section was eliminated, thereby reducing the volume of secondary waste. Deleterious effects to process performance due to losses of solvent components or buildup of metals in the solvent were not observed during the operating time of this test. The results also indicate numerous points where process and analytical improvements could be made to substantially enhance process performance.

## CONCLUSIONS

The FY-00 accomplishments associated with this project were contingent on the continued, successful collaboration between the INEEL and Khlopin Radium Institute (KRI) to apply the Fission Product Extraction Process to INEEL radioactive liquid waste. Laboratory data and preliminary dynamic testing at KRI were used to formulate a potential, preliminary flowsheet for time-wise extended dynamic testing at the INEEL in the centrifugal contactor mockup with simulated tank waste. In the flowsheet tested, 97.5% of the Cs, >99.992% of the Sr, >99.6% of the Ba, and 99.8% of the Pb were extracted from the simulated tank waste and recovered in the strip product. Lesser amounts of the major, bulk species of

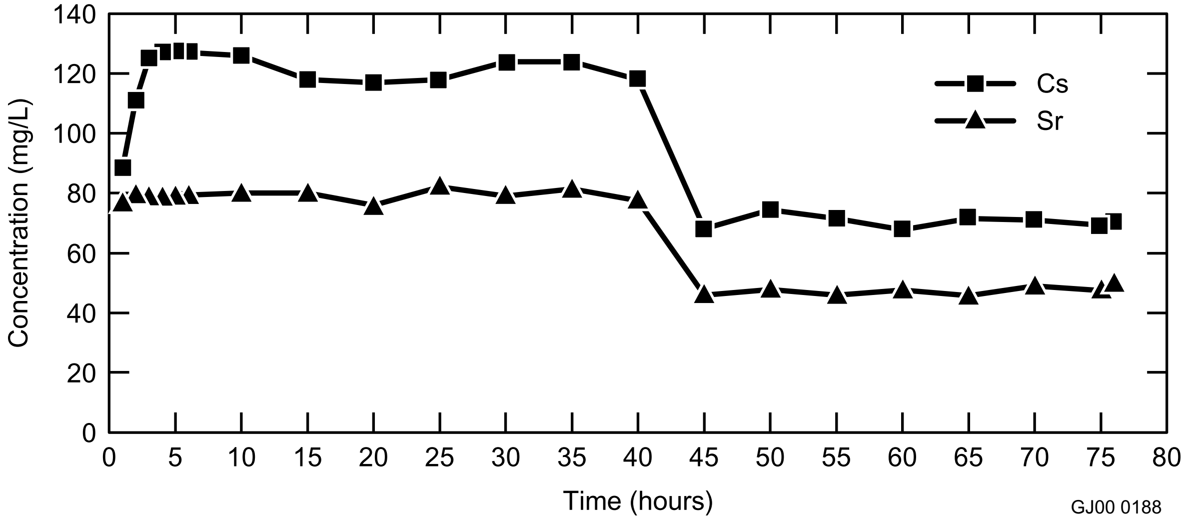

**Figure 5.** Time-wise concentration of Cs and Sr in the strip product.

Na, K, and Ca were also extracted and recovered in the dynamic test. Minor (<1%) of the Fe, Zr, Mo, and Hg followed the fission product surrogates to the final strip product solution. Extraction of Eu, used as an actinide surrogate, was negligible, indicating the process efficiently fractionates Cs and Sr (predominate fission products) from the transuranic fraction in INEEL tank waste. The dynamic flowsheet tested indicates process viability while incorporating significant changes and recent developments with regard to previously established and tested separation flowsheets. A new, less toxic organic phase diluent (FS-13) was evaluated as an alternative to m-nitrotrifluoromethyl benzene used in previous flowsheets. Guanidine carbonate was used as a substitute for hydrazine, concentrated nitric acid, and ammonium nitrate solutions, previously used as stripping and scrubbing reagents. Finally, the solvent wash and regeneration section of previous flowsheets was completely eliminated with positive results, thereby minimizing the quantity of secondary waste generated during the process.

While these process alterations resulted in a net, positive effect on the extraction process, the flowsheet developed and tested during this project still has substantial potential for improvement and optimization, and ultimately must be demonstrated on samples of actual INEEL tank waste. Future work would emphasize refinement of the organic phase composition for substantial increase in Cs removal efficiency, while maintaining a high Sr extraction efficiency. Methods to minimize waste (raffinate and strip) volumes should be explored. Potential strategies to reduce waste volumes include reducing or eliminating the initial 20 vol% dilution of the waste used in this test, decreasing the flow rate of scrub solution, and/or reducing the flow rate of the aqueous strip solution. An evaluation regarding the necessity of the scrub section or using different scrub solutions may provide an alternative means to reduce the raffinate volume. The temperature dependence of the Cs extraction distribution coefficient must be elucidated. Required analytical methods to accurately establish the PEG concentration in the organic phase must be developed. Finally, additional testing on samples of actual tank waste is necessary to validate flowsheet characteristics and process improvements.

## ACCOMPLISHMENTS

- In the flowsheet tested, 97.5% of the Cs, >99.992% of the Sr, >99.6% of the Ba, and 99.8% of the Pb were extracted from the simulated tank waste
- Extraction of Eu, used as an actinide surrogate, was negligible, indicating the process efficiently fractionates Cs and Sr (predominant fission products) from the transuranic fraction in INEEL tank waste
- A new, less toxic organic phase diluent (FS-13) was evaluated as an alternative to m-nitrotrifluoromethyl benzene used in previous flowsheets
- Guanidine carbonate was used as a substitute for hydrazine, concentrated nitric acid, and ammonium nitrate solutions, previously used as stripping and scrubbing reagents
- The solvent wash section, used in previous flowsheets, was successfully eliminated, resulting in process simplification and minimization of secondary wastes
- The concept of controlling PEG losses from the organic phase (due to solubility in aqueous phases) by adding PEG to the strip feed solution was verified. However, the results indicate additional efforts are required to quantify PEG solubility losses and develop accurate methods

to determine PEG concentration in the organic phase, allowing for accurate additions to the strip feed solution.

## REFERENCES

1. M.F. Hawthorme and T.D. Andrews, *J. Chem. Soc., Chem. Commun.,* 1965, 19, 443.
2. M.F. Hawthorne, D.C. Young and P.A. Wegner, *J. Am. Chem. Soc.,* 1965, 87, 1818.
3. J. Rais, P. Selucky, and M. Kyrs, *J. Inorg. Nucl. Chem.,* 1976, Vol. 38, pp. 1376-1378.
4. E. Makrlik and P. Vanura, *Talanta,* 1985, Vol. 32, No. 5, pp. 423-429.
5. M. Kyrs and P. Selucky, *J. Radioanal. Nucl. Chem. Articles*, Vol 174, No. 1, (1993) 153-165.
6. J. Rais, et. al, *J. Radioanal. Nucl. Chem.,* 1991, Vol. 148, No. 2, pp. 349-357.
7. P. Selucky, et. al., *Radiochem. Radioanal. Letters,* 1979, Vol. 38, No. 4, pp. 397-302.
8. Esimantovski V.M., et. al., "Technological Tests of HAW Partitioning with the use of Chlorinated Cobalt Dicarbolyde (ChCoDiC); Management of Secondary Waste," International Symposium Waste Management-92, Tucson Az., March 1-5, 1992.
9. E. V. Dzekun, Chief Engineer, MAYAK Production Association, Ozyorsk, Russia, *personal communiqué.*
10. I.V. Smirnov, et. al., "Combined Reprocessing of HLW by Universal Solvent on the Base of Cobalt Dicarbollyde and Phosphorylated Polyethylene Glycol," Spectrum'98, Denver, Colorado, USA, September 13-18, 1998, Proceedings, American Nuclear Society Inc, USA, 1998, p. 606-609.
11. T. A. Todd, et. al., "Countercurrent Treatment of Acidic INEEL Waste Using a Universal Extractant," Proceedings from the International Conference on Decommissioning and Decontamination and on Nuclear and Hazardous Waste Management, SPECTRUM '98, Denver, Colorado, September 13-18, 1998, vol. 1, pp. 743-747.
12. J. D. Law, et. al., "Demonstration of a Universal Solvent Process for the Separation of Actinides, Cesium and Strontium from Actual Acidic Tank Waste at the INEEL," Global '99, USA.
13. J. D. Law, et. al., "Demonstration of the UNEX Process for the Simultaneous Separation of Cesium, Strontium, and Actinides from Actual INEEL Tank Waste," INEEL External Report INEEL/EXT-99-00954, October 1999.

# Computational Simulation of Mechanical and Chemical Systems

### Randall A. LaViolette, Research Area Leader

For any problem, the ability to predict the outcome of a proposed solution is essential to making an informed decision concerning future research for, or deployment of, that solution. Recent advances in computation, both in terms of hardware and software, place reliable predictions within reach, often with less effort than required for a full demonstration. Therefore, the two-fold objective of this task is (1) to deliver a computational infrastructure consisting of hardware, software, and networking to INEEL scientists; and (2) the trustworthy prediction of the outcome of a wide variety of technologies, processes, or strategies that have been or soon will be proposed for solving Environmental Management needs. The following two projects constitute this task (Computational Simulation of Mechanical and Chemical Systems):

1. Computational Infrastructure Project

   Maintaining and operating a state-of-the-art hardware, software, and networking infrastructure for computational simulation.

2. Computational Simulation Project

   Employing state-of-the-art computational tools to predict and evaluate the outcomes of a wide variety of mechanical or chemical systems, specifically for the following problems:

   a. Chemical and molecular transport processes in liquids and solids

   b. Macroscopic dynamics of complex fluids and solids

   c. Fracture propagation in solids

   d. Determinism in time series

   e. Maintain, upgrade, and operate Squadron (beowulf-class parallel computer).

# Computational Simulation

**Randall A. LaViolette, Ray A. Berry, Eric D. Steffler,**
**Richard L. Williamson, Charles R. Tolle**

## SUMMARY

This project is divided into the following computational simulation (CS) tasks (task leaders are named in brackets):

| | | |
|---|---|---|
| (CH) | Chemical and molecular transport processes in liquids and solids | [R. LaViolette] |
| (TS) | Determinism and chaos in time series | [C. Tolle] |
| (FD) | Macroscopic dynamics of complex fluids and solids | [R. Berry] |
| (FP) | Fracture propagation in solids | [E. Steffler] |
| (BW) | Squadron (Beowulf cluster) operation | [A. Marley] |

The objective of this project is the delivery of new capability in, and results from, the computational modeling of chemical and physical processes that occur in systems studied by the Office of Environmental Management (EM) programs, especially those areas under the Idaho National Engineering and Environmental Laboratory (INEEL) Environmental Systems Research (ESR) Program. One of the themes that unify these tasks is that all contribute to the long-term scientific infrastructure of the INEEL. Another theme concerns the problem of *scale up*. This is the problem of elucidating the rules by which one can employ the results for small, even molecular systems in order to understand the behavior of complex systems. We have focused on the contaminated subsurface, which is a complex system consisting of heterogeneous and strongly interacting components that may interact over many different space and time scales. Tasks CH, FD, TS, and FP are concerned, particularly with the dynamics of chemical and physical processes, for one of a wide variety of space and time scales that affect the fate of contaminants in the subsurface or the outcome of proposed remediation strategies.

## PROJECT DESCRIPTION

This project consists of basic research. Some of the EM Science needs that are or can be addressed by this research are presented in Table 1. The CS Tasks (indicated by the two-letter code) are described in detail following Table 1.

**Table 1.** Selected EM science needs and CS subtasks.

| Selected EM Science Needs (alphabetical order) | CS Task |
|---|---|
| Chemical Sensor Principles | CH |
| Chemistry of Problem Constituents for HLW Vitrification | CH |
| Contaminant Mobility Beneath Tank Farms | CH, FD |
| Contaminant Transport in a Fractured Rock Vadose Zone | CH, FD |
| Decision Support Assistance for Remediation and Assessment Design | CH, FD, TS |
| Differences Between Saturated and Unsaturated Systems | FD |
| Effect of Subsurface Heterogeneities on Chemical Reaction and Transport | CH, FD |
| Fracture Toughness Properties for Carbon Steel Utilized for Nuclear Waste Containment Vessels | FP |
| Integration of Reactive Chemistry into Field-Scale Transport | CH, FD |
| Issue of Scale in Flow Prediction and Contaminant Remediation in Porous Media | CH, FD, TS |
| Low-Frequency Stress-Wave Stimulation for Enhanced Transport of NAPL Groundwater Contaminants | CH, FD |
| Mathematical Formulations of Chemical Reaction/Material Transport | CH, FD |
| Mechanisms of Line Plugging | FD |
| Moisture Flow and Contaminant Transport in Arid Conditions | FD |
| Physics of Fracture Flow and Transport in the Vadose Zone | FD, TS |
| Quantifying Uncertainty in Predictions of Remediation Performance | CH, FD, TS |
| Transport of Contaminants | CH, FD |
| Transport of HE and Metals in Fractured Rock and Surface Alluvial Systems | CH, FD |
| Vadose Zone Flow Simulation Tool Under Arid Conditions | CH, FD, TS |
| Water Fluxes and Solute Transport in Arid and Semiarid Environments | CH, FD |

## Chemical and Molecular Transport Processes in Liquids and Solids (CH)

The topics here come under the broad heading of computational and theoretical chemistry. Part of this work provides computational chemistry capabilities for a variety of tasks listed here, in other ESR tasks, and other tasks. Some of the latter include the study of solid acid catalysts in supercritical fluids, methane hydrates under seabed conditions, and hydrogen storage in intercalated graphite. All of these projects have paid for the labor involved in using these capabilities, but none could have paid to independently develop the capabilities that have been and continue to be developed under this task. The applications identified here are aimed at elucidating chemical and molecular transport processes in condensed phases. In these subtasks, the theory and techniques developed for isolated or simple chemical systems are incorporated in studies of more complex systems, and ultimately, the subsurface environment.

The connection between the structure of solvents around a solute and the corresponding thermodynamics is central to predicting solubility behavior from a molecular perspective. Recent work at Los Alamos National Laboratory (LANL) and the INEEL has suggested a simple procedure by which thermodynamic information can be extracted from the structures obtained from ab initio studies of solutes in associated liquids. We have studied test cases by employing the classical and quantum mechanical codes obtained from MSI (Molecular Simulations, Inc.) to obtain structures, which then can be analyzed with the new *quasi-chemical* theory reported by us last year. LANL supports Dr. Pratt in his share of the effort.

Ligand complexation may provide a route to immobilization or removal of contaminants from solid materials or minerals. We have begun to elucidate, through Monte Carlo calculations, the effective rate law for multidentate ligand complexation on a surface. Support for Dr. Redden came from other ESR tasks.

Computer simulation of contaminant transport in soils with randomly distributed biodegradation sites has revealed anomalies in both the degradation kinetics and transport. Although the phenomenon has been outlined for a simple model in a recent publication of ours, we have begun to apply this discovery to particular cases. Such an application requires input from the molecular to the macroscopic scale, from chemical and biochemical reaction dynamics to fluid dynamics. We have begun to elaborate on the simple model and explore anomalous transport for particular cases of interest.

Previously, we considered widely available materials as candidates for solid-state separation membranes. We have tried a different approach this year, namely, designing new materials from first principles. These new, and for the moment, hypothetical, hollow octahedral materials have been investigated computationally and show promise as solid-state separation membranes.

We have continued to integrate legacy and third-party Monte Carlo, molecular dynamics, and quantum mechanics codes into a common visualization environment for molecular modeling. The task included the examination of software offered both by private companies and national laboratories. The acquisition and implementation of these codes on the INEEL's SGI (Silicon Graphics, Inc.) multiprocessor ("Orion"), and the DEC (Digital Equipment Corporation) beowulf-class machine (see BW below), permit the modeling of more complex systems than had been previously available to us. The availability of a standard graphical user interface permits us to visualize the molecular dynamics in ways previously unavailable to us. Code development for the Beowulf-class machine will be essential because few (if any) commercial codes will run on it. We also have written utility codes, using MSI's Software Development Kit for the extraction and analysis of data produced by MSI code.

## Determinism and Chaos in Time Series (TS)

Many experiments, from the laboratory to field studies, can be expressed as the measurement of a time series. We expect to advance the state-of-the-art in the detection of determinism (e.g., periodicity) in complicated time series by exploiting recent advances in time-based clustering and fuzzy logic. The efforts under this project shifted away from the time-based clustering efforts of previous years in order to develop a new statistical measurement of texture. The concept that was explored is known as lacunarity. The term is derived from the Latin *lacuna* which means gap. Mandelbrot theorized that a texture could be described using three measures: fractal dimension, lacunarity, and connectivity.[1] Fractal dimension is well understood and there exists many means to estimate it; although many problems still exist, the concepts are well understood.[1–5] The same cannot be said of the latter two measures. The importance of being able to describe generic textures quantitatively must not be underestimated. The applications are wide ranging and include biofilm grow modeling,[6] to target detection and tracking.[2–5] This project was designed to investigate the principles behind lacunarity, develop a measure of it, and implement an estimation algorithm. Once a means for quantifying lacunarity is achieved, the time series analysis of biological systems can proceed under measurements of biofilm growth using this new statistic.

# Macroscopic Dynamics of Complex Fluids and Solids (FD)

The emphasis of this task remains on the research and development of advanced modeling tools permitting the exploration of problems in material dynamics such as reactive, multicomponent, multiphase, and multimaterial mixtures exhibiting complex interactive flow processes. As with last year's efforts, this year's activities touch, to varying degrees, on the same three areas of particle methods, multiphase mixtures, and nucleation. The bulk of the description given here will address the area receiving the most effort, that of particle methods.

Recently, we have been developing and testing several *meshless* or *grid-free* methods whereby the computational nodes have no permanent connectivity with near neighbor nodes, thus no mesh distortion occurs. These new methods can be applied to problems where traditional Eulerian and Lagrangian techniques fail, such as those of complex fluid, multiphase, reactive, and solid mechanics involving large deformation, fluid-fluid or fluid-solid interactions, and contorted geometry. Because of the context in which they are derived, several of the new meshless methods refer to their computational nodes as *particles* and the methods as *particle methods*. The particle method approach is envisioned to enable the simulation of a host of detailed pore-scale phenomena occurring in porous media such chemical transport through geological media, pore-level surface transport and surface-catalytic reaction, transport of microbes, and other transport which is difficult to simulate with currently available methods.

These meshless or particle methods for transient problems can be split into two major categories. The first category is composed of methods attempting to solve for bulk material motions by redefining the molecular particle masses and the molecular interaction forces of *molecular dynamics* methods to represent bulk particle masses and bulk interparticle forces, respectively. The resulting particle dynamics is that of a bulk material motion. Examples of this approach are *quasiparticle method*[7] and *dissipative particle dynamics*.[8] The second category comprised methods that attempt to solve the classical continuum mechanics PDE's (though possibly in integral or weak form). Several proposed methods fall into this category; for example, sophisticated interpolation routines for scattered data, modern variants of particle-in-cell methods, and meshless methods, such as the moving point semiimplicit (MPS) scheme,[9] generalized finite difference (GFD) scheme,[10] and the smoothed particle hydrodynamics (SPH) scheme,[11] along with its corrected forms.

A variant of the particle-in-cell method called material point method[12] is incorporated into the CFDLIB (a software library) multiphase, multimaterial, flow dynamics code as documented during the previous year's efforts.[13] Working with the LANL developers of CFDLIB, we have implemented and maintained the two latest versions released this year. CFDLIB continues to offer unparalleled capability for certain classes of multiphase, multimaterial flow problems, particularly with direct applicability to environmental concerns.

Significant effort was spent investigating the novel spatial differencing developed for the MPS scheme. Its spatial differencing uses a function of weighted sums of neighbor points similar to SPH. However, unlike SPH, to produce a spatial derivative (gradient, divergence, Laplacian, etc.) it does not integrate by parts, shifting the difference from the dependent variable to the weight function. On closer theoretical examination it was noticed that significant errors occurred with spatial derivative with nonuniform distribution of particles around the central particle. However, we believe we have developed a fix for this problem, which we currently plan to test and publish.

Significant effort was also spent researching, coding, and testing a GFD scheme to do heat conduction. The spatial differencing was basically a two-dimensional, second-order, Taylor series approximation of the dependent variable function that is least squares fit at each particle to the particles of the cloud associated with that particle. When the normal form equations were used, solutions using a two-step hybrid approach and an LU decomposition failed, presumably due to ill-conditioned matrices of the least squares fit. When the coding was rewritten to solve the least squares problem with polynomial basis functions using the quasiparticle solution method, the first and second order spatial derivatives were accurately produced.

Unlike the SPH method which, because it produces spatial derivatives through integration by parts, naturally gives Neumann type (normal direction gradient specification) boundary conditions at free surfaces, the MPS and GFD methods require explicit interface identification if Neumann boundary conditions are to be implemented. All three methods (MPS, GFD, and SPH) require boundary particle identification for implementation of Dirichlet type (dependent variable specification) boundary conditions. An automatic interface identification and tracking method was developed for the SPH scheme and will be detailed shortly.

Some of our research activities during the past year with the SPH method are discussed. SPH is based on the idea of treating material elements (fluid or solid) as extended clouds of material whose centers of mass constitute discrete computational points or *particles* which move according to the continuum conservation laws. As the motions of these particles are followed in time, problem variables such as density, velocity, deformation gradients, and stresses are obtained using integral interpolation functions or smoothing functions—thus, the name *smoothed* particle hydrodynamics. The substantial interest shown in this meshless Lagrangian method results from its promise to do away with the mesh-tangling problems which plague traditional Lagrangian calculations on a finite difference or finite element mesh. The Lagrangian feature of SPH is desired because it allows the computational points to be embedded in the material and thus reduces some of the material interface problems associated with Eulerian techniques. Furthermore, because of the SPH technique's ability to handle severe distortions, it can be applied to problems that historically have been reserved for Eulerian approaches.

For time-dependent problems, however, the SPH method still requires the integration of the discretized conservation equations forward in time. When explicit time integration is used, most traditionally used methods require a time step size inversely proportional to the material's sound speed to maintain numerical stability. SPH has a similar requirement. This results in a time-step size that is excessively small for computational efficiency for slow speed flows simulations (too many time steps are required) such as those described above. Some researchers have suggested that for low speed flows, the sound speed can be artificially lowered to enable larger time steps.[14] Our own research has indicated that this approach may give nonphysical results under some fairly deceptive circumstances. Traditionally used methods (particularly Eulerian methods) overcome this problem of disparate time scales by using partially or fully implicit time integration. This results in a time step inversely proportional to the material velocity. For low speed flow problems where material velocity is much lower than the material's sound speed, the implicit time integration is stable for much larger time steps and is thus more efficient for slow flow problems (a fewer number of time steps are required). Implicit time integration typically requires the inversion of large matrix equations. For such inversions, traditional Eulerian methods (fixed mesh, fixed connectivity, invariant node neighbors) can easily use specialized methods developed to take advantage of the structure of the matrices, typically sparse and banded. For SPH methods where nearest neighbor nodes are continually changing, it was initially believed that implicit and partially-implicit methods would not be effective.

One of the objectives of our research involved investigation of a *matrix-free* alternative method for achieving partially implicit time integration effects. This development is an extension of research begun previously at the INEEL known as the damped, artificial compressibility method.[15] Originally, this method was developed to accelerate low speed flow simulations (using explicit, fixed mesh methods) toward steady state. Our research was aimed at acceleration of a modified equation set toward a *pseudo-steady-state* attained at the end of each time step. With damped artificial compressibility, the governing equation, in Lagrangian form, for mass, internal thermal energy, and momentum balance are, respectively,

$$\frac{d\rho}{dt} = -\rho\nabla\cdot\vec{u}$$

$$\frac{de}{dt} = -\frac{p}{\rho}\nabla\cdot\vec{u} + \frac{Q}{\rho}$$

$$\frac{d\vec{u}}{dt} = -\frac{1}{\rho}\nabla q + \frac{\vec{S}}{\rho}$$

Where $\rho$ is the material density, $u$ is the material velocity, $p = p(\rho,e)$ is the material pressure, $e$ is the internal thermal energy, $Q$ is a collection of stress power, thermal conductivity and energy source terms, and $S$ is a collection of shear stress, body force, and source terms. The time derivatives are Lagrangian, following local material points. The variable $q$ is a pressure-like variable given by

$$\frac{dq}{dt} = \beta^2\frac{dp}{dt} - \frac{\beta^2}{\lambda}(q-p) - \rho D\frac{d}{dt}(\nabla\cdot\vec{u})$$

Where $\beta$ is the factor by which the effective sound speed is reduced, $\lambda$ is a relaxation time, and $D$ is an artificial bulk viscosity, all of which are discussed in Ramshaw and Mousseau.[15] This evolution equation for $q$ was developed[15] to reduce the effective sound speed by a factor $\beta$ and to accelerate the convergence to steady state by means of an appropriate damping term. Since the pressure $q$ appearing in the momentum equation artificially deviates from the equation of state pressure $p$ during the transient, the transient solution is therefore unphysical. However, Ramshaw and Mousseau claimed that, at steady state, the deviation of $q$ from $p$ vanishes and the proper physical steady state solution is obtained.[15]

It was hypothesized that this scheme could be extended to transient flows via a time-like iterative scheme:

$$\frac{\rho^{i+1}-\rho^i}{\Delta\tau} = -\frac{\rho^i-\rho^n}{\Delta t} - [\rho\nabla\cdot\vec{u}]^i$$

$$\frac{e^{i+1}-e^i}{\Delta\tau} = -\frac{e^i-e^n}{\Delta t} - \left[\frac{p}{\rho}\nabla\cdot\vec{u} + \frac{Q}{\rho}\right]^i$$

$$p^{i+1} = p\left(\rho^{i+1},e^{i+1}\right)$$

$$\frac{q^{i+1}-q^i}{\Delta\tau} = \beta^2\frac{p^{i+1}-p^i}{\Delta\tau} - \frac{\beta^2}{\lambda}\left(q^i-p^i\right) - \rho^i D\frac{(\nabla\cdot\vec{u})^n-(\nabla\cdot\vec{u})^{n-1}}{\Delta t}$$

$$\frac{\vec{u}^{i+1}-\vec{u}^i}{\Delta\tau} = -\frac{\vec{u}^i-\vec{u}^n}{\Delta t} - \frac{1}{\rho^{i+1}}\nabla q^{i+1} + \left[\frac{\vec{S}}{\rho}\right]^i$$

Where $\tau$ is the pseudo-time variable and $i$+1 and $i$ are successive iteration indexes. For each physical time step $\Delta t$, these equations would be marched out to a steady state in pseudo-time, the pseudo-time derivatives would then vanish, and $\rho$, $p$, and $u$ would converge to the new-time $(n+1)\Delta t$ values.

To expose problems peculiar to this extension, independent of problems that may result with coupling to SPH, the new approach was first to be developed and tested as a transient, fixed mesh method. To make this extension as close to that of SPH as possible, the transient, fixed mesh method selected was that of an explicit, node-centered, finite element method. Successful results here were requisite to the extending of this approach to SPH. It was found that the damped artificial compressibility method was severely lacking in robustness, requiring excessive effort to fine tune $\beta$, $\lambda$, and $D$, along with $\Delta\tau$ and $\Delta t$, to obtain acceptable solutions. Further development on this extension to SPH was dropped for the time being. It is recommend that a similar technique, as described by Mary, Sagaut, and Deville,[16] be developed in the future.

Efforts were shifted to the construction of a matrix-free, partially implicit (subsequently called pressure-implicit) solver for the SPH type particle method (the procedure we were initially trying to avoid with the extension of the damped, artificial compressibility method above). Consider the simplified conservation equations:

$$\frac{d\rho}{dt} = -\rho\nabla\cdot\vec{u}$$

$$\frac{de}{dt} = -\frac{p}{\rho}\nabla\cdot\vec{u}$$

$$\frac{d\vec{u}}{dt} = -\frac{1}{\rho}\nabla p$$

$$p = p(\rho, e)$$

Where the meanings of the variables are as stated above. An evolution equation for pressure was derived as

$$\nabla\cdot\left(\frac{\nabla p}{\rho}\right)^{*} - \frac{p^{*}}{\Delta t^{2}\left(\frac{p}{\rho}\frac{\partial p}{\partial e} + \rho\frac{\partial p}{\partial \rho}\right)^{n}} = -\frac{p^{n}}{\Delta t^{2}\left(\frac{p}{\rho}\frac{\partial p}{\partial e} + \rho\frac{\partial p}{\partial \rho}\right)^{n}} + \frac{1}{\Delta t}\left(\nabla\cdot\vec{u}\right)^{n}$$

Which is solved for $p^{*}$, the estimated new-time pressure. Using this estimate for new-time pressure, the density $\rho$, and internal energy $e$ are updated explicitly. If necessary, a final new-time pressure can then be determined from the equation of state. The second term on the left side and the first term on the right side of the Poisson type equation for calculating the pressure reflect the effects of the assumed local thermodynamic equilibrium by which the contribution from compressibility is included. The implicit pressure equation is to be solved using the Bi-CGSTAB method described by Van Der Horst.[17] When properly preconditioned, Bi-CGSTAB has shown very rapid convergence. Preliminary results with this pressure-implicit approach look encouraging and this research is continuing. Publication is planned for this work.

As mentioned, because it was becoming necessary (physically, mathematically, and numerically) to identify and track material and/or part interfaces, an algorithm was constructed to automatically perform this function. For example to model surface tension effects the material interfaces must be identified and its normal direction and curvature locally determined. An algorithm was developed based on the known weakness of the SPH method to compute spatial derivatives near a free surface. Because all of the particle methods have a common infrastructure, this method will work for all. The technique developed is similar to that described by Randles and Libersky.[18] First, a color function $\phi$, e.g., a constant value such as 1.0, is assigned to each particle of a body. The kernel estimate or SPH smoothed value of the $\phi$ is computed and the boundary is indicated by

$$\phi_i \neq \sum_{j \in N_i} \phi_j m_j W_{ij} / \rho_j$$

Where $m_j$ is the mass of the *jth* particle in the cloud of particles about particle *i*, $N_i$. A boundary either bordering empty space or a neighboring body of different kind is indicated when this inequality is sufficiently large. If a boundary is indicated by this inequality, then particle *i* is designated as a boundary particle and an estimate for the outward unit normal at *i*; then

$$\left(\nabla \phi\right)_i = -\sum_{j \in N_i} \phi_j m_j \nabla W_{ij} / \rho_j$$

$$n_i = \pm\left(\nabla \phi / \left|\nabla \phi\right|\right)_i \ .$$

The power of this technique is illustrated with the same configuration of a colliding droplet and solid ball as demonstrated in the FY 1999 Annual Report.[13] The droplet above is traveling downward at 100 m/s while the solid ball below is traveling upward at 100 m/s. The ensuing collision produces large deformation of the droplet interface and, subsequently, fractures which create new interface. Figure 1 shows this evolving interface identification and surface normal direction vectors. The droplet and the ball are given the same color function so the interface will show the two as combining bodies. Note that the significant increase of surface area as the algorithm interprets the latter stages of the droplet expansion as extensive fracturing, which is what it should do regardless of whether the fracturing is physical or numerical in origin.

## Fracture Propagation in Solids (FP)

The usefulness, lifetime, or safety of solid systems or components (e.g., waste containers, encapsulation matrices) is largely determined by fractures in solids. The ability to simulate and predict the behavior of fractures is therefore crucial to decisions about the choice of materials for these components, or estimates of the lifetimes of existing structures. The ability to predict the behavior of propagating cracks is important for an assessment of the behavior of solid components for long times, as might be required by waste container specifications for example. Current remediation techniques used to remove contaminated concrete can be improved by examining alternate, more efficient material breakup technologies based on a comprehensive understanding of fracture processes and numerical simulations. The task will continue to support projects in the materials dynamics area, especially coatings for environmental applications, corrosion and aging of solids, and decontamination/decommissioning. Secondly, this technique will be extended and verified via experimental comparison to elastic and elastic-plastic materials. Eventually, the research tool will analyze portions of full-scale structures/containers to assess the propensity for crack growth and estimate the time and conditions that would lead to catastrophic system failure.

This task is devoted to the development of computational capability and expertise to simulate (dynamic) propagating fractures in both elastic and elastic-plastic materials. Fracture modeling is one of the more challenging aspects of solid mechanics computations because of the large stress and strain gradients and microscopic spatial scales involved. Since many INEEL tasks have included the need for fracture modeling, the necessary capability and expertise to simulate static (nonpropagating) fractures has been well established. Such simulations are clearly limited, however, since fractures naturally propagate,

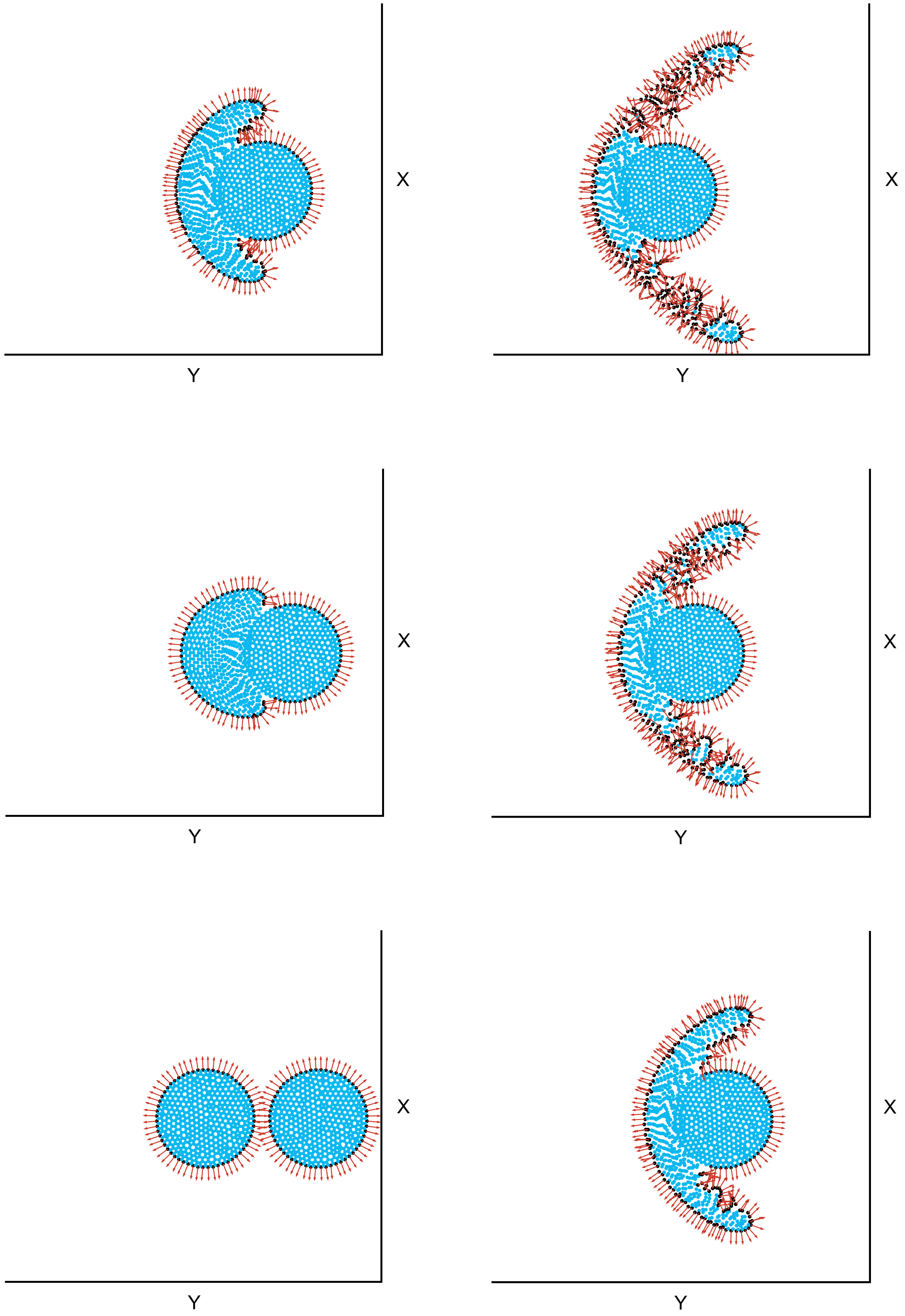

**Figure 1.** Droplet interface and subsequent fractures, showing new interface.

i.e., they evolve in time and space. The task has involved the use of the 2D Arbitrary Local Mesh Replacement (ALMR2D) method to compare numerically predicted fracture paths to published linear-elastic material fracture experimental results to validate/test the algorithm range of applicability. The current modeling capability, unique to the INEEL, is a direct result of FY-98/FY-99 accomplishments and cannot be done with commercial software. The subsequent sections give an overview of tasks completed in FY 2000 concerning the ALMR2D algorithm.

### Staff Training

The latest release of ALMR2D was installed on a workstation for INEEL staff access along the distribution of the latest ALMR algorithm user's manual. A comprehensive tutorial was also included which afforded interested personnel the opportunity to learn the programming conventions as needs were identified. The inherent capabilities of the algorithm to model/predict a crack trajectory without knowing the crack path is a powerful tool that only exists here at the INNEL within the fracture group.

### Experimental Work

The fracture test results of 2024 aluminum were conducted in an effort to quantify constraint effects on crack extension used as algorithm validation. Ms. Tonya Emerson, a graduate student from the University of California at Davis, was at the INEEL for the past summer to strengthen the collaborative efforts with the fracture group. The experimental work conducted during that time was used as benchmark information to refine/validate the ongoing development of the elastic-plastic algorithm.

Twenty-two 2024-aluminum specimens (fourteen 230 mm × 50 mm × 25.4 mm and eight 230 mm × 50 mm × 12.7 mm samples, respectively) were used for fracture tests. These dimensions were chosen to determine the constraint effects of this material and to use recorded engineering data to validate the elastic-plastic algorithm. A schematic of the test geometry is shown in Figure 2. Various positions of load application (1, 2, 3, and 4) were used to impose a variety of mixed mode crack tip stress fields that resulted in various crack trajectories.

After test completion, the specimens were completely separated to expose the crack surface. This exposure also enabled identification of fatigue crack profile, final crack front geometry, and the type of crack growth that occurred during corresponding events in recorded engineering data. While these tests establish a baseline for a full test matrix, additional experiments will be required to fully characterize the mixed mode fracture behavior of this material while developing a methodology for additional material. Once the process is refined, the minimum test matrix to determine material properties will be identified for any given engineering material. A typical data graph is shown in Figure 3, with the crack tip opening displacement (COD) and cross-head load.

### Brittle Coating

Protective coatings are often applied to metal materials, for example thermal spraying or as naturally grown oxide scales. Since these coating processes are typically done at high temperature and the substrate and coating posses significantly different thermal expansion coefficients, large and often detrimental thermal stresses are developed during cooling. At locations of significant geometry changes such as corners the stresses can be concentrated resulting in increased probability of fractures and thus undesirable failure of the brittle coating. In the DOE-BES Mechanically Reliable Surface Oxide (MRSOX) program here at the INEEL, significant modeling efforts have investigated the quantitative effects of these stress risers and the resulting fracture paths. In recent modeling efforts, a multiple crack

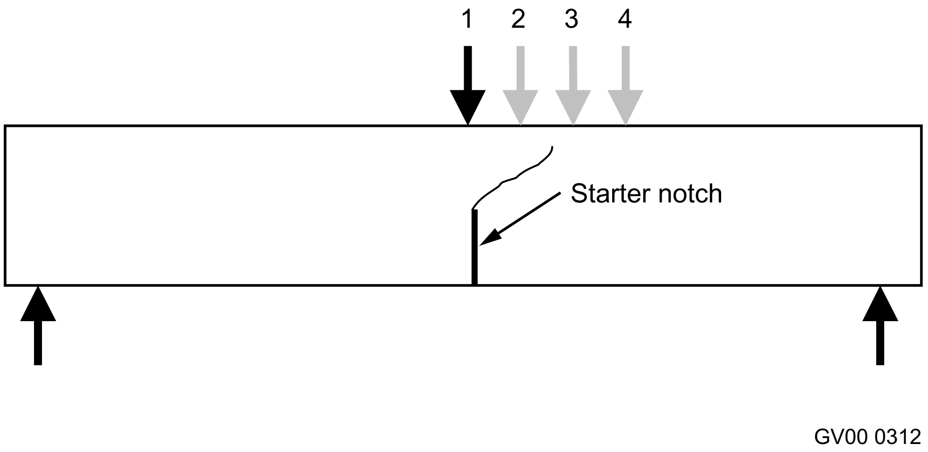

**Figure 2.** Three pt. bend bar geometry used for experimental work.

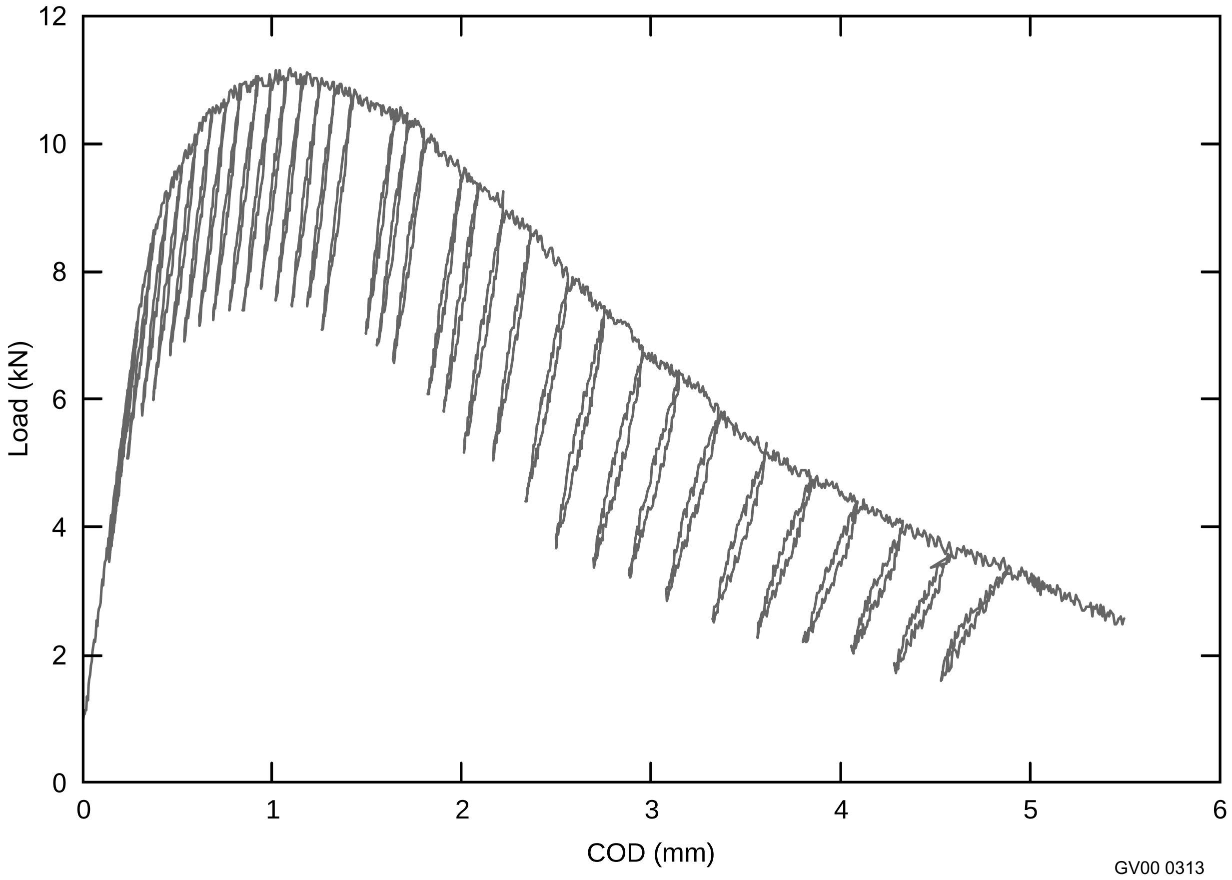

**Figure 3.** Typical engineering data acquired during 3 pt. bend test.

simulation has demonstrated the ability to predict crack extension in the brittle coating with initiation and extension in various locations. After a primary crack has extended and arrested, the redistribution of stress results in crack extension at other flaw locations. The primary drawback to this approach is that the crack paths need to be predefined. This is a significant limitation when complex stress fields and geometries are encountered, since the probable crack path of an actual system cannot be know before hand. An example of this type of model with multiple flaws is shown in Figure 4 and was produced using the commercial package ABAQUS.

FEFRAC was used to calculate similar crack geometries. A thermomechanical ABAQUS model was used to calculate the displacements along a coating to substrate interface. Since FEFRAC is currently only available for linear elastic materials, the ABAQUS calculated boundary displacements along the coating portion of the model were extracted and used as boundary condition input for FEFRAC. This two step process enabled the modeling of crack growth without guessing the probable fracture path. The geometry used by ABAQUS with the metal substrate and brittle coating is shown in Figure 5. Note the region of interest is at the corner of the model. Symmetry was used and only ¼ of the original component was modeled. Figure 6 shows a magnified image with the first flaw calculation introduced at 45 degrees through the corner.

The same boundary conditions were used with flaws introduced at 40 and 50 degrees. Figures 7–9 show large magnifications of the corner region of interest with extended flaw paths. Displacements are agnified for illustrative purposes. Note the significant crack path changes predicted by the model.

Additional analyses were applied to additional crack angles and material properties. The substrate in ABAQUS was defined as perfectly plastic for one case and work hardened in a second case. Other parameters were changed and the effects were compiled with typical results shown in Figure 10. Variable $c$ is crack length and $t$ is total scale thickness. Note the symmetry of the trajectories up to these load steps which is expected for this symmetric problem.

In the ABAQUS model illustrated in Figure 4 the secondary flaws grow and arrest at shorter flaw lengths as the distance from the maximum stress region is increased. This spatially makes physical sense except that there is a slight asymmetry in the stress contours surrounding the shorter flaws. If the stress intensity at the tips of these secondary flaws is both Mode I and Mode II, the maximum tensile stress direction may not be coincident with the required ABAQUS predefinition. This is evidenced in the initial numerical analysis of the same system using FEFRAC where the maximum stress surrounding the crack tip defines the direction of extension. If this can be confirmed with refined models, it will help explain why spallation of coating material consistently occurs near geometric features on actual components. With this knowledge, the geometric designs can be optimized to reduce and or eliminate this type of coating failure resulting in improved component integrity and cost savings.

The unique research code FEFRAC enables the fracture analysis group to model propagating cracks without the confines of crack path predetermination. The algorithm developed by Dr. Mark Rashid was supplied to the INEEL at no cost as a result of ongoing collaborative research. Dr. Rashid visited the INEEL and assisted in experiments that are currently being used to verify the latest elastic-plastic versions of the algorithm that will also be supplied to the INEEL at no cost. The working linear elastic version running at the INEEL has been used for a comprehensive analysis of the oxide scale problem. The algorithm has proven to be an improvement over traditional modeling methods in predicting crack path and has been used to supplement ongoing research in Coatings for Environmental Applications.

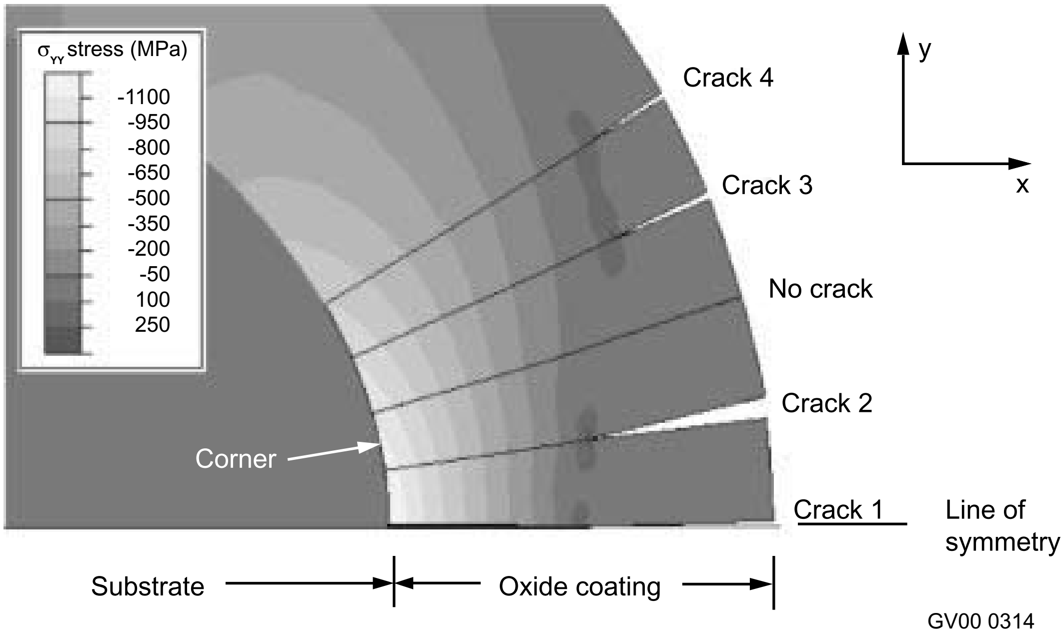

**Figure 4.** Multiple predefined crack ABAQUS model.

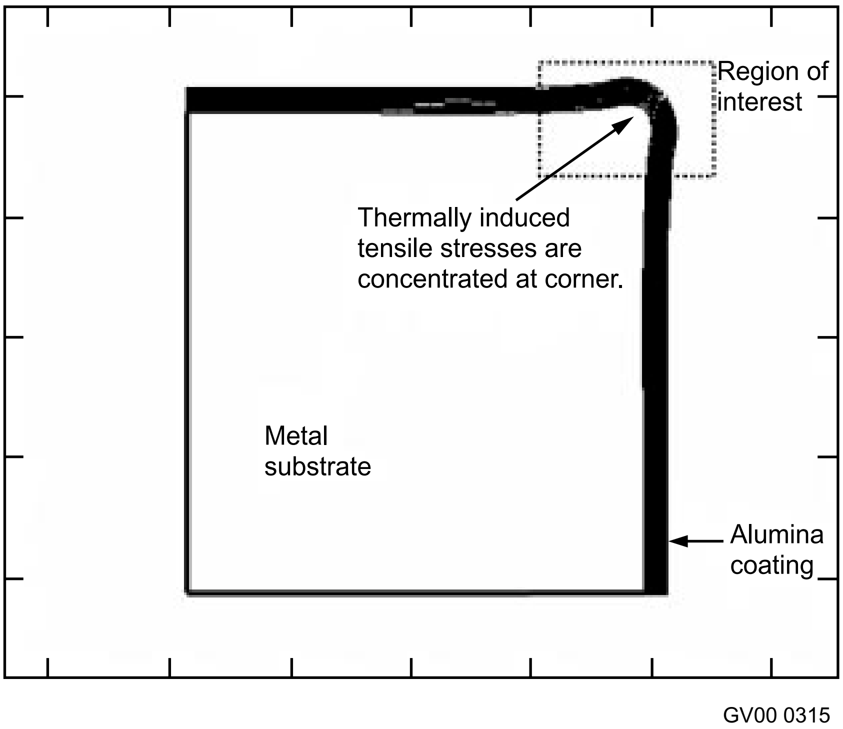

**Figure 5.** Overall model used in analysis showing the ¼ geometry with brittle coating and metal substrate.

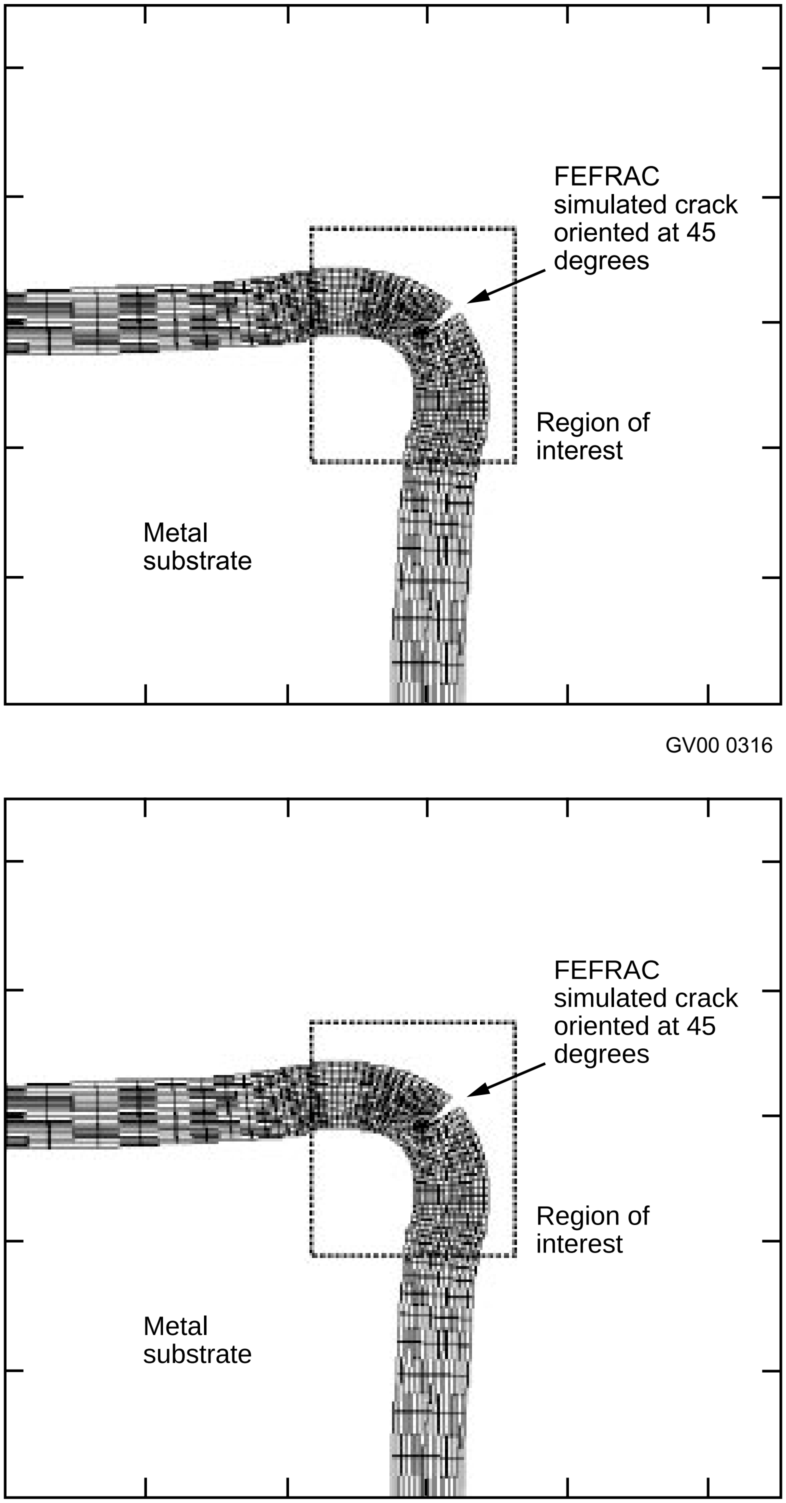

GV00 0316

**Figure 6.** Magnified image of corner model, showing initial 45-degree flaw introduction and resulting path.

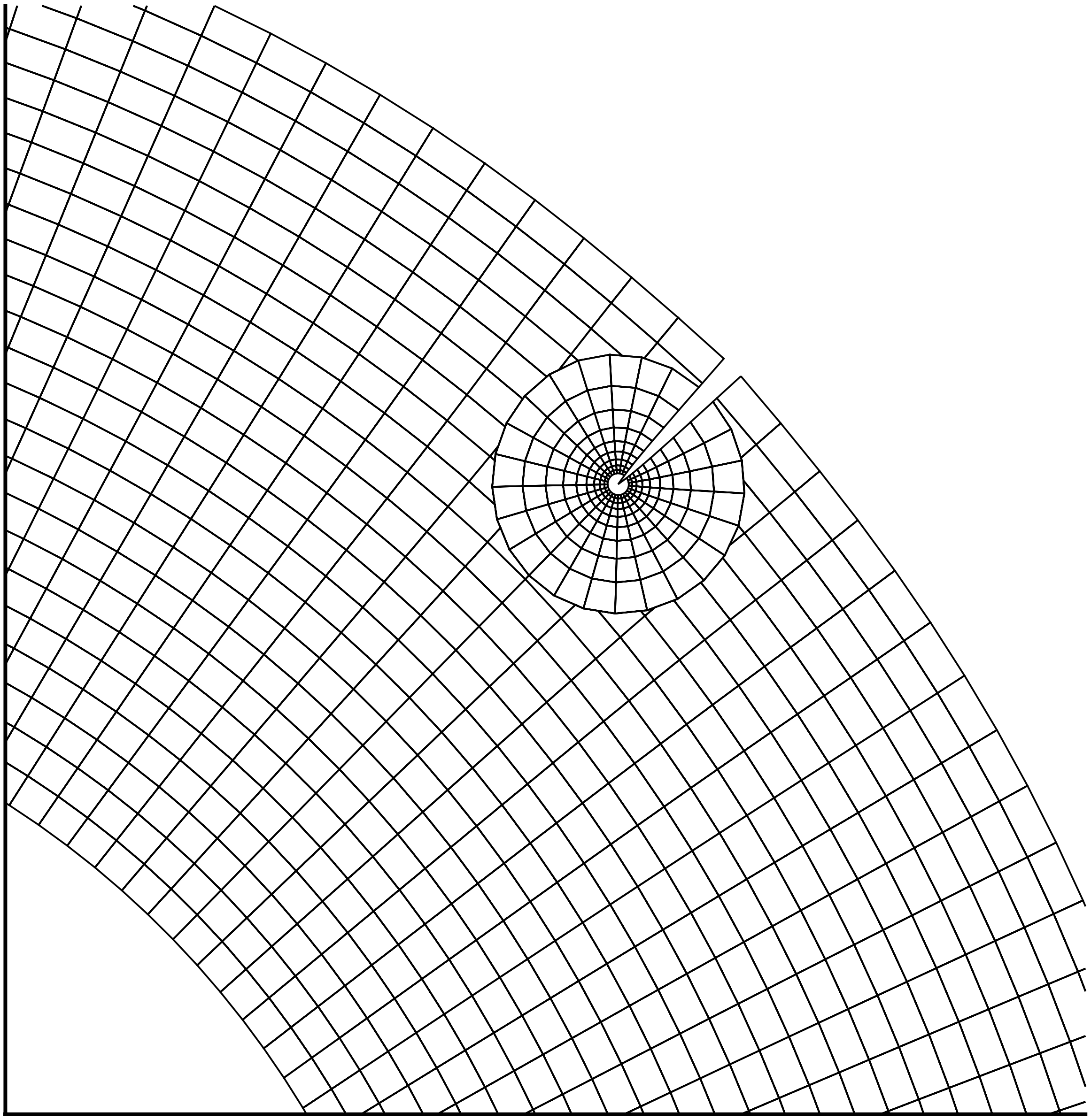

GV00 0317

**Figure 7.** FEFRAC predicted crack trajectory with initial flaw at 45 degrees at beginning of analysis.

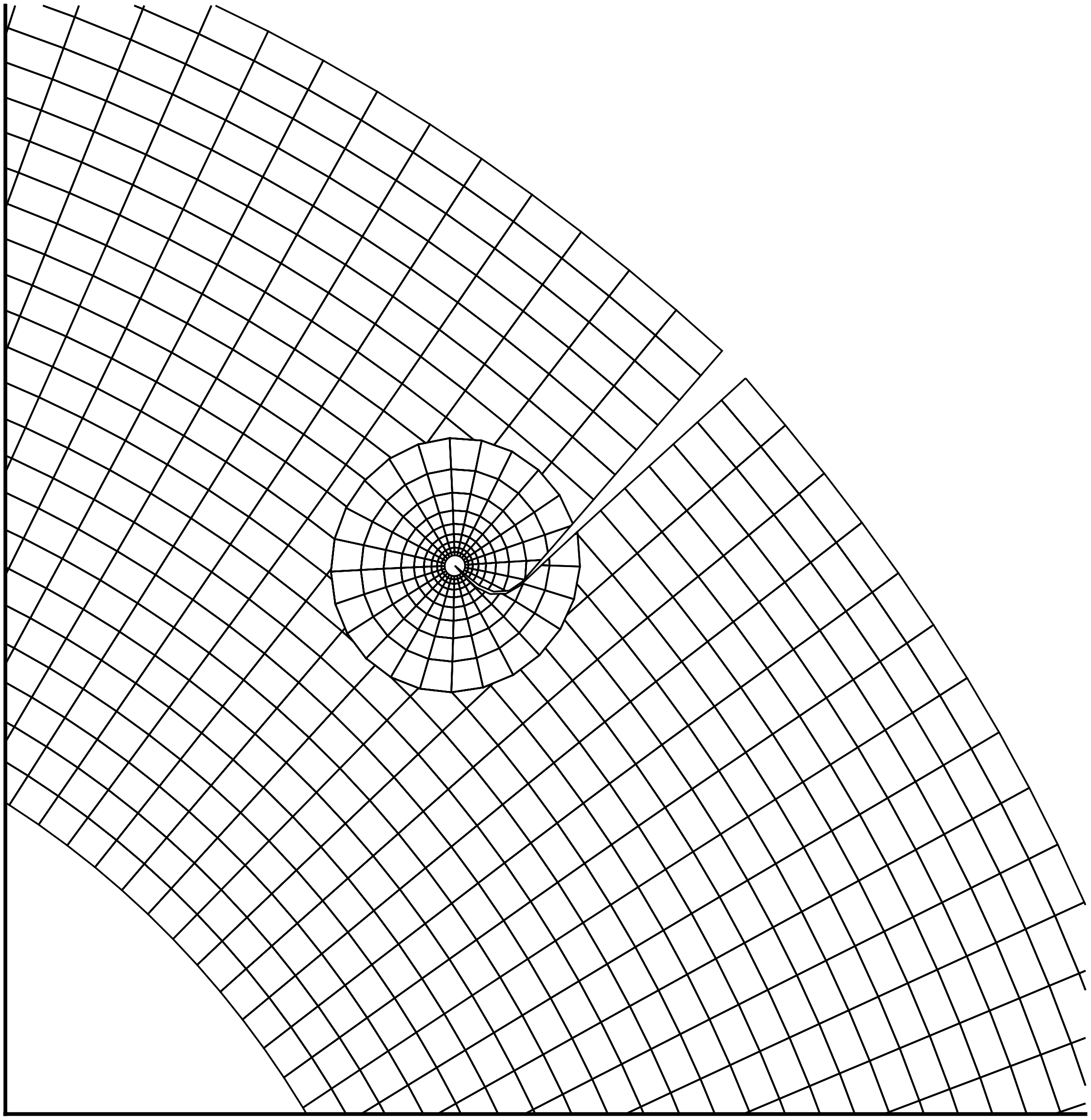

**Figure 8.** FEFRAC predicted crack trajectory with initial flaw at 45 degrees after 15 steps.

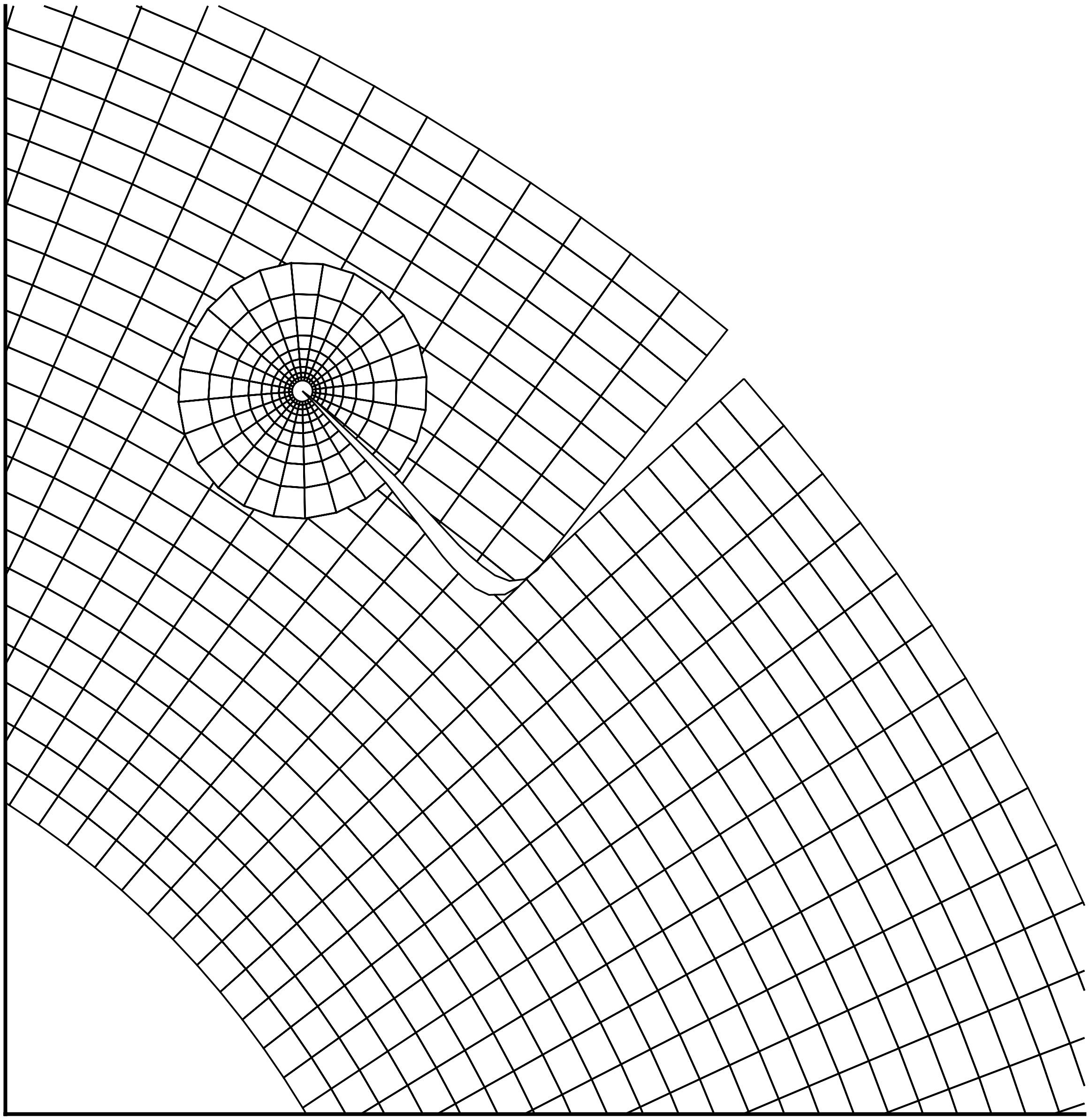

**Figure 9.** FEFRAC predicted crack trajectory with initial flaw at 45 degrees after 30 steps.

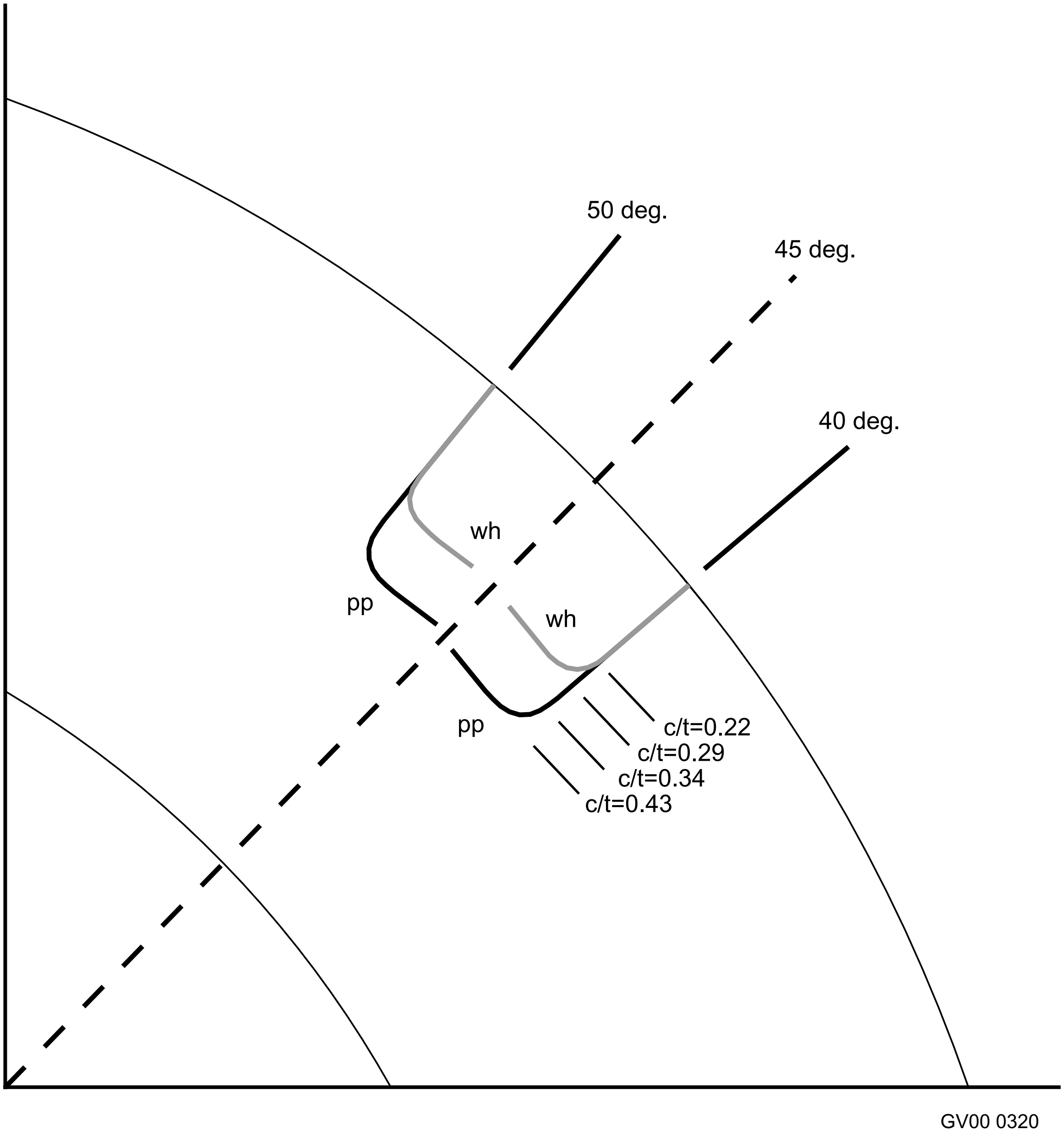

**Figure 10.** Multiple crack trajectories are shown for 40- and 50-degree initiation angles and the effects of perfectly plastic and work hardened substrates.

Numerical results indicate that FEFRAC predicted probable fracture paths that could be obtained in no other conventional finite element analysis packages. Ongoing and anticipated extensions of this work will extend the unique capabilities for fracture modeling at the INEEL to include analysis of elastic-plastic fracture.

## Squadron (Beowulf Cluster) Operation (BW)

Squadron is the Beowulf cluster built in FY-99 with operational funds from this task. Squadron consists of 27 DEC (now COMPAQ) 500a Alpha workstations containing a 533 MHz cpu, 4 Gby of hard disk, and 512K RAM (random access memory); ten of these processors were installed in FY-00. Nineteen AMD 650 MHz K7 processors, each with 512K RAM, have been ordered. All are (or will be) connected to a Cisco switch capable of connecting the 48 workstations in a heterogeneous array and supplying 10/100 networking. Squadron already runs a variety of home-grown and freeware message-passing parallel codes, and the CFDLIB from LANL. Squadron does not run the MSI computational chemistry code, but will run the GAMESS electronic structure code from Iowa State after some work, and the molecular dynamics code written this year for polymer diffusion simulation. Squadron provides, when fully configured and with finely tuned code, the fastest wall-clock computational speed at the INEEL.

## ACCOMPLISHMENTS

1. The project supported the discovery of

    - New materials with potential for applications in solid separation membranes
    - Anomalies in the transport of fluids in disordered media
    - Spontaneous chirality in achiral clusters and liquids
    - Significant errors in previous particle approaches to computational fluid dynamics
    - Anomalies in the kinetics of adsorption of multidentate molecules on mineral surfaces
    - New definition of lacunarity.

2. The project supported the development of novel approaches and code for

    - Predicting dynamic fracture propagation in solids
    - Detecting and reconstructing chaotic dynamics in noisy time series
    - Classifying complex patterns in two or three dimensions with the lacunarity
    - Generating random numbers
    - Simulating complex flow in geometrically complicated media
    - Calculating the solubility of ions and molecules in aqueous solutions
    - Estimating the solubility of gases in polymer membranes

- Modeling adsorption kinetics of complicated molecules
- A moving-least-squares particle method for more accurate spatial derivatives (tested with heat conduction equation)
- A method for detecting edges and interfaces on which boundary or other special conditions can be employed for fluid-dynamical particle methods in general
- A partially implicit, pressure based method for the solution of sph hydrodynamics
- A one-dimensional demonstration code coupling advection to the qmom scheme for nucleation and growth of nanocrystaline phase.

3. The project supported the implementation of the following additional capabilities:

   - Squadron (beowulf cluster), consisting of a dedicated 48-port CISCO switch with 27 DEC 500 MHz alpha processors and 19 AMD 650 MHz K7 processors (on order)
   - Computational chemistry codes: DMOL (MSI), GAMESS (Ames Lab), NWCHEM (PNNL).

## REFERENCES

1. B. B. Mandelbrot, “The Fractal Geometry of Nature: Updated and Augmented,” *W. H. Freeman and Company*, New York, NY, 1983).

2. D. Gorsich, C. R. Tolle, G. Gerhart, “Wavelet and Fractal Analysis of Ground Vehicle Images,” *8th Annual Ground Vehicle Survivability Symposium Proceedings* (1997).

3. D. Gorsich, C. R. Tolle, R. Karlsen, G. Gerhart, “Wavelet and Fractal Analysis of Ground Vehicle Images,” *1996 SPIE Symposium Proceedings* (1996).

4. C. R. Tolle, D. Gorsich, “Sub-Optimal Covers for Measuring Fractal Dimension,” *Proceedings of the 1996 Rocky Mountain NASA Space Grant Consortium Conference, University of Utah* (1996).

5. D. Gorsich, C. R. Tolle, R. Karlsen, and G. Gerhart, “Wavelet and Fractal Analysis of Ground Vehicle Signatures,” *7th Annual Ground Vehicle Survivability Symposium Proceedings* (1996).

6. Z. Lewandowski, D. Webb, M. Hamilton, and G. Harkin, “Quantifying Biofilm Structure,” *Wat. Sci. Tech*. 39 (7)(1999) 71.

7. A. M. Kristov, “Relation Between Spall Strength and Mesoparticle Velocity Dispersion,” *Internat. J. Impact Engrg.*, 23, pp. 477–487, 1999.

8. Pep Espanol, Mar Serrano, and Hans Christian Ottinger, “Thermodynamically Admissible Form for Discrete Hydrodynamics,” *Phys. Rev. Letters*, 83, pp. 4542–4545, 1999.

9. S. Koshizuka and Y. Oka, “Moving-Particle Semi-Implicit Method for Fragmentation of Incompressible Fluid,” *Nuclear Science and Engineering*, 123, pp. 421–434, 1996.

10. T. J. Liska, C. A. M. Duarte, W. W. Tworzydlo, “HP-Meshless Cloud Method,” *Comput. Methods Appl. Mech. Engrg.*, 139, pp. 263–288, 1996.

11. J. J. Monaghan, “Smoothed Particle Hydrodynamics,” *Annu. Rev. Astron. Astrophys.*, 30, pp. 543–574, 1992.

12. D. Sulsky, Z. Chen, and H. L. Schreyer, “A Particle Method for History-Dependent Materials,” *Comput. Methods Appl. Mech. Engrg.*, 118, pp. 179–196, 1994.

13. D. L. Miller, *Environmental Systems Research, FY-99 Annual Report*, INEEL Report INEEL/EXT-99-01008, January 2000.

14. J. P. Morris, P. J. Fox, and Y. Zhu, “Modeling Low Reynolds Number Incompressible Flows Using SPH,” *J. Comp. Phys.*, 136, pp. 214–226, 1997.

15. J. D. Ramshaw and V. A. Mousseau, “Damped Artificial Compressibility Method for Steady-State Low-Speed Flow Calculations,” *Computers & Fluids*, 20, pp. 177–186, 1991.

16. I. Mary, P. Sagaut and M. Deville, “An Algorithm for Low Mach Number Unsteady Flow,” *Computers & Fluids*, 29, pp. 119–147, 2000.

17. H. A. Van Der Vorst, “Bi-CGSTAB: A Fast and Smoothly Converging Variant of Bi-CG for the Solution of Nonsymmetric Linear Systems,” *SIAM J. Sci. Stat. Comput.*, 13, pp. 631–644, 1992.

18. P. W. Randles and L. D. Libersky, “Smoothed Particle Hydrodynamics: Some Recent Improvements and Applications,” Comput. Methods Appl. Mech. Engrg., 139, pp. 375–408, 1996.

# Computational Infrastructure

**Lance (Eric) Greenwade,**
**Melinda J. Cebull, Steven R. Woosley, Kari A. Holsberry, A. Shewmaker**

## SUMMARY

The computational infrastructure task has the charter to maintain the robust, effective, and modern set of computing technologies that support modeling and simulation of computational components of environmental problems. The charter includes support for all elements of computational work, including physical and process simulation, data analysis, archiving, and appropriate visualization and communication tools. Included were the system configuration, preventative maintenance, and routine operation of the Numerical Simulation Laboratory (NSL) located in Room 169 of the Engineering Research Office Building. FY 2000 efforts contain no new capability implementation or enhancements. The effort will continue a core multiprocessing computing capability, both shared and distributed memory, that is flexible, expandable, and incorporated into a well-designed product future. This project is divided into the following tasks: system configuration, preventative maintenance, routine operation. No new developments or hardware additions were planned. All systems maintained an availability of greater than 99% and a 50% increase in the number of users. In addition, the potential workload exceeded available resources for most of the year. New visibility for the INEEL was obtained in several areas with NSL staff presentations of peer-reviewed papers at three international technical conferences.[1,2,3]

## PROJECT DESCRIPTION

Planning for additional hardware was performed in two stages. The first focused on the equipment identified as part of the yearly INEEL General Purpose Capital Equipment (GPCE) requests, and the second as a part of the Environmental Sciences Candidate Research Products (ESCRP). The rapid growth in the number of users and the resulting increase in demand for processor time necessitated these upgrades. These plans for the upcoming hardware system upgrades and expansions were performed in a time effective manner that minimized the impact to users and programs. This entailed analyzing and evaluating the complex interconnection environment that encompasses the NSL. Although several GPCE requests were placed on the funded list, management removed these from consideration.

System configuration management improved dramatically this year by the addition of an experienced system administrator. This subtask included monitoring and maintenance of a large number of parameters that effect overall system performance and reliability. It includes, but is not limited to disk partitions, memory allocations, processor allocations, batch queues, and network interfaces. For the first time the NSL staff included an individual whose primary function was to monitor and maintain the facility. Hence, the NSL was able to move away from the previous fix-on-failure mode and into one with planned maintenance objectives focused on the high availability of computational resources.

The NSL presently consists of more than four dozen separate computing systems, including eight that incorporate parallel processing capability. There is also almost a terabyte of magnetic disk and a multiple terabit archive system that support the many users of the NSL. Preventative maintenance covers the system administration activities required to keep such a complex environment functioning effectively, including the avoidance of known hardware and software problems, by regular preventative maintenance and upgrades to the operating systems and user software environments. This is a proactive function that helps maintain the equipment in peak working order, greatly increasing the overall availability of the resources to the users. Approximately 70% of the FY 2000 budget was devoted to the purchase of maintenance agreements for both hardware and software in order to keep both current, to provide vendor support when questions arise, and to replace parts that malfunction.

User administration continues to be an important and time-consuming task. With the majority of INEEL users having minimal previous scientific computing experience, a good deal of time is required to get them up and functional on the equipment. This covers all the day-to-day activities associated with adding and removing users from the system. As such, user identifications, directories, groups, passwords, etc., must be effectively maintained across the diverse, heterogeneous NSL environment so that users can move as transparently as possible from machine to machine as their computing requirements dictate. An integral part of a robust system and user administration policy is the performance of system and user level backups on a regular basis. The present hardware configuration of the NSL severely limits the number of routine system and user file system backups to less than that necessary for a normal level of redundancy. Present procedures provide system and project level backups for archival purposes as the primary backup policy.

No development or implementation activities were funded for FY 2000. The computational infrastructure task was solely a maintenance operation. All development and new implementations for high performance computing and visualization were to be performed in various other program areas. The NSL staff did participate in several other high performance computing and visualization activities funded directly by EM Operations groups, but not directly associated with the Environmental Systems Research and Analysis (ESRA) Program.

## ACCOMPLISHMENTS

The NSL computing resource was maintained at an availability of greater than 99% for FY 2000. This was the highest level of availability ever achieved on scientific computing resources at the INEEL. The normal mode of operation was uptimes exceeding several months, with reboots only to reduce the indices of the process tables. There were several planned downtimes required for either hardware or software maintenance activities which were performed in a structured fashion that minimized the impact on users. Frequently several different maintenance activities were scheduled to occur during a given system downtime, therefore reducing the total number of times the systems were unavailable to users. This occasionally had the effect of a slightly longer downtime, but greatly increased the overall systems availability and decreased the number of times long running jobs were interrupted.

During FY 2000 there was a fairly dramatic increase in the number of people using NSL computational resources; the overall increase in the number of users was over 50%, with an increase of 200% on the 40 node AMD K7 cluster. Several important new program areas were represented by these users, including the advanced bioremediation at Test Area North, the atmospheric modeling supporting air quality at the Idaho Nuclear Technology and Environmental Center, spent fuel, and several thermohydraulics applications (RELAP). However, the largest group of new users came from various portions of the ESRA and ESCRP programs, including both users from existing areas as well as new ones.

An important achievement for FY 2000 was integrated user management across all platforms. With the NSL consisting of over four dozen different computers representing five different hardware families, uniform user access, file management, application availability, and data backup and archival becomes a challenging problem. The successful integration and uniform management structure allows users to take advantage of the most appropriate technology (hardware, software, or both) necessary for their tasks. Providing this capability in a seamless and efficient manner was a major accomplishment for the year.

The benchmark activities initiated in FY 1999 were extended this year, primarily through the efforts of a returning summer student from the University of Idaho. These efforts help classify the INEEL scientific computing capabilities with a set of metrics used throughout the rest of the community, DOE-wide, nationally, and internationally. The benchmark INEEL system provides a comparison of the present INEEL capabilities in this area with its peers around the nation. The implementation of the 40 node AMD K7 (Beowulf) cluster at the end of FY 1999 unofficially placed the INEEL on the Top 500 Supercomputer Sites list for the first time ever. Unfortunately the resources to prepare an official ranking submission were not available and the list has been updated twice in the subsequent months without any additions at the INEEL. As a consequence the INEEL's presently demonstrated capability is only 5.24 Gflops. This is in contrast to the 2,000–30,000 Gflops at DOE Defense Programs labs, 250-1,500 Gflops at DOE non-Defense Programs labs and 100–500 Gflops presently available at many U.S. and foreign universities. These performance numbers and the resulting analyses are being used as part of the computational infrastructure upgrade presently funded via the ESCRP.

In a related activity, members of the NSL staff introduced several developments from DOE's Accelerated Strategic Computing Initiative (ASCI) Data Models and Formats activities into INEEL Environmental Management (EM) applications. These activities were not supported by FY-00 activities from this task, but did leverage the FY 1999 activities in this area as well as those supported directly by the EM Operations customer. This activity provided an application independent interface between the surface modeling code and the tools used to analyze the results. This approach also facilitated the ability to store and retrieve global extremes and use an efficient hierarchical storage paradigm. The combination of these features allows for a greatly enhanced analysis process, and was the subject of an invited paper presented at an international conference in Paris, France in April 2000.[2] This approach, based on the paradigms and work-to-date of DOE's ASCI program, provides for an application independent, network centric, visualization of extremely large and complex data sets, without incurring the costs of application specific developments.

In another related activity, the NSL staff participated in the development of a parallel implementation of bioremediation code being used to model the trichlorethene issue and TAN. Although these activities were not supported by this task, they did leverage the previous year's activities and the stable operational environment, which was directly supported by this task. In this activity, a pre-existing, fortran-based simulation code was being used for the modeling activities. This was a single processor code that had executions times that were approximately one week in length. These long run-times were severely limiting the number of models that could be performed, especially due to the sequential nature of the modeling activities; i.e., one model had to be run and analyzed prior to performing a second. The EM Operations program supported the NSL staff in assisting the end user in the analysis of the code for parallelization opportunities, and then the subsequent implementation of those that promised the greatest short-term advantage. Initial results were surprisingly good with a speedup of 4.75 on five processors. Additional work produced a version of the code that ran on 10 processors and became the standard working version for the EM Operations activities. With this new version of the code, more complex models could be executed and analyzed in substantially less time than before, providing better data for decision making for the EM Operations staff. A peer-reviewed paper on this activity was presented in Noodwijk, Netherlands in May 2000.[1]

# REFERENCES

1. R. C. Arnett and L. E. Greenwade, "Parallel Processing of a Groundwater Contaminant Code," *Summit 2000 Proceedings, Noodwijk, Netherlands, May 2000*.

2. L. E. Greenwade, et al., "Effective Multiresolution Visualization for Subsurface Science," Invited Lecture, *SUPerG 2000 Proceedings, Paris, France, April 2000*.

3. L. E. Greenwade, et al., "Annexes E, F, G ISO-15444 Draft Information Standard," *ISO/IEC International DIS, Tokyo, Japan, April 2000*.

# Materials Dynamics

### Richard Wright, Research Area Leader

It is critical to understand mechanisms when establishing reliable intermediate and long-term storage of spent nuclear fuel and mixed waste. In particular, we must characterize those mechanisms that lead to the following: (a) protection or degradation in engineered barriers, (b) fundamental processes by which corrosive fluids are transported to storage systems and (c) transportion modes in environmental contamination. To help meet these needs, Materials Dynamics has focused on specific tasks in three areas: biocorrosion, impermeable coatings, and transport in porous media. The technical approach in each of these tasks has been to develop fundamental understanding of underlying mechanisms. Such knowledge assists in estimating defensible predictions for materials behavior over very long times. Only with mechanistic stratagies is it possible to control and mitigate degradation of materials.

## Description of Research Activities

*Biocorrosion Task: investigations of mechanisms in biologically assisted degradation of cladding materials in spent nuclear fuel.* The Biocorrosion Task focused on morphological characterization of bacteria in biofilms, microscopic methods to determine the relationship of biofilm formation to local electrochemical activity, and the influence of desiccation on biofilm morphology and adhesion. An additional subtask, to examine biofilm formation on radioactive fuel cladding samples, was conducted in collaboration with Argonne National Laboratory West in their hot cell facilities.

*Coatings Task fabrication of dense impermeable ceramic coatings for waste processing equipment and engineered barriers.* During Fiscal 2000, the Coatings Task concentrated on developing methods to determine properties of ceramic materials in the form of coatings (in contrast to handbook values for monolithic materials of similar composition) to use as input for numerical simulation of residual stress development during coating fabrication. The properties of interest in this study included fracture strength, elastic modulus, and thermal conductivity.

*Transport in Porous Media Task: studies on transport of contaminated fluids in porous or fractured media.* The Transport in Porous Media Task concentrated on determining the fundamental physics of pores and fractures in terms of their nature and bulk flow properties. The technical progress in each of the topical areas are described in detail in the following sections.

# Coatings for Environmental Applications

**Richard N. Wright, W. David Swank, and Jill K. Wright**

## SUMMARY

Coatings are being developed for a variety of Department of Energy Environmental Management needs, including thermal barriers for vitrification process equipment and corrosion barriers for long-term storage of spent nuclear fuel. One of the major factors influencing the long-term performance of coatings is the residual stress that arises during coating deposition. In this project, we have focused on identifying the sources of residual stress in ceramic coatings applied to metallic substrates using plasma spray methods and on developing methods to control the residual stress through optimization of processing parameters. Processing-induced tensile stresses are the major cause of failure in ceramic coatings.

Numerical simulation methods have been developed and validated that describe the individual components of total residual stress in a model system of $MgAl_2O_4$ ceramic coating on stainless steel substrates with a conventional Ni-Al bond coat. In addition to the well-known stress contributions from quenching the molten particles and from differences in thermal expansion between the coating and substrate upon cooling from the deposition temperature, we have shown that there is a significant residual stress associated with plasticity in the substrate as a result of steep thermal gradients during coating deposition.

Experimental methods have been developed to determine the constitutive behavior of the ceramic material in the form of the coating, where the behavior is considerably different from that of monolithic material because of coating defects and the superimposed residual stresses. Numerical simulations incorporating experimental values for coating elastic properties and fracture strength properly describe the nature and magnitude of the observed residual stress. We have further demonstrated that the metallic bond coat contributes significantly to the total residual stress and that by proper control of the process variables the stress arising from bond coat application can be varied from tensile, through essentially no residual stress, to substantial compressive stress. A compressive residual stress in the coating is generally desirable to suppress failure by cracking or debonding.

## PROJECT DESCRIPTION

Fabricating coatings by thermal spraying gives rise to residual stresses, which are a major driving force for failure and debonding of coatings. The stresses are due to quenching and mismatch. The quenching contribution is caused as the hot splats adhere to the cold substrate and contract as they cool from the temperature at impact. The contraction is constrained by the underlying substrate, and a tensile stress necessarily develops in the deposit. During the deposition process, steep thermal gradients arise as the coating and adjacent substrate material approach some local equilibrium temperature. These gradients provide an additional source of thermal stress, which can be considered a component of the quenching stress.

The mismatch contribution results from the difference in thermal expansion coefficients between the coating and the substrate materials as they cool from elevated temperature at the end of the spray process back to room temperature. When the coating is ceramic and the substrate metallic, this contribution typically results in a compressive stress in the coating. The net residual stress state depends on the sum of the quenching and mismatch contributions.

One of the most common ways to determine the residual stresses experimentally is by measuring the curvature of a thin sample.[1] Figure 1 shows a schematic of the curvature resulting from the quenching (without thermal gradients) and mismatch contributions for the case of a ceramic coating applied to a metallic substrate. The direction of curvature in the sample indicates the relative dominance of these two contributions for the model system of a ceramic coating on a metallic substrate. The curvature is dependent on both the change in temperature, $\Delta T$, and the difference in thermal expansion coefficients, $\Delta\alpha$. The $\Delta T$ can be separated into a quenching portion, $T_{splat}$-$T_{entire\ sample\ during\ deposition}$, which occurs during deposition, and a mismatch portion, $T_{entire\ sample\ during\ deposition} - T_{room}$, which occurs during final cooling. The $\Delta\alpha$ component applies only during final cooling as well.

The residual stress can be directly calculated from the curvature of the sample if certain assumptions are valid. Among these assumptions are perfect bonding of the coating, elastic deformation of the metal, and uniform curvature of the coupon. In reality, it is likely that debonding, localized plasticity, creep, and/or micro-cracking occur. Some of these features, for example plasticity and creep, can be accounted for using more complex finite element method (FEM) calculations. Others remain difficult to quantify.

## Finite Element Modeling

The long, narrow strip geometry developed for this study was used in the hope that residual stresses could be accurately calculated using straight-forward analytic solutions available from the literature,[2,3,4] or two-dimensional finite element models of the x-y plane (Figure 2). Several types of finite elements are available for this type of analysis, each with an inherent set of assumptions. A 3D model verified that the sample is under a biaxial stress condition, and thus stresses can be calculated accurately using analytic solutions, provided the materials remain linearly elastic. If nonlinearities such as plasticity or temperature dependence exist, stresses can be calculated using 2D generalized plane strain elements. All

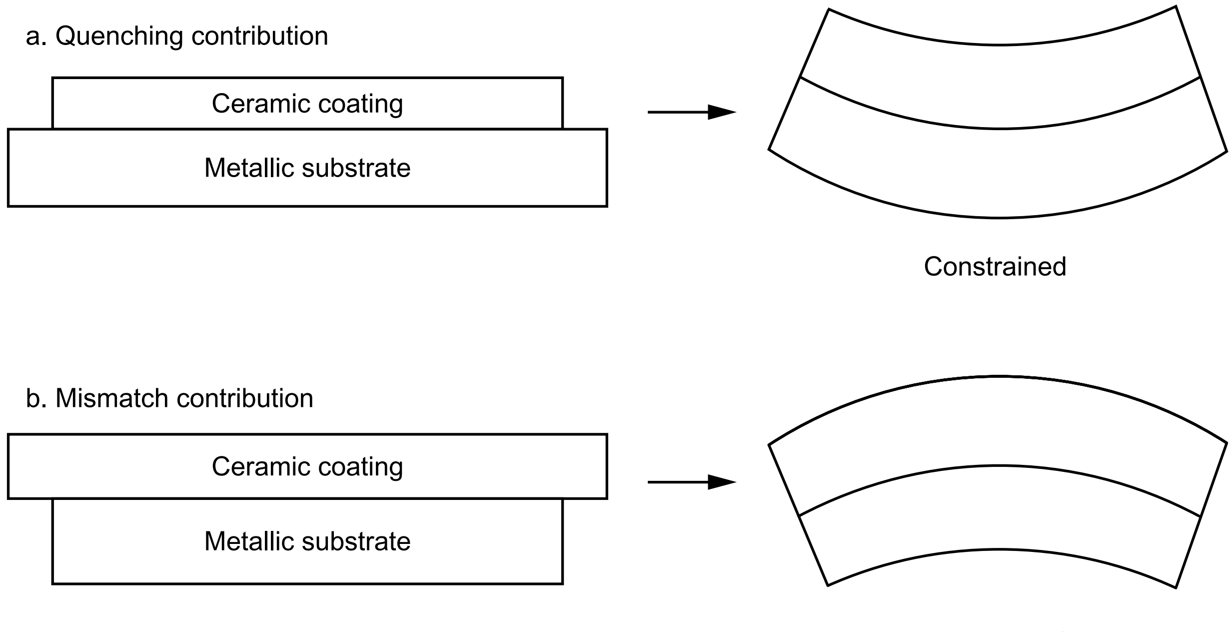

**Figure 1.** Schematic of curvature resulting from quenching and thermal expansion mismatch.

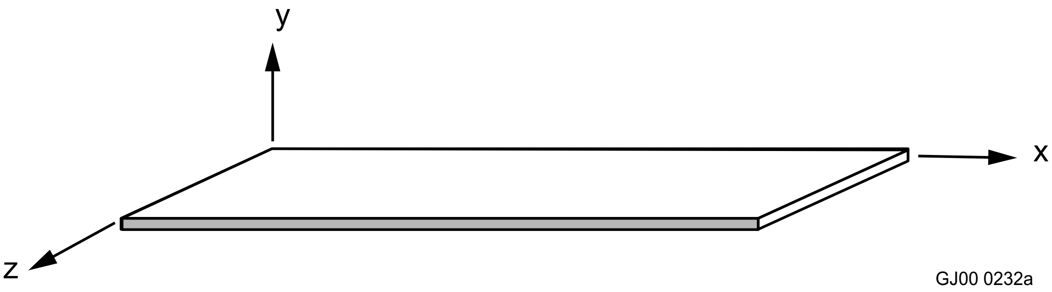

**Figure 2.** Sample schematic.

simulations used second order (quadratic) reduced integration elements. After a series of parametric numerical studies to examine these variables, a single column of elements through the thickness of the coupon with a periodic boundary condition was used to simulate an infinite plate, since results did not vary appreciably in the x or z direction (Figure 2) except near the edges. A large number of elements were required through the thickness to model accurately the large thermal gradient observed through the thickness. The mesh was constructed with 1000 elements, 500 each for the coating and the substrate.

In the experiments, the coatings were added a layer at a time, with each layer requiring two passes of the torch. During each pass, hot materials were added, and the torch heated one side while high-pressure laboratory air cooled the other side. The sample was removed from the torch while the air continued, and thus cooled for several seconds between each layer. After the last layer was added, the sample was cooled until it approached room temperature. In the model, elements in the coating portion of the mesh were turned off until their layer was added. However the active elements were constantly moving. To ensure that elements of new layers were added at the correct location, dummy elements using the same nodes were mapped over the deposit elements. The dummy elements have very low strength and do not affect the heat transfer of the active elements. Time-dependent properties such as creep were not considered, since cooling was reasonably rapid. The coatings and substrates were assumed to be perfectly bonded.

The temperature of the spinel particles was assumed to be 2300°C, based on measurements previously done at INEEL using a high-speed two-color pyrometer to determine the temperature of particles in flight. Although the temperature of metal splats upon impact with the substrate is probably in the vicinity of 2000°C, the melting temperature of the deposited metal was used as the initial deposit temperature. Since molten metal can support no load, no stress is generated during cooling from the actual deposition temperature to solidification, and that portion need not be modeled. In all cases, the initial temperature of the substrate was assumed to be 20°C.

Temperature histories were determined using FEM by matching the temperature history calculated at the back of the coupon with the experimentally-determined temperature histories at this location. Tabulated thermal properties for the various materials were used, along with estimated average gas properties from previous measurements on a similar plasma torch, to generate an approximate temperature history. The convective heating and cooling contributions were then calibrated by adjusting the average gas temperatures, velocities, and times to match the experimental temperature histories. Once these contributions were determined, the temperature histories were adequately modeled for all deposit materials by altering the deposit properties and deposition temperature. Temperatures computed throughout this analysis were used as input for stress analysis.

A finite element model of a thin (130 μm) bond coat applied to the stainless steel substrate was developed. The bond coat material is primarily Ni, with about 5% Al, so bulk tabulated properties for pure Ni were used. Initially it was assumed that the Ni was applied as a single layer and the entire x-y center plane of the coupon (Figure 2) was modeled. This calculation involved only two stages: obtaining thermal equilibrium between the hot deposited layer as it comes in contact with the cool substrate, and cooling the entire sample from that temperature to room temperature. The first stage results in quenching stresses, while the latter causes thermal expansion mismatch stresses. The steady-state temperature calculated by the model was 120°C. This value is in good agreement with the 90°C temperature obtained from a thermocouple attached to the back of a substrate during spraying. The actual specimen does not reach a steady state temperature during the thermal spray process, so the temperature measured on the back surface is expected to be lower.

The radius of curvature calculated by the FEM model is 5.29 m after deposition and 7.06 m after cooling to room temperature, with the sample curved toward the bond coat. These values are in good agreement with measured value of 4.4 m. Most of the curvature occurred during the quenching stage, and then somewhat relaxed during the mismatch stage because the thermal expansion coefficients used for Ni are less than those for stainless steel. Possible sources for the discrepancy between final modeled and measured curvatures include inaccurate material properties such as expansion coefficients and plasticity (especially at high temperatures), insufficient FEM mesh resolution, and the assumption that perfect bonding is maintained and that the sample reaches an intermediate steady-state temperature.

The preliminary bond coat model was modified to reflect the fact that it is applied in two layers (four passes). Layers of spinel were then added on top of the bond coat. Curvature trends of the FEM results are in good agreement with the experimental results (see Table 1). Most of the curvature is present after the bond coat has been applied, which reflects the dominance of the quenching effect for these spray conditions. The spinel layers cause a slight reduction in curvature.

Initial calculations assumed a spinel with no plasticity and an elastic modulus typical of a bulk material. Curvature results were three orders of magnitude higher than those measured experimentally. Frequently, thermally-sprayed ceramic coatings are modeled using a modulus of about 20% of the bulk modulus to account for cracking, debonding, and porosity in the coating.[5,6] This reduction in the modulus of the spinel results in about one-third the curvature initially and about half the curvature after all 10 layers have been applied. It is interesting to note that the 20% elastic modulus is lower than the modulus for the stainless steel substrate. The modulus was further reduced to about 6% of the bulk,

**Table 1.** Comparison of FEM and experimental curvature results.

| | Curvature (1/m) | | |
|---|---|---|---|
| | After Bond Coat | After Spinel | Reduction |
| Experiment | 0.267 | 0.206 | 0.062 |
| FEM | 0.686 | 0.613 | 0.073 |

based on ultrasonic Young's modulus measurements performed this year as described below. Although this very low modulus reduced the predicted curvature substantially, values were still about 200 times greater than experimentally-determined curvatures.

The properties of materials in thermally-sprayed coating are significantly different than the corresponding properties of monolithic materials.[5,6] It is very difficult to adequately characterize the properties because traditional mechanical property testing protocols assume that the material being tested is homogeneous and isotropic. Some work has been done on metallic materials where a thick coating is applied to a graphite substrate and the substrate subsequently removed by abrasion or burning. Or a parting layer such as boron nitride is applied on the substrate prior to coating application, allowing the coating to be mechanically removed. The major drawback of this type of technique is that the coating material is likely to have significant residual stress when adhered to a substrate; therefore, removing the substrate alters the condition of the material.

Despite these uncertainties, in general the properties ceramic coatings have been found to be significantly degraded compared to those of monolithic materials. In the absence of reliable experimental values, it is typical to assume that the elastic properties of a ceramic coating are 15 to 20% of handbook values. Metallic coatings have been less well studied, but it is typically assumed that the properties of the coating will be similar to handbook values since there is little cracking or porosity for metallic coatings. It has been shown, however, that the yield strength of NiCrAlY coatings increases substantially compared to mill products. This behavior is due to the very fine grain size and pinning of dislocations from a very fine dispersion of oxide particles created by interaction of the molten droplet with the process gases in flight, followed by mechanical mixing as the splat is formed on the substrate.

We are particularly concerned here with the properties of the ceramic $MgAl_2O_4$ coating. Microstructural characterization of this material has shown that there are a large number of cracks in the coating (for example, see Figure 3). This has been a particular focus of this work because we have observed that the nature and extent of cracking is a function of the process parameters. In every case we have noted that there are cracks between the individual layers of the coating and some cracking normal to the substrate. When observed with optical microscopy, the spinel coatings appear to be greater than 99% of theoretical density. High magnification examination of coating cross sections using scanning electron microscopy has shown that there is a significant fraction of unmelted particles entrained in the coating. These unmelted particles are fractured on a very fine scale and cannot be expected to have significant bulk mechanical properties.

The tensile fracture properties of $MgAl_2O_4$ coatings were determined from standard pull-tab experiments carried out according to ASTM standard C-633. In these tests, a coating is applied to a threaded cylinder of the same composition and prepared with the same surface treatment as the standard test coupons. A mating threaded cylinder is joined to the coating surface using an ASTM-specified adhesive and the coating is pulled to failure in tension. In the absence of a bond coat, the coating/substrate system failed at the bond line and the coating properties could not be determined. With a NiAl bond coat, failure occurred primarily through the coating and a valid tensile strength was determined. For a 1-mm-thick coating applied in 12 passes, the tensile strength was 13.8 MPa; for an identical coating applied using 24 passes the strength was 16.7 MPa. These values are the average of five tests for each condition. Note that for the latter case, this tensile strength value should be considered a lower limit since some failure of the bond was typically observed. These values compare with a handbook value of 190 MPa for monolithic $MgAl_2O_4$ tested in bending.

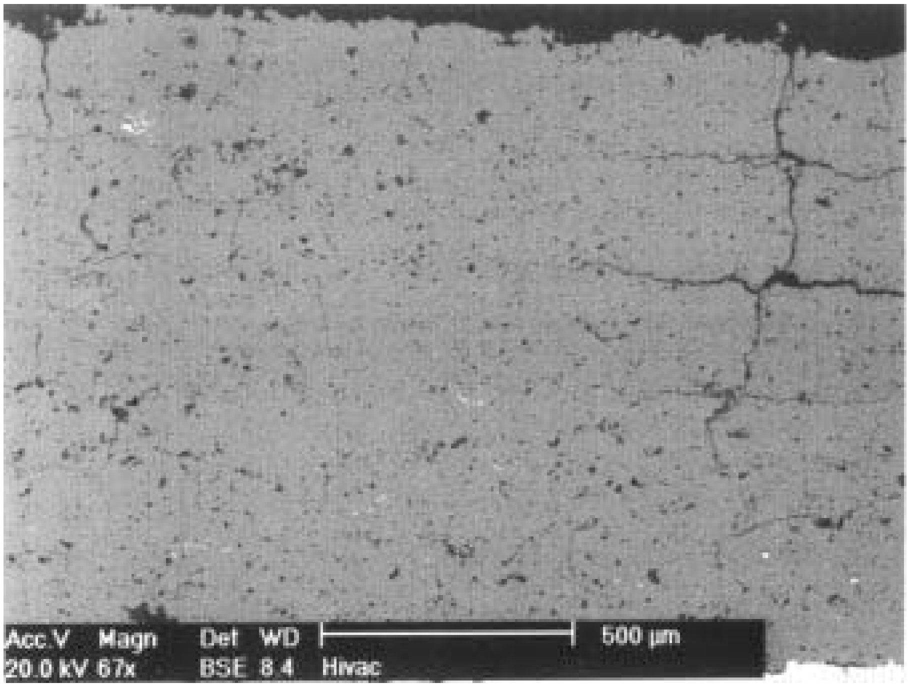

GJ00 0234

**Figure 3.** Backscattered scanning electron micrograph of a $MgAl_2O_4$ ceramic coating on a Type 304 stainless steel substrate.

In addition to tensile strength, which is essentially the fracture strength for a brittle ceramic material, the elastic properties of $MgAl_2O_4$ in the form of a coating are critical for the finite element simulations of residual stress. The modulus can be obtained from the elastic portion of the stress-strain curve from conventional mechanical property testing or by measuring the velocity of elastic waves through the coating. We attempted to measure the elastic properties using four-point bend testing; however, the coating typically failed at low loads, primarily by debonding from the substrate. Because of the low loads at failure and the mechanism of failure, we were unable to obtain reliable values of the elastic modulus using mechanical property methods.

To completely characterize the elastic properties of a material using ultrasonic elastic wave propagation, it is necessary to determine the velocity of both shear and longitudinal waves. A unique noncontacting ultrasonic measurement system has been developed at INEEL that induces elastic waves using laser irradiation and determines the time of flight of both shear and longitudinal waves using another laser system. Knowing the density of the material, it is a simple matter to determine the wave velocity from the time of flight. We attempted to apply this method to thermal-sprayed spinel coatings; however, attenuation of the relatively low-power laser-induced elastic waves resulted in insufficient signal to accurately measure the time of flight. An alternative method was developed to propagate longitudinal elastic waves through coatings on stainless steel substrates using a conventional quartz transducer, where a column of water is used between the transducer and the sample to focus the signal. This system is unable to support a shear wave; however, using a typical ratio of shear to longitudinal wave speeds for porous media we were able to estimate the Young’s modulus of the thermal-spray spinel coatings. The value obtained in this way was approximately 6% of tabulated values for monolithic material of the same composition.

The spinel coating is known to contain substantial microcracking and, therefore, as noted above, it is quite weak in tension. It has been argued that the material behaves similar to a brittle cast iron, which has failure strength in compression that is much higher than in tension. A case was run using a cast iron constitutive model that has been developed for ABAQUS. In this model, the ratio of strength in tension to that in compression is 1:10. A simpler approach is to model the spinel as a perfectly plastic material. Although the material is brittle, and does not 'yield' in the traditional sense, the microcracking results in gradual rather than catastrophic failure. In other words, it cannot support a load beyond a certain 'yield' or 'fracture' stress. A yield strength of 30 MPa, suggested by the cast iron constitutive model, reduced the final curvature to about 0.8. Further reduction to 10 MPa, a value estimated from pull tests as described above, caused a further small reduction. The cast iron model produced an even lower final curvature. It seems that the cast iron model should produce the same or higher curvature than the perfectly plastic model with a yield strength equal to the cast iron tensile strength, since the compressive strength is higher. This result is not currently understood, in part because the cast iron constitutive model required a material property (plastic Poisson's ratio) that is unknown for the spinel coating. Although the 'yielding' curvatures are still higher than the experimental values about 0.2, they are of the same order of magnitude and the curvature is in the correct direction.

The remaining difference between the numerical simulations and experimental curvature results are associated with plasticity introduced in the substrate by steep thermal gradients as the individual coating layers are applied. We have demonstrated through a detailed series of simulations that steep gradients are established in the substrate because the temperature on the deposition face increases to nearly 2000°C while the air-cooled rear face remains at less than 100°C. This causes a gradient in thermal expansion that is sufficient to cause nonuniform plasticity in the substrate during deposition, which in turn translates to curvature retained upon cooling to room temperature. This effect is small compared to the curvature observed after deposition of the bond coat since the metallic bond coat is sufficiently strong to transmit stress to the substrate. For the ceramic coating, which has both a low modulus and low effective plastic strength as described in detail above, the thermal gradient portion of the residual stress is a significant contribution to the total residual stress.

## Residual Stress Components in Metallic Coatings

As we noted in previous reports, the residual stress arising from the bond coat can dominate the total residual stress. This is thought to be because the mechanisms for the metallic coatings to shed residual stress after deposition are less effective than those for the ceramic coatings. To more fully explore the origins of residual stress, several cases of stainless steel deposited on stainless steel were modeled (without a bond coat) in an attempt to isolate the quenching effects. Experiments were conducted to support the modeling. The calculated curvature value of 2.9 for the stainless coating on a stainless substrate compares well with the measured value of 3.7. To further isolate the thermal expansion mismatch stress, an additional case was run with a coating having all the properties of the stainless steel except the thermal expansion coefficient, which was set to that of a spinel coating. The lower expansion of this case results in two distinct differences in the curvature from the stainless steel coating case. First, the curvature is lower at all times because the quenching effect is smaller. Quenching stress is determined by $\alpha\Delta T$, and $\alpha$ is smaller for the deposit. Second, the curvature has a negative slope during cooling between cycles because there is a $\Delta\alpha$ between the layers. There is less plastic strain in both the bottom of the substrate (because of less bending) and in the deposited layers (because of less contraction during quenching, i.e. lower $\alpha$). However, there is more plastic strain in the substrate near the interface, because it is bonded to the deposit layer and must accommodate the $\alpha\Delta T$ strain as it comes to local equilibrium.

Plasticity in the deposit results in much lower curvature at any given deposit thickness (time) compared to the purely elastic case. A plastic deposit requires less plastic strain to accumulate in the substrate, especially on the back, away from the interface. However, significant plasticity occurred in all cases whether the coating material was elastic or plastic, although the location (coating or substrate) and amount varies. Therefore, simple elastic calculations are not expected to be accurate. When the coating is not stiff, either because it plastically deforms or because it has a low modulus, sharp reversals can occur in curvature, displacement, or stress when plotted as a function of time. These spikes occur early in the cycle when the temperature of the newly deposited layer changes very rapidly and thermal gradients are high.

A calculation with 10 thinner (62-μm) layers had a curvature of 2.9, while 10 thicker (140-μm) stainless steel layers had a final curvature of 6.2. The thinner layers result in much less heat input, with the maximum temperature at the back of the substrate being about 90°C rather than 225°C. The maximum temperature calculated in the first layer is similar for the first couple of cycles, and then is also much less for the thin layer case. The curvature of the thinner layer is also less than 4.2, the curvature for the thicker layer case after only 4 layers, which results in a similar accumulated coating thickness (620 μm versus 560 μm). This 4-layer case had a curvature of 40 if no plasticity is considered for the coating.

For plasma-sprayed metallic coatings, we have shown that both the quench stress and the thermal gradient stress can be significant. Using a different deposition method, the high velocity oxygen fuel (HVOF) process, can result in cold working of the surface analogous to shot peening. While the quench stress is always tensile in nature, the peening stress can be compressive and amenable to significant variation through changes in process parameters. The total residual stress is more properly thought of as a sum of several contributions:

$$\sigma_{\mathrm{Total}} = \sigma_{\mathrm{CTE}} + \sigma_{\mathrm{Quench}} + \sigma_{\Delta T} + \sigma_{\mathrm{Peening}} + \sigma_{\mathrm{Substrate}}$$

where the stresses from differences in coefficients of thermal expansion and quenching are as described above. $s_{?T}$ is the stress arising from plasticity induced in the substrate by large thermal gradients from heating from the torch and deposition of hot particles, $\sigma_{\mathrm{Peening}}$ is the stress arising from local plastic deformation from impact of high velocity particles, and $\sigma_{\mathrm{Substrate}}$ is the residual stress in the substrate associated with surface preparation or heat treating prior to coating.

Plasma spray deposition is not expected to cause significant stress from peening because the particles are fully molten and have relatively low velocity. However, in the HVOF coating process metallic particles are typically sprayed at temperatures below their nominal melting point and at velocities on the order of 500 to 700 m/s. In this case, we expect that the peening stress will dominate and will leave the coating in a compressive residual stress state. To confirm this expectation, a series of experiments was carried out using Type 316 stainless steel powder to form coatings on Type 304 stainless steel substrates. This material system was chosen because the stainless steel powder has similar melting point to conventional bond coat materials, but the $\sigma_{\mathrm{CTE}}$ contribution to the stress will be very close to zero. Coupons were coated using plasma spray deposition with an increasing fraction of hydrogen gas added to systematically increase the particle temperature. All of these coatings were in tension and higher particle temperatures resulted in higher levels of tensile stress. This is consistent with the total residual stress dominated by the quenching stress.

Experiments with the HVOF process examined a series of different particle velocities with nearly constant particle temperature at about 100°C below the melting point. Residual stresses calculated from the total residual curvature as a function of particle velocity are shown in Figure 4. Negative stress values

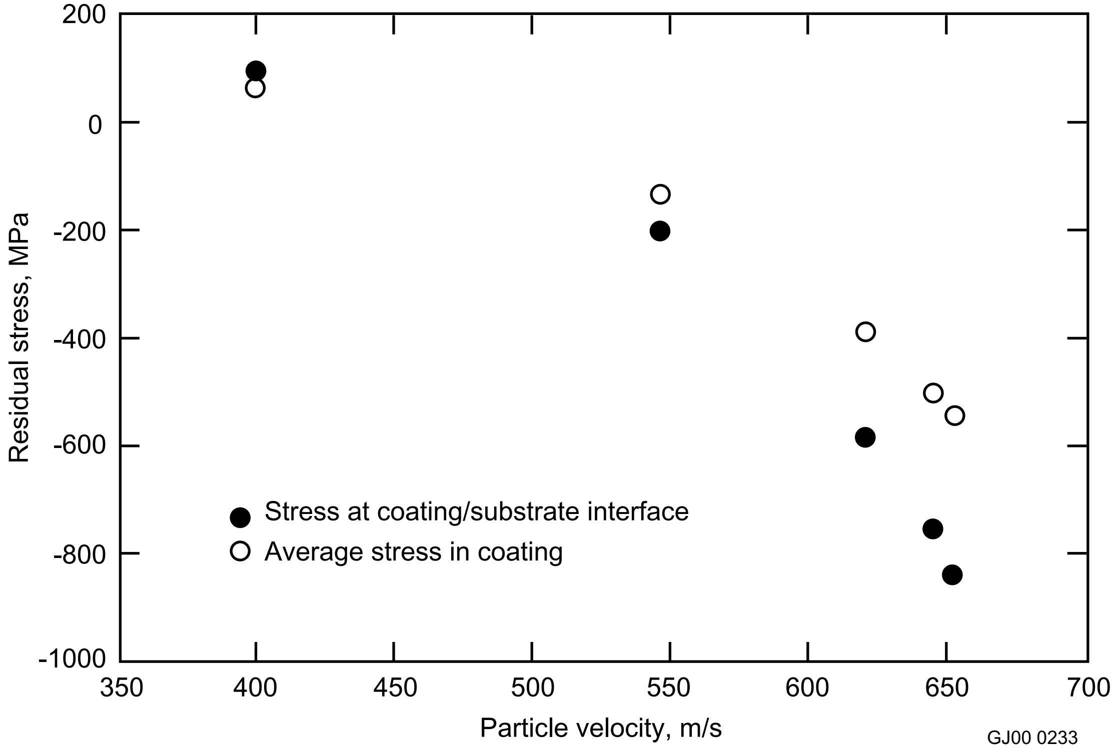

**Figure 4.** Total residual stress for Type 316 stainless steel coating on Type 304 stainless steel substrates as a function of particle velocity for a fixed particle temperature.

are compressive in this figure and positive values are tensile. It is evident from the figure that when using HVOF for stainless steel powder sprayed onto stainless steel coupons it is possible to vary the nature of the total residual stress from tensile to compressive. For the set of conditions examined here, an average particle velocity of 450 m/s will result in a coating/substrate couple with no residual stress.

Note that the indicated magnitude of the stresses in Figure 4 is likely to be unrealistically high since an elastic model was used to calculate the stresses and no doubt significant plastic flow will occur in the coating, and possibly the substrate, to reduce the stress. Nevertheless, we have demonstrated that it is possible to control the residual stress by controlling the particle temperature and velocity. Through proper choice of thermal spray systems and process control, the stress state can be varied from tensile to compressive. If the processing is done properly, there is no residual stress in the coating/substrate or a compressive stress in the coating can be established. This minimizes the probability of the coating failing by cracking or debonding.

## Thermophysical Property Measurements

Knowledge of the thermophysical properties of thermally sprayed coatings is crucial to properly designing coatings for environmental applications. Impermeable, thick ceramic coatings used for life extension of nuclear waste storage casks are one example. As the stored fuel decays, heat is transferred to the cask. Its temperature cycle must be calculated to predict thermally induced stresses and corrosion behavior, as well as to describe the heat load in the geological repository. The physical properties of thermally sprayed coatings do not always match those of the bulk material and, in fact, can vary widely depending on the spray process parameters. It is necessary to measure these properties for each coating design. Thermal conductivity is probably the most important thermal property to measure. We added the capability to determine thermal transport properties during this year. Two types of measurement techniques are available to determine thermal conductivity: transient and steady state. Both types provide a temperature gradient and then monitor the response of the material to the gradient. The difficulties with steady-state techniques are that the measurement requires access to both sides of the sample, the sample must conform to specified dimensions, and measurement time is lengthy to allow steady-state heat transfer coatings.

Transient techniques are popular due to their speed and simplicity. We examined three basic transient methods of measuring thermal conductivity for coating characterization: hot wire, transient plane source (TPS), and laser flash diffusivity. The hot wire technique, which involves inserting an electrically heated wire into the material and monitoring the temperature of the wire as a function of time, would be difficult to apply to thermally sprayed coatings. The TPS method, which is similar to the hot wire method, uses a circular heating element sandwiched between two identical pieces of the material to be tested. The heating element is operated under constant current conditions and its temperature is monitored to measure temperature rise over time. Thermal conductivity, diffusivity, and heat capacity can be determined from the data. There are several drawbacks to the TPS method. The technique is interfacial and depends on minimal contact resistance between the heating element and the material being tested. Also, if heat fully penetrates the sample, the air on the penetrated side becomes part of the heat transfer path, providing a false representation of the thermal property value. Therefore, the TPS method is difficult to apply to thin samples, <0.5 mm, which includes many thermally sprayed coatings. Furthermore, there is very little experience with this method for layered samples and at elevated temperatures.

In laser flash diffusivity a short pulse of heat is applied to one side of the sample using a laser pulse. The temperature rise on the opposite side of the sample is monitored as a function of time and the half time to full temperature rise is used to determine the thermal diffusivity. This can be combined with density and heat capacity data to calculate thermal conductivity. The laser flash method has some significant advantages over other transient measurement techniques for determining the thermal conductivity of sprayed coatings. A wide range of diffusivity values can be tested, including two- and three-layer samples and two-layer samples with contact resistance. Measurements can be carried out in oxidizing or inert atmospheres or under vacuum and at elevated temperatures (>1500°C). The data are easily corrected for heat loss and the finite time of the laser pulse. The measurement is also recognized by the American Society for Testing and Materials (ASTM E1461) and is used for over 80% of the thermal diffusivity measurements conducted worldwide.

For these reasons, we obtained a Netzch Instruments Laser Flash Apparatus. This instrument is fully computer automated for both data collection and analysis. It is able to vary the laser pulse width, which is necessary for thinner samples (coatings) and materials with high thermal diffusivity. The software also allows the heat loss and laser pulse width correction to be applied to two- and three-layer samples. With multi-layer samples, imperfect bonding at the coating/substrate interface changes the thermal response in a predictable manner. Changes in the shape of the time-temperature response curve are thus a reliable way of characterizing debonding in situ and are being used in this project to examine changes in physical properties of the coating induced by residual stress as a function of thermal cycling.

# ACCOMPLISHMENTS

We developed and experimentally validated numerical simulations that properly predict the total residual stress in plasma-sprayed $MgAl_2O_4$ coatings on Type 304 stainless steel substrates. The total residual stress in the ceramic coating arises from three contributions: quenching liquid particles on a relatively cool substrate, thermal expansion mismatch stress upon cooling to room temperature after fabrication, and plasticity in the substrate arising from the steep thermal gradients on each coating pass.

Experimental methods were developed to determine the fracture strength and elastic properties of the ceramic in the form of a plasma-sprayed coating, as compared to tabulated values for monolithic material for of the same composition. The fracture resistance of the coating is approximately 10% of the monolithic material's value. An effective plasticity criterion in the numerical simulations using the fracture properties is necessary to accurately describe the total residual stress.

Metallic bond coats are frequently necessary between metallic substrates and ceramic coatings to obtain reasonable adhesion. We demonstrated that the quenching contribution to total residual stress dominates the total stress for plasma-sprayed metallic bond coats and that the quench stress is always tensile. For high velocity oxygen fuel processed coatings, an additional stress contribution arises from cold work on the surface from particle impacts, akin to shot peening. By varying the process parameters the stress from bond coating can be controlled to be either tensile or compressive, or approximately neutral.

A laser flash thermal conductivity measurement system was purchased and installed. This system has been used to demonstrate that relaxation of residual stress after thermal cycling results from debonding of the coating from the substrate.

# REFERENCES

1. O. Kesler, J. Matejicek, S. Sampath, S. Suresh, T. Gnaeupel-Herold, P. C. Brand, H .J. Prask, "Measurement of Residual Stress in Plasma-Sprayed Metallic, Ceramic and Composite Coatings," Materials Science and Engineering, A257 (1998) 215-224.

2. C. H. Hsueh and A. G. Evans, "Residual Stresses in Metal/Ceramic Bonded Strips," Journal of the American Ceramic Society, 68(5) (1985) 241-248.

3. Y. C. Tsui and T. W. Clyne, "An Analytical Model for the Generation of Residual Stresses in Sprayed Coatings Deposited Progressively onto Planar Substrates," Thermal Spray: A United Forum for Scientific and Technological Advances, C. C. Berndt (Ed.), Published by ASM International, Materials Park, Ohio, 1997, 813-822.

4. Chin-Chen Chiu, "Residual Stresses in Ceramic Coatings as Determined from the Curvature of a Coated Strip," Materials Science and Engineering, A150 (1992) 139-148.

5. O. Kesler, M. Finot, S. Suresh and S. Sampath, "Determination of Processing-Induced Stresses and Properties of Layered and Graded Coatings: Experimental Method and Results for Plasma-Sprayed Ni-$Al_2O_3$," Acta Materialia, 42(2) (1997) 3123-3134.

6. Chin-Chen Chiu, "Elastic Modulus Determination of Coating Layers as Applied to Layered Ceramic Composites," Materials Science and Engineering, A132 (1991) 39-47.

# Corrosion and Aging

**Patrick J. Pinhero and Richard N. Wright**

## SUMMARY

Microbial influenced corrosion (MIC) is a problem of profound significance at the Idaho National Engineering and Environmental Laboratory (INEEL) as it relates to storage of spent nuclear fuel (SNF). The primary goal of this research is to mitigate MIC in SNF storage. FY 2000 research completed many extensions of FY 1999 studies. First, the radiation tolerance of microbes isolated from SNF environments, proven in FY 1999, was demonstrated in two subsequent and unrelated experiments in FY 2000. One study examined microbial vitality as a function of ultraviolet (UV) radiation within a laboratory environment. Results show direct correlation between cell pigmentation and cell survival, reds and pinks having highest radiation tolerances. A study conducted in collaboration with Argonne National Laboratory-West (ANL-W) demonstrated that microbes can survive an intense radiation environment, e.g., an ANL-W hot cell, and produce biofilms on irradiated cladding hulls. The ANL-W collaboration proves that biofilms form on irradiated stainless steel fuel cladding in a strong radiation field.

We used the Scanning Reference Electrode Technique (SRET) to comparatively examine the corrosive effects induced by a consortium of three microorganisms upon SNF cladding alloys: Al6061-T6, Type 304 stainless steel (SS304), and Zircalloy-4 (Zr4). The study showed local activity in both Al6061-T6 and Zr4 but uniform activity in SS304. Al6061-T6, as expected, demonstrated the highest net localized electrochemical activity of the three alloys. Advancing imaging techniques is a high priority for MIC research. It is necessary to identify and quantify MIC from both microbiological and chemical perspectives. We developed techniques for both Environmental Scanning Electron Microscopy (ESEM) and noncontact Atomic Force Microscopy (AFM) to examine the morphologies of microorganisms in natural conditions in preparation for studies relating to biofilm drying. Biofilm drying is important during the life cycle of SNF because many microorganisms are known to sequester radionuclides, thus creating a potential environmental risk. We initiated research focusing on developing microbial gene-specific fluorescent tags and Laser Confocal Fluorescence Microscopy (LCFM) for identifying specific microbes with spatially resolved corrosion regions. These techniques have potential to correlate the presence of certain microbes with observable corrosion activity. The recent addition of a postdoctoral research associate in the program has assisted in initiating development of a Scanning Electrochemical Microscope (SECM) for spatially resolving specific chemical reactions with respect to MIC.

## PROJECT DESCRIPTION

### Introduction

The Department of Energy is custodian of several thousand metric tons of spent nuclear reactor fuel (SNF), which is primarily the result of experimental nuclear reactor development and Naval reactor activities during the period of the Cold War. Also included in this stockpile is fuel from energy research. The long-term containment performance of the fuel under storage and disposal conditions is uncertain. Uncertainties have a direct bearing on the DOE's ability to license disposal methods. The EM Office emphasizes a fundamental need for identifying mechanisms that may adversely affect the performance of the fuel package during storage. Deleterious effects recognized as being incompletely characterized include corrosion and degradation rates for the fuel matrices, mechanisms that may lead to accelerated degradation of containers, and the effects of microbes on fuel packages.

Microbially influenced corrosion (MIC) is a known problem in various industries. For example, severe biofouling occurs in transport piping used in the petroleum industry. Sulfate-reducing bacteria (SRB) are of particular importance because they are responsible for souring oil and promoting MIC. Water content of just 1% is adequate to support substantial development of SRBs within a few weeks. At the INEEL, large *swimming pools* of water are used to temporarily store SNF as it cools prior to processing, transport, and final storage. During transition to final storage, the SNF is dried and then placed in containers for transport to repository for final deposition. Obvious questions arise given this scenario. Can microbes survive in temporary storage pools where SNF resides? What effect do the microbes, if present, have on the surface of the cladding? Do they initiate corrosion? Do they accelerate or exacerbate corrosion processes? Or, do they inhibit degradation of SNF cladding? If MIC is present, is it the result of one type of microbe, or is it a complex interaction induced by several classes of microbes? Does the chemistry change when the SNF is transitioned from wet to dry storage? This is by no means an exhaustive list of questions. Its purpose is to give some baseline for scientific inquiry.

## Tolerance of Bacteria to Ultraviolet Radiation

Reports of the observation of viable microbes in wet and dry SNF storage facilities are not novel, though it has not yet been unambiguously demonstrated that microbes can exist on SNF itself. Scientists in Canada have established a long-term study concerned with microbes introduced during construction of the Underground Research Laboratory.[19,20,17,18] Recently, a group of our colleagues at the INEEL published an account detailing the existence of organisms on coupons placed within two of the storage pools at Idaho Nuclear Technology Center (INTEC).[22] Although these research groups have observed microbes in storage facilities, nothing has been published thus far about the identity or radiation tolerance of the organisms. Resistance to radiation is significant because it implies that biofilms could survive on SNF.

It is well documented that some microbes, such as *Deinococcus radiodurans (D. radiodurans)* survive in a radiation-rich environment.[12] The tolerance of this organism to radiation may relate to its well-documented DNA repair mechanism, its peculiar cell wall/membrane structure, its high concentration of antioxidants, and its multiple copies of genetic information.[5] In FY 1999, we demonstrated the g-radiation sensitivity of microbes sampled and isolated from the INTEC SNF pools. The experimental study performed in FY 2000 focuses on determining the sensitivities of these same microbes to ultraviolet (UV) radiation.

Bacteria were grown overnight to mid-log stage. They were then streaked onto solid medium. Individual plates were exposed to a 15-W UV lamp 48 cm from the source (~0.27 mW/cm$^2$). Exposure times varied from 15 sec to 2 min; for *Deinococcus radiodurans,* the time varied from 15 sec to 8 min. Plates were observed for growth after 24–48 hr to determine how much UV radiation each species tolerated.

Preliminary results from the listed procedure are displayed in Figure 1. The color of the data bar represents the pigmentation of the identified microbe. With the exception of one outlying data point, the figure shows strong correspondence between pigmentation and UV-radiation survival. Bacteria with pink or orange pigmentation survived higher levels of UV than did those with yellow or no pigmentation. An associated experiment currently in progress is gathering more quantitative information about the numbers that survive irradiation. The population data will be compared with the results from last year’s g-radiation data and summarized in a peer-reviewed manuscript.

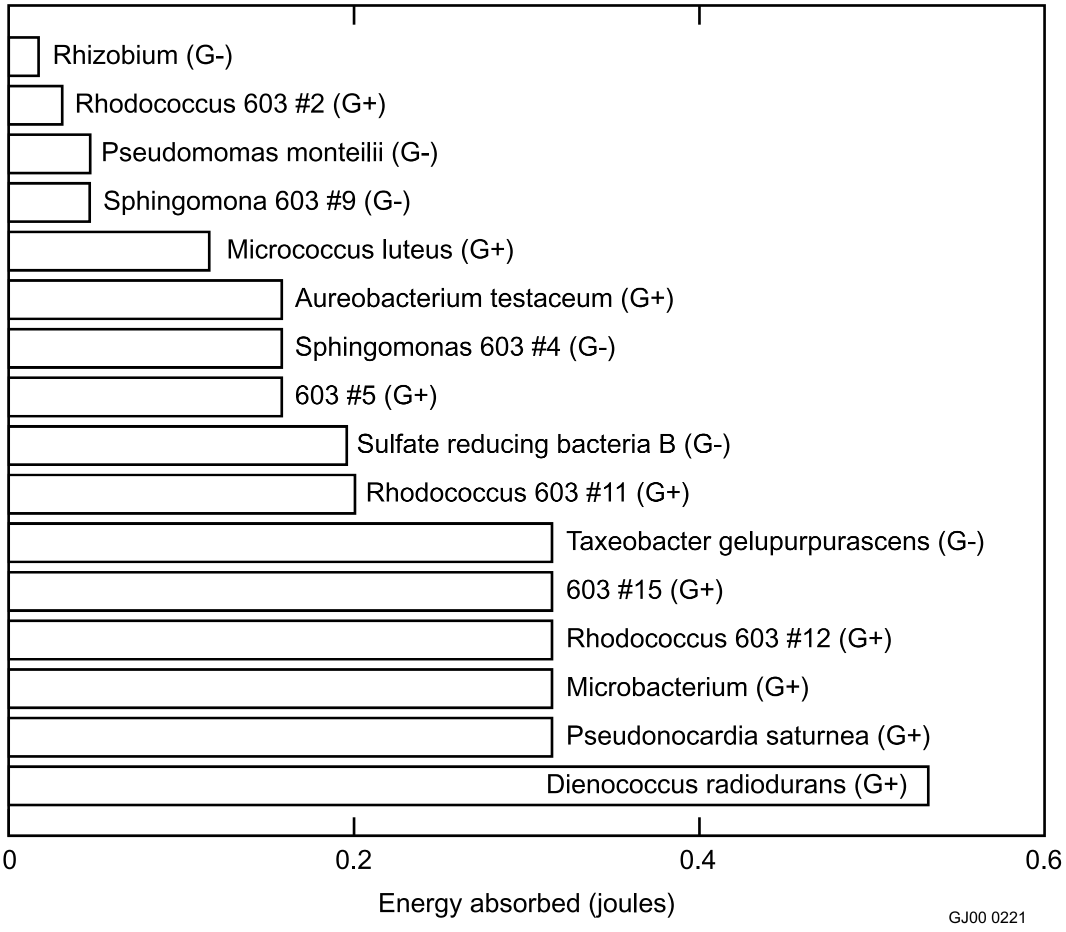

**Figure 1.** Graph of selected bacteria versus the total amount of absorbed UV energy required to kill the population. The color of each bar corresponds to the pigmentation of each bacterial colony. Note the correlation between prolonged survival and pink or orange pigmentation.

## Argonne National Laboratory–West Study

A fundamental criticism often heard from the SNF community is that microbes present in the pools are of no concern if they cannot survive on the claddings of irradiated fuel. Since we are limited in our capabilities to directly sample from fuel plates at INTEC, we established collaboration with the Analytical Chemistry hot cell group at Argonne National Laboratory-West (ANL-W) to conduct a proof-of-concept experiment. In this study, we introduced a large consortium of microbes to sealed vials containing SNF cladding hulls from Experimental Breeder Reactor II (EBR-II) fuel. The fuel was dissolved out of the hulls prior to introducing the microbes and kept in sealed jars positioned along the sides of a square test tube rack. The irradiated hulls have a residual radiation field of 40 rad/hour, and the rack positions see an average radiation field of 177 rad/hour. Five vials were placed within the test tube rack, all containing an irradiated fuel hull, four inoculated with the microbe consortium. The noninoculated vial containing an irradiated hull was used as a control for biological contamination within the confines of the experiment. An additional control containing a nonirradiated SNF hull inoculated with the microbe consortium was placed outside the field to check for survival in the background fields. The background fields arise from other objects in the ANL-W hot cell. The EBR-II cladding hulls were all composed of Type 304 stainless steel. Figure 2a shows four irradiated cladding hull segments used in the experiment.

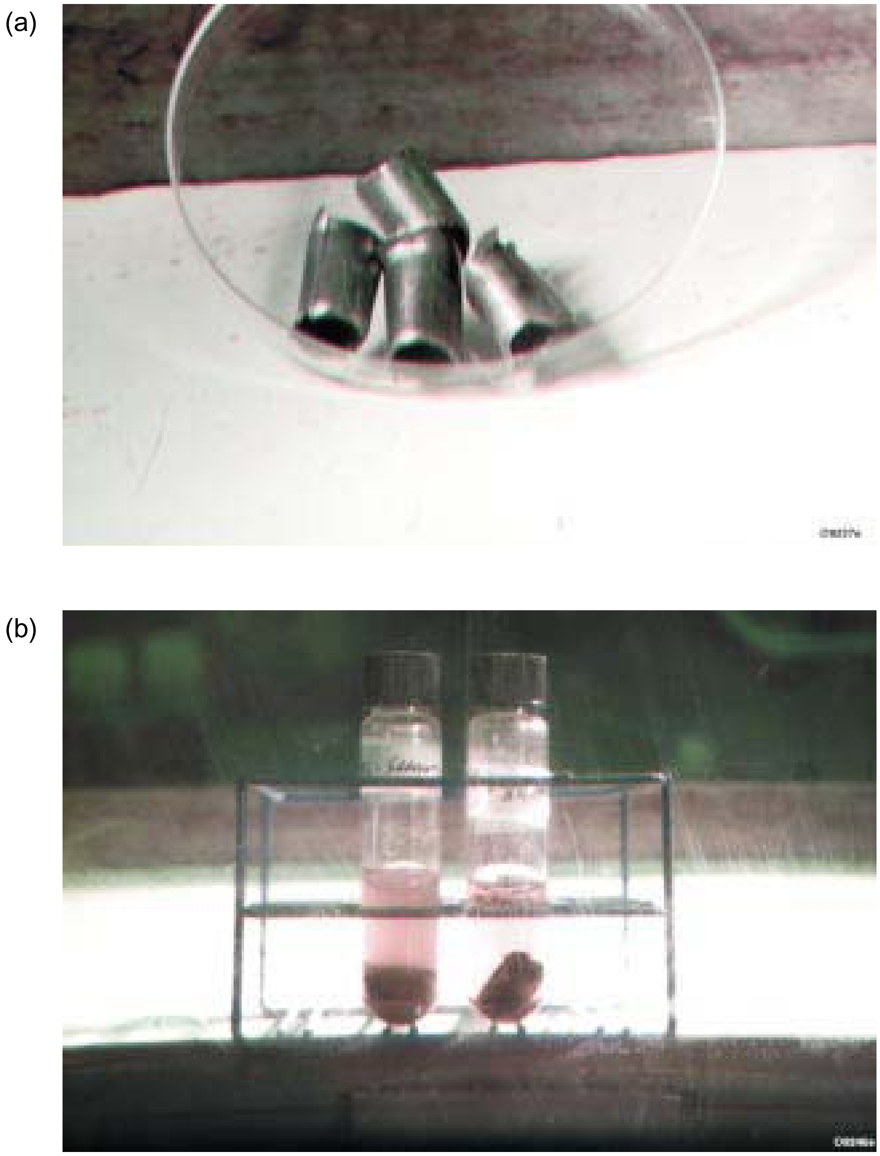

**Figure 2. (a)** The four irradiated cladding hull segments used for the biofilm growth experiment. The segments are from EBR-II blanket fuel elements that had been treated in the MK-V electrorefiner to remove the fuel. The segments had been soaked in 1% nitric acid and rinsed with sterilized water prior to placement into sterilized test vessels with media and microbes (except the control that had media only). A fifth, nonirradiated cladding hull segment of similar size was also used for the biofilm experiment, but is not shown in the photo. The dimensions of the hull segments are approximately 0.5 in. in diameter and 0.5 in. in length (1.3 × 1.3 cm); the hull material is 304 stainless steel. **(b)** Test vessels containing irradiated cladding hull segments and media solution. The photograph shows the test vessels through the hot cell window, Analytical Laboratory, ANL-W. The test vessel on the left contains irradiated hull segment 2 that was originally placed in a solution of media and 26 species of microbes. The irradiated hull on the right (hull 4) was originally placed in sterile media only and was used as a control. The experiment was initiated 3/22/00; the photo was taken 4/5/00, prior to sampling of cladding hull 2. The cloudy appearance of the solution on the left indicates healthy microbe activity. The clear solution of the control hull 4 on the right indicates no microbial growth.

Each of the vials was sampled at approximate one-month intervals. Figure 2b shows test vials containing both cladding hull segments and media solution. The vial on the left contains microbes; the one on the right is a control vial containing no bacteria. The total doses received by the hulls as sampled were 127 krad, 255 krad, 382 krad, and 510 krad. During each sampling, a serial dilution method was employed to sequentially lower the radiation present for handling and to thin the quantity of organisms present for ease of identification. Swabs were taken from both the insides and outsides of the cladding hull, and an aliquot was taken from the surrounding media. Both SRB vials and plating were used to isolate anaerobes and aerobes, as well as facultative bacteria. Figure 3a shows SRB vials for the experimental control. These display no SRB. Figure 3b was sampled from the interior of a hull segment in an inoculated vial irradiated for one month. Note the black suspension in the solution, indicating the presence of SRB. Both sets of vials, a and b, are serial dilutions from left to right, the left vial being the most concentrated. Serial dilutions provide us with an order of magnitude assessment of the approximate population surviving the total irradiation dose. Figure 4a shows streaked plates from the control sample. The apparent fungus probably resulted from contamination in the analytical hood at ANL-W, since it does not resemble any of the microbes introduced. Figure 4b shows two streaked plates sampled from an inoculated specimen.

Though we are in the process of interpreting the data from the ANL-W, we are confident that two conclusions can be drawn from a purely qualitative basis. First, bacteria grow to form biofilms on irradiated fuel hull segments in extremely high radiation fields. Second, SRBs remain active in this environment, which suggests that MIC is a real possibility with respect to SNF.

## Electrochemical Studies

Scanning Reference Electrode Technique (SRET) is an imaging tool that allows examination of local activity by measuring minute changes in electrochemical potential. In our experiments, we coupled a commercial SRET instrument, EG&G SVET 100, with an EG&G PAR 273A Potentiostat. This mating of instrumentation furnishes us with a method to examine the local breakdown of metal surfaces in different electrolytes. Using this method, we have studied five systems:

1. Type 6061-T6 Aluminum alloy (Al6061-T6) in a mixture of *Pseudomonas aeruginosa* (*P. aeruginosa*); *Deinococcus radiodurans* (*D. radiodurans*), and a mixed colony of sulfate reducing bacteria (SRBs)

2. Type 304 stainless steel (SS304) with the same three bacteria

3. Zircalloy-4 (Zr4) with the same three bacteria

4. Al6061-T6 in a chloride solution with the same three bacteria

5. Al6061-T6 in a “kitchen sink” consortium of all the bacteria in our inventory.

These studies involved multiple specimens in each of the mixtures. Each specimen measured 15000 mm in diameter, yielding an active electrode area of 1.767 $cm^2$. At one-week intervals, both a biotic and a sterile specimen were examined by acquiring SRET scans at open-circuit potential (corrosion potential), $E_{corr}$, and 10–15 SRET scans were subsequently acquired as a function of applied potential. The duration of each experimental study was 6 weeks.

Figure 5 displays an example set of SRET data. Panels (A), (B), and (C) are SRET images from a sterile Al6061-T6 sample after 15 days in a 50-mM $Cl^-$ solution. Panels (D), (E), and (F) are SRET scans for a specimen of Al6061-T6 in the same concentration of chloride, but inoculated with the three

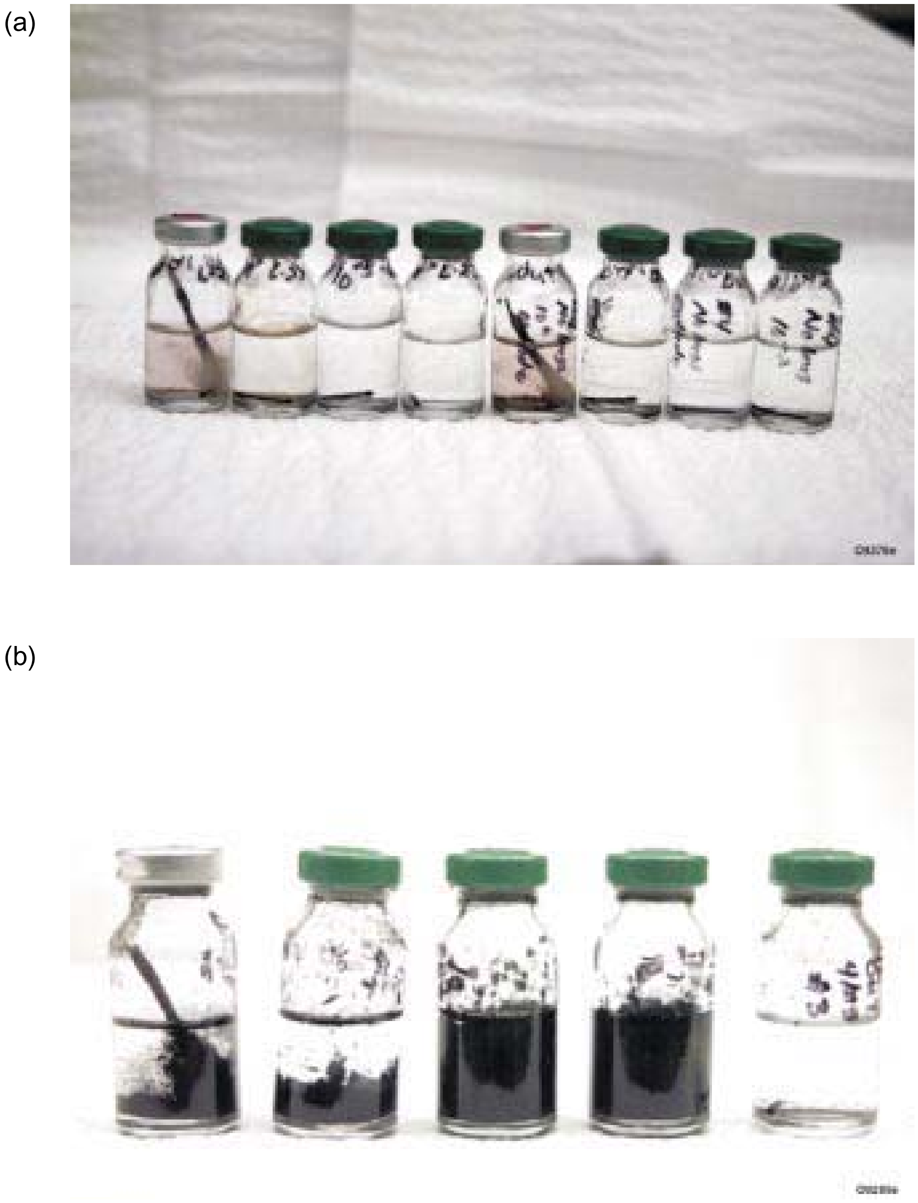

**Figure 3.** **(a)** SRB vials containing cotton swabs and subsequent serial dilutions from cladding hull 4 sampling. The test vessel containing hull 4 originally contained only sterile media, with no microbes added, and was used as an experimental control. The photograph shows two sets of four vials each containing the cotton swabs used to swipe the inside (left set) and outside (right set) of the hull. Subsequent serial dilutions were then made from the vial containing the swab. Sampling date is 6/27/00; date of photograph is 7/23/00. No microbial growth is observed from the sampling of the sterile control vessel. **(b)** Sulfate-reducing bacteria (SRB) vials containing the cotton swab (left-hand vial) used to sample the outside cladding hull 3, and vials containing subsequent 1:10 serial dilutions from the solution in the left-most vial. Black SRB growth is seen from the left-most vial containing the swab through (left to right) $10^{-1}$, $10^{-2}$, and $10^{-3}$ dilutions. The right-most vial is the $10^{-4}$ serial dilution, with no SRB growth observed. Cladding hull 3 was sampled using the cotton swab shown in the left vial on 4/25/00; the photograph was taken 5/16/00. The cotton swab used to sample the inside of cladding hull 3 showed black SRB growth to a dilution of $10^{-4}$.

**Figure 4.** **(a)** Streaked culture plates of control hull 4 cotton swab sampling (outside swab, upper left and inside swab, lower left as described in photograph 09377e) and plates to which solution from the control test vessel (hull 4) had been applied. The top right plate had 100 μL of media solution spread onto the plate, and the bottom right plate had 1:10 dilution of the test vessel solution applied. All plates remained clear, indicating no microbial growth for a period of three weeks. The fungus and possible bacteria growth observed on the two right hand plates and the top left plate are believed to be from contamination that occurred after the control samples had been applied to the plates. **(b)** Left, streaked culture plate from cotton swab sampling of the inside of cladding hull 3 (as described in photograph 09286e), and right, culture plate showing streaks from loop sampling of one of the colony regions from the original plate on the left. The sampling of the colony shown on the right occurred 5/11/00; the photograph was taken 5/16/00.

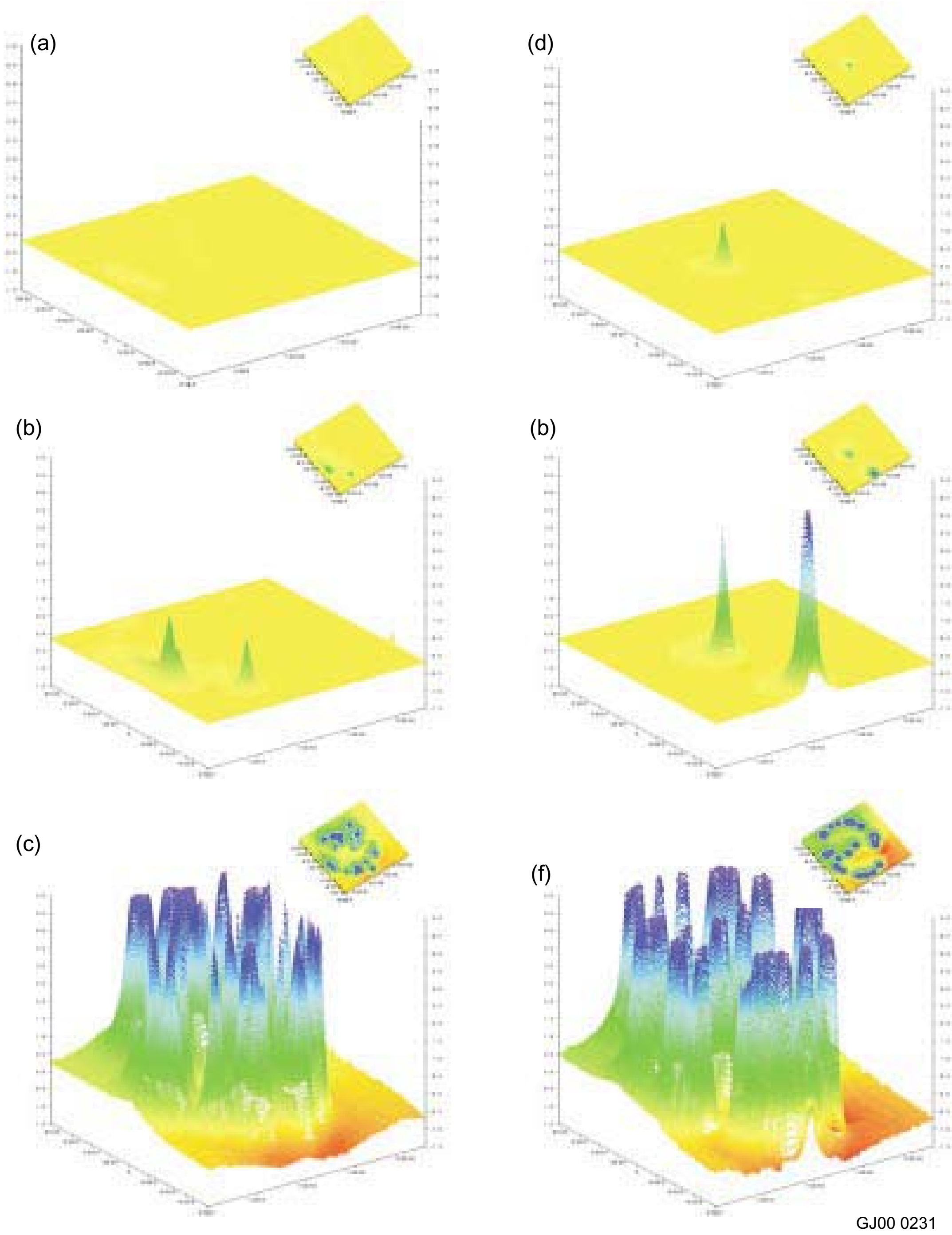

**Figure 5.** Each panel displays a 22000 × 16500 μm SRET image of the variances in micropotentials measured on a Al-6061 T6 substrate as a function of applied potential, $E_{appl}$. The electrolyte in all systems contained 0.1 M NaCl. The large image is a 3D perspective image for estimating the magnitude of response, which, full scale, measures 5 mV. The inset images in each panel show a top down perspective that yields information about the spacing and density of observed features. Images (a), (b), and (c) are a series of SRET scans for a sterile specimen (without microbes) after 22 days. Images (d), (e), and (f) are an analogous series of SRET scans for a biotic specimen (with microbes) after 23 days. Images (a) and (d) were acquired at $E_{corr}$ (-0.62 V), (b) and (e) are at $E_{pit}$, and (c) and (f) were at +1.6 V versus $E_{corr}$.

previously named bacteria. Each panel shows both a three-dimensional image of the surface and a top-down view of the surface (inset). This information aids in gauging the magnitude of electrochemical activity and the spatial displacement of this activity. Panels (A) and (D) were both acquired at the corrosion potential (-680 mV); panels (B) and (E) were both obtained at the pitting potential (-500 mV); and panels (C) and (F) were obtained at +1600 mV versus $E_{corr}$. At $E_{corr}$, panels (A) and (D), the sterile specimen displays no activity, while the biotic sample shows a local point at the very center of the sample. At the potential of $E_{pit}$, both specimens show new points of activity at their edges. At the final applied potential, frames (C) and (F), the biotic shows a larger net activity, i.e., more saturated peaks in 3D representation, but less breakdown within the interior of the specimen. In the inset image within frame (F), the outer circumference of the biotic specimen is clearly discernable. This leaves only three interior points of breakdown. The sterile specimen in panel (C) displays eleven interior points of local electrochemical activity. There are 19 local active points in the biotic specimen, yet 24 in the sterile specimen. The fact that the biotic specimen demonstrates one-third of the total number of interior active sites demonstrates that the microbial presence seems to inhibit corrosion activity by limiting the number of active sites.

Note that these SRET studies are preliminary. Pronounced effort is currently being applied to refining techniques to ensure that we are measuring overall corrosion effects and not mere attenuation of signal by a biofilm that carpets the surface. Additionally, we are in the process of refining our scans so that we can examine both breakdown and repassivation. This combined measurement will give us valuable information associated with the hysteresis formed by the breakdown and repassivation curves.

## Drying of Biofilms

After withdrawal from a nuclear reactor, SNF is temporarily stored at the reactor site, then transferred to one of the DOE SNF interim storage areas, e.g., INEEL, Hanford, or Savannah River. Upon receipt of SNF, the DOE site stores the fuel in interim wet storage environments where it can thermally cool. The time that a fuel remains in wet storage depends on the burn-up level of the fuel, but typically is in a range of 1–10 years. After the SNF has cooled, it is either reconditioned or is placed in interim dry storage. Fuel that is placed in interim dry storage is first dried under vacuum, up to a final temperature of 200–300°C. It is then loaded into an interim storage container and stored for some period until final transfer to a repository site, e.g., the DOE site at Yucca Mountain.

As stated, our MIC research at the INEEL concerns understanding the microbial factors that relate to the degradation of SNF cladding materials. Though wet storage environments are well regulated with respect to temperature, water quality, and potential contamination sources, degradation still occurs at an accelerated rate. A biological component has long been suspected as the dominant contributor to this observation. Our group is studying many aspects of the MIC problem. One facet focuses on developing microscopic techniques for investigating the effects of drying upon biofilm morphologies. This information will be useful for determining the potential risks imparted by the drying process, especially on biota that preferentially sequester radioisotopes.

The microbes used in our project comprise a mixture of those sampled from two INEEL wet storage facilities and American Type Culture Collection (ATCC) standards. Current stock includes over 35 species obtained from the INEEL site. Initial studies involved imaging pure microbial colonies applied to Type 304 stainless steel samples. For atomic force microscopy (AFM), the samples were allowed to dry briefly prior to imaging. For environmental scanning electron microscopy (ESEM), the samples were examined immediately after application of the microbes. Biofilms were grown static in glass dishes with the disk placed at about 60 degrees from horizontal. The solution was a mixture of bacteria and appropriate growth media in nanopure water.

The ESEM, an instrument derived from a scanning electron microscope, is unique in that few sample constraints exist and may image in a relatively high pressure of inert gas, such as water vapor. Figure 6a shows a diagram of the interface between the high-vacuum electron gun and high-pressure environmental chamber. These two portions of the instrument are separated by innovative pressure limiting apertures. Typical environmental chamber operating conditions are 2°C and 1–10 Torr of water vapor (40–100% relative humidity). Our instrument is a Phillips XL30 ESEM.

AFM images were taken using tapping mode (often called noncontact mode). Tapping mode AFM detects topological changes in the surface by measuring the dampening of an oscillating cantilever/tip as it tracks the surface (see Figure 6b). Our instrument (Picoscan, Molecular Imaging, Inc.) uses a magnetic field to oscillate the cantilever coated with magnetic material. Unlike most tapping mode instruments, only the cantilever oscillates. This allows precise control over the amplitude, and lower amplitudes can be used with lower stiffness cantilevers. Thus, less force is placed on the samples during imaging, which results in less sample perturbation when imaging soft materials.

Our initial efforts have focused on imaging microbial communities applied mechanically to metal surfaces. Figure 7 shows AFM and ESEM images of three different microbe cultures. These microbes range in their degree of desiccation tolerance, as can be observed in the puckering of the *Taxeobacter* sample, while the *Deinococcus* and *Micrococcus* samples maintain a rounded shape (note the linescan in the AFM images). It is interesting that less desiccation is observed for *Taxeobacter* with the ESEM (Figure 7f) than with the air-dried sample observed with the AFM (Figure 7c). It is well known that *Deinococcus* is desiccation tolerant, and it has been shown to resist high levels of radiation.[6] One commonly used method of preventing structural alterations in bacteria samples involves crosslinking (fixing) membrane proteins with aldehydes prior to sample preparation. Figure 8 compares fixed and nonfixed samples of a *Sphingomon*as bacteria culture. Both AFM and ESEM indicate the advantage of using this preparation technique to preserve the shape of bacteria prior to imaging. Future efforts will attempt to image bacteria under solution using AFM. This should be possible for bacteria that have attached themselves to the metal surface.

We have performed preliminary work on imaging biofilms. Figure 9 shows two images of Taxeobacter biofilms grown directly onto SS304 and dried for 24 hr prior to imaging.

The next step in this work will involve imaging biofilms after various stages of drying. The work will help determine the fate of biofilms following drying and placement in dry storage facilities. Another use of our imaging capability will involve correlating biofilm formation and the occurrence of pitting corrosion. These experiments will be performed with both pure and mixed cultures. In addition, we will image biofilms under solution using AFM to see dynamic events in biofilm growth and provide a more accurate picture of the native biofilm structure and evolution.

### In Vivo, Atomic Force Microscopy of Surface Proteins

The outer surface of bacteria, surface (S-) layer, possess unique structures that may initially determine its response to variations in environmental conditions. The roles fulfilled by the S-layer may include various functions, such as providing cell protection, determining both cell adhesion and cell recognition, acting as structural scaffolds for enzymes, and providing virulence factors.[11] It is known from electron microscopy (EM) that S-layer subunits may possess various symmetries. Linear (p1, p2), tetragonal (p4), and hexagonal symmetries (p3, p6) have been observed.[16] Owing to the highly periodic nature of S-layers, a variety of applications have been proposed. Most depend on the in vitro self-assembly capabilities of isolated S-layer subunits on the surfaces of solid substrates (e.g., silicon wafers,

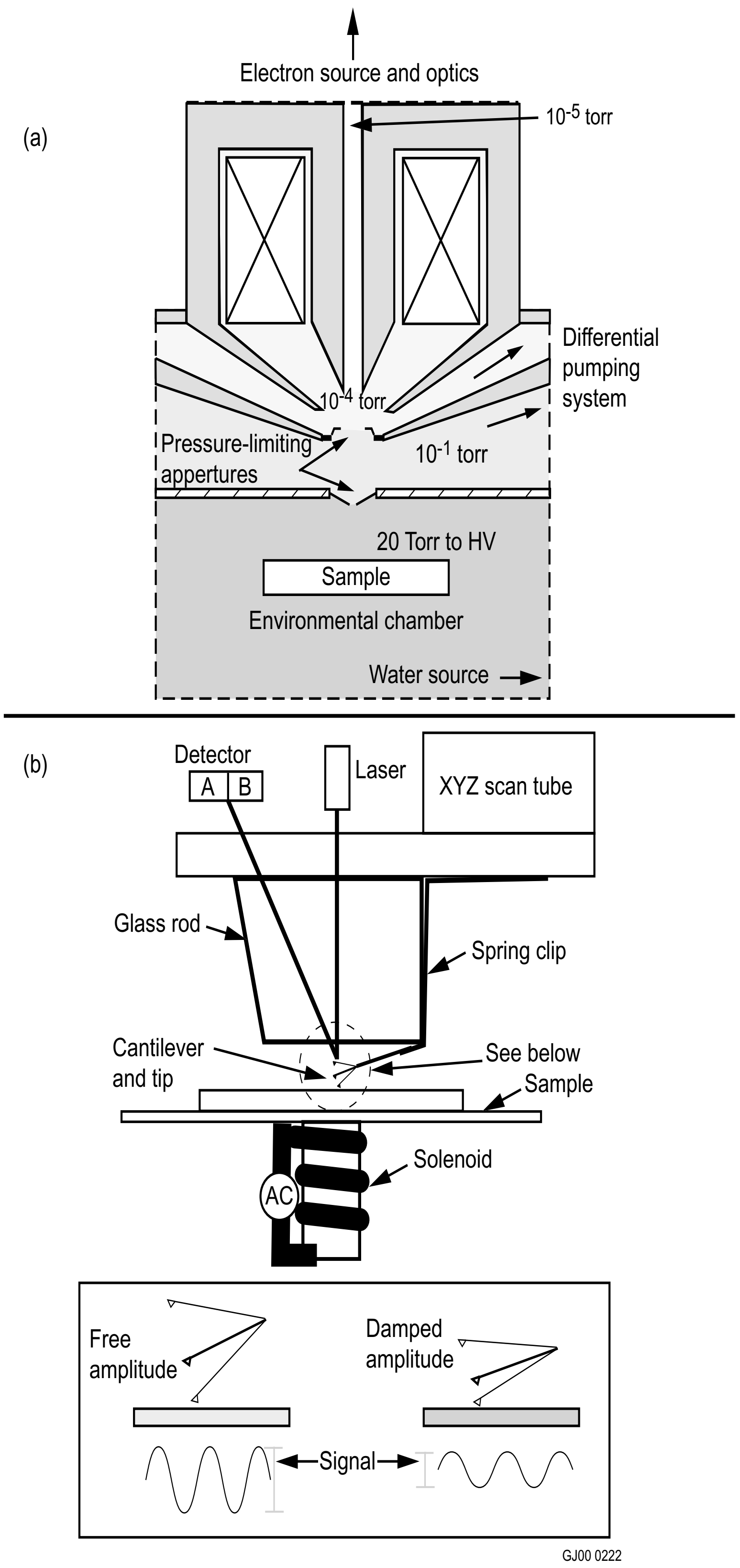

**Figure 6.** Diagrams of **(a)** ESEM differential pumping system, and **(b)** MAC mode AFM.

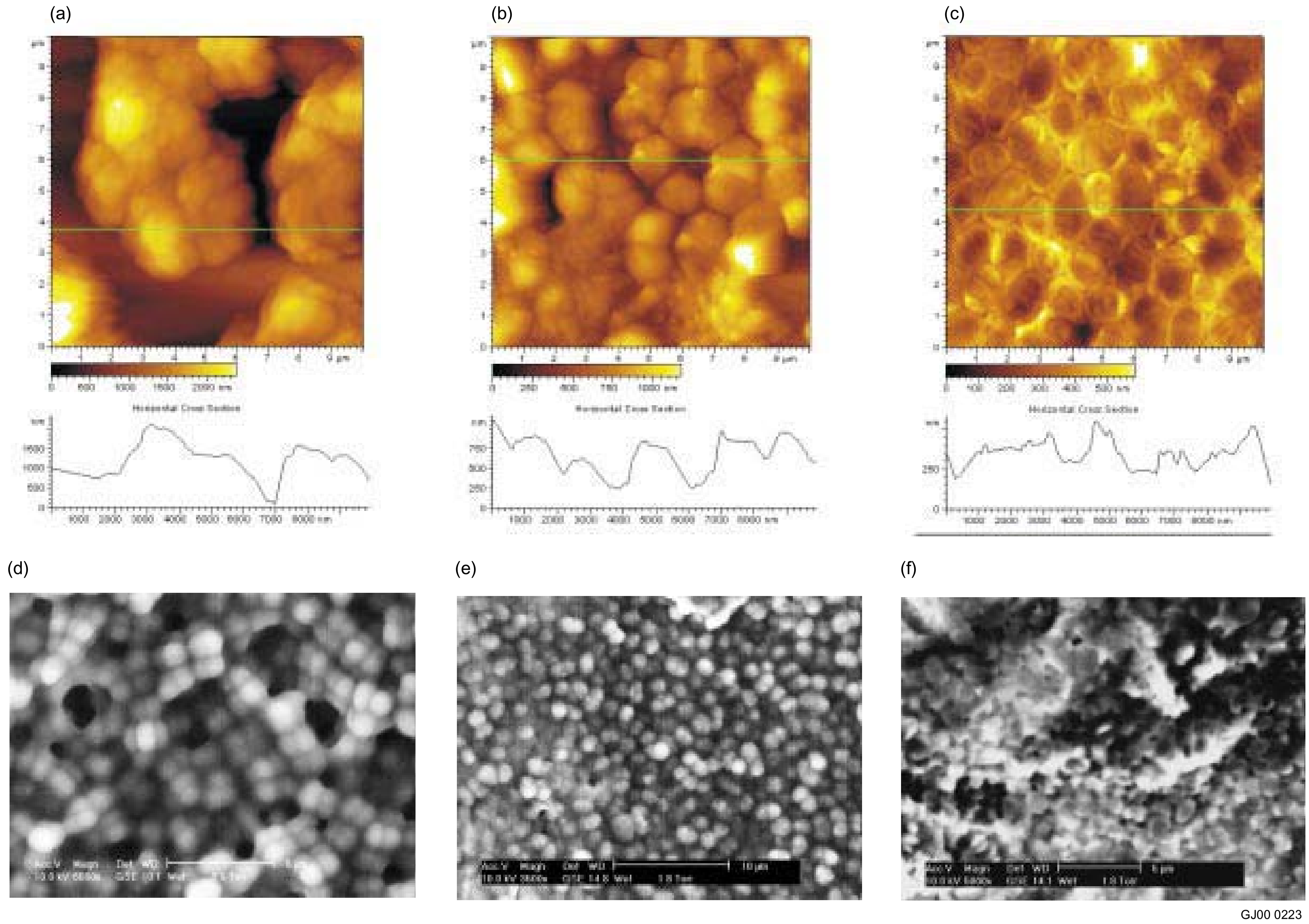

**Figure 7.** **(a)** AFM image of *Micrococcus*, **(b)** AFM image of *Deinococcus radiodurans*, **(c)** AFM image of *Taxeobacter*, **(d)** ESEM image of *Micrococcus*, **(e)** ESEM image of *Deinococcus radiodurans*, and **(f)** ESEM image of *Taxeobacter*.

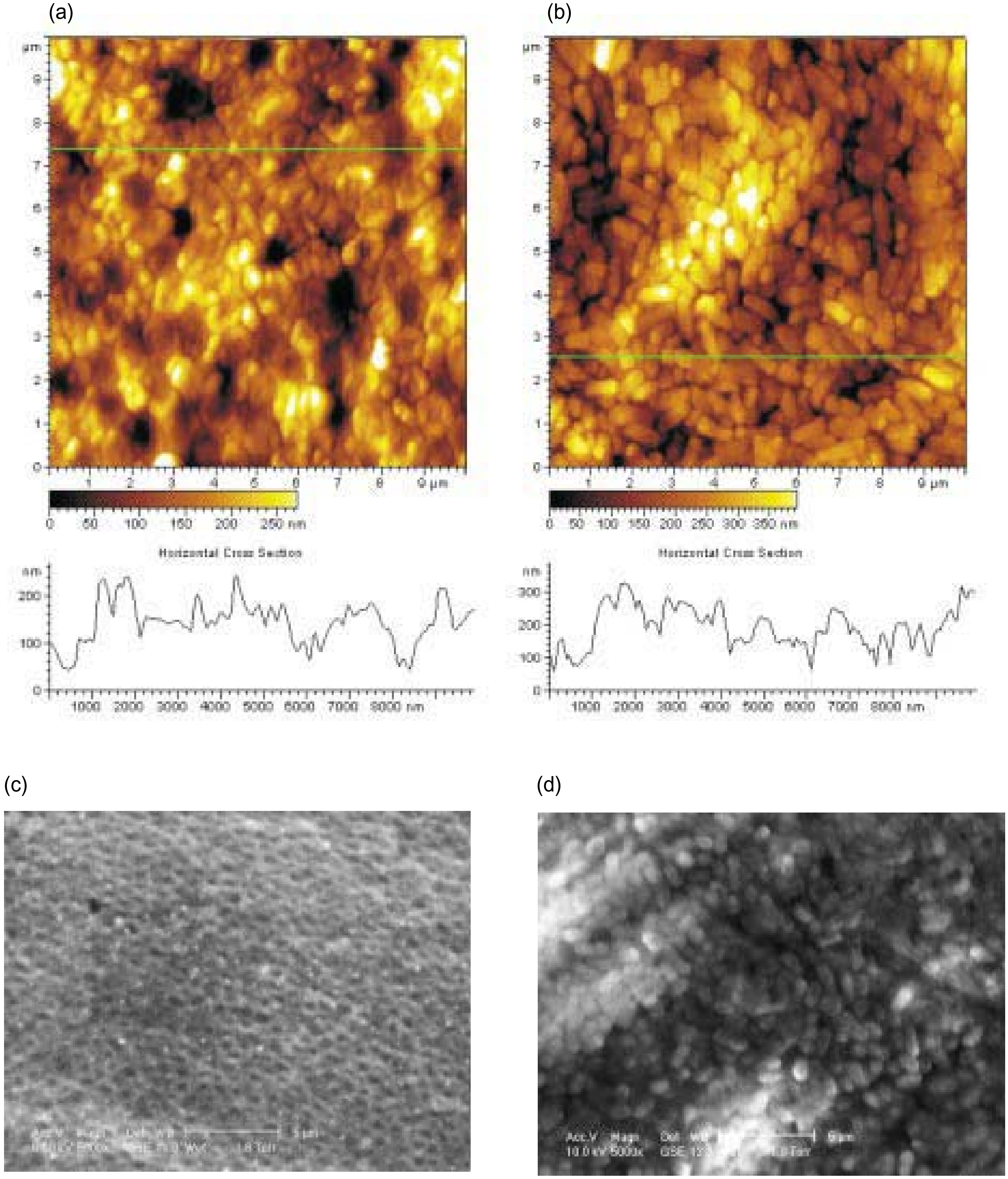

GJ00 0224

**Figure 8.** AFM images of *Sphingomonas* **(a)** without and **(b)** with paraformaldehyde fixing. ESEM image of *Sphingomonas* **(c)** without and **(d)** with paraformaldehyde fixing.

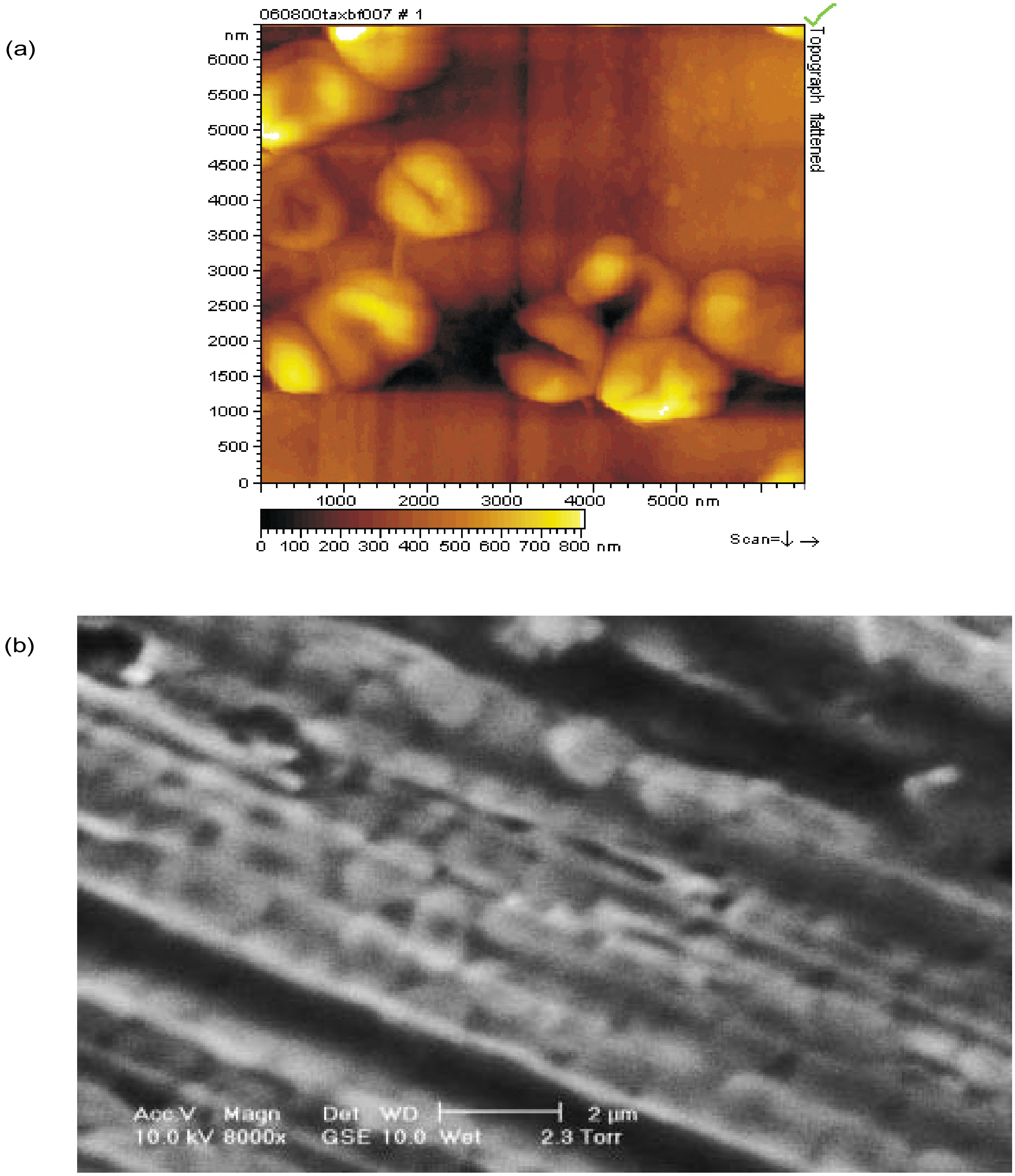

GJ00 0225

**Figure 9.** **(a)** AFM and **(b)** ESEM images of a Taxeobacter biofilm grown on 304 SS for one week and dried 24 hours prior to imaging.

polymer composites, and metals), Langmuir-lipid films and liposomes.

Traditionally, EM has been the tool of choice for viewing submicron structural details of S-layers. Nevertheless, due to the limited electron scattering efficiencies of the lighter elements (hydrogen, carbon, nitrogen, and oxygen) and the susceptibility of biomacromolecules to damage induced by a beam of high-energy electrons, biomolecules must often be processed prior to visualization with EM. Processing eventually extracts water, and thus contributes to a denaturing of the biological structures, which ultimately means that most of the details elucidating information about function are lost. Scanning probe microscopy (SPM) is a well-suited alternative technique for observing submicron detail of S-layers. SPM is based on the interaction of a finely constructed submicron probe with a small area of a specimen surface. A supreme advantage of SPM over EM is that it is nonintrusive, and therefore should yield a more natural, in vivo, representation of the true native structure of an organism.

The S-layer of *Deinococcus radiodurans* has p6 (i.e., hexagonal) symmetry. It is therefore commonly referred to as the hexagonally packed intermediate (HPI) layer. A lattice constant of 18 nm was determined with contact mode AFM.[10,2,3] Note that the HPI layer observed in these studies is extracted from the host organism with sodium dodecyl sulfate and immobilized on glass substrates by photo-crosslinking. The actual HPI surface examined in the studies are of the inner surfaces, not the outer surface, which is much more representative of what the surrounding environment contacts. Due to the pre-image processing and inversion of the HPI surface, the images acquired are no more representative of the true in situ HPI structure than are the surfaces observed with EM techniques.

We show here the first published AFM images of the HPI layer of *D. radiodurans* acquired in vivo. This is a first step in tailoring imaging techniques toward observing bacteria in their native state, unperturbed by sample preparation. Information about the native outer surface of *D. radiodurans* may shed light on its uniqueness with respect to radiation tolerance and desiccation resistance. The radiation tolerance of *D. radiodurans* has been well documented by our research group[6] and others.[7] Though the level of radiation tolerance displayed by *D. radiodurans* may be wholly a product of genetic factors, our group observed a loose correlation between g-radiation tolerance and cell wall structure in our study. The issue of desiccation resistance obviously strongly relates to variations in HPI structure. As bacteria begin to dehydrate, their surfaces contract and fold as a result of the reduction in volume. We have observed in other studies[4] that adjacent bacteria can self-assemble in cooperative response to dehydration processes. Examination of individual bacteria and changes in their associated S-layer structure may illuminate how biofilms respond to drying conditions.

*Deinococcus radiodurans* bacteria were cultured from pure ATCC standard strains. The bacteria were grown on agar solidified growth medium and removed from the plates by swabbing with a plastic wand and applying them to 304 stainless steel disks. The disks were 12.7 mm in diameter, 1.59-mm thick, and finely polished to 0.05 mm using diamond grit. The specimens were cleaned by sonicating them sequentially in acetone, then methanol, and finally deionized (DI) water. A drop of DI water was used to spread the bacteria evenly into an area approximately 5 mm in diameter. The sample was allowed to air dry in a covered petri dish. Upon drying, the bacteria form a smooth continuous film across the applied area. Imaging was performed on samples dried for at least 2 hr. After the initial drying process, no change in the imaging characteristics of the bacteria were observed over several days. The DI water was obtained from a Barnstead four-stage filtration system that yielded a resistance of 17.9 MΩ. Acetone and methanol were HPLC grade (Aldrich).

This work is a component of a larger research area examining the effects of drying processes on biofilms formed on the surfaces of materials used in the handling and storage of spent nuclear fuel. One of the fundamental issues to be addressed at the outset was to determine the morphologies of individual bacteria within natural environments. Most published information is based on characterization of bacteria in environments perturbed by stains, reduced pressure, or cryogenics. *D. radiodurans* was of particular importance in this study, as mentioned above, due to its known radiation tolerance and desiccation resistance. An AFM micrograph of *D. radiodurans* is shown in Figure 10A. In this image, four bacteria form a tetrad, a common structural conformation present in this particular species.[1] From the measured height profile, the bacteria are protruding approximately 500 nm above the level background. It is difficult to determine a real height, as the bacteria likely extend below the surrounding material. This surrounding background material is likely not the substrate, but a mixture of extracellular polymeric substances (EPS), culturing media, and salt precipitates. Centrifuging the bacteria prior to application seems to eliminate most of this material, but without any noticeable improvement in imaging quality for the bacteria. Our data support partial desiccation of the *D. radiodurans* bacteria, since the measurements show they are roughly half as high as they are wide (~1 μm). In addition to determining the general shape and size, we observed the finer detail of the bacteria cell wall (Figure 10A). This detail appears in the form of a folded structure resembling the texture of orange peel. Within the orange peel region are linear structures protruding approximately 25 nm from the surroundings. At higher magnification, we observed further detail in the linear structures, as demonstrated in Figure 10B. This image was acquired directly on the top of a single bacterium, resolving 20- to 50-nm structures.

At significantly higher magnifications, hexagonal lattices were observed near the interfaces between adjoining bacteria, shown in Figure 11. As mentioned in the introduction, *D. radiodurans* possess a hexagonally packed intermediate (HPI) protomer structure on their outer surface. For *D. radiodurans*, each hexagonal-shaped protomer unit consists of six proteins having a combined molecular mass of 655 kDa.[15] Figure 11A is the intersection of three bacteria, showing two somewhat different hexagonal domains. The domain to the lower left has units with a hexagonal shape and a central pore clearly visible. This domain has characteristics (unit diameter with pore) most commonly observed in our study. The more unusual domain located on the right side of the intersection has a somewhat larger unit size and a less distinct pore, though some units resemble those in the lower left. There appears to be continuity between the orientation of the domains on what is likely two different bacteria, going from lower left to upper right. A similar relationship is observed in Figure 11B, where the image was acquired near a tetrad interface. The center of the intersection in Figure 11B is near the center of the image, with each of the four bacteria extending into the corners of the image. The two bacteria on the left appear to possess similar orientations in their respective HPI structures, as do the two bacteria on the right. However, the HPI structures of the two bacteria on the left of the image appear to be misoriented from those of the two bacteria on the right. The angle of misorientation was measured to be approximately 30 degrees.

The highest resolution images of the HPI lattice are shown in Figure 12. These images clearly demonstrate the hexagonal symmetry characteristic of the HPI layer. They appear close-packed, the central pore having a measured depth of about 0.5 nm. Previous imaging of the HPI layer extracted and assembled onto mica surfaces has resolved six individual proteins composing each.[2] We were not able to achieve this level of resolution, possibly because (a) noncontact AFM does not yield the level of resolution afforded by contact mode AFM (because of the shorter interaction times between the probe tip and the surface), or (b) the outer carbohydrate structure remains intact in our studies, where in previous studies the layer might be stripped by the extraction process or by using contact mode AFM.

The in vivo images of the HPI layer show other interesting features when compared to layers formed by extraction/self-assembly. Figure 12A (and other images in this report) shows irregular packing of the units, with the rows deviating from linearity and the variation in height being quite pronounced along a row

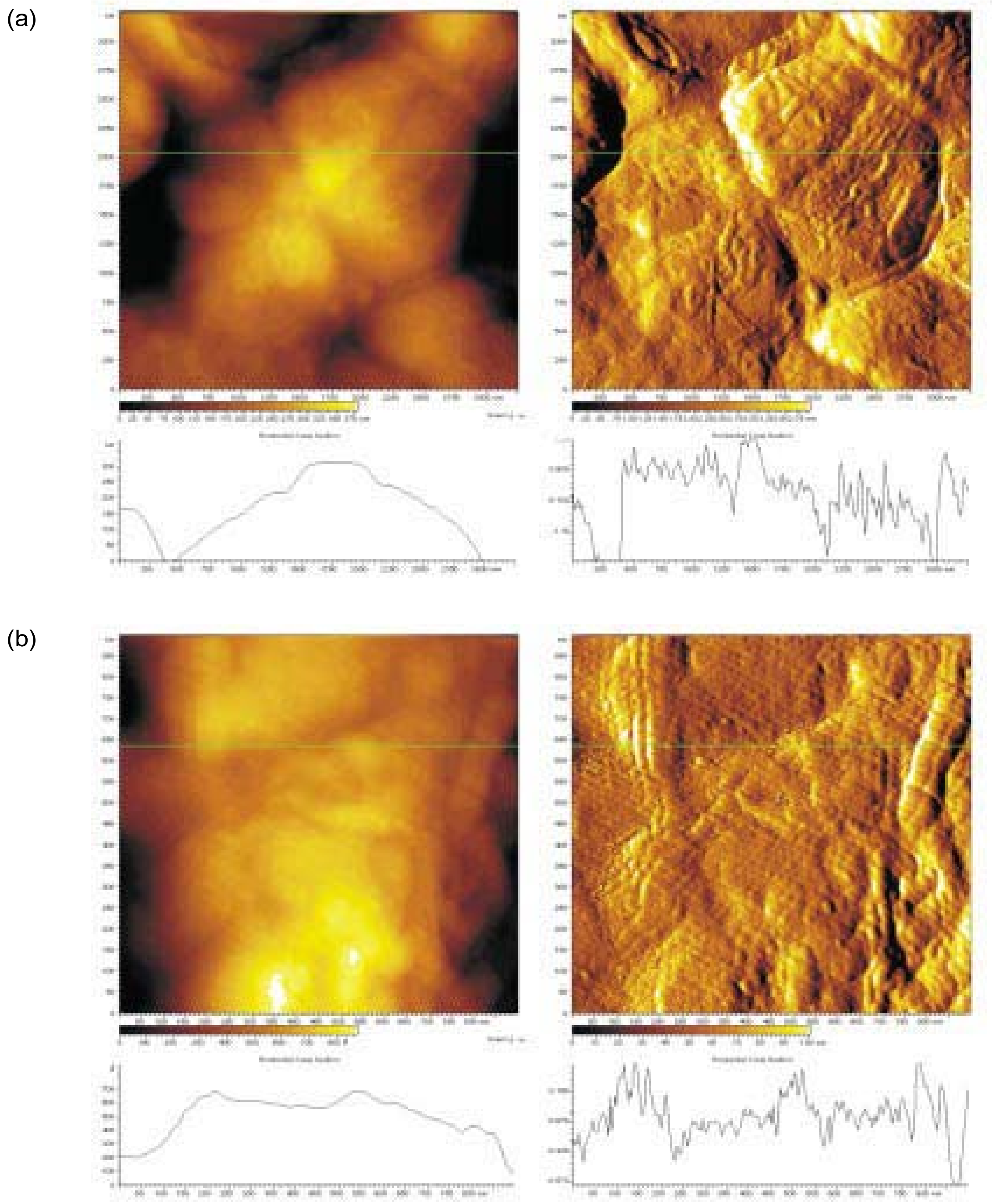

GJ00 0226

**Figure 10.** AFM micrographs of *D. radiodurans* (**A)** single tetrad and (**B)** resolution of bacteria wall structure.

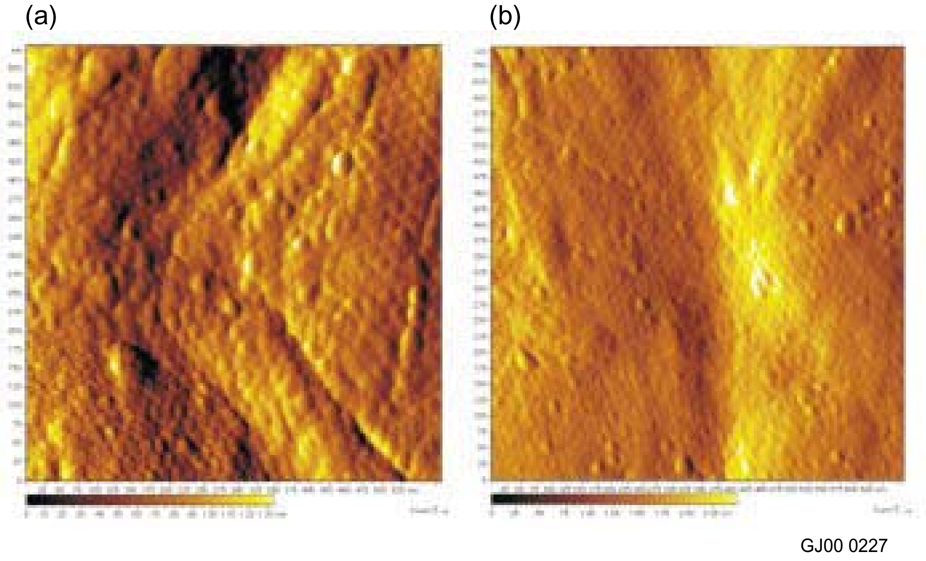

**Figure 11.** AFM micrographs showing the HPI layer (**a**) At the intersection of three bacteria and (**b**) at the center of a tetrad.

these measurements can result from slow scan axis drift or piezo hysteresis. This was confirmed by taking measurements using both directions of the slow scan (vertical) axis or by using a larger scan area. In another case, as shown in Figure 13, we have observed the HPI layer mixed with something close to the folding structure, suggesting that perhaps the defects we are seeing are due to a drying effect where the integrity of the cell wall is compromised by loss of internal volume.

Inasmuch as we saw a great variety of interunit distances in the HPI lattices, we performed statistical measurements of the HPI layer. The packing distances tabulated from 42 micrographs (acquired from different locations on three separate specimens) measured along all three row directions give an average distance of 21.21 +/- 2.52 nm. Previous values for HPI spacing from extracted proteins self-assembled onto mica was 18.0 nm.[10,3] Electron microscopy of freeze etched/thin sectioned samples has been performed and communicated,[8,9] but to our knowledge the details have not been published. Our measurements are somewhat larger than the values from the extracted samples. However, the extreme values of unit spacing (measured over at least 4 units) observed over all micrographs was 16.39 and 28.40 nm (not including the folded structures), which encompasses the values for the extracted protein. The range and high standard deviation also point to the large variation we see in the spacing of the HPI layer, values that lie beyond the measurement uncertainty for a calibrated scanning probe instrument. Thus, we are confident in assessing most of the observed variability to real sample variation.

Although we have seen the HPI layer near the interfaces of adjoining bacteria, it was not often observed at the tops of bacteria. However, in isolated cases, as shown in Figure 14, we were able to image a periodic array on the top part of the bacteria. The reason why we see the HPI structure mostly at the edges of the bacteria likely has to do with the dehydration process. Our measurements show the surface roughness is concentrated toward the center of the bacteria, which is composed of a folded structure having some periodicity in the chains. Large patches of HPI are likely not seen due to the roughness in this area. We expect that the volume loss at the center of dehydrated bacteria would be largest, and we are currently attempting to explain this observation with further imaging using different preparation and imaging conditions.

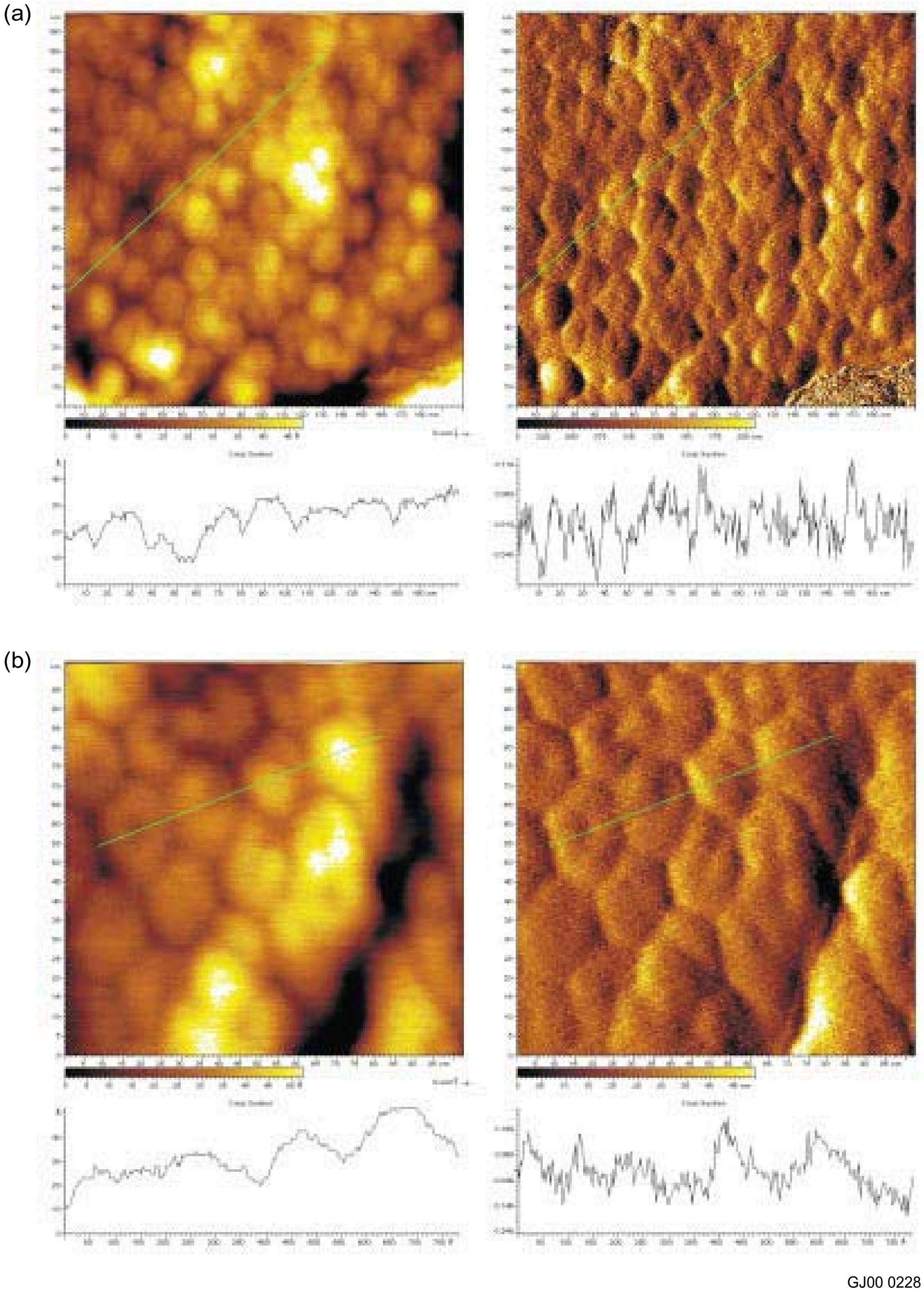

**Figure 12.** Two high-resolution AFM micrographs of the HPI layer near the intersection of bacteria.

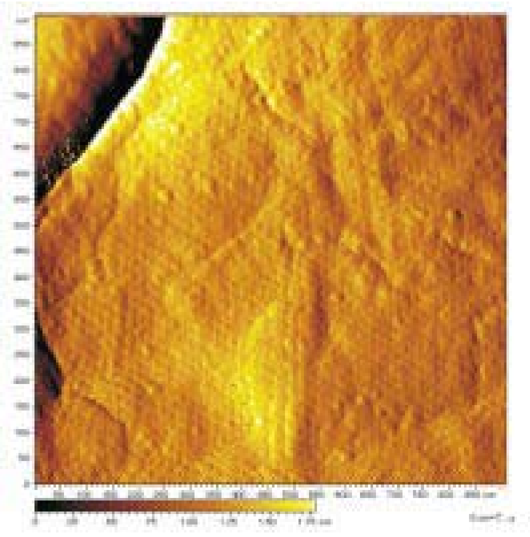

GJ00 0229

**Figure 13.** An AFM micrograph showing a mixed structure of HPI and folding structures.

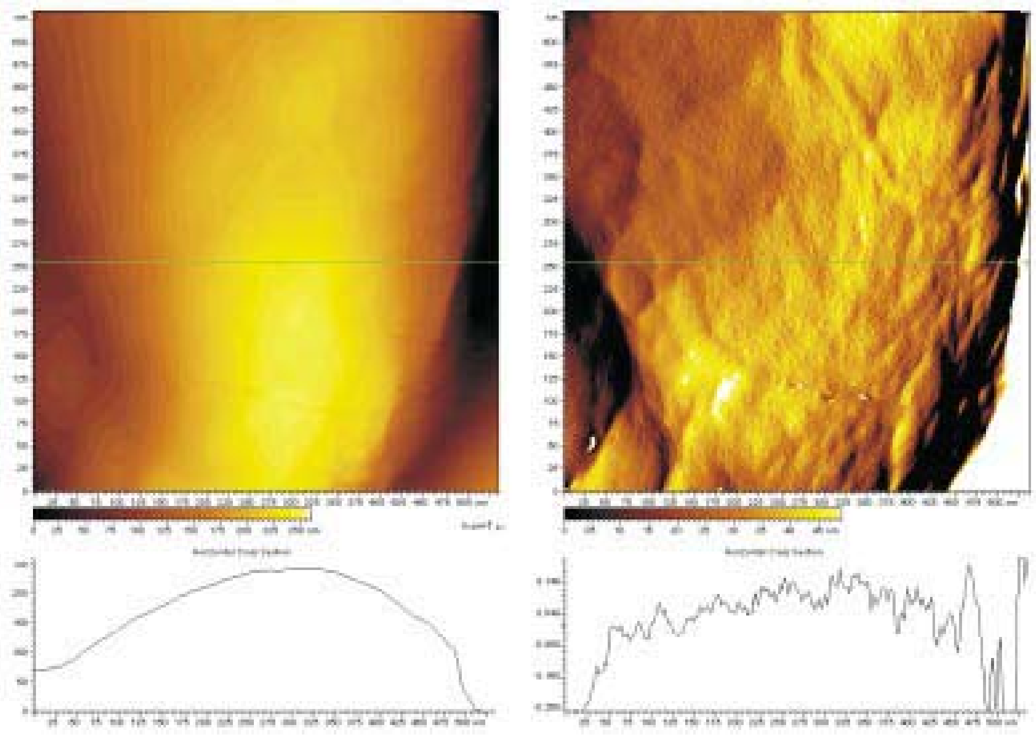

GJ00 0230

**Figure 14.** An AFM micrograph of a bacterium with HPI layer extending across the surface.

It appears that the regular structures observed near the interfaces of the bacteria are due to the HPI (S-layer) layer. Our observations parallel those reported using TEM and AFM of self-assembled proteins.[13,15,14] This is a significant finding if indeed it is the S-layer, as this demonstrates the potential for imaging outer cell wall structures in a natural state. We are somewhat confident that the cells were in a living yet dormant state, from the numerous reports of *D. radiodurans* surviving dry conditions.[1] We attempted some preliminary imaging of the bacteria under solution, but the bacteria appeared to float off the surface, even when the drying and solution were sequential. To prevent this, some methods of attachment should be attempted, such as surface modification, e.g., surface roughening. Imaging the S-layer in solution on the bacteria surface would be a significant step beyond the progress described here.

Our images raise one important question: why is there a variance between structures imaged on the top of the bacteria where the corrugated fold structure is seen versus images obtained at the outer edges where the HPI structure is observed? One possible explanation is that the bacteria are flattened by desiccation and the folded structure is due to the outer cell wall buckling to form the rougher orange peel texture. While it is tempting to think that the linear chains may be the HPI layer turned on its side, many of the observed folds exceed the approximately 4- to 9-nm height measured previously by a variety of techniques.[2,21] It is possible, however, that we are not achieving high resolution due to the rough corrugation of the cell wall or other factors. In that case, one would not expect to find a regular structure but a random arrangement with significant z-corrugation. Indeed, the structures that we observe in the center portions of the bacteria are of similar dimensions as the S-layer, and the linear chains possess unidirectional order. We also observe significant disorder in the HPI structures compared to those near perfect lattices observed by AFM and TEM. We ascribe this distortion to the collapsing of the inner structure and distortion of the cell wall caused by these strains.

## ACCOMPLISHMENTS

Radiation resistance of bacteria continued to be an area of focus during FY 2000. Collaboration with ANL-W provided means to test for microbial growth on actual SNF cladding hulls with strong radiation fields. This result is significant because it produced definitive evidence for the establishment of biofilms on cladding materials in radiation-rich environments. We have now shown that bacteria are not only present in the INTEC SNF pools (FY 1999 highlight), but that these bacteria can form biofilms on cladding materials within strong radiation fields. And our UV radiation tolerance study gave us another possible method for screening for radiation tolerance in microorganisms—correlation between radiation resistance and pigmentation. Results of these studies have been presented in peer forums. Preparation of peer-reviewed manuscripts detailing the UV/g-radiation studies and the ANL-W collaboration are currently in process.

We completed preliminary studies using the Scanning Reference Electrode Technique (SRET) in FY 2000. Modifications to the SRET instrument over the last quarter of FY 2000 now allow for quantitative measurement of local corrosion rates. We presented results of the preliminary studies at a focussed session of the Materials Research Society's National Meeting in Boston and at the American Society for Microbiology's Biofilms 2000 meeting in Big Sky. Presently, a manuscript detailing the preliminary studies is in preparation. The importance of the preliminary studies is that they offer qualitative evidence for corrosion inhibition produced by inoculation with a mixture of *P. aeruginosa*, SRBs, and *D. radiodurans*.

A very detailed study laying the foundation for future investigation of drying processes was initiated during FY 2000. This study looked at bacteria morphology within unperturbed, natural environments, i.e., no stains, fixation, etc. A manuscript is in preparation detailing this work.

The surface protein structure of *D. radiodurans* was examined, and we acquired high-resolution in vivo AFM images of the HPI layer within this bacteria. A manuscript has been submitted detailing this work.

In all, we delivered nine presentations at regional and national meetings, two of which were invited. Publication in the peer-reviewed literature is currently under focus.

## REFERENCES

1. Battista, J. R. *Annual Review of Microbiology* 1997, *51*, 203–24.

2. Baumeister, W.; Barth, M.; Hegerl, R.; Guckenberger, R.; Hahn, M.; Saxton, W. O. *Journal of Molecular Biology* 1986, *187*, 241–250.

3. Baumeister, W.; Karrenberg, F.; Rachel, R.; Engel, A.; Heggeler, B. t.; Saxton, W. O. *European Journal of Biochemistry* 1982, *125*, 535–44.

4. *Breckenridge, C. R.; Lister, T. E.; Pinhero, P. J. 2000.*

5. Brock, T. D.; Madigan, M. T. *Biology of Microorganisms*, 5 ed.; Prentice Hall: Englewood Cliffs, NJ, 1988.

6. *Bruhn, D. F.; Breckenridge, C. R.; Tsang, M. N.; Watkins, C. S.; Windes, W. E.; Roberto, F. F.; Wright, R. N.; Pinhero, P. J.; Brey, R. F. "Irradiation of Microbes from Spent Nuclear Fuel Storage Pool Environments"; Global'99: International Conference on Future Nuclear Systems, 1999, Jackson Hole, WY.*

7. Daly, M. J.; Minton, K. W. *Science* 1995, *270*, 1318.

8. Emde, B.; Heibe, E.; Karrenberg, F.; Baumeister, W. "Structural investigations on the cell wall of *Micrococcus radiodurans*"; Second International Congress on Cell Biology, 1980, Berlin.

9. Emde, B.; Wehrli, E.; Baumeister, W. "The topography of the cell wall of *Micrococcus radiodurans*"; 7th European Congress on Electron Microscopy, 1980, The Hague.

10. Engel, A.; Baumeister, W.; Saxton, W. O. *Proceedings of the National Academy of Science* 1982, *79*, 4050–4.

11. Firtel, M.; Beveridge, T. J. *Micron* 1995, *26*, 347–62.

12. Lin, C. L.; Tan, S. T. *International Journal of Radiation Biology* 1996, *69*, 493–502.

13. Moller, C.; Allen, M.; Elings, V.; Engel, A.; Muller, D. J. *BIOPHYSICAL JOURNAL* 1999, *77*, 1150–1158.

14. Muller, D. J.; Baumeister, W.; Engel, A. *JOURNAL OF BACTERIOLOGY* 1996, *178*, 3025-3030.

15. Muller, D. J.; Fotiadis, D.; Engel, A. *FEBS LETTERS* 1998, *430: (1-2) 105-111, Sp. Iss. SI JUN 23 1998*, 105–111.

16. Sara, M.; Sleytr, U. B. *Journal of Bacteriology* 2000, *182*, 859–868.

17. Stroes-Gascoyne, S.; Gascoyne, M. *Environmental Science and Technology* 1998, *32*, 317–26.

18. Stroes-Gascoyne, S.; Sargent, F. P. *Journal of Contaminant Hydrology* 1998, *35*, 175–190.

19. Stroes-Gascoyne, S.; West, J. M. *Canadian Journal of Microbiology* 1996, *42*, 349–366.

20. Stroes-Gascoyne, S.; West, J. M. *Fems Microbiology Reviews* 1997, *20*, 573–590.

21. Wang, Z. H.; Hartmann, T.; Baumeister, W.; Guckenberger, R. *Proceedings of the National Academy of Science* 1990, *87(23):9343-7*, 9343–7.

22. Wolfram, J. H.; Mizia, R. E.; Dirk, W. J. “Microbial Sampling of Aluminum-clad Spent Nuclear Fuel”; Corrosion 98, 1998, Houston, TX.

# Transport in Solid and Liquid Media

**Clinton DeW. Van Siclen**

## SUMMARY

This environmental systems research (ESR) project addresses the fundamental question: What are the relations between the macroscopic transport properties of a medium and its structure? A novel mathematical method for answering this question for arbitrarily complex media was developed over FY 1998 and 1999 (and recently published). This method has been applied during FY 2000 to fracture networks in recognition that subsurface contaminant migration at the INEEL, and many other DOE sites, occurs through fractured rock. In particular, algebraic expressions for the fluid permeability ($k$) and electrical conductivity ($\sigma$) of fracture networks have been derived, which together reproduce and explain experimental data relating $k$ and $\sigma$. This work significantly advances our understanding of the transport properties of fractured rock.

## PROJECT DESCRIPTION

Scientists now recognize that a network of fractures in the subsurface rock matrix, which would otherwise be relatively impermeable, provide the primary flow paths for what can be the extremely rapid movement of subsurface contaminants through the vadose zone and aquifer at the INEEL and other DOE sites.

Fracture systems are difficult to study because they are heterogeneous over all length scales. Fractures tend to occur in clusters, which are often highly anisotropic and tenuously connected to one another. The length distribution of fractures comprising a network may cover many orders of magnitude (millimeters to kilometers). Thus, the information gained from point measurements supplied by field investigations is limited. Similarly, the applicability of traditional modeling techniques is limited, because a continuum description or treatment of a fracture network is simply not valid.

There being no obvious way to proceed, we set ourselves the task (FY 2000) of explaining an unambiguous experimental result, namely, that the permeability ($k$) and the electrical conductivity ($\sigma$) of fluid-saturated, fractured rock exhibit a power law relationship, $k \propto \sigma^r$, as mechanical pressure is applied to the rock. This behavior is evident in Figure 1, which is a sampling of plots taken from the literature. Perhaps the surprisingly simple relationship between $k$ and $\sigma$ indicates some general (or universal) property of fracture networks, while the variation in the value of the exponent $r$ between samples ($1.5 \leq r \leq 2.8$) indicates some property that distinguishes between networks. Although the permeability of a fracture network is of primary interest in this project since fluid flow enables contaminant migration, the conductivity is also of interest since electrical resistivity measurements are often made to obtain information about the structure of the subsurface. This observed power law behavior is also relevant to the important fundamental issue of whether the electrical conductivity (easy to measure) of a porous medium can serve as an analogue for the fluid permeability (hard to measure).

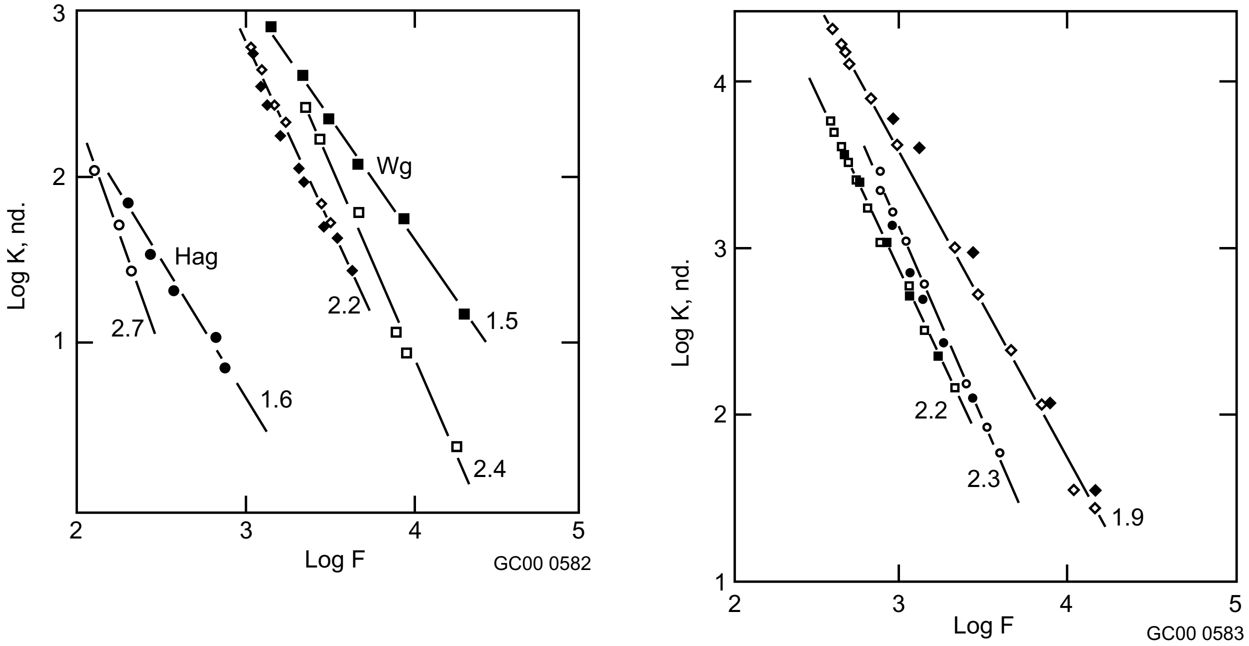

**Figure 1.** Experimental measurements of the permeability (*k*) and the formation factor (*F*) (proportional to $1/\sigma$) obtained for various types of fractured rock. These plots are from Walsh and Brace (1984), who included fits to the data points to highlight the power law relationship.

For the purposes of this project (i.e., to obtain analytical results), a fracture network is regarded as a collection of connected, locally planar fractures embedded in an impermeable matrix. Because the fluid flux and the electrical current flux are distributed differently among the flow channels comprising the network (reflecting the fact that the distribution of electrical current is that which minimizes the total power dissipation, while there is no corresponding global minimization principle for fluid flow), separate models for network permeability and conductivity are developed.

The transport properties of a rough, planar fracture can be expressed in terms of the *effective* fracture apertures $d_h$ and $d_e$, where the former equals the aperture of a *parallel plate* fracture (i.e., one with smooth, parallel sides) that produces the same volume flow rate as the planar fracture for a given fluid pressure difference, and the latter equals the aperture of a parallel plate fracture that produces the same electrical current as the planar fracture for a given potential difference. By a series of algebraic steps, such planar fractures are assembled into fracture networks having transport properties:

$$k = N_{\mathrm{A}} \frac{d_h^{\,3} w}{12 \tau_h} \tag{1}$$

and

$$\sigma = N_{\mathrm{A}} \sigma_0 \frac{d_e w}{\tau_e} \tag{2}$$

where

$w$ = the width of a representative planar fracture

$d_h$ and $d_e$ = the hydraulic and electric apertures, respectively, of the representative fracture

$N_A$ = the areal number density of fractures intersecting a cross-section of the material perpendicular to the applied fluid pressure or electrical potential gradient

$\sigma_0$ = the electrical conductivity of the fluid

$\tau_h$ and $\tau_e$ = fluid and current flow path tortuosity factors, respectively, determined by the *network* structure.

These expressions for $k$ and $\sigma$ constitute an *equivalent channel* model for transport in that $d_h$ and $d_e$ are taken to be representative of the planar fractures that constitute the network. The *connectivity* of the network is specified by the tortuosity factors $\tau_h$ and $\tau_e$.

Equations (1) and (2) can be combined to give

$$k \propto \sigma^r \frac{d_h^{\,3}}{d_e^{\,r}} \frac{\tau_e^{\,r}}{\tau_h} \tag{3}$$

where the proportionality constant containing $N_A$, $\sigma_0$, and $w$ is unaffected by pressure. Then $k \propto \sigma^r$ in agreement with experiment when both ratios $d_h^3/d_e^r$ and $\tau_e^r/\tau_h$ are slowly varying over the range of applied pressures. This is certainly the case for a fracture network consisting of a single, parallel plate fracture, where the exponent $r = 3$. The remainder of this report considers networks consisting of a single, planar fracture, for which it is shown that indeed $d_h^3 \propto d_e^r$, with slowly varying $r$, as pressure is applied. The question of whether $\tau_e^r \propto \tau_h$ is more difficult to address, although it is noted that this relation was found in the one case where $\tau_h$ and $\tau_e$ were determined experimentally for an isotropic, porous material.

The fluid permeability and electrical conductivity of single, planar fractures may be straightforwardly obtained by solving the Navier-Stokes equations and the Laplace equation, respectively, over the three-dimensional interior space of the fracture. However, these calculations are computationally intensive, which severely limits the number and size of fractures that can be studied. Instead, fluid flow is considered to be governed by a local *cubic law* inspired by the solution of the Navier-Stokes equations for parallel plate fractures. This gives rise to the two-dimensional Reynolds equation for fluid flow, which is typically solved for the local fluid pressures by the finite difference method (FDM). An analogous Reynolds equation was found for electrical current flow.

The two Reynolds equations are treated by the walker diffusion method (WDM) rather than solved by the FDM. A great virtue of the WDM (developed by the ESR project during FY 1999) is that it can produce useful analytical results as well as numerical results. Here, it gives the following algebraic relations for single, fluid-saturated, planar fractures:

$$k_1 = \frac{\langle d(\mathbf{r})^3 \rangle}{12 \langle d(\mathbf{r}) \rangle} D_h \tag{4}$$

$$d_h{}^2 = \frac{\langle d(\mathbf{r})^3 \rangle}{\langle d(\mathbf{r}) \rangle} D_h \tag{5}$$

$$\sigma_1 = \sigma_0 \, D_e \tag{6}$$

$$d_e = \langle d(\mathbf{r}) \rangle \, D_e \ . \tag{7}$$

The quantity $\langle d^n \rangle$ is the $n$th moment of the fracture aperture width distribution, and $D_h$ and $D_e$ can be shown to be functionals only of the fracture surface roughness and the degree of fracture closure. (It may be noted that $k_1$ and $\sigma_1$ are the transport properties of a single *disembodied* fracture; that is, no account is taken of the medium in which the fracture is embedded. In contrast, a fracture *network* necessarily includes the medium. This is a nontrivial distinction: for example, the conductivity $\sigma_1$ is scale invariant, while $\sigma$ is not.)

This set of equations together with Equations (1) and (2) show that there is no *fundamental* relationship between the permeability and the electrical conductivity of a planar fracture, despite the intentional similarity of their derivations. Thus, it is necessary to *calculate* (or measure) the transport properties of a variety of planar fractures with different geometries to discover any phenomenological relationship.

The simulated planar fractures are created from self-affine surfaces characterized by values for the roughness exponent $\zeta$ and the variance of the distribution of fracture surface heights. An example of a fracture with surfaces having $\zeta = 0.8$ (typical of real fracture surfaces) is given in Figure 2. The view is

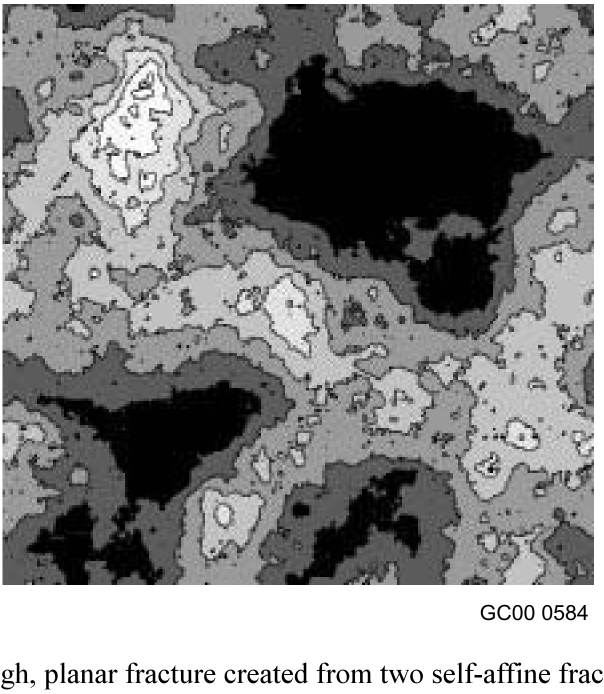
GC00 0584

**Figure 2.** Example of a rough, planar fracture created from two self-affine fracture surfaces. The view is normal to the fracture plane, the black regions indicating where the two surfaces touch and the contours of increasingly lighter shading signifying increasingly greater aperture.

normal to the fracture plane, with the black regions indicating where the two surfaces touch and the contours of increasingly lighter shading signifying increasingly greater aperture (the fractures used in the calculations were *not* contoured). The connected regions of relatively large aperture constitute flow channels through the fracture.

The WDM is used to determine the coefficients $D_h$ and $D_e$ for a variety of simulated fractures; these values are then used to calculate the quantities $d_h^3$ and $d_e$. The results are plotted in Figure 3. Each symbol identifies a set of fractures, where successive members of the set are obtained by further reducing the aperture of an initial fracture. Thus, the data points of a set, going from right to left, correspond to a planar fracture under increasing pressure, and the slope of a curve drawn through those data points gives the value of the power law exponent $r$ for that fracture. The straight lines with slopes 3, 2, and 1 are included in the plot to show that $r \to 3$ for fractures with well separated surfaces (i.e., large apertures) and that $1 \leq r \leq 3$ in agreement with experimental observations. The slope $r$ is clearly not constant for a set of fractures, but decreases slowly with decreasing aperture (increasing pressure). However, $r$ is effectively constant over the much narrower range of pressures that can be achieved experimentally (i.e., below the threshold pressure at which the rock responds inelastically). For reference, the last data point in each set corresponds to a planar fracture that is approximately 40% closed, a situation that is highly unrealistic.

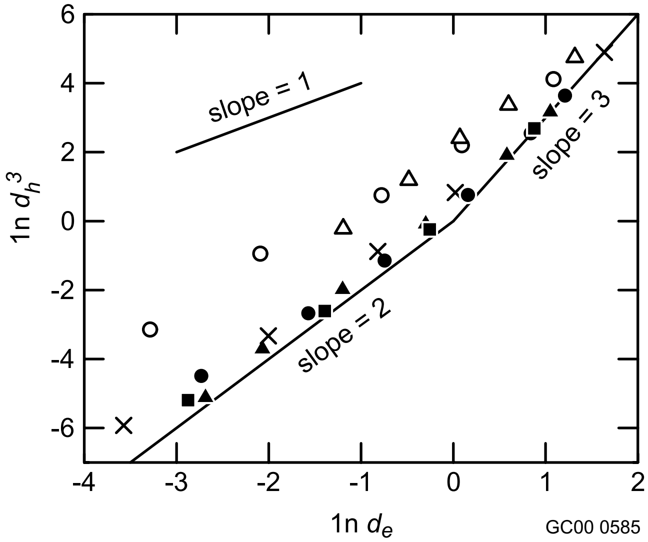

**Figure 3.** Computational results obtained for a variety of simulated, planar fractures. The variable $d_e$ is proportional to the electrical conductivity $\sigma$ of a fracture network comprised of a single fracture, while $d_h^3$ is proportional to the permeability $k$ of the network. The squares and triangles (circles) are data points for fractures with fracture surface roughness exponent $\zeta = 0.8$ (0). The filled (open) symbols indicate fractures created with a small (large) fracture surface height variance. The × are data points for fractures created from surfaces that are uncorrelated (i.e., surface heights are assigned randomly from a Gaussian distribution) and have a small height variance.

The most striking feature of Figure 3 is the alignment of data points with slope 2. The significance of the slope (or exponent) 2 becomes apparent when the partially closed fracture is regarded as a three-dimensional *porous* material; that is, as a collection of connected pores, all intersecting the fracture plane (Figure 2 can certainly be viewed in this way). An analysis for a porous medium, similar to that culminating in Equations (1) and (2) for the fracture network, produces the following relations:

$$k = N_{\mathrm{A}} \frac{\pi d_h'^2 \langle d'^2 \rangle}{128 \tau_h'} \tag{8}$$

and

$$\sigma = N_{\mathrm{A}} \sigma_0 \frac{\pi d_e'^2}{4 \tau_e'} \tag{9}$$

where the primed quantities characterize the porous medium. A representative sequence of linearly connected pores through which flow occurs has average cross-section $\pi \langle d'^2 \rangle / 4$, hydraulic diameter $d'_h$, and electric diameter $d'_e$. The analysis also shows that $d'_h = d'_e$ for such a system of linearly connected pores. Then, for the extreme case where the connected pores form smooth cylindrical tubes of uniform cross-section (so that $d'^2_h = d'^2_e = \langle d'^2 \rangle$), Equations (8) and (9) show that the permeability and electrical conductivity of the porous material follow the power law $k \propto \sigma^2$ as the pores are uniformly constricted. (The tortuosities $\tau'_h$ and $\tau'_e$ of flow tubes lying in the fracture plane will be little affected by pressure normal to the plane.) The opposite extreme is the case where the medium is comprised of distinct pores connected by narrow necks. Then, the effective cross-sections $d'^2_h$ and $d'^2_e$ decrease much more rapidly than the average pore/neck cross-section $\langle d'^2 \rangle$ as the pores and necks are constricted, so that $\langle d'^2 \rangle$ is effectively constant and $k \sim \sigma^1$. This analysis thus predicts the trends apparent in Figure 3: the value of $r$ tends toward 2 for systems of flow channels with relatively small variance in their diameter and toward 1 for systems of flow channels with relatively large variance in their diameter. In fact, the data points in Figure 3 imply the general rules that $r \approx 2$ when the ratio $\langle d \rangle / \sigma_d$ lies between 1 and 2, where $\sigma_d{}^2$ is the variance of the fracture aperture, and $r \to 1$ as $\langle d \rangle / \sigma_d \to 0$.

To briefly summarize, useful algebraic expressions for the fluid permeability $k$ and electrical conductivity $\sigma$ of fracture networks have been derived; together these expressions reproduce the experimentally observed power law relation between $k$ and $\sigma$. A planar fracture is found to increasingly resemble a porous medium as the fracture aperture decreases; this provides an explanation for the observed values of the power law exponent $r$. Evidence is presented that electrical current flow cannot be considered an analogue of fluid flow through fracture networks. Finally, it should be noted that this report is a greatly abbreviated version of a paper to be submitted for publication in the fall of 2000. Preprints are available on request.

## ACCOMPLISHMENTS

Progress has been made toward understanding the transport properties of fractured rock. Analytic models for the fluid permeability ($k$) and electrical conductivity ($\sigma$) of saturated, fracture networks have been developed for the purpose of reproducing and explaining the experimentally observed power law relation between $k$ and $\sigma$. A paper reporting this work will be submitted for publication in the fall of 2000.

# Characterization Science

### James Seydel, Research Area Leader

DOE's Environmental Management program faces a wide range of characterization and monitoring issues as it fulfills its responsibility for cleanup and monitoring of newly generated and legacy waste. Characterization of waste must be (a) before processing, (b) at contaminated sites during remediation, and, (c) often, after remediation. Characterization activities lead to understanding of the transport and fate of contaminates and are key to understanding natural attenuation processes. For example, accurate characterization of fissile material content is required when disposing of waste at the Waste Isolation Pilot Plant (WIPP) or spent nuclear fuel at the proposed Yucca Mountain Repository.

This research area supports development of a variety of techniques, which include nondestructive assay (NDA) instrumentation, nuclear spectroscopy, structure studies, sensor development, expert system development, and enhancement of existing instrumental techniques for environmental measurements. These techniques are leading to an improved capability for required characterization of boxed and drummed waste before its shipment to WIPP. Some of ESR's most immediate applications to operational problems are coming from nondestructive assay and nuclear spectroscopy research. Advancements in NDA instrumentation, nuclear structure data, and related software have already enhanced the INEEL's ability to characterize TRU waste. Work began in FY 2000 on developing advanced down-hole probes, based on NDA and nuclear structure work, which will be applicable to subsurface mapping of radionuclides and RCRA metals. The sensor development and instrumental enhancement activities address the needs of remediation activities and long-term monitoring, and the need for field portable characterization instruments.

# Adaptive Sensors

**Kenneth L. Telschow, Napoleon Thantu, Robert S. Schley**

## Summary

The sensing of environmental parameters, such as material properties, chemical concentrations, gas and liquid flow, etc., requires that measurements be noncontacting, nonintrusive, compatible with industrial environments, and highly sensitive and selective in the presence of large background effects. The goal of this research program was to investigate a new class of optical environmental sensors that use unique features of nonlinear optical processes. One optical process investigated was photorefractive dynamic holography for photoacoustic spectroscopic sensing applications. Theoretical and experimental characterization of a *containerless* photoacoustic spectroscopic measurement method were performed that demonstrated a sensitivity of 20 ppm for detection of hydrogen fluoride gas within the atmosphere with a path length of 60 cm. Modeling of this detection process showed that three orders of magnitude improvement is achievable with shot-noise limited detection. Even greater improvement is possible if longer paths are used.

The applicability of higher order optical nonlinearities for environmental chemical sensing were investigated through establishment of ultrafast femtosecond/picosecond laser expertise and facilities at the INEEL. This research task focused on environmental sensing based upon the third-order nonlinear optical response using materials that are transparent to the pump and probe light fields. Experimental measurements were conducted to demonstrate the efficacy of the technique to produce intensity dependent refractive index gratings that provide for large improvements in signal to noise detection sensitivity over conventional techniques. Optimal wave mixing geometries for reading out the grating information and the underlying physics of the nonlinear optical mechanism were studied. Various spectroscopic implementations of this ultrafast process were investigated and applied to relevant environmental detection problems. Seven publications and three conference presentations resulted from this research program.

## Containerless Photoacoustic Spectroscopy Using Dynamic Holographic Adaptive Sensing

The first environmental sensing application under study was photoacoustic spectroscopy, one of the most sensitive spectroscopic measurement approaches available for trace gas detection. This technique typically requires enclosing the sample within a container to trap a fixed volume of atmospheric gas. The goal of this work was to determine the sensitivity and limitations for containerless photoacoustic spectroscopy, using a dynamic holographic approach. Emphasis was placed on determining the ability to measure the absorption cross-section for a known molecular species from the heat generated during the photoacoustic process along the measurement beam. The ability of this approach to detect an important industrial environmental molecular species (hydrogen floride) was tested, and the minimum detectable limits were determined. Photorefractive nonlinear optical processing was employed to perform the interferometric measurement of optical phase shifts caused by the photoacoustic heating. The photorefractive approach allowed for dynamic holographic recording in a manner that can be used to compensate for unwanted environmental influences and to provide automatic alignment for interferometry that is useable outside of the laboratory.

## Experimental Measurement Setup

This project established the capability to perform containerless photoacoustic spectroscopy using a tunable Ti:Sapphire laser over the range of 700 to 1,000 nm and detection at 532 nm using a very stable solid state continuous Nd:YAG laser. The basic setup is shown in Figure 1. The excitation laser is modulated by a chopper and sent through a cell that contains controllable amounts of trace and background gases. The Ti:Sapphire laser is tuned to an absorption line of the trace gas. The absorbed light energy is ultimately transferred to the background gas producing alternating local temperature and density modulations in and near the beam path. Acoustic waves are also launched into the surrounding gas. The local heating in the gas produces a corresponding modulation in the index of refraction of the gas. A second detection laser beam passes through the absorption region and experiences a phase shift due to the index of refraction modulation. The nonlinear optical properties of the photorefractive material, bismuth silicon oxide (BSO), establish a grating that demodulates the small photoacoustic phase shift by interaction with a suitably modulated reference beam as indicated in the figure.

## Modeling the Photoacoustic Detection Process

A theoretical model of the containerless photoacoustic process was developed to compare with the experimental results and to determine the minimum detectable trace gas concentration for gasses with varying properties. Consider a temperature modulation produced by absorption of chopped laser radiation along a beam path of length, L (see Figure 1). Neglecting thermal diffusion, the fundamental component of the average temperature modulation along the detection beam path, as measured by lock-in detection, is given by

$$\Delta \mathrm{T} = \frac{(k_{\nu 0}\eta_0 + k_{\nu 1}\eta_1) I_0}{(\rho_0 C_{p0} + \rho_1 C_{p1})\pi^2 f} \tag{1}$$

where $k_{\nu 0,1}, \eta_{0,1}, \rho_{0,1}, C_{p0,1}$ refer to the optical absorption cross section, molecular concentration, mass density, and heat capacity of the background and trace gases, respectively. The optical absorption depends on the excitation laser wavelength and provides the selectivity for a particular molecular species. The $I_0$ factor describes the excitation laser intensity and the chopping, at the frequency, $f$ allows the use of lock-in detection techniques for high noise immunity. The factor $(1/p^2)$ accounts for the measurement selecting out only the fundamental frequency component in the chopped beam. When the excitation wavelength is chosen so that the background gas absorption coefficient is negligible, the above equation illustrates that the background gas primarily dampens the photoacoustic temperature fluctuation. This is a drawback to the photoacoustic approach as most measurement problems involve a background gas at one atmosphere.

The local heating along the beam path modulates the index of refraction of the gas through a small change in density. The net optical phase shift along the beam path is given by

$$\Delta\Phi = \frac{2\pi}{\lambda}\int\left(n(x, T_a + \Delta T) - 1\right)dx \approx \frac{2\pi \Delta n L}{\lambda} \tag{2}$$

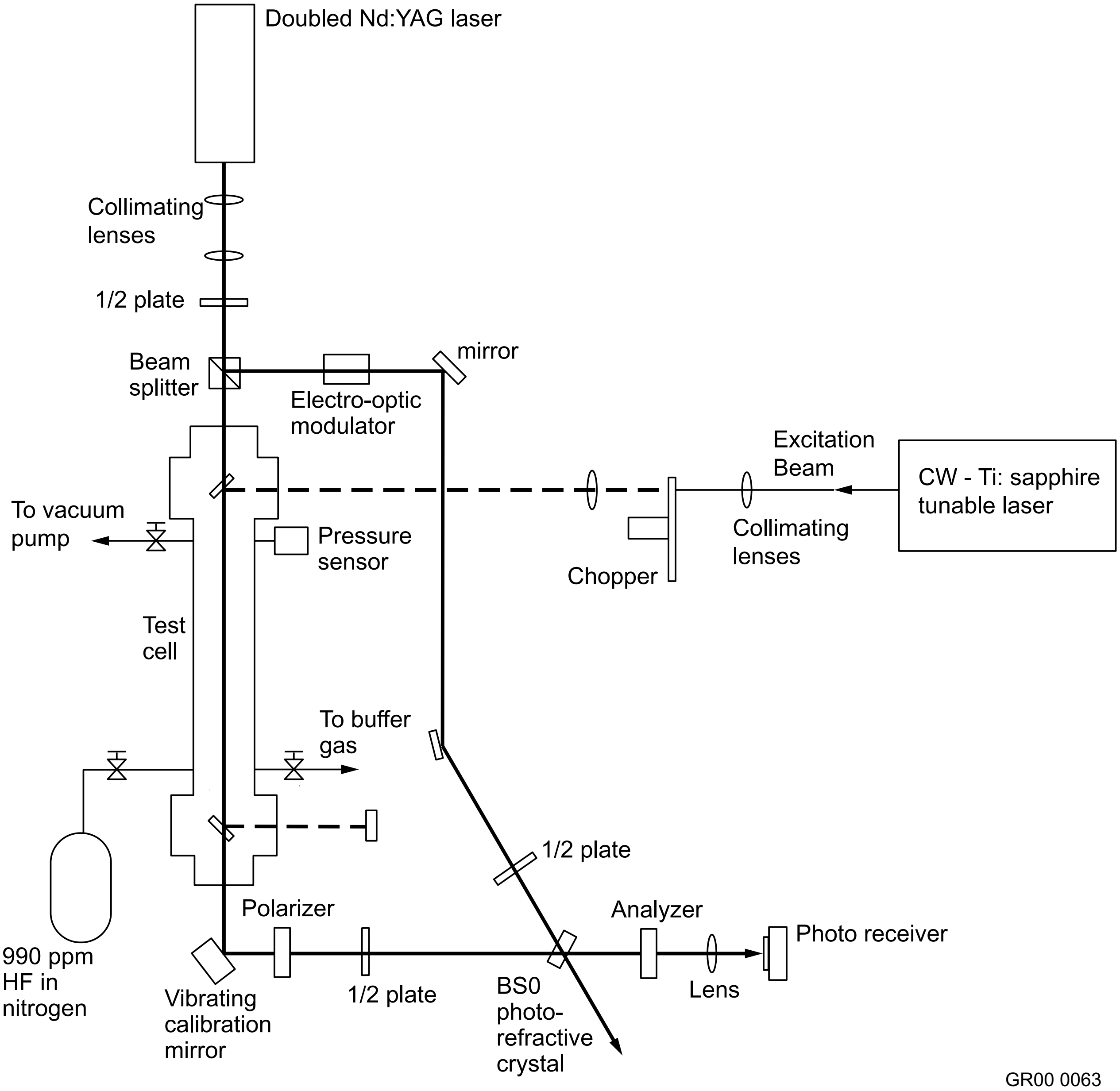

**Figure 1.** Experimental set up for *containerless* photoacoustic spectroscopy using a photorefractive nonlinear crystal.

where $L$ is the beam path length, l is the optical wavelength, $n(x,T)$ is the local temperature dependent index of refraction and $T_a$ is the ambient temperature. Optical interferometric detection techniques were used to demodulate the small photoacoustic phase shift. For a two-component gas mixture, the index of refraction is given by the Claussius-Mossotti relation,

$$\frac{n^2-1}{n^2+2}=\frac{R_{m0}\rho_0}{M_0}+\frac{R_{m1}\rho_1}{M_1} \tag{3}$$

where $R_{m0,1}(\frac{m^3}{mole})=\frac{N_A\alpha_{P0,1}}{3\varepsilon_0}$ with $N_A$ as Avogadro's number, $\alpha_{P0,1}(\frac{Cm^2}{V})$ the atomic or molecular polarizability, and $M_{0,1}$ (kg/mole) the molecular weight. The rise in temperature at constant pressure causes a change in index of refraction through

$$|\Delta n|\approx\frac{1}{2\varepsilon_0}|\alpha_{P0}\eta_0+\alpha_{P1}\eta_1|\left(\frac{\Delta T}{T_a}\right)\ . \tag{4}$$

Combining equations (1–3) produces the net photoacoustic phase shift as

$$\Delta\Phi=\left(\frac{2\pi L}{\lambda}\right)\left(\frac{I_0}{\pi^2 fT_a}\right)\left(\frac{\alpha_{P0}N_A}{2\varepsilon_0 M_0 C_{p0}}\right)\frac{\left(\eta_0+\left(\frac{\alpha_{P1}}{\alpha_{P0}}\right)\eta_1\right)}{\left(\eta_0+\left(\frac{M_1C_{p1}}{M_0C_{p0}}\right)\eta_1\right)}(k_{\upsilon1}\eta_1)\ . \tag{5}$$

The optical absorption cross-section for a given molecular transition at resonance is given by $k_v=\frac{S_{\upsilon\upsilon'}(T)}{\pi\gamma(p,T)}(cm^2/molecule)$, where $S_{\upsilon\upsilon'}(cm/molecule)$ is the line strength and $\gamma(p,T)(cm^{-1})$ is the half-linewidth. Values for these quantities were obtained from the HITRAN96 database of spectral lines and absorption cross-sections.[1]

The minimum detectable phase shift based on the shot noise limit was determined as

$$\Delta\Phi_{\min}=\sqrt{\frac{2hc\Delta f}{\lambda\eta P_o}}\ =\ \left(6.30x10^{-7}\right)\sqrt{\frac{\Delta f\,(Hz)}{\eta P_o\,(mwatts)}}\sqrt{\frac{1}{\lambda\,(nm)}} \tag{6}$$

where $hc=\left(6.626\cdot10^{-34}\,J\cdot\sec\right)\left(2.997\cdot10^{8}\,m/\sec\right)=1.986\cdot10^{-25}\,J\cdot m$. For a quantum efficiency of η=100%, detection bandwidth of $\Delta f$ = 1 *Hz*, and laser power of 5 mW, the detection "shot-noise" limit is calculated to be

$$\Delta\Phi_{\min} = \left(6.30x10^{-7}\right)\sqrt{\frac{1}{\lambda\left(nm\right)}} = 1.2\mathrm{x}10^{-8}\left(rad\,@\,532\text{ nm}\right). \tag{7}$$

The lowest concentration of a trace gas that could be detected using this spectroscopic technique can be determined from the minimum detectable phase shift and the gas parameters. If the noise levels of the current experimental setup could be reduced to the shot noise limit, hydrogen fluoride could be detected at the 1 ppb level for a 1-meter path length. By increasing the path length, the minimum detectable concentration could be further reduced.

## Trace Gas Measurement Results

In FY 1999 the photoacoustic measurements were calibrated using known amounts of water vapor in nitrogen. In FY 2000, photoacoustic measurements were performed on hydrogen fluoride\nitrogen mixtures at known absorption lines in the 800 to 900-nm range. Hydrogen fluoride was chosen since it is an industrially important gas that has relatively strong absorption lines within the tuning range of the laser. A certified mixture of 990 ppm hydrogen floride in nitrogen was obtained for the experiments from Matheson Gas Products. Hydrogen floride has seven absorption lines with intensities on the order of 1 × $10^{-21}$(cm/molecule) in the wavelength range of 870 to 890 nm. Several of the lines were investigated, but most of the data was collected for the strongest line at 11,1441.41 $\mathrm{cm}^{-1}$ which has a line intensity of 1.9 × $10^{-21}$($\mathrm{cm}^{-1}$/molecule). Measurements were made for 990 ppm hydrogen floride in nitrogen at sample gas pressures from 0 to 1,000 mbar. Figure 2 shows absorption peaks for the hydrogen floride/nitrogen mixture at several sample gas pressures. The dashed lines in the figures show Lorentzian fits of the absorption peaks. The asterisks indicate the linewidth used for the fit.

Early in the experiments, it was noticed that the signal decreased the longer the hydrogen floride was left in the test cell, and it was discovered that the hydrogen floride was reacting with the walls and windows in the test cell, depositing the gas onto the surfaces. Repetitive measurements on the same sample of gas over a period of 20 minutes revealed the rate at which the hydrogen floride was being depleted from the gas. Figure 3 shows a plot of the absorption peak area for scans of the same sample gas taken over a 20-minute period. The time constant was determined from the slope of the curve to be about 1,152 sec for a decrease to 1/e. These measurements show the sensitivity of this technique for monitoring gas adsorption onto surfaces within the ppm range.

Methods for increasing the signal-to-noise ratio were also investigated. Ideally, one would use a low chop frequency to maximize the index of refraction modulation of the trace gas and a low difference frequency between the signal and reference beams to maximize the signal produced through the photorefractive effect. However, this places both the chop and difference frequencies in the range of large ambient phase noise levels. It is possible to get a signal at difference frequencies above the crystal cutoff frequency using the photorefractive effect. However, the amplitude of the signal is reduced by 50% for the same detection beam phase shift. This reduction in signal amplitude can be off set by decreasing the chop frequency of the excitation beam. In the FY 1999 experiments, the chop frequency was around 400 Hz, and the difference frequency was around 19 Hz. During FY 2000 several sets of measurements were made on the HF/$N_2$ mixture using a chop frequency of 27 Hz and a difference frequency of 1,300 Hz. This technique increased the phase shift of the detection beam by a factor of ~8 and dropped the noise level by a little more than half. Figure 4 shows a comparison of the signal versus noise with chop frequencies of 389 Hz and 27 Hz. In each of these figures, the signal data were collected at a total gas pressure of about 1 bar. The absorption peaks shown in Figure 2 were recorded using a 27-Hz chop frequency. A signal-to-noise improvement factor of 18 was observed for these changes in measurement frequency.

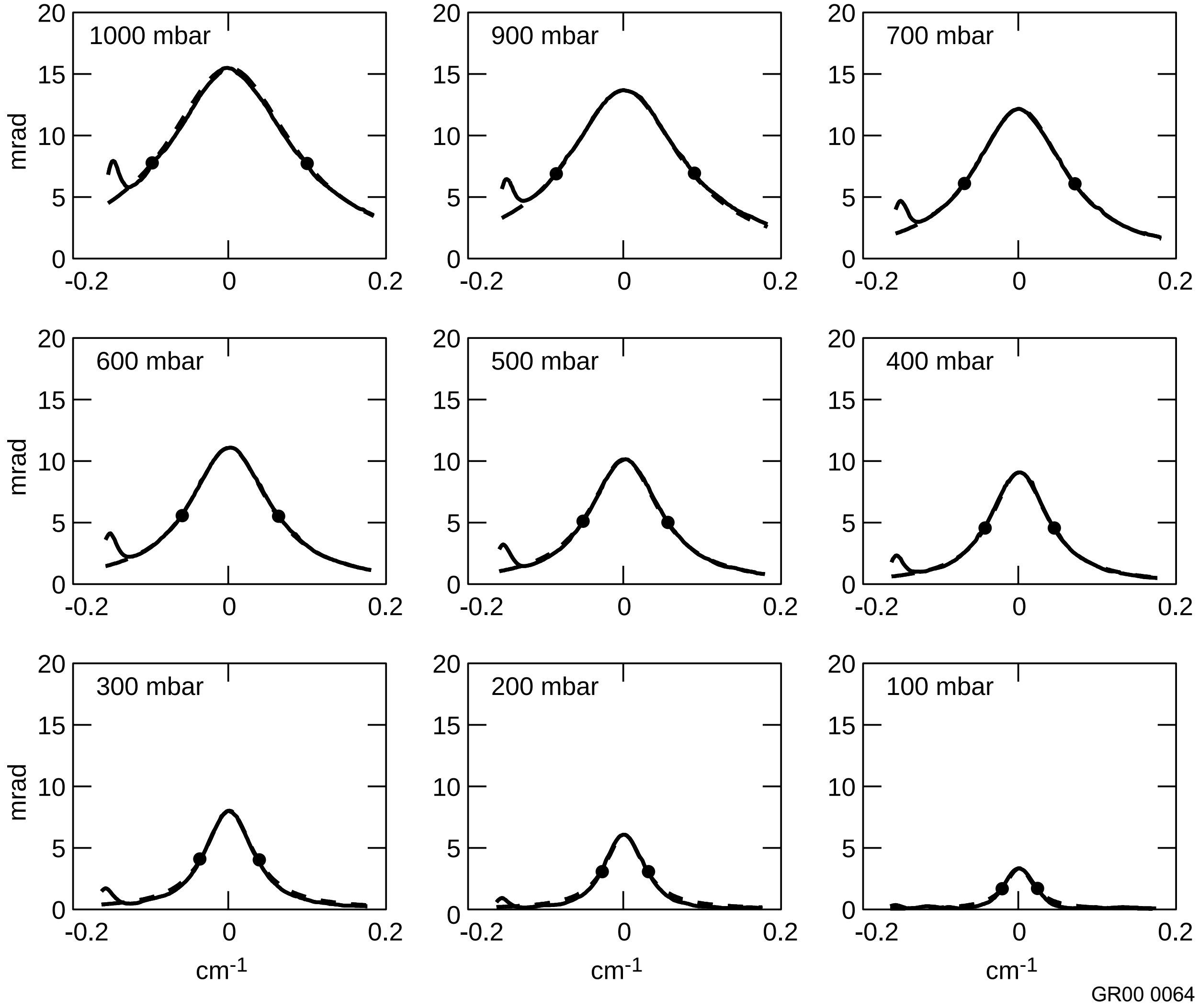

**Figure 2.** Absorption peaks for 990-ppm hydrogen fluoride in nitrogen at the gas pressure indicated. Dashed lines are Lorentzian fits of the peaks, using the optical linewidths between the two dots.

.

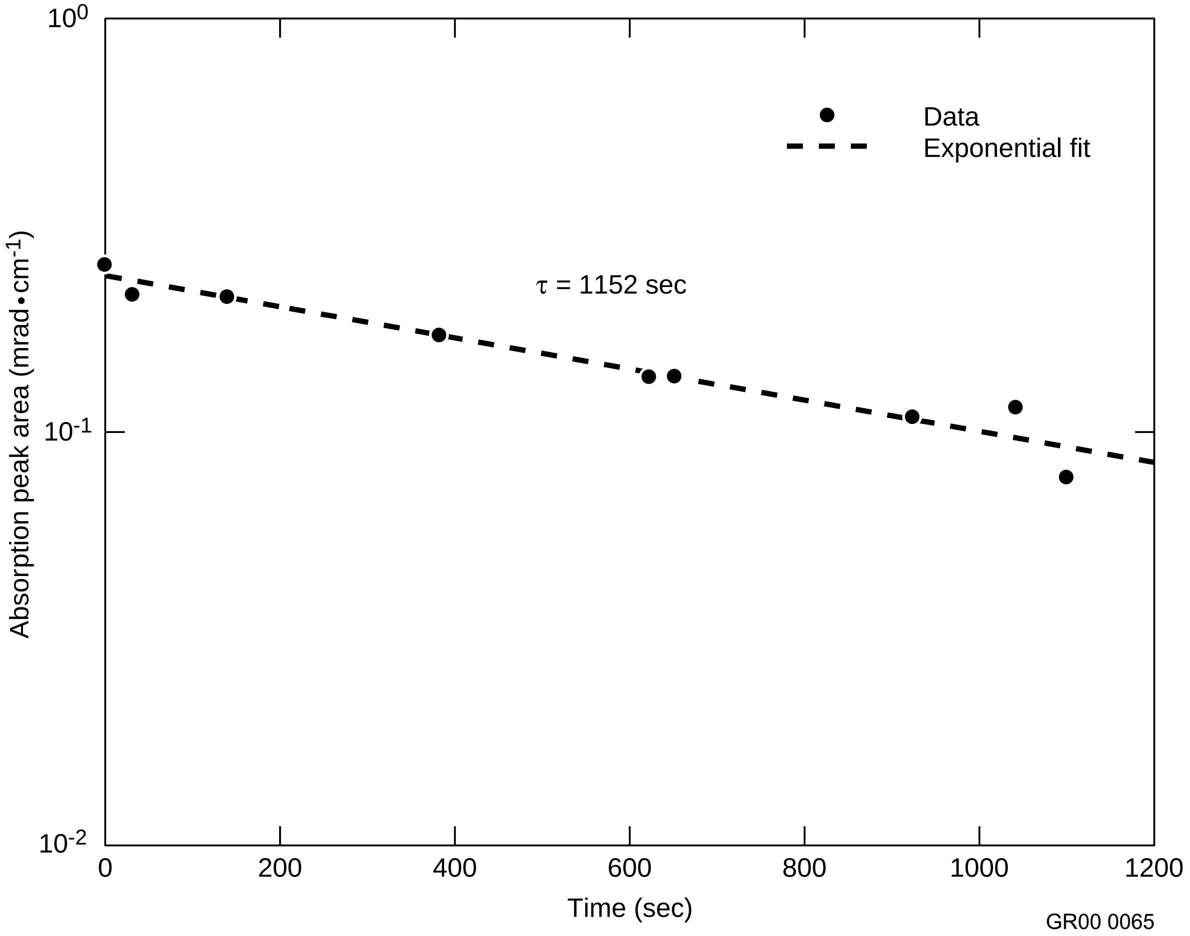

**Figure 3.** Decrease in the absorption peak area over time due to the reaction of the hydrogen fluoride with the walls and windows of the test cell.

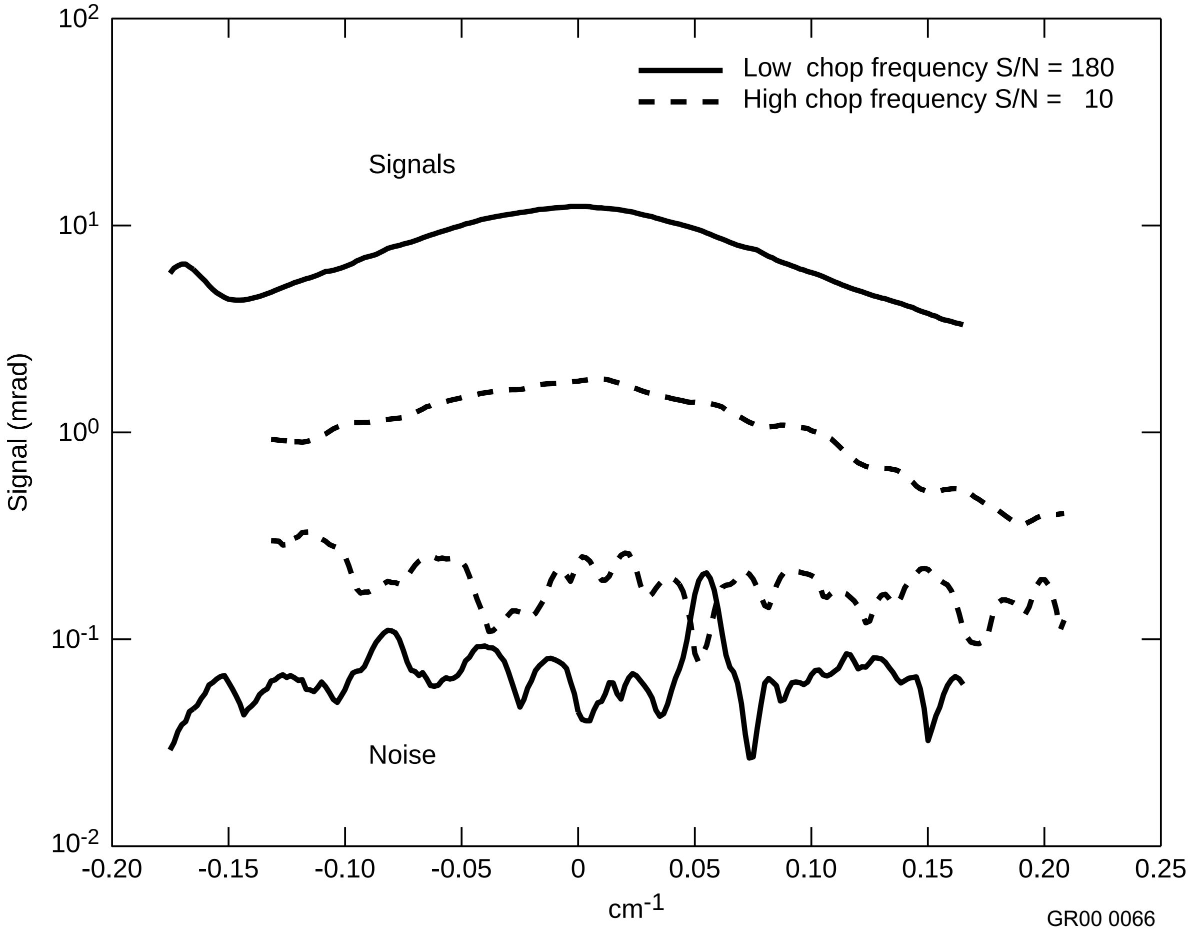

**Figure 4.** Improvement of signal and reduction of noise by increasing the difference frequency and decreasing the chop frequency (1 bar 990 ppm hydrogen floride in nitrogen).

Figure 5 shows the data versus theory for chop frequencies of 27 Hz and 389 Hz, respectively. The theory and data show very good agreement for the higher chop frequency of 389 Hz. At the lower chop frequency of 27 Hz, the signal was nearly eight times greater than the signal at the higher chop frequency, but was still only one third of that predicted by the model. The discrepancy between the theory and experimental data is attributed to thermal diffusion effects, which are not considered in the model and would have a greater impact at lower chop frequencies.

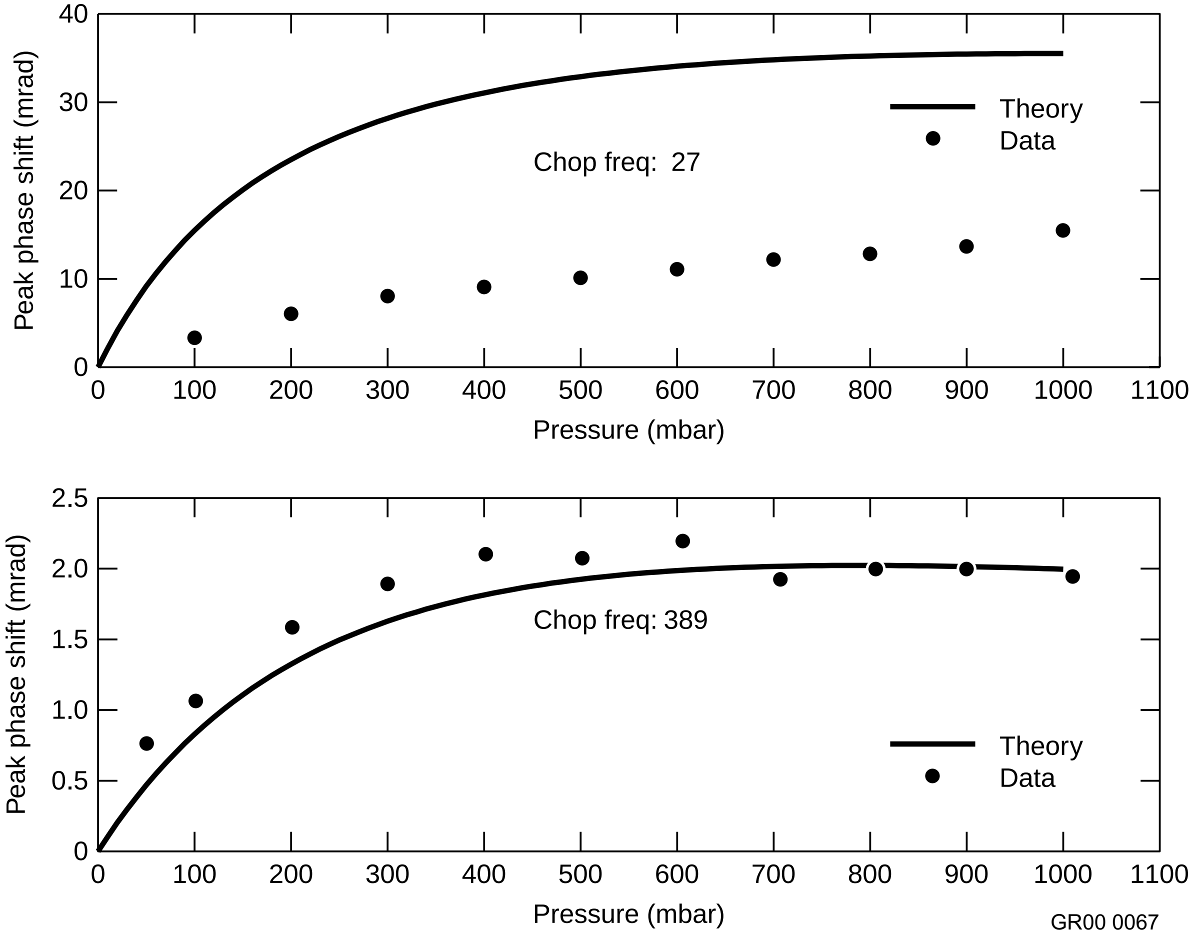

**Figure 5.** Comparison of data to the theory for 27-Hz chop frequency (top), and 389-Hz chop frequency (bottom) (990 ppm hydrogen floride in nitrogen at indicated pressure).

A mixture of 98 ppm HF/$N_2$ at 1,000 mbar total pressure was prepared and measurements were taken, using a chop frequency of 27 Hz and a difference frequency of 1,300 Hz. These measurements yielded a detection beam phase shift of ~0.4 mrad, which was still more than five times higher than the noise level. This puts the minimum detectable limit for HF with the current experimental noise level at less than 20 ppm.

An analysis of the minimum detectable trace gas concentration was performed using the photoacoustic model and the experimentally obtained noise level. The results are shown in Figure 6 as a series of phase shifts versus trace gas concentration for different line strengths. The trace gas concentration is listed in parts per million (ppm), and the model assumes the trace gas is buffered in one atmosphere of nitrogen. Data points for water vapor and HF buffered in one atmosphere of nitrogen are shown. The line strength for the particular absorption line of water measured was $4.2 \times 10^{-23}$ (cm/molecule), which lies on a line showing a minimum detectable concentration of about 1,000 ppm with the current experimental noise level. The line strength of HF was $1.9 \times 10^{-21}$(cm/molecule), which yields a minimum detectable concentration of less than 20 ppm, as noted above. The shot noise limit is also shown on the graph. Using the shot noise limit, the minimum detectable concentration of HF would be in the 1 ppb range. Even smaller concentrations can be measured by increasing the path length, increasing the excitation laser power, or using stronger absorption lines for the trace gas molecule as indicated. Generally, stronger absorption lines are observed in the infrared absorption region for wavelengths greater than 1 micron. The experimental noise level observed was determined to be due to phase noise in the lasers and from other vibrational and acoustic sources at low frequencies near the operating frequency. Improvements are possible with the use of additional photorefractive components to compensate for the noise sources. Such improvements are the subject of further study.

## Time-Domain Nonlinear Optical Techniques for Adaptive Sensing in Environmental Monitoring

Ultrafast research facilities were established at the INEEL in the past year with the addition of a new research team member experienced in ultrafast nonlinear optics and spectroscopy. An ultrashort pulsed laser system was acquired and the associated instrumentation and diagnostics established in one of our laboratories. Pulsed femtosecond/picosecond laser capability allowed unique investigations on a variety of materials. Specific optical nonlinear properties of molecular species allow the sample under investigation to become the sensing medium. A pump-probe experimental technique was employed for characterizing ultrafast dynamic events, such as ionic/charge transport and metastable chemical species in natural and artificially engineered materials.

Nonlinear optical techniques rely on properties of materials that exhibit a nonlinear dependence of the induced polarization on incident light fields. Sufficiently large incident light fields for accessing the nonlinear optical regime (though much less than typical interatomic or crystalline fields) are attainable with commercially available ultrashort pulsed lasers. Adaptive features in this approach are manifest in the ability of the sensing process to correct for environmental perturbations through either the ultrafast measurement time or the ability of the nonlinear process to provide optical holographic processing. Environmental perturbations that can be compensated for include, for example, atmospheric turbulence, sensor motion, extraneous optical radiation fields, and electronic noise that interfere with the sensing process and ultimately limit the minimum detectable parameters. Atmospheric turbulence can lead to phase front distortion of the laser beams that form an integral part of the sensing process. This phase distortion can be corrected through use of the nonlinear optical material's intensity dependence of the

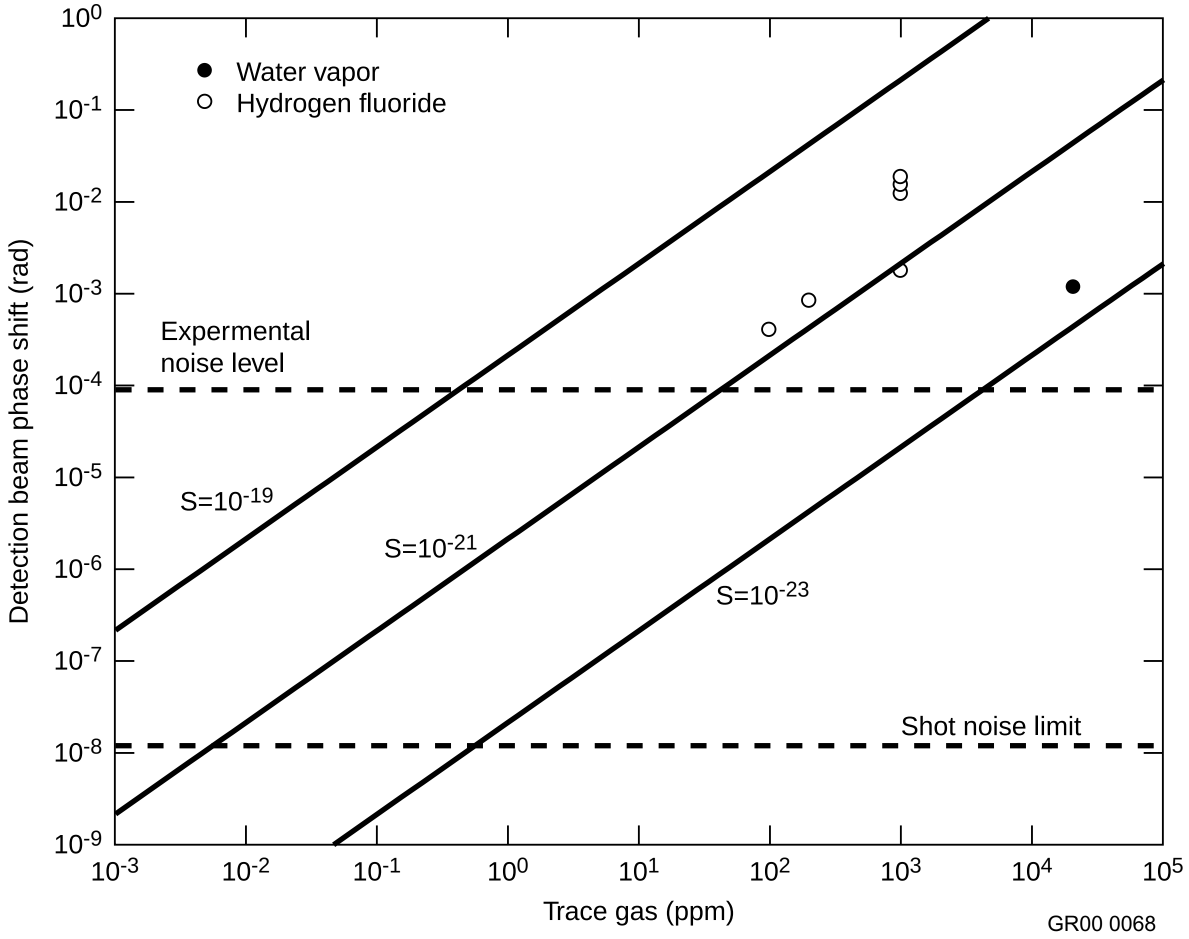

**Figure 6.** Theoretical detection limits calculated from the model for increasing absorption line strengths and experimental data of indicated trace gas buffered in 1 atmosphere of nitrogen.

index of refraction in a manner similar to the way deformable mirrors are employed to correct the phase-front distortion of starlight by the Earth's atmosphere in astronomy. If the material nonlinear optical response is derived from ultrafast (subpicosecond) processes, then the environmental sensor based upon this optical nonlinearity can process the desired information on a similar time scale,[2] within which much slower environmental perturbations are essentially constant. Furthermore, nonlinear optical techniques typically use intense, large-bandwidth, pulsed laser fields that dwarf normally weak background optical radiation fields. Therefore, adaptivity to environmental conditions is inherent in ultrashort time-domain nonlinear optical measurement techniques.

The pulsed laser system served as a resource to other ESR research projects for investigations requiring time-resolved measurements of ultrafast events or characterization of material nonlinear optical properties in condensed phases and gases. This high repetition-rate laser system benefits those measurements that require high peak power, but modest average power levels employing fast signal averaging techniques. In particular, time-resolved nonlinear optical techniques also are central to nonlinear optical material investigations being conducted through a joint effort with a number of academic institutions.

## Analysis of Benefits of the Ultrashort Time-Domain Optical Technique

The following analysis exhibits some of the reasoning behind the development of the ultrashort pulsed laser approach to spectroscopic measurements. In the weak field limit, the polarization induced by interaction between an intense optical field and a nonlinear optical material is given by

$$P = \varepsilon_0 \left( \sum_{j}^{3} \chi_{ij}^{(1)} E_j + \sum_{jk}^{3} \chi_{ijk}^{(2)} E_j E_k + \sum_{jkl}^{3} \chi_{ijkl}^{(3)} E_j E_k E_l + \dots\dots\dots \right) \tag{8}$$

where $X^{(n)}$ is the material susceptibility, the superscript indicates the order of the nonlinearity in the optical field, $E$, and $\varepsilon_0$ is the vacuum electric permittivity. In general, the susceptibility is a tensor, and, therefore, the polarization $P$ does not point in the same direction as $E$. The susceptibility is also, in general, a complex quantity of which the real part is associated with the index of refraction and the imaginary part contains information on the material absorption.

The first order interaction, $\chi_{ij}^{(1)}$, is commonly used in linear optical absorption and refraction measurements. Second-harmonic generation (SHG), sum-frequency generation (SFG), and the linear Pockels effect are examples of second-order nonlinear $\chi_{ijk}^{(2)}$ processes. An example of the Pockels effect is the field-dependent index of refraction in photorefractive materials that results from a space-charge field generated by optical excitation and subsequent diffusion and trapping of charge carriers. This second order effect was the basis for the photorefractive dynamic holography frequency-domain approach described earlier. In reference to SHG and SFG, the mixing process can produce an output optical product that is present only when this molecular species selective nonlinear process is present; that is, a *background free* measurement of a particular molecular species is produced. Due to inversion symmetry and the fact that the induced polarization changes sign upon a reversal of the electric field $E$, isotropic media and crystals belonging to centrosymmetric space groups are not $\chi_{ijk}^{(2)}$-active. Many molecular liquids and gases fall under this category, and their nonlinear optical response is of the $\chi_{ijkl}^{(3)}$ origin. However, many semiconductor materials such as ZnSe, CdTe, and GaAs, to name a few, and polymers exhibit photorefractivity and the third-order optical nonlinearity simultaneously. Environmentally relevant molecules adsorbed on surfaces of certain bulk materials can be spectroscopically analyzed because the presence of the surface breaks the symmetry resulting in net second order interaction activity. This fact allows use of frequency conversion techniques (SFG, SHG) that are sensitive only to the surface adsorbates, or certain interfaces, and not to the bulk, due to symmetry considerations. SHG and SFG methods employing ultrashort pulsed lasers provide environmental scientists with a new tool with which to probe interfacial dynamics (air/water, soil/water, etc.).[3] Selective probing of interfacial properties without interference from bulk species offers significant advantage over traditional spectroscopic techniques (absorption, fluorescence, Raman scattering) that cannot distinguish optical signals originating in the bulk from interfacial molecular species. The latter is especially true if the molecular species of interest are present in the bulk. The conversion efficiency for SHG and SFG scales as the square of the peak input power, implying that the use of high intensity lasers can greatly improve the measurement process signal-to-noise ratio over conventional techniques.

The dynamic holographic research and development effort on this adaptive sensors program relied on the electro-optic or $\chi_{ijk}^{(2)}$ process of semiconductor and polymeric materials. Much of this work was associated with using photorefractive materials to image environmental information contained in the phase and amplitude characteristics of the sensing optical fields. Imaging was achieved through the refractive index grating that is created when two continuous wave (CW) optical fields overlap inside the photorefractive material. The induced refractive grating can be described by[4]

$$n = n_0 + \frac{n_1}{2}\left[ e^{i\varphi}\left( \frac{E_1 E_2}{I_0} \right) \exp(-i\mathbf{K}\cdot\mathbf{r}) + c.c. \right] \tag{9}$$

where $n_0$ is the uniform index of refraction, $n_1$ is the amplitude of the index of refraction grating induced through the photorefractive effect, $I_0$ is the sum of the two optical field intensities, $\varphi$ is the spatial phase shift of the index grating with respect to the intensity grating resulting from interference of the two optical beams, and $\mathbf{K}$ is the grating wave vector. Equation (8) indicates that the index modulation is dependent on the contrast of the interference fringes, or the ratio of beam intensities. In the photorefractive process, an energy transfer from one beam to the other beam occurs only if the phase shift is nonzero. A nonzero phase shift characterizes a nonlocal response. On the other hand, Raman scattering, two-photon absorption (TPA), third-harmonic generation (THG), and the optical Kerr effect (OKE) are examples of the third-order nonlinear processes mediated by $\chi^{(3)}_{ijkl}$. Many specific optical nonlinearities of the targeted species are manifest only at high intensities and become available to be used for detection when ultrashort pulsed lasers are employed. This feature can lead to high selectivity in the optical spectroscopic process. In general, third-order nonlinear optical, or Kerr, media are characterized by a local response in which the index grating is in phase with the intensity grating. The induced index grating when two beams overlap in a Kerr medium is[4]

$$n = n_0 + n'_1 I_0 [1 + \cos(\mathbf{K}\cdot\mathbf{r})] \tag{10}$$

where $I_0$ is the sum of the square of the field amplitudes of each beam (here, the amplitudes are taken to be equal). Note that the amplitude of the induced index of refraction grating, $n'_1 I_0$, is directly proportional to the beam intensities (allowing the use of high intensity lasers to enhance the measurement signal-to-noise ratio) and is not phase-shifted from the resultant optical interference, given by the second term in Equation (9). The third-order response, in general, can be regarded as being local, and, in principle, cannot lead to energy transfer in two-beam coupling (although this is possible in four-wave mixing). As mentioned above, third-order nonlinear optical materials constitute a large class of materials often found in environmental sensing problems. In addition, since the process is local, third-order nonlinear optical responses are usually very fast, on the same time scale as that of the optical pulses (femtoseconds). Beam coupling efficiency can be enhanced by high peak powers that are routinely achievable with commercial ultrafast lasers, while keeping the average power to levels that do not lead to deleterious thermal effects on the material.

### The Pump-Probe Measurement Process

A pump-probe configuration was employed for the nonlinear optical experimental measurements. In a typical experiment, an intense, polarized optical pump pulse interacted with a nonlinear optical medium. Depending on the specific nature of the experiment, this interaction lead to excitation processes, such as electronic excitation and/or Raman scattering. The resultant material optical response manifested itself as an induced material polarization that radiates an optical field. This induced polarization was interrogated by a much weaker, polarized probe pulse. Variably delaying the probe pulse, with respect to the pump pulse, mapped out the temporal evolution of the induced polarization. This approach enabled complete characterization of the temporal nature of the response, without having to rely on the time resolution of the detector (the resolution here is limited only by the duration of the optical pulse), and the magnitude of the nonlinear optical coupling strength. Furthermore, the determination of each tensor component of $\chi^{(3)}_{ijkl}$, and its real and imaginary parts, was obtained. The pump and the probe beams function, respectively, as the reference and object beams when performing holographic recording and imaging. In this case, the two beams are made to overlap in space and time inside the nonlinear medium, and the resulting hologram is recorded by detecting the diffracted beam with a photodetector or CCD camera. A third beam also can be used and scattered from the induced grating, as in the transient grating or optical phase conjugation geometry. In the two-beam coupling geometry, the energy loss in the probe beam is given by $\mathrm{Im}\left[\mathbf{E}_2^* \cdot \mathbf{P}^{(3)}\right]$[5] (where $\mathbf{E_2}$ is the probe field vector and $\mathbf{P}^{(3)}$ is the induced polarization) at each point in the third-order nonlinear optical medium. Suppose that both pump and probe are polarized in, say, the x direction, and the response is given by

$$\chi^{(3)}_{effective} = \chi'_{xxxx} + i\chi''_{xxxx} \, . \tag{11}$$

The real part is proportional to the index of refraction that contributes to the phase grating and the imaginary part characterizes the nonlinear absorption that contributes to the amplitude grating. The change in the probe energy can be written as

$$\begin{aligned} \mathrm{Im}\left[\mathbf{E}_2 \cdot \mathbf{P}^{(3)}\right] = \mathrm{Im}\Big\{ & \int_{-\infty}^{\infty} E_2^*(t)E_1(t)\int_{-\infty}^{\infty} E_1^*(t')E_2(t') \times \left[\chi'_{xxxx}(t-t') + i\chi''_{xxxx}(t-t')\right]dt'dt \\ & + \int_{-\infty}^{\infty} E_2^*(t)E_2(t)\int_{-\infty}^{\infty} E_1^*(t')E_1(t') \times \left[\chi'_{xxxx}(t-t') + i\chi''_{xxxx}(t-t')\right]dt'dt \Big\} \, . \end{aligned} \tag{12}$$

Since the pump and probe pulses are derived from the same optical source with the probe being delayed with respect to the pump, their electric field amplitudes can be written as $E_1 = E(t)$ and $E_2(t) = E(t-\tau)e^{i\omega\tau}$. Then Equation (11) can be separated into three components:

$$\gamma(t) = \int_{-\infty}^{\infty} \left|E(t-\tau)\right|^2 \left|E(t')\right|^2 \chi''_{xxxx}(t-t')dt'dt \tag{12a}$$

$$\beta'(t) = \mathrm{Im}\left\{ \int_{-\infty}^{\infty}\int_{-\infty}^{\infty} E^*(t-\tau)E(t)E^*(t')E(t'-\tau)\chi'_{xxxx}(t-t')dt'dt \right\} \tag{12b}$$

and

$$\beta''(t) = \mathrm{Re}\left\{ \int_{-\infty}^{\infty}\int_{-\infty}^{\infty} E^*(t-\tau)E(t)E^*(t')E(t'-\tau)\chi''_{xxxx}(t-t')dt'dt \right\} . \tag{12c}$$

Equation (12a) is an incoherent term that is a convolution of the intensity autocorrelation function with the material response function. This contribution persists as long as the response function does. Equations (12b) and (12c), on the other hand, are coherent contributions to the diffracted beam that are nonzero only when the two beams are temporally and spatially overlapped inside the nonlinear medium so as to form a spatially modulated index grating. In the experiment, the contributions stemming from (12b) and (12c) can be distinguished from that of (12a) by modulating both pump and probe beams at certain frequencies and detecting the diffracted beam at the difference frequency. This analysis shows the various contributions to signal: two coherent contributions that are the focus when performing diffraction experiments and the other contribution that is relevant when characterizing the response in terms of its temporal nature using a two beam setup.

## Pump-Probe Experimental Results

A schematic of a pump-pump probe experimental configuration is given in Figure 7. Although this configuration is particularly suitable for two-beam diffraction and pump-probe OKE experiments, with slight modifications this setup can accommodate time-resolved transient grating and optical phase conjugation experimental configurations. Figure 8 illustrates a pulse sequence that was employed in diffraction experiments to read out the volume hologram recorded by a third-order nonlinear optical medium.

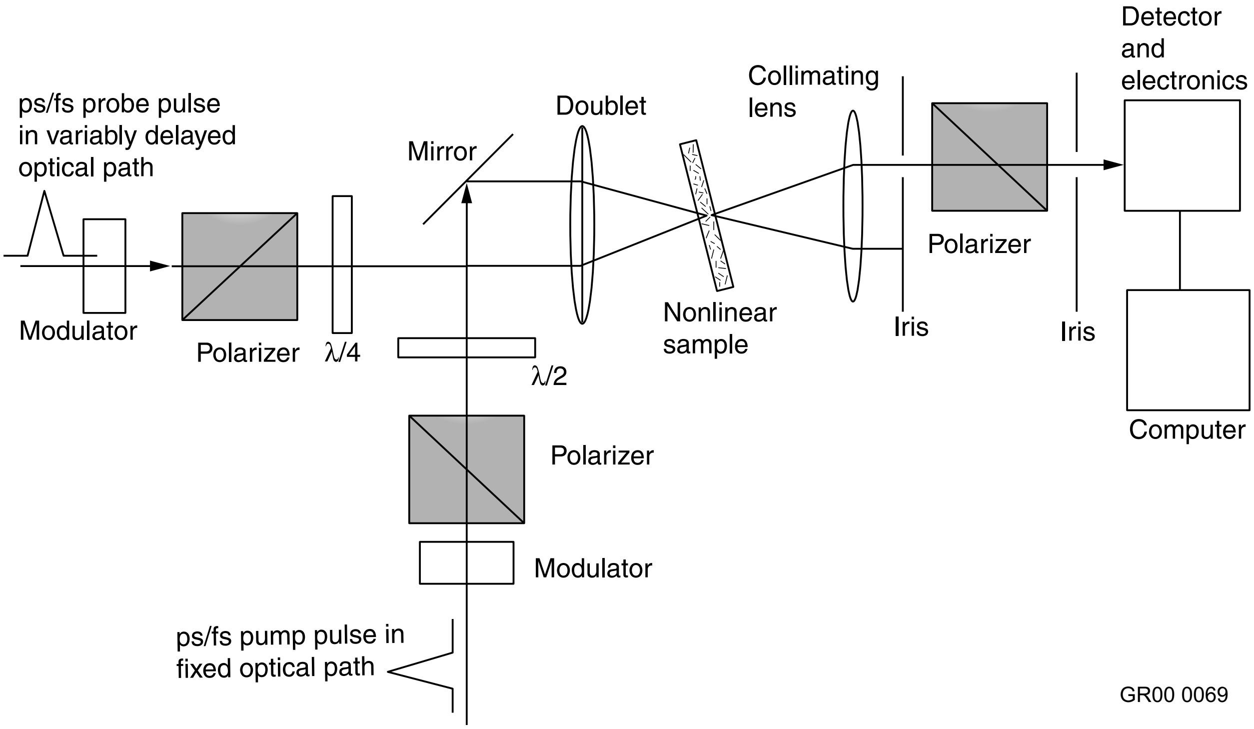

**Figure 7.** Schematic of the time-domain ultrashort pulse pump-probe experimental configuration.

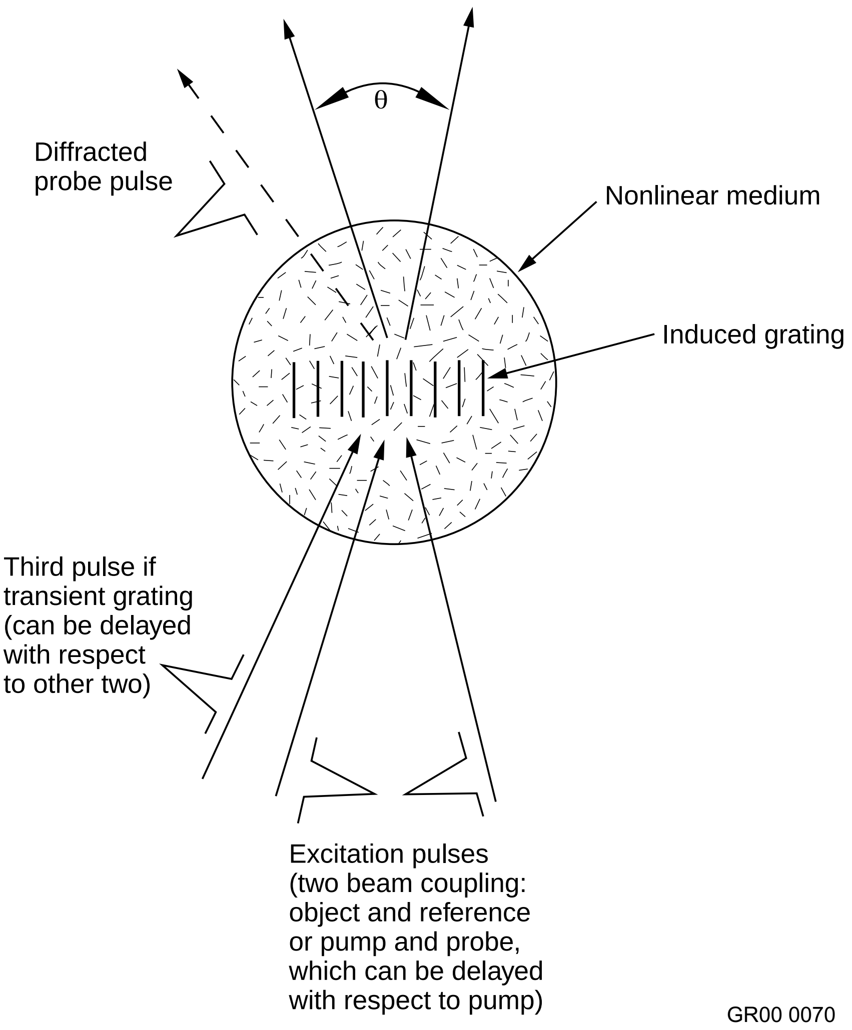

**Figure 8.** Pulse sequence in two and three beam diffraction experiments.

Initial experiments employed environmentally relevant molecular liquids, such as $CCl_4$, and explored ultrafast nonlinear optical techniques most suitable for sensitive chemical detection and analysis. Figure 9 shows the nonlinear optical response measurements of neat $CCl_4$. The experimental configuration used to measure this response is similar to the one depicted in Figure 7. The response has its physical origins in the birefringence induced by the pump pulse and its decay in the intermolecular and intramolecular vibrational motions and molecular reorientation. In the out-of-phase optical heterodyne detection configuration, the measured signal is linear in the real part of the third-order nonlinear optical response.[6] The nonlinear optical response waveforms in Figure 9 were obtained by varying the intensity of the 90-degree out-of-phase local oscillator in the heterodyne detection configuration. The measured waveforms show that the signal improves as the local oscillator intensity is increased. The noise floor in each measurement was on the order of a few microvolts and was uniform throughout the measurements.

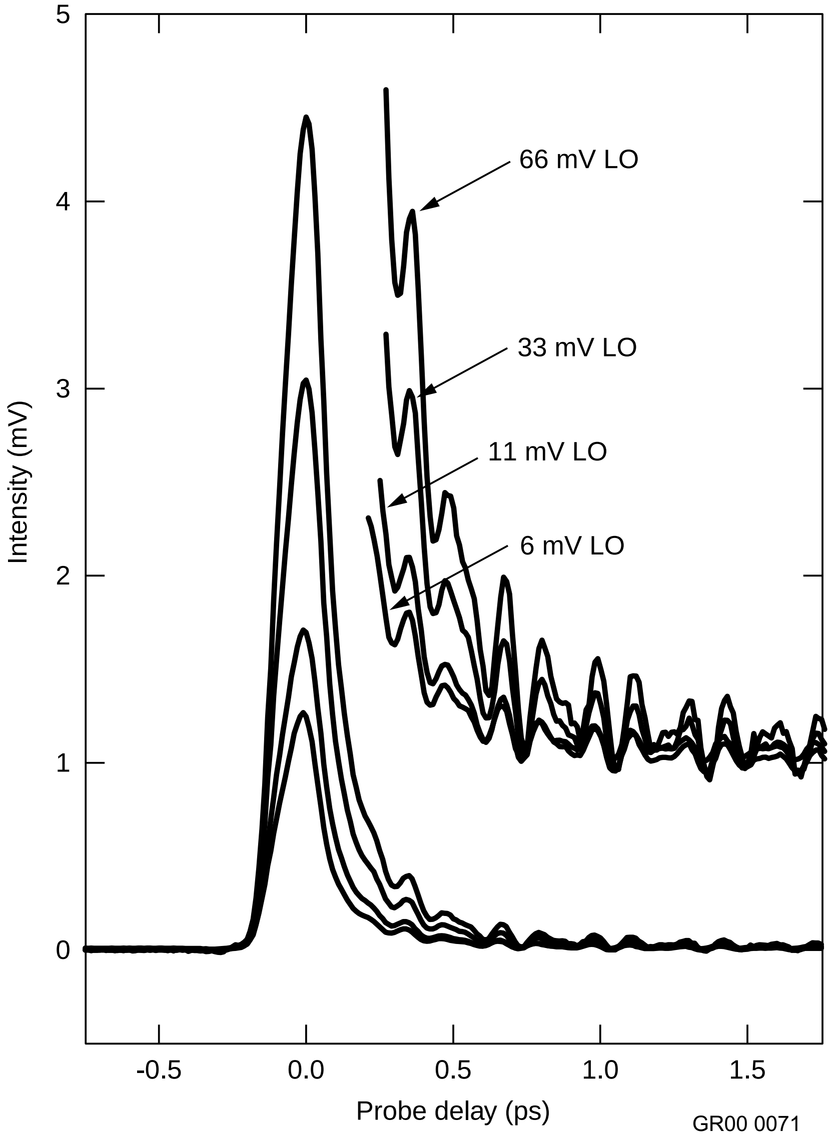

**Figure 9.** Third-order nonlinear optical response of $CCl_4$ as a function of local oscillator intensity measured with 100-fs optical pulses.

Figure 10 is the Fourier transform of one of waveforms in Figure 9 and shows the nonlinear optical frequency response function. The low-frequency broad peak is associated with intermolecular scattering intensity while the peaks at 218 and 314 $cm^{-1}$ are assigned, respectively, to $n_2$ and $n_4$ depolarized intramolecular Raman-active vibrations. The underdamped oscillations at delay times greater than ~0.25 picosecond in Figure 9 correspond to these two peaks in Figure 10. These intramolecular vibrational transitions can be used as the chemical signatures in spectroscopic analysis and detection of chemicals using this time-domain approach. Note that all of this is accomplished using a single femtosecond laser pulse. All depolarized Raman-active transitions that lie within the coherence bandwidth of the pump pulse are excited. The full-width-half-maximum bandwidth used in these measurements is ~200 $cm^{-1}$.

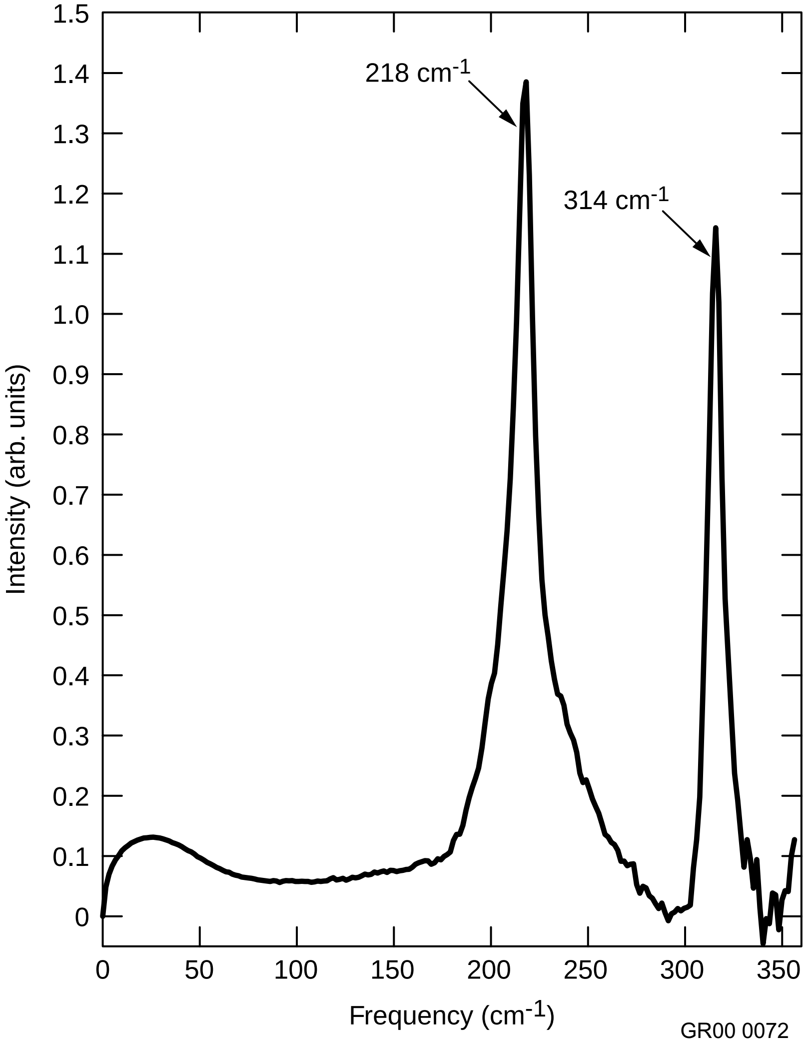

**Figure 10.** Measured Raman active vibrational frequency response of $CCl_4$.

The heterodyne signal is proportional to the squared modulus of the input laser beam intensity. If all experimental parameters except for the pulse energy are kept the same, then the heterodyned signal is proportional to the pulse energy of the input beam. The current measurements of heterodyned signal intensity scale proportionately by the same ratio of increment or reduction in the laser pulse energy with respect to the pulse energy (~nanojoules) employed in the above measurements. Since the nonlinear optical response is proportional to the molecular number density in the confocal region, the heterodyned signal is expected to decrease as the number density becomes smaller, for example, upon dilution or in gas phase. Current ultrashort pulsed laser technology is scalable not only for solid-state lasers but also for compact modelocked fiber lasers. Assuming the same level of background noise, if the current pulse energy was scaled up to the microjoule level, the current signal-to-noise ratio could be retained even if the number density was reduced by a factor of $10^6$. A much higher signal level is possible with the millijoule-level amplified femtosecond laser systems. The high pulse energy systems are especially suitable for detection and analysis in the dilute gas phase because of the less likelihood of interference from continuum generation and other nonlinear optical processes.

### INEEL Ultrafast Nonlinear Optical Characterization Facility

An experimental capability to completely characterize the material nonlinear optical properties (including the magnitude and temporal behavior of the nonlinear optical response) is central to the use and development of materials for potential holographic environmental sensing and imaging applications. Facilities are needed to perform nonlinear optical techniques that employ four-wave mixing, (optical heterodyne detected optical Kerr effect spectroscopy, optical phase conjugation, transient grating), two-beam coupling (using the material's third-order nonlinear response), the Z-scan beam distortion method, transient reflectance spectroscopy, and transient Raman spectroscopy. The previously described laser system operating at 76 MHz PRF with ~6 nJ of pulse energy and tunable from ~700 to 980 nm can be used in the research on many of the targeted nonlinear optical materials for use as environmental adaptive sensors. In order to cover all of the targeted materials, which not only include semiconductor materials but also molecular liquids and artificially engineered polymers that may be of use for environmental applications, a much larger tunable wavelength range of 200 to 4,000 nm and higher pulse energies (~μJ) are needed. The larger tunable range will make adaptive time-resolved techniques applied to trace gas detection versatile, and permit work on trace detection of many environmentally relevant molecules. Larger pulse energies are needed for laser excitation in the gaseous medium where molecular number densities are always orders of magnitude smaller than in the condensed phase and where sensitivities on the order of parts per billion or less are desired. In order to satisfy these requirements, future expansion is planned to establish a system that amplifies the laser pulse energy to the μJ level, produces a wide range of wavelengths by way of white light continuum generation or parametric amplification, and permits a variable pulse repetition frequency. The expansion will give the INEEL state of the art capabilities for a wide variety of fundamental and applied research on environmentally relevant problems.

| Future Facility Expansion | Vendor and Model Part No. |
|---|---|
| Ti:Sapphire regenerative amplifier, μJ energy pulses, rep. rate to 300 kHz | Coherent RegA 9000 |
| 10-watt all-solid-state pump laser for Ti:Sapphire regenerative amplifier | Coherent Verdi-V10 |
| BBO optical parametric amplifier tuning capability from ~0.250–3.5 mm | Coherent OPA 9800 |

## ACCOMPLISHMENTS

This project successfully performed the first proof-of-principle experimental *containerless* photoacoustic measurements using dynamic photorefractive holographic detection. Measurements were taken along laser beams less than one meter long and confirmed that the results were as expected from theoretical predictions. The minimum detectable trace gas concentration was determined based on the absorption line cross-section employed and the detection noise level. Methods and materials were identified to implement this spectroscopic method with the potential for ppb detectability at the shot noise level. Model calculations agree well with the experimental measurements and have yielded a minimum detectable concentration of about 20 ppm of hydrogen fluoride in one atmosphere of $N_2$ at room temperature using a single beam pass of about 60 cm. Several factors have been identified and quantified to improve this detectability, including improving the phase noise immunity of the photorefractive interferometric process, reducing laser and environmental phase noise, using faster and more sensitive photorefractive materials, using higher laser powers, and employing stronger absorption lines in the infrared region of the spectrum. Suitable scaling of these parameters allows extension of this technique to wide area spectroscopic imaging of trace gas concentrations in future work. These results are to be presented at the Photonics East conference, Advanced Environmental and Chemical Sensing Technology (ES09) session, November 5–8, 2000, Boston, Massachusetts, and subsequently published. A complete experimental and theoretical analysis has been made of the anisotropic diffraction properties of an important candidate photorefractive material, GaAs. These results have been shown to agree with predictions for the static two-wave mixing case and to produce a differential signal for dynamic phase modulation even when no two-wave mixing gain is present.[7] This is a new resultant property of anisotropic diffraction and the subject of a journal publication.[8] Imaging of phase modulations has been accomplished with GaAs beginning the process of extending the photoacoustic measurements to an imaging mode.

A new researcher experienced in ultrafast laser techniques has joined this project and established an ultrafast laser facility at the INEEL. The system includes an ultrafast femtosecond/picosecond laser system and appropriate instrumentation and diagnostics. A new task was begun on the use of ultrafast optical techniques for developing new environmental monitoring technology through highly selective optical nonlinearities that exist in selected molecular species. Two conference presentations were given based on the ultrafast measurement results and two manuscripts were submitted for publication in peer-reviewed journals.[8] An electrical engineering undergraduate student, Marshall Tolman, from the University of Wyoming worked on LabView software development for nontrivial time- and frequency-domain data analysis for femtosecond nonlinear optical experiments. He presented the work in a poster entitled *Pump-Probe Femtosecond Nonlinear Optical Spectroscopy of Molecular Liquids* on July 27, 2000 at the INEEL Research Center

## REFERENCES

1. HITRAN 1996, CD-ROM available from ONTAR Corp. North Andover, MA 01845-2000.

2. N. Thantu, J. S. Melinger, D. McMorrow, and B. L. Justus, “Ultrafast nonlinear optical response of CuCl nanocrystallite-doped glass in the transparent region,” *Nonlinear Optics: Principles, Materials, Phenomena and Devices*, 23, (1999).

3. K. B. Eisenthal, “Liquid interfaces probed by second-harmonic and sum-frequency spectroscopy,” *Chem. Rev.*, 96, 1343 (1996).

4. P. Yeh, “Two-wave mixing in nonlinear media,” *IEEE J. Quant. Electronics*, 25, 484 (1989).

5. S. L. Palfrey ad T. F. Heinz, “Coherent interactions in pump-probe absorption measurements: the effect of phase gratings,” *J. Opt. Soc. Am.*, B 2, 674 (1985).

6. W. T. Lotshaw, D. McMorrow, N. Thantu, J. S. Melinger and R. Kitchenham, “Intermolecular vibrational coherence in molecular liquids,” *J. Raman Spectrosc*. 26, 571 (1995).

7. K. L. Telschow, R. S. Schley, N. Thantu, V. A. Deason, and S. M. Watson, “Adaptive Sensing,” in *Environmental Systems Research, FY-99 Annual Report*, INEEL/EXT-99-01008, 273-292, January 2000.

8 See the section on Publications and Presentations in this report.

# Integrated Instruments for In Situ Chemical Measurements

**Peter M. Castle, William F. Bauer, John (Jack) Slater, Mark L. Stone**

## SUMMARY

One objective of this collection of research activities is to advance the state of environmental chemical analysis. The Integrated Instruments for In Situ Chemical Measurements tasks are carrying out research to address EM's field chemical analysis and long-term monitoring needs. In spite of many advances in chemical analysis instrumentation, there continue to be needs associated with characterization of remediation sites as well as long-term chemical monitoring at waste disposal facilities or after closure of sites. This task is directed at several of the important issues associated with environmental characterization and monitoring, such as measurement sensitivity, selectivity, sampling, and portability. The project was comprised of three tasks in FY 2000: enhancing ion mobility spectrometry (IMS), further investigations of separation membranes integrated with surface acoustic wave (SAW) devices, and the demonstration of a micromirror array spectrometer. The ion mobility spectrometry task had three subtasks: investigation of a new detector concept, using membrane sample introduction to enhance selectivity, and demonstration of laser photoionization as a more selective and portable ion source. This is the final year of support for the project.

## PROJECT DESCRIPTION

## Task 1. Enhancing Ion Mobility Spectrometry

### Subtask 1. Detection of Low-Energy Ions for Ion-Mobility Spectrometry (J. Slater)

***Background.*** The primary objective of this subtask, now completing the second year effort, is to enhance sensitivity for detecting analyte ions in an IMS system. The standard method for such ion detection is a charge collecting Faraday cup, which has no amplification capabilities, and therefore is limited to the detection of roughly $10^2$ or $10^3$ particles at a time with typical electronic noise levels. The purpose of this task is to explore a new technique for ion amplification that can operate at atmospheric pressure, unlike other high-gain detectors such as Channeltron electron multipliers. Success in this research would lead to instrumentation with substantially improved detection limits for environmental contaminants.

The concept being examined is based on the combination of two ideas. The first is to use an auger electron ejection mechanism at a metal surface to produce a free electron after impact by a positive ion, which is essentially the mechanism by which current is maintained at the cathode of a glow discharge. The probability that an ion ejects an electron from the cathode is called the Second Townsend coefficient, $\gamma_i$. The second idea is to use charge amplification at atmospheric pressure via electron avalanche in a high electric field (E-field) region between two electrodes. This is similar to detection strategies already used in high-energy physics when energetic particles generate free electrons in a gas. The free charge thus generated is detected as an electric current, with gains of $10^4$ common when operated in a linear mode and higher gains in saturated mode. The avalanche is a result of electrons gaining kinetic energy via the E-field, with subsequent ionization of other particles.

The primary challenge in this research is to generate the free electron starting from the ion we wish to detect. The ion does not cause further ionization and charge multiplication in an electric field because its momentum is lost during each collision with the background gas. By comparison, a free electron gains energy freely from an applied E-field until it makes an inelastic collision. However, when a positive ion strikes a metal surface, enough energy to remove an electron from the metal to the vacuum state is supplied by the energy of recombination. This is called Potential Electron Emission[1] and it involves an auger process in which an electron from the metal neutralizes the ion to an excited state, and this state decays via ejection of another electron from the metal to the vacuum level. Such electron emission is present as an unwanted effect in Geiger-Muller counters as a cause of secondary pulses.[2]

Potential electron ejection depends on the work function (W) of the metal, and the ionization potential (IP) of the impacting ion. Electron ejection is energetically possible only when $IP > 2W$. This condition is frequently satisfied, as work functions are often roughly 5 volts and the ionization potentials are often greater than 10 volts. If this condition is satisfied, the probability of releasing an electron from clean metal surfaces can be as large as 20%. For example, slow argon ions on aluminum have a 12% yield. Thus, if the yield were 10%, there is the potential to detect roughly one of every 1 of 10 ions, assuming every liberated electron is detectable electronically following the charge avalanche. If Faraday cup detection requires $10^3$ electrons, then this example would constitute a factor of 100 improvement. For negative ions, it may be possible to accelerate a negative ion to a point where the electron is detached, after which that electron can generate an avalanche. The negative ion presents a problem in that the electron, if liberated at all, may impact the anode before appreciable multiplication occurs.

Last year a conceptual design had been developed for an arrayed detector and critical laboratory tests were initiated. The initial tests apparently showed that an avalanche can be triggered by near-thermal ions. At that time, the path forward included optimization of the anode-cathode geometry, pressure scaling experiments, and addressing various manufacturability issues for a detector array. This year, reexamination of those results and much additional work indicates we cannot consistently demonstrate detection of low energy ions. In brief, this means that the experiments have not been successful and that the anticipated mechanism does not at present appear to be a viable approach to efficient detection of low energy ions.

***Discussion.*** As mentioned in the Background section, the initial premise for this work was that electron ejection on the cathode surface, followed by electron avalanche detection, could provide an improved detector for IMS applications by perhaps a factor of 100. However, examination during this project has shown that two factors undermine the premise.

The first problem is dissociative recombination. Consider at first an atomic argon ion. The desired Auger recombination proceeds in multistep fashion by drawing an electron from the surface, forming an excited neutral atom, and then ejecting another electron to the vacuum level upon relaxation of the excited atom, i.e.,

$Ar^+ + \text{surface} \rightarrow Ar^* + \text{surface} \rightarrow Ar + \text{surface} + e$

where $e$ is the free electron. Now in the case of a generic diatomic molecular ion, $M_2^+$, a competing process is

$M_2^+ + \text{surface} \rightarrow M^* + M + \text{surface}$

where an electron has been donated by the surface and the energy of recombination is shared between an excited state and kinetic energy of the neutral atoms. No electron is ejected in this case. The preference for dissociation over electron ejection can be very large for some molecules, and may generally be large for organics. For example, the compilation of Little[3] shows that for $CH_4^+$, $CH_3OH^+$, and $C_2H_5OH^+$, Dissociation is favored over electron ejection *by about 8 orders of magnitude*. Note that these three gasses are extreme examples of low electron emission, since they have been used in Geiger counters to suppress secondary counts. Even if one wished to detect slow $Ar^+$ ions, at atmospheric pressures the drift region conversion process

$Ar^+ + Ar + Ar \rightarrow Ar_2^+ + Ar$

tends again to produce a molecular ion with subsequently lower probability for electron ejection at the cathode. Branching ratios between dissociation and electron ejection for a wide range of molecular ions are not available in the literature.

A second problem has to do with oxidation and other surface contaminants of the cathode that are generally present in real world, i.e., “dirty,” surfaces. One of the few quantitative comparisons available between ultra clean and dirty surfaces is the work of Phelps[4] with argon discharges. It shows that the presence of adsorbed gas and oxidation can reduce the Second Townsend coefficient by roughly two orders of magnitude for slow $Ar^+$ ions under the conditions studied. The electron yield for the clean surface is about 12%. The work of Hofer and Varga[5] also shows significant reduction of electron yield from tungsten under $Ar^+$ impact after carefully controlled exposure to oxygen. In this case reductions of roughly two orders of magnitude are interpreted in terms of a modification in the density of states in the combined system of the impacting ion, gas layer, and surface.

Note also that the requirement for potential emission, namely that the ionization potential be at least twice work function of the cathode surface, can be violated for some ions. For example, the work function of tungsten is about 4.5 eV and the ionization potential of $C_2H_6S_2$ is only 7.4 eV. However, values in the 9 to 10-volt range are more typical of organics. In long drift columns there is also a tendency for charge exchange reactions to produce positive ions with the lowest (least electron affinity) ionization potential. This could exacerbate the energetics problem in principle, but organics will generally already have lower ionization potentials than the background gas. There has been considerable work over many years to tailor cathode surfaces for low work functions, for example with films of alkaline earth metals. However, these approaches generally produce surfaces that must remain at high vacuum. Another possibility is reduction of the work function via a very high E-field, as would be found in field emission conditions, but this would also likely require high vacuum conditions. Our experiments with carbon fibers as a cathode material were motivated by this concept. Note that true field emission should not be confused with the corona emission from pointed electrodes, which produces electrons through another mechanism that is not relevant to this discussion.

Finally, we note that if the low Second Townsend coefficient problem can be solved, the issue of manufacturability for large arrays is not as daunting as might be expected. There has been considerable progress in the fabrication of arrayed electrodes similar to what would be required here by the high-energy physics community[6] largely through the use of photolithographic techniques. We appreciate the cooperation of the primary U.S. group active in such fabrication techniques, residing at Purdue University.[7]

We are left with the conclusion that our negative results are most likely the result of a dissociative recombination process that has a very low electron yield.

## Subtask 2. Membrane Development/Characterization for MIMS and IMS Applications (M. Stone)

***Background.*** The ability to carry out fast, chemical analysis measurements on environmental samples in the field is a desirable attribute in the environmental remediation arena. Environmental water samples, for instance, often contain solid matter (colloidal or other) that interferes with many standard analytical techniques. One of the novel integrating aspects of this work is the use of selective thin polymer membranes to presort and preconcentrate analytes prior to their detection in these analytical methods. In this task the membrane materials are developed and then characterized by placing them at the inlet port of a membrane introduction mass spectrometer (MIMS). See Figure 1.

MIMS has made large strides in capability improvement since its introduction.[8] The main progress has been in systematic design changes that have allowed this technique to measure analytes in the parts-per-trillion range with samples that have had no special handling or pretreatment. In spite of these improvements, however, the most important component of MIMS—the membrane—has not been optimized. In this subtask, membranes have been selected, tested, and evaluated as candidates in applications involving chlorocarbon analysis. The results showed interesting responses by different polymers that may make them good candidates for improved analytical capabilities needed for many EM-relevant cleanup and monitoring applications. Additionally, these membranes are anticipated to provide sample preconditioning for an IMS that operates on a different principle from MIMS but has equal or greater sensitivity. In addition to its sensitivity, the IMS is a much smaller and more portable device than the MIMS and is already in use in some field applications.

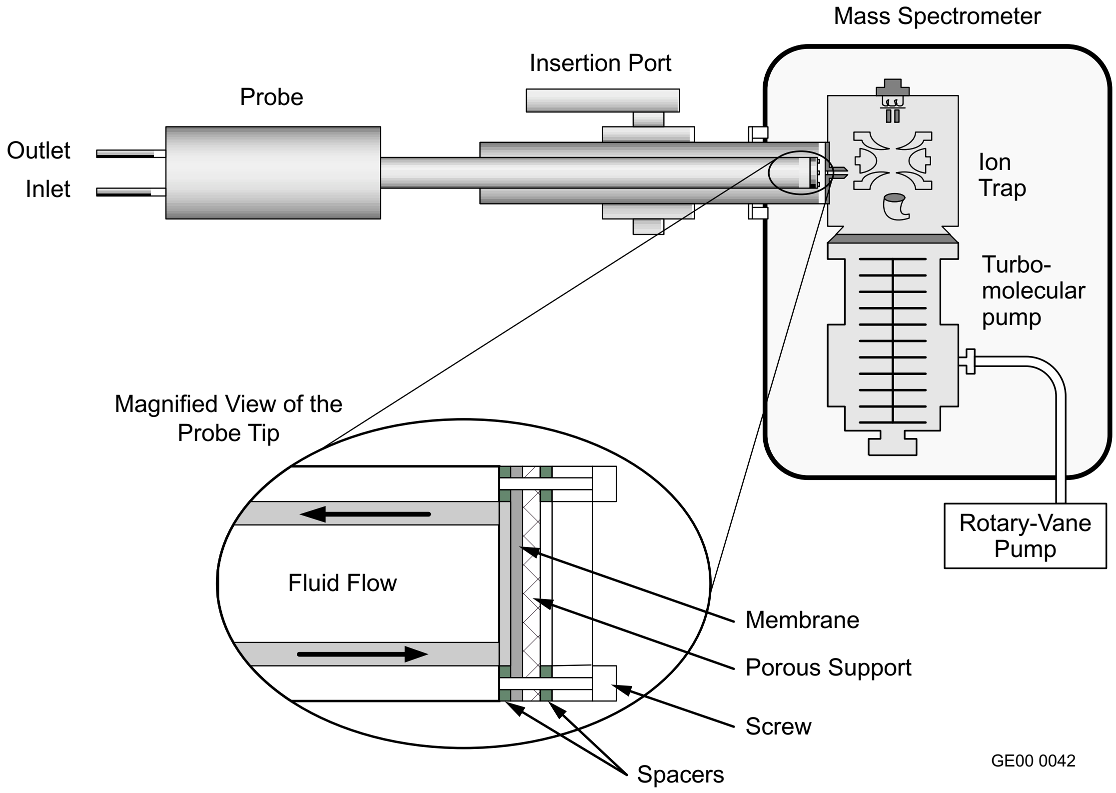

**Figure 1.** MIMS insertion probe assembly.

***Results.*** The results of exposing a number of membrane materials to methylene chloride are given in Table 1. It was surprising that none of the polymers served as good semipermeable membranes for methylene chloride. Some small peaks were observed, but mostly erratic behavior occurred. There were several polymers that passed too much water to be used.

The results for exposure to TCE are given in Table 2. Several of the membranes worked very well in this case. Viton, polyurethane, Sensicare gloves, and nitrile rubber gloves all gave good results. Viton gave the lowest detection limit of 2 ppb.

Carbon tetrachloride exposure results are given in Table 3. Only the Sensicare gloves showed any quantifiable permeability of 20 ppm.

Table 4 contains the results for the chloroform experiments. Polyethylene, Viton, and Sensicare materials gave measurable peaks, all in the low ppm.

The results obtained are very important from the point of view of developing an array of materials that can be used to distinguish between these closely related analytes. The objective was to see if membranes might be developed that either individually or in use as an array might be preconcentrators that would take the place of a gas chromatograph for use in sensor applications such as microsensors on a chip. The results not only showed that families of analytes (such as chlorocarbons) can permeate the membranes, but that an array of membranes or polymer coatings on devices such as SAW devices could be used to identify individual components within a family of compounds.

The idea of using membranes for other analytical instrumentation was tested using both a silicone membrane and a polyphosphazene membrane in front of an ion mobility spectrometer (IMS). Figure 2 is a photograph of the system. It shows how the output of a membrane cell is directed at the inlet port of the IMS detector. This paves the way for exploring how to improve instrument sensitivity by using the selective specificity of the membranes for many types of analytical devices. In these experiments a water feed stream was pumped (recirculated) over one face of the polymer membrane (47 mm in diameter). A low volume sweep gas (20–50 ml/min) was passed over the other side of the membrane. At first, pure water was used to get a background check of the system. Then an analyte (methylene bromide in this set of experiments) was injected into the feed stream. When a microsyringe was used to deliver only 10 µl of methylene bromide into the feed stream (250-ml water), it took only a few seconds before a large bromide peak was observed. It was so large that the IMS detector had to be 'aired' out for a few minutes to recover. After several minutes, the silicone membrane was exchanged for a polyphosphazene membrane. No new analyte was added, and in just a few minutes a strong bromide peak was obvious. Figure 3 shows the baseline control scan, a scan using the silicone rubber membrane (PDMS, polydimethylsiloxane), and a scan using the polyphosphazene membrane (designated Z1002a).

The IMS system is remarkably sensitive, and with the addition of a membrane in front of the sample inlet, many benefits can be realbized. Membranes can be tailored for specific analytes, they are simple to use, they greatly reduce sample preparation time, and they serve as preconcentrators for the system. After observing how easy it was to configure the system and how clear and strong the signals were, many new potential applications of this combination of technologies are now being identified.

**Table 1.** Polymer response to methylene chloride.

| | Polymer | Mfg., Part Number | Thickness (inches) | Actual Thickness | $MeCl_2$ (200 ppm) | Comments |
|---|---|---|---|---|---|---|
| 1a. | Natural rubber | Fisher 11-393-88C<br>Phoenix PL600TM | 0.005 | 0.005 | | Water leaked through. |
| 1b. | Natural rubber | Lab Safety 23169 | 0.016 | 0.012 | | Water leaked, pulled and tore easily. |
| 2a. | PVC (polyvinylchloride) | Fisher 96-334 (Oak) | 0.0236 | 0.005 | | Water leaked through while on probe. |
| 2b. | Vinyl exam gloves | Fisher 11-394-36D | 0.008 | 0.005 | | Water leaked through while on probe. |
| 3. | Sensicare Maxxim Medical | Fisher 11-127-51D | 0.007 | 0.005 | Small peaks | Didn't leak high baseline. |
| 4a. | Polyethylene | Fisher 11-394-100C | 0.00125 | 0.0022 | Small peaks | Didn't leak. |
| 4b. | Polyethylene | Fisher 11-394-110C | 0.00175 | 0.0015 | Erratic baseline | Didn't leak high baseline. |
| 5. | Viton Fluoroelastomer | Lab Safety 6647-9 | 0.01 | 0.01 | No peaks | Didn't leak. |
| 6. | Butyl rubber | Lab Safety 14567 | 0.007 | 0.009 | | Water leaked through. |
| 7a. | Polyurethane | Lab Safety 6975 | 0.005 | 0.005 | No peaks | Didn't leak. |
| 7b. | Polyurethane | Lab Safety 10050 | 0.0015 | 0.002 | Small peaks | Didn't leak high baseline. |
| 8. | Neoprene | Lab Safety B8159 | 0.017 | 0.017 | Erratic baseline | Didn't leak. |
| 9. | Nitrile | Fisher 11-388-31<br>N-Dex | 0.016 | 0.005 | No peaks | Didn't leak. |

**Sources**

1a. Phoenix Medical Technologies, P.O. Box, Andrews, South Carolina 29510

2a. Oak Technical Inc., 4835 Darrow Rd., Stow, Ohio 44224-1431.

3. Maxxim Medical, 10300 49th Street North, Clearwater, Florida 33762, 727-561-2100.

**Table 2.** Polymer response to TCE.

| Polymer | Thickness Mfg., Part Number | Actual (inches) | Thickness | TCE | Comments |
|---|---|---|---|---|---|
| 1a. Natural rubber | Fisher 11-393-88C<br>Phoenix PL600TM | 0.005 | 0.005 | | Water leaked through. |
| 1b. Natural rubber | Lab Safety 23169 | 0.016 | 0.012 | | Water leaked, pulled and tore easily. |
| 2a. PVC polyvinylchloride | Fisher 96-334 (Oak) | 0.0236 | 0.005 | | Water leaked through while on probe. |
| 2b. Vinyl Exam Gloves | Fisher 11-394-36D | 0.008 | 0.005 | | Water leaked through while on probe. |
| 3. Sensicare Maxxim Medical | Fisher 11-127-51D | 0.007 | 0.005 | 20 ppb | Didn't leak. |
| 4a. Polyethylene | Fisher 11-394-100C | 0.00125 | 0.0022 | | Didn't leak, pressure rises (TCE). |
| 4b. Polyethylene | Fisher 11-394-110C | 0.00175 | 0.0015 | | Didn't leak, high baseline, swamped detector (TCE). |
| 5. Viton Fluoroelastomer | Lab Safety 6647-9 | 0.01 | 0.01 | 2 ppb | Didn't leak. |
| Butyl rubber | Lab Safety 14567 | 0.007 | 0.009 | | Water leaked through |
| 7a. Polyurethane | Lab Safety 6975 | 0.005 | 0.005 | 20 ppm | Didn't leak |
| 7b. Polyurethane | Lab Safety 10050 | 0.0015 | 0.002 | | Didn't leak, pressure rose (TCE) |
| 8. Neoprene | Lab Safety B8159 | 0.017 | 0.017 | No peaks | Didn't leak. |
| 9. Nitrile | Fisher 11-388-31<br>N-Dex | 0.016 | 0.005 | 20 ppm | Didn't leak, odd-shaped peaks (TCE). |

## Sources

1a. Phoenix Medical Technologies, P.O. Box, Andrews, SC 29510

2a. Oak Technical Inc., 4835 Darrow Rd., Stow, OH 44224-1431.

3. Maxxim Medical, 10300 49th Street North, Clearwater, FL 33762, 727-561-2100.

**Table 3.** Polymer response to carbon tetrachloride.

| Polymer | Mfg., Part Number | Thickness (inches) | Actual Thickness | TCE | Comments |
|---|---|---|---|---|---|
| 1a. Natural rubber | Fisher 11-393-88C<br>Phoenix PL600TM | 0.005 | 0.005 | | Water leaked through. |
| 1b. Natural rubber | Lab Safety 23169 | 0.016 | 0.012 | | Water leaked, pulled and tore easily. |
| 2a. PVC (polyvinylchloride) | Fisher 96-334 (Oak) | 0.0236 | 0.005 | | Water leaked through while on probe. |
| 2b. Vinyl exam gloves | Fisher 11-394-36D | 0.008 | 0.005 | | Water leaked through while on probe. |
| 3. Sensicare Maxxim Medical | Fisher 11-127-51D | 0.007 | 0.005 | 20 ppm | Didn't leak. |
| 4a. Polyethylene | Fisher 11-394-100C | 0.00125 | 0.0022 | | Didn't leak. |
| 4b. Polyethylene | Fisher 11-394-110C | 0.00175 | 0.0015 | No peaks | Didn't leak, high baseline. |
| 5. Viton Fluoroelastomer | Lab Safety 6647-9 | 0.01 | 0.01 | Negative peaks | Didn't leak. |
| 6. Butyl rubber | Lab Safety 14567 | 0.007 | 0.009 | | Water leaked through. |
| 7a. Polyurethane | Lab Safety 6975 | 0.005 | 0.005 | No peaks | Didn't leak. |
| 7b. Polyurethane | Lab Safety 10050 | 0.0015 | 0.002 | | Didn't leak . |
| 8. Neoprene | Lab Safety B8159 | 0.017 | 0.017 | No peaks | Didn't leak. |
| 9. Nitrile | Fisher 11-388-31<br>N-Dex | 0.016 | 0.005 | No peaks | Didn't leak. |

## Sources

1a. Phoenix Medical Technologies, P.O. Box, Andrews, South Carolina 29510

2a. Oak Technical Inc., 4835 Darrow Rd., Stow, Ohio 44224-1431.

3. Maxxim Medical, 10300 49th Street North, Clearwater, Florida 33762, 727-561-2100.

**Table 4.** Polymer response to chloroform.

| Polymer | Mfg., Part Number | Thickness (inches) | Actual Thickness | TCE | Comments |
|---|---|---|---|---|---|
| 1a. Natural rubber | Fisher 11-393-88C<br>Phoenix PL600TM | 0.005 | 0.005 | | Water leaked through. |
| 1b. Natural rubber | Lab Safety 23169 | 0.016 | 0.012 | | Water leaked, pulled and tore easily. |
| 2a. PVC polyvinylchloride | Fisher 96-334 (oak) | 0.0236 | 0.005 | | Water leaked through. |
| 2b. Vinyl exam gloves | Fisher 11-394-36D | 0.008 | 0.005 | | Leaks water through. |
| 3. Sensicare Maxxim Medical | Fisher 11-127-51D | 0.007 | 0.005 | 2 ppm | Didn’t leak. |
| 4a. Polyethylene | Fisher 11-394-100C | 0.00125 | 0.0022 | 2 ppm | Didn’t leak. |
| 4b. Polyethylene | Fisher 11-394-110C | 0.00175 | 0.0015 | 2 ppm | Didn’t leak. |
| 5. Viton Fluoroelastomer | Lab Safety 6647-9 | 0.01 | 0.01 | 20 ppm | Didn’t leak. |
| 6. Butyl rubber | Lab Safety 14567 | 0.007 | 0.009 | | Water leaked through. |
| 7a. Polyurethane | Lab Safety 6975 | 0.005 | 0.005 | No peaks | Didn’t leak. |
| 7b. Polyurethane | Lab Safety 10050 | 0.0015 | 0.002 | No peaks | Didn’t leak. |
| 8. Neoprene | Lab Safety B8159 | 0.017 | 0.017 | No peaks | Didn’t leak. |
| 9. Nitrile | Fisher 11-388-31<br>N-Dex | 0.016 | 0.005 | No peaks | Didn’t leak. |

**Sources**

1a. Phoenix Medical Technologies, P.O. Box, Andrews, South Carolina 29510

2a. Oak Technical Inc., 4835 Darrow Rd., Stow, Ohio 44224-1431.

3. Maxxim Medical, 10300 49th Street North, Clearwater, Florida 33762, 727-561-2100.

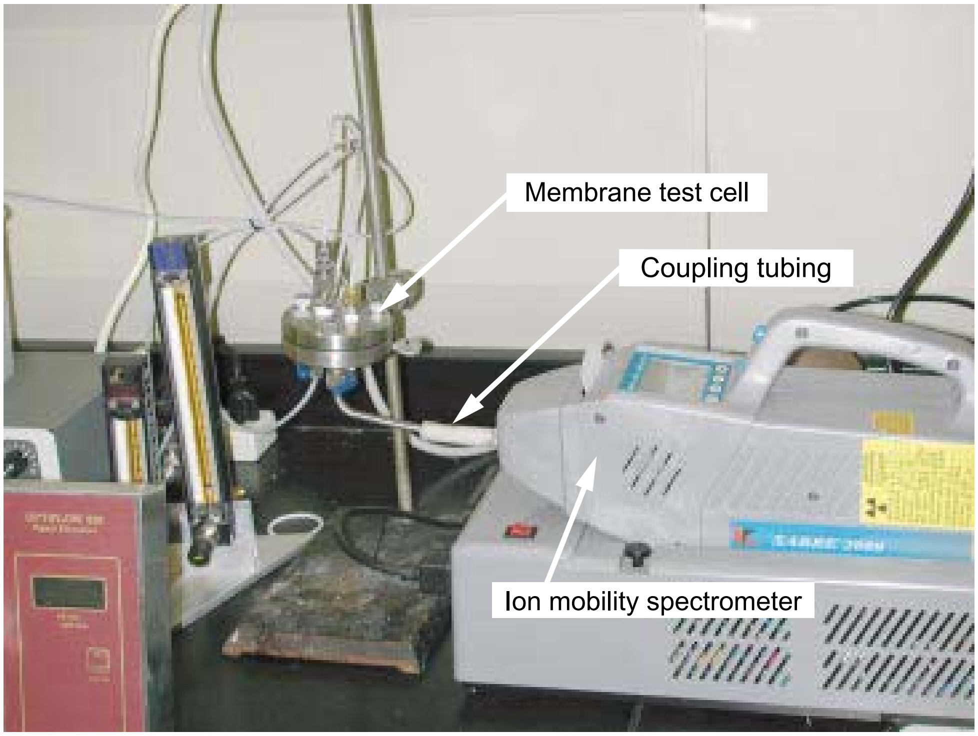

GE00 0050

**Figure 2.** Membrane separation cell interfaced to an ion mobility specrometer.

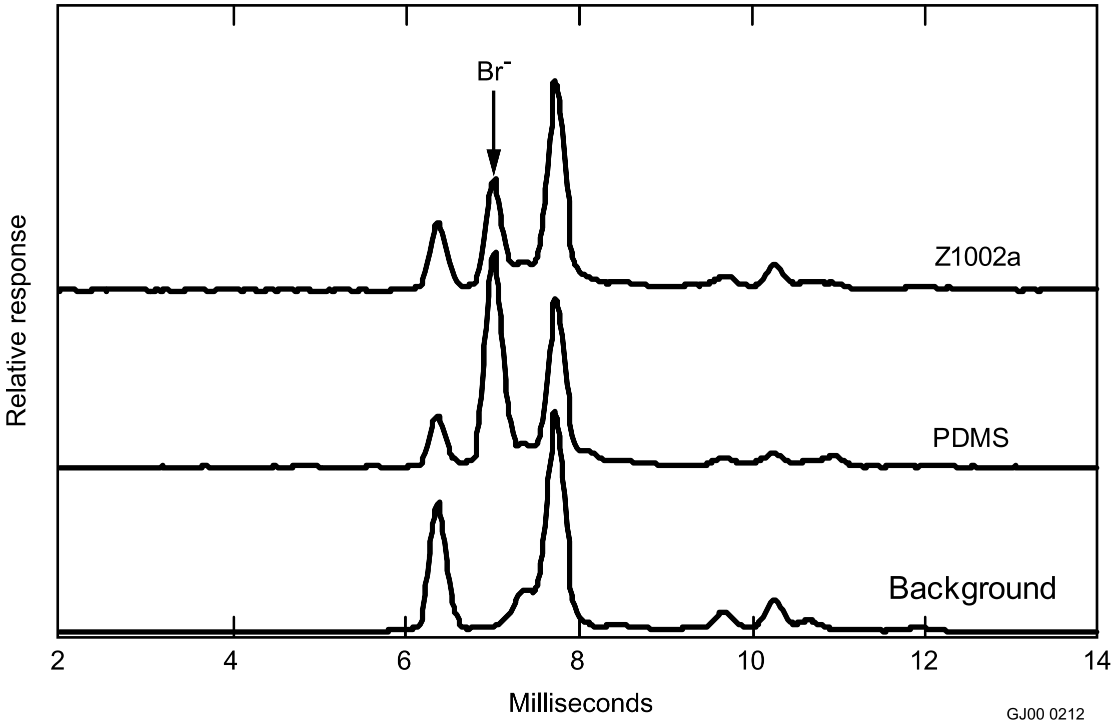

GJ00 0212

**Figure 3.** Results of scanning for bromide in ion mobility specrometry using membnrane reconcentrators.

### Subtask 3. Photoionization Source for an IMS (P. Castle, J. Partin)

***Background.*** The objective of this work is to enhance the sensitivity and broaden the applicability of IMS to analytes of concern in the EM program. This work will lead to the elimination of the $^{63}$Ni source and the ion gating grid of the traditional IMS by directly photoionizing the analyte molecules with a UV laser operating at 266 nm (frequency quadrupled Nd YAG laser). We have demonstrated the technique in the absence of the gating grid, relying on a narrow (~10 ns) laser pulse to provide the timing gate.

There are several significant aspects of IMS addressed by this work. The first is that the formation of the ions of the target analyte is no longer dependent on the proton affinity of the analyte or the electron attachment cross section of the molecule. The analyte molecules are directly ionized by photoionization. The second is the elimination of the ion gate grid. Since the laser pulse is extremely narrow (on the order of 10 ns), the ion formation process is limited to this time period and is not a continuous ionization process as is found when using the standard $^{63}$Ni source. The ion gate grid has traditionally been a design, production, and mechanically difficult link in IMS instrumentation. The pulsed laser provides its own timing gate. The third depends on the advent and continuous refinement of diode laser pumped ND YAG laser systems. This continuing development, which will be enhanced by advances in vertical cavity surface emitting laser (VCSEL) sources for pumping Nd YAG lasers, will provide increasingly compact and more efficient sources of 266 nm, pulsed radiation. Lincoln Laboratories has produced a compact integrated micro laser package that produces 15 mW/pulse that is not far from the power levels at which the experiments described here were carried out. These advances in laser sources will provide the opportunity to decrease the size of the combined electronic and instrumental package and lead to field deployable instrumentation based on this technology.

While others have investigated the use of photoionization[9–15] as an ion source for IMS , only one other group[12] has taken advantage of the fact that many pulsed lasers by virtue of their narrow pulse widths (time) can eliminate the need for a gate pulse grid in an IMS system. Much of the work that is reported in the literature is more than 5 years old. Laser systems have advanced significantly in that time. The ability to ionize analytes directly, rather than rely on ion molecule reactions and the vagaries of proton affinities and electron attachment cross sections of individual molecules, is a significant advantage for an analytical system.

***Experimental and Results—***Initial work that has been conducted has demonstrated that a pulsed laser can be used as an ion source without an ion gate grid. Figures 4–7 show the IMS spectra generated by pulsed laser ionization (at 248 nm, generated by a krypton fluoride excimer laser) with a pulse energy of about 40 mJ in an ionization volume of about 0.18 cm$^3$ (22kW/cm$^3$).

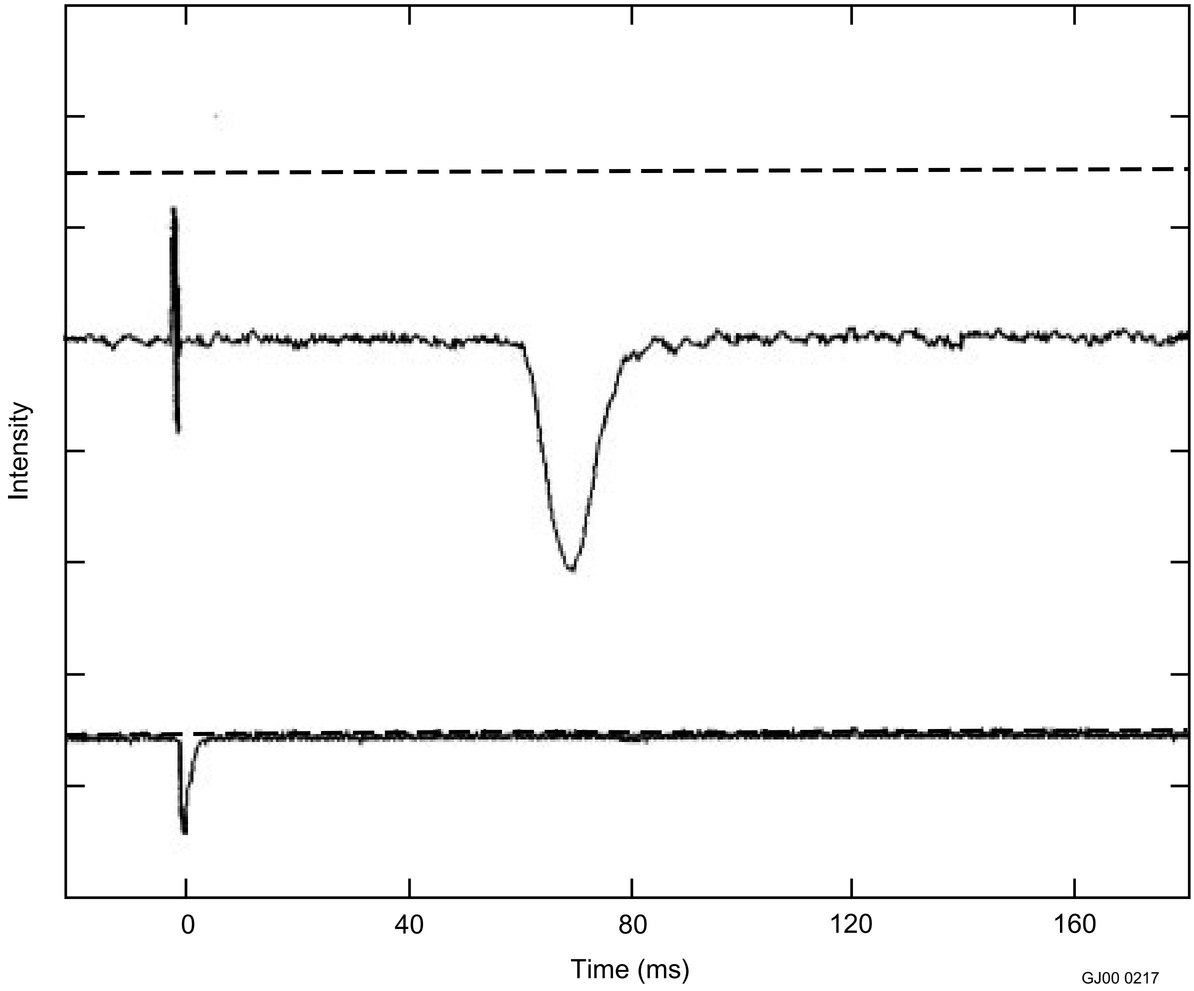

**Figure 4.** Photoionization IMS spectrum of methanol.

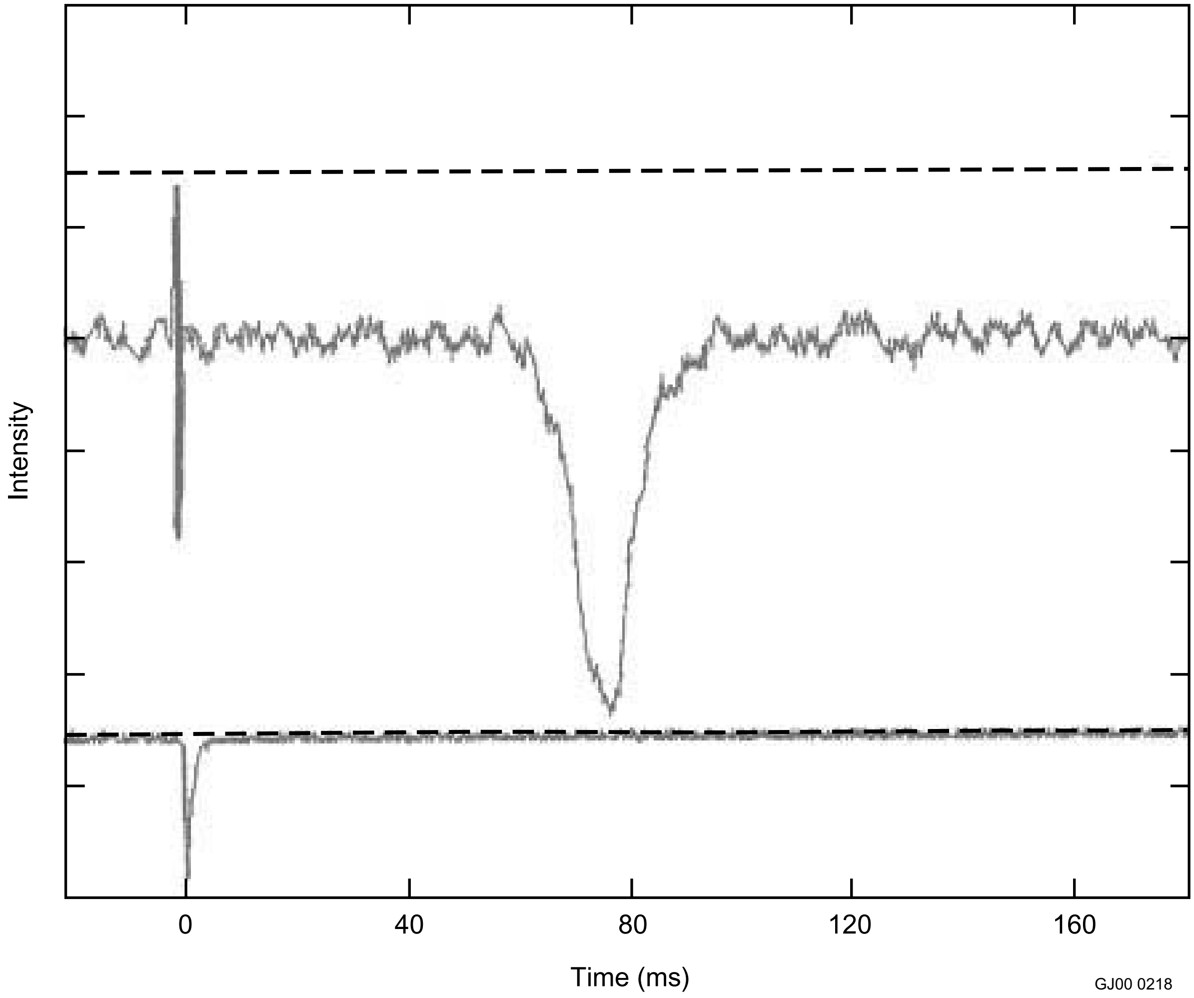

**Figure 5.** Photoionization IMS Spectrum of ethanol.

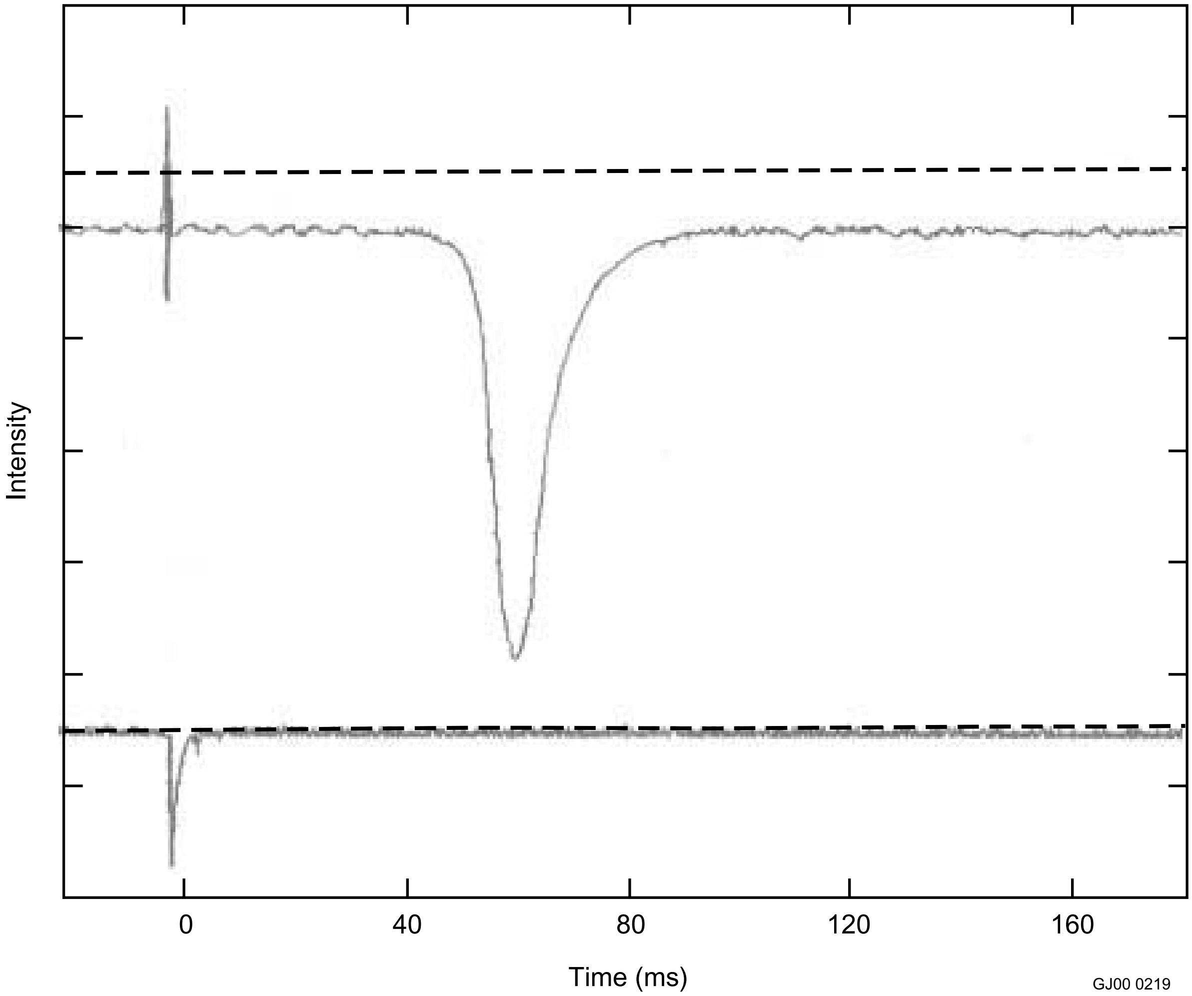

**Figure 6.** Photoionization IMS spectrum of naphthalene.

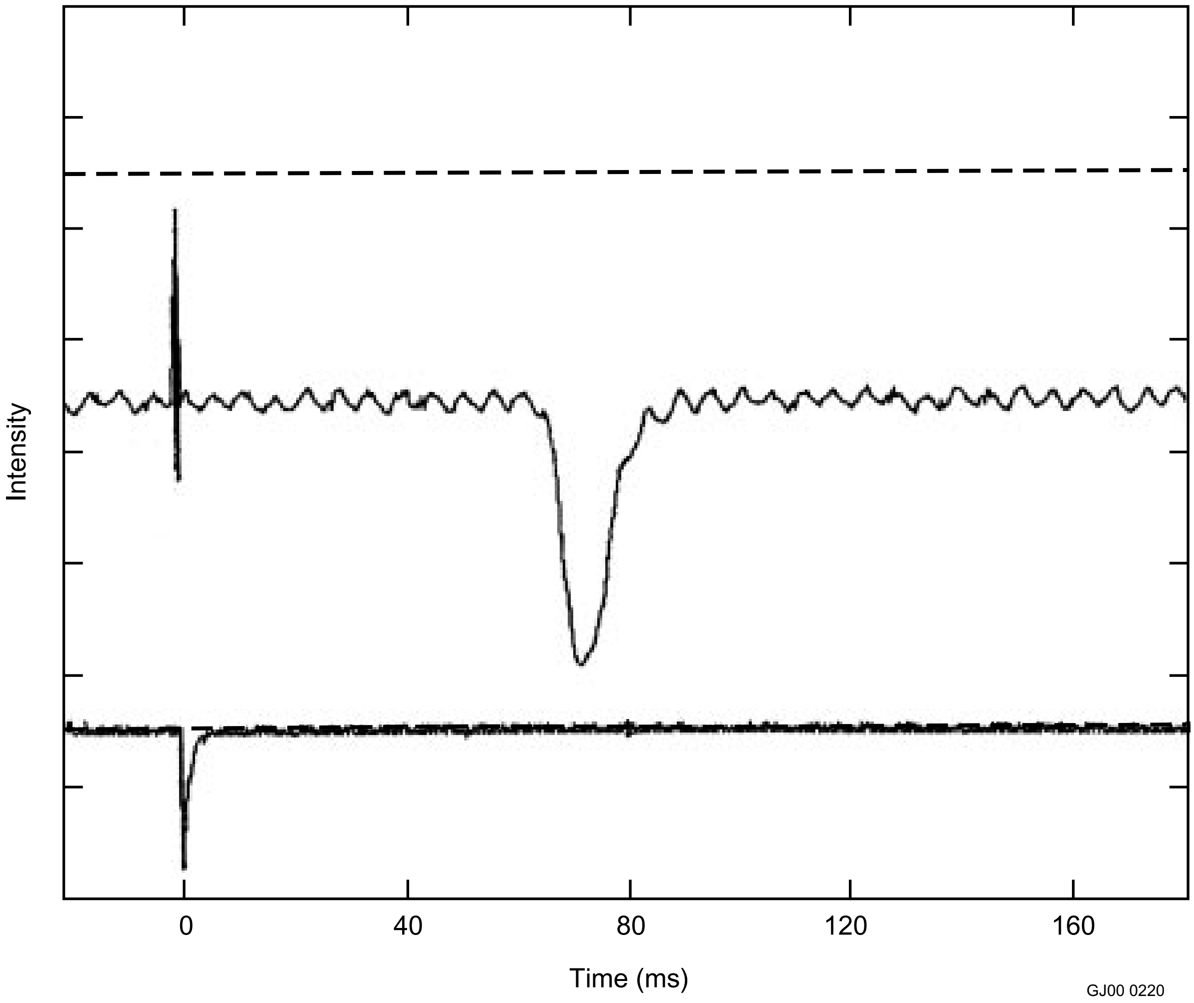

**Figure 7.** Photoionization IMS spectrum of acetone.

These spectra demonstrate the ability of laser radiation of a constant wavelength to produce photoions from differing molecules. Further work needs to be carried out to understand both the implications of resonant and nonresonant photoionization processes with respect to sensitivity and selectivity. In addition the peaks in the spectra shown above are broader than is usually experienced in IMS. Work must be done to understand and eliminate this broadening mechanism.

## Task 2. Membrane/SAW Detector System Development

### Peter Castle

### Background

This task had as its objective the development of a system that combined the results of the selective membrane studies, previously discussed in conjunction with the IMS, with SAW detection technology. The premise has been that selective membranes placed upstream of the SAW detector as well as coatings of the same materials on the surfaces of the devices would provide selectivity and additional sensitivity to compounds such as halogenated hydrocarbons, e.g., trichloroethylene, carbon tetrachloride, methylene chloride. These compounds are of interest to DOE-EM as primary contaminants of concern in subsurface contaminant plumes and in monitoring the long-term performance of waste disposal cells. We believed that successful demonstration of this concept would be a step in the direction of developing reliable long-term monitoring systems for DOE's subsurface monitoring needs.

***Experimental and Results***—The original experimental setup shown in Figure 8 was modified by replacing the valves with mass/flow controllers. In addition, in some instances the bubbler was replaced by a gas cylinder containing a known concentration of a halocarbon in nitrogen. The uncoated SAW did not respond to the halocarbons and responded only weakly to more polar compounds such as methanol and acetone. We were unsuccessful in coating the SAWs with the polymeric materials tested above in Subtask 2. A quartz crystal microbalance (QCM) system has recently become available. QCM devices, while not as sensitive as SAWs, are easier to coat and work with. The principle of combining the permeable membrane with a coated detector may be more easily demonstrated using a coated QCM, and, if successful, a means to coat a SAW will be devised.

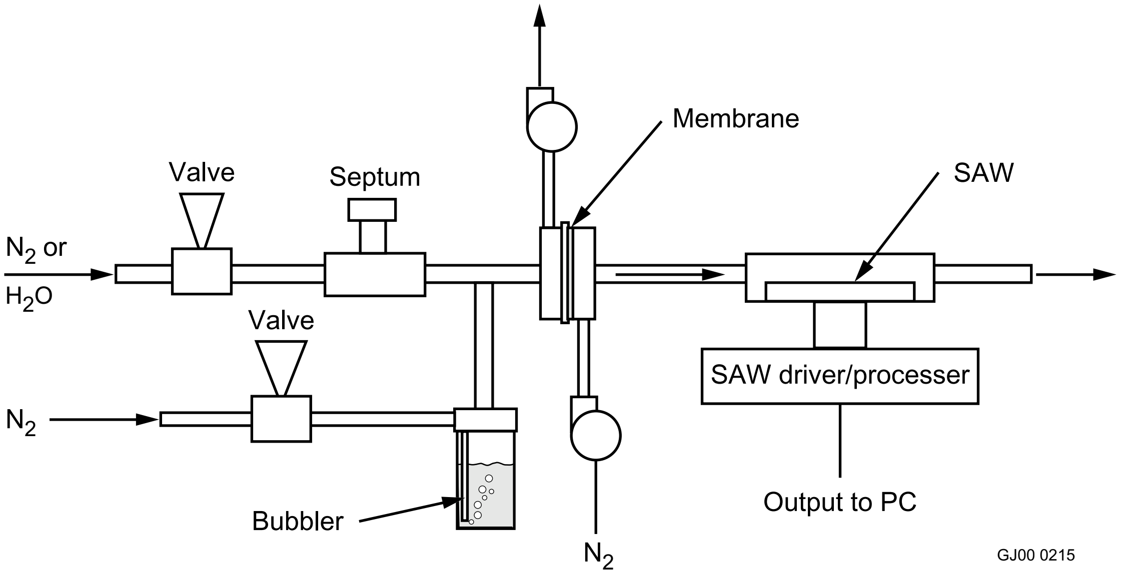

**Figure 8.** Membrane/SAW experimental setup.

## Task 3. A Two-Dimensional Imaging Spectrometer Using Digital Micromirror Arrays and a Single Photomultiplier Tube

**W. Bauer, G. Lassahn, F. White**

### Background

The objective of this project is to design and build a prototype of a novel two-dimensional imaging spectrometer using two digital micromirror array devices (DMAs or DMDs), a grating, and a photomultiplier tube. This project will also help to define scientific applications for the exiting technology named DMA, which is being developed for high-resolution digital TV and projection. The combination of the high optical throughput, versatility, and potential multiplex advantages provided by the DMAs coupled with the use of a sensitive photomultiplier tube will make the proposed instrument more sensitive and selective than any comparable imaging spectrometers that are currently available at a lower cost. The high throughput, multiplex advantage provided by the DMAs and the use of a sensitive photomultiplier tube could significantly enhance the achievable lower detection limits over that of a charge coupled device (CCD) camera. The resulting instrument will be quite powerful. It will have a raw hardware cost of ~\$10K.

Two-dimensional spectral imaging, sometimes referred to as hyperspectral imaging, has a variety of diverse applications spanning the micro- to macroscopic scale and a variety of scientific fields, e.g., microbiology, chemistry, geochemistry, forensics, environmental, astronomy and agriculture. An example of the value of true two-dimensional spectral imaging is given by the comparison of the Landsat and AVIRIS satellites. Both cover the spectral range of approximately 350–2,500 nm and both use their motion to image the surface in a push broom like technique. The Landsat satellites cover this range with seven broad band filters while the AVIRIS uses a grating to disperse it onto CCDs to get 244 wavelengths (10-nm bandpass) of the same spectral region. The Landsat can identify vegetation in a particular field on the earth's surface. The AVIRIS cannot only identify vegetation in the field but can use the spectrum to identify the specific crop growing in that field.[16]

Unfortunately, the common laboratory instrumentation for two-dimensional spectroscopic imaging is not typically as very versatile as the AVIRIS. Most laboratory *spectral imaging* systems depend on a very limited set of bandpass filters for spectral selection and either a CCD camera or mechanical devices such as a *moving stage* or raster scanning system for spatial selection. The filters incorporated into these spectroscopic imaging systems severely limit the number of applications that the instrument can be used for. Not only is the wavelength selection limited, but the bandpass is frequently too large for optimum selectivity or to successfully employ mathematical techniques to extract the information. In fluorescence microscopy, the bandpass of most filters used is on the order of 10–40 nm. Liquid crystal tunable filters (LCTF) and acousto-optical tunable filters (AOTF) are commercially available and can be used for more versatile wavelength selection in imaging applications.[17,18] However, the light throughput, relatively wide bandpasses, requirement for an expensive CCD detector and price of these devices may still be limiting for many applications. LCTFs range in price from as little as ~\$5K for a wide bandpass model to more than \$30K for a model with resolution sufficient for Raman imaging. Grating or prism instruments are much cheaper but require a moving stage to acquire an image at multiple wavelengths unless only 1D spatial information is required (i.e., the spatial information along the entrance slit of the spectrometer if a 2D array detector such as a CCD is used).

Two-dimensional spectral imaging systems employing a moving stage are simply too slow to be used for most routine applications. Collection of a single two-dimensional spectral image can take several hours using this technique. With the use of a CCD camera, an image can be obtained in much less than one second or by integrating for several seconds to enhance the signal-to-noise ratio (S/N). Spectral images with a CCD can be obtained; but a filter wheel, AOTF, LCTF or moving stage with a slit entrance to a polychrometer are necessary. Acquisition time using the CCD camera is generally on the order of minutes. While CCD cameras are readily available, their sensitivity can be limited for many low-light applications like fluorescence or Raman imaging. Intensified CCD cameras appropriate for many low-light applications are commercially available but cost on the order of \$15–\$25K. These high sensitivity CCD cameras are still as much as 100x less sensitive than a photomultiplier tube, which can have an acquisition or replacement cost of less than \$2K dollars, including electronics.

Hadamard spectroscopy or imaging is performed by making a series of n measurements of n masks of n elements. The individual responses at the n elements are then calculated via a set of simultaneous equations. In its simplest terms this is basically a least squares solution described by M = S·I, where M represents a vector of n measurements. S is a Sylvester matrix derived from a Hadamard matrix, describing which of the n elements are on or off during each of the n measurements, and I is the vector of the actual response at each of the n elements that is to be determined. Because multiple elements are on during each measurement, the Hadamard technique provides a multiplex advantage that can significantly increase the S/N.

Hadamard encoding using either mechanical,[19] AOTF,[18] or liquid crystal devices (LCD)[19,20] as masks has been used to allow otherwise common spectroscopic and microscopic equipment to be used to collect spectra and images with either single or multiple detector elements. The multiplex advantage associated with the Hadamard encoding has improved the S/N for these imaging and spectroscopic applications. The latest developments in Hadamard spectrometers and spectral imaging devices have employed digital micromirror array devices (DMA).[21,22] DMAs are a two dimensional array of micromirrors (16 $\mu m^2$ separated by 1 μm) mounted on a SRAM chip. The development of DMAs is being driven by the digital television and projection market, therefore, it is expected that these devices will become common place and even less expensive in the future. For spectroscopy applications, these devices hold much promise because they can be addressed rapidly (<20 μsec compared to ~10 msec on a LCD), do not suffer from light leakage or photodegradation like LCDs[23] and are ultimately much cheaper than CCDs. Currently, a projector with a single DMA is ~$2–3K. Using DMAs for other spectroscopic applications involving atmospheric chemistry has also been suggested.[24]

## Proposed Instrument

The DMA spectroscopic and two-dimensional spectroscopic imaging applications to date have employed a single DMA. We have been attempting to build a two-dimensional spectral imaging instrument employing two DMA devices. This instrument will be highly versatile and should ultimately cost <$20K. Figure 9 is a highly simplified schematic of the two-dimensional spectral imaging system design generated using OSLO LT 5.4 optical design software. The imaging spectrometer will consist of an input source using OSLO LT 5.4 optical design software. The imaging spectrometer will consist of an input source

## Experimental

Because the manufacturer of the DMAs (Texas Instruments, TI) does not sell them directly, the only way to acquire one is to purchase a video projector that contains one. Therefore, two such projectors (Davis, DL 450) were purchased along with a photomultiplier tube (Hitatchi, R928), including the necessary power supplies, housings and electronics (PTI, Model 814 PMT detection system), and a multifunction card for a PC (National Instruments, PCI-MIO-16E-1) to acquire the data from the photomultiplier tube and to ultimately change voltages on the PMT, operate shutters, etc., as necessary.

The light source was removed from the DL-450 projector along with a light pipe, lens, and mirror assembly used to image the light from the source through the filter wheel and onto the DMA. The feedback signal from the light source was mimicked by applying a 5-Vdc signal to pin 40 of the TI formatter interface. Originally, the filter wheel was removed and a pulse sent at ~120 Hz to the color wheel index signal on pin 31 of the formatter interface. There were some minor problems with the synchronization that caused the DMA to flutter. The filter wheel was replaced to eliminate this problem. The filter wheel does not in any way interfere with the incoming light from the DMA. For simplicity and demonstration purposes it was decided to leave the output lens assembly in place and use it as the input lens. The output lens optics of the projector were such that a collimated image could be directed at the photomultiplier tube

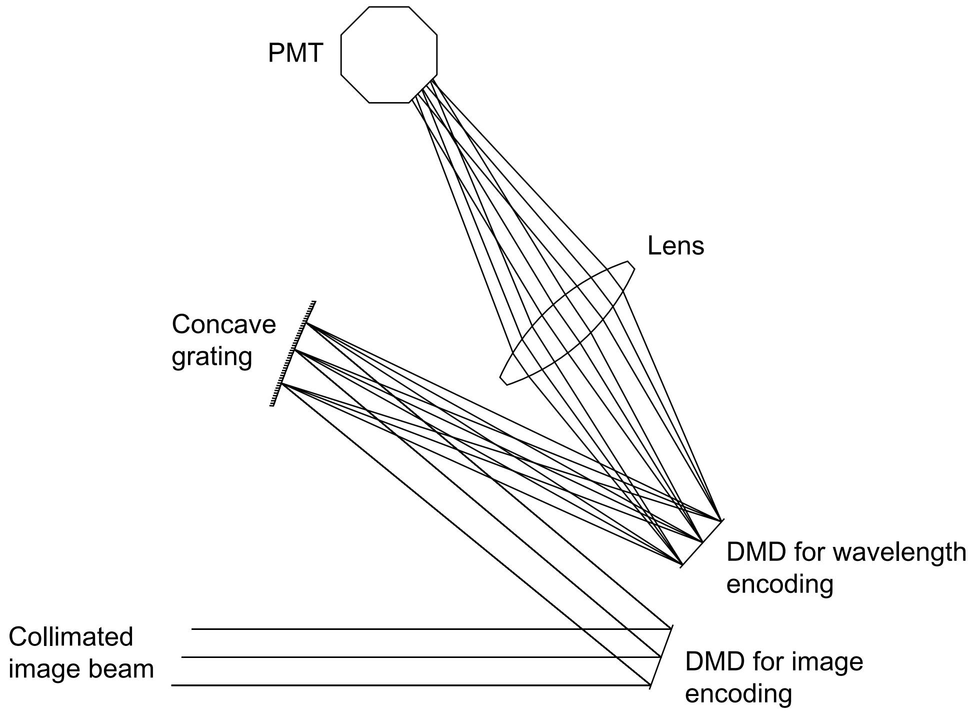

GJ00 0215

**Figure 9.** Conceptual schematic of 2-D imaging spectrometer.

which was mounted on the end of a tube which was put in place of the removed mirror assembly.

For ease and simplicity, we originally expected to operate the instrument and process the images using LabView (National Instruments) and/or MatLab (The Mathworks, Inc., V5.3). The DMA is actually controlled by the TI Digital Light Processing (DLP) processors, which behave just like a video display device such as a monitor. To have complete control of the DMA, one must have complete control of the video display screen. Unfortunately, Window NT and 98 do not generally allow this and LabView and MatLab do not have functions that allow this capability. We therefore had to begin developing the DMA control software in C++. The resulting program is MA13. The current version of the MA13 program controls the DMA via the TI DLP processing electronics.

The DMA is treated as a device 800 usable pixels wide by 600 pixels high. An image is projected onto the DMA, and each pixel does or does not reflect the part of the image on that pixel. The pixels are controlled by treating the DMA as a monitor screen and writing a black-and-white pattern to that screen. A pixel that is written as white reflects toward the detector, and a pixel written as black does not. Thus, the DMA acts as a device that masks an image, allowing transmission of the parts of the image that fall on white DMA pixels and blocking transmission of the parts of the image that fall on black DMA pixels. In MA13, by necessity, the mask that is imposed on the DMA also appears on the user's console monitor, so the user sees a black-and-white pattern that is the same as the mask on the DMA. In normal operation, for each mask that is written to the DMA, the program acquires one data point that is the value of the intensity averaged over the masked image. The resulting ASCII data and image are stored as files with dat and tif extensions, respectively.

MA13 is set up to create a sequence of masks, regularly spaced in time. MA13 can create any of four types of mask sequence: MovingSlit, RasterScan, HadamardLinear, and HadamardFolded.

In a MovingSlit sequence, each mask has a narrow white region, with a height of 600 pixels (the full screen height) and a user-selectable width that is normally much smaller than the screen width of 800 pixels. This mask is intended to function like a spectrometer slit, and we will refer to the white region as a slit. In the first mask of the sequence, the slit is at the left edge of the screen, and in each successive mask the slit is just to the right of the previous slit position. The sequence terminates when there is not room at the right side of the screen to display one more full-size slit; a partial-width slit is NOT displayed. This mask sequence is intended to act as a moving spectrometer slit. Or, in other words, it is intended to sample a two-dimensional image in which the only interesting intensity variations are in the horizontal direction; intensity variations in the vertical direction are averaged out. If the image projected onto the DMA is the spectrally dispersed image of a spectrometer entrance slit, the sequence of data points recorded with this sequence of masks would comprise a spectrum, intensity versus wavelength.

In the RasterScan sequence, each mask has a rectangular white region with user-selected height and width, normally small compared to the screen size. In successive masks of the sequence, this region is scanned raster-fashion over the screen, starting at the top left corner, proceeding across the screen to the right edge (one row), moving to the left edge one space down from the top and proceeding across the screen again (second row), and so forth until the last mask has the white rectangle at or near the bottom right of the screen. Only those masks that display the full rectangle are used; a partial rectangle mask is NOT displayed. This mask sequence is intended to sample a two-dimensional image.

In the HadamardLinear sequence, each mask is like several slits of the MovingSlit sequence displayed simultaneously. The user selects the number of elements, which we will call N. The program allows only certain values of N, those values for which the program can construct a Hadamard matrix of size N (N rows and N columns). The value of N must be such that N, N/12 or N/20 are powers of 2. The sequence comprises N-1 masks, each of which is a different combination of N/2 white slits and N/2-1 black slits (N is always an even number). The N-1 data points corresponding to these N-1 masks can be mathematically manipulated to give a different set of N-1 values, which would be nominally the same as the first N-1 values that would be recorded by a MovingSlit scan with the same slit width. The difference is that the Hadamard scan gives a better trade-off between total data acquisition time and certain types of noise in the data. The maximum number of slits allowed is 799 (N = 800) corresponding to a slit width of 1 DMA pixel.

The HadamardFolded sequence is analogous to the RasterScan sequence, just as the HadamardLinear sequence is analogous to the MovingSlit sequence. Each mask in the HadamardFolded sequence is a pattern of N-1 rectangular regions, N/2 of which are white and N/2-1 of which are black. If N-1 is a prime number, each of the rectangular regions is like a slit, being as high as the screen, and the N-1 rectangular regions are displayed side by side. In this case, there is not much point in using the HadamardFolded mask sequence. On the other hand, if N-1 is factorable, e.g., if N-1 = I×J, with I and J both integers greater than 1 and less than N-1 and I greater than J, then the pattern of rectangles is "folded" into I columns by J rows, and each rectangle is more nearly square than the slit shape. The N-1 data values from this sequence can be mathematically manipulated to get a set of N-1 different values that are nominally the same as the N-1 values that would obtain from the **RasterScan** sequence with the same size of rectangular region. Again, the advantage of the Hadamard sequence is the improved time-noise trade-off. The maximum number of elements that the current program allows in a Hadamard image is 6,399 (N = 6,400) producing an 81 × 79 element image where each element corresponds to a 9 × 7 box of DMA pixels. Larger Hadamard matrices can be generated but better memory management schemes will need to be developed to handle them.

## Results and Discussion

The simplest, most direct way to operate the DMA is via the TI DLP processors which are the basis of the TI provided *engine* for all DMA based projectors. The single DMA chip DLP processor, such as in the Davis DL450 receives the incoming image information and determines the contribution of each color at each pixel element. The DMA mirrors are then switched in sync with a spinning filter wheel containing red, green, blue and a clear section. The individual mirrors can be switched at rates of up to 50,000 times per second. The filter wheel spins at a rate in sync with the screen refresh rate (e.g., 60 Hz). The individual mirrors are switched on and off for lengths of time during each color section of the wheel cycle to give the individual contributions for each color presented. Each cycle of the wheel occurs in less time than is discernable by the human eye. Figure 10 is a trace from the PMT showing the basics of the DLP processing for the colors black, white, red, green and blue. The wheel actually cycles at twice the screen refresh rate of 60 hz. Even with a screen color of white, there is considerable switching of the mirrors during each section of the filter wheel.

The noise contributions of this continuous mirror switching by the DLP processor can be significant. In fact, when scanning the DMA using a single analog-to-digital (A/D) conversion for each mask, the noise for pixels where there is appreciable light intensity is high enough to effectively decrease the effective S/N for those masks. During Hadamard imaging, the S/N actually decreases significantly rather than increases, because most measurement masks have a significant number of pixels with measurable signals switched on. The *noise* in the resultant signal can be minimized by signal averaging for periods of at least 8 milliseconds (i.e., at least one cycle of the filter wheel). Alternatively, the application of an electronic time constant filter to the signal can effectively eliminate the effect of the continuous mirror switching. The PTI, Model 814 PMT detection system has user selectable time constants ranging from 0.05 to 500 milliseconds (by factors of 10). Figure 11 demonstrates the effectiveness of the application of the longer time constants to the output signal. Unfortunately, after the application of a spectroscopic or

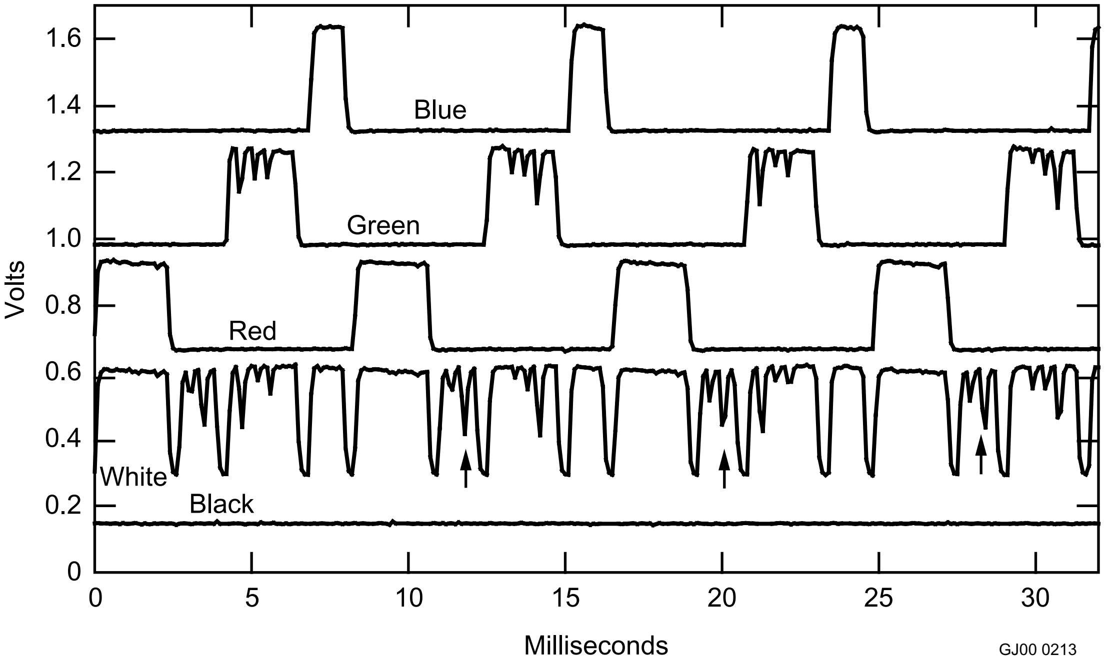

**Figure 10.** DMD activity, using the TI DLP processing electronics when illuminated by a constant energy source, with screens set to black, white, red, green, and blue. The arrows correspond to the *clear* section of the filter wheel used in the TI DLP processor.

imaging mask to the DMA, one must delay for a period at least as long as the time constant to record the signal. To optimize data collection speed, time constants and associated delays in the range of about 8.3 to 17 milliseconds should be used.

To assess the characteristics of the DMD imager/spectrometer using the TI DLP processor electronics, simulated spectra/images, the modified DMA projector was placed in a light tight box. At one end of the box, a mask with a series of holes was placed and through which either room light or light from a dc source allowed entered the box. Figure 12 shows a raster scanned image and a Hadamard-scanned image at the maximum resolution MA13 allows for a Hadamard image. As expected, the Hadamard image has reduced noise and a significantly enhanced S/N. Table 5 shows the improvements in the standard deviation and S/N for normalized data from Hadamard and raster scanned images obtained under identical conditions. The averaging of points for each mask written to the DMA generally improves the S/N by the expected factor. The S/N of the Hadamard images/scans with one data point per mask are generally the same as the corresponding raster scanned image. This S/N enhancement is not as great as would be predicted for unknown reasons.

For spectroscopic and imaging applications of the DMA, the cycling of the mirrors by the TI DLP™ Processor electronics as shown in Figure 10 and 11 is less than optimal because it severely limits the rate at which spectra and images can be obtained with reasonable S/N. Operating the DMA as a video display device using the DLP processors also potentially limits the application of the DMA for rapid kinetic studies because the mirrors will not remain *on* continuously during rapidly decaying signals. An additional problem with the operating the DMA device via the DLP processing electronics is that Windows generally does not allow more than one video display device to be employed at one time. When two video display devices are allowed, they are generally operated as a single “wide” screen. Thus making an

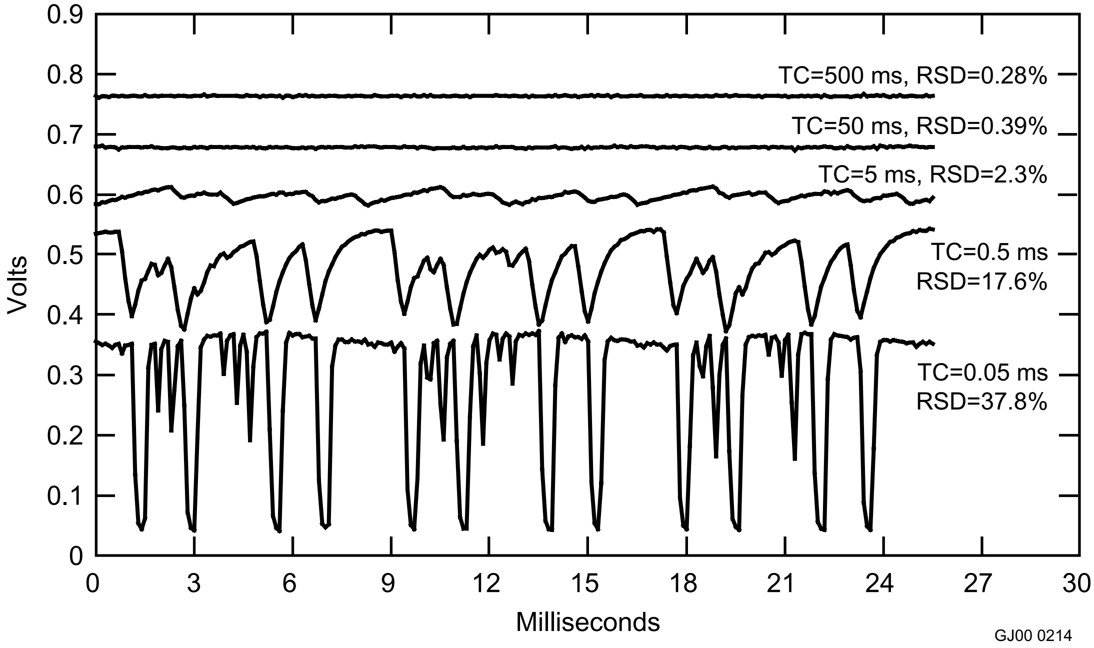

**Figure 11.** DMA activity, using the TI DLP processing electronics when illuminated by a constant energy source, with the screen set to white and the time constant on the PMT signal varied from 0.05 to 599 nukkusecibds.

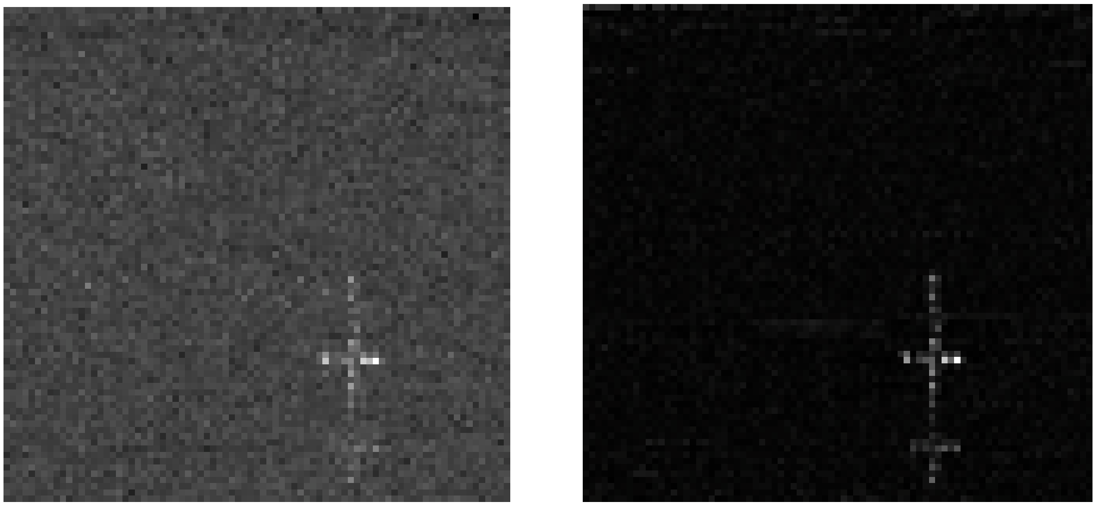

**Figure 12.** Raster scan (left) and Hadamard-acquired images of a pattern of lit dots using the TI DLP processing electronics. Each image element is 9 x 7 DMA pixels. The Hadamard image has 6,399 elements.

**Table 5.** Signal-to-noise characteristics of DMA operating as a spectrometer or imaging device, using the DLP processing with a time constant of 50 ms.

| Analysis Type | Number of Averaged Points per Mask | Standard Deviation | S/N Ratio |
|---|---|---|---|
| 2-D Raster Scan Image | 1 | 0.037 | 20 |
| | 17 | 0.0124 | 76 |
| Hadamard Image | 1 | 0.0128 | 75 |
| | 17 | 0.0087 | 110 |
| Moving Slit Scan | 1 | 0.0443 | 20 |
| | 17 | 0.013 | 74 |
| Hadamard Slit Scan | 1 | 0.0212 | 41 |

imaging spectrometer using two DMA devices would require either two computers (one for each DMA), deploying two masks on a *split* screen, or employment of a more expensive TI DLP processor, which employs three DMD devices.

Rochester Microsystems, Inc. (RMI) of Rochester, NY has been produced a potential solution to the limitations imposed by Windows and the TI DLP processor. In collaboration with the researchers at the Max Planck Institute (microscopy application) and the Rochester Institute of Technology (astronomy application), RMI has developed and is marketing a controller for the 848 × 600 pixel DMAs produced by TI for nonprojector applications. This controller allows the DMA to be operated reliably at full frame update rates of 625–10,000 frames/second. Communication with the DMA using the RMI controller is via a 10base-T Ethernet connection; so, ultimately many DMAs could be controlled at one time.

After learning of the RMI controllers and their potential, we decided not to pursue creating our own controller and purchased one. The MA13 program has been modified to support the RMI controller. In early September 2000, we expect to be able to test the RMI controller for our applications and by the end of September to test a 2-DMA application using a video display device DMA and a DMA in the RMI controller.

## ACCOMPLISHMENTS

- Developed the techniques/methodologies to produce high quality, thin film membranes composed of natural rubber, polyvinyl chloride, vinyl rubber, polyethylene, Viton fluoroelastomer, butyl rubber, polyurethane, and neoprene.
- Tested all of these eight materials against the following series of chlorinated hydrocarbons: chloroform, carbon tetrachloride, methylene chloride, and trichloroethylene.
- The system was modified to use a gas feed stream. Upper parts per billion toluene in argon and nitrogen were observed. This type of configuration could possibly be used to monitor chlorocarbon vapors in the vadose zones at contaminated DOE sites.
- Configuring a membrane as a preconcentrator to an ion mobility spectrometer worked remarkably well and was extremely easy to do. It took only a few minutes to easily detect 10 µl of methylene bromide in 250 ml of water.
- Photoionization IMS spectra for four different organic molecules were produced.
- A DMA based projector was modified to be used as an imaging device or spectrometer.
- A software application has been developed to use a DMA as an imaging device or spectrometer using the native TI DLP electronics.
- To allow multiple DMA devices to be used at one time, a controller recently developed by Rochester Microsystems, Inc., has been purchased.
- The software application has been modified to allow operation of a DMA in the new controller.

## REFERENCES

1. R. A. Baragiola, Electron Emission from Slow Ion-Solid Interactions, New York: John Wiley & Sons, 1994, pg. 190–259.

2. S. C. Brown, *Basic Data of Plasma Physics,* New York: AIP Press, 1994, pg. 259–270.

3. P. F. Little, *Handbuch der Physik*, ed. by S. Flugge, Berlin: Springer-Verlage, 1956, pg 619–622.

4. A. V. Phelps and Z. L. Petrovic, "Cold-cathode discharges and breakdown in argon: surface and gas phase production of seconcdary electrons," *Plasma Sources Science Technology,* 8, 1999, pg. R21-R44.

5. W. Hofer and P. Varga, "Adsorbate Dependent Neutralization of Ions Near A Surface," *Nuclear Methods in Physics Research B2*, 1984, pg 391–395.

6. F. Sauli, "Gas detectors: Recent developments and future perspectives," *Nuclear Instruments & Methods in Physics Research A*, 1998, pg 189–201.

7. Dr. J. Miyamoto, Dept. of Physics, Purdue University.

8. Scott Bauer, "Membrane introduction mass spectrometry; an old method that is gaining new interest through recent technological advances," *Trends in Analytical Chemistry*, 14 (5), 1995, 202–213.

9. "Plasma Chromatography with Laser Produced Ions," D. M. Lubman, M. N. Kronick, *Anal. Chem. 54(9), 1546–51 (1982).*

10. "Discrimination of Isomers of Xylene by Resonance Enhanced Two-Photon Ionization," D. M. Lubman, M. N. Kronick, *Anal. Chem. 54(13), 2289 (1982).*

11. "Ion Mobility Detector for Gas Chromatography with a direct Photoionization Source," M. A. Baim, R. L. Eatherton, H. H. Hill, Jr., *Anal. Chem. 55(11), 1761–66 (1983).*

12. "Effects of Laser Beam Parameters in Laser Ion Mobility Spectrometry," G. A. Eiceman, V. J. Vandiver, C. S. Leasure, G. K. Anderson, J. J. Tiee, W. C. Danen, *Anal. Chem. 58(8), 1690–95 (1986).*

13. "Laser Desorption and Ionization of Solid Polycyclic Aromatic-Hydrocarbons in Air with Analysis by Ion Mobility Spectrometry," G. A. Eiceman, G. K. Anderson, J. J. Tiee, W. C. Danen, *Anal. Letter 21(4), 539–52 (1988)*

14. "Performance of an Ion Mobility Spectrometer for use with Laser Ionization," J. Gormally, J. Phillips, *Int. J. Mass Spectrom., 107(3), 441–51 (1991).*

15. "The Laser Desorption of Organic Molecules in Ion Mobility Spectrometry," J. Gormally, J. Phillips, *Int. J. Mass Spectrom., 112(2-3), 205–14(1992).*

16. N. Short, "Remote Sensing and Image Interpretation & Analysis in Remote Sensing Tutorial (an Online Handbook)," Applied Information Sciences Branch at NASA's Goddard Space Flight Center, http://rst.gsfc.nasa.gov/, Updated: 5/99.

17. P. J. Treado, I. W. Levin, and E. N. Lewos, "Indium Antimonide (Insb) Focal Plane Array (Fpa) Detection for Near-Infrared Imaging Microscopy," *Applied Spectroscopy*, Vol. 48, No. 5, 1994**,** pp. 857.

18. J. F. I. Turner, and P. J. Treado, "Near-Infrared Acousto-Optic Tunable Filter Hadamard Transform Spectroscopy," *Applied Spectroscopy*, Vol. 50, No. 2, 1996**,** pp. 277.

19. M. K. Bellamy, A. N. Mortensen, R. M. Hammaker, and W. G. Fateley, "Chemical Mapping in the Mid- and Near-Ir Spectral Regions by Hadamard Transform/Ft-Ir Spectrometry," *Applied Spectroscopy*, Vol. 51, No. 4, 1997**,** pp. 477–486.

20. W. G. Fateley, R. M. Hammaker, J. V. Paukstelis, S. L. Wright, E. A. Orr, A. N. Mortensen, and K. J. Latas, "Application of a Two-Dimensional Hadamard Encoding Mask for the Imaging of Thin-Layer Chromatography Plates by Laser-Induced Fluorescence or Surface-Enhanced Raman Scattering and for Use with a Photoacoustic Detector to Generate Three-Dimensional Photoacoustic Images," *Applied Spectroscopy*, Vol. 47, No. 9, 1993, pp. 1464–1470.

21. Q. S. Hanley, P. J. Verveer, M. J. Gemkow, D. Arndt-Jovin, and T. M. Jovin, "An Optical Sectioning Programmable Array Microscope Implemented with a Digital Micromirror Device," *Journal of Microscopy-Oxford*, Vol. 196, 1999, pp. 317–331.

22. R. A. DeVerse, R. A. Hammaker, and W. G. Fateley, "Hadamard Transform Raman Imagery with a Digital Micro-Mirror Array," *Vibrational Spectroscopy*, Vol. 19, 1999, pp. 177–186.

23. L. J. Hornbeck, "From Cathode Rays to Digital Micromirrors: A History of Electronic Projection Display Technology," *TI Technical Journal*, Vol. July–September, 1998, pp. 7–46.

24. Chakrabarti, "Ground Based Spectroscopic Studies of Sunlit Airglow and Aurora," *Journal of Atmospheric and Solar!Terrestrial Physics*, Vol. 60, 1998, pp. 1403–1423.

# Intelligent Nonintrusive Methods for Characterization

**Timothy J. Roney, John C. Determan, Dennis C. Kunerth, Timothy A. White**

## SUMMARY

This research addresses measurement interpretation and advanced measurements for use in characterizing nuclear waste and resolving industrial inspection problems. Three tasks are emphasized: interpretation and automated processing of nuclear waste characterization data, material characterization using electromagnetic methods, and three-dimensional imaging in constrained environments. All three areas of research pose challenges of a basic nature but also hold promise for useful application in several DOE programs, including transuranic waste characterization and spent nuclear fuel characterization. Research in interpretation and automated processing focused on developing an expert system to validate nuclear assay data from waste characterization systems installed at the INEEL. In FY 2000, we completed a prototype expert system. INEEL data validation physicists tested the system, with highly encouraging results. Significantly, the INEEL has decided to fund deployment of the expert system. Two additional projects funded by groups outside the INEEL have resulted from this research. FY 2000 research in electromagnetic material characterization concentrated on assembly and testing of an eddy-current system having neural network-based data processing capabilities. The research developed neural network processing techniques to improve the amount and quality of information that can be extracted from pulsed eddy-current test signals. Various neural networks were implemented and tested. The work demonstrated that neural networks can be successfully trained and applied to drum inspection problems. The objective in 3-D imaging research was to develop capabilities to acquire and process 3-D images on objects in challenging imaging situations. We designed and completed a laboratory x-ray imaging system in FY 2000 and used it to acquire data representing imaging systems that may be deployed in difficult field circumstances. Questions regarding system alignment and scatter for 2-D and 3-D x-ray imaging systems were addressed in collaboration with the University of Utah. Results from both studies proved to be very useful in improving image quality of existing imaging systems at the INEEL and within the medical imaging community.

## PROJECT DESCRIPTION

## Task 1. Automated Processing of Waste Characterization Data

Intelligent processing for waste characterization research had two thrusts in FY 2000: (1) development of a prototype expert system for review/validation of nondestructive waste assay data and (2) development of a system for automatically generating classification rules from data used in expert systems. Note that the expert system is being deployed at the Stored Waste Experimental Pilot Plant (SWEPP) at the INEEL as a direct result of this research. In addition, the research has generated two external customers for the expert system.

### Prototype Expert System

Nondestructive assay waste characterization data generated for the National Transuranic Program must be of known and demonstrable quality. We are developing, therefore, a generic expert system framework to review and validate nondestructive assay data. Each nondestructive assay measurement must receive independent technical review by a qualified expert. With hundreds of raw and reduced data acquired on each waste drum and hundreds of thousands of such drums in the national inventory, a large and costly data review/validation effort is mandated. The generic expert system implements the process of data review within a set of expert system rules, and within an object-oriented framework that can be easily customized for application at sites with different nondestructive assay configurations and waste inventory properties. The program, NDA-DRXS (NonDestructive Assay–Data Review Expert System), receives as input all the neutron and gamma assay measurement data from a batch of waste drums and verifies the data against a wide variety of criteria, including known constant values that must be matched, known limiting values that must not be exceeded, and many internal consistency checks. The system outputs a list of messages indicating which data were successfully reviewed, which data failed the review, and what the final disposition of the drum should be (i.e., accept, reject, remeasure, recalculate, or analyze more thoroughly). This system will likely reduce the review effort ten-fold, as all the necessary checks are performed within seconds, leaving the reviewer to isolate the root causes of problems detected in any drum.

Central to the system is a set of rules that captures the generic logic of the data review process. These rules are grouped into phases of operation, as shown in Figure 1. The diagram indicates that the system transitions through a sequence of phases where distinct activities take place. There are separate phases for initializing review of overall batch characteristics, as opposed to initializing the system for review of individual assays within a batch. Rules in these phases initialize item-list *objects* (a basic unit of software in an object-oriented programming language) that are used to control the review process. The verification phase then follows, in which applicability of rules to specific data objects is checked, and if the rule is applicable to the object, the specific data review is performed. At this stage, messages

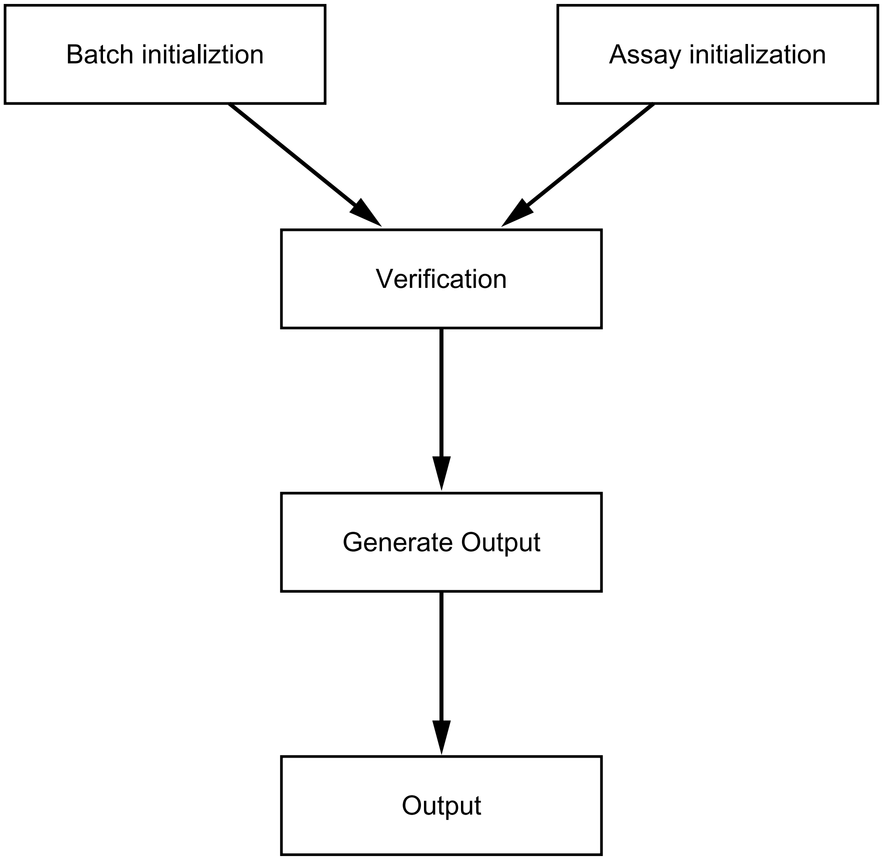

**Figure 1.** Schematic of the NDA data review process.

regarding the inapplicability of a rule to an object, or the success of a specific check, are created. Items that were either inapplicable to or successfully checked by a particular rule are removed from the item-list controlling review by a particular rule. By the end of this phase, the item-lists contain only data objects that failed tests to which the objects were applicable. In a subsequent phase, Generate Output, messages indicating failure of specific objects against specific rules are created, by referencing those objects that still remain in an item list, as are messages regarding the final disposition of the drum. In the final phase, Output, all messages created by the system are printed in a specific order to facilitate interpretation.

Figure 2 shows an abbreviated object model of the system. At the highest level, there is software generic to any implementation. Software specific to a given implementation are derived from these generic data objects. Item-lists are used for controlling the data review process, and the specific data_item objects to be checked by each type of rule are included in an item-list for that rule. The data_item object defines fields and operations that all specific data objects will contain; specific data objects to be reviewed are derived from data_item, and are specific to a given implementation. Summary lists are generic to the system, but the lists' contents are specific to a given implementation. Summary lists include all the item-list objects for rules that result in a given classification.

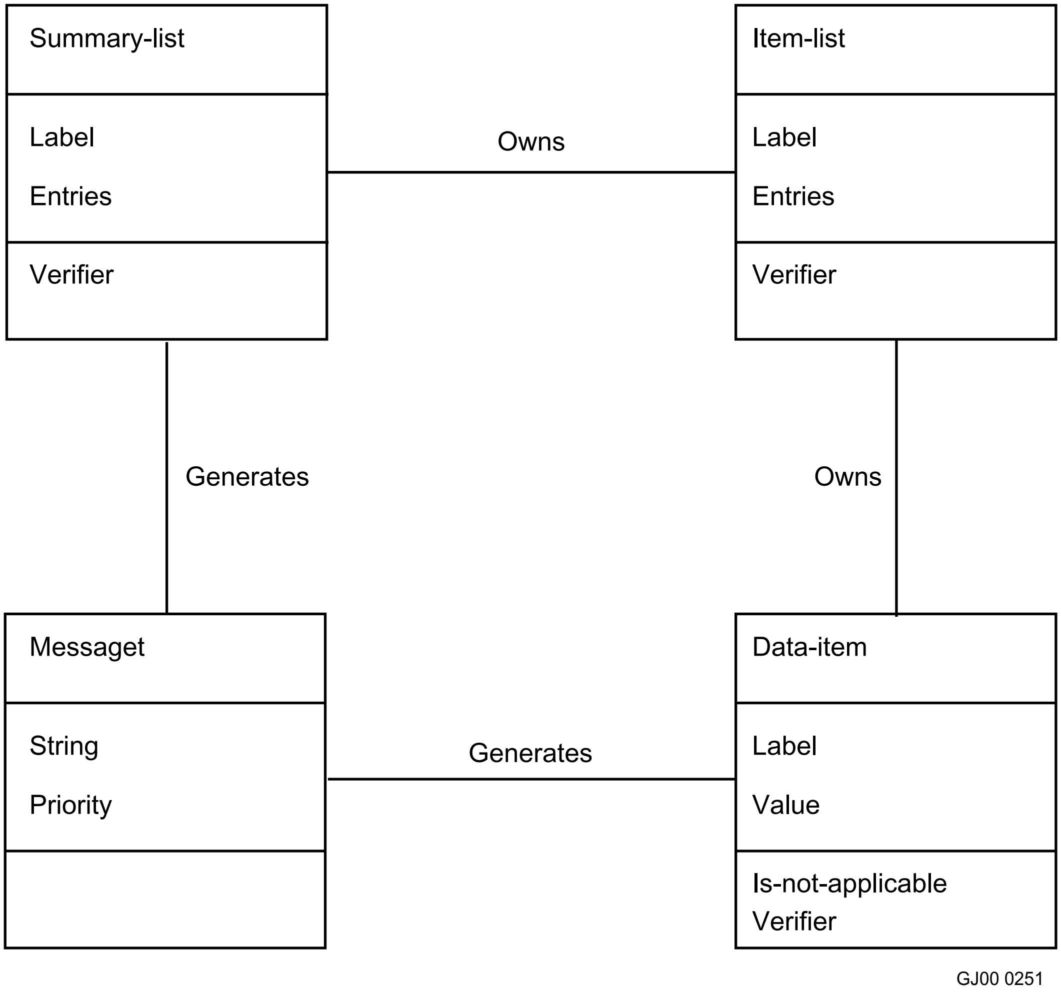

**Figure 1.** Abreviated object model of the system.

Development of the rules for the SWEPP data review expert system occurred in three stages: (1) rules for verifying PAN data from sludge drums, (2) rules for verifying gamma spectroscopy data, (3) rules for verifying PAN and gamma data from debris waste drums. The rules applicable to sludge waste forms were considered also applicable to debris waste. The rules presented have been corrected based on review and testing through the end of FY 2000; however, further testing and review will be performed. One notable outcome of the review was that the rules developed specifically for debris waste were determined to be valid for sludge as well; hence, there is really only one set of rules, all equally applicable to sludge or debris waste forms. While some rules verify PAN data and others verify Gamma data from a functional point of view, this is not a significant distinction.

Development of the Nondestructive Assay Data Review Expert System is nearly to the point of deployment at the SWEPP Facility. Direct funding has aided the effort to produce the required software quality assurance documentation. Deployment is currently scheduled for the first quarter of FY 2001. Specifically, design of the user interface has been improved based on feedback from beta-testing by SWEPP data reviewers, errors in rule specification have been detected and corrected, and additional rules have been identified and coded.

Four software quality assurance documents are associated with this project, all of them currently undergoing review: software requirements specification, software test plan, software design document, and a user's manual. When these documents have been reviewed and approved, formal acceptance testing can be performed. At this point, the system can be installed, and after a minimum of 1 calendar month of operational experience, an audit can be performed. At that time, the code would be fully certified by WIPP. Additional information on the expert system may be found in the following two reports:

> John C. Determan, Greg K. Becker, *Application of Expert System Technology to Nondestructive Waste Assay Data Review*, INEL/EXT-98-00016, February 1998.
>
> John C. Determan, Greg K. Becker, Scott D. Matthews, *Development of the Nondestructive Assay Data Review Expert System,* INEEL/INT-2000-01271, September 2000.

### Automatic Rule Generation

Generating rules in expert systems is typically achieved manually by interviewing experts in the field being modeled and by coding the rules in an appropriate language. Generating rules automatically allows determining rules from knowledge implicitly embedded in data that an expert has classified. This is useful because a primary reason for developing an expert system is to relieve overworked professionals who have no spare time for eliciting knowledge. We have developed a genetic algorithm (GA)-based data clustering algorithm for generating fuzzy logic[1] expert system rules. Genetic algorithms are used in diverse fields, such as simulating biological and social systems, and for optimizing scientific and engineering design problems. We have used them in the later context. They automate exploration of a large design space in a manner that is biased toward finding the best permutations of design parameters. In our work, they were used to examine large amounts of example data and find rules that predict the patterns in the data.

GAs derive their name from the fact that they mimic the processes of evolution and natural selection to determine optimized solutions to problems. A data structure represents a problem to be solved (e.g., a collection of key design parameters) and is referred to as a genome or chromosome, and, continuing the analogy, the individual parameters are referred to as genes, and their possible values are alleles. An initial population of these genomes is created, either randomly or in some more intentional manner. In any population, some members will represent better solutions to the problem at hand than others. GAs use some mathematical estimate of the worth of a solution, called a fitness function, to distinguish among the solutions in the population. The processes of genetic reproduction and mutation are also mimicked. GAs follow a cycle of the form (1) generate a population, (2) use a fitness function to measure the worth of each member, (3) use the fitness function to select members of the population for reproduction into the succeeding generation (where all members have some chance of being selected, but members with better fitness are more likely to be selected), and (4) use the reproductive and mutational operators to form a new population from the genes of the members selected for reproduction. An example that comes to mind is the manner in which nondimensional parameters are used in the design of prototypes for scaled testing. As long as the significant parameters of the problem remain in specified ranges, the forces acting on the scaled prototype represent the forces acting on the full-scale design. Experimenters could design a function of the nondimensional parameters of the problem that indicates which designs are better; however, the calculation would not be able to indicate the best solution. In this example, a generate-and-test procedure would be applied until a reasonably good solution was found. A GA, in the context of engineering design, is an automated, smart, generate-and-test algorithm. By mimicking reproduction and natural selection, GAs quickly focus even a random initial population toward the most promising regions of the design space, and find good solutions.

Data clustering is a statistical method of detecting commonality between data points and classifying the data points into clusters of similar data points. Classification algorithms generally divide sample data into two groups: test data and training data. The training data are used to develop the classification method; the test data are used to verify the performance of the method. We have examined the ability of GAs to perform data clustering on training data, with a method we call genetic data clustering. Rule generation algorithms must face two major questions: (1) how many clusters exist in the data, and (2) how are ambiguous regions of the data, where clusters may overlap, treated? The first point determines how many rules are found. The second affects rule accuracy. Data clustering algorithms possess adjustable parameters that affect the number of clusters found, and the membership profiles of the clusters. We used GAs in our initial work to determine values for these adjustable parameters, but with some experience, we realized that GAs could tackle data clustering more directly and efficiently. Instead of representing algorithm parameters, the genome could represent the cluster membership profiles and the number of clusters in the data. An advantage of performing genetic data clustering is that GAs are probabilistic, and ambiguous data points have some probability of being assigned to any cluster. With a good objective function, and appropriate genetic operators, natural selection should find good data clusters. However, grouping problems are difficult for GAs, due to tight constraints on how the genome can be mutated and crossed. In grouping problems, a GA must neither duplicate nor remove alleles from the genome, and ordinary genetic operators do not guarantee these properties. Therefore, the genetic data clustering problem could be expected to shed light on an area of interest in the Evolutionary Computing community: combinatorial or grouping problems.

GAs cluster the data, but the next step is to form rules from the clusters. If the data points consist of features X and Y, and classification Z, then each cluster of data implicitly represents a rule of the form “if X and Y fall in specific ranges, then Z will tend have a specific value.” Different functional forms can be imposed on the data to relate X, Y, and Z, and the assumed functional form is referred to as the rule representation. We assumed that the rule inputs and output were related through Gaussian functions.

We introduced several innovations that improve both the speed of the rule-generation process and the accuracy of the generated rules. Our work also contributes to the application of GAs to combinatorial problems in general. First, we inverted the rule generation process described above. Our genetic data clustering (GDC) algorithm first locates data points in the training data that belong together; it then calculates exact means and standard deviations over these clusters; finally, it builds fuzzy rules from the cluster means and standard deviations, as before. This procedure bypasses the time-consuming process of backpropagation. We designed crossover and mutation operators specifically for data clustering. We used self-adaptive techniques, including variable length chromosomes and a variable probability of mutation. We performed tests to examine the effect of the probability of crossover.

We tested our method on both large and small data sets from the literature. The Fisher Iris data relate the species of Iris plants to a set of four characteristics: the widths and lengths of the petals and sepals of Iris plants from four species. There were 300 plants, 75 from each species, in the study. We used these data because they frequently appear in the literature and would be familiar to researchers. Another frequently used data set is a collection of LANDSAT satellite image data. The set consists of tens of thousands of pixels of data, where each has been painstakingly classified (manually) as to the soil/vegetation characteristics represented by the pixel. The size of this data set makes it a more significant challenge for classification.

We enhanced the automatic rule generation system to work on large data sets, and tested it against both large and small data sets from the literature. The tests revealed both strengths and weaknesses of the approach, and indicate where future work should be undertaken. The primary conclusions derived from this work are as follows:

- We used the Fisher Iris data and LANDSAT satellite image data to compute ideal classification rules by a simple manual procedure. We used these rules to show that the GDC algorithm computes rule sets are as good as the rule representation format will allow.

- We tested the algorithm against several data sets, both large and small, including the Anderson and Fisher Iris data, a LANDSAT satellite image data set, and three sets of nondestructive assay waste characterization data. Overall, the results indicate that the GDC algorithm achieved average performance compared to a suite of classification algorithms found in the literature.[2] The rule representation format was the primary limitation to performance.

- An improvement to the rule representation format produced a considerable reduction in the error rate of the GDC calculations on the satellite image data (and to a much lesser extent on the Iris data). This observation confirms that a primary limitation to performance of the GDC algorithm is the rule representation format.

- Comparison of our results on the above data sets with results from the ELENA project[3] indicates that classification rules generated by our method achieve about average results, but it also indicates that the rule representation, not the performance of the GDC algorithm, is the primary limitation to performance.

- We tested three sets of neutron assay data with the GDC algorithm, and these tests showed moderate to high levels of performance. The preceding conclusions, however, shed some light on limitations that could be affecting performance of the GDC algorithm on the neutron data sets. The neutron data sets are quite small, and while their performance is good, it is likely that a primary limitation in their performance is the paucity of data. It is also likely that, as with the satellite image data, the rule representation form is a limiting factor in their performance. Alternative rule representations should also be considered, but only after addressing the issue of data set size.

Future work in automated rule generation should concentrate on the following:

- Investigation of different rule representations to see what different results they obtain with different inductive biases. Geographic data, such as the satellite image data, are possibly fractal in nature, and this consideration might lead to a whole different range of basis functions for rule representation.
- Detailed study of the nature of waste nondestructive assay data to suggest better rule representations for these data. In addition, more thorough investigation is needed in the area of an appropriate data input set for rule generation from waste nondestructive assay data.

In a somewhat different direction, the GDC could also be compared with rule generation by neural networks, or hybrid neural-genetic methods.

Over the past year, we presented our work at two widely recognized conferences and received inquiries from four organizations concerning NDA-DRXS. These conferences were the 7th Nondestructive Waste Assay Characterization Conference, Salt Lake City, Utah, May 23-25, 2000 (Determan and Becker, 2000),[4] and Spectrum 2000, Chattanooga, Tennessee, Sept 24-28, 2000 (Determan, Becker and Matthews, 2000).[5] The organizations interested in NDA-DRXS included two private companies that provide NDA services, Antech, and Canberra Industries, both in regard to work being performed at the Rocky Flats Environmental Test Site in Colorado, and two DOE facilities, Los Alamos National Laboratory and Savannah River Site. Work is currently in progress for Canberra Industries and Los Alamos National Laboratory to apply NDA-DRXS to their needs.

## Task 2. Automated Material Characterization Using Electromagnetic Measurements

The objective of this task is to develop real-time, multifrequency eddy-current data inversion technologies for automated material characterization and nondestructive evaluation. The significance of the work is development of data processing tools that permit the use of pulsed/multifrequency eddy-current technologies for material characterization, including automated/real-time applications for various complex structures. Some of these complex structures of specific interest to DOE-EM include spent fuel, waste storage containers, protective metal coatings, and composite or graded metal structures. Previous work using advanced pulsed/multifrequency eddy current techniques for the determination of waste storage drum integrity demonstrated the need to develop improved data processing techniques.[6,7] Mutifrequency techniques inherently provide more information than conventional single/dual frequency approaches, but methods to extract the information have been limited to peak or minimum amplitude sampling in a specified time window. This approach is satisfactory for tests having only one or two variables, but for inspections where specimen conditions such as internal/external corrosion, dents, labels, and/or complex geometry exist (see Figure 3) more test variables are introduced. Consequently, more information needs to be used to identify and characterize the various signal contributions and extract the desired information.

We have investigated and used two approaches for eddy-current data inversion: model-based and neural networks. Model-based approaches are relatively complicated, making implementation difficult and typically slow, but have potential to address complex material conditions. Neural networks are simple and fast but limited by training methodologies and scope. The application, along with the attributes/limitations of each inversion approach, will determine which technique can be applied. The desire to implement a technology that can provide real-time processing of data resulted in our emphasizing a neural network approach.

**Figure 3.** Extended storage of waste drums has resulted in degradation. Nondestructive evaluation techniques will be required to determine container integrity.

We developed and tested several neural networks using data collected from carbon steel calibration strips containing various thickness steps, ranging from 20 to 70 mils. Lift-off was introduced into the measurement process via twelve nonconducting shims ranging from 0.5 to 30 mils. We determined that the best results were obtained from networks using selected eddy-current signal features believed to be characteristic of changes in both thickness and liftoff. Figure 4 shows the definitions of the signal features selected. Figures 5 and 6 illustrate how the features change with thickness and lift-off. The neural networks and training found to be functional used three layer back propagation with nine nodes in the input layer, five nodes in the hidden layer, and one output node. Typically, the nine feature inputs are first scaled by a sigmoid squashing function to obtain outputs between 0 and 1:

$$Sig(x) = \frac{1}{1+e^{-x}} \quad . \tag{1}$$

The sums of the weighted inputs are taken in the hidden layer and weighted and summed again in the output layer. The value is then squashed by the sigmoid function, and the thickness/lift-off is output in percent of the trained range. There are two networks used, one for the thickness determination and one for the lift-off determination.

Figure 7 presents the test results from one specific set of neural networks and data set. The plot compares actual thickness and lift-off to neural network-determined values. For this test, we acquired

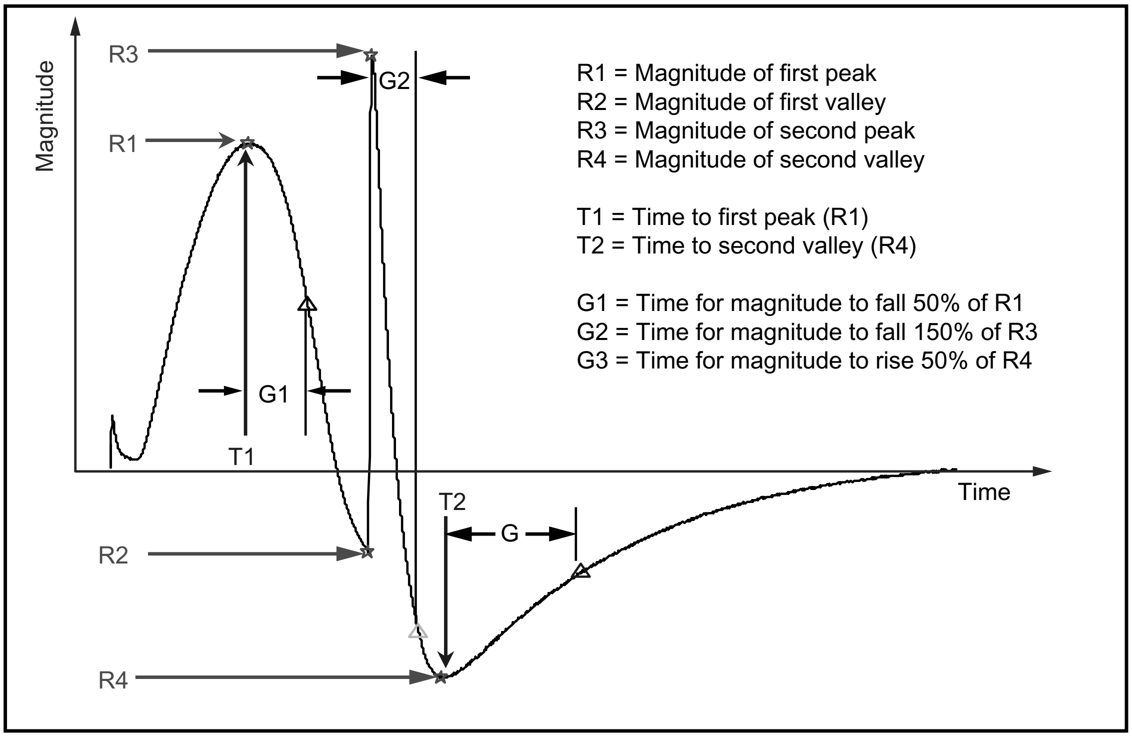

**Figure 4.** Selected eddy-current signal features were used to train neural networks. Features were selected based on their response to changes in thickness and lift-off.

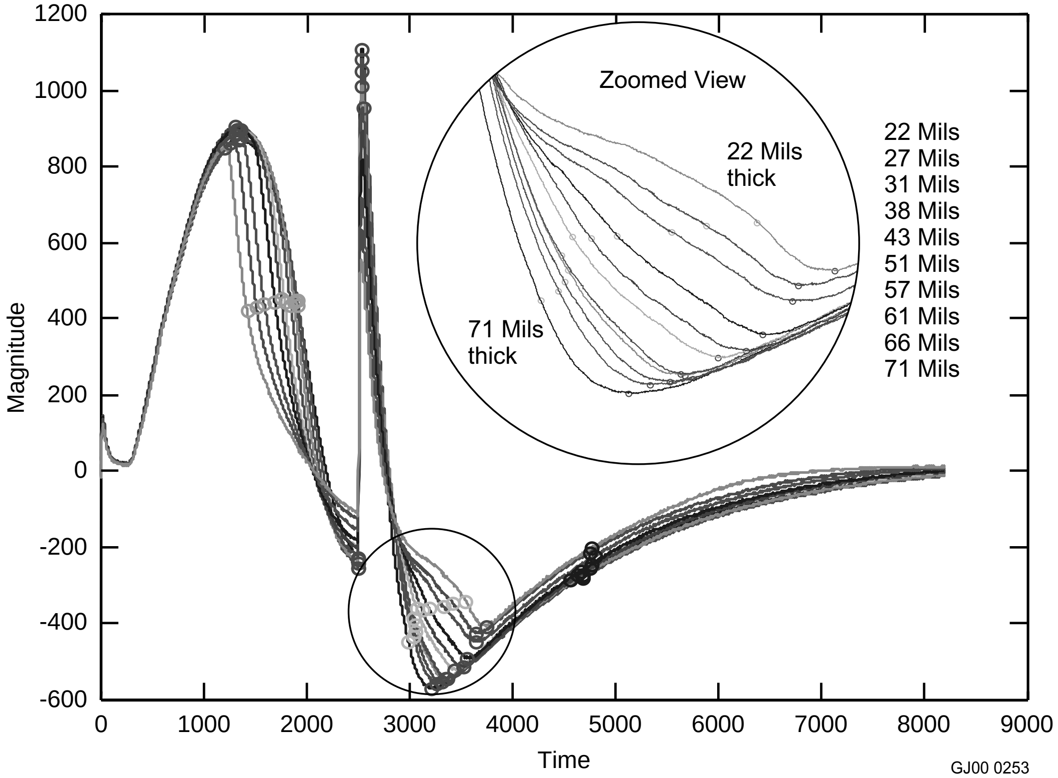

**Figure 5.** Calculated features with change in thickness.

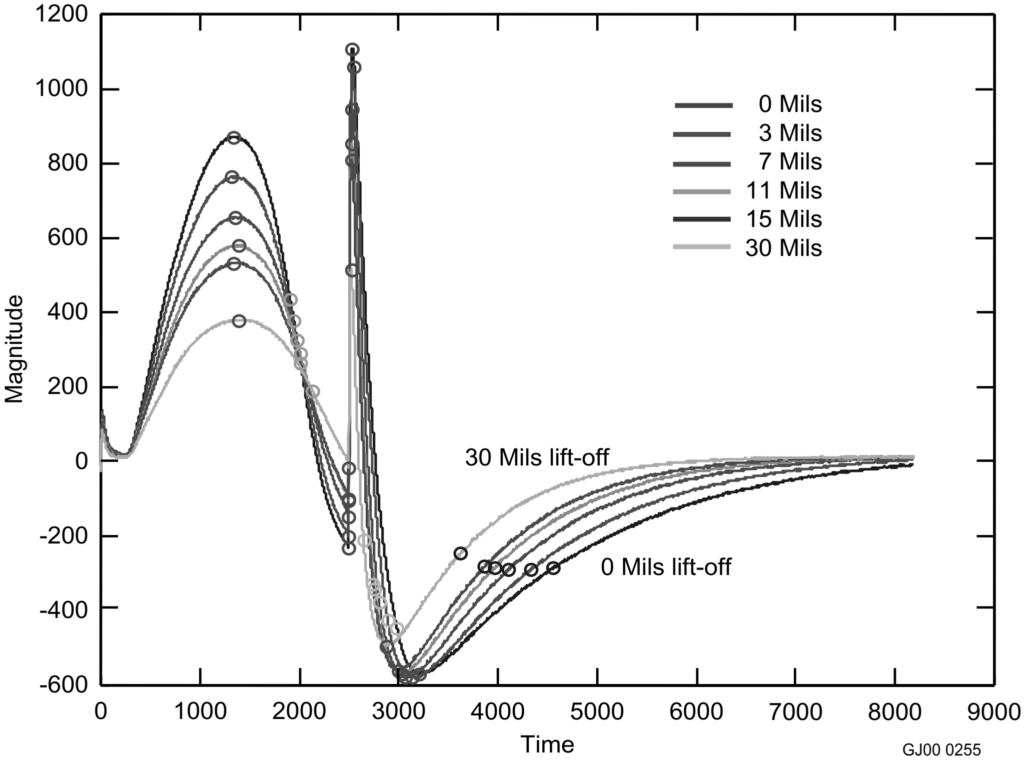

**Figure 6.** Calculated features with change in lift-off.

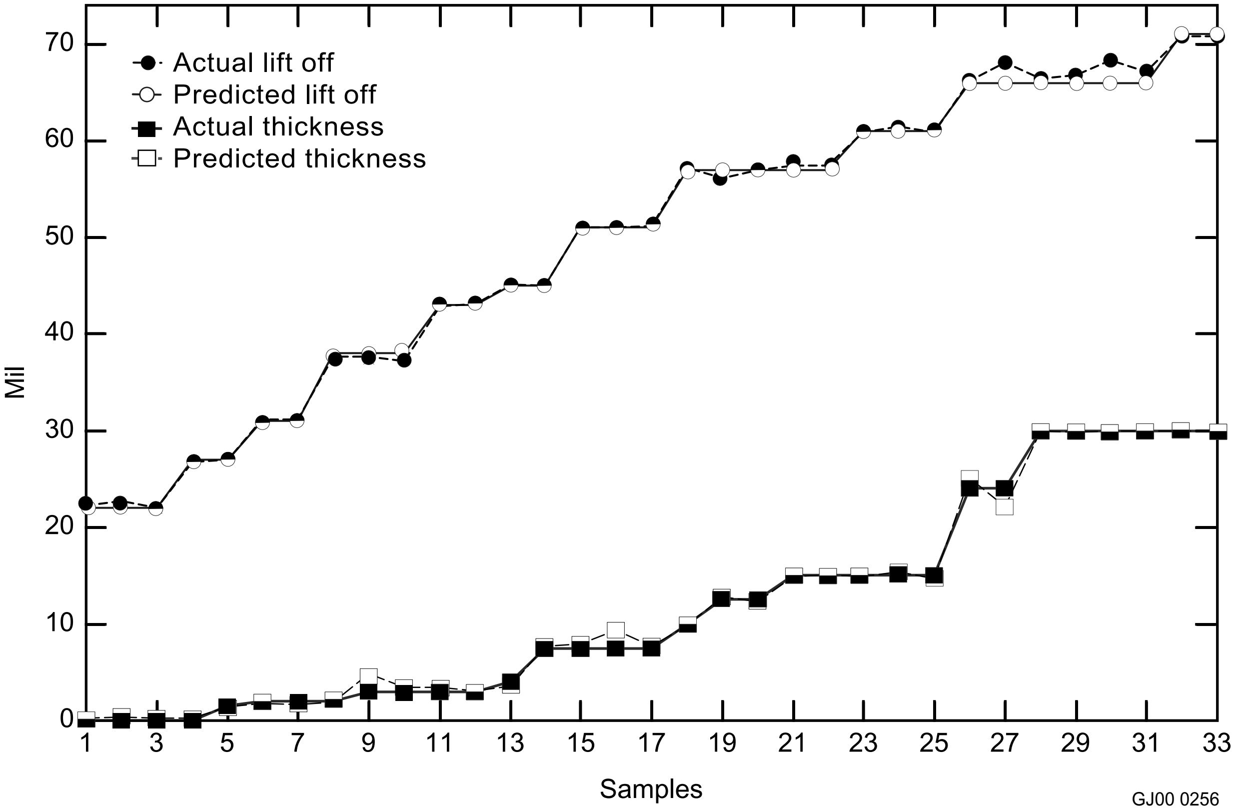

**Figure 7.** Comparison of actual thickness and lift-off values to those determined by neural network.

132 waveforms using various lift-off and plate thickness values. Random samples of three fourths of these waveforms were used to train the network. The other quarter was used to test the accuracy of the network. The thickness prediction closely follows the actual values until it reaches the upper range of the thickness where increased error is observed. Whether this is from lack of electromagnetic field penetration or inadequate network training has not been determined. The significance of the results obtained is that neural networks can be used as an efficient data processing tool for pulsed eddy-current responses.

The objective of the work in FY 2000 was to develop a pulsed eddy-current system that implements the neural network technology and is capable of scanning curved surfaces typical of waste storage drums. Figures 8 and 9 present a schematic of the system developed and a test sample geometry. We implemented a software approach to the neural network as a means to obtain versatility, but this resulted in a reduced scanning speed owing to the processing time for the data. The network itself is fast, but the feature extraction involves a significant amount of data processing within the MatLab environment. Modifications to the system that will improve speed include a faster processor and incorporation of the feature extraction code directly into the LabVIEW environment where motion control and data acquisition already occurs. Other issues addressed during FY 2000 included probe design and the means to accommodate test parameters such as labels, surface corrosion, variations in electrical conductivity and magnetic permeability, and dents.

Of interest is a probe design that minimizes the effects of geometry, i.e., curved surfaces and edges, yet provides sufficient field to penetrate the highly permeable carbon steel sheet. Of the various probe designs evaluated, a cup-core design using a high permeability core material proved to be the most effective, providing both adequate penetration and a means to locally confine the field, therefore reducing edge effects. We addressed probe wobble on the curved surfaces by reducing size, machining the probe face to match the radius of curvature of the test samples, and/or adding mechanical stops that maintained constant lift-off relative to test sample surface.

Inspecting actual objects such as waste drums will introduce additional test parameters that may affect the eddy-current response, and thus measurement accuracy. The ability to train a neural network to identify and address each of the different variables is limited by the ability to acquire a significant number of representative responses. Representative responses can be obtained from actual test samples or from analytical models, but both approaches require significant output of resources and effort. A possible means to overcome the problem is to train a neural network to identify responses atypical of either thickness or simple lift-off variations. However, this approach is limited by its inability to provide information regarding the source of the atypical response or differentiate contributions from variables that modify the eddy-current response in the same fashion as thickness or lift-off. To investigate the potential of this approach, we trained and tested networks using typical and atypical signal feature data sets. The atypical data sets were generated by randomly modifying individual features. Testing of the networks using independent data sets demonstrated that successful determination of measurement character could be made 98% of the time. These results suggest that for the waste drum example, signal features representing thickness and lift-off have a characteristic pattern, and that small variations from this pattern can be recognized and flagged by a neural network. Although not demonstrated in the laboratory, this provides the means to assess measurement confidence.

## Task 3. X-ray Imaging in Constrained Environments

An objective of this task was to develop capabilities to acquire and process 3-D images on objects inaccessible from all sides. This situation arises in spent nuclear fuel storage and industrial processing.

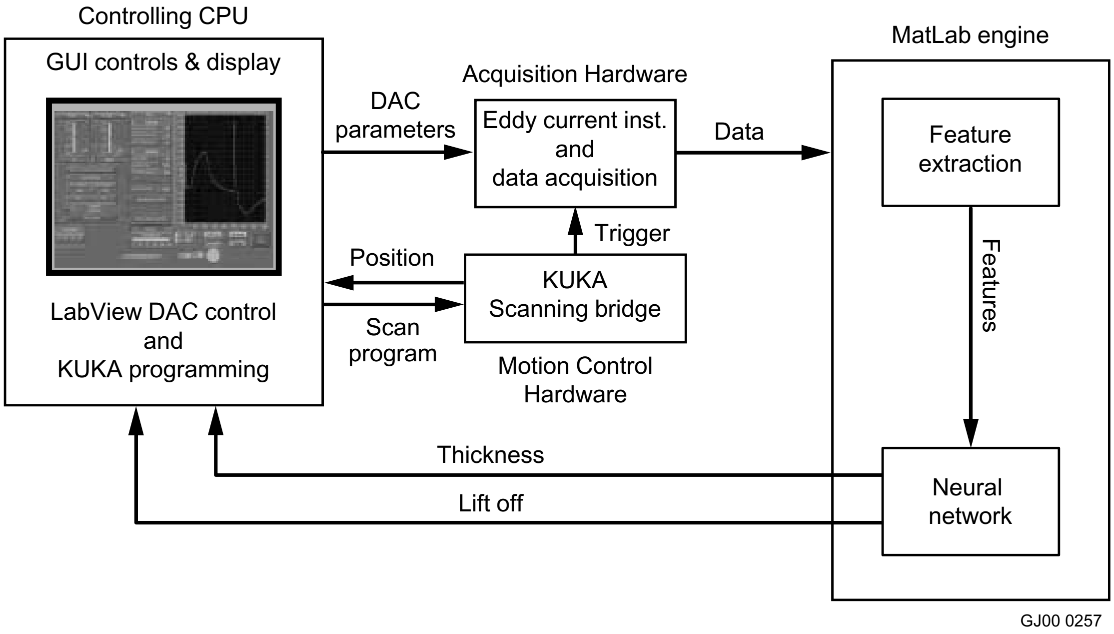

**Figure 8.** Pulsed eddy-current system configuration.

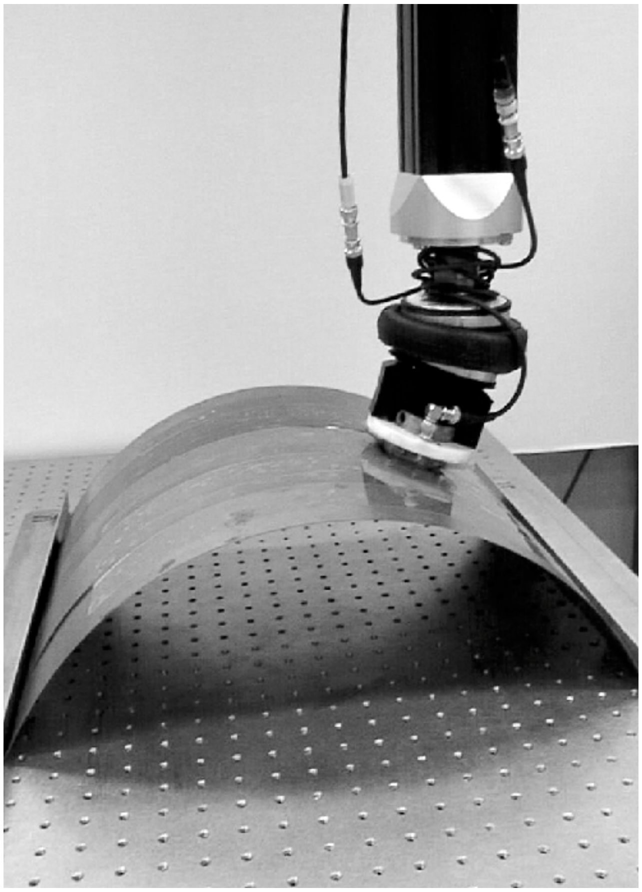

**Figure 9.** Test sample geometry.

Before FY 2000, we designed and built a transportable imaging system capable of digital radiography (DR) and three-dimensional (3-D) computed tomography (CT). Software to control motion, data acquisition, and image display was written in FY 2000. The system was used to acquire data that allowed system characterization and calculation of system alignment parameters necessary to ensure good image quality in portable imaging systems.

Another goal of this task was to conduct a set of experiments and simulations that would improve our ability to design efficient and effective imaging systems for challenging imaging situations. We used our prototype system above to investigate the effects of Compton scatter[8] and system misalignment[9,10] on image quality. Computer modeling experiments have verified some of the results of the Compton scatter experiments. Collaborators at the University of Utah developed another simulation package to investigate system misalignment issues.

The goals of our three-dimensional (3D) imaging task were to

- Develop data-collection strategies for challenging imaging geometries, i.e., geometries in which access to all views of an object are impossible
- Develop simulation tools to as aids in system design and for understanding imaging artifacts
- Develop data-processing algorithms for processing these data to obtain 3D images of the objects under consideration
- Develop image-processing and visualization tools for conveying the information in the images to an operator/observer.

As an example of an imaging challenge, consider the task of determining the contents of a single container of hazardous material located in a field of similar containers. For conventional 3D x-ray imaging, it is necessary to view the container from all directions. However, in this scenario, it may not be possible to move any of these containers, and thus it may be impossible to achieve a good (access from 360°) imaging geometry. Information about the contents of the container—type of item, number of items, condition of items—may be required, and this information may be difficult to obtain. Determining as much information as possible about this container from a limited number of views, and conveying that information to an operator, is the goal of this subtask.

As a tool toward achieving these goals, we have built and tested a laboratory x-ray imaging system that can obtain images in a variety of imaging geometries. In addition, we have worked with researchers at the University of Utah Medical Imaging Research Laboratory to develop algorithms for processing images from a variety of imaging configurations, including incomplete-projection data sets. We have also developed image visualization and manipulation code that has been used extensively in this and other projects. The following sections discuss the hardware and software accomplishments of this task and suggest directions for continued research.

## IMAGING HARDWARE

The x-ray imaging system consists of a flat-panel detector, a three-axis object manipulator, an x-ray source, and a data-acquisition/image-processing computer. A photograph of the imaging system is shown in Figure 10. The indirect-conversion flat-panel imager has an active area of 300 × 400 $mm^2$ with a pixel pitch of 0.127 mm. The detector output is a 2304 × 3200-pixel, 12-bit image with an effective dynamic

**Figure 10**. The x-ray imaging system. The flat-panel imager is the gray rectangular object in the background. The imager is surrounded by a lead *picture frame* that protects the detector electronics from x-rays. In front of the detector is the object manipulator (rotate, vertical translate, and horizontal translate stages). In the foreground is the 300-kVp x-ray source used to collect the images shown in this document.

range of about 10 bits. The detector readout is fairly slow (~4-sec/image at the fastest readout rate), but is sufficient for a laboratory imaging system.

The object manipulator consists of a rotational stage upon which the object to be imaged is located, a vertical translation stage upon which the rotate stage is mounted, and a horizontal stage that moves the vertical stage toward and away from the detector. The rotational stage is used to acquire images of an object from different viewing angles; motion is essential for computed tomography (CT) data acquisition. The vertical stage is used to collect multiple images of objects that are too tall for a single shot and for helical CT imaging (discussed below). The horizontal stage can be used to move the object closer to the source to obtain a magnified image.

We have available a variety of x-ray sources that can be used in this system. All of the images collected to date have been with a portable x-ray generator with a maximum output of 300 kVp/3.0 mA. This source is not ideally suited to this system because the x-ray focal spot is large, about 1.5-mm diameter. The large focal spot allows only a small amount of magnification before blurring (often called image unsharpness) degrades the image. In order to effectively use the spatial resolution of the detector, the system should be operated with x-ray sources that have focal-spot sizes on the order of 0.01 mm.

There are three principal modes of operation for the imaging system. Single radiographs can be acquired by manipulating the object into position and *snapping* a single image. This mode is useful for determining coarse orientation of internal components of an object, for example. The second imaging mode is circular-trajectory data acquisition in which multiple radiographs of the object are collected as the object is rotated through a series of small angular increments. This is referred to as circular-trajectory data collection because, from the objects frame of reference, the x-ray source and detector move along a circle as images are acquired. If enough images are collected in a single rotation, these images form a sufficient data set for a three-dimensional (3D) CT reconstruction. After the full set of images are acquired, the images can be viewed rapidly in sequence to simulate images from a real-time imaging system. The third imaging mode involves both a small angular step and a small vertical step between images in a sequence. Data from this motion are said to come from a helical trajectory. This type of data is interesting from a CT perspective because it allows 3D imaging of objects that are larger (*taller*) than the detector; one could imagine collecting images as the source and detector spiral up and around a tall object. Three-dimensional reconstruction of these data poses interesting theoretical problems because it falls into a class of problems in which there are incomplete projections of the object (i.e., the entire object to be reconstructed is not present in each projection).

## IMAGING SOFTWARE

The imaging system is entirely controlled through a LabVIEW graphical user interface (GUI). A screen shot of the interface is shown in Figure 11. The motors and detector are controlled via this interface. We have implemented all three modes of operation described above. Experience developing imaging system solutions using LabVIEW allowed us to quickly generate a working interface. However, we discovered in using this interface and attempting to implement some rudimentary image processing that LabVIEW is not the most efficient platform for manipulating large 2D or 3D arrays such as radiographic or tomographic images.

We used another programming language, IDL (interactive data language), to create a GUI for collecting and manipulating a single image. The IDL environment is an efficient one in which to quickly process and display large data sets, and we were able to build very quickly a small interface that includes some advanced image processing capabilities. Unfortunately, motion control is very difficult within IDL, so we must rely on the LabVIEW interface for multiple image acquisition.

We developed four important suites of tools for image processing and analysis:

1. Routines to correct for nonuniformities in the detector response
2. A set of routines for CT reconstruction from a variety of source/detector trajectories (including circular and helical trajectories)
3. Routines for ray-trace simulation of x-ray imaging systems (these routines are useful for determining if an imaging geometry will provide adequate images or for determining the source of reconstruction artifacts)
4. Monte Carlo simulation of fan and cone-beam imaging systems (this tool is useful for investigating the effects of image-degradation processes such as Compton scatter).

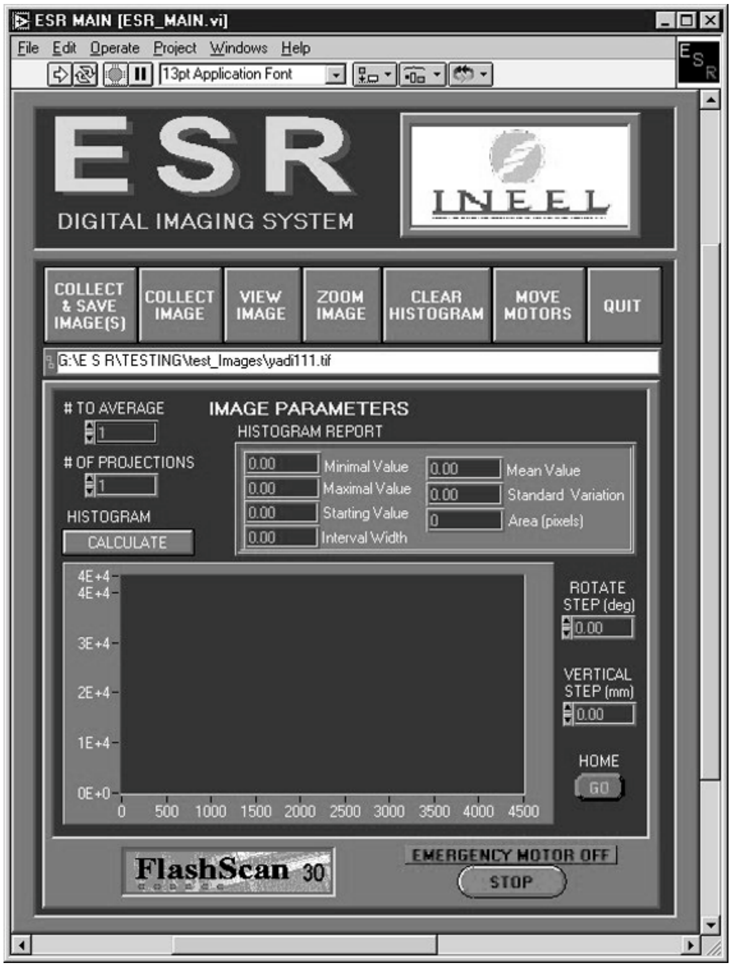

G:\E S R\TESTING\test_Images\yadi111.tif

# TO AVERAGE 1

# OF PROJECTIONS 1

0.00 Minimal Value
0.00 Maximal Value
0.00 Starting Value
0.00 Interval Width
0.00 Mean Value
0.00 Standard Variation
0 Area (pixels)

ROTATE STEP (deg) 0.00

VERTICAL STEP (mm) 0.00

**Figure 11** [File XRAY-2]. The graphical user interface (GUI) used to control the x-ray imaging system. This interface controls the movement of the object manipulator and acquires and saves images from the imager. It is also possible to control the x-ray source through this interface, though that option has not yet been implemented. A limited amount of image processing is also available through this interface.

The first two sets of routines have been integrated into graphical user interfaces (GUIs) and can be used easily by the operator of the image-acquisition system. The other tools are more difficult to use. The image reconstruction and ray-trace utilities are the result of several years collaboration with the Medical Imaging Research Laboratory (MIRL) at the University of Utah.

In order to perform a high-resolution CT reconstruction, it is necessary to understand the alignment of critical imaging components. Examples of critical alignment parameters include the location of the detector with respect to the x-ray source, location and orientation of the axis of rotation, and orientation of the detector. We have shown, for example, that a misorientation of less than 0.3 degree in the detector position can result in a noticeable artifact.[8] When designing and building an imaging system, it is important to either build the system to very tight specifications so that these alignment parameters are known, or to provide a method to measure these parameters should the alignment parameters change. We have chosen to adopt the second approach because we are interested in reconfigurable volume-imaging systems. Reconfigurable systems are always subject to minor changes in component (source, detector, object stage) placement. Hence, it is necessary to measure these system alignment parameters.

In collaboration with Dr. Fred Noo and Dr. Rolf Clackdoyle at MIRL, we developed a test object and algorithm for determining the system alignment parameters by evaluating images collected with this object.[9,10] The object consists of a thin plastic plate containing either two or three small (5 to 10 mm diameter) ball bearings, depending on whether the system is to be aligned for circular- or helical-trajectory CT. Radiographs are collected as the object is rotated in discrete steps through 360 degrees. The projections of the object, if summed together, form either two or three ellipses on the detector, depending on the number of balls in the phantom. Evaluation of the size and orientation of the ellipses allows us to precisely determine the values of nine alignment parameters critical for CT reconstruction. Figure 12 shows a radiograph of the object and an image that is the sum of a set of radiographs. The next challenge will be to develop a similar alignment strategy for less conventional imaging situations.

Finally, we developed a suite of tools for image display, including volume rendering tools for visualizing 3D CT data. Processing of single images and sets of radiographs or 2D slices from a 3D volume is straightforward and implemented in a user-friendly GUI. The volume rendering interface is not as advanced and will require more automated processing before we can consider it a finished product.

## X-RAY IMAGING SUMMARY

We assembled and used the imaging system to acquire single radiographs and CT data from a variety of objects. The system has also served as a valuable test bed for understanding the operation of and correction algorithms needed for flat-panel imaging systems. We used this system hardware and the knowledge gained from the research in cone beam tomography and system alignment in developing imaging systems for several other projects. The system will be continue to be valuable as a

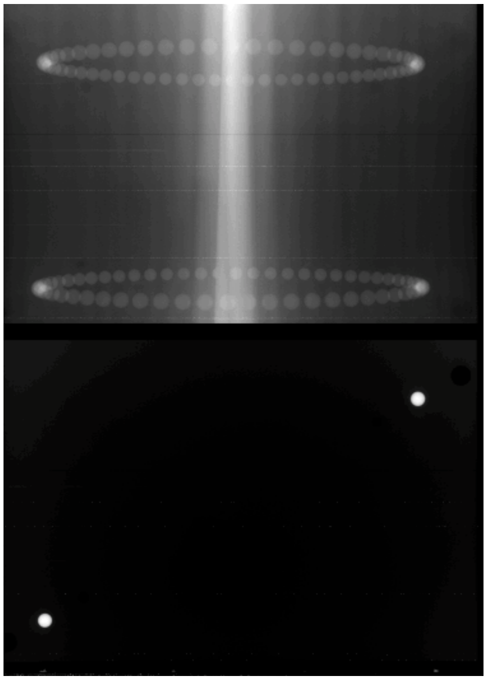

**Figure 12** [File XRAY-3]. A single radiograph and the summation of 60 projections of the alignment object. The set of radiographs were obtained at 6-degree increments. The parameters of the ellipses found by determining the centroids of the projections of the balls are used to determine the values of nine alignment parameters critical for high-resolution CT reconstructions.

nondestructive evaluation tool at the INEEL and for further research into limited-view and truncated-projection CT. Figure 13 shows an example radiograph and CT slice collected with the system.

We developed a suite of data-collection, image-processing, and image-visualization tools using a variety of software packages and programming languages. Some of the development focussed on user-friendly interfaces in order to make these tools more accessible to other researchers at the INEEL. Most development focussed on algorithms and data-collection strategies for nonconventional radiographic and CT imaging. In collaboration with MIRL, we developed tools for system alignment and CT reconstruction from both complete and truncated data sets.

## ACCOMPLISHMENTS

A prototype expert system for data validation in waste characterization was demonstrated, tested, and well received by INEEL data validation physicists.

The expert systems research performed in this project has evolved to the point of becoming an asset to site operations in waste characterization at the Radioactive Waste Management Complex (RWMC) at INEEL. During FY 2001 the prototype expert system will be deployed at RWMC to be used in the data validation process of waste destined for the Waste Isolation Pilot Plant (WIPP).

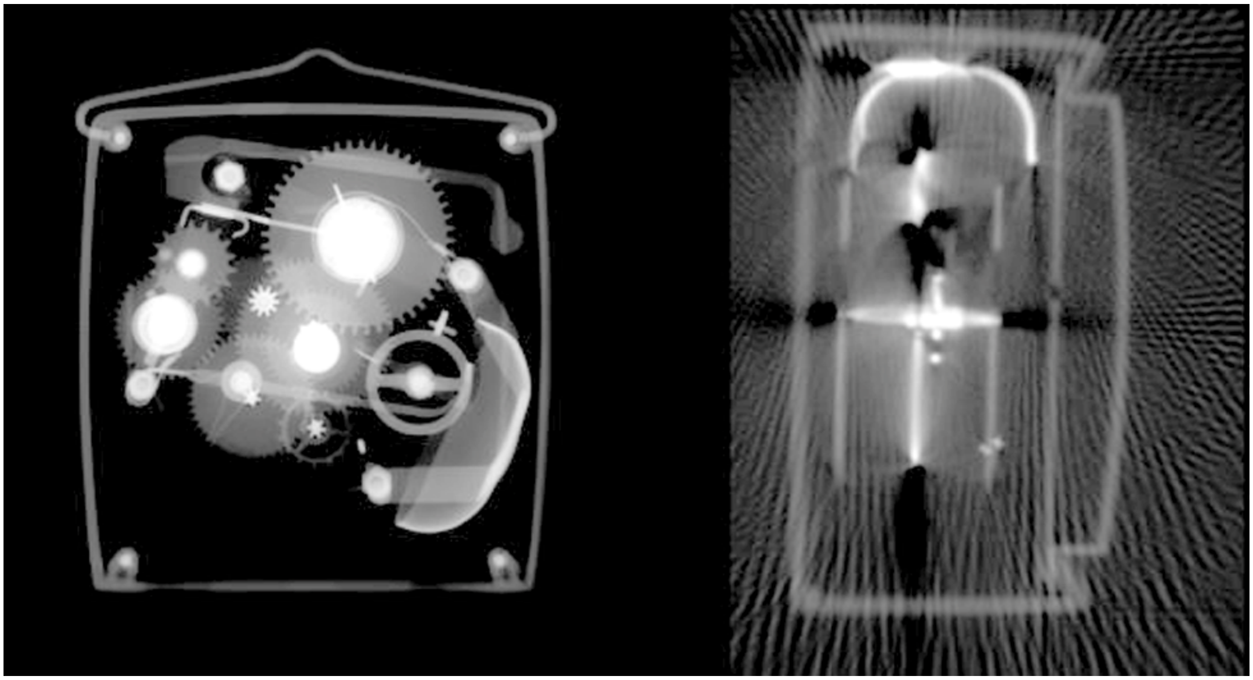

**Figure 13** [File XRAY-4]. A single radiograph of a darkroom timer and a CT slice from a 3D reconstruction. We used a set of 180 projections of the timer in the reconstruction. The slice is from near the bottom of the object; a cross section of the bell can be seen at the top of the slice. The streaking artifact (low-intensity radial lines) is characteristic of data collected with insufficient angular sampling.

Two private organizations have become interested in the Nondestructive Assay–Data Review Expert System (NDA-DRXS): Antech, and Canberra Industries, both in regard to work being performed at the Rocky Flats Environmental Test Site in Colorado. Two DOE facilities, Los Alamos National Laboratory and Savannah River Site have also expressed interest. Externally funded work arising as a direct result of research performed in this project is currently in progress for Canberra Industries and Los Alamos National Laboratory to apply NDA-DRXS to their needs.

The work in automated rule generation has served as one researcher's Computer Science Master's Thesis, and a journal article covering this material is in progress.

A pulsed eddy current system having neural network data processing capabilities has been designed and assembled. The knowledge and experience gained from this exercise provides the basis through which the eddy current inspection of complex structures such as waste containers can be addressed.

A 3-D cone beam x-ray imaging system has been designed and assembled to acquire single radiographs and computed tomography data from a variety of objects. The system serves as a valuable test bed for understanding the operation of, and correction algorithms needed for, flat-panel x-ray imaging systems. Our research results have already been applied to the improvement of field-portable x-ray imaging systems used by the US Army. The laboratory system will be continue to be valuable as a non-destructive evaluation tool at the INEEL and for further research into limited-view and truncated-projection CT.

A suite of data-collection, image-processing, and image-visualization tools utilizing a variety of software packages and programming languages has been developed. Some of this development has been focused on user-friendly interfaces in order to make these tools more accessible to end users and other researchers at the INEEL. A majority of the development has been focused on algorithms and data-collection strategies for non-conventional radiographic and CT imaging. In collaboration with the Medical Imaging Research Laboratory at the University of Utah we have developed tools for system alignment and CT reconstruction from both complete and truncated data sets. These tools have already been applied to INEEL systems and have potential for being used in the medical imaging field.

The x-ray imaging work has advanced collaboration with both the University of Utah and Idaho State University resulting in publications that are relevant to both the medical imaging and industrial inspection communities.

## REFERENCES

1. L. A. Zadeh, 1965, "Fuzzy Sets," *Information Control*, Vol. 8, pp. 338–353.

2. F. Blayo et al., 1995, "Benchmarks," *Enhanced Learning for Evolutive Neural Architecture*, ESPRIT Basic Research Project 6891, R3-B4-P.

3. C. Aviles-Cruz, J.L. Voz, D. Van Cappel, 1995, "Databases," *Enhanced Learning for Evolutive Neural Architecture*, ESPRIT basic Research Project 6891, R3-B1-P.

4. J. C. Determan, G. K. Becker, 2000, "A Prototype Generic Expert System Architecture for Data Review and Validation," *Seventh Nondestructive Assay Waste Characterization Conference, Salt Lake City, Utah, May 23-25, 2000.*

5. J. C. Determan, G. K. Becker, S. D. Matthews, 2000, “Expert System Technology for Nondestructive Waste Assay Data Review,” *Proceedings of SPECTRUM 2000, Chattanooga, Tennessee, September 24-28, 2000.*

6. D. C. Kunerth, T. K. O’Brien, L. Philipp, R. M. Suguitan, 1996, “Pulsed Eddy Current Thickness Measurements of Thin Ferromagnetic Materials Through Corrosion,” *Proceedings of the First US-Japan Symposium on Advances in NDT, Kahuku (Island of Oahu), Hawaii, June 24-28, 1996*, pp. 281-286.

7. T. K. O’Brien and D. C. Kunerth, 1995, “Pulsed Eddy Current Thickness Measurements of Transuranic Waste Containers,” *4th Nondestructive Assay and Nondestructive Examination Waste Characterization Conference, Salt Lake City, Utah, October 24-26, 1995*, pp. 331-340.

8. T. A. White, T. J. Roney, R. J.Pink, F. Noo, R. Clackdoyle, M. Smith, W.F. Jones, “Comparison of fan- and cone-beam imaging capabilities on a portable x-ray imaging system,” *Developments in X-ray Tomography II,* Ulrich Bonse, editor*, Proceedings of SPIE*, vol. 3772, pp. 138-146, 1999.

9. F. Noo, C. Mennessier, R. Clackdoyle, T. A. White, and T. J. Roney, 1999, “Non-iterative Methods for Scanner Calibration in Cone-beam Tomography,” *Proceedings of the 1999 International Meeting on Fully Three-Dimensional Image Reconstruction in Radiology and Nuclear Medicine, Zuiderduin Hotel, Egmond aan Zee, The Netherlands, June23–26,* 1999, pp. 155–158.

10. F. Noo, R. Clackdoyle, C. Mennessier, T.A. White, and T. J. Roney, 2000, “Analytic Method Based on Identification of Ellipse Parameters for Scanner Calibration in Cone-beam Tomography,*” Physics in Medicine and Biology*, Vol. 45, pp. 3489-3508.

# Nondestructive Assay

**Yale D. Harker**

**Jerald D. Cole, Mark W. Drigert, J. K. (Jack) Hartwell,
John W. Mandler, Christopher A. Mcgrath, Charles V. McIsaac**

## SUMMARY

This research is advancing the state of the art in nondestructive assay (NDA). The main thrust is to develop signatures that will improve NDA by providing more detail concerning isotopics and improving the overall accuracy of data. To meet the objective, the project is divided into four tasks: (1) fission physics research, (2) radiation transport analysis, (3) high-count-rate systems development, and (4) downhole probe development. All address present and future NDA needs of spent nuclear fuel (SNF), contact-handled transuranic (CH-TRU) waste, remote-handled (RH-TRU) transuranic waste programs and environmental monitoring and remediation programs. The following paragraph presents a synopsis of FY 2000 highlights.

In the area of fission physics, the prompt fission fragment decay correlation matrices have been developed for thermal neutron-induced fission of $^{235}$U and $^{239}$Pu. The data acquisition phase of the $^{233}$U fission experiment has commenced, and a second fission experiment, located at the Oak Ridge Electron Linear Accelerator (ORELA), is now planned. In the area of radiation transport analysis, North Carolina State University's (NCSU's) radiation transport code (CEARPGA) has been modified to make it more amenable for INEEL field applications of prompt neutron gamma activation analysis. In a second area of radiation transport analysis, an analytical gamma analysis package for use in absolute assays using passive gamma-based assay systems has been successfully tested using gamma spectrometry data taken on real CH-TRU waste assays at the Stored Waste Examination Pilot Plant (SWEPP) on the INEEL. In the area of high-count-rate systems development, a data acquisition and processing system using a Motorola Power PC processor and a LynxOS operating system for use with high-count-rate, multidetector assay systems, has been developed and is being tested on the Multi-Detector Analysis System. In addition, two commercial, digital-signal-processor (DSP) based pulse-height-analysis (PHA) systems were tested to evaluate their high-count-rate performance. Both DSP systems performed well at input count rates that would challenge all but the most specialized analog spectrometry systems. In the area of downhole probe development, the conceptual designs for two downhole probes have been completed and major components are on order. An existing facility at the INEEL Test Reactor Area has been converted to support downhole probe calibration and testing.

## PROJECT DESCRIPTION

### Fission Physics Research

The fission research is a fundamental research program to do two things in support of Environmental Management (EM) programs:

1. Develop a database of correlated fission fragment decay data (referred as the correlation matrix) for use in analyzing correlated gamma and neutron data from the newly developed multidetector array nondestructive assay technique. This technique has the unique capability

to identify the fissile nuclide producing the event from the emitted particles from each correlated fission event.

2. Use the correlated fission data to research the physics of fission.

The fission correlation matrix data will be used by two programs at the INEEL, the Spent Nuclear Fuel (SNF) Program and the Remote Handled Transuranic (RH-TRU) Program. Support of these programs means that the fundamental information being determined from the fission experiments, after evaluation and validation by the Nuclear Data Project, will be used for nondestructive analysis of fuel and waste in support of their final disposition by the U.S. Department of Energy (DOE).

For the past 2 years the experimental program has been conducted at the Argonne National Laboratory/Intense Pulsed Neutron Source (ANL/IPNS). During this time, an array of 10 high-purity germanium (HPGe) detectors with bismuth germanate (BGO) Compton suppression shields (CSS) and eight BC501 liquid scintillation detectors have been used to collect multiparameter coincidence data on the induced fission of $^{235}$U, $^{239}$Pu, and $^{233}$U. This is the first time such data have been collected.

The multiparameter data are stored in a list-mode format such that the experiment may be *replayed* in an off-line computer. When data are taken and stored in this manner, the analysis can be done in such a way that it is the same as doing the experiment over with different detector configurations and trigger conditions. The importance of this is that the fission data contains information on approximately 800 isotopes. This information is not only the traditional spectroscopy data of gamma-ray energy versus intensity, but time relationships between radiation emitted, both particle and gamma ray. In addition, the prompt isotope yields can be obtained without having to correct for beta-decay feeding. Explicit neutron and gamma-ray multiplicity is available as is multifragment branching ratios. The measurements lead to discoveries of new decay modes and strongly perturbed states of nuclei as is seen in ternary fission.

The fission data sets represent a unique resource of information that should and will be maintained and analyzed for many years. Data sets from the spontaneous fission experiments that we took in 1992 are still being analyzed and yielding new information. This long time line of analysis is a primary reason that we are the lead laboratory in a collaboration of groups to perform these experiments and analyze the data.

At the start of FY 2000, we were finishing a period of two long data collections on $^{235}$U and $^{239}$Pu. The experimental equipment was in need of extensive repairs and a general overhaul as the system deteriorates over time and use. In addition, we had planned to replace the HPGe detectors and the CSS units with our own. The units that were initially in the experimental setup were loaned from ANL Physics Division. According to the original loan arrangement, the INEEL ordered 11 HPGe detectors from EG&G ORTEC and 11 BGO CSSs from Bicron to replace the ANL detectors. However, Dr. Robert Janssens, point of contact with ANL Physics, proposed that we keep the ANL detectors and CSSs and use our new units in another setup. This plan was agreed to and much of the FY 2000 experimental effort was focused on repairing the ANL detectors. These repairs were completed in July and the detector array was returned to experimental operation in August 2000 with the start of the $^{233}$U run.

During the year, the 11 new HPGe detectors and CSS units were received and tested. These were shipped in August to Vanderbilt University, where a new detector stand is being produced. In early FY 2001, these detectors and the new stand will be installed at Oak Ridge National Laboratory (ORNL)/ORELA, which has been selected as the site of the second fission experiment. There will be further discussions of this later in this report.

With respect of analysis of the fission data, Dr. Rahmat Aryaenijad has been working to extract specific signatures of fission from the $^{235}$U correlation matrix constructed in FY 1999. These signature gamma rays will be used to establish that fission is being detected in the Multidetector Analysis System (MDAS) tests being conducted at ANL-W's Transient Reactor Test Facility.

The correlation matrix from the $^{239}$Pu experiment was constructed during the past year. In FY 1999, the sorted gamma-gamma coincidence matrices for the $^{235}$U induced fission data were built. A background-subtracted version of the gamma-gamma coincidence matrices has also been generated. The $^{239}$Pu-induced fission measurements were completed well ahead of the scheduled completion milestone, December 1999 (Milestone 2 in the FY 2000 work package). The early completion was due to having a higher than expected neutron flux at the INEEL fission experiment station at IPNS, consequently the desired number of fission events was achieved ahead of schedule. These plutonium and uranium correlation matrices and the raw list-mode data were sent to our Russian collaborators at JINR, Dubna, Russia. The correlation matrices were also sent to the Nuclear Physics group at Vanderbilt University. The raw data have not been set to Vanderbilt but will be transferred later in FY 2001.

A special experimental run was performed at IPNS during the May through June time scale that involved a mixed sample of $^{235}$U, $^{239}$Pu, and $^{238}$U that was a piece of Hanford N-Reactor fuel. The objective was to look at a mixed fission source with a high background activity and perform data analysis on fission product gamma rays. This demonstration was performed in support of RH-TRU and SNF programs and used the experimental stand developed for the INEEL fission studies at IPNS. The two programs mentioned supported the additional cost of this run. A formal external report is being prepared and will be issued by the end of FY 2000 or the beginning of FY 2001. Copies of this report will be sent to the appropriate sponsors of the basic fission work. This special experiment used five of our new detectors before they were sent to Vanderbilt where they have been performing flawlessly. This experiment focused on identifying contamination in samples and targets. We will try to repeat this run in FY2001 with another sample with greater fissile mass than the piece of spent fuel we used in FY 2000.

The purchase order was placed for a $^{237}$Np target that will be used in FY 2001. We have ordered 10 grams of neptunium in metallic form that >90% $^{237}$Np and <0.01% uranium and/or plutonium. The material will be welded into a stainless-steel encapsulation. This has been ordered from Russia at a cost of less than $13,000. The delivery of this source is tentatively scheduled for first half of FY 2001.

Agreement has been reached with ORNL to set up a second experiment for induced fission at ORELA. ORELA has a broader range of neutron energies available than IPNS and will provide another variable in the experiment by being able to tag each event by neutron energy. We will begin setting up the equipment in ORELA in October 2000. Another advantage of ORELA is that it is a nuclear physics facility under DOE/SC-OHENP, whereas IPNS is a materials science facility under DOE/SC-BES. This will allow us greater latitude in the material and experiments planned. Also, ORELA is planning to allow us to occupy an entire experimental hall of five beam lines. This will mean we will not have conflicts with other experimental programs in our immediate area or have to share a beam line with other experiments.

The opportunity to perform experiments at ORELA came because ORNL scientific management learned of our fission work and saw it as an ideal fit to a facility they have. They also saw it as a good science effort that would bring visibility to their facility for basic research. This parallels the meeting at ANL with several people interested in furthering their fission studies. They were Samit (Sam) Bhattcharyya (ANL Technology Development (TD), Division Director), Tom Yule (TD, Associate

Division Director), and Phillip Finck (TD, Associate Division Director). The Technology Development Division is responsible for IPNS. They are also capable of making contacts for us with other offices/ agencies inside and outside the DOE that could lead to a broader base of support for these studies.

## Radiation Transport Analysis

### Transport Analysis Related to Prompt Gamma Neutron Activation Analysis

Over the last 2 years the INEEL has been working with NCSU in developing a version of NCSU's radiation transport code called CEARPGA, for use in quantitative analysis of prompt gamma neutron activation analysis (PGNAA). At the outset of this task it was determined that CEARPGA had to be modified to better meet the needs of the INEEL and DOE complex. Major aspects of these modifications are:

- CEARPGA must be able to accommodate source/target/detector geometries associated with applications at the INEEL and the DOE complex

- To readily make cross comparisons, CEARPGA must have an input material/geometry specification format compatible with that of the widely used Monte Carlo Neutron Particle (MCNP) transport code

- CEARPGA must be able to simulate responses from gamma rays arriving in coincidence.

The FY 2000 objective was to improve the NCSU method for predicting gamma-ray spectra from PGNAA and then to test these improvements against measured PGNAA gamma-ray spectra. In particular, the following subtasks were performed: (1) the NCSU CEARPGA computer code was generalized to use the same geometry and materials input as the MCNP code, (2) methods for obtaining detector response functions were investigated, and (3) the capability within the CEARPGA code for simulating the effects of gamma-ray coincidences was developed.

North Carolina State University has completed development of the protocol for generalizing the geometry and material input for the CEARPGA code and modification of the CEARPGA code has been completed. CEARPGA now uses a general geometry in the same format as the geometry input for MCNP. A standard deviation calculation for each channel in CEARPGA has also been added. This should give a good indication of any "big weight" problems that might occur and, when used in the Library Least-Squares approach, will give the appropriate smaller amount of weight to library channels that have large standard deviations.

The analysis method used in CEARPGA relies on detector response functions—either measured or computed. To support this analysis, there has been a subtask on developing detector response function via Monte Carlo computer methods. Computed detector response functions are needed because there are not enough mono-energetic gamma-ray sources to provide an adequate database for CEARPGA analysis based on measurements alone. In this development, two generalized Monte Carlo transport codes, MCNP and Cylindrical Transport (CYLTRAN), were used. The MCNP code has been implemented on INEEL computers but the CYLTRAN code has not. As a first step in this effort, CYLTRAN was fully implemented and checked out on our computers.

Several series of calculations were performed to investigate the effects of detector parameters (e.g., diameter and depth of center hole, thickness of dead layer, rounding of detector edges) on the detector response using both MCNP and CYLTRAN. Since CYLTRAN is limited to cylindrical geometry, it was very difficult to model the standard INEEL PGNAA bismuth shield geometry and volume sources using CYLTRAN. Therefore, comparisons between MCNP and CYLYTRAN were performed using the same cylindrically symmetric geometry and point sources. These tests indicated some unexpected differences. For example, for the hydrogen capture gamma ray (2.223 MeV), CYLTRAN gave about a 6% higher peak efficiency but approximately the same total efficiency as did MCNP. CYLTRAN also gave higher escape peaks for an incident 1.33-MeV gamma ray. There were also differences in the intensities of the 511-keV peak (due to pair production in the shield and detector housing) and the bismuth x-ray peaks (due to gamma-ray interactions in the bismuth shield). These differences are critical because without accurate detector response functions the CEARPGA analysis will not be accurate. Further investigations of these effects were initiated and are ongoing.

North Carolina State University began investigating how to include gamma-ray coincidences in their model that predicts gamma-ray spectra from fast and thermal neutron interactions in media. Gamma-ray coincidences often occur in capture gamma measurements and they must be taken into account. As part of this effort, NCSU initiated experiments to measure gamma rays in coincidence for thermal neutron capture reactions on a selected list of elements, in particular, elements important for the use of PGNAA in the coal industry. In a parallel effort, INEEL researchers initiated an effort to extract the required gamma-ray coincidence information from the Evaluated Nuclear Structure Data Files (ENSDF) and to manipulate these data into a form NCSU can use to modify the CEARPGA code.

### Gamma-Ray Transport Analysis for Simple Spectrometer Assay Systems

Many NDA systems are being employed to characterize waste contained in 208-liter drums. The systems range from simple passive assay systems to computed tomography systems. Generally speaking, the more complex the assay system the better the accuracy that can be expected for the assay result. However, this accuracy comes at a cost in terms of capital outlay and/or production rate. In many cases, the added costs cannot be justified by the requirements. We believe that the accuracy of passive gamma-ray assay systems can be greatly improved by using representative efficiency calculations, which account for simple variations in the source distributions and absorption in the matrices. Reported here are the results of a small research task that explored the potential of using a simple method for calculating the absorption-modified efficiency for each drum assay (this approach is referred to as the *analytical analysis approach*). The technique relies mainly on the data obtained from the gamma-ray spectrum and a physical description of the waste volume; i.e., volume radius, height, and density. It assumes that during data acquisition the drum is rotating; therefore, the azimuth variations in the source distribution are smeared out by the rotation. It also assumes that the radial and axial variations in source distribution can be represented by simple functions and that the matrix density is constant. These assumptions greatly reduce the complexity of the calculational problem and provide a reasonable alternative to more costly and time-consuming tomographic techniques.

A computer code that operates in real time (while the assay data are being acquired) was written to calculate the attenuated gamma-ray efficiency as a function of gamma ray energy and source distribution. The geometry used in the computer code assumes a 208-liter drum being rotated in front of an array of gamma-ray detectors, which is typical of most gamma-ray based drum assay systems. Based on the attenuated efficiency data, a least squares regression analysis of at least four gamma peaks associated with the decay of $^{239}$Pu (i.e., 129 keV, 208 keV, 345 keV, and 414 keV) is used to determine the optimal estimate of plutonium mass. Plutonium was the first element analyzed using this approach, but the method is equally applicable to other nuclides as long as they have measurable multiple gamma lines that are relatively widely dispersed with respect to energy. Relative to this approach being applied to other nuclides, this analysis approach has been applied to the assay of $^{241}$Am, and the preliminary results are very similar to those reported here for plutonium.

This analysis approach was first tested on surrogate drum data involving eight different waste matrices. The results of these tests are listed in Table 1. For the surrogate drum cases, the source distribution was known and radial and axial dimensions were modeled exactly. For these cases, the measured plutonium mass values were within 2% of the known plutonium mass values.

**Table 1.** Surrogate drum tests of the analytical analysis approach to gamma based drum assay.

| Matrix | 129 keV R[a] | 203 keV R[a] | 345 keV R[a] | 375 keV R[a] | 413 keV R[a] | Average R[a] | Std. Dev. R[a] |
|---|---|---|---|---|---|---|---|
| Zero matrix | 0.9584 | 0.9832 | 0.9581 | 0.9675 | 0.9884 | 0.9712 | 0.0142 |
| Inorganic sludge | 1.006 | 1.007 | 0.9782 | 1.004 | 1.016 | 1.002 | 0.0143 |
| Organic sludge | 1.003 | 0.9921 | 0.9554 | 0.9649 | 0.979 | 0.9788 | 0.0194 |
| Mixed metals | 1.049 | 0.9662 | 0.9875 | 1.011 | 1.028 | 1.008 | 0.0326 |
| Filters | 1.013 | 1.012 | 0.9755 | 0.9972 | 1.006 | 1.001 | 0.0154 |
| Combustibles | 1.014 | 1.022 | 0.9917 | 1.008 | 1.012 | 1.009 | 0.0112 |
| Glass | 1.01 | 1.018 | 0.9946 | 0.9927 | 1.017 | 1.066 | 0.0121 |
| Graphite | 1.001 | 1.024 | 0.9587 | 1.007 | 1.031 | 1.004 | 0.0283 |

---

a. R is the ratio of the measured Pu-239 mass to the known Pu-239 mass = 2.861g.

The analytical analysis approach was also tested on real waste drum assay data taken by the SWEPP Gamma Ray Spectrometer (SGRS), a modified Canberra $Q^2$ gamma spectrometer system. For the real waste cases, the source distributions were not known, but the analysis assumed them to be uniform. The results of the testing on real waste drums are given in Table 2 for 10 of the 84 assays tested and shown in Figure 1 for all 84 cases. In the real waste tests, the average SGRS Pu mass, as determined by the analytical analysis approach, is 15% below the Pu mass as determined by radiochemistry. This agreement was achieved using the computer-generated attenuated gamma-ray efficiency curves and the analytical analysis approach. No empirical adjustments were made to the SGRS results.

Gamma data taken by the SGRS as part of the WIPP Performance Demonstration Program (PDP) Cycle 6B were also analyzed using this approach. The results are shown in Table 3 and they exhibit similar characteristics to the real waste assay results; i.e., the measured plutonium mass is 13% below the known value. If this analysis approach had been used in the actual PDP test, the SGRS would have passed both the PDP accuracy and precision requirements as an absolute assay system.

A paper on this analysis approach was presented at the 7th NDA Waste Characterization Conference held in Salt Lake City in May 2000. Parts of this analysis approach are currently being implemented in the gamma software packages designed for the SWEPP gamma spectrometer systems; i.e., SGRS and Waste Assay Gamma Spectrometer (WAGS). Full implementation of this analysis approach on SGRS and WAGS is scheduled for the first half of FY 2001.

**Table 2.** Real Waste, 10 Sludge Drum Test of the analytical analysis approach to gamma based drum assay.

| Drum Bar Code | SGRS $^{239}$Pu Mass | Error | SGRS Pu Mass | Error | Radio-Chemistry Pu Mass | Error | Percent Recovery | Error |
|---|---|---|---|---|---|---|---|---|
| 000513 | 0.156 | 0.035 | 0.166 | 0.037 | 0.21 | 0.02 | 79 | 19 |
| 003325 | 0.210 | 0.026 | 0.224 | 0.028 | 0.30 | 0.02 | 75 | 11 |
| 004221 | 1.292 | 0.008 | 1.375 | 0.008 | 1.89 | 0.13 | 73 | 5 |
| 005698 | 0.257 | 0.023 | 0.273 | 0.025 | 0.31 | 0.03 | 88 | 12 |
| 010549 | 0.762 | 0.011 | 0.811 | 0.011 | 1.03 | 0.11 | 79 | 8 |
| 012287 | 5.283 | 0.049 | 5.623 | 0.052 | 6.08 | 0.53 | 92 | 8 |
| 024498 | 2.006 | 0.069 | 2.135 | 0.074 | 1.71 | 0.01 | 125 | 4 |
| 030186 | 0.158 | 0.029 | 0.169 | 0.031 | 0.34 | 0.01 | 50 | 9 |
| 031166 | 1.573 | 0.023 | 1.675 | 0.025 | 1.76 | 0.02 | 95 | 2 |
| 032674 | 0.323 | 0.010 | 0.344 | 0.011 | 0.35 | 0.01 | 97 | 4 |
| | | | | | | avg = | 85 | |
| | | | | | | sdev = | 19 | |

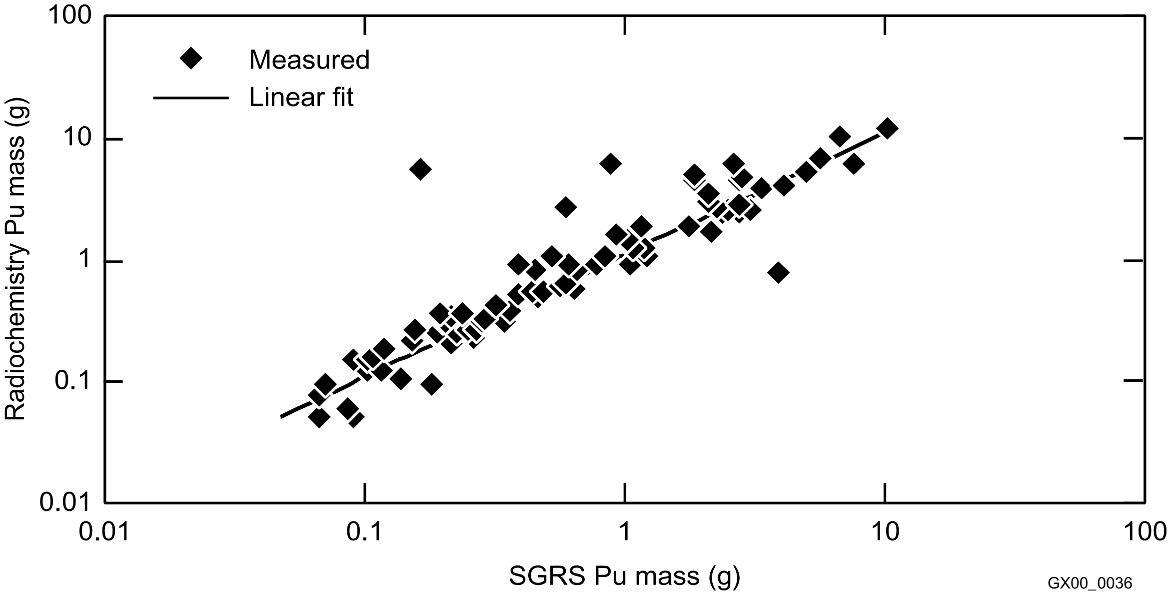

**Figure 1**. Real waste, 84 sludge drum, test of the analytical analysis approach.

**Table 3.** PDP-6B Sludge drum test of the analytical analysis approach to gamma based drum assay. Known Pu mass = 104.35g

| File Name | SGRS Pu mass | Error | % error |
|---|---|---|---|
| PDP5.001 | 91.07 | 0.97 | 1.07 |
| PDP5.002 | 90.70 | 0.66 | 0.73 |
| PDP5.003 | 91.57 | 0.45 | 0.49 |
| PDP5.004 | 91.86 | 0.87 | 0.94 |
| PDP5.005 | 91.06 | 0.48 | 0.52 |
| PDP5.006 | 92.40 | 0.52 | 0.57 |
| average | 91.44 | | |
| std | 0.57 | | |
| % RSD | 0.54 | | |
| %Recovery | 87.63 | | |

## Downhole Probe Development for Subsurface Characterization

A downhole probe development task was added to the ESR/NDA program in FY 2000. This task is in response to an increasing need to characterize subsurface deposits of radioactive and nonradioactive sensitive materials prior to removal or remediation. A primary example of the use of downhole probes would be the characterization of radioactive waste buried at the Subsurface Disposal Area (SDA) at the INEEL Radioactive Waste Management Complex (RWMC). These wastes are reported to have transuranic waste, beta/gamma waste, and RCRA materials such as cadmium and carbon tetrachloride. The recent borehole logging demonstration in Pit 9 clearly showed the capability of a germanium-detector-based borehole probe to provide information about the disposition of materials of interest in the SDA. The results of the project also illustrated the importance of obtaining additional and more detailed information about the principal constituents of interest—chlorine and plutonium. The accuracy and precision of the lower and upper limits of sensitivity were not sufficient to develop unambiguous models of their distribution. In a meeting where the data from the project were reviewed, a panel of experts on nuclear measurements and logging recommended that future efforts focus on being able to measure plutonium to the level of 10 nCi/gm and chlorine to the level of 5,000 ppm in the vapor phase in the interstitial dirt. They also recognized that significant improvements are necessary in the design of a gamma-ray probe to enhance its capability for measuring elements of interest over the wide range of concentrations likely to be encountered.

Based on lessons learned from the INEEL/SDA experience, it was determined that two types of advanced downhole probes would greatly benefit the INEEL buried waste and monitor well characterization programs. The first probe will use a neutron generator as the neutron source and a cooled HPGe detector. It will use the PGNAA technique to identify and quantify nonradioactive materials, such as cadmium and carbon tetrachloride. The second probe will also use a neutron generator (in this case a Zetatron[a] is required) and two detector packages that can be interchanged. The second

---

[a] Zetatron is a specific design of the pulsed neutron generator, which was originally developed as a nuclear weapons trigger. Its advantage for this application is that it produces no *dark current* neutrons between bursts.

probe, with a neutron detector package installed, will be designed to determine fissile concentrations—primarily $^{239}$Pu and $^{235}$U. The second probe, with a gamma detector installed, will be used to determine porosity and neutron absorption cross section of the bulk media surrounding the access hole. Porosity and neutron absorption parameters are needed to interpret data logs properly.

In addition to the development of the gamma and neutron probes, a facility is needed at the INEEL to test and calibrate the probes as well as to benchmark calculational codes. The facility must be able to simulate actual borehole geometry and bulk media surrounding the borehole.

### Gamma Probe Basic Design

The gamma-ray probe must be able to operate in a number of different modes. The following modes are discussed further below:

- Passive
- Inelastic
- Capture
- Delayed Activation
- Decay Time.

The passive mode is intended to look for radioactive elements that emit gamma rays from radioactive decay. Typical elements that may be seen in this mode at the INEEL are plutonium, americium, potassium, and the uranium and thorium decay series. Because of the energy resolution, it may well be practical to detect gamma rays from $^{235}$U as well as initial $^{238}$U decays, thus being able to separate enriched uranium, and deposited uranium that is part of the geological environment. While using this mode, no external source is required and measurements can be performed on material located within a few inches of the bottom of the borehole.

The inelastic mode makes use of a pulsed neutron generator that emits a narrow “pulse” of 14 MeV neutrons. Before these neutrons slow down to thermal energies, they may interact with nuclei through inelastic scattering or through an $(n,x)$ reaction, where $x$ stands for a charged particle, two neutrons, or a high energy gamma ray. Because all these reactions occur within a microsecond of when the neutron is produced, the gamma rays must be detected during the neutron burst. Detecting these gamma rays during a burst from the accelerator provides an enhancement of a factor of typically 5–10 in the intensity of the inelastic gamma rays as compared with those resulting from thermal neutron capture (which can be viewed as a background for this measurement). Elements such as carbon and oxygen can be more readily detected in this spectroscopy mode. Because this mode uses a neutron generator, which is located at the bottom of the tool, the effective depth of the inelastic scattering measurements is 4 to 5 feet from the bottom of the borehole.

The capture mode looks at gamma rays produced between neutron bursts. Within a few tenths or hundredths of microseconds after a neutron burst has ended, all neutrons will have been thermalized. They then diffuse through the environment until they are captured by a nucleus, which produces prompt capture gamma rays. By measuring capture gamma rays exclusively between the bursts of the neutron generator, interference from inelastic gamma rays is removed from the acquired spectrum, thus improving the signal to noise ratio. Elements that can typically be determined by capture gamma rays are silicon, iron, calcium, sulfur, chlorine, titanium, boron, gadolinium, hydrogen, chromium, nickel, and copper. Again, because this mode uses the pulsed neutron generator, measurements can be made no closer than 4 to 5 feet from the bottom of the hole. However, a configuration should be available where an isotopic source (e.g., $^{252}$Cf) can be used that allows measurements to be made within about 1 to 2 feet of the bottom of the hole.

The delayed activation mode makes use of the creation of a radioactive ground state or isomeric state following a neutron-induced reaction. At some later time, this radioactive ground state (or isomer) will decay and emit a characteristic gamma ray. Because these decays occur at a later time, there is little background (except for that resulting from natural activity) to be detected so the measurement can be very sensitive. If a combination of factors such as cross section, half-life, and gamma-ray branching ratios are favorable, it is sometimes possible to detect elements at concentrations as low as 1 ppm. Elements that can be readily seen in this mode include aluminum, manganese, vanadium, calcium, magnesium, chlorine, gold, and sodium.

The decay time mode is really a multiscaling mode intended to measure the time it takes for thermal neutrons to be absorbed by the nuclei in the environment. While spectroscopic measurements can be performed during this mode the (primarily capture) gamma rays are not efficiently produced for spectroscopy. The decay time provides a measure of the thermal neutron absorption cross section, which is a useful parameter for describing the environment and is necessary for relating the gamma ray count rates to elemental concentrations. Since this mode uses the pulsed neutron generator, measurements can be made only to within about 4 to 5 feet of the bottom of the hole.

As is standard for downhole probes, the components are stacked vertically inside a sealed cylindrical enclosure. A multiple lead cable bundle is attached to the top of the enclosure and extends to the surface. Signals are transmitted over this cable bundle to the instrumentation at the surface.

- At the top of the assembly are line drivers designed to drive the signals over 700 feet of cable to the surface instrumentation.

- Power supply modules are located below the line drivers.

- Below the power supplies are the DSP and the DSP driver. (See the section on High-Count-Rate System Development for a description of DSP technology.) The addition of DSP technology in this probe means that digital signals, not analog signals, will be transmitted up the 700 feet of cable to the surface instrumentation. This is a major advancement over the current borehole technology.

- The HPGe detector and cryostat will be positioned below the DSP and DSP driver modules.

- The neutron generator will be positioned at the bottom of the probe.

- A heavy metal shield will be positioned between the neutron generator and the germanium detector to shield the detector from direct radiation from the neutron generator.

The overall length of the probe will be approximately 120 inches and the diameter will be less than 4.5 inches. These dimensions are compatible with the present and planned test holes at the RWMC/SDA and some of the monitor wells located throughout the INEEL.

## Neutron Probe Design

The neutron probe employs a method called the prompt fission neutron (PFN) technique and the tool is frequently referred to as the PFN probe. It is based on the differential die-away method (referred to as the decay time mode above) of detecting fissile material. The theory of operation is based on detecting fission neutrons produced by thermal neutron-induced fission of $^{239}$Pu or $^{235}$U. In PFN mode of operation, a Zetatron neutron generator produces a pulse of 14 MeV neutrons, which in turn thermalize in the media surrounding the borehole. Once thermal equilibrium is achieved, the thermal neutron population decays (or dies) away due to diffusion/leakage or absorption. The thermal neutron die-away follows a simple exponential decay with respect to time. The die-away constant, t, is the time for the neutron population to be reduced by *1/e,* where *e* is the base of natural logarithms. Some of the thermal neutrons are absorbed by $^{239}$Pu or $^{235}$U atoms entrained in the media and produce fission events and an average of 2 to 3 prompt neutrons per fission. The average energy of the fission neutrons is around 2 MeV. Since the prompt fission neutrons are energetic they will not be absorbed as readily in the media. Therefore, there is a significant probability that fission neutrons will be detected by the fast-neutron detectors on the PFN probe. The term *fast neutron detector* means that the detector is sensitive to high-energy neutrons and is not sensitive to thermal neutrons. Since the prompt fission neutrons were produced by thermal neutron-induced fission, the fast neutron detector signal from these events will follow the same characteristic die-away as the interrogating thermal neutron population. The integral of the fast neutron detector time distribution—fast neutron detector counts versus time following the Zetatron pulse—is therefore proportional to the concentration of fissile material in the media. The data acquisition process of neutron burst followed by fast neutron count is repeated for each neutron burst in the data acquisition cycle.

The sensitivity of this method depends on many factors but a critical aspect with regard to sensitivity is the fact that the neutron generator must not produce dark current neutrons between primary pulses. These dark current neutrons are not distinguishable from the fission neutrons and therefore contribute to the background and limit the ultimate sensitivity of the method. This is why the Zetatron type of neutron generator, which shuts off completely between primary pulses, is critical to PFN tool design.

Primary use of the PFN probe is for tracking plutonium migration. This was identified as a critical piece of data not obtainable by any other method. In addition to providing data about the buried waste in the SDA, the PFN probe would also have capabilities to measure contaminants in existing and future monitor wells extending into the basalt outside the SDA. In the configuration discussed, it will be capable of tracking plutonium at very low levels. The instrument can also measure the saturated porosity of hydrogenous liquid independently of the concentration of neutron absorbing materials (Pu and Cl) in the SDA. This *porosity/capture cross section* mode uses an array of gamma ray detectors in place of the fast neutron detectors. The gamma detection method increases the depth into the formation at which the saturated porosity and absorption effects are gauged.

The fast neutron detector package consists of six to eight 0.5-inch diameter by 5-inch active length $^{3}$He proportional counters embedded in a cylinder of polyethylene. The polyethylene is in turn surrounded by a 0.040 in-thick cover of cadmium. Cadmium stops all thermal neutrons from reaching the $^{3}$He detectors and the polyethylene inside the cadmium moderates the fast neutrons passing through the cadmium down to thermal neutron energies where they are more likely to be detected by the $^{3}$He detectors.

The gamma detector package consists of two NaI(*Tl*) scintillation detectors operated as simple gamma detectors.

The detector electronics for either the neutron detectors or the gamma detectors consist of preamplifier/amplifier/discriminator modules in which TTL discriminator pulses are passed up through the 700 feet of cable to acquisition electronics at the surface. Data will be stored as individual event records, which for this probe, will contain the time the event occurred. Die-away analysis is then performed using software based analysis routines. The advantage of event or LIST mode data acquisition is that there is great flexibility in data analysis and the fact that the data can be analyzed in different ways to arrive at different parameters.

The PFN probe modules and vertical stacking are similar to the gamma probe configuration with the exception that the neutron generator is a Zetatron and is located above the detector package rather than below the detector, as is the case for the gamma probe. In this configuration the PFN probe can scan close to the bottom of a borehole.

### Downhole Probe Calibration and Test Facility

In addition to designing and building borehole probes, we are also designing a calibration facility that will be located in the former Engineering Test Reactor Critical (ETRC) facility at the INEEL Test Reactor Area. The ETRC is being converted for use in downhole probe development in conjunction with a D&D program that is responsible for removing items left over from previous programs. The former ETRC canal pit will be backfilled with gravel. A test structure consisting of a test hole extending to the bottom of the ETRC canal pit surrounded by removable surrogate assemblies will be positioned in the gravel. The test configuration will allow for calibration and testing with different materials and source distributions surrounding the test hole.

## High Count Rate Systems Development

Almost all NDA systems are involved in processing high data rates, either due to high count rates or to the large number of data being accumulated and processed from large arrays of detectors. Even when NDA systems are involved in environmental monitoring, situations exist where high-count rates are expected. For example, environmental monitoring may involve active interrogation, such as the PGNAA and PFN downhole probes discussed above. Even in the case of passive gamma counting of contact-handled transuranic waste, high count rates are present because of the strong activity from $^{241}$Am decay. Obviously, assays involving RH-TRU waste and SNF have to deal with high count rates. The goal of this task is to advance the state of the art (in particular the INEEL's capabilities) in the area of field-able, wide-dynamic-range data collection and analysis systems.

### Advanced Data Acquisition System

The work carried out under this project continues the development of compact data acquisition designed to collect and preprocess the digitized information collected from a multidetector coincidence system. The system is designed to collect all pertinent information of a detected radiation event, perform front-end data validation, and to format the data for long-term storage and subsequent detailed analysis. The system is also designed to make use of distributed computing environment to spread the data processing tasks over a set of moderate sized computing platforms.

The first implementation of this system is being used by the MDAS currently under development to characterize SNF and RH-TRU, and by the measurement system performing the fission studies at IPNS.

***Conversion to PowerPC Processor-Based System.*** In FY 2000, the work on the data acquisition and data processing system concentrated on moving the system to a new hardware platform and operating system. The original system was based on a Motorola 88110 RISC processor, packaged in a VME form-factor, running System V/R4 UNIX. This processor and operating system software, while well established, is no longer being updated or well maintained. It was decided to move to a Motorola PowerPC processor based system running LynxOS. LynxOS is a real-time operating system available from LynxWorks (formerly Lynx Real-Time Systems). The PowerPC processor was chosen because of its increased processing capabilities and a clear upgrade path. The previous 88110 processors used in the original system had maximum clock-speeds of 50 MHz. The new PowerPC 604 and 750 processors run at a clock speed of 330 MHz. One of the important limiting factors in the speed of the data acquisition system is the speed that the processor can readout the VME hardware memories that collect the digitized measurement information from the front-end electronics. The previous hardware could perform this readout at a maximum of about 2 Mbytes/sec. The new PowerPC processor can perform that readout at over 4 Mbytes/sec, which greatly exceeds the throughput possible from the signal processing electronics. The original design of the data acquisition system called for the need for high speed network connections for transmitting the experimental measurement data between a number of distributed data processing tasks and storage media. At the time FDDI was the only network protocol that had the transmission capabilities needed. In upgrading to the PowerPC based system it was decided to make use of 100 BaseT networking hardware. This choice of network hardware is less expensive and would make it easier to integrate a set of measurement systems into an already existing facility network. The results of the various hardware improvements has lead to a three-fold increase in data throughput as determined by use of the simulation and test functions built into the data acquisition system software.

***Progress Toward a Network-Distributed Data Acquisition System.*** Included in this second phase system implementation is the goal to incorporate network-distributed processing features into the structure of the data acquisition system. These features include remote control of the data acquisition processes and distributed processing of the collected measurement data. This capability serves two purposes. The first is to reduce the amount of time that the front-end processor needs to process each buffer of measurement information. When the memory module that's collecting the digitized measurement data is full it is taken offline and the information is read out and processed. If there is a second memory in the system, data collection will be shifted to that module. If the second memory module fills before the data acquisition system can finish processing the previous buffer, data collection will stop until one of the memories can be made available again. With the distributed processing, the front-end processor would immediately send the data buffer over a network connection to one or more separate tasks for processing. It would then be able to process and clear the next full memory buffer in a much shorter time period thus decreasing the overall measurement system dead-time.

The second use for this distributed processing model is to form the basis of a distributed array of compact measurement stations for monitoring environmental conditions around a facility. The information would be collected by each of the independent monitoring systems that would transmit the information, using standard network protocols and hardware, back to a central collection point for collating and processing.

Transmission of the digitized data to a remote data analysis process has been operational for some time. Implementation of the networked control interface for the different data acquisition and processing tasks is now in the process of being tested and optimized. Once the control interface is completed, the distributed processing capabilities of the data collection and processing system will be complete.

### High-Count Rate DSP Testing

Two commercial digital gamma-ray spectrometers coupled to a high-purity-germanium (HPGe) detector with a transistor reset preamplifier (TRP) were tested to evaluate their high-count rate performance at input rates up to 600 kcps. These tests evaluated the total system throughput, peak centroid stability, peak shape parameters, and the quantitative accuracy of the system dead time and pulse pileup corrections as a function of input rate at five gamma-ray energies between 121.8 and 1,408.0 keV.

For the measurements performed in these tests, the throughput of the DSA2000 was superior to that of the DSPEC$^{PLUS}$, perhaps partially due to the more stringent pulse pile-up rejection criteria used in the DSPEC$^{PLUS}$. Both units exhibited similar resolution values at half the maximum peak height at all tested energies from 122 to 1,408 keV; however, at rates up to 245 kc/s the DSPEC$^{PLUS}$ exhibited superior peak widths at one-fiftieth maximum (FW0.02M.) This again is probably due to the more stringent pulse pile-up rejection criteria of the DSPEC$^{PLUS}$.

The DSA2000 operated reliably at the highest tested rate of 603 kc/s. At this highest rate the DSPEC$^{PLUS}$ never incremented its live timer, and the system throughput was too low to allow a fair assessment of the system performance. Both DSPs performed well at input rates that would challenge all but the most specialized analog spectrometry systems.

The two digital spectrum processors that were tested are a Canberra Industries DSA2000 (Serial Number 12982656) and an ORTEC DSPEC$^{PLUS}$ (Serial Number 130).[b] The acquired spectra from both DSPs were carefully analyzed using the interactive spectrum analysis feature of our PCGAP code.[1]

These DSPs use trapezoidal digital filter shaping primarily defined by a rise time and a flat top width. The digital filter settings for both units were set to a rise time of 2.8 μs and a flat top of 0.6 μs. These settings are roughly equivalent to an analog semi-Gaussian shaping time of 2 μs. Both DSPs were set for comparable signal shapes; however, a less stringent pile-up rejection criterion was used on the DSA2000. The Canberra DSA2000 allows the operator to select a spacing parameter (the PUR Guard setting) that affects the action of the pile-up rejecter (PUR). By adjusting the PUR Guard setting the operator can select the acceptable time interval between the end of an event's flat top and the initial rise of a following event. Since the selected value for the PUR Guard has an effect on the system throughput, the manufacturer suggests a series of simple tests to determine an optimum setting. We performed these tests and chose a relaxed PUR setting. The ORTEC DSPEC$^{PLUS}$ does not have an operator-selectable PUR setting, and requires a complete return to baseline between acceptable events.

The sources used for the evaluation of the two digital spectrometers were a set of proportional activity $^{152}$Eu sources that have been used for years at our laboratory.[2,3,4] This set consists of 11 mounted point sources of $^{152}$Eu carefully prepared by weight aliquoting from a master solution. The relative source strengths are known to better than 0.1% and are documented as "Normalization Factors" (NF) recorded in the source documentation and engraved on the source mount.

For each acquired spectrum, the system throughput was calculated by integrating the spectral counts and dividing the total stored counts by the recorded system real time in seconds. Figure 2 compares the measured throughput of the two tested units. The DSA2000 exhibits superior throughput characteristics for all tested input rates above about 40 kc/s. This may be partially due to the less stringent PUR setting of the DSA2000.

In each spectrum, the strong $^{152}$Eu photopeaks at 121.8, 344.3, 778.9, 964.0, and 1,408.0 keV were evaluated to determine the stability of the peak positions and amount of peak broadening as a function of input rate. The 1,408-keV peak centroid shift as a function of input rate for both DSPs is presented

---

[b] The manufacturers loaned the units used in this work. Their support is appreciated.

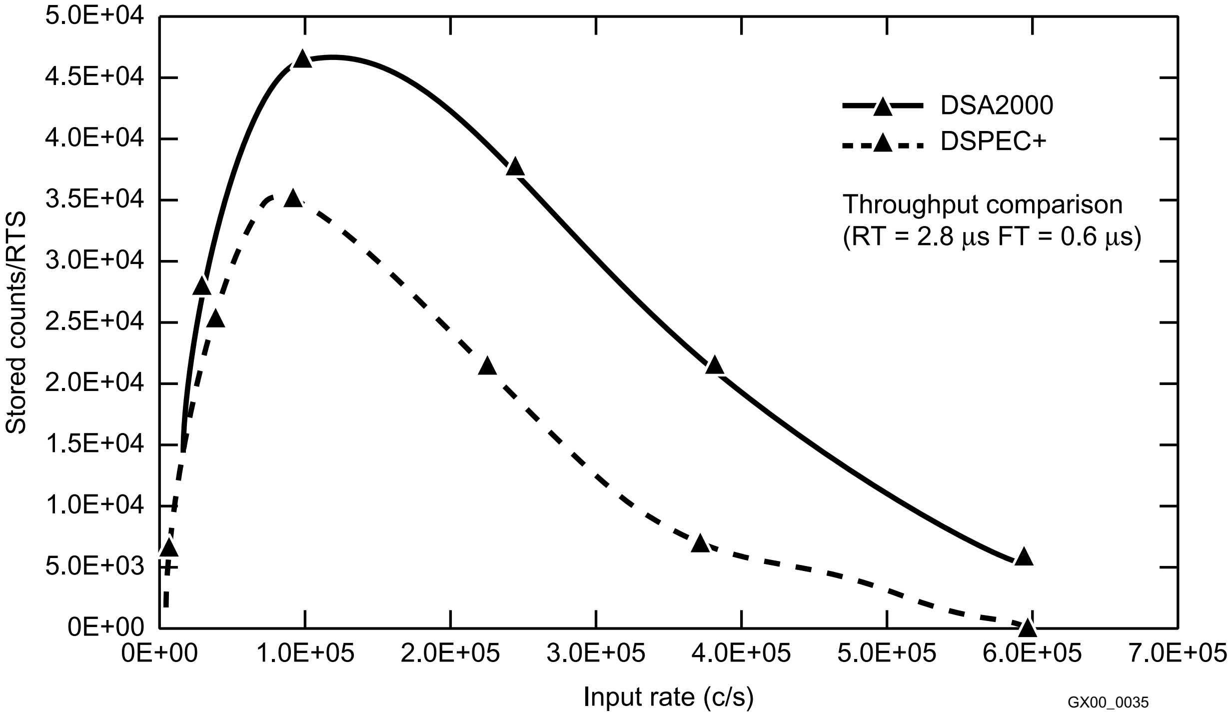

**Figure 2.** Comparison of the throughput, calculated as stored counts per real time second of acquisition time, as a function of input rate for the two tested DSPs. The digital filter shaping for both units was RT = 2.8 ms and FT = 0.6 ms. The source was $^{152}$Eu.

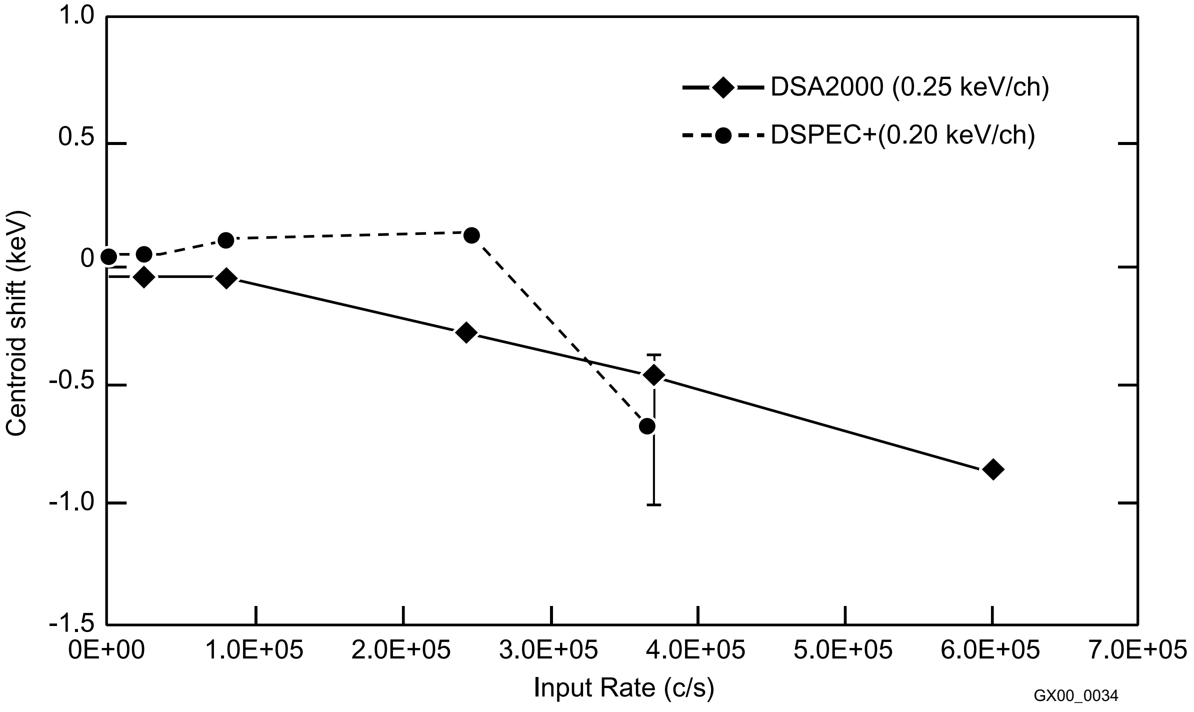

**Figure 3.** Comparison of the centroid peak shift in keV of the 1,408-keV line as a function of input rate for the DSA2000 and the DSPEC$^{\text{PLUS}}$.

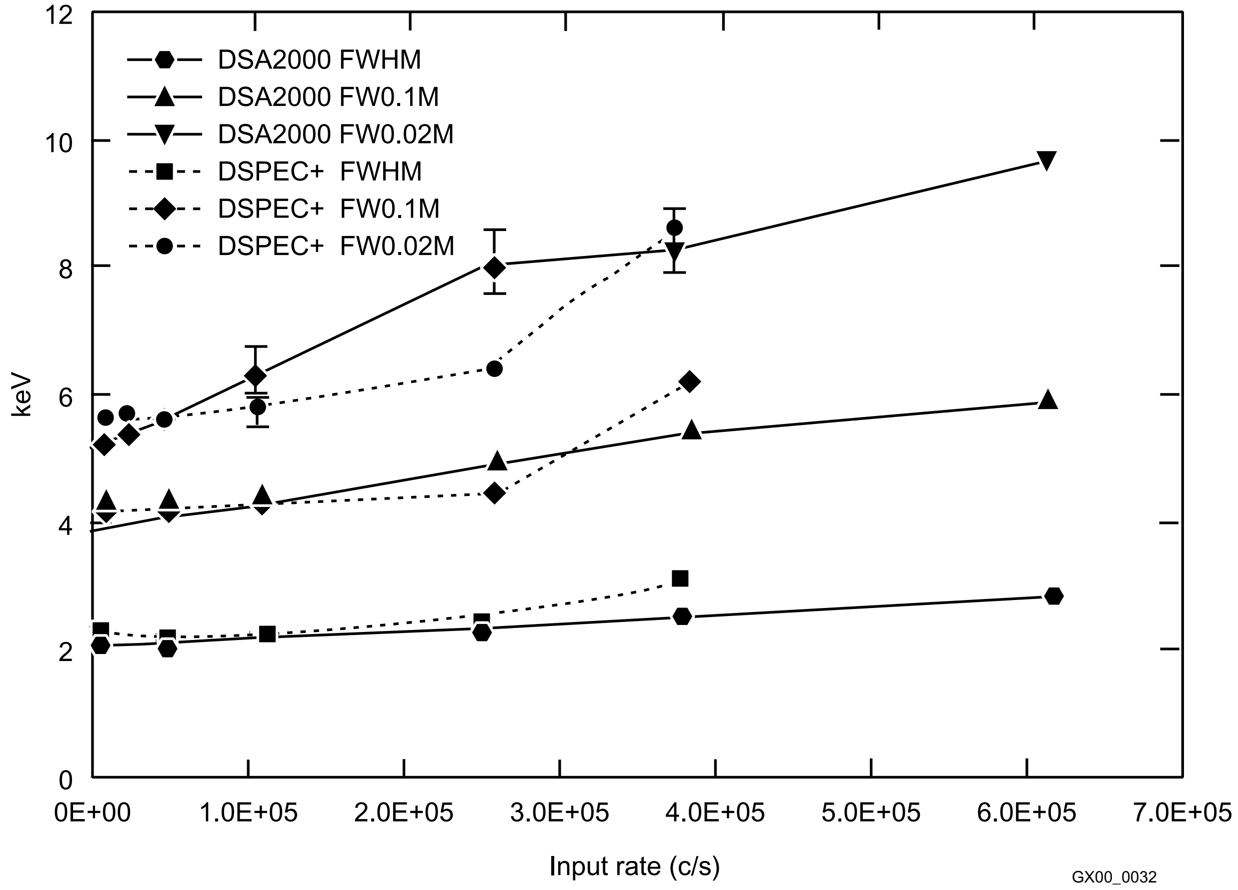

**Figure 4.** Comparison of peak shape parameters for the 1,408-keV peak of $^{152}$Eu determined for the DSA2000 and the DSPEC$^{\text{PLUS}}$.

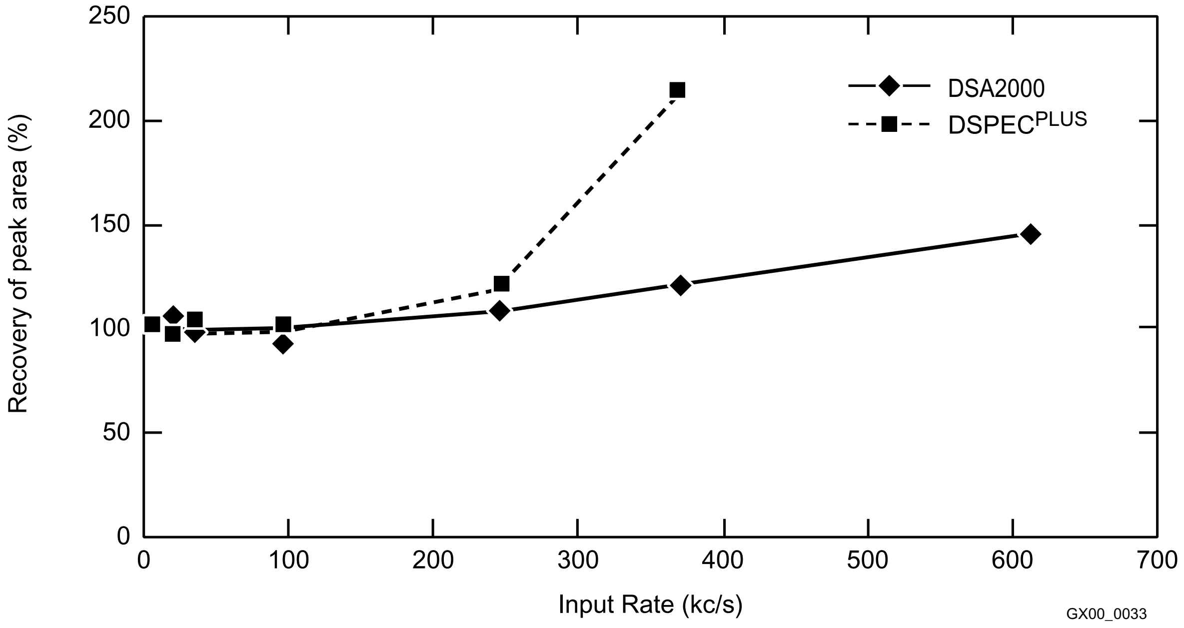

**Figure 5.** A comparison of the %Recovery values determined for the DSA2000 and the DSPEC$^{\text{PLUS}}$ at 1,408 keV.

graphically in Figure 3. The measured widths of the 1,408-keV peak from both DSPs are compared graphically in Figure 4.

An additional advantage of the proportional source technique is that it allows a direct evaluation of the quantitative accuracy of system corrections for dead time and pulse pile up losses (Reference 2). If the corrections are perfect, then for a given photopeak, the net peak counts per second measured on each source divided by the relative source strength (NF) should equal the net counts per second recorded for that photopeak on the lowest activity (NF = 1.0000) reference source. The %Recovery values measured for both DSPs at 1,408 keV line are compared graphically in Figure 5.

The performance of the rate effects correction circuitry in both of these DSPs was very good in these tests. Both units gave accurate results up to about 100 kc/s. Beyond this rate, the accuracy suffered, but the DSA2000 remained within 20% of the correct value up to 370 kc/s. The quantitative performance of the DSPEC$^{PLUS}$ in these tests is similar to that measured using resistive feedback preamplifier systems by other researchers,[5] while that measured for the DSA2000 is better than that reported by others.

## ACCOMPLISHMENTS

After extensive down time due to detector repair and scheduled accelerator maintenance, the data acquisition phase of the $^{233}$U fission experiment at IPNS has started. We expect to continue through December 2000.

Tentative agreement for a second fission experiment at ORELA has been reached. The ORELA experiment will allow more flexibility in terms of neutron energy and target materials that can be used.

The PGNAA analytical code CEARPGA has been modified so that it can be used to analyze PGNAA data taken at the INEEL. The input format has been made to be compatible with the Monte Carlo transport code MCNP.

The analytical analysis approach to gamma-based drum assay has been tested using surrogate waste forms, real waste assays, and PDP tests. So far, the results indicate that the analytical analysis approach would make simple gamma spectrometer type assay systems capable of meeting the assay requirements as specified in the WIPP Waste Acceptance Criteria.

The design of two downhole probes, one for PGNAA and one for fissile material detection, is currently at the end of the concept design stage. Certain long lead-time components are on order. An existing facility at the INEEL/TRA has been converted to a testing and calibration facility for the downhole probe development project.

The advanced high-count-rate data acquisition system based on a Motorola PowerPC processor and a LynxOS operating system has been developed. This new architecture is faster and more adaptable.

A study of the high-count-rate performance characteristics of commercial DSP PHA has been completed. The new DSP based PHA systems performed well at input count rates that would challenge all but the most specialized analog PHA systems.

# REFERENCES

1. E. W. Killian and L. V. East, “PCGAP, A Code for the Routine Analysis of Gamma-Ray Pulse-Height Spectra on a Personal Computer,” *J. Radioanal. Nucl. Chem.*, 233, 109 (1998).

2. R. J. Gehrke, J. W. Rogers, and J. D. Baker, User’s Description of a Set of $^{152}$Eu Sources of Precisely Known Relative Strengths and Accurately Known Activity, U.S. Department of Energy Report EGG-PHY-1981 (1981).

3. J. K. Hartwell and S. G. Goodwin, “Pulser Injection with Subsequent Removal—Implementation and Applications,” *IEEE Trans. Nucl. Sci.,* NS-36, 615 (1989).

4. R. J. Gehrke, E. W. Killian, L. V. East, J. M. Hoggan, S. G. Goodwin, and G. D. McLaughlin, “A portable photon analysis spectrometer for the assay of X- and gamma-ray emitting radionuclides,” *J. Radioanal. Nucl. Chem.*, 233, 225 (1998).

5. S. Pommé and G. Kennedy, “Pulse loss and counting statistics with a digital spectrometer,” *Applied Radiation and Isotopes,* 52, 377 (2000).

# Nuclear Structure Research

**J. W. Mandler and R. J. Gehrke**

## SUMMARY

The objective of this project was to perform nuclear structure research that builds and expands the INEEL's current nuclear physics expertise and provides nuclear data useful to both the basic and applied communities. Six related research areas were pursued: (1) high-accuracy γ-ray measurements, (2) actinide decay scheme studies, (3) nuclear data measurements for prompt (n,n'γ) reactions, (4) γ-ray measurements for (n,γ) reactions, (5) very low-level radiation detection, and (6) prompt γ rays from α-induced reactions. In order to bring together the required expertise and carry out this project, we developed collaborations with two other national laboratories, eight colleges and universities, two foreign laboratories, and an international collaboration.

The high-accuracy γ-ray measurement technique was demonstrated by developing a relative efficiency curve accurate to ~0.1% over the energy range 433–2,754 keV. The accuracy of this curve is approximately an order of magnitude better than had previously been attained. We developed a method to determine the age of waste and the presence of $^{237}$Np in waste from the grow-in of granddaughters of $^{241}$Am over time. The intensity of $^{226}$Ra a decay to the 186-keV excited state was accurately determined (to ± 0.5%), thereby resolving a long-standing discrepancy. Gamma-ray production rates and cross sections for Si and O were developed from previously unanalyzed LANSCE (Los Alamos Neutron Scattering Center) data. We obtained approval for beam time on LANSCE and performed our own measurements on Na and I. Successfully obtaining beam time on LANSCE was a positive sign that our experimental work was accepted and that these data are needed. Many proposed experiments do not receive approval for beam time. Our method for ultra purification of mass-separated $^{100}$Mo was very successful. Up to two orders of magnitude reduction in trace natural radionuclides in the purified $^{100}$Mo was realized. We developed an experiment suitable for use by a small Rocky Mountain college to study prompt gamma neutron activation analysis using cosmic-ray produced neutrons. Reaction γ rays from (α,n) and (α,p) reactions induced by α particles from actinides were studied. Using these γ rays and a model of the SWEPP (Stored Waste Examination Pilot Plant) γ-ray system to calculate the efficiency for a particular γ ray, we were able to predict (within 30%) the measured neutron flux from (α,n) reactions in about one-third of a sample of TRU 55-gal waste drums.

## PROJECT DESCRIPTION

### Introduction

The objective of this project was to perform nuclear structure research that builds and expands the INEEL's current nuclear physics expertise and provides nuclear data useful to both the basic and applied communities. Six related research areas were pursued: (1) high accuracy γ-ray measurements, (2) actinide decay scheme studies, (3) nuclear data measurements for prompt (n,n'γ) reactions, (4) γ-ray measurements for (n,γ) reactions, (5) very low-level radiation detection, and (6) prompt γ rays from α-induced reactions. All six areas address the need to improve the known nuclear data to either (a) verify and validate our present understanding of nuclear structure and the interactions of radiation with matter, or to (b) provide a foundation to be used to improve our current understanding of and ability to predict nuclear parameters, such as level energies and transition probabilities. Research in these six areas resulted in furthering the knowledge of nuclear structure, expanding the database that is required to develop new nuclear models and improve existing nuclear models, providing data necessary for practical applications using nuclear techniques (e.g., data needed for modeling, for analysis of assay data), and building the INEEL's capabilities in $\gamma$-ray metrology.

This work has direct EM relevance. For example, the actinide decay scheme studies provided data on the gamma rays emitted by actinides that was useful in solving a measurement issue that arose at SWEPP and that is helping us understand the logging data obtained at Pit 9. The (n,n'$\gamma$) and (n,$\gamma$) measurements are providing $\gamma$-ray production rates needed in modeling efforts to develop techniques to obtain quantitative data from prompt gamma neutron activation analysis, a technique that is needed for probe-hole logging at RWMC (Radioactive Waste Management Complex). Studies of the prompt $\gamma$ rays from $\alpha$-induced reactions has enabled us to identify the chemical form of some of the americium in Pit 9, and it is needed in the development of improved techniques to assay waste containing plutonium and americium.

Research Areas 1 and 4 focused on improving the known accuracy of nuclear parameters, providing a better understanding of nuclear structure models, and enhancing the INEEL's $\gamma$-ray metrology capability. Research Area 4 focused on verifying whether all uniquely defined prompt $\gamma$-ray transitions following neutron capture are being identified and correctly placed in the level scheme. This exercise ensures the correctness and completeness of the level scheme or identifies the need to reinvestigate it.

Research Area 2 provided new and better nuclear structure information for high-mass and also for short-lived nuclides. The decay schemes for some of these nuclides have never been adequately studied, and, in some cases, there are inconsistencies in $\gamma$-ray emission probabilities.

As a result of Research Area 3, new nuclear structure information (especially of the higher-energy levels) was obtained. This information will prove useful in testing evaluated cross sections and in testing nuclear models relating to nuclear states, transition multipolarities, and level densities. In addition, our knowledge of the $\gamma$ rays emitted upon neutron capture and neutron inelastic scattering continues to be enhanced, especially as to how the intensities of these $\gamma$ rays vary with neutron energy. This information is very important in attempts to accurately model the $\gamma$ rays emitted when a neutron interacts with matter. Current application models are relatively crude. Assumptions are currently made that are not totally correct because of lack of suitable theoretical models to precisely calculate interactions of neutrons with mater. This is due in turn to a lack of data concerning neutron capture and inelastic scattering cross sections at different neutron energies. When adequate data are finally obtained for a sufficient number of neutron energies, a theoretical model that more precisely describes $\gamma$-ray yields resulting from (n,$\gamma$) and (n,n'$\gamma$) reactions at varying neutron energies should be developed and validated.

Research Areas 2 and 3 have focused on expanding the present knowledge of nuclear structure and making this information available to the scientific community in an up-to-date Web site database. Research in these areas expands the knowledge-base of prompt $\gamma$ rays emitted for reactions initiated by a wider range of neutron energies than is presently in the database and improves the quality of the present prompt and decay data. The results of these tasks have immediate application to radioanalysis. Accurate radioanalysis depends directly upon accurate $\gamma$-ray energies, emission probabilities, and level schemes. The currently available tables of prompt $\gamma$-ray energies and intensities in units of $\gamma$ rays per 100 captures are limited mainly to thermal neutron energies, and even these have many errors, including wrong assignments, inaccurate energies, and inadequately known intensities. The same is the case for g rays from inelastic scatter of fast neutrons. The new fundamental understanding of nuclear structure obtained from Research Areas 2 and 3 will allow new practical applications for radioanalysis. For example, with a more detailed set of data from multiple neutron energies, prompt gamma neutron activation analysis (PGNAA) is more likely to be successfully expanded from a qualitative to a quantitative technique for more matrices, elements, and isotopes. This will allow PGNAA to be applied to a wider variety of mining and industrial applications.

Research Area 5 has had the indirect benefit of furthering our present knowledge of very low-level radiation detection. Very low-level radiation detection and analysis of peaks from very weak transitions is required for radioanalysis and for basic nuclear physics research, such as studies of low-intensity nuclear transitions and the Neutrino-less Experiment Using Molybdenum-3 (NEMO-3) studies to determine whether the neutrino has mass. These areas are important in that they directly affect nuclear models and our knowledge of nuclear parameters. The mass of the neutrino is important in determining whether the universe is open (will expand forever) or closed (will ultimately stop expanding and then collapse). Very low-level radiation detection is also important in applications such as measuring radioactivity at and below the environmental level, reducing the radioactivity in ultra-pure materials (such as semiconductors), measuring radioactive uptake by plants, performing tracer studies, and determining the radioactivity in the body. Our goal has been to apply good counting techniques that reduce the continuum under peaks and to reduce background levels during counting so that smaller, less radioactive samples can be assayed to currently required accuracy, thereby enhancing the signal and reducing the amount of waste to be disposed.

Research Area 6 focused on studying the $(\alpha,n)$ and $(\alpha,p)$ reactions on low-Z elements likely to be present in transuranic (TRU) waste, and to measure the nuclear properties (e.g., energies, relative intensities) for the associated prompt $\gamma$ rays. This will provide the baseline data required for deducing the number of $(\alpha,n)$ reactions occurring in waste, and hence the nonfission neutrons, by measuring the prompt $\gamma$ rays associated with the $(\alpha,n)$ and $(\alpha,p)$ reactions. Being able to deduce the number of $(\alpha,n)$ reactions will provide a means to correct the present assay technique (which consists of counting the fission neutrons and a-induced neutrons) for measuring fissile material in TRU. Successful demonstration of this technique will improve the accuracy of the assays.

The specific areas of research are discussed in more detail in the following sections.

## Research Area 1: High Accuracy $\gamma$-Ray Measurements

### *Background*

Up to the current time, the most precise measurements of relative $\gamma$-ray intensities with Ge semiconductor detectors have been accurate to within ~0.5%. Some recent work at the University of Michigan has suggested that it is possible to increase the accuracy to ~0.1% over a limited energy range of 661 to 1,332 keV. If the ability of attaining this accuracy can be verified and the energy range can be expanded, then benefits can be realized in our knowledge of nuclear structure. For example, an experiment has been proposed (by a Texas A&M professor) to determine one of the parameters of $\beta$ decay (i.e., the vector coupling constant, $G_V$) by a very precise relative $\gamma$-ray intensity measurement. This experiment cannot be performed until the efficiency determination methodology discussed here is fully developed at energies down to at least 74 keV. In addition, highly calibrated Ge detectors can be used to obtain better $\gamma$-ray intensities for various radionuclides. Besides directly improving the database of $\gamma$-ray data at the National Nuclear Data Center at BNL,[1] such measurements can be used to improve the data that is deduced from such $\gamma$-ray intensities. This includes the log *ft* values, which are a measure of the "speed" of the $\beta$ decay transition branches from the parent to the daughter nuclide. These log *ft* values are often used by evaluators to deduce the spins and parities of the daughter levels and determine information of interest for nuclear structure studies.

Internal-conversion coefficients give the ratio of the probability of an excited nuclear level emitting an atomic electron to that for a $\gamma$-ray photon in its process of de-excitation. Historically, the best measurements of these coefficients have uncertainties of about 1%. In many radionuclide decays, it is possible to deduce the K conversion coefficients from a measurement of the relative intensities of the $\gamma$ ray, the K x-ray, and the K fluorescence yield. If the precise relative efficiency curve can be developed and extended down to the region of the K x-rays, it may be possible to make some very precise measurements of internal-conversion coefficients. These values can then be used to test the results of theoretical model calculations of these coefficients. This is an issue of current interest since a new code to calculate these values is being prepared (cooperative effort of Russian scientists and those at ORNL), and it will be of interest to show that its results are better than the previous calculations.

### *Objectives*

The specific objectives of this research area have been to: (1) develop collaborations with academic and national laboratory researchers, (2) develop a highly accurate method for determining the relative full-energy peak efficiency of a Ge $\gamma$-ray detector and to demonstrate that this method can give accuracies of ~0.1%, (3) extend the method to the energy range 53–2,754 keV, (4) model detectors for collaborators to accuracies required for their nuclear structure applications, and (5) compare the capabilities of various Monte Carlo methods to calculate relative full-energy peak efficiencies for Ge $\gamma$-ray detectors.

### *Collaborations*

Collaborations were developed with Lawrence Berkeley National Laboratory (LBNL), Sandia National Laboratory, University of Michigan, Idaho State University, Albion College, Texas A&M University, North Carolina State University, Institute of Isotope and Surface Chemistry in Budapest, Bucharest University, and Physikalisch-Technische Bundesanstalt (PTB) in Germany.

### *Accomplishments*

We performed Monte Carlo calculations (using the CYLTRAN code) of the full-energy peak efficiency ($\varepsilon_p$) for a University of Michigan 100% p-type Ge detector. Comparison of these Monte Carlo results with precise measurements performed by the University of Michigan verified, at the 0.1% level, the validity of the physics modeling within the Monte Carlo code. These comparisons also indicated that the Monte Carlo method is able to produce accurate predictions for the g-ray energy range investigated (i.e., 433–1,332 keV) when the dimensions and active volume of the detector are accurately known. We then used the Monte Carlo results to compute relative $\varepsilon_p$ values at intermediate $\gamma$-ray energies to aid in the numerical interpolation of the efficiency at any desired energy within the range of the data.

These Monte Carlo results were used along with the measurements made with the University of Michigan Ge detector for nuclides that have $\gamma$ rays with very well known relative intensities ($^{108m}$Ag and $^{24}$Na) to expand the efficiency curve range to 433 to 2,754 keV. This resulted in a relative efficiency with an uncertainty of about 0.1% for this entire energy range. Therefore, our collaboration with the University of Michigan and Albion College successfully developed a highly accurate relative $\varepsilon_p$ curve for a HPGe detector to an accuracy of about 0.1% over the energy range 433–2,754 keV. The accuracy of this curve is approximately an order of magnitude better than had previously been obtained. Table 1 shows a comparison of the calculated and measured results. The results of this work were published in *Nuclear Instruments and Methods in Physics Research A*. In addition, this work was presented to and

**Table 1.** Ratios of pairs of efficiencies.

| Nuclide | γ-energies | Ratio of Efficiencies |  | Percent Difference |
|---|---|---|---|---|
|  |  | Measured | Monte Carlo |  |
| $^{108m}$Ag | 433, 614 | 1.2610(12) | 1.2620(16) | 0.08 |
| $^{108m}$Ag | 614, 722 | 1.1127(11) | 1.1119(15) | -0.07 |
| $^{94}$Nb | 702, 871 | 1.1473(19) | 1.1481(12) | 0.07 |
| $^{46}$Sc | 889, 1120 | 1.2070(13) | 1.2078(18) | -0.03 |
| $^{48}$Sc | 983, 1312 | 1.2070(13) | 1.2078(18) | 0.07 |
| $^{60}$Co | 1173, 1332 | 1.0879(12) | 1.0858(15) | -0.19 |
| $^{24}$Na | 1368, 2754 | 1.7128(29) | 1.7146(18) | -0.10 |

discussed with our international collaborators. It should be noted that the detector active volume and associated dimensions and charge collection properties are often not known well enough to achieve 0.1% accuracy with Monte Carlo calculations.

The capability to accurately model the γ-ray response of Ge detectors is extremely important in the development of nondestructive assay techniques such as PGNAA and bore-hole/probe-hole logging techniques. Without this capability, PGNAA cannot become a truly quantitative technique useful for assay of heterogeneous waste at the INEEL and other DOE facilities. In addition, the interpretation of bore-hole/probe-hole logging data requires accurate modeling of the Ge detectors used. This is especially important for applications concerning highly heterogeneous conditions such as those at Pit 9 and other RWMC locations.

A collaboration with John Hardy, Texas A&M University, was developed. A major emphasis of our work for this collaboration has been to extend the energy range of the highly accurate $\varepsilon_p$ method down to 74 keV, to extend the method to the calculation of a total efficiency ($\varepsilon_t$) curve, and to model the Texas A&M detector using the Monte Carlo code CYLTRAN. Highly accurate $\varepsilon_p$ and $\varepsilon_t$ curves for the energy range 74–600 keV are needed to support Texas A&M in determining one of the parameters of β decay by a very precise relative γ-ray intensity measurement.

Sets of $\varepsilon_p$ and $\varepsilon_t$ curves were calculated for the Texas A&M Ge detector. These calculations were done for the energies of the γ rays from the decay of $^{133}$Ba from 53 to 383 keV for sources at 15 and 100 cm from the detector. The statistical uncertainties of these calculated efficiencies, determined from the number of counts in the peak, range from 0.1% to 0.3%. Using the CYLTRAN Monte Carlo code and γ rays from $^{137}$Cs, $^{60}$Co, and $^{88}$Y, the relative efficiency curve was expanded to 53–1,836 keV for the Texas A&M detector. This encompasses the complete energy range required by Texas A&M.

In support of another collaboration, a preliminary set of Monte Carlo calculations was performed to determine the peak/total ratios for a Ge detector at the Institute of Isotope and Surface Chemistry in Budapest. The calculations were done for γ-ray energies of 662, 1,332, and 2,754 keV for the Budapest shielded geometry. Researchers in Budapest, Hungary, have made careful measurements of the efficiency of a Ge detector over an energy range that extends up to 11 MeV. The collaboration with the researchers in Budapest will give us experience developing highly accurate efficiency curves for collimated (or partially collimated) and shielded detectors and will, together with our other collaborations, give us experience with determining efficiencies over a 50 keV to 11 MeV energy range.

A collaborative effort was initiated to compare the ability of the various Monte Carlo methods to model HPGe detector response. The collaboration includes researchers from LBNL, the University of Michigan, and Romania, in addition to the INEEL. Each research group uses a different Monte Carlo computer program, and each is to model the University of Michigan detector using their particular computer program. We have completed our portion of the work. The work by the other three groups awaits completion. When all of the work is complete, we will draft a paper for publication showing comparisons of the results.

A major accomplishment of our work has been the establishment of a network of people who are interested in combining their efficiency measurements with our experience in using the Monte Carlo electron and photon transport code (CYLTRAN) to improve the precision of these efficiency curves by calculating the efficiencies for energies between the measured values. This network includes persons at other laboratories who are specifically interested in making high-quality measurements.

Our work has shown that there may be a problem with the completeness of the physics in the Monte Carlo codes we use that describes the interactions of $\gamma$ rays above 3 MeV. This involves the ratios of areas of the full-energy, the single-escape, and the double-escape peaks. We performed Monte Carlo calculations of these ratios for detectors at the University of Michigan, LBNL, and Budapest for comparison with their measured data. The measured and calculated ratios do not agree as well as expected. This difference was also shown to exist for calculations performed by LBNL with the MCNP Monte Carlo code. In addition, the calculations we performed using CYLTRAN and MCNP indicated that the results from the two codes do not agree as well as expected. Because of these agreement problems, we invited one of the Sandia National Laboratory authors of CYLTRAN to join our collaboration to see if there are some limitations in this code at these energies. Since all of the participants in our collaboration are very capable researchers, we can expect to improve the physics algorithms used in these codes and thereby advance the field of $\gamma$-ray spectrometry, especially in the determination of peak and total efficiency curves for Ge detectors.

In order to extend the usefulness of this highly accurate relative efficiency curve, we have pursued converting it to a highly accurate absolute efficiency curve. In order to accomplish this, highly accurate (having an uncertainty of about 0.1%) calibration sources are required. The accuracy of the activities of these sources must be at least about an order of magnitude better than what is currently available (which are accurate to about 1.5%). These sources would be used to convert our precise relative efficiencies to absolute efficiencies. Discussions were held with the French and German radioactivity standards laboratories, Laboratorie National Henri Becquerel (LNHB) and Physikalisch-Technische Bundesanstalt (PTB), respectively, concerning the possibility of providing these highly accurate efficiency calibration sources. Initially, both laboratories expressed interest in this project. PTB provided, at no cost to us, two $^{60}$Co sources with quoted accuracies of ±0.06%. This is a considerable contribution since low-count rate calibration methods had to be applied to high-count rate sources and the associated corrections and their uncertainties determined.

## Research Area 2: Decay Schemes for Heavy Mass and Short-Lived Nuclides

### Background

The long a-particle decay chains of high-mass nuclides such as $^{233}$U, $^{235}$U, and $^{238}$U have some short-lived progeny (e.g., $^{221}$Fr, $^{217}$At, $^{213}$Bi) for which the decay schemes have not been well studied.[1,2] In other cases, due to the lack of accurately measured emission probabilities, the x-ray intensities from one member of the chain do not agree with those from another member of the chain (e.g., $^{226}$Ra chain).[1,2]

The results of these decay scheme studies have provided new and better nuclear structure information. In addition, these decay chains are of interest in various practical applications, such as the assay of residue and waste from the production of weapons, reactor fuel, and radwaste, but have not been fully used because the above inconsistencies limit the accuracy of the information obtained from the use of the daughter products in the radioanalysis.

### Objectives

The specific objective of this research area was to study the decay of actinides and to provide an extensive actinide database of practical use to the γ-ray spectrometry practitioners. This includes: (1) developing the necessary radiochemistry methods to give pure sources of the desired elements (some of which have short half-lives), (2) measuring high-quality Ge γ-ray spectra, and (3) when necessary, measuring the γ-ray energies and intensities for the individual nuclides and the decay chain. It also includes making this information available to the scientific community in an easily accessible form, i.e., a web site.

### Collaborations

Collaborations were developed with the University of Michigan and Washington State University.

### Accomplishments

A collaboration was developed with the University of Michigan to perform high-precision γ-ray spectral measurements on radionuclides of interest (both actinides and nuclides used to support Research Area 1). Our collaborators at the University of Michigan developed techniques for chemical separation of $^{229}$Th and its daughters and used this technique on approximately 100 μg of acceptably clean $^{229}$Th. Measurements of the γ-ray spectra from $^{233}$U and $^{229}$Th and their short-lived daughters were performed at the University of Michigan using a Ge detector. Measurements of the γ-ray spectra from $^{233}$U using Loax γ-ray detectors were also completed at both the INEEL and the University of Michigan.

Our University of Michigan collaborators performed high-precision measurements of γ-ray spectra from radionuclides with very well known relative intensities and energies for use in demonstrating the accuracy of the efficiency curves developed in Research Area 1. They then used the highly accurate efficiency curves developed in Research Area 1 to perform highly accurate measurements of γ-ray intensities for selected radionuclides and investigated nuclear structure parameters. A set of high-precision γ-ray spectra from $^{24}$Na at various distances to show coincidence summing trends was obtained. Spectra taken at 99 cm show the very weak 4,237 keV γ ray with an area three standard deviations above the continuum (see Figure 1). Spectra taken at 0 cm show the 5,235 keV sum (sum of cascade γ rays emitted upon depopulation of the 5,235 keV level in $^{24}$Mg). A set of high-precision γ-ray spectra with good statistics at high energies was obtained from $^{49}$Ca. Sets of high-precision γ-ray spectra from $^{91,92}$Sr-$^{91,92}$Y have been completed. This work resulted in much improved γ-ray spectra for $^{91}$Sr-$^{91}$Y and

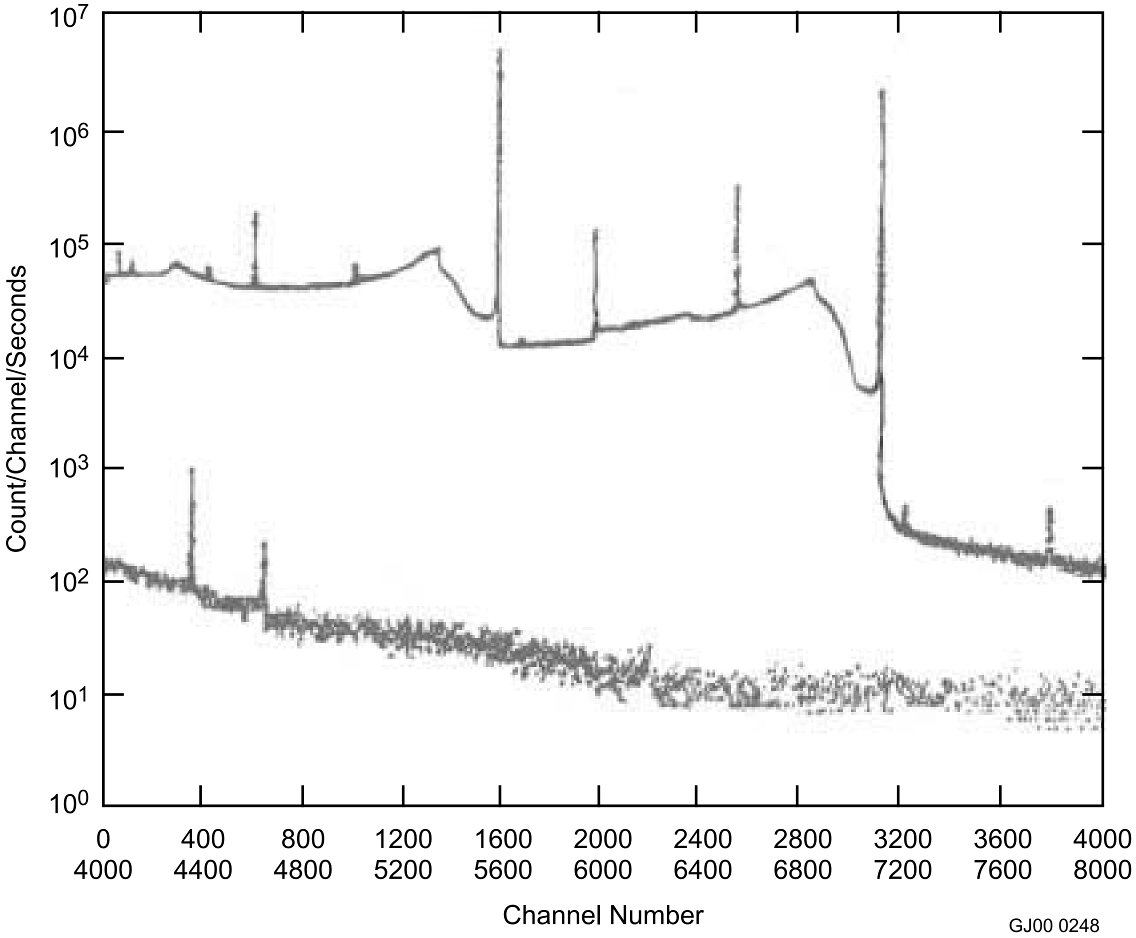

**Figure 1.** High-precision γ-ray spectrum from $^{24}$Na showing weak 4,237 keV γ ray.

slightly improved γ-ray spectra for $^{92}$Sr-$^{92}$Y. A set of high-precision γ-ray spectra from $^{108m}$Ag was obtained with the Loax detector.

Researchers at the University of Michigan performed a very careful and lengthy measurement of the γ-ray spectrum from the decay of $^{49}$Ca (8.7 m half-life). Since they used the same detector as used in the Research Area 1 study (but at a different source distance), we were able to provide accurate relative efficiencies for the $^{49}$Ca γ-ray energies. As a result, this work provides γ-ray intensities for this decay that are from 10 to 100 times more accurate than the currently available data. These highly accurate intensities will then be used to develop highly accurate decay scheme information (i.e., significantly more accurate values than currently known). This will provide correspondingly more accurate β-decay branch intensities and related log *ft* values (i.e., reduced transition probabilities), which are important to β-decay theory.

Working with the University of Michigan and Texas A&M University (where the β-decay studies are being performed) is enhancing the INEEL's collaboration efforts with universities, providing increased visibility for the INEEL in the nuclear physics community, and further enhancing the expertise of INEEL's nuclear science research personnel.

At the INEEL, nuclear data, including γ-ray spectra and decay data, were completed for the following radioactinides: $^{226}$Ra, $^{232}$U, $^{233}$U, $^{235}$U, $^{238}$U, "aged" $^{237}$Np, $^{238}$Pu, $^{239}$Pu, $^{240}$Pu, "aged"

$^{241}$Pu, $^{242}$Pu, "aged" $^{241}$Am, $^{243}$Am, $^{243}$Cm, $^{244}$Cm, and $^{245}$Cm. These radioactinides with their decay schemes, ENSDF downloaded data, and γ-ray spectra will be added to an updated INEEL Gamma-ray Center web site. These data have already found wide use at the INEEL in resolving waste issues and in correcting erroneously reported reaction γ rays as from $^{241}$Am decay. Spectra from depleted uranium are currently being used in an effort to develop methods to determine the attenuation of γ radiation in waste drums when they contain large amounts of actinides, especially depleted uranium. A manuscript titled, "Artifact (alpha,n) Reaction Gamma-ray peaks as $^{241}$Am Decay Gamma Rays," has been accepted for publication in the Journal of Radioanalytical and Nuclear Chemistry. This paper was prompted by a previously published article (Abdulrahman Abdul-Hadi, "Gamma-spectrum of $^{241}$Am," Journal of Radioanalytical and Nuclear Chemistry 231 (1998) 147). Upon comparing the author's results with our measurements, we discovered that the author misidentified α-induced reaction γ-rays as coming from the decay of $^{241}$Am. Proper identification of the γ rays from $^{241}$Am is very important. First, if the γ rays are erroneously attributed to the decay of $^{241}$Am, then they must be fit into the decay scheme, and this will result in errors in our knowledge of the nuclear structure (i.e., the nuclear levels). Second, since the $^{241}$Am γ rays are frequently used for assay of transuranics, if γ rays are erroneously attributed to $^{241}$Am, then assay results can be incorrect due to interference corrections. Accurate knowledge of transuranic content is especially important for waste shipment (e.g., to WIPP). It is hoped that our paper will assist researchers and operations personnel in avoiding assay errors related to the misidentification of peaks.

An investigation of the age of waste was carried out by looking for and then measuring the intensities of γ rays from daughter nuclides. The presence of $^{237}$Np in $^{241}$Am-contaminated waste was determined by observation of the $^{233}$Pa granddaughter that grew in over time. Observation of this progeny was unexpected because of the very long half-life of $^{237}$Np (2 million years). A paper, titled "Information in Spectra from Sources Containing "Aged" $^{241}$Am as from TRU Waste," documenting the results of this work has been accepted for publication in Waste Management. A paper titled "Peeling the Onion? The Gamma-ray Spectrometry of TRU Waste," was completed and presented at the 7th NDA Waste Characterization Conference held during May in Salt Lake City. This paper, which is published in the meeting proceedings, reported on the use of the 440 keV γ-ray peak from $^{213}$Bi, a progeny of $^{233}$U, as useful in the identification of aged $^{233}$U. It also reported on the use of the 312 keV g ray emitted in the decay of the granddaughter $^{233}$Pa for verifying the age of the $^{241}$Am-containing waste and for determining the possible presence of $^{237}$Np in excess of that formed in the decay of the $^{241}$Am activity.

Our collaboration with Washington State University resulted in a very accurate (±0.5%) determination of the $^{226}$Ra α decay to the 186-keV excited state. This work resolves a long-standing inconsistency in the literature for the past 30+ years in the $^{226}$Ra 186-keV emission probability that was reported by studies resulting from measurements based on the $^{226}$Ra mass standard and those based on $^{226}$Ra decay parameters. Our results agree, within statistical error, with the results based on the mass standard. A paper, titled "Precise Determination of the Intensity of $^{226}$Ra Alpha Decay to the 186-keV Excited State," documenting this work was reported at the Fifth International Conference on Methods and Applications of Radioanalytical Chemistry (MARC-V) Conference, and it will also be published in the *Journal of Radioanalytical and Nuclear Chemistry*. This work received very positive reviews from Dr. Garmon Harbottle of Brookhaven National Laboratory (BNL) and Jerome Simon from the United Kingdom who requested a copy of the "timely" work.

A paper titled "Radioactinide Additions to the Electronic Gamma-Ray Spectrum Catalogue" was presented at the MARC-V Conference. The paper will also be published in the *Journal of Radioanalytical and Nuclear Chemistry*. The presentation announces the addition to the INEEL Gamma-ray Center web site of actinide nuclear data and γ-ray spectra taken on present-day Ge spectrometers for use by educators, regulators, researchers, and technologists using and applying nuclear radiation. We also received and accepted an invitation to present a paper titled “Extension of the Electronic Gamma-ray Spectrum Catalog Web Site” at the CAARI 2000, 16th International Conference on the Application of Accelerators in Research and Industry.

## Research Area 3: Nuclear Data Measurements for Prompt (n,n’γ) Reactions

### *Background*

The γ-ray energies and intensities for many multi-isotope elements produced from prompt reactions are fragmentary, with data measured in great detail for some of the isotopes and minimal or no data for other isotopes.[1,3,4] There still remain some γ-ray transitions that have not been well measured or placed in their level schemes or decay schemes and have important nuclear structure implications or limit radioanalysis results.

Definitive γ-ray energy and intensity information is needed to more accurately assay complex matrices. This information will also provide new nuclear structure information (especially of the higher-energy levels) to test evaluated cross sections and to test theoretical nuclear models for their ability to identify various types of states, transition multipolarities, and level densities. Additional knowledge of the γ rays emitted upon neutron capture and neutron inelastic scattering is needed for assay applications. For example, very little is known about how the spectrum of emitted γ rays changes as the neutron energy changes. When this information is obtained, models can be developed to predict how this γ-ray emission changes with neutron energy. Such models are very important in the application arena.[5–10]

Prompt gamma neutron activation analysis (PGNAA) is an assay technique that could greatly benefit from a comprehensive database of γ-ray energy and intensity information for (n,γ) and (n,n’γ) reactions. PGNAA is potentially a very powerful technique for determining elemental content and the minor impurities in a material, and the state-of-the-art is making possible assays of trace levels of RCRA elements in an ore or waste that indicates the need for special handling or disposal. If PGNAA is to be developed for expanded use in quantitative elemental analysis, it will be necessary for Monte Carlo modeling codes to have access to accurate reaction data for neutron/γ-ray/electron transport so that all modes of interaction with matter including those occurring in the detector can be properly handled, even in complex (multi-element) matrices.

### *Collaborations*

A collaboration with the Los Alamos Neutron Science Center (LANSCE) located at the Los Alamos National Laboratory (LANL) was developed for obtaining previously unanalyzed LANSCE data and for performing measurements at LANSCE. Personnel from Idaho State University joined the collaboration to assist us in making the measurements.

### *Objectives*

The specific objective of this research area was to obtain data concerning the γ-ray energies and intensities (in γ’s per particle interaction) as a function of neutron energy for neutron-induced reactions on elements of interest. The scope of work for this research area involved obtaining and analyzing previously unanalyzed data from LANSCE and using highly calibrated Ge detectors to measure the γ-ray energies and intensities from (n,n’γ) reactions on selected high-purity elemental samples at a variety of neutron energies up to 14 MeV.

## ***Accomplishments***

Investigations of the state-of-the-art of nuclear data relating to prompt $\gamma$ rays from neutron-induced reactions were performed. We concluded that for quality applications using PGNAA, better cross sections and $\gamma$-ray production rates are required. Detailed information concerning $\gamma$-rays intensities from neutron inelastic scattering is only known for a fission-neutron spectrum. Very little is known for discrete neutron energies, although there is some information for 14-MeV neutrons. In order to accurately model nondestructive assay (NDA) techniques using fast neutron reactions, the $\gamma$ rays from neutron inelastic scattering need to be known as a function of neutron energy. In addition, the Evaluated Nuclear Structure Data File (ENSDF) energies for capture $\gamma$ rays are reasonable, but the intensities (i.e., $\gamma$ rays per 100 captures) are not complete (e.g., intensities for many $\gamma$ rays are not available).

We identified facilities that are adequate for carrying out our scope of work. For high-energy neutron studies, the LANSCE facility at LANL is most appropriate for the measurement of $\gamma$ rays from high-energy neutron reactions. LANSCE has obtained $\gamma$-rays spectra from (n,x'$\gamma$) reactions for a small set of elements and neutron energies ranging from 2 or 4 MeV to 100 MeV, depending on the element. A few preliminary $\gamma$-rays spectra were obtained from LANSCE. Analysis of these spectra indicated that the LANSCE data is of interest to us. Data currently exist for some of the elements of interest to us (i.e., those that are useful in PGNAA applications), but not for all. In addition, it will take some effort to retrieve and use the existing data. Therefore, a collaboration was developed with LANSCE for the purpose of (1) retrieving all existing data of interest to us, (2) providing assistance in analyzing these data, and (3) performing measurements to collect new data.

Work on retrieving the first set of existing data (i.e., those for oxygen and silicon) including neutron binning of the data and measurement of fluences, was carried out by LANSCE personnel. We installed the computer codes needed to analyze the spectra on our computers. We then analyzed the data, identifying $\gamma$-rays peaks, calculating $\gamma$-rays intensities, and generating production rates and cross sections. Figure 2 shows plots of the resulting cross sections for fast-neutron bombardment of oxygen. Subsequently, we discovered that LANSCE data existed for boron, carbon, nitrogen, sodium, magnesium, sulfur, calcium, titanium, and manganese. We, therefore, had LANSCE personnel retrieve these data. We will generate production rates and cross sections after we evaluate the quality of these data.

A proposal to measure $\gamma$ rays from (n,x'$\gamma$) reactions for other elements of interest for which no data currently exist was developed and submitted to LANSCE. The LANSCE Program Advisory Committee (PAC) approved our measurements, stating, "The committee supports a vigorous coordinated program of measurements [of gamma-ray yields]." This is a very positive sign of acceptance of our experimental plan and the need that exists for these data. Few proposed experiments receive approval for beam time. This is a major step in allowing us to build a program of measurements to fill a glaring nuclear data need.

We were allowed one period of beam time at LANSCE during FY 2000. Our first target of interest was NaI. This compound was selected because a large amount of PGNAA work is currently performed using NaI(Tl) detectors. We obtained a suitable sample of NaI and measured the $\gamma$-ray production rates for iodine. We will be allowed additional beam time during FY 2001 and will make measurements on additional elements of interest.

Discussions were initiated with Anton Tonchev (Idaho State University) on a collaboration with him in the study of photonuclear physics on high-spin isomeric targets.[11] Discussions have involved the production and purification of long half-life isomers with high spin states. Dr. Tonchev presented a seminar on this subject at the INEEL. Interest in high-spin states derives from the fact that high-spin states are important to the investigation of nuclear structure effects. These states may have significant

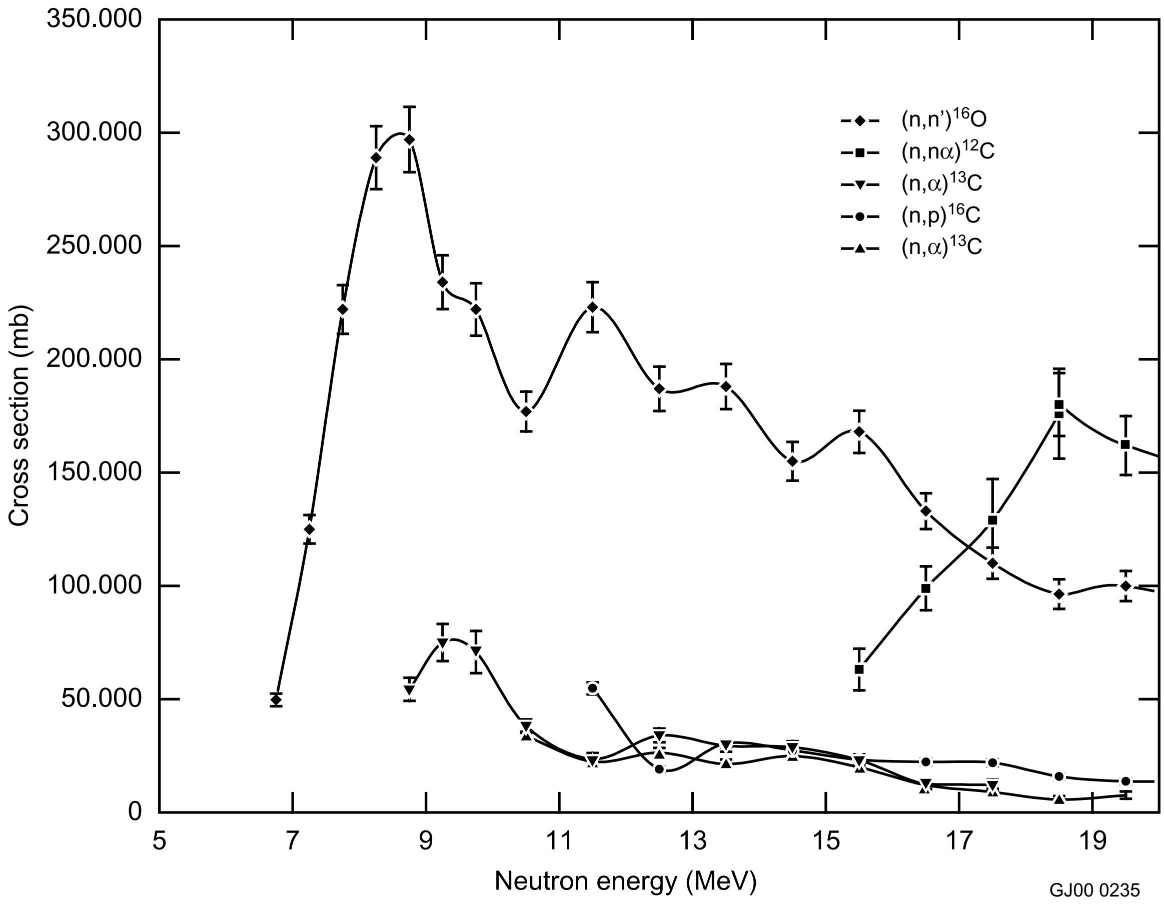

**Figure 2.** Measured cross sections for fast neutron bombardment of oxygen.

absorption cross sections in comparison with usual nuclei due to the nuclear structure, possible alteration of deformation and nuclear radius, and also the level density of the compound nucleus. The identification of several high-spin state long half-life isomers is being conducted. Since we have sufficient amounts of some of the required isomers in storage (e.g., ~20 μCi of $^{108m}$Ag), we expect a collaborative effort to begin during FY 2001.

## Research Area 4: Measurement of Additional g Rays in (n,g) Reaction

### ***Background***

If one observes all of the prompt γ rays following thermal neutron capture, the sum of the products of the γ-ray energies and intensities (in γ's per decay) should add up to the energy of the neutron capture state. For low-mass nuclides the level schemes (and hence the γ-ray spectra) are simple enough that existing experimental data are complete and this relationship holds. But, for medium and heavy mass nuclides the level schemes and, therefore, the spectra are very complex, causing the discrete peaks to lose their identity and become part of the continuum due to the very high density of nuclear levels participating in the nuclear de-excitation. Under these conditions, the historical peak analysis techniques only extract the data for a fraction of the emitted γ rays. For these nuclides, because the above sum is incomplete, it is much less than the energy of the capture state.[3,12]

This work focused on developing a more complete understanding of the statistical nature of γ-ray emission from high-energy states. (During FY 2000, we received a request for advice on how to compensate for the lack of completeness in these data and for practical ways to analyze these complex spectra.)

### Objective

The specific objective of this research area was to increase our knowledge of the energies and intensities of these γ rays emitted in (n,γ) reactions. One approach is to develop and apply a method to extract the data for a continuous spectrum of γ rays in addition to the data for the discrete lines that are normally observed. This methodology requires spectrum de-convoluting software which, in turn, requires detector response functions for monoenergetic γ rays. These response functions must be determined from a combination of measured γ-ray spectra from simple radionuclide decays and Monte Carlo calculations. Another approach is to measure as many of the individual γ rays as possible using coincidence techniques, a very time-consuming task.

### Collaborations

A collaboration with North Carolina State University (NCSU) was developed in order to use their thermal neutron beam to investigate (n,γ) reactions using γ–γ techniques. Tentative collaborations with the National Institute of Standards and Technology (NIST) and the Institute of Isotope and Surface Science (Budapest) were developed in order to perform investigations using their thermal neutron (NIST) and cold neutron (NIST and Budapest) beams.

### Accomplishments

Discussions were held with a number of basic and applied researchers to determine their data needs. We found that more information concerning the unaccounted for γ rays and γ-ray coincidences from (n,γ) reactions was, indeed, a current need, especially by groups using prompt gamma neutron activation analysis and by groups developing models to predict γ-ray spectra from (n,γ) reactions in bulk material. In order to scope the issue of the fraction of γ-ray energy unaccounted for, data from ENSDF for selected thermal neutron (n,γ) reactions were obtained and analyzed to determine if all the energy resulting from thermal neutron capture can be accounted for by the known γ rays. Results indicated that for the low-Z isotopes (e.g., thermal neutron capture in $^{28}$Si and $^{34}$S), both the energy resulting from thermal neutron capture and the γ transitions from the capture state are adequately accounted for. For the medium-Z and high-Z isotopes, however, only a small fraction of the neutron capture energy and the gamma transitions from the capture state are accounted for. For example, for thermal neutron capture in $^{113}$Cd, only about 32% of the neutron capture energy and about 11% of the transitions from the capture state are accounted for. For thermal neutron capture in $^{155}$Gd, only about 31% of the neutron capture energy and about 20% of the transitions from the capture state are accounted for. This is due to the fact that only a limited fraction of the discrete gamma rays are seen in capture γ-ray spectra. A large fraction of the γ rays are in the unresolved continuum.

A study of methods for extracting the γ rays from the continuum was initiated and a potential candidate method was identified. Investigation of this method indicated that it would not provide results with the accuracy we would like. It would provide information concerning the γ rays in an energy interval, but it could not provide information concerning individual γ rays. While the former would be useful to us (especially for modeling applications), the latter is required if level information is desired. It appears that the most appropriate way to obtain additional data is to use advanced experimental methods to measure and identify additional discrete γ rays from neutron capture. By a combination of using the cleanest neutron beams available together with large Ge detectors and anti-Compton and γ–γ techniques, we expect to obtain information on additional γ rays from neutron capture reactions.

A collaboration was developed with North Carolina State University (NCSU) to use their thermal neutron beam for (n,γ) measurements using γ-γ techniques, and the design of experiments was initiated. The first step was to evaluate the available nuclear data to determine what nuclear levels for a given isotope would be expected to be populated in an (n,γ) reaction but for which no γ rays have yet been observed. Researchers at NCSU developed a list of isotopes for which this type of enhanced γ-ray transition information is needed. We expanded the list and then evaluated a selection of low- and medium-mass isotopes. Subsequently, NCSU performed a series of measurements of γ rays from (n,γ) reactions using γ-γ techniques. The measurements were successful and showed promise, but they indicated that better results might be obtained if the small Ge detectors used by NCSU would be replaced by larger Ge detectors. Scheduling was completed for the initiation of (n,γ) measurements at NCSU during the last quarter of FY 2000. However, because of travel restrictions, we were not allowed to perform these measurements. We now expect to begin them during the first few months of FY 2001.

We identified other facilities that are adequate for carrying out our scope of work. Capture γ-ray spectra were obtained from the National Institute of Standards and Technology (NIST) and from the Institute of Isotope and Surface Chemistry, Budapest, Hungary. These facilities are currently leaders in capture γ-ray studies. Both have operating neutron beams we could use. The Institute of Isotope and Surface Chemistry has a cold neutron beam, and NIST has both thermal and cold beams. Computer routines were developed to read these data files so that the spectra can be analyzed with PCGAP's GINA interactive analysis program for γ-ray energies and peak areas. A comparison of the results of the analysis of the spectra obtained from the two facilities indicated that those from the Institute of Isotope and Surface Chemistry are higher quality. This is due to the cleaner characteristics of the neutron beam at the Institute of Isotope and Surface Chemistry and the fact that they routinely use Compton-suppressed detectors. It was concluded that we could use the NIST facility for our work with thermal neutrons, but at present the Institute of Isotope and Surface Chemistry is superior for our cold neutron work. Our work will consist of performing high-quality singles measurements that have not yet been done with large (>50% relative efficiency) Ge detectors and to use γ-γ coincidence techniques to study γ cascades not otherwise discernable in singles measurements so that they may be placed in the level scheme. In order to carry out these measurements, tentative collaborations with NIST and the Institute of Isotope and Surface Chemistry were developed. Our current plans are to perform initial measurements at NCSU (a facility on which it is easier for us to obtain beam time), perfect our instruments and techniques, obtain preliminary data, and then go to the NIST and/or Institute of Isotope and Surface Chemistry facilities.

The measurements in Research Areas 3 and 4 require the design of specialized detector-shield setups. In order to adequately design these experiments, the use of Monte Carlo neutron and γ-ray transport is required. In the course of performing Monte Carlo modeling studies to design our setups, we discovered some differences between the results generated by MCNP as compared to those generated by CYLTRAN. In particular, although both codes seem to give comparable total efficiencies, the peak efficiencies differ in some cases. Therefore, we initiated a detailed investigation to learn more about the magnitude and extent of the differences between the results generated by CYLTRAN and MCNP. Additional unexpected differences in escape and the 511 keV peak intensities were found when preliminary MCNP and CYLTRAN results were compared. A collaboration with researchers at other laboratories and institutions was developed for further investigation of this issue (see Research Area 1).

Our involvement in technical societies and in organizing sessions for technical meetings has been very useful to the Nuclear Structure Research Project (especially Research Areas 3 and 4), the Environmental Systems Research and Analysis Program, and the INEEL during the year. Not only does it give the Nuclear Structure Research Project's personnel visibility, it has allowed us to invite authors to present papers on other INEEL research in the Environmental Systems Research and Analysis Program (such as the Nondestructive Assay Project) and other INEEL projects. In addition, it brought us into contact with researchers with whom we expect to collaborate in the future. It also brought us into contact with a recent Ph.D. on a postdoctoral assignment at LANSCE who accepted an employment offer from us and joined our staff in November 1999.

## Research Area 5: Very Low-Level Radiation Detection

### *Background*

The ability to detect and quantitatively measure very low levels of radiation and peaks from very weak transitions is becoming more important to both the basic and applied nuclear physics communities. The applied nuclear physics community needs new instruments and techniques for the measurement of very low levels of radioactivity in the environment, biological media, and ultra-pure materials. Not only must the lower limit of detection be reduced, the accuracy of the quantitative results must also be improved. This can be achieved either by increasing the efficiency of the radiation detection technique or by using advanced methods to reduce the spectral continuum and the background through optimizing the counting conditions. For example, large arrays of shielded detectors can be used. Anti-Compton techniques can be used to reduce the spectrum background, thereby increasing the signal-to-noise ratio. Shielding can be employed up to massive amounts (e.g., locating the counters far underground) to reduce the natural background. Chemical separations can be performed in order to reduce the amount of natural radioactive materials in the sample. Our participation in the Neutrino-less Experiment Using Molybdenum-3 (NEMO-3) gives us the opportunity to participate in an international collaboration that is making advances in using all these methods. To study double beta decay (and, if successful, measure the mass of the neutrino), requires the development of techniques to detect very low levels of radiation and ultra-purification techniques to remove trace amounts of natural radioactive materials from mass-separated $^{100}$Mo. The experience gained with this collaboration is being applied at the INEEL to solve DOE's problems.

The NEMO-3 will result in a better understanding of the dynamics of the universe via knowledge of the mass of the neutrino. Our participation in the NEMO-3 will result in new separations technology that can be applied not only to the manufacture of ultra-pure materials but also in isotope production (e.g., isotope production at ATR). With the new radiation measurement instruments and techniques, our ability to study low intensity nuclear transitions and to accurately determine the radioactivity in the environment, materials, and biological media will be enhanced. In particular, the lower limit of detection will be reduced and the statistical accuracy of measurements will be improved. In some cases, sample size can then be reduced while achieving the same accuracy. This could result in a significant reduction of laboratory radwaste. The improvement in accuracy or reduction in radwaste would be a definite asset in the ongoing competition to do things better, faster, and cheaper.

### *Objective*

The objective of this research area was to enhance the INEEL's expertise in the area of very low-level radiation measurement. Specific objectives were to continue our participation in the NEMO-3, develop a method for ultra-purification of molybdenum, ultra-purify the $^{100}$Mo required by the experiment, and participate in the design and implementation of the very low-level radiation measurements and in methods for reduction of the spectral continuum

### *Collaborations*

The INEEL continued participation in the NEMO-3, the international collaboration performing the double beta decay experiment. This collaboration involves an international collaboration of U.S., French, Russian, and Hungarian scientists. Mount Holyoke College was one of our close collaborators in this effort.

### *Accomplishments*

The INEEL (1) continued its involvement in the NEMO-3 international collaboration that is performing this experiment; (2) developed radiochemistry separation methods to remove the natural radioactivity from mass-separated stable $^{100}$Mo for the double beta decay experiment; (3) developed an improved method to minimize the particle size of the Mo (to less than 10 microns); (4) separated a preliminary sample of natural Mo that, when tested, proved to be the purest ever produced and pure enough to meet the needs of the double beta decay experiment; and (5) purified approximately 4 kg of mass separated $^{100}$Mo.

Development of a method for ultra-purification of Mo was highly successful. Up to about two orders of magnitude reduction was realized for some nuclides. This purification meets the strict NEMO-3 requirements. This was demonstrated by measurements performed at the NEMO-3 experimental facility at Modane, France, that showed that the ultra-purified $^{100}$Mo contained no g-ray emitting isotopes detectable above the background. Table 2 shows the exceptional separation obtained in a typical batch of ultra-purified $^{100}$Mo. Almost as important as purifying the $^{100}$Mo, our procedure results in very low losses of Mo. For example, in this batch of 680 g of $^{100}$Mo, the loss was only 5 grams of $^{100}$Mo. This is very important due to the very high value of $^{100}$Mo ($6,700 per gram in the U.S.). Our losses of $^{100}$Mo were well below the requirements of the NEMO-3 collaboration, which was 5% or ~34 grams.

Through the INEEL Academic Exchange Program, we awarded a faculty fellowship to Prof. S. Sutton of Mount Holyoke College and an undergraduate fellowship to Ms. C. Riddle of Idaho State University. Both individuals worked on the $^{100}$Mo separation task. At the end of the 1999 summer internship period, there was a contest at each of the INEEL facilities where fellowship students presented their summer accomplishments. Ms. Riddle was chosen as the Test Reactor Area's representative to present her work on $^{100}$Mo purification to the complete laboratory. Prof. Sutton presented our work at a NEMO-3 experimenters' meeting at Prague, Czech Republic. He also presented an invited paper

**Table 2.** Results of chemical Purification of $^{100}$Mo.

| Radioisotope | Initial Activity (dpm/kg) | Final Activity (dpm/kg) | NEMO-3 Requirements (dpm/kg) |
|---|---|---|---|
| $^{214}$Pb-Bi | 0.24 ± 0.04 | < 0.02 | 0.02 |
| $^{234}$Th | 16 ± 2 | < 1 | |
| $^{40}$K | 8.3 ± 0.6 | < 0.4 | |
| $^{235}$U | 5.0 ± 0.4 | 0.06 ± 0.02 | |
| $^{238}$Ac | 0.14 ± 0.05 | < 0.06 | |
| $^{208}$Tl | 0.08 ± 0.02 | < 0.01 | 0.001 |
| $^{212}$Pb | 0.19 ± 0.05 | < 0.06 | |

discussing the NEMO-3 instrument at the 1999 Winter Meeting of the American Nuclear Society in Long Beach, California.

A white paper describing the $^{100}$Mo purification and the NEMO-3 experiment was developed and is being used to obtain outside funding for this work. A potential DOE sponsor has been identified, and we are now negotiating with him to obtain FY 2001 funding. Four papers concerning the NEMO-3 experiment were published. We are also working on a Mo purification paper that will be submitted to Nuclear Instruments and Methods. We gave a presentation on our Mo purification work for the NEMO-3 experiment at the Northwest Regional American Physical Society meeting held during May 2000 in Eugene, Oregon.

Serge Jullian (leader of the NEMO-3 experiment) and Dominique Lalanne presented seminars at the INEEL and at Idaho State University (ISU) and held discussions with staff members of both organizations. The possibility of ISU joining the NEMO-3 collaboration was discussed. ISU's role would potentially include performing: (1) calculations regarding interactions of internal and external neutrons and $\gamma$ rays with the NEMO-3 detector, and (2) experiments at the Idaho Accelerator Center involving the injection of 2–4 MeV electrons into a NEMO-3 plastic scintillator detector and the careful monitoring of the output signal as a function of time.

Dr. Sean Sutton (our Mount Holyoke College collaborator) presented a paper on NEMO-3 and molybdenum purification and backgrounds in the NEMO-3 detector at a special conference (Carolina Symposium on Neutrino Physics. Sean Sutton and John Baker gave a talk to the Physics Department at Idaho State University (ISU). It was very similar to the talk given at the University of South Carolina. Dr. Sutton also studied a problem that our Russian colleagues are having in the area of making composite foils using the purified molybdenum. It seems to be related to the temperature of the final reduction of the molybdenum. If the temperature is too high, the molybdenum forms aggregates, and if too low, it is not completely reduced. This causes problems when the molybdenum is mixed with water and polyvinyl alcohol. The Russians were getting a rubbery mixture rather than a paste, making it very difficult to spread the molybdenum evenly upon the mylar film. With Dr. Sutton's assistance, the problem was satisfactorily solved.

During June 2000, John Baker attended the NEMO-3 source production meeting in France and presented a paper titled, "Chemical Purification of Molybdenum Samples for the NEMO-3 Experiment." This paper has subsequently been submitted for publication in Nuclear Instruments and Methods A. During the meeting, Baker had the opportunity to tour the Marie Curie Museum with Helene Langdevin, daughter of Irene Joliot and granddaughter of Marie Curie, conducting the tour. John visited the Frejus Underground Laboratory in Modane, France, and was apprised of the status of the NEMO-3 experiment. Presently there are five detectors, three of which are completely wired and operational. While at the Frejus underground laboratory, John was able to observe the first tracking of ionizing particles through the Geiger cells and into the plastic scintillator detectors where they are analyzed. Philippe Hubert of the University of Bordeaux and Director of the Frejus Underground Laboratory gave John a copy of a $\gamma$-ray spectrum of chemically purified, enriched calcium fluoride that was to be used in another (Russian) double beta decay experiment at this laboratory. There were several $\gamma$-ray lines that were unidentified, and John volunteered to have our staff try to identify these lines. Robert Gehrke successfully identified these lines as coming from $^{249}$Cf and all of the progeny down to $^{233}$Pa. This identification significantly helped that experiment.

Studies were performed on reducing the continuum under $\gamma$-ray peaks in order to detect lower levels of $\gamma$-ray activity. A draft of a paper for publication in *Radioactivity and Radiochemistry* is being prepared on the acquisition of $\gamma$-ray spectra through the application of methods that reduce the continuum under the $\gamma$-ray peaks. This paper discusses: (1) the impact of pulse pileup on spectral quality, (2) the impact of counting at close source-to-detector distances, (3) the importance of using beryllium absorbers to prevent high-energy $\beta$ particles from reaching the detector, (4) counting with large (relative efficiency >70%) Ge detectors, and (5) reducing the ambient background from the room, shield, and spectrometer itself. Examples of these effects will be provided as figures in the paper.

A summer student, Marcus C. Chisolm on a fellowship from Howard University in Washington, D.C., spent nine weeks at the INEEL with our group. We gave him a research problem involved with very low-level radiation detection, namely, to study neutron interactions using cosmic ray-produced neutrons as the neutron source. He conducted experiments with water, boron, and chlorine using a 7.6 × 7.6 cm NaI(Tl) $\gamma$-ray detector in a 10-cm-thick lead shield and a portable analyzer. The experiment served two purposes: (1) to study effects of importance to the characterization of waste using prompt gamma neutron activation analysis, and (2) to develop a set of simple experiments that can be conducted at a small Rocky Mountain college at an elevation of about 4,500 ft or more. (These experiments can be carried out at colleges at lower elevations with the addition of a very weak isotopic neutron source, whose strength is so low as to make it unsuitable for other purposes.)

The experiments were highly successful. In the annual competition held between the summer students at the INEEL, Marcus' work was judged to be in the top seven for the year 2000. In addition, an invitation was received and accepted to present a paper titled "Prompt Gamma-ray Neutron Activation Analysis without the Neutron Source" at the 2000 Winter Meeting of the American Nuclear Society.

## Research Area 6: Prompt $\gamma$ Rays from $\alpha$-induced Reactions

### *Background*

The assay of transuranic (TRU) waste is often accomplished by measuring fission neutrons associated with the fissile isotopes. Frequently, this technique is limited by the presence of neutrons arising from ($\alpha$,n) reactions on low-Z elements due to large amounts of $^{241}$Am in the waste. These ($\alpha$,n) and associated ($\alpha$,p) reactions also emit prompt $\gamma$ rays.[13] If the prompt $\gamma$-ray to $\alpha$-induced neutron emission ratios can be measured, then it would be possible to deduce the number of ($\alpha$,n) reactions occurring in the waste from the prompt $\gamma$-ray emission rates.[14, 15] Corrections, therefore, could then be made to the assay technique by subtracting out from the total neutron rate the component due to the ($\alpha$,n) reactions to arrive at the neutrons from fission. In addition, these prompt g rays could be used to deduce the chemical form of the $^{241}$Am, since they are fingerprints for the nuclides undergoing the ($\alpha$,n) or ($\alpha$,p) reaction.

### *Objective:*

The specific objective of this research area was to study ($\alpha$,n) and ($\alpha$,p) reactions on low-Z elements likely to be present in TRU waste, to measure the nuclear properties (e.g., energies, relative intensities) for the associated prompt $\gamma$ rays, and to test the method to determine the feasibility of providing a correction for the TRU assay technique.

### *Collaborations:*

A collaboration is under consideration with Stephen Croft (presently at Canberra Industries). We are assessing published data he brought to our attention regarding production rates of ($\alpha$,n) and ($\alpha$,p) reactions in TRU waste that he and others measured.

### ***Accomplishments***

An extensive literature review was performed to identify the known gamma rays from ($\alpha$,n) and ($\alpha$,p) reactions and a review of $\gamma$-ray spectra from waste containers being stored at the INEEL to determine whether $\gamma$ rays from ($\alpha$,n) and ($\alpha$,p) reactions are present in these spectra (which have not been optimized for observation of these $\gamma$ rays). The literature review identified a paper that lists the partial $\gamma$-ray cross sections for $\alpha$-induced reactions on several low-Z elements.

We obtained the necessary experimental data for fluorine ($\alpha$,n) reactions. With these data, it is possible to calculate the number of neutrons that would be expected for a specific number of detected reaction $\gamma$ rays of a specific energy. One needs only the $\gamma$ efficiency, the neutron efficiency, $\gamma$-ray and neutron absorption corrections for the matrix, and the neutron to $\gamma$ ratio (n/$\gamma$ ratio). The n/$\gamma$ ratio is determined by comparing the total ($\alpha$,n) cross section at a particular $\alpha$ energy to the partial cross section for $\gamma$ rays of a particular energy, at the same $\alpha$ energy. It should be possible to go to the $\gamma$-ray spectra that contain some of these reaction $\gamma$ rays and calculate the number of neutrons that would have been expected and compare this to the number of neutrons that were measured.

A model of the SWEPP $\gamma$-ray system has been constructed that allows us to calculate the efficiency for a particular $\gamma$-ray energy. Within the next few months, a system should be in place at SWEPP that will calculate the neutron and $\gamma$-ray efficiencies for individual barrels. This will provide the capability to automate the calculation of the number of ($\alpha$,n) neutrons in a particular barrel.

Using the available literature values, we were able to calculate the numbers required to approximate the ($\alpha$,n) neutron flux by measuring the $\gamma$-ray flux. SWEPP appears to be an ideal test bed for this technique because we have access to data from drums for which extended $\gamma$-ray measurements were made. Using available SWEPP data, our first step was to produce convincing evidence that the observed $\gamma$ rays do, in fact, result from ($\alpha$,n) reactions. This was fairly straightforward, and the evidence is very convincing. The next step was to calculate the neutron fluxes. At first glance, the calculated neutron fluxes did not match the measured fluxes from the SWEPP data files. Further investigation indicated that we needed to reanalyze the SWEPP data to account for the matrix self-absorption effects. Comparisons were made between the number of reported neutrons from ($\alpha$,n) reactions and the neutrons measured from the 583 keV reaction $\gamma$ ray for 27 well characterized drums containing TRU waste. The numbers of neutrons expected are in reasonable agreement (within 30%) for about one-third of the drums. Continued progress on this front will rely on the development of a more effective way to measure the $\gamma$-ray efficiency of individual drums and on our ability to identify all reactions contributing to $\alpha$-induced reactions resulting in the emission of neutrons. Certain tasks related to this work are being carried out by another project. As these tasks are accomplished, our task will use their results to achieve our goal of using the reaction $\gamma$ rays to deduce the neutrons from ($\alpha$,n) reactions.

The above results are very encouraging and indicate that measuring reaction $\gamma$ rays may be an effective method for calculating the resulting ($\alpha$,n) neutron flux and providing a useful correction for the passive neutron assay measurement.

A paper titled "Peeling the Onion? The Gamma-ray Spectrometry of TRU Waste," which was presented at the 7th Nondestructive Assay Waste Characterization Conference, reported on the use of $\gamma$ rays, resulting from ($\alpha$,n) and ($\alpha$,p) reactions due to high $^{241}$Am activity, for identifying several light-element components of the waste matrix and measuring the neutron fluence created by ($\alpha$,n) reactions. At that conference, a meeting was held with Stephen Croft from the U.K. and now with Canberra Industries. He indicated a willingness to share some information regarding production rates of ($\alpha$,n) and ($\alpha$,p) reactions in TRU waste. This information has been received and is being evaluated.

We previously intended to obtain (α,n) and (α,p) production rates from sources prepared from $^{241}$Am in intimate contact with a low-Z element. We now believe that an alternate and possibly better way to obtain production rates for these reactions is to measure them at a particle accelerator that accelerates α particles. Facilities that can best accommodate these measurements are being identified. In the meantime, however, we are still planning to prepare at least one radioactive source of $^{241}$Am in intimate contact with a low-Z element such as fluorine (e.g., $^{241}$Am in a KF matrix). Initial measurements with a commercial source based on the $^{13}$C(α,n)$^{16}$O reaction producing a γ ray at 6,129 keV have been performed to demonstrate the technique.

## Accomplishments

The Nuclear Structure Research Project was initiated during the middle of FY 1999. Six related research areas were pursued: (1) high accuracy γ-ray measurements, (2) actinide decay scheme studies, (3) nuclear data measurements for prompt (n,n'γ) reactions, (4) γ-ray measurements for (n,γ) reactions, (5) very low-level radiation detection, and (6) prompt γ rays from α-induced reactions. During the past 1-1/2 years of the project, a number of accomplishment have been realized.

We have successfully developed collaborations with universities and other national laboratories including Los Alamos National Laboratory, Lawrence Berkeley National Laboratory, University of Michigan, Texas A&M University, Idaho State University, Washington State University, North Carolina State University, Albion College, Mount Holyoke College, Institute of Isotope and Surface Chemistry (Budapest), Bucharest University, Physikalisch-Technische Bundesanstalt (PTB) in Germany, and the NEMO-3 (an international collaboration that includes researchers from France, Russia, Hungary, and the United States).

Technical accomplishments include the following.

We demonstrated the method for determining the relative efficiency curve of a Ge γ-ray detector that is accurate to ~0.1% over the energy range 433–2,754 keV. The accuracy of this curve is approximately an order of magnitude better than had previously been attained. This was accomplished by performing Monte Carlo calculations to determine the efficiency for a Ge detector and then comparing the results with precise measurements. These comparisons verified, at the 0.1% level, the validity of the physics modeling within the Monte Carlo Code itself and thereby indicated that the Monte Carlo method is able to produce accurate predictions for γ rays in the energy range 53–2,754 keV. We then extended the low end of the range down to 53 keV to accommodate the needs of Texas A&M University. This work was well received by the technical community and has generated considerable interest both nationally and internationally.

Our work has shown that there may be a problem with the completeness of the physics in the Monte Carlo codes we use to describe the interactions of γ rays above 3 MeV. This involves the ratios of areas of the full-energy, the single-escape, and the double-escape peaks. Calculated ratios do not agree as well as expected with experimental values.

We obtained from PTB two $^{60}$Co sources with very accurately known activities (~0.1%). These will be used to extend our method for obtaining highly accurate total efficiency curves for Ge γ-ray detectors.

Our collaborators at the University of Michigan have performed a very careful and lengthy measurement of the γ-ray spectrum from the decay of $^{49}$Ca (8.7 m half-life). Our new relative efficiency method provided highly accurate relative efficiencies for the $^{49}$Ca γ-ray energies, and as a result, this work provides γ-ray intensities for this decay that are from 10 to 100 times more accurate than the previously available data and aids in the assignment of transition multipolarities, spins, and parities for the respective levels.

High-precision γ-ray spectra were obtained from various isotopes of Am, Cm, Np, Pu, Ra, Th, and U. The decay schemes for $^{229}$Th and $^{233}$U were studied. We developed a method to determine the age of waste containing $^{241}$Am and the presence of $^{237}$Np by investigating the grow-in of daughters/granddaughters over time. We also determined the intensity of $^{226}$Ra a decay to the 186-keV excited state of $^{222}$Rn, thereby resolving a long-standing discrepancy.

We retrieved previously unanalyzed LANSCE data for high-energy neutron interactions on 11 light elements and constructed γ-ray production rates and cross sections for silicon and oxygen. We successfully obtained approval for beam time on LANSCE and performed our own measurements on sodium and iodine. Obtaining approval by the LANSCE Program Advisory Committee and subsequent beam time on LANSCE is a very positive sign of acceptance of our experimental work and the need that exists for these data. Few proposed experiments receive approval for beam time. Subsequently, we performed measurements at LANSCE, obtaining spectra of prompt γ rays, from which we will develop excitation functions. The γ-ray production rates and cross sections developed by this work provide a type of nuclear information that has never before been available.

We were very successful in developing a method for ultra purification of mass-separated $^{100}$Mo, separating from it trace quantities of natural radioactive material (e.g., $^{232}$Th, $^{235}$U, $^{238}$U and their daughters and $^{40}$K). Up to two orders of magnitude reduction was realized for some nuclides with very low losses of $^{100}$Mo. This purification reduced the levels of radioactive impurities by up to two orders of magnitude and met the needs of the international NEMO-3 double beta decay experiment. We subsequently purified approximately 4 kg of $^{100}$Mo for NEMO-3. We developed an experiment suitable for use by a small Rocky Mountain college to study prompt gamma neutron activation analysis using cosmic-ray-produced neutrons. This method can be used by colleges at lower elevations if they supplement the cosmic-ray-produced neutrons with a very weak isotopic neutron source (one whose strength is so low as to make it unsuitable for other purposes). This work generated an invitation that was accepted to present a paper titled, “Prompt Gamma-ray Neutron Activation Analysis without the Neutron Source,” at the 2000 Winter Meeting of the American Nuclear Society.

We investigated (α,n) and (α,p) reaction g rays induced by α particles from actinides. Using these γ rays and a model of the SWEPP γ-ray system to calculate the efficiency for a particular γ ray, we were able to predict (within 30%) the measured neutron flux from (α,n) reactions in about one-third of a 27-drum sample of TRU 55-gal waste drums. In addition, the results of the work proved useful in the analysis of γ-ray spectra obtained from probeholes in Pit 9 at the INEEL. The chemical form of $^{241}$Am was identifiable in many cases.

- Developed and demonstrated a method for determining the relative efficiency curve of a Ge γ-ray detector that is accurate to ~0.1% over the energy range 433-2,754 keV, which is approximately an order of magnitude better than had previously been attained.

- Used our relative efficiency curve method to provide γ-ray intensities for the decay of $^{49}$Ca that are from 10 to 100 times more accurate than the previously available data to aid in the assignment of transition multipolarities, spins, and parities for the respective levels.

- Discovered an apparent problem with the completeness of the physics in Monte Carlo codes used to describe the interactions of $\gamma$ rays above 3 MeV.

- Obtained from Physikalisch-Technische Bundesanstalt two $^{60}$Co sources with very accurately known activities (~0.1%) for use in extending our method for obtaining highly accurate total efficiency curves for Ge $\gamma$-ray detectors.

- Measured high-precision $\gamma$-ray spectra from various isotopes of Am, Cm, Np, Pu, Ra, Th, and U. Studied the decay schemes for $^{229\mathrm{Th}}$ and $^{233}$U.

- Developed a method to determine the age of waste containing $^{241}$Am and the presence of $^{237}$Np by investigating the grow-in of daughters/granddaughters over time.

- Determined the intensity of $^{226}$Ra $\alpha$ decay to the 186-keV excited state of $^{222}$Rn, thereby resolving a long-standing discrepancy.

- Retrieved previously unanalyzed LANSCE data for high-energy interactions on 11 light elements and constructed $\gamma$-ray production rates and cross sections for silicon and oxygen.

- Obtained approval for beam time on LANSCE and performed our own measurements on sodium and iodine. Obtaining approval by the LANSCE Program Advisory Committee and subsequent beam time on LANSCE is a very positive sign of acceptance of our experimental work and the need that exists for these data.

- Developed a method for ultra purification of mass-separated $^{100}$Mo, separating from it trace quantities of natural radioactive material (e.g., $^{232}$Th, $^{235}$U, $^{238}$U and their daughters, and $^{40}$K). This purification reduced the levels of radioactive impurities by up to two orders of magnitude and met the needs of the international NEMO-3 double beta decay experiment. A total of 4 kg of $^{100}$Mo was purified.

- Developed an experiment suitable for use by a small Rocky Mountain college to study prompt gamma-ray neutron activation analysis using cosmic-ray-produced neutrons.

- Investigated the feasibility of using ($\alpha$,n) and ($\alpha$,p) reaction $\gamma$ rays induced by a particles from actinides to correct the results of TRU assay systems. Using these $\gamma$ rays and a model of the SWEPP $\gamma$-ray system to calculate the efficiency for a particular $\gamma$ ray, we were able to predict (within 30%) the measured flux from ($\alpha$,n) reactions in about one-third of a 27-drum sample of TRU 55-gal waste drums.

- Used the data developed in the ($\alpha$,n) and ($\alpha$,p) studies in the analysis of Pit 9 probe-hole logging data. The chemical form of the buried americium was identified.

# REFERENCES

1. J. K. Tuli, ed., Nuclear Data Sheets.

2. R. B. Firestone, Table of Isotopes, 8th Edition, V. S. Shirley, Editor, volumes 1 & 2, A Wiley-Interscience Publication, John Wiley & Sons, Inc., New York, 1996.

3. M. A. Lone, R. A. Leavitt, and D. A. Harrison, "Prompt Gamma Rays from Thermal-Neutron Capture," Atomic Data and Nuclear Data Tables, 26 (1981) 511-559.

4. A. M. Demidov et al., Atlas of Gamma-ray Spectra from Inelastic Scattering of Reactor Fast Neutrons, Atomizdat, 1978.

5. A. R. Dulloo, F. H. Ruddy, T. V. Congedo, J. G. Seidel, and R. J. Gehrke, "Detection Limits of a Laboratory Pulsed Gamma Neutron Activation analysis System for the Noindestructive Assay of Mercury, Cadmium, and Lead," Nuclear Technology, 123 (1998) 103.

6. J. Salgado and C. Oliveira, "Corrections for Volume Hydrogen Content in coal Analysis by Prompt Gamma Neutron Activation Analysis, Nuclear Instruments and Methods in Physics Research," B66, (1991) 465.

7. C. M.. Shyu, R. P. Gardner, and K. Verghese, "Development of the Monte Carlo-Library Least-Squares Method of analysis for Neutron Capture and Prompt Gamma-Ray Analyzers," Nuclear Geophysics, 7, 2, (1993) 241-268 and 153-182.

8. A. R. Dulloo, T. V. Congedo, F. H. Ruddy, B. Petrovic, J. G. Seidel, A. Haghighat, M. E. McIlwain, R. J. Gehrke, L. Van Ausdeln, and L. O. Johnson, "Evaluation of Pulsed Gamma Neutron Activation Analysis for the NDA of RCRA Metals in 55-Gallon Mixed-Waste Drums," 7th NDA Waste Characterization Conference, Salt Lake City, Utah, May 23 –25, 2000. Report No. INEEL/EXT-2000-0002, 2000.

9. R. P. Gardner, P. Guo, A. Sood, C. W. Mayo, R. J. Gehrke, and C. L. Dobbs, "Monte Carlo Aided Treatments of the Nonlinear Inverse PGNAA Measurement Problems for Various continuous On-line Applications," Journal of Radioanalytical and Nuclear Chemistry, 233 (1998) 105.

10. R. P. Gardner, A. Sood, Y. Y. Wang, L. Liu, P. Guo, and R. J. Gehrke, "Single Peak versus Library Least-Squares Analysis Methods for the PGNAA of Vitrified Waste," Journal of Applied Radiation and Isotopes, 48 (1997) 1331.

11. A. P. Tonchev and J. F. Harmon, "Excitation of the $^{180m}$Ta Isomer in ($\gamma$,n) Reactions and Its Astrophysical Relevance," Applied Radiation and Isotopes 52 (2000) 873.

12. G. Molnar and R. Firestone, Prompt Gamma-ray reference of energies and intensities given at the Modern Trends in Activation Analysis conference in 1999 in Bethesda, MD

13. E. B. Norman, K. T. Lesko, T. E. Chupp, P. Schwalbach, and M. A. Faccio, "Gamma-Ray

Production Cross Sections for Alpha-Particle Induced Reactions on $^{19}$F and $^{23}$Na," Radiation Effects, 94 (1986) 307.

14. S. Croft, "The Thick Target ($\alpha$, n) Yield of Fluorine compounds For a Broad Range of Actinides," Proceedings of ESARDA's 19th Annual Symposium on Safeguards and Nuclear Material Management, Montpellier, France, May 13–15, 1997, Report No. EUR 17665 EN, page 397.

15. E. W. Lees and D. Lindley, "Neutron Production From (a, n) Reactions in $^{241}$AmO$_2$," Annuals of Nuclear Energy, 5 (1978) 133.

# Science and Technology Foundation

### Peter M. Castle

The Science and Technology Foundation's portion of the program integrates research, analyzes the research portfolio, and facilitates external program reviews. In FY 2000, the foundation added the Long-Term Stewardship task to its activities. The Science and Technology Integration activity has the responsibility for monitoring the EM complexwide technology and science needs in such databases as the OST Needs Management System. Understanding these needs is necessary to ensure that the ESR research portfolio is addressing issues of importance to EM. An additional function within the Science and Technology Integration activity is to maintain connections with the focus areas and offer transition avenues for ESR science and technology into operations, and to facilitate transition of a portion of the investment in the EM Science Program into Operations. The ESR portfolio technical content and the technical content of the collaborative effort between ESR and the EM Science Program are subjected to peer reviews arranged through this portion of the ESR program.

The FY 2000 Long-Term Stewardship project was a two-fold activity. One aspect focused on science issues of Long-Term Stewardship, such as identifying and modeling ecological indicators to be used in long-term monitoring, surveillance, and prediction. The other aspect included an initial needs assessment and preliminary development of a roadmap template to be used for Long-Term Stewardship throughout the DOE complex. Both activities are highlighted in this report.

# Science and Technology Integration

**Peter M. Castle**

## Summary

The objectives of the Science and Technology Integration (STI) task are to maintain relevance of the Environmental Systems Research (ESR) research portfolio to the science and technology needs of the U.S. Department of Energy, Environmental Management Program, and to ensure quality of the technical content. STI also forges links between the ESR research, INEEL operations, and EM focus areas. Activities that support these objectives include an annual cross-walk of the ESR's programmatic content against EM's science and technology needs catalogued in the Office of Science and Technology's Technology Management System database. The STI task arranges annual external panel review of the technical content of the ESR program.

## Description of Research Activities

The STI task of the Science and Technology Foundation in the ESR Program provides analysis and interface capabilities. We direct our analyses to understand the science and technology development needs of the EM Program complexwide. The understanding allows us to evaluate the ESR portfolio to ensure that the research is relevant to EM problems. Analysis focuses on the research programs funded by the EM Science Program (EMSP) and the EM focus areas to avoid duplicating ongoing EM-funded work. Also, STI has been responsible for arranging for external reviews the of the ESR program each year.

We conduct our analysis of the ESR portfolio against complexwide needs and research activities using various EM-managed databases. The EM Science Program maintains a database, accessed through their homepage (*http://www.em.doe.gov/science/*), that contains information concerning all funded EM Science Program projects. EM-50 maintains the Technology Management System (TMS), accessed through their homepage (*http://ost.em.doe.gov/tms/Home/Entry.asp?Show=Sites*). In addition to listing all EM-developed technologies, TMS contains a list describing both basic science and technology development needs. Individual Site Technology Coordination Groups, associated with many of the U.S. Department of Energy (DOE) Operations Offices, supply the entries for the database. The data in TMS describe technology and science gaps and opportunities associated with ongoing or anticipated operations uncovered by the coordination groups during their interaction with operations personnel. The research activities within the ESR portfolio can all be linked to one or more of the needs in TMS.

The Environmental Systems Research program is committed to act as a bridge to help mature EMSP research progress from their basic science orientation to applications orientation. We assist the focus areas in their effort to harvest the results of the EM Science Program-funded research. STI serves as the interface for the focus areas and ESR. STI works with the focus areas to identify EMSP research projects of future value to the focus areas and to the capabilities of the INEEL that need further development before they can be adopted. Since the INEEL is the designated EM laboratory, the ESR program is responsible for deploying its research and making its capabilities available not just at the INEEL but complexwide. We establish interfaces to accomplish these activities with the EMSP and the focus areas.

Environmental Systems Research has proposed to work with the focus areas to determine which of the 1996 EMSP projects being carried out at universities match needs identified in the baseline planning. When the focus areas define their prioritized list of EMSP projects, ESR evaluates the projects to determine their ultimate value to the INEEL and determine which will strengthen ESR research capabilities. When suitable matches are found, ESR intends to co-fund researchers at both the INEEL and the universities. Possibly, ESR may offer postdoctoral appointments and sabbaticals to research groups. Given the current INEEL Subsurface Science Initiative, the initial effort is to prioritize EMSP projects that would involve the Subsurface Contaminants (SubCon) focus area. In 1996, SubCon prioritized a list of EM Science Program projects having relevance to SubCon's future needs. While it was originally hoped that two of these programs could be funded through the ESR, eventually only one was funded, and that by a different mechanism. With the expanded emphasis on subsurface science at the INEEL, we anticipate that the connection with SubCon will be maintained and strengthened. There should be additional opportunities in the future to cooperate with SubCon to harvest EMSP research beneficial to SubCon and the INEEL.

Environmental Systems Research views external review of the research and research directions as an important part of maintaining a viable and credible research portfolio. In FY 1998 and 1999, two of the research areas selected from five each year were reviewed by a panel of persons chosen for their expertise and reputation in fields of research relating to ESR research areas. The FY 2000 review panel comprised subject area experts recruited from various universities and the US Geological Survey. They conducted their review in conjunction with review of the projects in the Environmental Systems Research Candidates Program over four days in late July. This review was different from previous reviews in two ways. With the exception of ESR tasks not to be carried into FY 2001, they reviewed the entire ESR and ESRC program. For the ESR portion, the review emphasis was on the proposed research for FY 2001 rather than the accomplishments of FY 2000. Most proposed research tasks withstood the review.

## Accomplishments

With help from SubCon, we identified two 1996 high-priority EMSP projects for continuation and obtained funding for one of them. We completed a report that linked the ESR research portfolio with EM's complexwide needs, as compiled in the Office of Science and Technology's Nuclear Materials Safeguards database. In conjunction with the ESRC and LDRD programs, we facilitated the FY 2000 external panel review of ESR projects. We worked with the INEEL Fellows and the Technology Deployment Center to develop strategies for integrating operations and R&D and to establish contacts with operations managers and directors responsible for effecting this integration. And we arranged for a presentation by WAG managers of their technology development needs to an audience of ESR and Environmental Forum researchers.

# Long-Term Environmental Stewardship Project

**Sharon Berrett**

## SUMMARY

*Long-term stewardship* is defined by the Department of Energy (DOE) as the physical controls, institutions, information, and other mechanisms needed to ensure protection of people and the environment at sites where DOE has completed or plans to complete cleanup. Once DOE completes stabilization, cleanup, and disposal of waste, some sites will not be released for unrestricted use because residual contaminants are present or because waste or facilities have been deliberately entombed. These sites may require long-term surveillance and maintenance or long-term physical and administrative controls.

The Long-term Environmental Stewardship Project comprises two disparate tasks:

- Task 1. Development of "Needs Assessment and Technology Baseline Report."

  This task involved developing a report that assesses technological needs and inventorying existing technologies that support long-term stewardship activities in support of the Long-term Stewardship Roadmapping effort.

  The Draft Initial Needs Assessment and Technology Baseline Inventory 2000 supports activities and site managers associated with long-term stewardship. The draft report can be viewed in its entirety on the Internet at http://emi-web.inel.gov/lts.

- Task 2. Identification of scientific issues relating to long-term stewardship. Two specific subtasks were addressed:

  Task 2.1. The project developed criteria for selecting ecological indicators for long-term stewardship and established an approach to address the long-term stewardship of DOE lands and resources. The approach included a process and criteria to select site-specific long-term ecological indicators to be used for long-term monitoring and surveillance.

  Task 2.2. The project developed a model to predict performance for long-term stewardship based on established ecological indicators. The model was created using systems dynamics to demonstrate the ability to predict performance of institutional controls put in place for long-term stewardship.

## PROJECT DESCRIPTION

### Task 1 Needs Assessment and Technology Baseline Report 2000

The INEEL is DOE's lead laboratory for the Long-term Stewardship Program (LTS). This responsibility includes defining the program through a needs assessment and technology baseline. Task 1 outlines the plan for developing the Long-term Stewardship Program. INEEL will engage science and technology support throughout the DOE complex to coordinate present and future LTS research and development needs. The INEEL is well suited for this assignment owing to its many EM missions and its technical expertise developed as lead DOE EM laboratory.

We determined long-term stewardship science and technology needs using a process to obtain consistent, fully integrated, and coordinated results. This needs identification process used existing Office of Science and Technology (OST) processes as a starting point, but we expanded it through interviews with EM science and technology user organizations and with stakeholders and regulators. Our process included review of a wide variety of data, including existing documentation, data bases, and data sources (i.e., NMS, STCGs, Focus Areas, dispositions maps), and information gathered from site interviews, workshops, and technical review committee meetings.

We published a technology baseline report for Congress, Department of Energy program directors, and other decision-makers with information about existing and emerging technologies that apply to long-term stewardship needs. The information will be useful in determining funding priorities and directions for research. The information is critical for decision-makers in meeting the three goals of the Long-Term Stewardship Science and Technology Program: (1) reduce long-term stewardship costs, (2) improve the reliability of remedy performance, and (3) reduce the uncertainty of long-term site performance.

The report identifies long-term stewardship needs and existing and emerging technologies that apply or might apply to long-term stewardship needs and activities. At minimum, the key elements of a long-term stewardship program include monitoring, inspection, maintenance (both preventive and minor corrective maintenance), site security and hazard communication, information management, and long-term continuing operations. These elements are discussed in Chapter Three of the report (see http://emi-web.inel.gov/lts).

We also created an initial LTS science and technology roadmap template in which we identified the gaps between needs and current technologies. Our report, Long-Term Stewardship Science and Technology Roadmap Framework, compares the baseline inventory to the specific long-term stewardship technology needs identified in the initial needs assessment. This comparison (or gap analysis) highlights needs that existing or developing technologies do not address. The roadmap proposes a living process for moving forward with developing technologies to fill those gaps and meet long-term stewardship technology needs.

## Task 2.1 Criteria for Selecting Ecological Indicators for Long-Term Stewardship

The goal of this task was to develop an approach to identify and define the key components of ecological health and associated indicators and to develop a model to demonstrate the ability to evaluate options for long-term stewardship.

In many cases, habitat disturbance and associated impacts (e.g., permanent habitat loss or conversion and disturbance to exotic species) continue to be some of the greatest assaults to the environment and may pose the greatest long-term risk to the system.

We developed an approach to help determine site-specific assessment questions to establish key components of ecological health and associated indicators for long-term stewardship. The approach includes a process to formulate assessment questions, select candidate indicators, and arrive at detailed indicator evaluation criteria. A report detailing the approach is available from the Integrated Environmental Services Department.

Long-term monitoring and surveillance can best be accomplished by applying a suite of resource indicators. A good indicator is one that is repeatable and well-understood and reflects the overall health (i.e., integrity and/or sustainability) of the resource. This health can be assessed on a variety of scales, ranging from an individual organism to a population, community, or an entire ecosystem. However, developing a useful suite of indicators capable of providing the information necessary to determine the health of the resource can be extremely difficult.

The approach to developing long-term indicators of ecological health at the INEEL is largely modeled on pertinent portions of the Environmental Protection Agency's Environmental Monitoring and Assessment Program (EMAP). The approach is designed to detect cumulative impacts of natural and anthropogenic influences on the condition of ecological resources rather than effects caused by a limited set of individual stressors.

Because the INEEL lies within the sagebrush/steppe communities of the Snake River Plain, EMAP information on Desert and Rangeland Ecosystems will be applied where possible. The EMAP Desert and Rangeland Ecosystems group has developed a framework based on four classes of ecological indicators: response, exposure, habitat, and stressor. *Indicator* is defined as "any expression of the environment that quantitatively estimates the condition of ecological resources, the magnitude of stress, the exposure of biological components to stress, or the amount of change in condition."

Response indicators describe ecological conditions. Exposure and habitat indicators explain observed differences (spatial) or changes (temporal) in response indicators. Stressor indicators identify possible causes for changes in exposure and habitat indicators. Table 1 lists indicators specific to semiarid ecosystems. Table 2 shows how various indicators could be applied at the INEEL.

The framework can be used to develop a suite of indicators to evaluate the health of ecosystems at the INEEL. Where possible, these indicators should draw upon existing information, including data sets and historical monitoring programs. We anticipated, however, that little information will be available that can be related easily to ecosystem health. Candidate indicators should be evaluated for (a) conceptual soundness, (b) feasibility of implementation into a routine monitoring program, (c) statistical behavior, and (d) utility in resource assessment.

## Selection of Criteria for Ecological Indicators

The purpose of establishing criteria to evaluate potential indicators of resource status is to define a priori the characteristic properties that an indicator or indicators should possess in order to be effective. This approach is recommended to avoid some of the problems common to many existing monitoring programs whereby ecological indicators fail to provide the information necessary to evaluate the condition of the resource being monitored (D.L. Peterson et al. 1992; J. Peterson et al. 1992). The criteria developed should be used to bound potential ecological indicators in a manner that will better ensure that the data produced are of known quality and are collected most cost-effectively. Furthermore, monitoring programs must be designed on a site-specific basis. An ecological monitoring program designed for one scenario will not necessarily be applicable to another.

Table 3 is a list of criteria we suggest for evaluating the effectiveness of indicators for assessing the status of lands and resources. These criteria are of varying importance, and reaching consensus of opinion regarding the relative importance of each criterion may be difficult. Furthermore, the relative importance of each may vary between sites. The goal in applying these or other criteria is to obtain a consistent, generic approach to selecting indicators. This approach can be applied in virtually any situation (i.e., any combination of source and receptor of interest), but the output must be considered site-specific.

**Table 1.** List of indicators.

**A.** **Core Indicators (**for routine measurement to detect changes occurring at the regional level)

1. Primary productivity
2. Landscape pattern
3. Foliar chemistry
4. Soil chemistry
5. Riparian ecosystem integrity
6. Water erosion
7. Grazing
8. Energy balance
9. Water balance
10. Weather and climate
11. Ground water quality
12. Frequency and biomass of nitrogen fixing plants

**B.** **Retrospective indicators** (for establishing the magnitude of modern changes in the context of a long-term record)

1. Tree/shrub growth
2. Pollen record
3. Woodrat midden record
4. Charcoal

**C.** **Faunal indicators**

1. Fluctuating asymmetry
2. Tissue concentrations
3. Distribution and nest density of harvester ants and termites
4. Demographics
5. Species abundance

**Table 2.** Example application of indicators and process information.

| Indicator | Category | Index Period | Measurements | Variability | Problems |
|---|---|---|---|---|---|
| Primary productivity | Response or ecosystem function | Peak times of productivity | Total chlorophyll<br>Annual wood increment<br>C, H, O isotopes in wood | High | Labor intensive<br>Need for ancillary data |
| Landscape pattern | Exposure or landscape habitat | Late spring, early summer, cloud-free days | Landsat thematic mapper data of elevation, rock, and soil units, habitat classification, mechanical disturbance, development, drainage density, habitat fragmentation, fire | No spatial variability (100% coverage)<br>Temporal <10% | |
| Foliar chemistry | Response or biomarker | Peak biomass * | Tissue concentration of N, P, K, Ca, Mg, Na, S, Fe, Mn, Zn, Cu, B, Ti, Al, Mo, Cl, Si. Ni. Pb. | 20% or less spatially | Lack of baseline data by species. Lack of understanding of optimum sampling time. |
| Soil chemistry | Exposure or ambient concentration OR Response/ ecosystem function | | | | |

**Table 3.** Indicator Evaluation Criteria

| Criteria | Definition |
|---|---|
| **Essential Criteria** | |
| Unambiguously interpretable | Relates unambiguously to a recognized environmental value or assessment question and quantitatively conveys the same information for most resource sampling units within a regional resource class. |
| Ecologically responsive | Responds to stressors and to changes in the condition of the resource across most pertinent habitats within a regional resource class. |
| Index period stability | Exhibits low-measurement error and temporal variation during an index period. |
| Amendable to synoptic survey | Can be quantified by synoptic monitoring or by cost-effective automated monitoring. |
| High signal-to-noise ratio | Possesses sufficiently high signal strength (when compared to natural annual or seasonal variation) to allow detection of ecologically significant changes within a reasonable time frame. |
| Nominal-subnominal criteria | Possess documented or identifiable thresholds or patterns of trends that identify the nominal or subnominal condition of the resource. |
| Minimal environmental impact | Sampling produces minimal environmental impact. |
| **Desirable Criteria** | |
| Available method | Possesses a generally accepted and standard measurement method that can be applied on a regional scale. |
| Historical record | Has an existing historical data base or one that can be generated from accessible data sources. |
| Retrospective | Relates to past conditions by way of retrospective analyses. |
| Anticipatory | Provides an early warning of widespread changes in ecological condition or processes. |
| Cost effective | Has low incremental cost relative to its information. |
| New Information | Provides new information: that is, does not merely duplicate data already collected by cooperating agencies. |

Source: Breckenridge, R. P., W. G. Kepner, and D. A. Mouat, Environmental Monitoring and Assessment 36: 45-60, 1995.

# Task 2.2 Model to Predict Performance for Long-Term Stewardship

The purpose of this task was to model the key components of ecological health and associated indicators associated with INEEL lands. From this work we will be able to evaluate options for long-term environmental stewardship.

We used system dynamics to examine and evaluate activities necessary for successful long-term environmental stewardship. System dynamics is an analytical approach that examines complex systems through the study of the underlying system structure. A complex system comprises many elements, which interact over time to form a unified whole. Thorough understanding of system structure can lead to an explanation of the performance of a complex system over time and in response to both internal and external perturbations. By understanding a system's underlying structure, one can predict how the system will react to change.

In order to demonstrate this approach, we developed a model of a waste cap system that could be implemented at the INEEL (see Figure 1). The model took into account the amount of precipitation, infiltration, transpiration, and runoff to estimate the potential migration of waste accumulated in the soil below the cap. The model allows for examining the effects on contamination migration caused by such phenomena as changes in surface water (in the form of precipitation and irrigation) and changes in ground cover due to fires or grazing. The model serves two purposes. The first was to educate

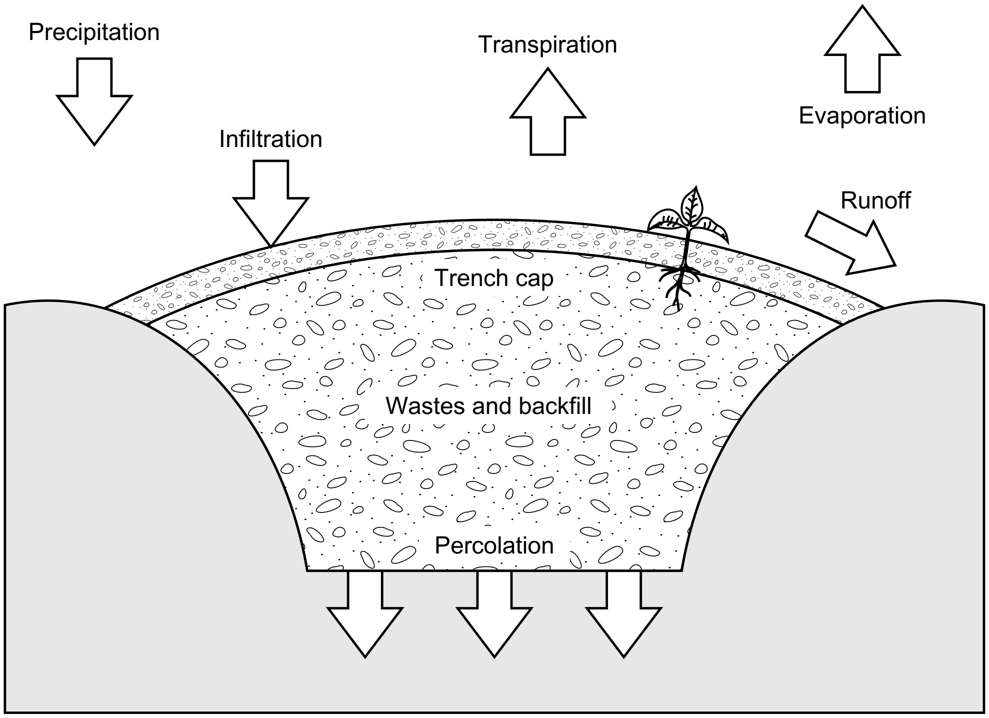

**Figure 1.** Cap and cover model user interface.

stakeholders about the complexity of the entire system. It visually identifies the various components of the system and management scenarios. The second was to allow stakeholders to engage in a game simulation and to test different long-term management scenarios so they could see the long-term effects of their management decisions.

This *systems* approach (see Figure 2) can be applied to other issues associated with basic habitat disruption during cleanup or other activities occurring at the sites. In many cases, habitat disturbance and associated impacts (e.g., permanent habitat loss or conversion, exotic species) continue to be some of the greatest assaults to the environment and may pose the greatest long-term risk to the system. There is great need to start addressing the long-term issues in addition to contaminant-related impacts and risks. This will need to be a key component in developing long-term stewardship strategies for the DOE laboratory complex.

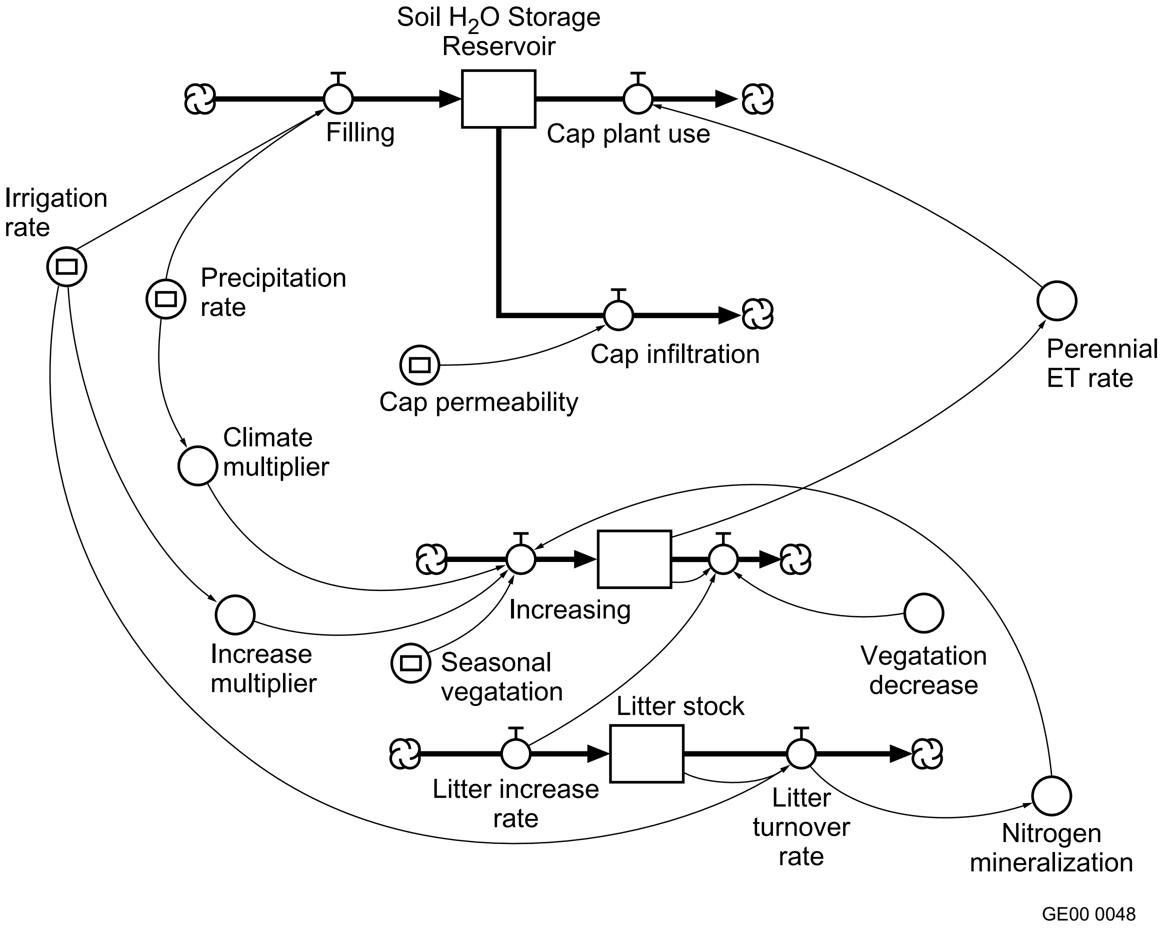

**Figure 2.** Logic diagram for cap and cover model.

## ACCOMPLISHMENTS

We developed a decision analysis model for a waste cap system that can be implemented at the INEEL. The model uses adjustable parameters such as precipitation, infiltration, transpiration, and runoff to estimate the potential migration of waste accumulated in the soil below the cap. The model examines the effects on contamination migration caused by such phenomena as changes in surface and changes in ground cover due to fires or grazing. The model has two purposes. The first is to educate stakeholders about the complexity of the entire system. It visually identifies the various components of the system and management scenarios. The second is to allow stakeholders to engage in a game simulation and test different long-term management scenarios and to see the long-term effects of their management decisions.

We created an initial Long-term Stewardship Program science and technology roadmap template, which identifies gaps between LTS needs and current technologies. Our report, Long-Term Stewardship Science and Technology Roadmap Framework, compares the baseline inventory to the specific long-term stewardship technology needs identified in the initial needs assessment. This comparison (or gap analysis) highlights needs that are not addressed by existing or developing technologies. The roadmap proposes a living process for moving forward with developing technologies to fill those gaps and meet long-term stewardship technology needs.

## REFERENCES

R. P. Breckenridge, W. G. Kepner, and D. A. Mouat, "A Process for Selecting Indicators for Monitoring Conditions of Rangeland Health," *Environmental Monitoring and Assessment* 36: 45-60, 1995.

D. L. Peterson, et al., *Guidelines for Evaluating Air Pollution Impacts on Class I Wilderness Areas in California*, USDA Forest Service Pacific Southwest Research Station General Technical Report PSW-GTR-136.

J. Peterson, et al., *Guidelines for Evaluating Air Pollution Impacts on Class I Wilderness Areas in the Pacific Northwest,* USDA Forest Service Pacific Northwest Research Station, General Technical Report PNW-299 1992.

# Appendix A

# Peer Reviewed Publications

# APPENDIX A

## Peer Reviewed Publications

### Biochemical and Geochemical Reactions on Environmental Surfaces

Redden, G., J. Bargar, et al. (1999). “Citrate Enhanced Adsorption of U(VI) on Goethite: Characterization Of Uranyl Speciation Using EXAFS.” *J. Colloid Interface Sci.*, submitted.

### Reactive Transport in Variably Saturated Heterogeneous Media

Hull, L. C., M. N. Pace, and G. D. Redden, “Adsorption Parameters for Radioactive Liquid-Waste Migration”, *Scientific Basis for Nuclear Waste Management*, Materials Research Society, (in press).

Johnson, R. W. and Landon, M. B., “A B-Spline Collocation Method To Approximate The Solutions To The Equations Of Fluid Dynamics,” *Proceedings of the 3rd ASME/JSME Joint Fluids Engineering Conference, July 18-23, San Francisco, Forum F-217, 1999.*

Sisson, J. B., A.L. Schafer, and J.M. Hubbell, “Vadose Zone Monitoring System for Site Characterization and Transport Modeling,” *Scientific Basis for Nuclear Waste Management*, Material Research Society, (in press).

### Transport Phenomena in Geologic Porous Media

O’Connell, S.P., Lawson, R.D., Watwood, M.E. and Lehman, R.M. 2000. “A BASIC Program For Reduction Of Data From Community-Level Physiological Profiling Using Biolog Microplates: Rational And Critical Interpretation Of Data.” *J. Microbiol. Meth.* 40(3): 213-220.

Genter, R.B. and Lehman, R.M. 2000. “Metal Toxicity Ascertained By Algal Population Density, Heterotrophic Substrate Utilization, And Fatty Acid Profile In A Small Stream.” *Environ. Toxicol. Chem.* 19(4): 869-878.

Garland, J.L. and Lehman, R.M. 1999. “Dilution/Extinction Of Community Phenotypic Characters To Estimate Relative Structural Diversity In Mixed Communities.” *FEMS Microbiol. Ecol.* 30(4): 333-343.

Lehman, R.M., Roberto, F.F., Earley, D., Bruhn, D.F., Brink, S.F., O’Connell, S.P., Delwiche, M.E. and Colwell, F.S. “Attached And Unattached Microbial Communities In Closely-Paired Groundwater And Core Samples From An Acidic, Crystalline Rock Aquifer.” Submitted *to Applied and Environmental Microbiology*.

Lehman, R.M., Colwell, F.S., Bala, G.B. “Partitioning Of Microbial Communities Between Basalt And Groundwater In Laboratory Core Floods.” In preparation *for Applied and Environmental Microbiology*

Sisson, J.B. and J.M. Hubbell, 1999, “Water Potential to Depths of 30 Meters in Fractured Basalt and Sedimentary Interbeds,” in *Proceedings of the International Workshop on Characterization and Measurement of Hydraulic Properties of Unsaturated Porous Media*, ed. by M.Th. van Genuchten, F.J. Leij and L. Wu, U.S. Salinity Laboratory, Riverside, CA. pp. 855-865.

Hubbell, J.M. and J.B. Sisson, October 19, 1999, Patent Number 5, 969,242, US patent and Trademark Office, “Isobaric Groundwater Monitoring Well”, Assignee Lockheed Martin Idaho Technologies Company, Idaho Falls, Idaho, 19 claims, 7 drawing sheets.

### Selective Mass Transport in Polymers

F. F. Stewart, M. K. Harrup, R. P. Lash, M. N. Tsang, “Synthesis, Characterization and Thermal Stability of Phosphazene Terpolymers with 2-(2-Methoxyethoxy)ethoxy and Diacetone D-Glucofuranosyl Pendant Groups,” *Polymer International*, 2000, 49(1), p. 57.

F. F. Stewart, R. E. Singler, M. K. Harrup, E. S. Peterson, R. P. Lash, “Electron Beam Crosslinking of Fluoroalkoxy, Methoxyethoxyethoxy and Substituted Phenoxy Polyphosphazenes: Physical and Chemical Characterization and Comparison to a Thermally Induced Free Radical Process and Ionic Complexation,” *J. Appl. Polym. Sci,*. 2000, 76(1), p. 55.

F. F. Stewart, M. K. Harrup, T. A. Luther, C. J. Orme, R. P. Lash, “Formation of Pervaporation Membranes from Polyphosphazenes Having Hydrophilic and Hydrophobic Pendant Groups: Synthesis and Characterization,” *J. Appl. Polym. Sci.,* in Press.

F. F. Stewart, T. A. Luther, M. K. Harrup, R. P. Lash, “Reactions and Polymerization of Hexa(tert-butylhydroquinone)cyclotriphosphazene: A New Method for the Preparation of Soluble Cyclomatrix Phosphazene Polymers,” *J. Appl. Polym. Sci.,* in Press.

C. J. Orme, M. K. Harrup, T. A. Luther, R. P. Lash, K. S. Houston, D. H. Weinkauf, F.F. Stewart, “Characterization of Gas Transport in Selected Rubbery Amorphous Polyphosphazene Membranes,” *J. Membrane Sci*., submitted.

### Pore Size and Morphology Control for Solid and Polymer Matrices

Harrup, M. K.; Stewart, F. F., “Improved Method for the Isolation and Purification of Water-Soluble Polyphosphazenes” *J. Appl. Poly. Sci.*, 2000, 78(5), 1092.

Wertsching, A. K.; Cotten, G. B.; Harrup, M. K.; “Examination of the Physical Properties of Polyphosphazene Silicate Nanocomposites Using Novel Synthetic Strategies.” *Chem. Mater.* 2000, Submitted.

Harrup, M. K.; Stewart, F. F.; Wertsching, A. K. “Self-Doped Molecular Composite Battery Electrolytes” U. S. Patent Pending, Filed, July 28, 2000.

### Adsorption and Absorption Materials for Molecular Separations

P.J. Martellaro, G.A. Moore, A.E. Gorenbain, E.H. Abbott and E.S. Peterson, *Sep. Sci. Technol.* Accepted (2000).

G.A. Moore, P.J. Martellaro and E.S. Peterson, *Studies in Surface Science and Catalysis*, 129, (2000), 765.

P.J. Martellaro, G.A. Moore, E.S. Peterson, “Surfactant Mediated Copper Sulfide Synthesis and Bulk Copper Sulfide Acid Treatment for Sorbent Development,” In preparation for submission to *Colloids and Surfaces A*.

## Computational Simulation

D. A. Dahl, C. L. Atwood and R. A. LaViolette, "A Random-Walk Pseudorandom Byte Generator", *Appl. Math. Modelling* 24 771 (2000)

C. R. Tolle, J. L. Budzien and R. A. LaViolette, "Do Dynamical Systems Follow Benford's Law?", *Chaos* 10 331 (2000)

R. A. LaViolette and M. T. Benson, "Density Functional Calculations Of A Hypothetical Neutral Hollow Octahedral Molecule With A 48-Atom Framework: Hydrides And Oxides Of Boron, Carbon, Nitrogen, Aluminum And Silicon", *J. Chem. Phys.* 112 9269 (2000)

R. A. LaViolette, J. L. Budzien and F. H. Stillinger, "Inherent Structure Of A Molten Salt", *J. Chem. Phys.* 112 8072 (2000)

This is in addition to the following papers that were published previously under this project:

R. A. LaViolette, M. E. Watwood, T. R. Ginn, and D. L. Stoner, "Spatial Disorder And Degradation Kinetics In Intrinsic Biodegradation Schemes", *J. Phys. Chem.* 103 4480 (1999)

C. R. Tolle, and R. W. Gundersen, "Searching for Determinism in Erratic Signals: Fuzzy Time-Based Clustering of Delay Vectors", *Intelligent Engineering Systems Through Artificial Neural Networks 8*, edited by C. H. Dagli, (ASME Press, New York) 1998.

L. R. Pratt and R. A. LaViolette, "Quasi-Chemical Theories Of Associated Liquids", *Mol. Phys*. 94 909 (1998)

J. L. Budzien, J. D. McCoy, J. G. Curro, R. A. LaViolette, and E. S. Peterson, "The Solubility Of Gases In Polyethylene: Integral Equation Study Of Standard Molecular Models", *Macromolecules* 31 6669, erratum 8653 (1998).

J. L. Budzien, J. D. McCoy, D. H. Weinkauf, R. A. LaViolette, and E. S. Peterson, "Solubility Of Gases In Amorphous Polyethylene", *Macromolecules* 31 3368 (1998)

## Corrosion and Aging

T.E. Lister and P.J. Pinhero, "In-vivo Atomic Force Microscopy of Surface Proteins within *Deinococcus radiodurans*", submitted to *Langmuir*, 9/2000.

## Transport in Solid and Liquid Media

C. DeW. Van Siclen, "Walker Diffusion Method For Calculation Of Transport Properties Of Composite Materials," *Physical Review E*, Vol. 59, No. 3, 1999, pp. 2804-2807.

C. DeW. Van Siclen, "Anomalous Walker Diffusion Through Composite Systems," *Journal of Physics A: Mathematical and General*, Vol. 32, 1999, pp. 5763-5771.

## Adaptive Sensors

Napoleon Thantu, "Femtosecond Optical Heterodyne Detected Raman Induced Kerr Effect Spectroscopy for Chemical Analysis," submitted for publication in *Applied Optics*.

Dale McMorrow, Napoleon Thantu, Valeria Kleiman, Joseph S. Melinger and William T. Lotshaw, "Analysis of Intermolecular Coordinate Contributions to Third-Order Ultrafast Spectroscopy of Liquids in the Harmonic Oscillator Limit," submitted for publication in the *Journal of Physical Chemistry*.

R. S. Schley, K. L. Telschow and J. Holland, "Static and Dynamic Two-Wave Mixing in GaAs," *Applied Optics: Lasers Photonics and Environmental Optics*, 4348-4354 (August 20, 2000).

Napoleon Thantu, "Time-Resolved Optical Heterodyne Detected Raman Induced Kerr Effect Spectroscopy for Chemical Analysis," in *Laser Applications to Chemical and Environmental Analysis*, *OSA Technical Digest* (Optical Society of America, Washington DC, 2000), post-deadline paper PD5.

Dale McMorrow, Napoleon Thantu, Valeria Kleiman, Joseph S. Melinger and William T. Lotshaw, "Analysis of Intermolecular Coordinate Contributions to Third-Order Nonlinear-Optical Response of Liquids with a Quantum Harmonic-Oscillator Model," in *Nonlinear Optics: Materials, Fundamentals and Applications, OSA Technical Digest* (Optical Society of America, Washington DC, 2000), pp. 273-275.

D. Wright, A. Grunnet-Jepsen, M. A. Diaz-Garcia, J. D. Casperson, B. Smith, M. S. Bratcher, M. S. DeClue, J. S. Siegel, W. E. Moerner, and R. J. Twieg, "Trapping Studies on Photorefractive Polymers," *Proc. Soc. Photo-Opt. Instrum. Engr.* 3471, 60-71 (1998).

K.L. Telschow, V. A. Deason, R. S. Schley and S. M. Watson, "Imaging of Lamb Waves in Plates for Quantitative Determination of Anisotropy using Photorefractive Dynamic Holography," *Reviews of Progress in Quantitative NDE*, Vol. 18A, edited by D. O. Thompson and D. E. Chimenti (Plenum Press, New York, 1998) pp. 999-1005.

## Integrated Instruments for In Situ Chemical Measurements

M. L. Stone, G. L. Gresham, and L. A. Polson, "Characterization Of Two Polyphosphazene Materials As Membranes In Membrane Introduction Mass Spectrometry," *Analytica Chimica Acta*, 407, 2000, pp. 311-317.

## Intelligent Nonintrusive Methods for Characterization

F. Noo, R. Clackdoyle, C. Mennessier, T. A. White, and T. J. Roney, "A Direct Analytic Method For Scanner Calibration In Cone-Beam Tomography," *J. of Optical Society of America A* (submitted).

J. C. Determan, G. K. Becker, "Automatic Expert System Rule Generation on Nondestructive Waste Assay Data at the Idaho National Engineering and Environmental Laboratory," *Journal of Evolutionary Computation* (submitted).

F. Noo, R. Clack, T. J. Roney, and T. A. White, "The Dual-Ellipse Cross Vertex Path For Exact Reconstruction Of Long Objects In Cone-Beam Tomography," *Phys. Med. Biol.* 43, 1998, 797–810.

F. Noo, R. Clackdoyle, C. Mennessier, T. A. White, and T. J. Roney, "Analytic Method Based On Identification Of Ellipse Parameters For Scanner Calibration In Cone-Beam Tomography," *Phys. Med. Biol.*, Accepted for publication August, 2000.

## Nondestructive Assay

R. J. Gehrke, L. V. East, Y. D. Harker, "Information in Spectra from $^{241}$Am as from TRU Waste," *Waste Management 20* (2000) pg. 555-559.

## Nuclear Structure Research

R.G. Helmer, R.J. Gehrke, J.R. Davidson, J.W. Mandler, "Scientists, Spectrometry, and $\gamma$-Ray Spectrum Catalogues 1957-2007," *Journal of Radioanalytical and Nuclear Chemistry* 243 (2000) 109.

M.A. Ludington and R.G. Helmer, "High-Accuracy Measurements and Monte Carlo Calculations of the Relative Efficiency Curve of an HPGE Detector from 433 to 2754 keV," *Nuclear Instruments and Methods in Physics Research A* 446 (2000) 506.

R.J. Gehrke, L.V. East, and Y.D. Harker, "Information in Spectra from Sources Containing "Aged" $^{241}$Am as from TRU Waste," accepted for publication in *Waste Management*.

R.J. Gehrke, "Artifact (alpha,n) Reaction Gamma-ray peaks as $^{241}$Am Decay Gamma Rays," accepted for publication in the *Journal of Radioanalytical and Nuclear Chemistry*.

R.J. Gehrke, J.R. Davidson, P.J. Taylor, R. Helmer, and J.W. Mandler, "Radioactinide Additions to the Electronic Gamma-ray Spectrum Catalogue," accepted for publication in the *Journal of Radioanalytical and Nuclear Chemistry*.

S.P. LaMont, R.J. Gehrke, S.E. Glover, and R.H. Filby, "Precise Determination of the Intensity of $^{226}$Ra Alpha Decay to the 186-keV Excited State," accepted for publication in the *Journal of Radioanalytical and Nuclear Chemistry*.

R. Arnold, C. Augier, J. Baker, A. Barbash, D. Blum, V. Brudanin, A.J. Caffrey, J.E. Campagne, E. Caurier, D. Dassie, V. Egorov, T. Filipova, R. Gurriaran, J.L. Guyonnet, F. Hubert, Ph. Hubert, S. Jullian, O. Kochetov, I. Kisel, V.N. Kornouknov, V. Kovalenko, D. Lalanne, F. Laplanche, F. Leccia, I. Linck, C. Longuemare, Ch. Marquet, F. Mauger, H.W. Nicholson, I. Pilugin, F. Piquemal, J-L. Reyss, X. Sarazin, F. Scheibling, J. Suhonen, C.S. Sutton, G. Szklarz, V. Timkin, R. Torres, V.I. Tretyak, V. Umatov, I. Vanyushin, A. Vareille, Yu, Vasilyev, and Ts. Vylov, "Testing The Pauli Exclusion Principle With The NEMO-2 Detector," *Eur. Phys. J.A*, 6 (1999) 361.

R. Arnold, C. Augier, J. Baker, A. Barbash, D. Blum, V. Brudani, A.J. Caffrey, J.E. Campagne, E. Caurier, D. Dassie, V. Egorov, T. Filpova, R. Gurriaran, J.L. Guyonnet, F. Hubert, Ph. Hubert, S. Julian, I. Kisel, O. Kochetov, V.N. Kornoukhov, V. Kovalenko, D. Lalanne, F. Laplanche, F. Leccia, I. Linck, C. Longuemare, Ch. Marquet, F. Mauger, H.W. Nicholson, I. Pilugin, F. Piquemal, J-L. Reyss, X. Sarazin, F. Scheibling, J. Suhonen, C.S. Sutton, G. Szklarz, V. Timkin, R. Torres, V.I. Tretyak, V. Umatov, I. Vanyushin, A. Vareille, Yu. Vasilyev and Ts. Vylov, "Double Beta Decay Of $^{96}$Zr," *Nuclear Physics A* 658, 299 (1999).

R. Arnold, C. Augier, J. Baker, A. Barbash, D. Blum, V. Brudanin, A.J. Caffrey, J.E. Campagne, E. Caurier, D. Dassie, V. Egorov, T. filipova, R. Gurriaran, J.L. guyonnet, F. Hubert, Ph. Hubert, S. Jullian, I. Kisel, O. Kochetov, V.N. Kornoukhov, V. Kovalenko, D. Lalanne, F. Laplanche, F. leccia, I. Linck, C. Longuemare, ch. Marquet, F. Mauger, H.W. Nicholson, I. Pilugin, F. Piquemal, J-L. reyss, X. Sarazin, F. Scheibling, J. Suhonen, C.S. sutton, G. Szklarz, V. Timkin, R. torres, V.I. Tretyak, V. Umatov, I. Vanyushin, A. Vareille, Yu. Vasilyev, and Ts. Vylov, "Limits On Different Majoron Decay Modes Of $^{100}$Mo, $^{116}$Cd, $^{82}$Se and $^{96}$Zr For Neutrinoless Double Beta Decays In The NEMO-2 Experiment," submitted for publication in *Nuclear Instruments and Methods A*.

R. Arnold, C. Augier, J. Baker, A. Barbash, D. Blum, V. Brudanin, A.J. Caffrey, J.E. Campagne, E. Caurier, D. Dassie, V. Egorov, T. filipova, R. Gurriaran, J.L. guyonnet, F. Hubert, Ph. Hubert, S. Jullian, I. Kisel, O. Kochetov, V.N. Kornoukhov, V. Kovalenko, D. Lalanne, F. Laplanche, F. leccia, I. Linck, C. Longuemare, ch. Marquet, F. Mauger, H.W. Nicholson, I. Pilugin, F. Piquemal, J-L. reyss, X. Sarazin, F. Scheibling, J. Suhonen, C.S. sutton, G. Szklarz, V. Timkin, R. torres, V.I. Tretyak, V. Umatov, I. Vanyushin, A. Vareille, Yu. Vasilyev, and Ts. Vylov, "Influence Of Neutrons And Gamma Rays In The Frejus Underground Laboratory," submitted for publication in *Nuclear Instruments and Methods A*.

# Presentations

### Biochemical and Geochemical Reactions on Environmental Surfaces

Redden, G. D. and J. A. Davis (1999). "Surface Complexation Models In Solute Transport: Issues Of Practicality And Applicability For Transport Modeling." *Materials Research Society National Meeting, Boston, MA*, Materials Research Society.

Redden, G. D. and R. A. Laviolette (2000). "Evaluation Of The Mass Action Expression Coefficients For Multidentate Complexation On Mineral Surfaces." *ACS Washington National Meeting, Washington D.C.*, American Chemical Society.

Hull, L., G. Redden, et al. (1999). "Adsorption Parameters For Radioactive Liquid Waste Migration." *Materials Research Society National Meeting, Boston, MA*, Materials Research Society.

### Reactive Transport in Variably Saturated Heterogeneous Media

Hull, L. C., M. N. Pace, and G. D. Redden, "Adsorption Parameters for Radioactive Liquid-Waste Migration," *Materials Research Society Fall Meeting, Symposium on Scientific Basis for Nuclear Waste Management, Boston, MA, December 1999*.

Johnson, R. W., "Development of a B-Spline Collocation Method for CFD," accepted to be presented at *ASME Fluids Engineering Division Summer Meeting, May 29-June 1, 2001, New Orleans, LA*.

Mattson E.D., and J.B. Sisson, "Vadose Zone Characterization Equipment Development At The INEEL", *Advanced Vadose Zone Characterization Workshop, Hanford, WA., Jan 19-20, 2000.*

Mattson E.D., R. Jacobson, and G. Matthern, "Sensing the Vadose Zone: A CenSSIS Perspective, Problem Overview", *Sensing the Vadose Zone: A CenSSIS Perspective Workshop, Boston University Photonics Center, Boston, MA, Feb 16, 2000*.

Mattson, E.D., “Laboratory to Field: Application of Meso-scale Experiments”, *INEEL Meso-scale Subsurface Research Workshop, Salt Lake City, May 8-9, 2000.*

Sisson, J. B., A.L. Schafer, and J.M. Hubbell, “Vadose Zone Monitoring System for Site Characterization and Transport Modeling” *Materials Research Society Fall Meeting, Symposium on Scientific Basis for Nuclear Waste Management, Boston, MA, December 1999.*

Sisson, J.B., A. L. Schafer, J.M. Hubbell, “Water Content and Water Potential in Deep Vadose Zones,” *Soil Science Society of America 91st Annual Meeting, Salt Lake City, UT, Oct 31-Nov 4, 1999*

### Transport Phenomena in Geologic Porous Media

Kauffman, M.E., Holman, H.-Y., Lehman, R.M., Martin, M.C., McKinney, W.R. 2000. “Investigation Into The Biochemistry Of Bacterial Attachment Using Synchrotron Radiation-Based Fourier Transform Infrared Microscopy.” *Society of Applied Spectroscopy, Snake River Section Fifth Biennial Summer Meeting, Sun Valley, ID, August, 2000.* (Recipient of the Ray Woodriff Student Presentation Award)

O’Connell, S.P., Watwood, M.E., Lehman, R.M., Colwell, F.S. 2000. “Optimized Recovery Of Microbial Community DNA From Groundwater.” Abstract, *Intermountain Branch Meeting of the American Society for Microbiology, Provo, UT, April, 2000.* (Recipient of Student Presentation Award, Environmental Microbiology Section)

Ingram, J.C., Colwell, F.S., Lehman, R.M., Bauer, W.F., Shaw, A. 2000. “Interrogation Of Intact Microorganisms By Static Secondary Ion Mass Spectrometry.” Abstract, *American Society for Mass Spectrometry, 2000.*

Kauffman, M.E., Holman, H.-Y., Lehman, R.M., Martin, M.C., McKinney, W.R. 1999. “Application Of Synchrotron Radiation-Based Fourier Transform Infrared Spectromicroscopy To The Investigation Of Bacterial Attachment To Aluminum And To Mineralogically-Heterogeneous Geologic Substrata.” Abstract, *Advanced Light Source Users Conference, Berkeley, CA, Oct., 1999.*

Kauffman, M.E., Holman, H.-Y., Lehman, R.M., Martin, M.C., McKinney, W.R. 1999. “Investigation Of Bacterial Attachment To Distinct Mineral Phases Within Heterogeneous Geologic Substratum Using Synchrotron Radiation-Based Fourier Transform Spectromicroscopy.” Abstract, *Fall Meeting of the American Geophysical Union, SF, CA, Dec., 1999.*

Garland, J.L. and Lehman, R.M. 1999. “Dilution/Extinction Of Community Phenotypic Characters To Estimate Relative Bacterial Species Diversity In Mixed Communities.” Abstract, *ASM Conference on Microbial Biodiversity, Chicago, IL, Aug., 1999.*

O’Connell, S.P., Colwell, F.S., Lehman, R.M., and Watwood, M.E. “Groundwater Microbial Species Diversity As Affected By Trichloroethylene In Microcosm Experiments.” Abstract, *ASM Conference on Microbial Biodiversity, Chicago, IL, Aug., 1999.*

Wilson, M.S., Lehman, R.M. and Colwell, F.S. 1999. “Comparison Of Culture- And Non-Culture- Based Methods For Measuring Abundance Of Methanotrophic Bacteria In A Deep Basalt Aquifer.” Abstract, *International Symposium on Subsurface Microbiology - 1999, Vail, CO, Aug., 1999.*

Lehman, R.M., Bala, G.A., Robertson, E.P., and Colwell, F.S. 1998. "Bacterial Partitioning Between Mobile And Immobile Phases In Saturated Basalt." Abstract, *Eighth International Symposium on Microbial Ecology, Halifax, Canada, Aug., 1998.*

Lee, B. D., Walton, M. R., Doherty, J. L. and Apel, W. A. "Biologically Mediated Mobilization of Uranium Adsorbed to Iron Oxide Coated Sand." *219th American Chemical Society National Meeting. San Francisco, CA. March 26-30, 2000.*

Hubbell, J.M. and J. B. Sisson, "Variability of Water Potential in Deep Vadose Zones at Arid and Humid Sites," *November 1, 1999, 91st Annual Meeting, Soil Science Society of America, Soil Water Flux and Potential, Division S-1, Soil Physics, Salt Lake City, UT, SSSA*

Sisson, J.B, A.N. Schafer and J.M Hubbell, "Vadose Zone Monitoring system for Site Characterization and Transport Modeling," *Material Research Society Conference, Boston, November 30, 1999.*

J. M. Hubbell, "Installation and Operation of the Advanced Tensiometer and Cone Penetrometer Tensiometer, The Path Forward for RWMC Operable Units 7-10 & 7-13/14," *Meeting of Region 10 Environmental Protection Agency, DOE-ID, and Idaho State Department of Environmental Quality, Idaho Falls, ID., April 6, 1999.*

"Advanced Tensiometer and Cone Penetrometer Tensiometer" displayed on Capitol Hill on April 10, 2000 in the DOE Science and Technology Complex-Wide Exhibit, Washington D.C.

"Advanced Tensiometer", April 25-27, 2000, displayed as part of the INEEL Technology Deployment Center's exhibit at the Environmental Management Science Program National Workshop in Atlanta, GA.

### Selective Mass Transport in Polymers

M. K. Harrup, F. F. Stewart, "Inorganic Membrane Research at the INEEL," *Session T1038-Posters-Interactive Networking in Separations, Annual AICHE Meeting, Dallas, TX., November 1999,* invited.

F.F. Stewart, T.A. Luther, M.K. Harrup, R.P. Lash, "A Novel Synthesis of Polyesters Containing Hexa-(tert-butylhydroquinone)cyclotriphosphazene," *Division of Polymer Chemistry, Symposium on Hybrid Organic and Inorganic Materials, 219th National Meeting of the American Chemical Society, San Francisco, CA, March 2000, POLY 303.*

F.F. Stewart, M.K. Harrup, T.A. Luther, C.J. Orme, D.H. Weinkauf, "Pervaporation of Water-Alcohol Mixtures using Chemically Modified Phosphazene Polymers," *Symposium on Gas/Vapor Separations and Pervaporation (Paper 11), 11th North American Membrane Society Meeting, Boulder, CO, May 2000.*

F.F. Stewart, M.K. Harrup, T.A. Luther, C.J. Orme, "Polyphosphazene Membrane Separations at the INEEL," *Joint 55th Northwest/16th Rocky Mountain Regional Meeting of the American Chemical Society, Idaho Falls, ID, June 2000, Paper 095.*

K. S. Houston, D. H. Weinkauf, F.F. Stewart , "Plasma Treatment of Rubbery Membrane Materials for Gas Separations," *11th Annual Rio Grande Regional Symposium on Advanced Materials, Albuquerque, NM, October 1999.*

K. S. Houston, D. H. Weinkauf, F.F. Stewart, "Plasma Treatment of Rubbery Membrane Materials for Gas Separations," *11th North American Membrane Society Meeting, Boulder, CO, May 2000.*

C. J. Orme, F. F. Stewart, M. L. Stone, "Gas Transport Properties of a Series of Tri-Substituted Phosphazene Polymers," *Joint 55th Northwest/16th Rocky Mountain Regional Meeting of the American Chemical Society, Idaho Falls, ID, June 2000, paper 047.*

M.K. Harrup and F.F. Stewart, "Inorganic Membrane Research at the INEEL," *Joint 55th Northwest/16th Rocky Mountain Regional Meeting of the American Chemical Society, Idaho Falls, ID, June 2000, paper 060.*

T.A. Luther, M.K. Harrup, F.F. Stewart, "$^{1}$H, $^{13}$C, $^{15}$N, and $^{31}$P NMR Spectroscopic Study of Isotopic $^{15}$N Labeled Polyphosphazenes," *Joint 55th Northwest/16th Rocky Mountain Regional Meeting of the American Chemical Society, Idaho Falls, ID, June 2000, paper 145.*

### Pore Size and Morphology Control for Solid and Polymer Matrices

Harrup, M. K.; Stewart, F. F. "Inorganic Membrane Research at the INEEL" *AIChE Fall National Meeting; November 1999.*

Harrup, M. K.; Wertsching, A. K.; Stewart, F. F. "Phosphazene Silicate Nanocomposites. A Survey of Materials Properties and Synthetic Methods Using New Catalysts." *219th National Meeting of the American Chemical Society; March 2000.*

Harrup, M. K.; Stewart, F. F. "Inorganic Membrane Research at the INEEL" *55th Northwest Regional Meeting of the American Chemical Society; June 2000.*

Lash, R. P.; Harrup, M. K.; Wagner, S. M.; "Investigation of Poly(Dichlorophosphazenes) Using Dilute Solution Characterization Techniques" *55th Northwest Regional Meeting of the American Chemical Society; June 2000.*

Wey, J. E.; Harrup, M. K.; "Purification of a Phosphazene Polymer Using a Lower Critical Solubility Temperature Approach" *55th Northwest Regional Meeting of the American Chemical Society; June 2000.*

Wertsching, A. K.; Harrup, M. K.; "Phosphazene Silicate Nanocomposites. New Experimental Protocols." *55th Northwest Regional Meeting of the American Chemical Society; June 2000.*

Luther, T. A.; Harrup, M. K.; Stewart, F. F.; "$^{1}$H, $^{13}$C, $^{15}$N, and $^{31}$P NMR Spectroscopic Study of Isotropic 15N Labeled Polyphosphazenes" *55th Northwest Regional Meeting of the American Chemical Society; June 2000.*

### Adsorption and Absorption Materials for Molecular Separations

P.J. Martellaro, G.A. Moore, A.E. Gorenbain, E.H. Abbott and E.S. Peterson, "Environmental Application of Mineral Sulfides for the Removal of Gas Phase Hg(0) and Aqueous $Hg^{2+}$. *11th Symposium on Separation Science and Technology, Gatlinburg, TN Oct 18-21, 1999.*

P.J. Martellaro, G.A. Moore and E.S. Peterson, "Mercury Sorption Characteristics of Nanoscale Metal Sulfides," *Poster Presentation at Access in Nanoporous Materials II, Banff, Canada May 25-28,2000.*

P.J. Martellaro, G.A. Moore and E.S Peterson, "Metal Sulfides as Sorbents for Elemental and Ionic Mercury." *ACS Northwest Regional Meeting, Idaho Falls, ID June, 15 2000.*

## Computational Simulation

G. D. Redden and R. A. LaViolette, "Evaluation of the Mass Action Expression Coefficients for Multidentate Complexation on Mineral Surfaces", *220th Meeting of the American Chemical Society, Washington D.C., 20-24 August 2000.*

R. A. LaViolette and M. T. Benson, "Clusters and Solids of 48-Atom Octahedral Molecules", *West Coast Theoretical Chemistry Conference, Salt Lake City UT, 26-28 June 2000.*

R. A. LaViolette and M. T. Benson, "Clusters and Solids of 48-atom octahedral molecules", *Joint Northwest-Rocky Mountain Regional Meeting of the American Chemical Society, Idaho Falls ID, 15-17 June 2000.*

R. A. LaViolette, "Do Dynamical Systems Follow Benford's Law?" *83rd Statistical Mechanics Meeting, Rutgers University, Piscataway NJ, 7-9 May 2000.*

R. A. LaViolette and D. L. Stoner, "Spatial Disorder And Degradation Kinetics In Intrinsic Biodegradation Schemes", *219th Meeting of the American Chemical Society, San Francisco CA, 19-24 March 2000.*

This is in addition to the following talks presented previously at national meetings or university seminars under this project:

M. M. Rashid and R. Roy, "Experimental Comparison and Model Assessment for a Novel Approach to Inelastic Fracture", *5th U. S. National Congress on Computational Mechanics, U. of Colorado, Boulder, CO, 4-6 Aug, 1999.*

J. L. Budzien, J. D. McCoy, J. G. Curro, and R. A. LaViolette, "A Simple Relation for the Solubility of Gases in Polymers", *Centennial Meeting of the American Physical Society, Atlanta GA, 20-26 Mar. 1999.*

R. A. LaViolette, "Spatial Disorder & Degradation Kinetics In Soil Restoration", *Physical Chemistry Seminar, University Of Oregon, Eugene OR, 15 Feb. 1999.*

R. A. LaViolette, "Spatial Disorder & Degradation Kinetics In Soil Restoration", *Physical Chemistry Seminar, University Of Cincinnati, Cincinnati OH, 21 Jan. 1999.*

C. R. Tolle, and R. W. Gundersen, "Searching for Determinism in Erratic Signals: Fuzzy Time-Based Clustering of Delay Vectors", *ANNIE '98, St. Louis MO, 1-4 Nov. 1998.*

## Corrosion and Aging

P.J. Pinhero, C.S. Watkins, "Imaging Microbiologically-Influenced Pitting Corrosion of Spent Nuclear Fuel Cladding Material with a Scanning Reference Electrode Technique (SRET)", *MRS1999 Symposium QQ18: Microbial Processes in Waste Management, December 1, 1999, Boston, MA.*

P.J. Pinhero, "Microbial-Assisted Corrosion of Spent Nuclear Fuel Cladding Materials", *Northwest & Rocky Mountain Joint Regional Meeting of the American Chemical Society, June 15-17, 2000, Idaho Falls, ID.* (Invited)

C.R. Breckenridge, T.E. Lister, and P.J. Pinhero, "Microscopic Characterization of Drying Effects in a Biofilm on Spent Nuclear Fuel Cladding Materials", *Northwest & Rocky Mountain Joint Regional Meeting of the American Chemical Society, June 15-17, 2000, Idaho Falls, ID.*

C.S. Watkins, M.N. Tsang, and P.J. Pinhero, "The Modification and Application of a Coupled-Cell Technique in the Study of Microbiologically Influenced Corrosion", *Northwest & Rocky Mountain Joint Regional Meeting of the American Chemical Society, June 15-17, 2000, Idaho Falls, ID.*

D.F. Bruhn and P.J. Pinhero, "UV and $\gamma$-Radiation Resistance of Microbes Isolated from INEEL SNF Pools", *Northwest & Rocky Mountain Joint Regional Meeting of the American Chemical Society, June 15-17, 2000, Idaho Falls, ID.*

C.R. Breckenridge, T.E. Lister, and P.J. Pinhero, "Microscopic Characterization of Microbe Morphologies in Natural Environments", *American Society for Microbiology Biofilms 2000, July 16-20, 2000, Big Sky, MT.*

C.S. Watkins and P.J. Pinhero, "Using a Scanning Reference Electrode Technique (SRET) to Image Microbiologically-Influenced Pitting Corrosion of Spent Nuclear Fuel Cladding Material", *American Society for Microbiology Biofilms 2000, July 16-20, 2000, Big Sky, MT.*

D.F. Bruhn, C.R. Breckenridge, M.N. Tsang, C.S. Watkins, W.E. Windes, F.F. Roberto, R.N. Wright, and P.J. Pinhero, "Gamma and UV Irradiation of Microbes from INEEL SNF Storage Pools", *American Society for Microbiology Biofilms 2000, July 16-20, 2000, Big Sky, MT.*

P.J. Pinhero, "Investigations into the Microbial-Influenced Corrosion of Spent Nuclear Fuel Cladding Materials", *GRC-Aqueous Corrosion, July 22-28, 2000, New London, NH.* (Invited).

## Adaptive Sensors

K. L. Telschow and R. S. Schley, "'Containerless' Photoacoustic Spectroscopy using Photorefractive Interferometry," *Photonics East conference, Advanced Environmental and Chemical Sensing Technology (ES09) session, 5-8 November, 2000, Boston, MA*

Dale McMorrow, Napoleon Thantu, Valeria Kleiman, Joseph S. Melinger and William T. Lotshaw, "Analysis of Intermolecular Coordinate Contributions to Third-Order Nonlinear-Optical Response of Liquids with a Quantum Harmonic-Oscillator Model," *August 6-10, 2000, Kauai-Lihue, HI.*

Napoleon Thantu, "Time-Resolved Optical Heterodyne Detected Raman Induced Kerr Effect Spectroscopy for Chemical Analysis," *Laser Applications to Chemical and Environmental Analysis, February 11-13, 2000, Santa Fe, NM.*

## Integrated Instruments for In Situ Chemical Measurements

Mark L. Stone, Linda A. Polson, and Garold L. Gresham, "Analysis of Chlorocarbon Transport Through Polymeric Membranes Using Membrane Introduction Mass Spectrometry," *Northwest Regional American Chemical Society Meeting, Idaho Falls, ID, June 15, 2000.*

Linda A. Polson, Mark L. Stone, and Garold L. Gresham, "Characterization of Phosphazene Materials as Membranes in Membrane Introduction Mass Spectrometry (MIMS)," *poster (070) at the 2000 Northwest and Rocky Mountain Joint Regional Meeting, Idaho Falls, ID, June 15-17, 2000.*

Linda Polson, Mark Stone, and Gary Gresham, "Membrane Introduction Mass Spectroscopy (MIMS): An Overview of System Components and Variables," *National American Chemical Society Meeting, Washington, D.C., August 22, 2000.*

## Intelligent Nonintrusive Methods for Characterization

J.C. Determan , G.K. Becker, S. D. Matthews, "Expert System Technology for Nondestructive Waste Assay Data Review," *Proceedings of SPECTRUM 2000, Chattanooga, TN, September 24-28, 2000.*

J.C. Determan , G.K. Becker, "A Prototype Generic Expert System Architecture for Data Review and Validation," *Seventh Nondestructive Assay Waste Characterization Conference, Salt Lake City, Utah, May 23-25, 2000.*

J.C. Determan, J.A. Foster, "Using Chaos in Genetic Algorithms." *Proceedings of the 1999 Congress on Evolutionary Computation, Vol. 3, 2094-2101. Piscataway, New Jersey: IEEE Press.*

J.C. Determan, G.K. Becker, "Expert Systems and Case-Based Reasoning for Learning Nondestructive Assay Data Review," *Sixth Nondestructive Assay and Nondestructive Examination Waste Characterization Conference, Salt Lake City, Utah, November 17-19, 1998.*

J.C. Determan, G.K. Becker, "Expert System Technology for Nondestructive Waste Assay," *Tenth Conference on Innovative Applications of Artificial Intelligence, Madison, Wisconsin, July 26-30, 1998.*

G.K. Becker, J.C. Determan, "Expert System Technology for Nondestructive Waste Assay," *39th Annual Meeting of the Institute of Nuclear Materials Management, Naples, Florida, July 26-30, 1998.*

J. T. Johnson, D. C. Kunerth, C. R. Tolle, and L. G. Allred, "Neural Network Processing of Pulsed Eddy Current Responses," A*SNT 1999 Fall Conference, Phoenix, AZ Oct. 11-15, 1999.*

D. C. Kunerth, C. R. Tolle, J. T. Johnson, and L. G. Allred, "Neural Network Processing of Pulsed Eddy Current Responses," *WANTO Meeting, Sandia National Laboratory, Albuquerque, NM, Feb 22-26, 1999.*

F. Noo, R. Clackdoyle, T. A. White, and T. J Roney, "Image Reconstruction From Misaligned Truncated Helical Cone-Beam Data," *1999 IEEE Nuclear Science Symposium and Medical Imaging Conference, Seattle, WA, October 1999.*

T. A. White, T. J. Roney, R. J. Pink, M. Smith, R. Clackdoyle, and F. Noo, "Comparison Of Fan- And Cone-Beam Imaging Capabilities On A Portable X-Ray Imaging System," *SPIE 44th Annual Meeting, Denver, CO, July 1999.*

T. J. Roney, T. A. White, R. J. Pink, and M. Smith, “Field-Portable Gamma Ray and X-Ray Inspection Systems,” *37th Weapons Agency Nondestructive Testing Organization (WANTO) Meeting, Sandia National Laboratories, Albuquerque, NM, Feb 22–26, 1999.*

F. Noo, T. A. White, R. Clackdoyle, and T. J Roney, “Estimation of Geometrical Parameters in Spiral CT,” *2000 IEEE Nuclear Science Symposium and Medical Imaging Conference, Lyon, France, Oct 2000.*

## Nondestructive Assay

J. D. Cole, M. W. Drigert, R. Aryaeinejad, E. L. Reber, J. K. Jewell, J. H. Hamilton, A. V. Ramayya, C. J. Beyer, G. M. Teer-Akopian, T. Y. Organessian, G. S. Popeko, A. V. Daniel, “Using New Fission Data with the Multi-Detector Analysis System for Spent Nuclear Fuel,” *Proc. of the International Conference Perspectives in Nuclear Physics*, J. H. Hamilton, H. K. Carter, R. B. Piercey, eds., World Scientific Publishing Co. River Edge, NJ, 1999, p. 35.

J. W. Mandler, R. Gardner, “Application of PGNAA to Ore Mining and Processing,” *4th Topical Meeting on Industrial Radiation and Radioisotope Measurement Applications (IRRMA), October 3-7,1999, Raleigh, NC.*

J. K. Jewell, E. L. Reber, and non-INEEL collaborators, “$^{5}$He Ternary Spontaneous Fission Yields from $^{252}$Cf and $^{235}$U,” *Proceedings of the American Physical Society, Division of Nuclear Physics meeting, Asilomar, California, October 14-17, 1999.*

J. K. Jewell, E. L. Reber, and non-INEEL collaborators, “Ternary Spontaneous Fission of $^{252}$Cf,” *Proceedings of the American Physical Society, Division of Nuclear Physics meeting, Asilomar, California, October 14-17, 1999.*

J. K. Jewell, E. L. Reber, and non-INEEL collaborators, “Prompt Gamma-Ray Coincidences from $^{235}$U Induced Fission,” *Proceedings of the American Physical Society, Division of Nuclear Physics meeting, Asilomar, California, October 14-17, 1999.*

J. K. Jewell, E. L. Reber, and non-INEEL collaborators, “Neutron and Gamma-Ray Detectors for the Multi-Detector Analysis System,” *Proceedings of the American Physical Society, Division of Nuclear Physics meeting, Asilomar, California, October 14-17, 1999.*

J. D. Cole, “The Use of Large Arrays of HPGe Detectors and the Study of Fission”, *Transactions of the American Nuclear Society 1999 Winter Meeting, Long Beach, CA, November 14 –18, 1999*, Vol. 81, pages 112-113.

R. P. Gardner, W. A. Metsally, E. S. El Sayyed, C. W. Mayo, J. W. Mandler, R. J. Gehrke, “Preliminary Feasibility Studies of the Absolute Determination of Elemental Amounts in Small Samples in Thermal Neutron Beams by Coincidence PGNAA,” *Proceedings of the Fifth International Conference on Methods and Applications of Radioanalytical Chemistry, Kailua-Kona, Hawaii, April 9 – 14, 2000.*

E. L. Reber, J. D. Cole, R. Aryaeinejad, M. W. Drigert, J. K. Jewell, “Multi-Detector Analysis System,” *Proceedings of the 7th Nondestructive Assay Waste Characterization Conference, Salt Lake City UT, May 22-26,2000,* INEEL/EXT-2000-0002.

Y. Harker, W. Y. Yoon, G. W. Twedell, C. V. McIsaac, "Absolute Gamma-Ray Assay of Transuranic Waste Containers using the Passive Gamma-Ray Technique and an Analytical Method of Container-Specific Efficiency Curve Generation," *Proceedings of the 7th Nondestructive Assay Waste Characterization Conference, Salt Lake City UT, May 22-26,2000,* INEEL/EXT-2000-0002.

R. J. Gehrke, J. K. Hartwell, C. A McGrath, E. W. Killian, Y. D. Harker, G. W. Twedell, D. M. May, L. V. East, C. V. McIsaac, "Peeling the Onion? The Gamma-Ray Spectrometry of Transuranic Waste," *Proceedings of the 7th Nondestructive Assay Waste Characterization Conference, Salt Lake City UT, May 22-26,2000,* INEEL/EXT-2000-0002.

Y. D. Harker, E. W. Killian, C. V. McIsaac, "Generating Counting Efficiency Curves for the SWEPP Gamma-Ray Spectrometer from Experimental Counting Efficiency Data using a Transform Technique," *Proceedings of the 7th Nondestructive Assay Waste Characterization Conference, Salt Lake City UT, May 22-26,2000,* INEEL/EXT-2000-0002.

J. D. Cole, E. L. Reber, R. Aryaeinejad, M. W. Drigert, J. K. Jewell, "Non-Destructive Analysis using the Multi-Detector Analysis System", *Transactions of the American Nuclear Society 2000 Annual Meeting,, San Diego, CA, June 4 –8, 2000.*

### Nuclear Structure Research

R.G. Helmer and C. van der Leun, "Recommended Standards for Gamma-ray Energy Calibration," *Tenth International Symposium on Capture Gamma-Ray Spectroscopy and Related Topics, Santa Fe, NM, August 30 – September 3, 1999*, invited presentation

R.J. Gehrke, J.K. Hartwell, C.A. McGrath, E.W. Killian, Y.D. Harker, G.W. Twedell, D.M. May, L.V. East, and C.V. McIsaac, "Peeling the Onion: The Gamma-ray Spectrometry of TRU Waste," *7th NDA Waste Characterization Conference, Salt Lake City, UT, May 23-25, 2000.*

R.J. Gehrke, J.R. Davidson, P.J. Taylor, R. Helmer, and J.W. Mandler, "Radioactinide Additions to the Electronic Gamma-ray Spectrum Catalogue," *Fifth International Conference on Methods and Applications of Radioanalytical Chemistry (MARC-V Conference), April, 2000.*

S.P. LaMont, R.J. Gehrke, S.E. Glover, and R.H. Filby, "Precise Determination of the Intensity of $^{226}$Ra Alpha Decay to the 186-keV Excited State," *Fifth International Conference on Methods and Applications of Radioanalytical Chemistry (MARC-V Conference), April, 2000.*

J.D. Baker and K. , "Mo Purification for the NEMO-3 Experiment," *Northwest Regional American Physical Society meeting, Eugene, Oregon, May, 2000.*

R.J. Gehrke, "The Role of the INEEL in Ionizing Radiation Measurements and Standards," *Idaho State University, College of Engineering Graduate Seminar Series, Pocatello, Idaho, September 10, 1999.*

S. Jullian and D. Lalanne, "NEMO-3 Experiment," *Idaho State University, Pocatello, Idaho, March, 2000.*

S. Sutton and J.D. Baker, "NEMO-3 and Molybdenum Purification," *Carolina Symposium on Neutrino Physics, University of South Carolina, Columbia, South Carolina, March, 2000.*

S. Sutton and J.D. Baker, “NEMO-3 and Molybdenum Purification,” *Idaho State University, Pocatello, Idaho, March, 2000.*

R.J. Gehrke, J.K. Hartwell, R.G. Helmer, B.D. Harlow, “ISOCS Results for Test Geometries,” *1999 Canberra Users’ Meeting, Boulder, CO, May 24-28, 1999.*